frontiers | Research Topics

Computational methods in cardiac electrophysiology

Edited by
Matthijs Cluitmans, Richard David Walton and Gernot Plank

Published in
Frontiers in Physiology

ISSN 1664-8714
ISBN 978-2-8325-2925-6
DOI 10.3389/978-2-8325-2925-6

About Frontiers

Frontiers is more than just an open access publisher of scholarly articles: it is a pioneering approach to the world of academia, radically improving the way scholarly research is managed. The grand vision of Frontiers is a world where all people have an equal opportunity to seek, share and generate knowledge. Frontiers provides immediate and permanent online open access to all its publications, but this alone is not enough to realize our grand goals.

Frontiers journal series

The Frontiers journal series is a multi-tier and interdisciplinary set of open-access, online journals, promising a paradigm shift from the current review, selection and dissemination processes in academic publishing. All Frontiers journals are driven by researchers for researchers; therefore, they constitute a service to the scholarly community. At the same time, the *Frontiers journal series* operates on a revolutionary invention, the tiered publishing system, initially addressing specific communities of scholars, and gradually climbing up to broader public understanding, thus serving the interests of the lay society, too.

Dedication to quality

Each Frontiers article is a landmark of the highest quality, thanks to genuinely collaborative interactions between authors and review editors, who include some of the world's best academicians. Research must be certified by peers before entering a stream of knowledge that may eventually reach the public - and shape society; therefore, Frontiers only applies the most rigorous and unbiased reviews. Frontiers revolutionizes research publishing by freely delivering the most outstanding research, evaluated with no bias from both the academic and social point of view. By applying the most advanced information technologies, Frontiers is catapulting scholarly publishing into a new generation.

What are Frontiers Research Topics?

Frontiers Research Topics are very popular trademarks of the *Frontiers journals series*: they are collections of at least ten articles, all centered on a particular subject. With their unique mix of varied contributions from Original Research to Review Articles, Frontiers Research Topics unify the most influential researchers, the latest key findings and historical advances in a hot research area.

Find out more on how to host your own Frontiers Research Topic or contribute to one as an author by contacting the Frontiers editorial office: frontiersin.org/about/contact

Computational methods in cardiac electrophysiology

Topic editors
Matthijs Cluitmans — Maastricht University, Netherlands
Richard David Walton — Université de Bordeaux, France
Gernot Plank — Medical University of Graz, Austria

Citation
Cluitmans, M., Walton, R. D., Plank, G., eds. (2023). *Computational methods in cardiac electrophysiology*. Lausanne: Frontiers Media SA.
doi: 10.3389/978-2-8325-2925-6

The authors declare that the research was conducted in the absence of any commercial or financial relationships that could be construed as a potential conflict of interest.

Table of contents

frontiers | Frontiers in Physiology

TYPE Editorial
PUBLISHED 21 June 2023
DOI 10.3389/fphys.2023.1231342

OPEN ACCESS

EDITED AND REVIEWED BY
Ruben Coronel,
University of Amsterdam, Netherlands

*CORRESPONDENCE
Matthijs Cluitmans,
m.cluitmans@maastrichtuniversity.nl

RECEIVED 30 May 2023
ACCEPTED 12 June 2023
PUBLISHED 21 June 2023

CITATION
Cluitmans M, Walton R and Plank G (2023), Editorial: Computational methods in cardiac electrophysiology.
Front. Physiol. 14:1231342.
doi: 10.3389/fphys.2023.1231342

Editorial: Computational methods in cardiac electrophysiology

Matthijs Cluitmans[1]*, Richard Walton[2] and Gernot Plank[3]

[1]Department of Cardiology, Cardiovascular Research Institute Maastricht, Maastricht University, Maastricht, Netherlands, [2]INSERM Institut de Rythmologie et Modélisation Cardiaque (IHU-Liryc), Pessac, Aquitaine, France, [3]Gottfried Schatz Research Center for Cellular Signaling, Metabolism and Aging, Medical University of Graz, Graz, Styria, Austria

KEYWORDS

electrophysiolgy, arrhythmias (cardiac), technology, digital twin, personalized medicine, signal processing, methodology

Editorial on the Research Topic
Computational methods in cardiac electrophysiology

Introduction

Cardiac electrophysiology research increasingly relies on computational methods to connect experimental and clinical observations to understand underlying mechanisms. These methods process experimental data, such as optical mapping and body-surface potential mapping, and model biophysical processes, such as the behavior of electrical sources within the heart and the electrical potential fields linked to these. Signal processing from experiments and clinical recordings helps elucidate electrophysiological properties across various domains, while computational modeling offers a theoretical understanding. Patient-specific models increasingly help interpret observations and improve individual cardiac electrical behavior approximations. Consequently, advancements in computational methodologies are vital for gaining new insights into cardiac electrophysiology and arrhythmias.

Here, we review papers published in the Frontiers in Physiology Research Topic on "*Computational methods in cardiac electrophysiology*," and share a perspective on the potential future impact of such technology (Figure 1).

Body-surface potential mapping, electrocardiographic imaging, and optical mapping

Body-surface potential mapping (BSPM) may provide information beyond the 12-lead electrocardiogram (ECG), which is particularly relevant for extraction of therapy predictors in complex (chaotic) rhythms such as atrial fibrillation (AF). Zhong et al. used BSPM signals to predict AF recurrence after catheter ablation therapy. They combined single-time instant BSPMs with temporal-attention block, which allowed the training of a 3D convolutional neural network (3D-CNN) with BSPMs over time to predict AF recurrence. The advantage of using BSPM without performing noninvasive

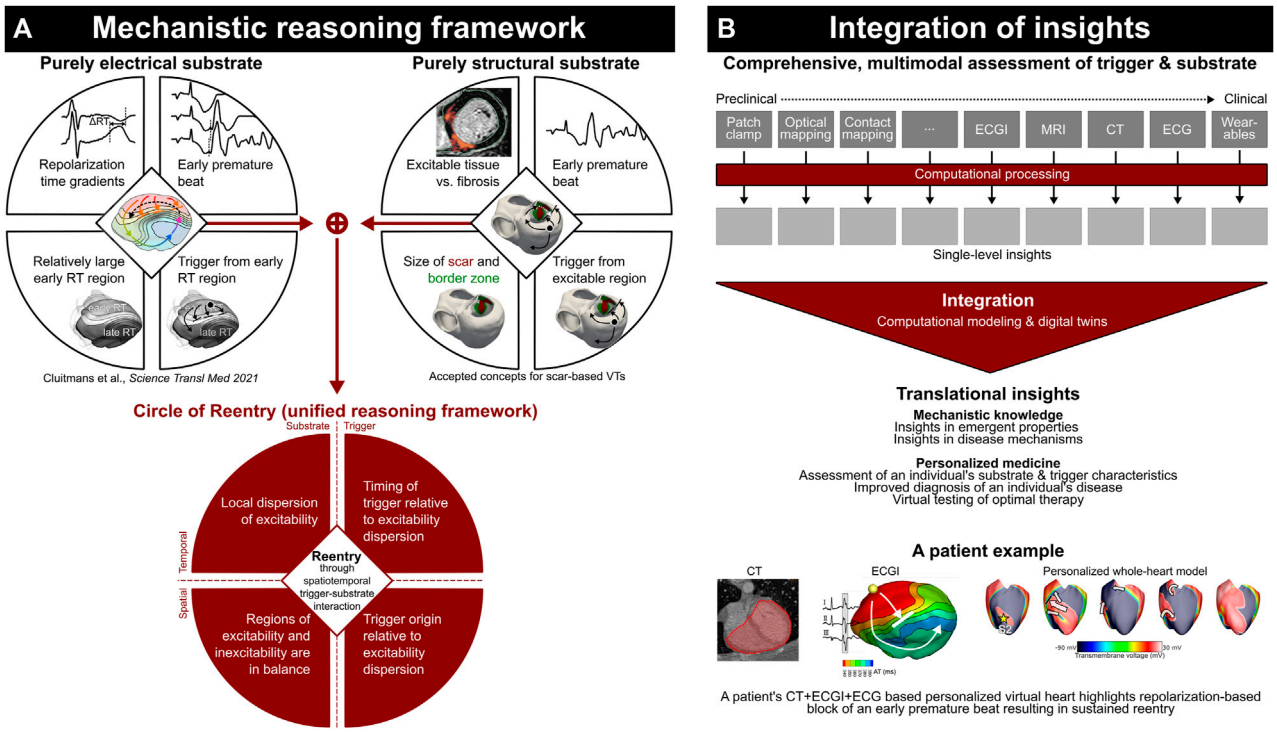

FIGURE 1
Current mechanistic reasoning frameworks highlight the complex spatiotemporal interaction of trigger and substrate **(A)**; computational modeling is essential to integrate detailed assessment of trigger and substrate characteristics to obtain translational insights **(B)**. Adapted from Cluitmans et al., 2023, licensed CC-BY-4.0.

inverse mapping techniques (called electrocardiographic imaging, ECGI) is that it avoids ECGI's particular intricacies and pitfalls. Melgaard et al. have performed such inverse mapping but have limited it to a simplified, potentially more stable, approach. They restrict their inverse technique to the 12-lead ECG and a generic (non-personalized) geometry. Their method was able to noninvasively localize the latest electrically activated region in patients with LBBB, which is relevant for lead placement during CRT implantation. Although the use of generic geometries forfeits the need for imaging in patients, it likely affects the accuracy with which abnormalities can be localized in the heart. This was also studied by Molero et al., who investigated the effect of the density of personalized digitized torso meshes in patients with AF undergoing ECGI. They found that including the exact positions of the electrodes on the patient's torso directly in the mesh (thus matching electrodes with mesh nodes) drastically reduces the need for high-density meshes. Their findings suggest that meshes primarily composed of electrode positions may contain sufficient geometric detail for accurate inverse reconstructions (if sufficient electrodes are present).

In two companion papers, Meng et al. introduced a novel formulation of ECGI and then applied this method to the less-studied intracardiac approach. First, the method of fundamental solutions (MFS) was employed to map intracardiac (catheter-based) signals to the endocardium of the heart. MFS is a meshless ECGI approach that has been applied to inverse torso-heart mapping, but not yet to inverse catheter-heart (intracardiac) mapping. They studied the intracardiac MFS approach and found that it outperforms traditional (mesh-based) approaches and is theoretically simpler to set up. Subsequent application of this method in patients with AF showed that it is a feasible mapping method, but catheters must be large enough to capture features of complex rhythms (Meng S. et al.).

Combined, these papers add important insights to the field: For some applications, BSPM or simplified ECGI approaches (based on the 12-lead ECG) may be sufficient; and for more complex applications such as intracardiac mapping, meshless approaches may be better suited than the traditional mesh-based approaches with more complex requirements. Sometimes, simpler is better.

With the advent of telehealth, a robust quality assessment of input data from (wearable) sensors is essential. Castiglioni et al. used cepstral analysis, a method to identify the periodicity of a signal, for single-lead electrocardiograms to quantify the quality of the recording. Even if multiple electrodes are available, defining the most informative metrics remains an ongoing process, as illustrated by Kappel et al., who assessed three quantitative indices to predict whether a uniform ablation strategy resulted in AF termination (Kappel et al.).

Optical mapping plays a major role in unraveling arrhythmia mechanisms in experimental investigations. Such mechanisms may be partially based on complex interactions

between transmembrane voltage and intracellular calcium. Uzelac et al. developed a method that allows simultaneous recording of these quantities in a single-camera optical mapping setup. This allows the quantitative characterization of their dynamic interactions that play a role in arrhythmogenesis at the tissue level. Among others, dynamics may be the result of inflammation, which was studied with computational models to begin unraveling the underlying complex interactions by Bi et al.

Tissue modeling, organ modeling, and digital twins

Traditionally, computational models have been indispensable in experimental studies to facilitate more accurate analysis and to infer mechanisms underlying cardiac function. Driven by recent methodological advances, cardiac modeling has also begun to appear in clinical applications as a means of aiding in diagnosis and stratification, or—by exploiting their mechanistic nature that allows to predict therapy outcomes—for the optimal planning of therapies. All of these application scenarios pose different challenges, many of which are addressed in this Research Topic.

Overall, cardiac modeling benefits from methodological advances leading to improved robustness, accuracy and numerical stability (Barral et al.). It also profits from more accurate biophysical representation of mechanisms, such as electro-mechanical force generation at the cellular level (Bartolucci et al.) or of atrial electrophysiology in experimentally important porcine models (Peris-Yagüe et al.). Models also play a pivotal role in gaining insight into the relationship between key pathological processes in cardiac diseases such as myocardial fibrosis and their reflection in the most important observable physical measurements, that is, intracardiac electrograms. The computational methodology for best representing the impact of fibrosis in models on electrograms was comprehensively reviewed by (Sánchez and Loewe).

At the forefront of cardiac modeling research is the development of methodologies for generating anatomically accurate and physiologically detailed computational models calibrated to patient data at an individual level. Such personalized models represent data acquired from individuals with high fidelity, or are statistically representative of a group of patients. Such digital twin models or virtual cohorts are now gaining importance in clinical applications, in the medical device industry as well as in regulatory policy. Furthering these arguably most advanced models of cardiac function to deliver on these high promises relies on improving several critical aspects. Most importantly, model calibration must be achieved with high fidelity by comparing to clinically observable data. These calibration processes must be streamlined and automated to create digital twins with sufficient reliability within feasible timeframes. Gillette et al. reported the first biophysical whole-heart electrophysiology model that can be executed with real-time performance, and is able to match the ECG of the modelled subject using a topologically and physically detailed model of the entire cardiac conduction system. Beetz et al. proposed a novel data-driven approach to investigate physiological patterns linked to electrophysiological activity and mechanical deformation (Beetz et al.). These vary considerably between individual patients and across cardiovascular diseases. They developed a multi-domain variational autoencoder network that integrates electrocardiogram and MRI-based 3D anatomy data into a unified model. Demonstrating high fidelity reconstruction and generation of realistic virtual populations, their approach enhances cardiovascular disease classification and supports the creation of accurate computational models, capturing disease and patient variability. Doste et al. proposed utilizing cardiac models for accurately and non-invasively determining the site of origin of ectopic beats in outflow tract arrhythmias prior to ablation therapy, to improve intervention outcomes. They enriched the training data with simulation-based synthetic data to train a machine-learning classification model. Their study demonstrated that simulated data are pivotal for enhancing training classification algorithms to achieve sufficiently accurate localization of the sites of origin.

Personalized computational methodology is ideally positioned—and perhaps critical—to assess an individual's true risk for arrhythmias, as it is increasingly recognized that simplified concepts such as "wave length," "scar volume," and "reduced ejection fraction" are insufficient to accurately assess this. This is particularly true when addressing both electrical and structural abnormalities, as can be studied using the recently introduced unifying "Circle of Reentry" (Cluitmans et al., 2023), Figure 1A. Although such reasoning frameworks may be all-encompassing, they are dependent on a complex spatiotemporal interaction of their elements. This necessitates computational assessment not just to process the complex data at the level of each single modality, but also to integrate findings to understand emergent behavior and arrive at an accurate risk assessment of an individual's heart characteristics (Figure 1B).

Artificial intelligence (AI), although relatively unaddressed in this collection of papers, is expected to significantly change our scientific understanding (Krenn et al., 2022). Although its 'black-box' approach may initially seem unsuitable to obtain new insights, it can uncover patterns and may be well suited to explore new or unstructured data. Even when the biophysics of a field are relatively well-understood—as is arguably the case for cardiac electrophysiology—an interaction between "fuzzy" AI and 'exact' biophysics may yield new insights (Cluitmans, 2023). And AI in Digital Twins may help to augment data that is required for personalization but may not be directly available in a particular individual.

Conclusion

In conclusion, the papers presented in this Research Topic on "*Computational methods in cardiac electrophysiology*" collectively contribute to advancements in computational methods that can transform the understanding, analysis, and treatment of cardiac arrhythmias. By focusing on the development of robust and accurate models, as well as innovative approaches to personalize patient care, these methodologies pave the way for better clinical applicability and predictive outcomes. The integration of artificial intelligence and machine learning techniques, which have seen rapid growth and

adoption in recent years and months, is poised to propel the field forward, enabling deeper insights and more effective treatment strategies. Overall, the synergy of computational electrophysiology, AI, and experimental and clinical data holds great promise for improved diagnostic accuracy, patient-specific therapeutic planning, and an enhanced understanding of complex cardiac interactions, ultimately contributing to better patient outcomes and quality of life.

Author contributions

All authors listed have made a substantial, direct, and intellectual contribution to the work and approved it for publication.

Conflict of interest

The authors declare that the research was conducted in the absence of any commercial or financial relationships that could be construed as a potential conflict of interest.

Publisher's note

References

Cluitmans, M. (2023). Fuzzy meets exact: The synergy between large language models and biophysics. *Transform. Med.Tech*. 2023. Available at: https://www.transformingmed.tech/p/the-synergy-between-llm-and-biophysics-models.

Cluitmans, M. J. M., Bayer, J., Bear, L. R., ter Bekke, R. M. A., Heijman, J., Coronel, R., et al. (2023). The circle of reentry: Characteristics of trigger-substrate interaction leading to sudden cardiac arrest. *Front. Cardiovasc. Med.* 10, 1121517. doi:10.3389/FCVM.2023.1121517

Krenn, M., Pollice, R., Guo, S. Y., Aldeghi, M., Cervera-Lierta, A., Friederich, P., et al. (2022). On scientific understanding with artificial intelligence. *Nat. Rev. Phys.* 412 4, 761–769. doi:10.1038/s42254-022-00518-3

frontiers in Physiology

ORIGINAL RESEARCH
published: 11 February 2022
doi: 10.3389/fphys.2022.812968

Methodology for Cross-Talk Elimination in Simultaneous Voltage and Calcium Optical Mapping Measurements With Semasbestic Wavelengths

Ilija Uzelac[1]*, *Christopher J. Crowley*[1], *Shahriar Iravanian*[2], *Tae Yun Kim*[3], *Hee Cheol Cho*[3,4,5] *and Flavio H. Fenton*[1]

[1] School of Physics, Georgia Institute of Technology, Atlanta, GA, United States, [2] Division of Cardiology, Section of Electrophysiology, Emory University Hospital, Atlanta, GA, United States, [3] Department of Pediatrics, Emory University School of Medicine, Atlanta, GA, United States, [4] Department of Biomedical Engineering, Emory University School of Medicine, Atlanta, GA, United States, [5] The Sibley Heart Center, Children's Healthcare of Atlanta, Atlanta, GA, United States

OPEN ACCESS

Edited by:
Richard David Walton,
Université de Bordeaux, France

Reviewed by:
Callum Michael Zgierski-Johnston,
University Heart Center Freiburg, Germany
Jack Rogers,
University of Alabama at Birmingham, United States

***Correspondence:**
Ilija Uzelac
ilija.uzelac@physics.gatech.edu

Specialty section:
This article was submitted to Cardiac Electrophysiology, a section of the journal Frontiers in Physiology

Received: 11 November 2021
Accepted: 03 January 2022
Published: 11 February 2022

Citation:
Uzelac I, Crowley CJ, Iravanian S, Kim TY, Cho HC and Fenton FH (2022) Methodology for Cross-Talk Elimination in Simultaneous Voltage and Calcium Optical Mapping Measurements With Semasbestic Wavelengths.
Front. Physiol. 13:812968.
doi: 10.3389/fphys.2022.812968

Most cardiac arrhythmias at the whole heart level result from alteration of cell membrane ionic channels and intracellular calcium concentration ($[Ca^{2+}]_i$) cycling with emerging spatiotemporal behavior through tissue-level coupling. For example, dynamically induced spatial dispersion of action potential duration, QT prolongation, and alternans are clinical markers for arrhythmia susceptibility in regular and heart-failure patients that originate due to changes of the transmembrane voltage (V_m) and $[Ca^{2+}]_i$. We present an optical-mapping methodology that permits simultaneous measurements of the V_m - $[Ca^{2+}]_i$ signals using a single-camera without cross-talk, allowing quantitative characterization of favorable/adverse cell and tissue dynamical effects occurring from remodeling and/or drugs in heart failure. We demonstrate theoretically and experimentally in six different species the existence of a family of excitation wavelengths, we termed semasbestic, that give no change in signal for one dye, and thus can be used to record signals from another dye, guaranteeing zero cross-talk.

Keywords: optical mapping, semasbestic wavelength, isosbestic point, fluorescent dyes, transmembrane voltage, intracellular free calcium concentration, alternans

1. INTRODUCTION

Heart failure (HF) is a global epidemic, affecting more than 64 million people worldwide (James et al., 2018) and is increasing in prevalence. In the US, about 6.9 million people have been diagnosed with HF, with an expected 24% increase to nearly 8.5 million by 2030 (Benjamin et al., 2018). The prognosis is poor: 20% die within 1 year and 80% within 8 years, resulting in over 655,000 deaths annually (Virani et al., 2020) in the US alone. More than half of HF deaths are due to ventricular fibrillation (Packer, 1985), and despite decades of study, the mechanisms by which HF predisposes patients to these ventricular arrhythmias are not well-understood. As a result, few treatment options are available. It is, therefore, crucial to identify how HF leads to the development of life-threatening cardiac arrhythmias. Although it is well-known that fibrosis and myocardial ischemia (Tomaselli and Zipes, 2004) can cause conduction abnormalities and cardiac arrhythmias, there is growing recognition that abnormal intracellular calcium cycling plays a fundamental role in the pathology

of HF (Hoeker et al., 2009; Aistrup et al., 2011). Many studies have shown that disruptions in intracellular calcium concentration ($[Ca^{2+}]_i$) cycling, along with the complex voltage-calcium bidirectional coupling, can lead to action potential (AP) repolarization abnormalities that promote arrhythmias (Balijepalli and Kamp, 2008, 2011; Hoeker et al., 2009; Louch et al., 2010; Aistrup et al., 2011). This necessitates the development of effective methods that can investigate simultaneously the dynamics of the cell's transmembrane voltage (V_m) and $[Ca^{2+}]_i$ in cardiac tissue.

Optical mapping, developed in the mid-1970s, is the perfect methodology for the study of V_m -$[Ca^{2+}]_i$ in cardiac electrophysiology due to a high spatial and temporal resolutions. In essence the method originally consisted in measuring changes in V_m from changes in fluorescence intensity using V_m sensitive dyes. For example, electrochromic V_m dyes bind to the cell's membrane, and their absorption and emission spectra blue-shifts a few nanometers as the cell membrane depolarizes. By blocking the excitation light and part of the emission spectra with a long-pass-filter (LPF) placed over an electro-optical sensor (camera), fluorescence intensity is measured in practice (**Figure 1**). For small spectra shifts, the normalized change in fluorescence intensity ($\Delta F/F$) is given by (F - F_0) / F_0, where F_0 is the fluorescence intensity when the cell's membrane is polarized (the resting membrane potential), and F when the cell's membrane is depolarized (any other transmembrane potential) which to first approximation it is linearly proportional to the cell's transmembrane potential and thus closely reproduce the action potential (**Figure 1D**). With unprecedented high spatial and temporal resolution, optical mapping with V_m sensitive dyes have been used to characterize wave propagation across the tissue surface (Barone et al., 2020) and depth (Kelly et al., 2013), during regional ischemia (Sidorov et al., 2011) and provide evidence of reentrant waves as mechanisms of lethal arrhythmias such as ventricular tachycardia and fibrillation (Davidenko et al., 1992; Gray et al., 1998; Cherry and Fenton, 2008) that affect the electro-mechanical coupling (Christoph et al., 2018). Additionally, invasive and non-invasive techniques can also be characterized using optical mapping, such radio-frequency ablation outcome (Paredes et al., 2020; Pollnow et al., 2020), and low-energy defibrillation techniques (Li et al., 2011; Ji et al., 2017; Uzelac and Fenton, 2020). However, for a complete understanding of arrhythmic mechanisms, simultaneous measurements of V_m and $[Ca^{2+}]_i$ are needed. Simultaneous measurement of V_m-$[Ca^{+2}]_i$ reveals spatial dispersion of AP repolarization and $[Ca^{+2}]_i$ transients (CaT) (Uzelac et al., 2017) which is one of the mechanisms leading to ventricular arrhythmias (Pastore et al., 1999; Watanabe et al., 2001; Gizzi et al., 2013).

Historically, the first dual optical mapping systems were designed in 2000 by Choi and Salama (2000) with RH-237 V_m and Rhod-2 AM $[Ca^{+2}]_i$ dyes, and by Laurita and Singal (2001) with Di-4-ANEPPS V_m and Indo-1 AM $[Ca^{+2}]_i$ dyes. These systems used overlapping excitation bands for the two dyes with separate emission bands split and sent to the two photodetectors, one to measure V_m and one for $[Ca^{+2}]_i$ with a spatial resolution of 16 × 16 pixels. Since then, other dual systems with higher resolution (Holcomb et al., 2009) have been developed, including those designed with a single camera for monolayers (Scull et al., 2012) and whole hearts (Lee et al., 2011, 2012a,b,c; Herron et al., 2012). The advantages of a single detector based systems include: (i) Significantly less expensive as they do not require multiple detectors/cameras; (ii) There is no need for spatial alignment of the detectors to have the same field of view, increasing complexity of setups, and possible decrease of the field of view (Holcomb et al., 2009); (iii) No need to use a dichroic mirror to separate the V_m and $[Ca^{+2}]_i$ fluorescence signals for each sensor, decreasing light intensity, that is signal to noise ratio (SNR).

While optical mapping recordings have been considered technically challenging and expensive, advances in recent years have made the necessary equipment affordable enough (Marina-Breysse et al., 2021) to become a standard technique in many labs. Different methods have been proposed to achieve dual V_m and $[Ca^{2+}]$ optical mapping measurement. Two-camera setups require complex spatial alignment of the cameras and optical elements to split the two fluorescent signals, with only one signal reaching each camera (Holcomb et al., 2009). The complexity of the two-camera setups can be avoided by a single camera for dual V_m and $[Ca^{2+}]_i$ signal measurements. The fundamental principle behind single-camera-based methods is to separate the V_m and $[Ca^{2+}]$ fluorescence signals based on differences in excitation and/or emission spectra of the two dyes used. Existing methods (Lee et al., 2011, 2012a,c) are limited to the particular choice of fluorescent dyes, significantly limiting their application. Additionally, there is no established methodology for designing and implementing a single-camera-based dual V_m and $[Ca^{2+}]_i$ measurement technique which provides zero-cross talk of the two fluorescence signals. The excitation light band for a V_m dye preferably would not excite a $[Ca^{2+}]_i$ dye and vice versa. However, true spectral separation is not possible (with currently available dyes), but illuminating at a wavelength where one or the other dye is not sensitive to the parameter of interest is sufficient. This is essential as the complex bidirectional coupling between V_m and $[Ca^{2+}]_i$ (Shiferaw and Karma, 2006) is important when investigating under which HF conditions (Gorski et al., 2015) V_m or $[Ca^{2+}]_i$ are responsible for triggering an arrhythmia.

This study presents a theoretical framework to analyze and select the optimal dyes/filters combination to achieve zero-cross talk for dual V_m - $[Ca^{2+}]$ optical mapping applications for simultaneous measurement of V_m and $[Ca^{2+}]_i$ signals, using a single sensor. The methodology is based on alternating excitation bands for each fluorescent dye in sync with the camera, recording each signal in alternating frames in order to overcome the challenges of mutual cross-talk of the two signals. Excitation at wavelengths we term semasbestic results in no change of fluorescence of a voltage-sensitive dye as V_m changes, which is suitable to excite a $[Ca^{2+}]_i$ dye with no cross-talk. We demonstrate the existence of a family of these excitation wavelengths and the advantage of this methodology experimentally with optical mapping measurements performed in six different animal species, while also showing how previous methods exhibit signal cross-talk. Furthermore, optical-mapping methods using V_m and $[Ca^{+2}]_i$ dyes have a broad range of applications, suitable for research of cardiomyocyte cultures (Fast and Ideker, 2000), studying drug effects on heart

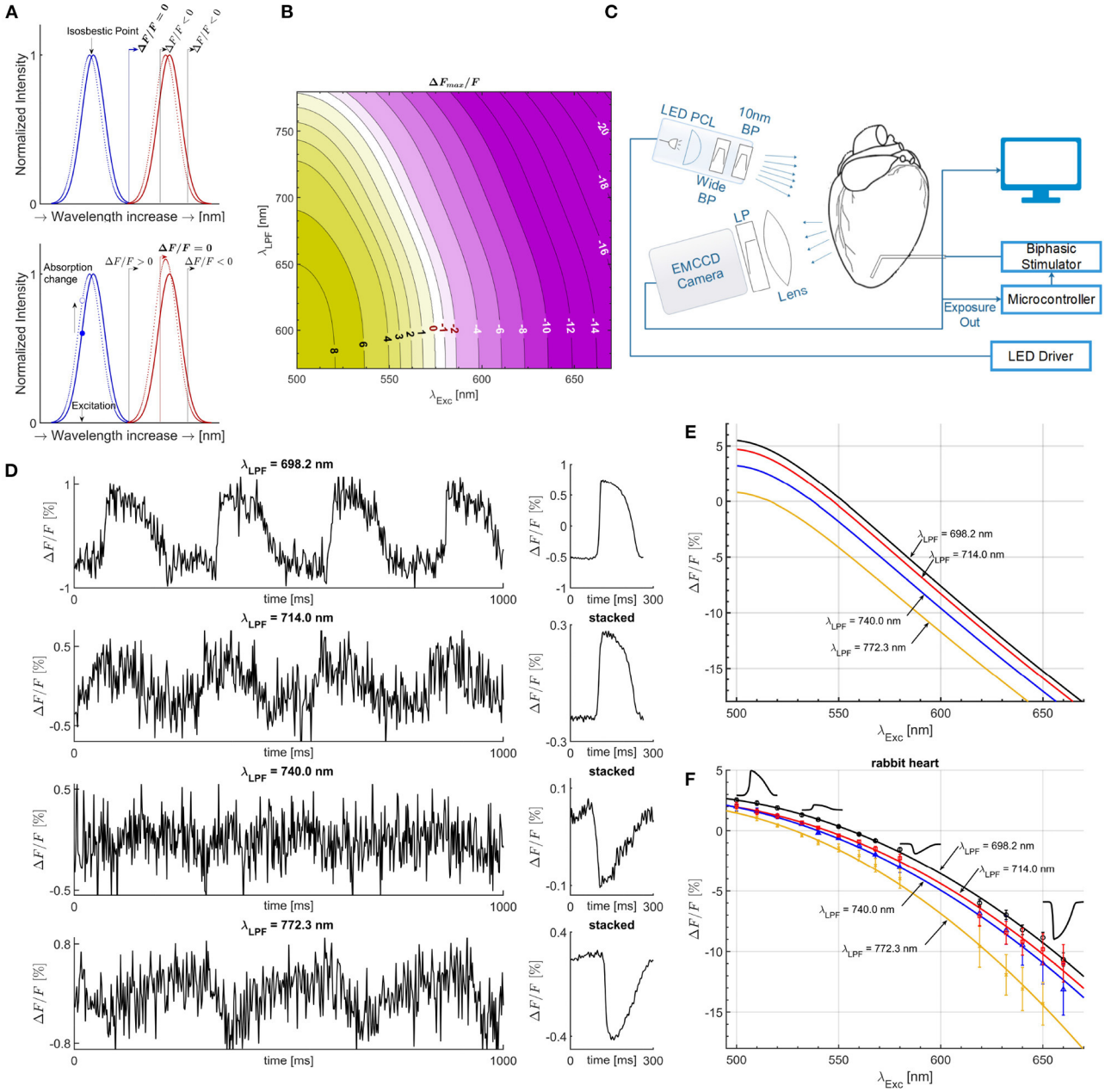

FIGURE 1 | Mechanisms of measurement with an electrochromic V_m dye. **(A)** The Gaussian absorption (blue) and emission curves (red) are good fits for a given electrochromic V_m dye for illustration purposes, with solid lines for polarized membrane and leftward shifted dotted lines for maximally depolarized membrane by a propagating AP. For excitation at the *isosbestic* point and for a given LPF on the camera side passing only part of the emission spectra, as illustrated with the solid (black) vertical lines, $\Delta F/F$ is always negative. $\Delta F/F = 0$ can only be achieved if the entire emission spectrum is obtained (solid blue vertical line), thereby not dependent on the optical setup, the λ_{LPF} value. Excitation left of the *isosbestic* point results in an amplitude increase of the emission spectra due to absorption coefficient increase with the shift of the absorption spectra. Depending on the filter λ_{LPF}, overall $\Delta F/F$ sign can be negative or positive, and in between, there is a particular λ_{LPF} such that positive change cancels the negative change resulting in $\Delta F/F = 0$, for specific λ_{Exc}, termed *semasbestic* wavelength. **(B)** Theoretically calculated map of $\Delta F/F$ magnitude values as a function of λ_{Exc} and λ_{LPF}, showing the transition from positive to negative $\Delta F/F$, and continuous line of *semasbestic* wavelengths, $\Delta F/F = 0$ isochrone line, for each λ_{Exc} - λ_{LPF} pair. **(C)** Illustration of the experimental setup. **(D)** APs from optical mapping measurements on isolated rabbit heart near a *semasbestic* wavelength. A 10 nm wide BP excitation filter was used of 540 nm nominal center wavelength along different LPFs on the camera's side. Due to low $\Delta F/F$ values SNR is low. However, ensemble averaging (stacking) increases SNR without filtering in post-processing. **(E)** Quadratic fit curves from $\Delta F/F$ simulated values **(B)**, for four different LPFs of the same λ_{LPF} values as LPF used in $\Delta F/F$ measurements on isolated hearts. **(F)** Quadratic fit curves from $\Delta F/F$ magnitude values for four different LPFs. Optical mapping recordings were performed on isolated rabbit heart for across a wide range of excitation wavelengths, from 500 to 660 nm. Zero crossings correspond to the *semasbestic* wavelengths. All λ_{LPF} values of LPFs are experimentally measured.

electrophysiology (Bedut et al., 2016; Streit and Kleinlogel, 2018; Gunawan et al., 2021; Uzelac et al., 2021), gene therapies on V_m and $[Ca^{2+}]_i$ dynamics in cardiac tissue and in other organs such as the brain (Baker et al., 2005; Ma et al., 2016; Turrini et al., 2017) as well as in other biological systems driven by V_m and $[Ca^{2+}]_i$ dynamics like in C-Elegans (Venkatachalam et al., 2016).

2. MATERIALS AND METHODS

Previously published methods of simultaneous measurement of V_m-$[Ca^{2+}]_i$ with a single sensor (Lee et al., 2011, 2012b,c), have incorrectly used the term *isosbestic* point of a V_m dye as a suitable excitation wavelength (λ_{Exc}) for $[Ca^{2+}]_i$ dye, expecting no change in measured V_m fluorescence. While *isosbestic* points (Ahmed and Connor, 1979; Shynkar et al., 2004; Tai et al., 2004; Nič et al., 2009; Bachtel et al., 2011; Uzelac et al., 2019) are defined as the excitation wavelengths at which the total absorbance of a fluorescent dye does not change in response to a change of V_m (**Figure 1A**; **Supplementary Figure 1**), it was instead applied as the excitation wavelength at which there is no measurable change in V_m fluorescence signal, expressed as $\Delta F/F = (F - F_0)/F_0 \approx 0$, where F_0 is the fluorescence intensity when the cell's membrane is at the resting membrane potential, and $F = F(V_m)$ is the intensity at any other cell membrane potential.

Isosbestic point is defined as the excitation wavelength at which the absorption spectra for polarized cell membrane and the shifted absorption spectra for maximally depolarized membrane, intersect each other (Bachtel et al., 2011) (**Figure 1A**). Therefore, when illuminating at an isosbestic point, the absorption coefficient changes minimally (can be approximated to zero), and the integral over the entire emission spectra remains the same. This implies $\Delta F/F = 0$, only if the LPF placed on the camera side passes the entire emission spectra. In practice, this is not possible as cameras have limited dynamic rang, and in common use the LPF on the camera side blocks part of the emission spectra to increase the absolute $\Delta F/F$ value (**Figure 1A**).

In this study, we show that *isosbestic* points, which are an intrinsic property of fluorescent dyes and as such do not depend on the optical filters transmission properties and sensor spectral response used in many optical mapping setups, are not necessarily the correct wavelengths to use to prevent cross-talk and in fact can give large V_m signal (see top panel V_m signal in **Figure 1D** obtained with the same optical filter values and the same camera used in Lee et al. (2012b) what authors mistakenly considered to be an isosbestic point excitation). In this study, we establish a methodology to design bi-modal optical-mapping systems with the selection of the correct optical filters, given a choice of V_m and $[Ca^{2+}]_i$ dyes. We demonstrate that for a given electrochromic V_m dye, a continuous range of excitation wavelengths exist that result in $\Delta F/F = 0$ (no fractional change of fluorescence) dependable on a given a LPF cut-on wavelength (λ_{LPF}) and the spectral response of the camera used. We have termed such a family of wavelengths as *semasbestic* (self-extinguishable) wavelengths, which are a function of the λ_{LPF} for a particular V_m dye. *Thus, V_m and $[Ca^{2+}]_i$ dyes can be excited with different wavelengths in alternating frames, the V_m with a wavelength outside of a $[Ca^{2+}]_i$ dye's absorption spectrum and the $[Ca^{2+}]_i$ dye within the absorption spectra of the V_m dye, but using a semasbestic wavelength for the V_m dye, to achieve zero cross-talk for both signals.*

The absorption and emission spectra of electrochromic V_m dyes bound to a cardiac cell membrane and shift a few nanometers toward blue as the membrane depolarizes (Loew, 1982) (**Figure 1A**). The *isosbestic* point, is the intersection of the absorption curves for the polarized (−80 mV) and fully depolarized (approximately +20 mV) membrane (**Figure 1A**), typically occurring near the peak of the absorption spectrum (Ahmed and Connor, 1979; Bachtel et al., 2011; Uzelac et al., 2019). Excitation at the *isosbestic* point results in a leftward shift of the emission curve without changing in amplitude. Therefore, the only case in which no change in V_m signal can be measured ($\Delta F/F = 0$), occurs when using an LPF on the camera side that passes the entire emission spectra for both (polarized/depolarized cell membrane) curves (**Figure 1A**).

Excitation with wavelengths shorter than the *isosbestic* (**Figure 1A**) increases the absorbed light, resulting in an increased amplitude of the shifted emission spectrum. For the emission spectrum range, approximately left of the emission peak, $\Delta F/F$ is positive, and for the range right of the peak, $\Delta F/F$ is negative. With LPF on the camera side, the actual measured fluorescence signal represents integrated emission spectra from the filter λ_{LPF}, and the overall sign of $\Delta F/F$ can be positive or negative depending on λ_{LPF}. A *semasbestic* wavelength will be then the excitation wavelength such that integrated intensity over the emission spectra starting from λ_{LPF} results in $\Delta F/F = 0$. Therefore, *Semasbestic* wavelengths depend on the λ_{Exc} and the λ_{LPF} used, resulting in continuous line of $\Delta F/F = 0$ values (**Figure 1B**).

To demonstrate the existence and usefulness of *semasbestic* wavelengths, we used the near infra-red electrochromic V_m dye JPW-6003 (**Supplementary Figure 1**) in isolated Langendorff perfused hearts of six animal species, fish (N = 2), Guinea pigs (N = 2), rabbits (N = 12), cats (N = 6), pigs (N = 7), and sheep (N = 2), totaling 31 experiments, in addition to monolayers cultured from neonatal rat hearts. Details of experimental materials and methods, including heart excision and preparation, cell culture monolayers preparation, excitation light sources, emission optical filters characterization, absorption and emission spectra of the JPW-6003 V_m dye, as well as methods used to obtained $\Delta F/F = 0$ *semasbestic* points experimentally and their statistical analysis, are provided in the **Supplementary Materials**.

3. RESULTS

$\Delta F/F$ values were measured in isolated heart experiments stained with V_m dye JPW-6003, and excited with a series of different excitation light bands using 10 nm wide bandpass (BP) excitation filters of nominal center wavelengths ranging from 500 to 671 nm. The filters were coupled to either green or red LED collimated light (**Figure 1C**), and for four different LPFs used on the camera side (**Supplementary Figure 2**). The excitation

light band of each BP filter was modeled with a single effective excitation wavelength (**Supplementary Figure 3**).

For each LPF-BP filter combination (out of the 60 possible), optical mapping recordings of V_m were obtained for a duration of 2–10 min (depending on the amplitude of $\Delta F/F$ signal), acquiring a sequence of images with the V_m across the tissue, at 500 FPS at a resolution of 128 × 128 pixels. For signals of low $\Delta F/F$ values close to the *semasbestic* wavelengths, where signal to noise ratio (SNR) decreases (**Figure 1D**), the longer recordings (10 min) were used to perform action potential (AP) stacking (ensemble-averaging) (Uzelac and Fenton, 2015) in post-processing. The stacking procedure significantly improved SNR to precisely obtain the small $\Delta F_{max}/F$ magnitude values (**Figure 1D**; **Supplementary Figure 4**).

For each isolated experiment and each LPF, *semasbestic* wavelengths were obtained as zero values of the fit curves of $\Delta F/F$ magnitudes obtained for different excitation BP filters. The range of semasbestic wavelength hypothesized theoretically matches well with those obtained experimentally (**Figures 1E,F**). Among obtained *semasbestic* wavelengths from the different animal species, no statistically significant difference was observed, with the largest variation found only in pig hearts (**Figure 2A**). We attribute this difference to the surface fatty tissue layer (that other animals did not have) attenuating non-linearly the emitted fluorescence spectra (van Veen et al., 2004), which resulted in a small leftward shift of the *semasbestic* wavelengths. One-way ANOVA tests were performed with and without the *semasbestic* wavelengths obtained in pig hearts, and found that even when including the *semasbestic* wavelengths of the pig hearts, *P*-values did not reach statistical significance ($P < 0.05$ was considered statistically significant). Therefore, *semasbestic* wavelengths (**Figure 2B**) appear to be independent of animal species, and a curve can be fitted to relate *semasbestic* wavelengths as a function of λ_{LPF} for V_m JPW-6003 dye, (**Figure 2C**).

Any *semasbestic* wavelength is suitable to excite a $[Ca^{2+}]_i$ dye. However, in practice using off-the-shelf filters it is expected some mismatch with the filter effective excitation wavelength from the ideal *semasbestic* wavelength. Any mismatch will result in a cross-talk, the presence of the V_m signal while measuring the $[Ca^{2+}]_i$ fluorescence signal. However, for the excitation wavelengths of up to 10 nm from the ideally suitable *semasbestic* wavelength, the fractional change of V_m fluorescence is less than 0.5% (**Figure 2D**). Staining a heart in addition with a $[Ca^{2+}]_i$ dye and assuming the same baseline fluorescence levels of the two dyes, the fractional change of 0.5% will results in ∼0.25% fractional change of both fluorescence signals combined, attributed to $V_m - Ca$ cross-talk. In practice for $V_m - Ca$ single-camera measurements, a relative fluorescence change measured in *Ca* fluorescence channel, of for example 5% means that 0.25% of the measured fluorescence change is attributed to the unwanted V_m signal.

To further demonstrate the proof of concept for $V_m - Ca$ cross-talk minimization for each of the four LPF filters, V_m measurements with JPW-6003 dye only were performed using alternating excitation bands in sync with the camera frame rate (500 Hz at a resolution of 128 × 128 pixels). The sequence of images was recorded with the odd frames corresponding to ideally no change in V_m fluorescence (DFF = 0) and even frames corresponding to the change in V_m signal fluorescence **(Figure 3)**. For odd frames, the off-the-shelf BP excitation filters were used chosen to match as close as possible the ideal *semasbestic* point corresponding to each of the four different LPFs, and coupled with 525 centered green LED. For even frames, the BP excitation filter of the effective λ_{Exc} = 660.0 nm wavelength was used. For each of the four validation tests with different LPF, the amount of $V_m - Ca$ cross-talk is around 0.25% except for λ_{LPF} = 698.2, which is around 0.4%. The cross-talk is represented as a fractional change in the V_m dye fluorescence. The optical action potential traces corresponding to the same image pixel for even and odd image sequences for direct comparison. As off-the-shelf BP filters were used, the amount of cross-talk depends on the difference between the BP filter effective wavelength from the semasbestic point. Based on the measurement (**Figure 3**), sensitivity is minimal for λ_{LPF}^{nom} = 740.0 nm, using a BP filter of effective excitation wavelength of 5 nm off the *semasbestic* point and resulting in $\Delta F/F$ less than 0.25%.

4. DISCUSSION

The range of different *semasbestic* wavelengths of a given V_m dye provides flexibility in the design of an optical mapping system for simultaneous single-camera V_m - *Ca* recordings, as it is not limited to a single choice of excitation and emission filters, and V_m and *Ca* fluorescence dyes. The design parameters include the optimal excitation wavelength for a V_m dye (that maximizes $\Delta F/F$), choice of $[Ca^{2+}]_i$ dye and its excitation wavelength (*semasbestic* point), the dual-band pass optical filter on the camera side, and suitable LEDs coupled with excitation filters. Availability of LEDs, optical excitation filters, and the dual-band pass filter of desired spectral properties based on the theoretical design are additional constraints that need to be considered. To begin with the parameters optimization, the first step is to choose a V_m dye.

4.1. V_m Dye Selection

Selection of the V_m dye determines the range of *semasbestic* wavelengths. For optical mapping method optimization with a chosen V_m dye, the first step is to determine the V_m dye emission spectra to optimize $\Delta F_{max}/F$. For a chosen JPW-6003 dye its absorption and emission spectra are shown in **Supplementary Figure 1**. Excitation of the V_m dye with longer wavelengths than the *isosbestic* point and using longer λ_{LPF} on the camera side, increases $\Delta F_{max}/F$ magnitude (**Figures 1B–F**; **Supplementary Figure 5**). However, the SNR decreases for longer λ_{LPF} due to less fluorescence light reaching the detector. A common practice is to choose λ_{LPF} between the V_m dye emission peak and 50% of the peak, the range from 708 to 775 nm for JPW-6003 dye (**Supplementary Figure 1**). Considering suitable and currently available deep red high-power LEDs,

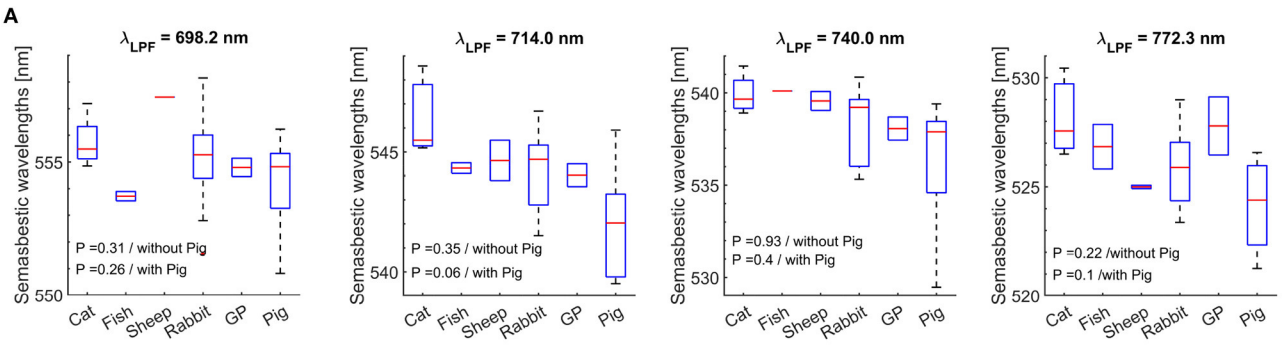

B

λ_{LPF} = 698.2 [nm]	N	Mean [nm]
Cat	6	555.7 ± 5.1
Fish	2	553.7 ± 2.2
Sheep	1	557.4 ± 2.4
Rabbit	12	555.1 ± 3.5
GP	2	554.8 ± 7.5
Pig	7	554.2 ± 2.0
All	30	555.2 ± 4.5

λ_{LPF} = 714.0 [nm]	N	Mean [nm]
Cat	3	546.4 ± 2.1
Fish	2	544.3 ± 7.1
Sheep	2	544.6 ± 2.2
Rabbit	12	544.3 ± 4.5
GP	2	544.0 ± 8.5
Pig	6	542.1 ± 2.0
All	27	544.3 ± 5.3

λ_{LPF} = 740.0 [nm]	N	Mean [nm]
Cat	4	539.9 ± 3.0
Fish	1	540.1 ± 1.5
Sheep	2	539.6 ± 1.4
Rabbit	10	539.0 ± 5.8
GP	2	538.1 ± 4.7
Pig	7	536.4 ± 4.1
All	26	538.8 ± 4.1

λ_{LPF} = 772.3 [nm]	N	Mean [nm]
Cat	3	528.2 ± 2.9
Fish	2	526.8 ± 7.2
Sheep	2	525.0 ± 3.0
Rabbit	10	526.0 ± 3.5
GP	2	527.8 ± 4.6
Pig	4	524.2 ± 3.3
All	23	526.3 ± 4.6

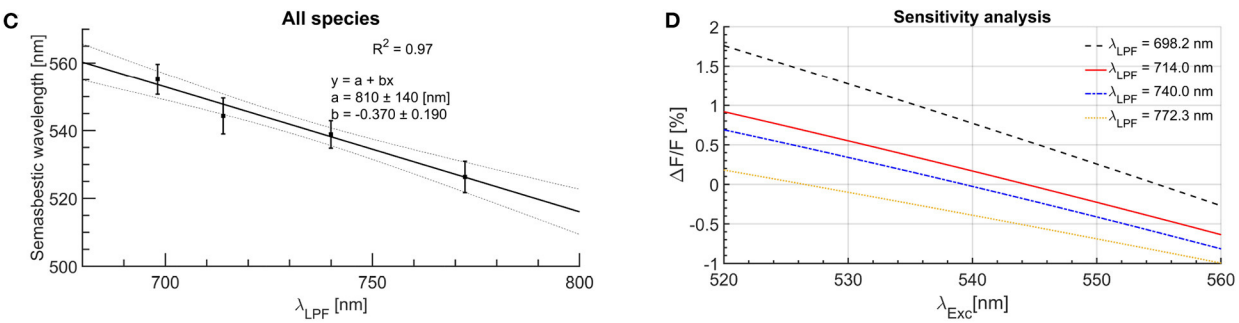

FIGURE 2 | The *semasbestic* wavelengths across all experiments for JPW-6003 V_m dye. **(A)** Box plots are a statistical representation of *semasbestic* wavelength averaged for each species. The ends of each box are the upper and lower quartiles, with the median marked as a horizontal line inside the box. The whiskers lines represent the upper and lower extremity. The P-values represent results of one-way ANOVA analysis with and without the *isosbestic* points from isolated pig hearts experiments. **(B)** The mean values and uncertainties of experimentally obtained *semasbestic* points across all species for different LFPs used on the camera. **(C)** A linear curve fit relating the range of *semasbestic* wavelengths corresponding to different λ_{LPF}. **(D)** Sensitivity analysis near the *isosbestic* wavelength for different LPFs. Experimentally obtained $\Delta F/F$ magnitude values were averaged across all species for the same LPF-BP filter pairs. Excitation wavelengths for up to 10 nm off the *semasbestic* wavelength result in less than 0.5% in the fractional change of the V_m signal.

the optimal choice is to use peak emission LEDs around 660 nm.

4.2. $[Ca^{2+}]_i$ Dye Selection

Selection of the suitable $[Ca^{2+}]_i$ dye is constrained with the range of the *semasbestic* wavelengths corresponding to the selected range of λ_{LPF} values, from 708 to 775 nm. From the equation shown in **Figure 2C**, the corresponding range of *semasbestic* wavelengths range from 523 to 548 nm, suitable to excite $[Ca^{2+}]_i$ dyes such as Cal-520, Rhod-2, and Rhod-4. In this study, we choose Rhod-2 dye with a peak absorption at 552 nm. However, commercially available LEDs offer peak emission around 525 nm, decreasing emission intensity toward the Rhod-2 absorption peak, making excitation at 540 nm a suitable trade-off. Another important aspect to consider is to avoid overlap of the $[Ca^{2+}]_i$ dye absorption spectra with the chosen JPW-6003 V_m dye excitation wavelength of 660 nm. Rhod-2 $[Ca^{2+}]_i$ dye absorption spectrum effectively reaches zero above 625 nm, making Rhod-2 dye a suitable choice for $[Ca^{2+}]_i$ measurement.

4.3. Dual-Band Pass Filter

A dual-bandpass optical filter is required on the camera to pass the emitted fluorescence from both dyes. With the chosen 540 nm *semasbestic* wavelength, the V_m dye band is determined from the λ_{Exc} vs. λ_{LPF} curve (**Figure 2C**) to start at ∼730 nm. The first filter band corresponding to the Rhod-2 emission spectra can be from 560 and up to 610 nm. The lower band limit is imposed by excitation BP filter centered at 540 nm so that its transition band effectively reaches zero ($< \ 10^{-4}$) at 560 nm. The upper limit is determined to avoid overlap with the V_m emission spectra to minimize cross-talk, the presence of V_m signal in

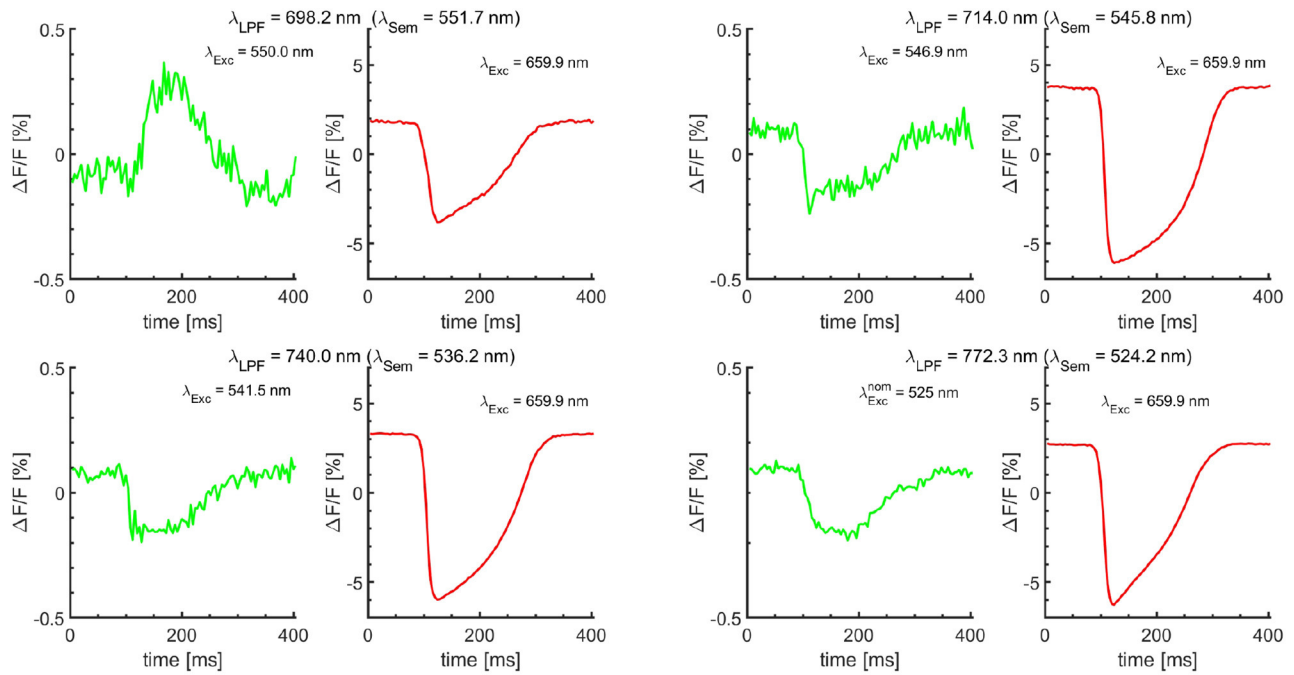

FIGURE 3 | Single-camera dual V_m measurements. The V_m dye was excited with alternating excitation bands, using a 660/10 excitation BP filter in even frames. Odd frames were acquired using off-the-shelf excitation BP filters selected to closely match the *semasbestic* points (λ_{Sem}) corresponding to the λ_{LPF} of the four LPFs. λ_{Exc} wavelengths are effective excitation wavelengths of the BP filters. Their nominal center wavelengths are listed in **Supplementary Figure 3**. λ_{Exc}^{nom} = 525 nm is the nominal center wavelength of 20 nm wide (OD6) BP filter (Semrock). Shown optical action potential signals are obtained using the stacking procedure from a single pixel, averaging at least 400 periods without any filtering. The stacking resolves small V_m signal changes buried under the noise level, which could be interpreted as no change in V_m signal in the odd frames otherwise. The cross-talk, the presence of V_m signal due to the differences between the filters effective excitation wavelength and corresponding *semasbestic* points is less than 0.25% for most LPF. The sensitivity to the difference is the lowest for λ_{LPF} = 740.0 nm, resulting in $\Delta F/F$ amplitude of less than 0.25% using excitation wavelength of more than 5 nm different from the ideal semasbestic point.

the 560–610 nm filter band when the Rhod-2 dye is excited (**Supplementary Figures 1**, **6**).

4.4. Excitation Filters

The LED bell-shaped emission curve results in non-uniform excitation spectra passing through the BP excitation filter. For example, the light intensity passed through the 10 nm wide 540 nm centered BP filter is higher for the wavelength range left of the 540 nm than for the range right of the 540 nm, resulting in different effective (mean) excitation from the nominal 540 nm center wavelength. Since this effective excitation wavelength has to match the *semasbestic* wavelength, any mismatch will result in a non-zero $\Delta F/F$ value. However, the introduced error is small, and the V_m signal change is less than 0.5% using an excitation wavelength in the ±10 nm range around the *semasbestic* wavelength. The fractional changes were measured only with the V_m dye. Adding the *Ca* dye, the amount of cross-talk will be even lower, as the fractional change is measured in respect to the summed baseline fluorescence of both dyes (**Figure 2D**). For the V_m dye excitation, the width and spectral non-uniformity of the passed light are not critical. With a 660 nm centered LED, BP filters with a 660 nm center wavelength of up to 50 nm BP width can be used. The limits are imposed to avoid excitation of the Rhod-2 dye, and a practical limit is due to the LED's bell-shaped emission curve.

4.5. Practical Design With Applications

The optical mapping setup with optimized parameters may come at a high cost requiring the manufacturing of custom filters. However, flexibility in the choice of the *semasbestic* wavelengths provides leverage in the choice of design parameters while still minimizing the cross-talk for single-camera based simultaneous V_m - *Ca* measurements to use off the shelf filters. The dual BP filter is the most important for the system design as it determines the *semasbestic* wavelength. Additionally, any mismatch between the off-the-shelf BP filter effective excitation wavelength and the *semasbestic* wavelength will result in V_m to *Ca* cross-talk. However, as outlined above, the amount of cross-talk is less than 0.25% when the difference between the BP filter effective excitation wavelength and the *semasbestic* point is less than 5 nm (**Figures 2D**, **3**).

For practical realization, we choose an off-the-shelf dual BP filter, of optical density (OD) 6 (Chroma), with the first passband of 560–610 nm, and the second LPF band of the nominal 700 nm wavelength (effective 698.2 nm) (**Supplementary Figure 7**). Based on the equation (**Figure 2C**),

the corresponding *semasbestic* wavelength for JPW-6003 V_m dye is 551.7 nm. The closest off-the-shelf 10 nm wide BP filter of 550 nm (nominal wavelength) center wavelength (Edmund Optics) was chosen to be used for Rhod-2 *Ca* dye excitation (**Supplementary Figure 3**). An additional OD6 LPF of nominal λ_{LPF} = 575 nm (Chroma) was placed over the dual BP filter to avoid overlap between the 550/10 BP excitation filter and the 560–610 nm passband of the dual-band pass filter. This design narrows the Rhod-2 *Ca* emission spectra range to the 575–610 nm range resulting in reduced *Ca* fluorescence intensity reaching the camera sensor. However, this was a necessary trade-off using off-the-shelf optical filter filters. For the V_m dye excitation, a 10 nm wide OD4 BP filter of 660 nm nominal center wavelength was used (Edmund Optics). A green LED with 525 nm peak (Luminous Devices) coupled with 550/10 nm BP filter for Rhod-2 *Ca* dye excitation was used, and a red 660 nm peak LED (LEDEngin) coupled with the 660/10 nm BP for V_m dye excitation (**Supplementary Figure 8**).

Quantification of spatiotemporal discordant alternans of V_m-$[Ca^{2+}]_i$ in cardiac tissue. The optical mapping system with the design parameters described above was used to measure V_m - $[Ca^{2+}]_i$ signals with a single-camera in isolated hearts of Rabbit, Cat, Guinea Pig, Pig (**Figure 4**), and monolayer cell culture of neonatal rats (**Figure 5**). A restitution protocol was performed for each species, where V_m - *Ca* signals were recorded at decreasing pacing cycle lengths (PCLs) until a conduction block or ventricular fibrillation (VF) occurs. At shorter PCLs, instabilities in V_m or $[Ca_i]$ at the cellular level lead to the development of beat to beat alternans in action potential duration (APD) (Pastore et al., 1999), and intracellular calcium duration (CaD) (Uzelac et al., 2017). Through tissue-level coupling, these instabilities lead to complex and irregular spatial dispersion in AP repolarization and in CaD (**Figure 4**), forming dangerous spatially discordant alternans. Spatially discordant alternans are equivalent to T-wave alternans in clinical ECGs (Pastore et al., 1999; Uzelac et al., 2021), the clinical marker for arrhythmia susceptibility and sudden cardiac death (Walker and Rosenbaum, 2003; Verrier et al., 2009). Among species, the differences in ionic membrane channel densities such as potassium repolarization channels and lack of specific ionic channels create differences in AP morphology. In addition, through V_m - *Ca* bidirectional coupling, other differences across species exist in terms of handling the intracellular *Ca* cycling (**Figure 4**). For rabbit, cat, and guinea pig heart, alternans in *Ca* seem to drive V_m alternans leading to spatial dispersion of AP repolarization. In contrast, no alternans are observed in V_m nor *Ca* signals for pig hearts, yet pig hearts develop VF at faster PCLs in the restitution protocols. Understanding these differences across species could lead to a better understanding of different arrhythmia mechanisms modalities and relate them to human heart physiology to more complete understanding arrhythmia in human hearts, devise novel treatments, and help with the global epidemic of HF.

5. CONCLUSIONS

This study presents a methodology to achieve zero cross-talk (smaller than SNR after stacking) in a single-camera bi-modal optical mapping design based on *semasbestic* wavelengths. The presented guidelines show how to optimize *semasbestic* wavelengths to achieve zero cross-talk among V_m and *Ca* signals, while optimizing signals amplitudes as well. With off-the-shelf bandpass excitation filters of slightly different effective excitation wavelengths than corresponding *semasbestic* wavelengths (**Figure 3**) we achieved near zero-cross talk. For a true zero cross-talk, custom manufactured bandpass filters matching the *semasbestic* point would be needed, and one would need to take into account the LED excitation light spectral profile within the filter passband. The absorption spectra of a given electrochromic V_m dye is spectrally shifted when the dye is bounded within a cell membrane due to a strong interaction between the dye's molecule electric dipole momentum and the cell membrane electric field (Matson et al., 2012). Therefore, contemporary spectroscopy methods to obtain the dye absorption and emission spectra, dissolving the dye in a solvent such as ethanol and using a spectrometer, would result in different *semasbestic* wavelengths than when performing equivalent measurements on isolated hearts stained with the dye. In this study we conclude that obtained *semasbestic* wavelengths for a given electrochromic V_m dye, are dependent only on the excitation wavelength λ_{Exc} and corresponding λ_{LPF} of the dye emission band. As validated on isolated hearts of six different species, the *semasbestic* wavelengths seems to be independent of the species (as validated on six different species and cell culture monolayers).

In the published literature of simultaneous measurement of V_m-$[Ca^{2+}]_i$ with a single sensor (Lee et al., 2011, 2012b,c), authors used the same EMCCD camera model and the dual-bandpass filter of 700 nm LPF cut-on wavelength for the JPW-6003 V_m fluorescence showing no visible V_m signal when excited with 540 nm centered band, subsequently used for Rhod-2 Ca dye excitation. However, our findings are different. As shown in **Figure 1D**, excitation at 540 nm with LPF of 700 nm nominal cut-on wavelength resulted in apparent presence of V_m signal. Therefore, exiting Rhod-2 dye with 540 nm centered bandpass filter and using the dual-band pass filter of 700 nm LPF band for V_m fluorescence results in a cross-talk which can be further minimized with the presented methodology for cross-talk elimination.

While the presented methodology is demonstrated with the *semasbestic* wavelengths of JPW-6003 V_m dye and using Rhod-2 $[Ca^{2+}]_i$ dye, the described methodology does not depend on the choice of the dyes. It applies to any other electrochromic V_m resulting in a different set of *semasbestic* wavelengths. Therefore, depending on the user's need, we provide a range of *semasbestic* excitation wavelengths that can be used with JPW-6003 V_m sensitive dye, and a methodology to obtain the same for other V_m sensitive dyes. We followed the common practice in optical mapping to use an LPF to record V_m signal fluorescence. Excitation on the positive-slope side of the excitation spectrum induced an increase in fluorescence during an action potential, which is balanced by recording from the negative-slope side of the emission spectrum. Other classes of *semasbestic* points may exist with different designs of the emission filter. For example, it is also possible to create a *semasbestic* wavelength along the negative-slope side of the excitation spectrum and balance this by recording from a band on the positive-slope side of the

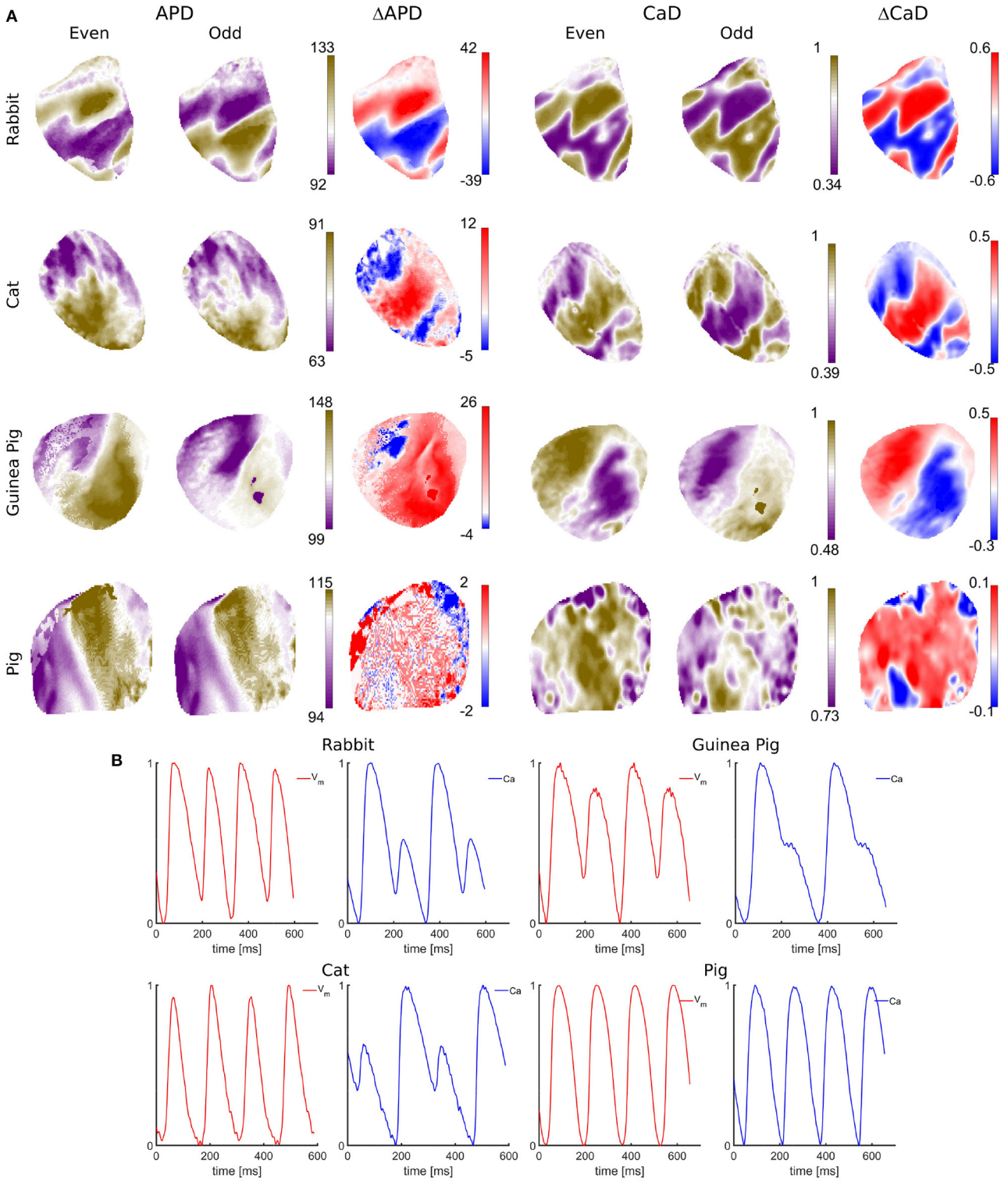

FIGURE 4 | Single-camera dual V_m – *Ca* measurements in isolated hearts of different species. **(A)** Arrhythmic effects under dynamic pacing, shown as spatial dispersion of APD and CaD across tissue for different species for even and odd beats. The spatial dispersion indicates an increased susceptibility to arrhythmia. APD values are obtained from 50% signal rise in amplitude till 50% AP repolarization. Numbers to the right indicate 3rd and 97th percentile APD values expressed in milliseconds. CaD values are obtained as the integral from 50% rise in amplitude till 50% decrease. Blue-red patterns show variations in APD and CaD (ΔAPD, ΔCaD) between even and odd beats (discordant alternans), showing regions alternating out of phase and separated with the nodal lines (white lines). Spatially discordant alternans are the counterpart of T-wave ECG alternans, a well-known marker for arrhythmia susceptibility. Although all species do develop arrhythmia under dynamic pacing, the electrophysiology across species is very different. Spatially discordant alternans are the most pronounced in rabbits, while pig hearts show very little APD and CaD dispersion, with insignificant differences between even and odd beats. **(B)** V_m and *Ca* representative AP signals showing temporal alternans for different species.

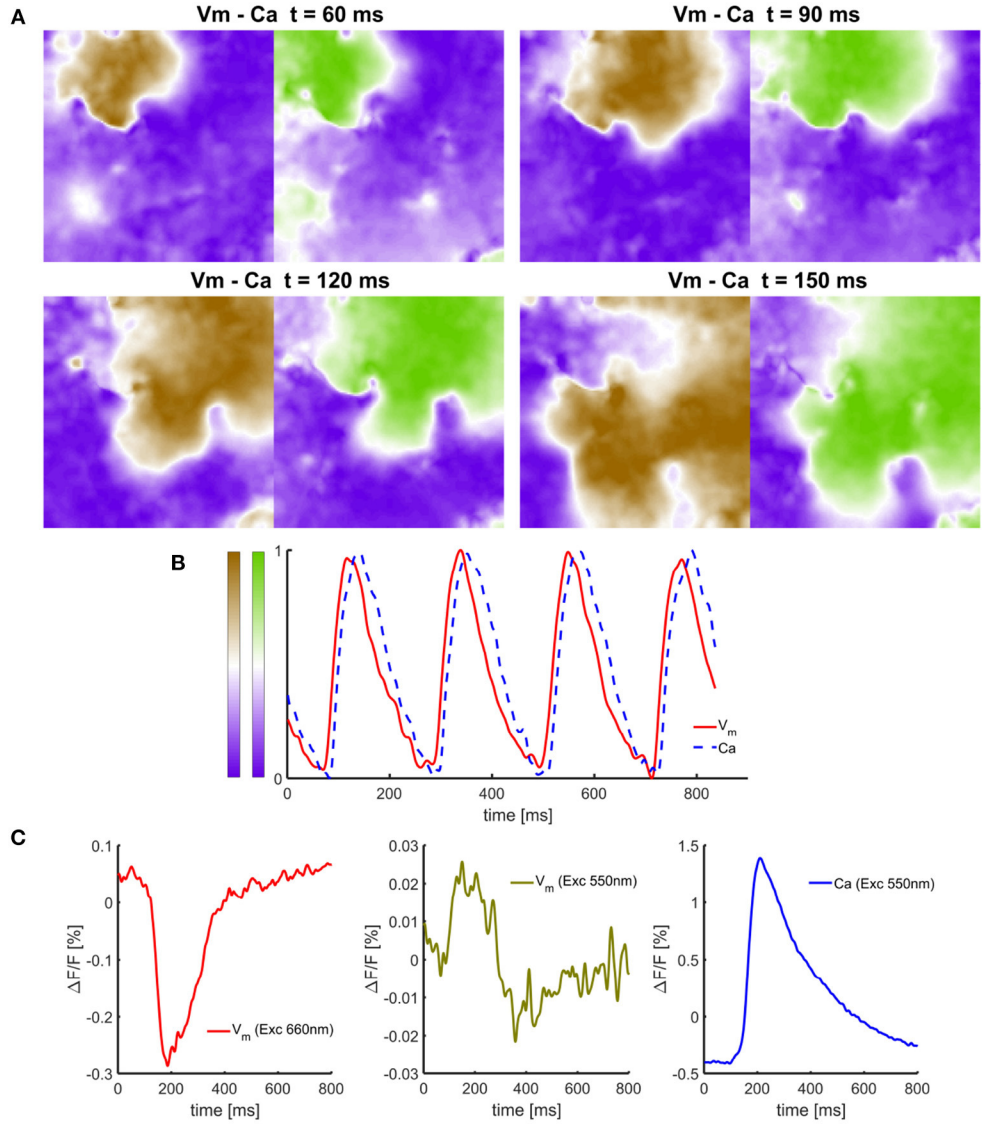

FIGURE 5 | Simultaneous single-camera-based measurements of V_m and Ca signals in isolated cell culture monolayers of neonatal rats. **(A)** Time-snapshots of V_m - *Ca* dynamic at different time points illustrating the presence of anchored spiral wave and spatial loss of correlation between propagating V_m wavefront from *Ca* dynamics. **(B)** Normalized V_m and *Ca* signals obtained from processed raw recordings showing *Ca* signal lagging in time. **(C)** Representative unfiltered V_m and *Ca* signal traces with no filtering expressed as a relative change. In cell culture monolayers, *Ca* signals have significantly higher SNR than V_m signals originating only from the dye bound to the cell membrane. The amount of cross-talk and the presence of V_m signal in *Ca* signal with excitation at near the semasbestic point (Exc550) results is a small yet negligible cross-talk compared to the amplitudes of the signals.

emission spectrum. However, the close separation between the dye absorption and emission spectra (**Supplementary Figure 1**) may preclude such an approach for JPW-6003 dye, while it may be feasible for other V_m dyes.

Optical mapping methods using fluorescent dyes are well-established and very important to measure signals from cells and tissue. The use of optical mapping systems is rapidly growing. Nowadays, it is becoming a common tool in many research labs as the equipment is no longer prohibitively expensive (Lee et al., 2017) with novel advances in CMOS sensor technology. The increasing number of research groups are using optical mapping to investigate V_m-$[Ca^{+2}]_i$ on biological tissues, and optical mapping methods are even becoming accessible in university classrooms. Simultaneous measurement of V_m and $[Ca^{2+}]_i$ enables many studies in the area of electrophysiology related to the V_m and $[Ca^{2+}]_i$ dynamic and their bidirectional coupling. For example, cardiac arrhythmia can be caused by AP spatial dispersion driven with *Ca* alternans at the cellular level (Uzelac et al., 2017) (**Supplementary Videos 1**, **2**). Dual V_m and $[Ca^{2+}]_i$ measurements are necessary to understand the underlying mechanism leading to arrhythmia (Groenendaal et al., 2014), and optical mapping studies can be performed even in combination

with contractions (Christoph et al., 2018) to study the mechanical stretching effects on cardiac electrophysiology. Time-resolved series of V_m and $[Ca^{2+}]_i$ signals at high spatiotemporal resolution are generally applicable to other electrophysiology related studies besides HF. For example, many drugs affect the AP repolarization phase blocking the potassium channels and prolonging the APD, the cellular mechanism of long-QT. Optical mapping provides integrative studies at both the cellular and tissue level to understand how drugs affect the ionic channel currents and intracellular *Ca* dynamics and to understand the drug's safety profile and associated antiarrhythmic or proarrhythmic at the tissue level (Uzelac et al., 2020, 2021), which would not be possible to understand, studying the drug's effect at the cellular level only. The methodology developed here can also be used to investigate other biological systems with V_m-$[Ca^{+2}]_i$ driven dynamics such as the brain (Rad et al., 2017) the pancreas (Yang and Berggren, 2006), smooth (Nelson et al., 1990), and skeletal (Flucher and Tuluc, 2017) muscle among others.

DATA AVAILABILITY STATEMENT

The raw data supporting the conclusions of this article will be made available by the authors upon reasonable request.

ETHICS STATEMENT

The animal study was reviewed and approved by the Office of Research and Integrity Assurance at Georgia Institute of Technology and T3 Labs (Translation Testing and Training Laboratories, Inc.), Institutional Animal Care and Use Committee (IACUC) protocols A18012 and A15002.

AUTHOR CONTRIBUTIONS

IU performed the study design, designed and performed the experiments, and analyzed and interpreted the data. CC contributed to data interpretation, theoretical postulations, and calculations. SI provided critical comments to the study. HC and TK contributed with isolated monolayer cell culture preparation and assisted in related experiments. FF contributed to study design and experiments. All authors worked in writing and reviewing the manuscript.

FUNDING

This study was supported by grants NIH 1R01HL143450-01, National Science Foundation 1446675, American Heart Association 15POST25700285, NHLBI R01HL143065, NHLBI R01HL147270, NHLBI R01HL157363, 20TPA35260085, and Department of Defense GRANT12901705 (PR191598).

ACKNOWLEDGMENTS

We would like to thank the Neurophysiology Laboratory, Laboratory for Drug Delivery, and T3 Labs at Georgia Tech for heart donations.

SUPPLEMENTARY MATERIAL

The Supplementary Material for this article can be found online at: https://www.frontiersin.org/articles/10.3389/fphys.2022.812968/full#supplementary-material

REFERENCES

Ahmed, Z., and Connor, J. (1979). Measurement of calcium influx under voltage clamp in molluscan neurones using the metallochromic dye arsenazo III. *J. Physiol.* 286, 61–82. doi: 10.1113/jphysiol.1979.sp012607

Aistrup, G. L., Balke, C. W., and Wasserstrom, J. A. (2011). Arrhythmia triggers in heart failure: the smoking gun of $[Ca^{2+}]_i$ dysregulation. *Heart Rhythm* 8, 1804–1808. doi: 10.1016/j.hrthm.2011.06.012

Bachtel, A. D., Gray, R. A., Stohlman, J. M., Bourgeois, E. B., Pollard, A. E., and Rogers, J. M. (2011). A novel approach to dual excitation ratiometric optical mapping of cardiac action potentials with di-4-anepps using pulsed led excitation. *IEEE Trans. Biomed. Eng.* 58, 2120–2126. doi: 10.1109/TBME.2011.2148719

Baker, B. J., Kosmidis, E. K., Vucinic, D., Falk, C. X., Cohen, L. B., Djurisic, M., et al. (2005). Imaging brain activity with voltage-and calcium-sensitive dyes. *Cell. Mol. Neurobiol.* 25, 245–282. doi: 10.1007/s10571-005-3059-6

Balijepalli, R. C., and Kamp, T. J. (2008). Caveolae, ion channels and cardiac arrhythmias. *Prog. Biophys. Mol. Biol.* 98, 149–160. doi: 10.1016/j.pbiomolbio.2009.01.012

Balijepalli, R. C., and Kamp, T. J. (2011). Cardiomyocyte transverse tubule loss leads the way to heart failure. *Future Cardiol.* 7, 39–42. doi: 10.2217/fca.10.113

Barone, A., Gizzi, A., Fenton, F., Filippi, S., and Veneziani, A. (2020). Experimental validation of a variational data assimilation procedure for estimating space-dependent cardiac conductivities. *Comput. Methods Appl. Mech. Eng.* 358, 112615. doi: 10.1016/j.cma.2019.112615

Bedut, S., Seminatore-Nole, C., Lamamy, V., Caignard, S., Boutin, J. A., Nosjean, O., et al. (2016). High-throughput drug profiling with voltage-and calcium-sensitive fluorescent probes in human ipsc-derived cardiomyocytes. *Am. J. Physiol. Heart Circ. Physiol.* 311, H44–H53. doi: 10.1152/ajpheart.00793.2015

Benjamin, E. J., Virani, S. S., Callaway, C. W., Chamberlain, A. M., Chang, A. R., Cheng, S., et al. (2018). Heart disease and stroke statistics-2018 update: a report from the american heart association. *Circulation* 137, e67–e492. doi: 10.1161/CIR.0000000000000573

Cherry, E. M., and Fenton, F. H. (2008). Visualization of spiral and scroll waves in simulated and experimental cardiac tissue. *N. J. Phys.* 10, 125016. doi: 10.1088/1367-2630/10/12/125016

Choi, B.-R., and Salama, G. (2000). Simultaneous maps of optical action potentials and calcium transients in guinea-pig hearts: mechanisms underlying concordant alternans. *J. Physiol.* 529, 171–188. doi: 10.1111/j.1469-7793.2000.00171.x

Christoph, J., Chebbok, M., Richter, C., Schröder-Schetelig, J., Bittihn, P., Stein, S., et al. (2018). Electromechanical vortex filaments during cardiac fibrillation. *Nature* 555, 667–672. doi: 10.1038/nature26001

Davidenko, J. M., Pertsov, A. V., Salomonsz, R., Baxter, W., and Jalife, J. (1992). Stationary and drifting spiral waves of excitation in isolated cardiac muscle. *Nature* 355, 349–351. doi: 10.1038/355349a0

Fast, V. G., and Ideker, R. E. (2000). Simultaneous optical mapping of transmembrane potential and intracellular calcium in myocyte cultures. *J. Cardiovasc. Electrophysiol.* 11, 547–556. doi: 10.1111/j.1540-8167.2000.tb00008.x

Flucher, B. E., and Tuluc, P. (2017). How and why are calcium currents curtailed in the skeletal muscle voltage-gated calcium channels? *J. Physiol.* 595, 1451–1463. doi: 10.1113/JP273423

Gizzi, A., Cherry, E., Gilmour Jr, R. F., Luther, S., Filippi, S., and Fenton, F. H. (2013). Effects of pacing site and stimulation history on alternans dynamics and the development of complex spatiotemporal patterns in cardiac tissue. *Front. Physiol.* 4, 71. doi: 10.3389/fphys.2013.00071

Gorski, P. A., Ceholski, D. K., and Hajjar, R. J. (2015). Altered myocardial calcium cycling and energetics in heart failure–A rational approach for disease treatment. *Cell Metab.* 21, 183–194. doi: 10.1016/j.cmet.2015.01.005

Gray, R. A., Pertsov, A. M., and Jalife, J. (1998). Spatial and temporal organization during cardiac fibrillation. *Nature* 392, 75–78. doi: 10.1038/32164

Groenendaal, W., Ortega, F. A., Krogh-Madsen, T., and Christini, D. J. (2014). Voltage and calcium dynamics both underlie cellular alternans in cardiac myocytes. *Biophys. J.* 106, 2222–2232. doi: 10.1016/j.bpj.2014.03.048

Gunawan, M. G., Sangha, S. S., Shafaattalab, S., Lin, E., Heims-Waldron, D. A., Bezzerides, V. J., et al. (2021). Drug screening platform using human induced pluripotent stem cell-derived atrial cardiomyocytes and optical mapping. *Stem Cells Transl. Med.* 10, 68–82. doi: 10.1101/2020.07.14.203232

Herron, T. J., Lee, P., and Jalife, J. (2012). Optical imaging of voltage and calcium in cardiac cells & tissues. *Circ. Res.* 110, 609–623. doi: 10.1161/CIRCRESAHA.111.247494

Hoeker, G. S., Katra, R. P., Wilson, L. D., Plummer, B. N., and Laurita, K. R. (2009). Spontaneous calcium release in tissue from the failing canine heart. *Am. J. Physiol. Heart Circ. Physiol.* 297, H1235–H1242. doi: 10.1152/ajpheart.01320.2008

Holcomb, M. R., Woods, M. C., Uzelac, I., Wikswo, J. P., Gilligan, J. M., and Sidorov, V. Y. (2009). The potential of dual camera systems for multimodal imaging of cardiac electrophysiology and metabolism. *Exp. Biol. Med.* 234, 1355–1373. doi: 10.3181/0902-RM-47

James, S. L., Abate, D., Abate, K. H., Abay, S. M., Abbafati, C., Abbasi, N., et al. (2018). Global, regional, and national incidence, prevalence, and years lived with disability for 354 diseases and injuries for 195 countries and territories, 1990-2017: a systematic analysis for the global burden of disease study 2017. *Lancet* 392, 1789–1858. doi: 10.1016/S0140-6736(18)32279-7

Ji, Y. C., Uzelac, I., Otani, N., Luther, S., Gilmour, R. F. Jr., Cherry, E. M., et al. (2017). Synchronization as a mechanism for low-energy anti-fibrillation pacing. *Heart Rhythm* 14, 1254–1262. doi: 10.1016/j.hrthm.2017.05.021

Kelly, A., Ghouri, I. A., Kemi, O. J., Bishop, M. J., Bernus, O., Fenton, F. H., et al. (2013). Subepicardial action potential characteristics are a function of depth and activation sequence in isolated rabbit hearts. *Circ. Arrhythmia Electrophysiol.* 6, 809–817. doi: 10.1161/CIRCEP.113.000334

Laurita, K. R., and Singal, A. (2001). Mapping action potentials and calcium transients simultaneously from the intact heart. *Am. J. Physiol. Heart Circ. Physiol.* 280, H2053–H2060. doi: 10.1152/ajpheart.2001.280.5.H2053

Lee, P., Bollensdorff, C., Quinn, T. A., Wuskell, J. P., Loew, L. M., and Kohl, P. (2011). Single-sensor system for spatially resolved, continuous, and multiparametric optical mapping of cardiac tissue. *Heart Rhythm* 8, 1482–1491. doi: 10.1016/j.hrthm.2011.03.061

Lee, P., Calvo, C. J., Alfonso-Almazán, J. M., Quintanilla, J. G., Chorro, F. J., Yan, P., et al. (2017). Low-cost optical mapping systems for panoramic imaging of complex arrhythmias and drug-action in translational heart models. *Sci. Rep.* 7, 1–14. doi: 10.1038/srep43217

Lee, P., Klos, M., Bollensdorff, C., Hou, L., Ewart, P., Kamp, T. J., et al. (2012a). Simultaneous voltage and calcium mapping of genetically purified human induced pluripotent stem cell-derived cardiac myocyte monolayers. *Circ. Res.* 110, 1556–1563. doi: 10.1161/CIRCRESAHA.111.262535

Lee, P., Taghavi, F., Yan, P., Ewart, P., Ashley, E. A., Loew, L. M., et al. (2012b). In situ optical mapping of voltage and calcium in the heart. *PLoS ONE* 7, e42562. doi: 10.1371/journal.pone.0042562

Lee, P., Yan, P., Ewart, P., Kohl, P., Loew, L. M., and Bollensdorff, C. (2012c). Simultaneous measurement and modulation of multiple physiological parameters in the isolated heart using optical techniques. *Pflügers Arch. Eur. J. Physiol.* 464, 403–414. doi: 10.1007/s00424-012-1135-6

Li, W., Janardhan, A. H., Fedorov, V. V., Sha, Q., Schuessler, R. B., and Efimov, I. R. (2011). Low-energy multistage atrial defibrillation therapy terminates atrial fibrillation with less energy than a single shock. *Circ. Arrhythmia Electrophysiol.* 4, 917–925. doi: 10.1161/CIRCEP.111.965830

Loew, L. M. (1982). Design and characterization of electrochromic membrane probes. *J. Biochem. Biophys. Methods* 6, 243–260. doi: 10.1016/0165-022X(82)90047-1

Louch, W. E., Hake, J., Jølle, G. F., Mørk, H. K., Sjaastad, I., Lines, G. T., et al. (2010). Control of ca2+ release by action potential configuration in normal and failing murine cardiomyocytes. *Biophys. J.* 99, 1377–1386. doi: 10.1016/j.bpj.2010.06.055

Ma, Y., Shaik, M. A., Kim, S. H., Kozberg, M. G., Thibodeaux, D. N., Zhao, H. T., et al. (2016). Wide-field optical mapping of neural activity and brain haemodynamics: considerations and novel approaches. *Philos. Trans. R. Soc. B Biol. Sci.* 371, 20150360. doi: 10.1098/rstb.2015.0360

Marina-Breysse, M., Garcia-Escolano, A., Vila-Garcia, J., Reale-Nosei, G., Alfonso-Almazán, J. M., Yan, P., et al. (2021). A complete and low-cost cardiac optical mapping system in translational animal models. *Front. Physiol.* 12, 696270. doi: 10.3389/fphys.2021.696270

Matson, M., Carlsson, N., Beke-Somfai, T., and Nordén, B. (2012). Spectral properties and orientation of voltage-sensitive dyes in lipid membranes. *Langmuir* 28, 10808–10817. doi: 10.1021/la301726w

Nelson, M., Patlak, J., Worley, J., and Standen, N. (1990). Calcium channels, potassium channels, and voltage dependence of arterial smooth muscle tone. *Am. J. Physiol. Cell Physiol.* 259, C3–C18. doi: 10.1152/ajpcell.1990.259.1.C3

Nič, M., Jirát, J., Košata, B., Jenkins, A., and McNaught, A. (2009). *IUPAC Compendium of Chemical Terminology*. IUPAC, Research Triagle Park, NC.

Packer, M. (1985). Sudden unexpected death in patients with congestive heart failure: a second frontier. *Circulation* 72, 681–685. doi: 10.1161/01.CIR.72.4.681

Paredes, J., Pollnow, S., Dössel, O., and Salinet, J. (2020). "The influence of cardiac ablation on the electrophysiological characterization of rat isolated atrium: preliminary analysis," in *2020 Computing in Cardiology* (Rimini: IEEE), 1–4. doi: 10.22489/CinC.2020.265

Pastore, J. M., Girouard, S. D., Laurita, K. R., Akar, F. G., and Rosenbaum, D. S. (1999). Mechanism linking t-wave alternans to the genesis of cardiac fibrillation. *Circulation* 99, 1385–1394. doi: 10.1161/01.CIR.99.10.1385

Pollnow, S., Schwaderlapp, G., Loewe, A., and Dössel, O. (2020). Monitoring the dynamics of acute radiofrequency ablation lesion formation in thin-walled atria-a simultaneous optical and electrical mapping study. *Biomed. Eng.* 65, 327–341. doi: 10.1515/bmt-2019-0013

Rad, M. S., Choi, Y., Cohen, L. B., Baker, B. J., Zhong, S., Storace, D. A., et al. (2017). Voltage and calcium imaging of brain activity. *Biophys. J.* 113, 2160–2167. doi: 10.1016/j.bpj.2017.09.040

Scull, J. A., McSpadden, L. C., Himel, H. D., Badie, N., and Bursac, N. (2012). Single-detector simultaneous optical mapping of V_m and $[Ca^{2+}]_i$ in cardiac monolayers. *Ann. Biomed. Eng.* 40, 1006–1017. doi: 10.1007/s10439-011-0478-z

Shiferaw, Y., and Karma, A. (2006). Turing instability mediated by voltage and calcium diffusion in paced cardiac cells. *Proc. Natl. Acad. Sci. U.S.A.* 103, 5670–5675. doi: 10.1073/pnas.0511061103

Shynkar, V. V., Klymchenko, A. S., Duportail, G., Demchenko, A. P., and Mély, Y. (2004). "Ratiometric fluorescence measurements and imaging of the dipole potential in cell plasma membranes," in *Biophotonics Micro-and Nano-Imaging* (Strasbourg: International Society for Optics and Photonics), 118–130. doi: 10.1117/12.545768

Sidorov, V. Y., Uzelac, I., and Wikswo, J. P. (2011). Regional increase of extracellular potassium leads to electrical instability and reentry occurrence through the spatial heterogeneity of apd restitution. *Am. J. Physiol. Heart Circ. Physiol.* 301, H209–H220. doi: 10.1152/ajpheart.01141.2010

Streit, J., and Kleinlogel, S. (2018). Dynamic all-optical drug screening on cardiac voltage-gated ion channels. *Sci. Rep.* 8, 1–13. doi: 10.1038/s41598-018-19412-z

Tai, D. C.-S., Caldwell, B. J., LeGrice, I. J., Hooks, D. A., Pullan, A. J., and Smaill, B. H. (2004). Correction of motion artifact in transmembrane voltage-sensitive fluorescent dye emission in hearts. *Am. J. Physiol. Heart Circ. Physiol.* 287, H985–H993. doi: 10.1152/ajpheart.00574.2003

Tomaselli, G. F., and Zipes, D. P. (2004). What causes sudden death in heart failure? *Circ. Res.* 95, 754–763. doi: 10.1161/01.RES.0000145047.14691.db

Turrini, L., Fornetto, C., Marchetto, G., Müllenbroich, M., Tiso, N., Vettori, A., et al. (2017). Optical mapping of neuronal activity during seizures in zebrafish. *Sci. Rep.* 7, 1–12. doi: 10.1038/s41598-017-03087-z

Uzelac, I., Crowley, C. J., and Fenton, F. H. (2019). "Isosbestic point in optical mapping theoretical and experimental determination with di-4-anbdqpq

transmembrane voltage sensitive dye," in *2019 Computing in Cardiology Conference (CinC)* (Singapore: IEEE), 1.

Uzelac, I., and Fenton, F. H. (2015). "Robust framework for quantitative analysis of optical mapping signals without filtering," in *2015 Computing in Cardiology Conference (CinC)* (Nice: IEEE), 461–464. doi: 10.1109/CIC.2015.7408686

Uzelac, I., and Fenton, F. H. (2020). "Personalized low-energy defibrillation through feedback based resynchronization therapy," in *2020 Computing in Cardiology Conference (CinC)* (Rimini: IEEE), 1–4. doi: 10.22489/CinC.2020.471

Uzelac, I., Iravanian, S., Ashikaga, H., Bhatia, N. K., Herndon, C., Kaboudian, A., et al. (2020). Fatal arrhythmias: Another reason why doctors remain cautious about chloroquine/hydroxychloroquine for treating covid-19. *Heart Rhythm*. 17, 1445–1451. doi: 10.1016/j.hrthm.2020.05.030

Uzelac, I., Ji, Y. C., Hornung, D., Schröder-Scheteling, J., Luther, S., Gray, R. A., et al. (2017). Simultaneous quantification of spatially discordant alternans in voltage and intracellular calcium in langendorff-perfused rabbit hearts and inconsistencies with models of cardiac action potentials and ca transients. *Front. Physiol*. 8, 819. doi: 10.3389/fphys.2017.00819

Uzelac, I., Kaboudian, A., Iravanian, S., Siles-Paredes, J. G., Gumbart, J. C., Ashikaga, H., et al. (2021). Quantifying arrhythmic long qt effects of hydroxychloroquine and azithromycin with whole-heart optical mapping and simulations. *Heart Rhythm* 2, 394–404. doi: 10.1016/j.hroo.2021.06.008

van Veen, R. L., Sterenborg, H., Pifferi, A., Torricelli, A., and Cubeddu, R. (2004). "Determination of vis-nir absorption coefficients of mammalian fat, with time-and spatially resolved diffuse reflectance and transmission spectroscopy," in *Biomedical Topical Meeting* (Miami: Optical Society of America), doi: 10.1364/BIO.2004.SF4

Venkatachalam, V., Ji, N., Wang, X., Clark, C., Mitchell, J. K., Klein, M., et al. (2016). Pan-neuronal imaging in roaming caenorhabditis elegans. *Proc. Natl. Acad. Sci. U.S.A*. 113, E1082–E1088. doi: 10.1073/pnas.1507109113

Verrier, R. L., Kumar, K., and Nearing, B. D. (2009). Basis for sudden cardiac death prediction by t-wave alternans from an integrative physiology perspective. *Heart Rhythm* 6, 416–422. doi: 10.1016/j.hrthm.2008.11.019

Virani, S. S., Alonso, A., Benjamin, E. J., Bittencourt, M. S., Callaway, C. W., Carson, A. P., et al. (2020). Heart disease and stroke statistics-2020 update: a report from the american heart association. *Circulation* 141, e139–e596. doi: 10.1161/CIR.0000000000000757

Walker, M. L., and Rosenbaum, D. S. (2003). Repolarization alternans: implications for the mechanism and prevention of sudden cardiac death. *Cardiovasc. Res*. 57, 599–614. doi: 10.1016/S0008-6363(02)00737-X

Watanabe, M. A., Fenton, F. H., Evans, S. J., Hastings, H. M., and Karma, A. (2001). Mechanisms for discordant alternans. *J. Cardiovasc. Electrophysiol*. 12, 196–206. doi: 10.1046/j.1540-8167.2001.00196.x

Yang, S.-N., and Berggren, P.-O. (2006). The role of voltage-gated calcium channels in pancreatic β-cell physiology and pathophysiology. *Endocrine Rev*. 27, 621–676. doi: 10.1210/er.2005-0888

Conflict of Interest: IU is the owner of Aleksa Tech Inc., a manufacturer of power sources for LED illumination in optical mapping measurements.

The remaining authors declare that the research was conducted in the absence of any commercial or financial relationships that could be construed as a potential conflict of interest.

Publisher's Note: All claims expressed in this article are solely those of the authors and do not necessarily represent those of their affiliated organizations, or those of the publisher, the editors and the reviewers. Any product that may be evaluated in this article, or claim that may be made by its manufacturer, is not guaranteed or endorsed by the publisher.

frontiers in Physiology

ORIGINAL RESEARCH
published: 10 March 2022
doi: 10.3389/fphys.2022.812535

A Mathematical Model for Electrical Activity in Pig Atrial Tissue

Víctor Peris-Yagüe[1,2], *Tony Rubio*[3,4], *Funsho E. Fakuade*[3,4,5], *Niels Voigt*[3,4,5], *Stefan Luther*[1,3,4] *and Rupamanjari Majumder*[1,3,4]*

[1] Biomedical Physics Group, Max Planck Institute for Dynamics and Self Organisation, Gottingen, Germany, [2] Centre de Formaćio Interdisciplinària Superior (CFIS), Universitat Politècnica de Catalunya, Barcelona, Spain, [3] Institute of Pharmacology and Toxicology, University Medical Center Göttingen, Georg-August University, Gottingen, Germany, [4] German Center for Cardiovascular Research (DZHK), Partner Site Göttingen, Gottingen, Germany, [5] Cluster of Excellence "Multiscale Bioimaging: From Molecular Machines to Networks of Excitable Cells" (MBExC), Georg-August University, Gottingen, Germany

State of the art mathematical models are currently used to bridge the gap between basic research conducted in the laboratory and preclinical research conducted on large animals, which ultimately paves the way for clinical translation. In this regard, there is a great need for models that can be used alongside experiments for in-depth investigation and validation. One such experimental model is the porcine atrium, which is commonly used to study the mechanisms of onset and control of atrial fibrillation in the context of its surgical management. However, a mathematical model of pig atria is lacking. In this paper, we present the first ionically detailed mathematical model of porcine atrial electrophysiology, at body temperature. The model includes 12 ionic currents, 4 of which were designed based on experimental patch-clamp data directly obtained from literature. The formulations for the other currents are adopted from the human atrial model, and modified for porcine specificity based on our measured restitution data for different action potential characteristics: resting membrane potential, action potential amplitude, maximum upstroke velocity and action potential duration and different levels of membrane voltage repolarization. The intracellular Ca^{2+} dynamics follows the Luo-Rudy formulation for guinea pig ventricular cardiomyocytes. The resulting model represents "normal" cells which are formulated as a system of ordinary differential equations. We extend our model to two dimensions to obtain plane wave propagation in tissue with a velocity of 0.58 m/s and a wavelength of 8 cm. The wavelength reduces to 5 cm when the tissue is paced at 200 ms. Using S1-S2 cross-field protocol, we demonstrate in an 11.26 cm square simulation domain, the ability to initiate single spiral waves (rotation period $\simeq$ 180 ms) that remain stable for more than 40 s. The spiral tip exhibits hypermeander. In agreement with previous experimental results using pig atria, our model shows that early repolarization is primarily driven by a calcium-mediated chloride current, I_{ClCa}, which is completely inactivated at high pacing frequencies. This is a condition that occurs only in porcine atria. Furthermore, the model shows spatiotemporal chaos with reduced repolarization.

Keywords: ionic model, pig atria, spiral waves, large animal, cardiac electrophysiology

OPEN ACCESS

Edited by:
Richard David Walton,
Université de Bordeaux, France

Reviewed by:
Arun V. Holden,
University of Leeds, United Kingdom
Oleg Aslanidi,
King's College London,
United Kingdom
Carlos Sanchez,
University of Zaragoza, Spain

***Correspondence:**
Rupamanjari Majumder
rupamanjari.majumder@ds.mpg.de

Specialty section:
This article was submitted to Cardiac Electrophysiology, a section of the journal Frontiers in Physiology

Received: *10 November 2021*
Accepted: *28 January 2022*
Published: *10 March 2022*

Citation:
Peris-Yagüe V, Rubio T, Fakuade FE, Voigt N, Luther S and Majumder R (2022) A Mathematical Model for Electrical Activity in Pig Atrial Tissue. Front. Physiol. 13:812535. doi: 10.3389/fphys.2022.812535

1. INTRODUCTION

Atrial fibrillation (AF) is the most common sustained form of cardiac arrhythmia occurring in humans. Its effective treatment requires a detailed understanding of the underlying mechanisms at the genetic, molecular, cellular, tissue and organ levels. To study the complex mechanisms underlying the development, maintenance and termination of cardiac arrhythmias, preclinical research models are required. These models range from *in vitro* cell cultures to *in vivo* small and large animal hearts. However, translational research necessitates a proper understanding of the results from animal experiments in the human context, for which it is very important that the preclinical results are well-understood and validated. Currently, this is achieved through simulations of state-of-the-art mathematical models alongside experimentation on large animals. In particular, a model that is extensively used by experimentalists to advance surgical management of AF, is that of the pig atria. However, until now, an ionically detailed mathematical model for pig atrial tissue has been lacking, and researchers have been forced to rely on mathematical models from other animal species to understand their experimental observations.

Typical large animal heart models include that of dog, sheep, goat, pig, etc. In studies on cardiac arrhythmias, especially atrial fibrillation (AF) it is a challenge to find the right animal model. This is mainly because the reliable inducibility of sustained AF requires some form of chronic intervention, which is often associated with a large cost of maintenance and time limitations. The porcine atrial model overcomes this challenge by providing an acute, reliable and reproducible model for sustained AF (Lee et al., 2016). This model can be used at length to test experimental procedures and drugs that are intended for translational purposes under various disease conditions. To make matters more favorable, the cardiac anatomy, electrophysiology and coronary circulation of pigs are very similar to those of humans (e.g., heart mass: 148–383 g in humans vs. 250–400 g in pigs; heart to body mass ratio: 0.4 in humans vs. 0.32 in pigs; heart rate: 60–80 in humans vs. 68–100 in pigs, etc.) For a detailed comparison of human and pig parameters, we refer the reader to Table 1 of Clauss et al. (2020). Thus, an electrophysiologically detailed mathematical model of the porcine atria is definitely a important tool to have in translational research.

In this study, we present the first detailed mathematical model of the pig atria, based on experimental patch-clamp data from literature and our own restitution experiments on pig atrial tissue, using sharp-electrode technique. In two dimensions, we demonstrate its ability to produce and sustain stable meandering spiral waves. We characterize the spatiotemporal meander pattern, report the dominant frequencies and the effect of system size on the stability of the spiral pattern. In particular, we highlight some fundamental differences in the role of Cl^- currents and Ca^{2+} dynamics in the early repolarisation phase of AP in pigs with respect to humans, a crucial difference to be accounted for in the translatability of results, from pigs to humans, in future *in vitro* and *in vivo* experiments. We further go on to propose a model for AF using an altered set of parameters that allows us to have a state of electric turbulence in pig atrial tissue.

2. MATERIALS AND METHODS

All animal care and use procedures were carried out exclusively by appropriately trained staff and were in accordance with the German Animal Welfare Act and reported to the local animal welfare officers. The handling of the animals prior to the experiments and the humane, animal welfare procedures strictly followed animal welfare regulations, in accordance with German legislation, local regulations and the recommendations of the Federation of European Laboratory Animal Science Associations (FELASA). All scientists and technicians involved have been accredited by the responsible ethics committee (Lower Saxony State Office for Consumer Protection and Food Safety - LAVES).

Experimental Recordings

Trabecular muscles were isolated and excised from a whole right atria, and placed in a custom-built recording chamber under continuous perfusion of heated (37°C) and carbonated (5% CO_2, 95% O_2) Tyrode's solution containing (in mM): NaCl 126.7, KCl 5.4, $MgCl_2$ 1.1, $CaCl_2$ 1.8, $NaHPO_4$ 0.42, $NaHCO_3$ 22, glucose 5.5, pH = 7.45 at least 45 min before measurement, for accommodation.

Borosilicate glass capillaries (Hilgenberg, Germany) were pulled using a horizontal pipette puller (Zeitz, Germany). Electrical resistance was 30–40 MΩ. Pipettes were backfilled with 3M KCl.

Tissues were electrically stimulated with a 1 ms monophasic pulse using a custom-made electrode (FHC, USA). Pulse amplitude was pre-defined as 30% higher than the value necessary to trigger an action potential. After successful tissue impalement, and after reaching steady state activity, the tissue was then subjected to a train of electrical stimulation at increasing frequencies (0.25, 0.5, 1, 2, 3, and 4 Hz). AP onset at 5 Hz proved difficult and inconsistent.

Membrane potential signals were amplified using a Sec-05-X (npi, Germany) amplifier, digitized using LabChart PowerLab, and acquired and saved with LabChart Pro 7 software (both: ADInstruments, New Zealand).

Analysis was performed using LabChart pro and GraphPad Prism 7 (GraphPad Software Inc., USA). The average value of 10 consecutive action potentials were calculated in LabChart Pro. The following parameters were measured: resting membrane potential (RMP), action potential maximum upstroke velocity (dV/dtmax), action potential amplitude (APA) and the action potential duration at 20, 50 and 90% of repolarisation (APD_{20}, APD_{50}, and APD_{90}, respectively).

Mathematical Model

The fitting of IV curves from experimental data by Li et al. (2004) was carried out by minimization of the squared error between the simulated and experimental data using Python's Scipy module (Virtanen et al., 2020). For this purpose, a function was created in Python that would recreate the patch-clamp experiments as in Li et al. (2004), and output the simulated IV curve. The

morphology of each individual current and its gating variables was initially taken directly from the human atrial model by Courtemanche et al. (1998) and corrected accordingly to match experimental data. Fitting was done by matching normalized IV curves first, and then adjusting conductance values to match the non-normalized experimental IV curves.

Overall AP morphology and restitution curves were later matched by re-adjusting conductance values of the different currents, and simulating AP evolution for stimulation at different cycle lengths. Slight changes were made to currents not fitted from Li et al. (2004) to better adjust experimental restitution curves. See the Results section for detailed explanations of each individual current.

3. RESULTS

We developed a mathematical model for a native atrial cardiomyocyte, isolated from the excised atrium of a healthy adult pig. The equivalent electrical circuit representing the cell membrane is shown in **Figure 1**.

It consists of a membrane capacitance, C_m, connected in parallel with several nonlinear conductances (G_X) and batteries (E_X). The net current (I_{ion}) flowing across the cell membrane at any instant is the sum of individual currents flowing through the various branches of the circuit. Thus, the time-evolution of the transmembrane voltage V can be described using the following ordinary differential equation. (Equation 1)

$$\frac{dV}{dt} = -\frac{I_{ion} + I_{stim}}{C_m} \tag{1}$$

Here I_{stim} represents the external stimulus current that needs to be applied to the cell membrane to invoke an action potential (AP). We describe I_{ion} as a sum of 12 ionic currents (Equation 2):

$$\begin{aligned} I_{ion} = {} & I_{Na} + I_{K1} + I_{ClCa} + I_{Kur} + I_{Kr} + I_{Ks} \\ & + I_{Ca,L} + I_{p,Ca} + I_{NaK} \\ & + I_{NaCa} + I_{b,Na} + I_{b,Ca} \end{aligned} \tag{2}$$

V is measured in millivolts (mV), time (t) in milliseconds (ms), C_m in picofarads (pF), and all currents in picoamperes per picofarad (pA/pF). All conductances G_X are measured in nanosiemens per picofarad (nS/pF), and intracellular and extracellular ionic concentrations ($[X]_i$, $[X]_o$) are expressed in milimolar (mM). The fast Na^+ current is represented by I_{Na}, the inward rectifier K^+ current by I_{K1}, ultrarapid rectifier K^+ current is given by I_{Kur}, rapid and slow delayed rectifier K^+ currents by I_{Kr}, I_{Ks}, respectively, *L-Type* Ca^{2+} current by $I_{Ca,L}$, Ca^{2+} pump current by $I_{p,Ca}$, the Sodium-Potassium and Sodium-Calcium pump currents by I_{NaK}, I_{NaCa}, respectively, and the background Na^+ and Ca^{2+} currents by $I_{b,Na}$, $I_{b,Ca}$, respectively. Uniquely in the pig atrial model, the transient outward current is represented only by a calcium-mediated chloride current, I_{ClCa}.

The formulation of subcellular Ca^{2+} uptake and release by the sarcoplasmic reticulum (SR) is retained from the work of Luo and Rudy (1994). The three main currents involved are the Ca^{2+} uptake current, I_{up}, the Ca^{2+} release current I_{rel} and the Ca^{2+} transfer current between the network SR (NSR) and junctional SR (JSR), I_{tr}. The model also includes a leak current from the SR into the cytoplasm, $I_{up,leak}$, as described by Courtemanche et al. in their model for the human atrial cardiomyocyte (Courtemanche et al., 1998).

To invoke action potentials in tissue, we applied a stimulus current of 7 nA for 4 ms. The mathematical description of each ionic current is provided in the **Supplementary Appendix**, together with a list of model parameters and initial values.

Membrane Currents

Fast Sodium, I_{Na}

We describe the fast Na^+ current according to the Courtemanche-Ramirez-Nattel (CRN) model for human atrial cardiomyocytes (Courtemanche et al., 1998), which uses a Hodgkin-Huxley type formulation (see Equation 3) taken from the Luo-Rudy model (Luo and Rudy, 1994):

$$I_{Na} = g_{Na} m^3 h j (V - E_{Na}) \tag{3}$$

Here m is the activation gate; h and j are the two inactivation gates. In order to make the model pig-specific, we used

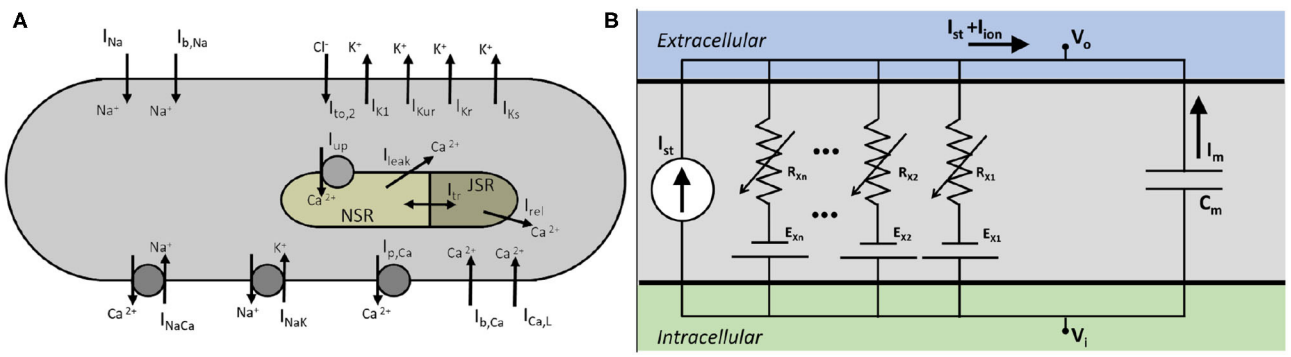

FIGURE 1 | (A) Schematics of a pig atrial cardiomyocyte model, showing transmembrane currents and the basic structure of the Ca^{2+} dynamics. **(B)** Electrical circuit equivalent of the cell.

Equation (3) to fit experimentally obtained I_{Na} current-voltage (IV) characteristics and/or current traces from patch-clamp measurements. However, in the absence of these experimental data, we followed an alternative approach. Since I_{Na} is the dominant active current during the upstroke phase of an AP, (the other current being the inward rectifier, I_{K1}, which is orders of magnitude smaller than I_{Na}), we considered it to be primarily responsible for the AP amplitude (APA) and maximum upstroke velocity ($\frac{dV}{dt}_{max}$). Thus, we used the complete model (considering all currents, pumps and exchangers) to fit experimentally obtained APA and $\frac{dV}{dt}_{max}$ data, at various pacing frequencies, i.e., APA- and $\frac{dV}{dt}_{max}$ restitution, by tuning only the I_{Na}.

Numerical fitting of these restitution data, using Equation (3) to describe I_{Na} instructed us to apply the following adaptations: (*i*) raise the maximum channel conductance (g_{Na}) by 80% with respect to humans; (*ii*) increase the time constant of activation (τ_m) by a factor 1.7; and (*iii*) increase the time constant of inactivation (τ_h, τ_j) by a factor 2. The kinetics of the activation and inactivation gates are shown in **Figures 2A,B**. With the applied modifications, the I_{Na} current traces turned out to be as in **Figure 2C** and the IV curve, as shown in **Figure 2D**.

L-Type Calcium Current, $I_{Ca,L}$

The L-type Ca^{2+} currrent ($I_{Ca,L}$) was modeled according to previous literature (Courtemanche et al., 1998; Ramirez et al., 2000; Pandit et al., 2001; Majumder et al., 2016), based on the Hodgkin-Huxley formalism:

$$I_{Ca,L} = g_{Ca,L} d f f_{Ca} (V - 65.0) \tag{4}$$

Here $g_{Ca,L}$ is the channel conductance, d and f the voltage-gated activation and inactivation variables, respectively, and f_{Ca} is a calcium-mediated gating variable defined by:

$$\tau_{f(Ca)} = 2, \quad f_{Ca,\infty} = \frac{1}{1 + \frac{[Ca^{2+}]_i}{0.00035}} \tag{5}$$

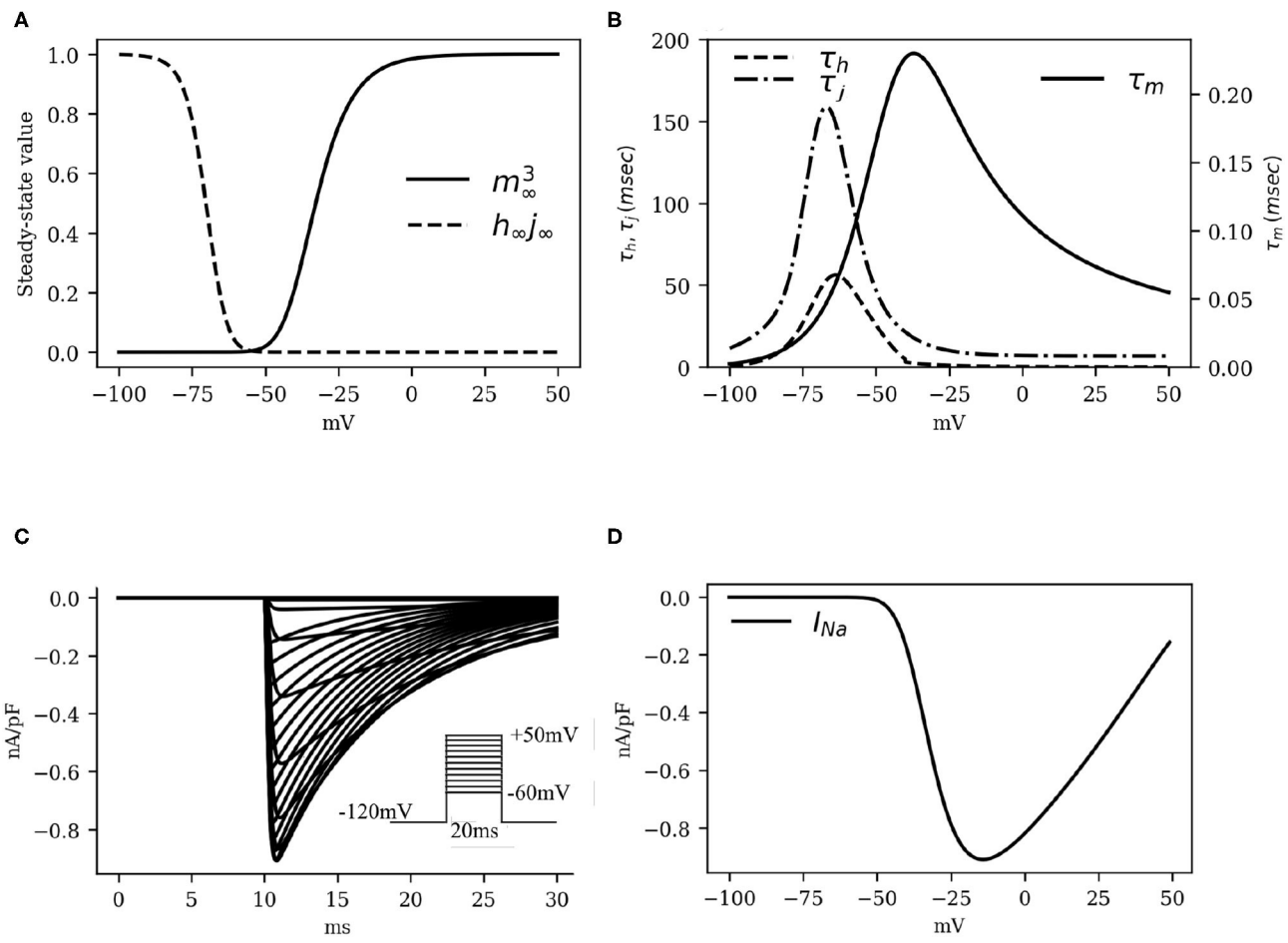

FIGURE 2 | The kinetics of the fast Na^+ current I_{Na}. **(A)** Activation and inactivation characteristics of the steady state gating variables m (raised to cubic power), h and j (combined as the product $h_\infty j_\infty$). **(B)** Voltage dependence of the time constants for activation (τ_m) and fast and slow inactivation (τ_h and τ_j, respectively). **(C)** Simulated traces of I_{Na} (traces at 5mV steps from minimum to maximum in the inset). **(D)** I_{Na} Current-Voltage characteristics.

In particular, the gating behavior of $I_{Ca,L}$ follows the human CRN model, with a $+5\,mV$ shift in the activation kinetics to decrease the activation window along with the overall $I_{Ca,L}$ that is necessary for the fitting of action potential duration restitution properties. As $I_{Ca,L}$ is considered to be largely responsible for the plateau phase of the action potential, decreasing (increasing) this current by small amounts can lead to sharp decrease (increase) in the action potential duration without lowering (raising) the resting membrane potential by substantial amounts. Our patch-clamp measurements showed that the amplitude of $I_{Ca,L}$ was $\simeq 3.25 \pm 0.75$ pA/pF. This value imposed a constraint on the choice of g_{CaL}. The kinetics of L-type Ca^{2+} channel, as well as the IV characteristics of the I_{CaL} are shown in **Figure 3**.

Inward Rectifier Potassium Current, I_{K1}

The I_{K1} is known to play a major role in determining the resting membrane potential (RMP) of excitable cardiac cells in many animal species, with the current reversing its direction of flow close to the actual RMP value. Given that our sharp-electrode measurements on pig atrial tissue suggested a more depolarised (positive) RMP value than that reported in human atrial cardiomyocytes (Courtemanche et al., 1998), we modified the parameters of the CRN I_{K1} formulation to make the current pig-specific.

To this end, (*i*) we shifted the reversal potential of I_{K1} by −5 mV, as has been done previously in some large animal models, such as the sheep (Butters et al., 2013), (*ii*) we reduced the maximum channel conductance of I_{K1} by 9% relative to the human model (Courtemanche et al., 1998), (*iii*) we decreased the slope of activation of the I_{K1} IV curve by 10%; and (*iv*) we shifted the half-rise potential by +10 mV. Thus, I_{K1} in the pig atrial model is described according to Equation (6). These adjustments enabled us to fit the shape of the action potential duration restitution curves at the 80–90% repolarization, while trying to balance the effects of $I_{Ca,L}$ and other rectifier currents. The IV curve for I_{K1} as shown in **Figure 4**.

$$I_{K1} = g_{K1} \cdot \frac{V - E_K - 5}{1 + exp(0.063 \cdot (V + 70))} \tag{6}$$

Ultrarapid Potassium Current, I_{Kur}

Recent work by Ehrlich et al. (2006), indicates that pig atrial tissue exhibits a bi-exponential inactivation. Pandit et al. (2011) developed a model for the ultrarapid K^+ current, that reproduces the experimental data of Ehrlich et al. (2006). We used the

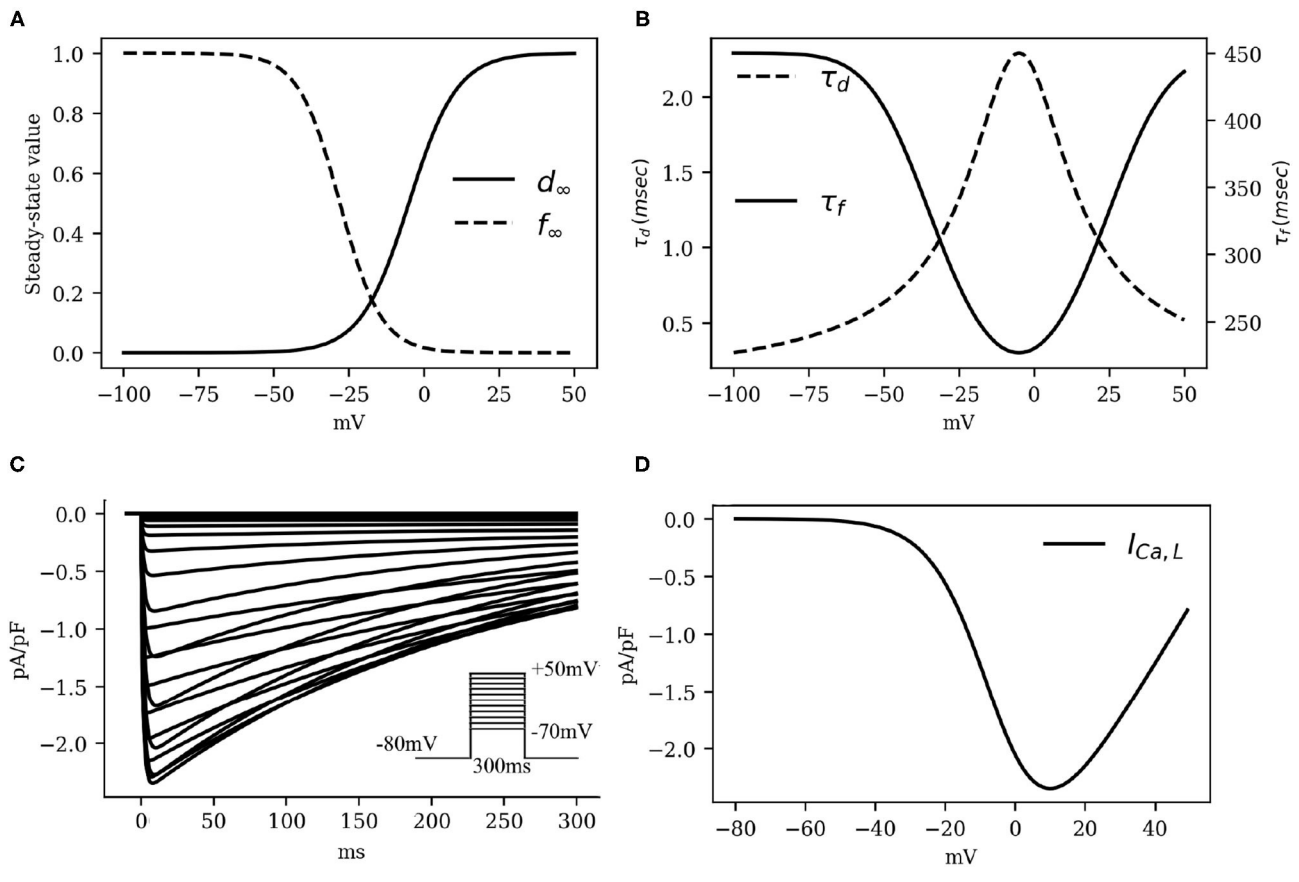

FIGURE 3 | The kinetics of the fast L-type Ca^{2+} current I_{CaL}. **(A)** Activation and inactivation characteristics of the steady state gating variables *d* and *f*. **(B)** Voltage dependence of the time constants for activation (τ_d) and voltage-gated inactivation (τ_f). **(C)** Simulated traces of I_{CaL} (traces at 5mV steps from minimum to maximum in the inset). Intracellular Ca^{2+} concentration was kept constant at $[Ca^{2+}]_i = 0.0001\,mM$. **(D)** I_{CaL} Current-Voltage characteristics.

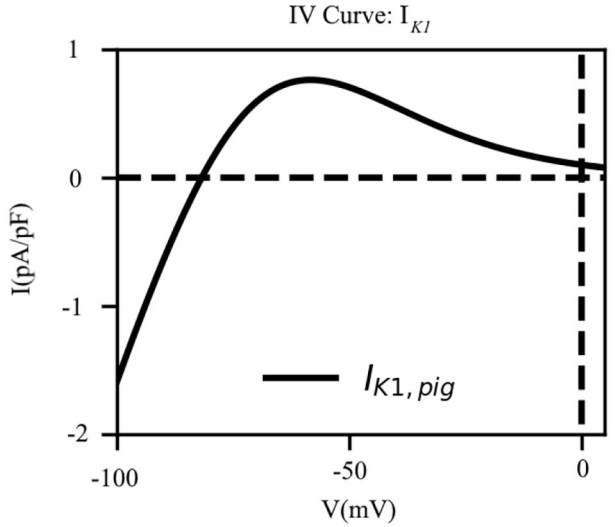

FIGURE 4 | The current-voltage characteristic of the inward rectifier K^+ current (I_{K1}). The direction of flow of the current across the cell membrane reverses at $E_K = -81.76\,mV$ which is close to our experimentally measured resting membrane potential.

formulation of Pandit et al. (2011) to describe I_{Kur} in our model for the pig atrial tissue (see Equation 7)

$$I_{Kur} = g_{Kur} \cdot u_a^3 \cdot (au_{i,f} + bu_{i,s}) \cdot (V - E_K) \tag{7}$$

Here g_{Kur} is the channel conductance, u_a the activation gate, E_K the reversal potential of K^+, and $u_{i,f}$ and $u_{i,s}$ the fast and slow inactivation components, respectively. $(a, b) = (0.25, 0.75)$ are weights applied to the inactivation gates. It is interesting to note that the approach by Pandit et al. is similar to that of Aguilar et al. for the human atria. However, in the latter case, the inactivation of I_{Kur} is given by $u_i = u_{i,f} \cdot u_{i,s}$ instead of a sum of the variables (Aguilar et al., 2017). The conductance of I_{Kur} is described according to Equation (8).

$$g_{Kur} = g_{Kur,amp}\left[0.005 + \frac{0.05}{1 + \exp(-\frac{V-15}{13})}\right] \tag{8}$$

Here $g_{Kur,amp}$ is an adjustable parameter whose value is determined during the final stages of model development (see section 3.2, for more details). **Figures 5A,B** show the activation and inactivation kinetics of I_{Kur}, whereas, a comparison between the current-voltage characteristics, as measured in experiments by Ehrlich et al. (2006) and that produced using our model, is presented in **Figure 5C**.

Rapid Delayed Rectifier Current, I_{Kr}

The rapid delayed rectifier current (I_{Kr}) was formulated similar to the original CRN model (Courtemanche et al., 1998), but with altered half-rise voltage ($V_{1/2}$), slope of the correction value, and the steady-state of the single gating variable, such that the obtained IV characteristic curve matches with the experimental IV curve of Li et al. (2004):

$$I_{Kr} = g_{Kr} \cdot x_r \cdot \frac{V - E_K}{1 + exp(\frac{V-79.4825}{8.2217})} \tag{9}$$

Initially, the conductance g_{Kr} was set at $0.0065\,pA/pF$ to match the non-normalized IV curve. However, this value was tuned during the final stages of model development to match the pig atrial APD restitution curves at the tissue level. The steady-state value ($x_{r,\infty}$) of the gating variable x_r is described according to Equation (10):

$$x_{r,\infty} = \frac{1}{1 + exp(\frac{-(V-4.4451)}{9.3305})} \tag{10}$$

Note that, $V_{1/2}$ of $x_{r,\infty}$ is shifted by $+20mV$ relative to the CRN model, whereas, the slope of the x_r kinetic is slightly decreased (Courtemanche et al., 1998). The gating behavior of x_r is described in **Figures 5D,E**. Unavailability of sufficient experimental data led us to retain the temporal dynamics of the gating variable x_r from the CRN model (Courtemanche et al., 1998). **Figure 5F** shows the comparison between the experimental and simulated IV curves for I_{Kr}.

Slow Delayed Rectifier Current, I_{Ks}

We retained the slow delayed rectifier current formulation from the original CRN model (Courtemanche et al., 1998):

$$I_{Ks} = g_{Ks} \cdot x_s^2 \cdot (V - E_K) \tag{11}$$

The maximum channel conductance g_{Ks} was adjusted to fit the restitution properties. The gating variable x_s, and time constant τ_s are described according to Equations (12) and (13), respectively.

$$x_{s,\infty} = \left[\frac{1}{1 + exp(-\frac{V-p_1}{p_2})}\right]^{1/2} \tag{12}$$

$$\tau_s = \frac{1}{2} \cdot \left[\frac{1}{4 \times 10^{-5} \cdot \frac{(V-p_1)}{1-exp(-\frac{V-p_1}{17})} + 3.5 \times 10^{-5} \cdot \frac{(V-p_1)}{exp(\frac{V-p_1}{9})-1}}\right], \tag{13}$$

Here, parameters p_1 and p_2 have values 18.802 and 12.6475 mV, respectively, obtained by fitting experimental data from Li et al. (2004). The close resemblance of these values with those used in the human atrial tissue model (Courtemanche et al., 1998) suggests that electrophysiologically, human atrial I_{Ks} and pig atrial I_{Ks} are very similar. **Figures 5G,H** show the steady state kinetic and time constant, respectively, of I_{Ks}, whereas, the model-generated IV curve is compared with experimental data from Li et al. in **Figure 5I**.

Transient Outward Current, I_{to}

I_{to} in most species is composed of two components: a potassium current ($I_{to,1}$) and a chloride current ($I_{to,2}$, also referred to as I_{ClCa}).

$$I_{to} = I_{to,1} + I_{to,2} = I_{to,1} + I_{ClCa} \tag{14}$$

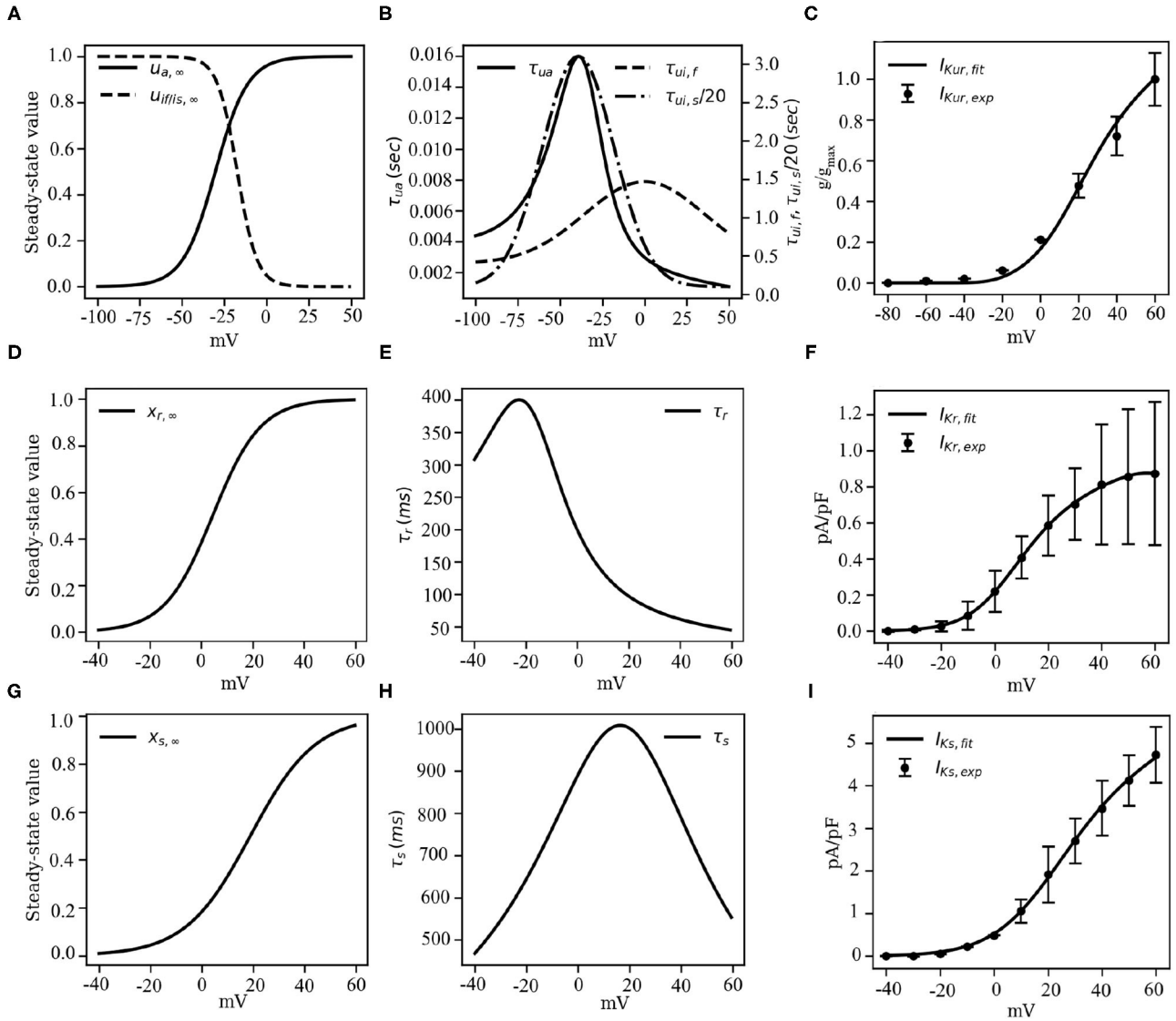

FIGURE 5 | Channel kinetics and current-voltage characteristics of the rectifying K^+ currents I_{Kur}, I_{Kr} and I_{Ks}. **(A)** Voltage-dependence of steady-state activation ($u_{s,\infty}$) and inactivation ($u_{if,\infty}$ of $u_{is,\infty}$) probabilities of I_{Kur}. **(B)** Voltage-dependence of the time constants of activation (τ_{ui}) and inactivation (τ_{uf} or τ_{us}) of I_{Kur}, reduced by a factor of 20. **(C)** Comparison between the model-generated IV curve for I_{Kur} and the IV curve reported by Ehrlich et al. (2006) based on experiments. **(D)** Voltage-dependence of steady-state activation ($x_{r,\infty}$) probability of I_{Kr}. **(E)** Voltage-dependence of the time constant of activation (τ_r) of I_{Kr}. **(F)** Comparison between the model-generated IV curve for I_{Kr} and the experimentally obtained IV curve from Li et al. (2004). **(G)** Voltage-dependence of steady-state activation ($x_{s,\infty}$) probability of I_{Ks}. **(H)** Voltage-dependence of the time constant of activation (τ_s) of I_{Ks}. **(I)** Comparison between the model-generated IV curve for I_{Ks} and the experimentally obtained IV curve from Li et al. (2004).

Although the presence of I_{ClCa} has been reported in multiple species and tissues (Zygmunt and Gibbons, 1991; Gomis-Tena and Saiz, 1998; Ramirez et al., 2000; Xu et al., 2002; Bondarenko et al., 2004; Wang and Sobie, 2008), including human atria (Wang et al., 1987, 1993), it is generally observed that $I_{to,1}$ forms the predominant component, scoring over I_{ClCa} in both strength and duration of activity, as a transient outward current (Wang et al., 1993; Bondarenko et al., 2004). However, in a study by Li et al. (2004), it was reported that pig atrial I_{to} is unique, in the sense that it is a completely calcium-driven chloride current (Li et al., 2003, 2004; Schultz et al., 2007). Thus, in our model, we incorporated this feature by modeling I_{ClCa} according to Equation (15), and experimental data from Li et al. (2004).

$$I_{to} \equiv I_{ClCa} = g_{ClCa} \cdot q_{Ca}(V - E_{Cl}) \tag{15}$$

For the choice of formulation of I_{ClCa} we considered various candidates (Gomis-Tena and Saiz, 1998; Ramirez et al., 2000; Bondarenko et al., 2004; Wang and Sobie, 2008). In the end, we decided to use Equation (15), which is a formulation for I_{ClCa} in a canine atrial model (Ramirez et al., 2000). The reason for choosing this formulation was that it allowed a fairly accurate reproduction of the bell shape of the IV curve and the same

general upward trend present in the experimental data of Li et al. (2004).

Here g_{ClCa} is the channel conductance, E_{Cl} the Cl^- reversal potential and q_{Ca} the sole gating variable of the channel, which follows the typical gating behavior of a Hodgkin-Huxley-type gating variable:

$$q_{Ca}(t) = q_{Ca,\infty} - (q_{Ca,\infty} - q_{Ca,0}) \cdot e^{-\frac{t-t_0}{\tau_{Ca}}}$$
$$q_{Ca,\infty} = 1 - \left[\frac{1}{1 + \left(\frac{F_n}{1.1e-10}\right)^3}\right], \quad \tau_{Ca} = 2 \tag{16}$$

F_n is the flux of Ca^{2+} into the myoplasm. F_n shows a strong correlation with the sharp release of Ca^{2+} from the SR in the initial stages of AP (through the SR release current, I_{rel}), giving I_{ClCa} the fast dynamics of a transient outward current. Also, the inactivation of I_{rel} gives I_{ClCa} a significant bell-shape in its IV curve, something universally observed in I_{ClCa} (Tseng and Hoffman, 1989; Gomis-Tena and Saiz, 1998; Hiraoka et al., 1998; Ramirez et al., 2000). In the case of our model, we shifted the inactivation of I_{rel} by $+40\,mV$ and increased the slope of inactivation to fit experimental results from Li et al. (2004).

Figure 6 shows the IV curve for I_{ClCa}, as obtained using our model of the pig atrial tissue, overlaid on experimental data from Li et al. (2004). The simulated current activated earlier than in experiments, but with a good overall qualitative behavior.

Summary of Currents

Table 1 presents a summary of all currents adjusted in the model, along with references to the experimental data used and the parameters adjusted.

Restitution Studies

The cell model thus developed reflects ionic current properties obtained from different cell samples patched under different experimental conditions and by different groups around the world. It is unreasonable to expect that the resulting model would represent the electrophysiology of a real porcine atrial cell just by combining these currents. We need some degree of tuning to ensure that the resulting cell responds electrophysiologically in the same way as an average cell isolated from a porcine tissue sample. Therefore, we move to the next step in model development, i.e., tuning with restitution. Refining a model to ensure that it is able to reproduce the electrical properties of the heart at tissue and organ level requires detailed studies of

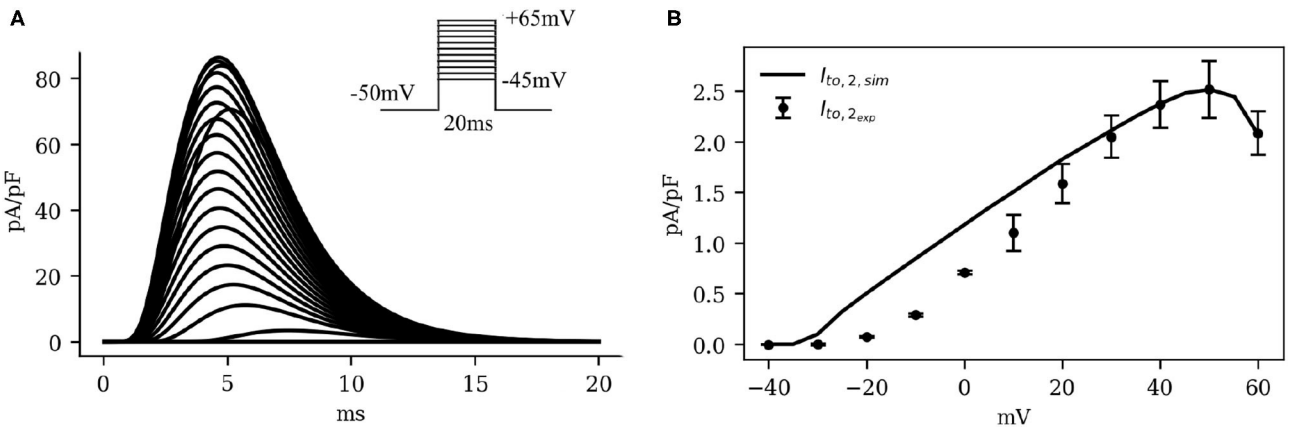

FIGURE 6 | (A) Simulated traces (traces at 5mV steps from minimum to maximum in the inset) and **(B)** Current-voltage characteristics of I_{ClCa}, showing experimental data (dots with error bars) from Li et al. (2004), overlaid on the model-generated curve (solid). Note the significant bell-shape of the curve at high positive voltage values.

TABLE 1 | Summary of currents.

Current	Source	Species	Parameters adjusted	Experimental data source
I_{Na}	Luo and Rudy (1994)	Guinea-pig	g_{Na}, τ_m, τ_h, τ_j	our APA and dV/dt_{max} restitution data
I_{K1}	Courtemanche et al. (1998)	Human	g_{K1}, slope, half-rise, reversal potential	our RMP and APD_{80}-APD_{90} restitution data
$I_{Ca,L}$	Courtemanche et al. (1998)	Human	$g_{Ca,L}$, d_∞, τ_d, τ_f, τ_j	our$APD_{20} - APD_{50}$ restitution and patch clamp data (for maximum current)
I_{Kur}	Pandit et al. (2011)	Pig	$g_{Kur,amp}$	our $APD_{10} - APD_{30}$ restitution data
I_{Kr}	Courtemanche et al. (1998)	Human	g_{Kr}, $x_{r,\infty}$	Li et al. (2004) and our $APD_{60} - APD_{90}$ restitution data
I_{Ks}	Courtemanche et al. (1998)	Human	g_{Ks}, $x_{s,\infty}$	Li et al. (2004) and our $APD_{60} - APD_{90}$ restitution data
$I_{Cl,Ca}$	Ramirez et al. (2000)	Dog	$g_{Cl,Ca}$, w(of I_{rel})	Li et al. (2004) and our $APD_{10} - APD_{20}$ restitution data
I_{NaK}	Luo and Rudy (1994)	Guinea-pig	$I_{NaK,max}$	our $APD_{70} - APD_{90}$ restitution data
I_{NaCa}	Luo and Rudy (1994)	Guinea-pig	$I_{NaCa,max}$	our $APD_{70} - APD_{90}$ restitution data

model restitution. In cardiac electrophysiology, restitution refers to the property by which parameters such as the duration of an electrical action potential (APD) or the conduction velocity (CV) of a propagating signal vary with time between successive stimuli applied to excitable cardiac tissue. In order to study restitution, the model was extended to higher spatial dimension.

Spatial Extension of the Model to Higher Dimensions

To simulate wave propagation in 1 dimension and above, we added a diffusion term to Equation 1, such that the spatiotemporal evolution of the voltage is given by

$$\frac{\partial V}{\partial t} = -\frac{I_{ion} + I_{stim}}{C_m} + D\nabla^2 V \tag{17}$$

We used a value 0.00126 cm^2/ms for the diffusion coefficient D. This choice of D allowed our model to reproduce the experimentally observed conduction velocity of 58 cm/s from Jang et al. (2019).

For numerical integration of Equation (17), we used a Forward Time Centered Space (FTCS) scheme, with a space differential $\Delta x = \Delta y = 0.022$ cm. The timestep chosen for the simulations was $\Delta t = 0.02$ ms and all coding was done using Python or C, with MPI-based parallelization.

Action Potential Duration (APD)

The amount of time, during an action potential, when the membrane voltage of an excited cardiac cell is more positive than a chosen threshold, is called the action potential duration (APD) at that threshold. Typically, this threshold value is measured on the basis of degree of repolarisation of the cell membrane. Thus, APD_X refers to the amount of time during an AP, when the cell membrane is more than X% repolarised, or, less than X% depolarised.

When cardiac tissue is electrically stimulated using a train of pulses at a particular frequency, the morphology of the AP adapts to the applied pacing frequency. This reflects in the APA, RMP, $\frac{dV}{dt}_{max}$ and APD values at all possible levels of repolarization. Such studies are conducted to investigate the restitution behavior of the model or the tissue sample. We performed sharp-electrode measurements on pig atrial tissue to obtain APD restitution (APDR) data. We used these data to make final adjustments to the model, to perfect its electrical response to high frequency stimulation. In both experiments and simulations, pig atrial tissue was stimulated at $0.25, 0.5, 1, 2, 3, 4\,Hz$, and action potentials were recorded.

We adjusted model parameters to find the most optimal parameter set that simultaneously fit each of these restitution curves with minimal deviation from measurement. Specifically, we adjusted the maximum conductance values of several currents. The final selection of conductance values is listed in **Table 2**.

The overlays of our experimental and simulated data for each of the following parameters: APA, RMP, $\frac{dV}{dt}_{max}$, and APD_X, for X = 10, 20, 30, 40, 50, 60, 70, 80, and 90% repolarization are shown in **Figure 7**.

TABLE 2 | Conductance values and maximal currents after fitting restitution data.

Conductance	Value (nS/pF)
g_{K1}	0.08218
g_{Na}	13.9900
$g_{Kur,amp}$	0.45539
g_{ClCa}	0.15731
g_{Kr}	0.01730
g_{Ks}	0.0594
$g_{Ca,L}$	0.06574
Maximal current	Value (pA/pF)
$I_{NaK,max}$	0.94935
$I_{NaCa,max}$	2304

Note that pig APDR curves show an interesting feature that distinguishes the model from most other mammalian species that we know of. In the early stages of repolarisation (i.e., up to APD_{50}), an overall downward trend is observed for stimulation cycle lengths greater than 1,000 ms (see **Figures 7D–H**). This could be due to inactivation of I_{ClCa} at high pacing frequencies: slower and lesser calcium uptake causes a decrease in I_{ClCa}, which significantly slows down initial AP repolarization, causing an overall higher early APD at high pacing frequencies with respect to low-frequency pacing.

To test this hypothesis, we measured intracellular calcium flux and I_{ClCa} in simulated restitution experiments. **Figure 8** shows the resulting restitution curves for peak calcium flux and peak I_{ClCa} at different stimulation cycle lengths in the simulated model. A clear dependence of peak values on cycle length can be observed, and both quantities decrease significantly with a decrease in cycle length. This is indeed indicative of an initial AP repolarization phase that is heavily dependent on calcium dynamics. To the best of our knowledge, this behavior is exclusive to the pig, and might have profound implications in the translatability of studies on arrhythmia control and termination from pigs to other species.

To summarize, the pig atrial model is capable of reproducing experimentally recorded porcine APs at different pacing frequencies within experimental deviations (**Figures 9A,E–G**). The discrepancies between the experimental traces show the variable nature of electrophysiology, in particular in the atria (Cherry and Fenton, 2007), and the model is good at finding a compromise and reproducing an AP with average traits within experimental tolerances. **Figures 9B–D** show the temporal evolution of each of the transmembrane currents considered in Equation (2). With this basic model, we now begin our study of electrical wave propagation at the tissue level.

Wave Propagation in 2D

Electrical stimulation of a quiescent 2D domain containing pig atrial cardiomyocytes leads to propagation of an excitation wave. Our studies confirm that at frequencies below 5 Hz, the paced waves propagate with uniform and identical wavefront and waveback conduction velocity. Electrical pacing at higher

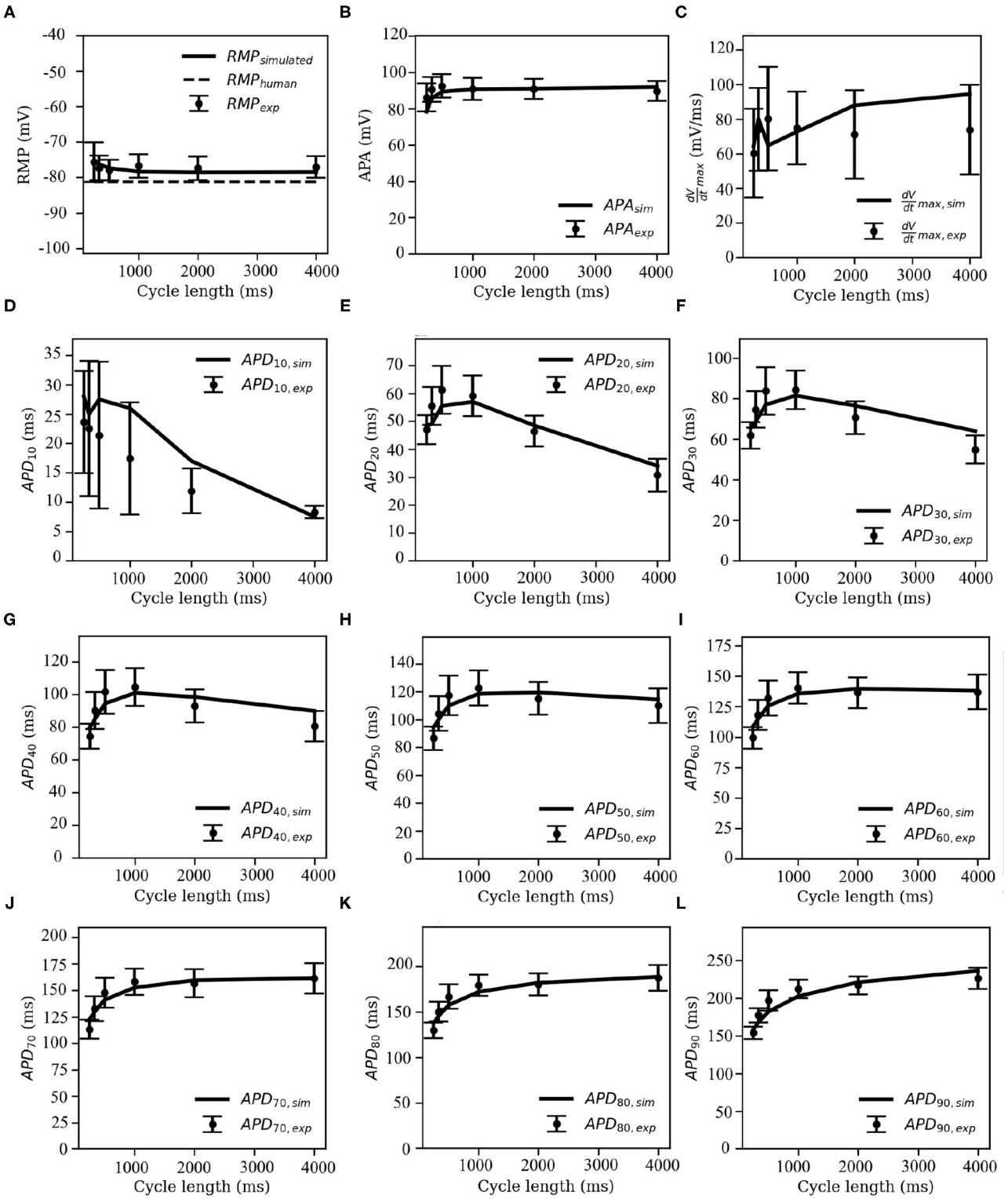

FIGURE 7 | Restitution curves for **(A)** resting membrane potential (RMP), **(B)** action potential amplitude (APA), **(C)** maximum upstroke velocity ($\frac{dV}{dt}_{max}$), and **(D–L)** action potential duration (APD_X), at $X = 10, 20, 30, 40, 50, 60, 70, 80$, and 90% repolarisation of the membrane voltage. Solid black lines indicate the model-generated data, whereas the markers (with error bars) represent our data obtained from sharp-electrode experiments.

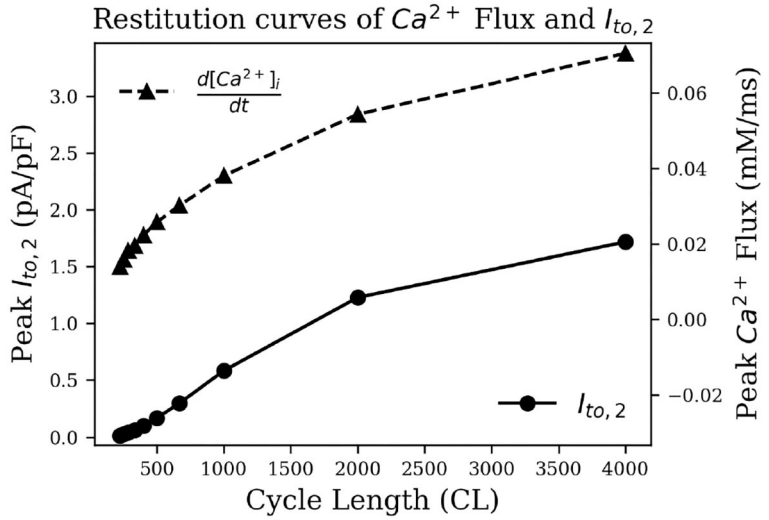

FIGURE 8 | Restitution curve of peak intracellular calcium flux (dashed) and peak I_{ClCa} (solid).

frequencies does not lead to 1:1 capture. This is because the effective refractory period of the cells is approximately 215 ms. **Figure 10A** shows snapshots of plane wave propagation through a 2D domain containing identical pig atrial cardiomyocytes. The simulated wavelength (WL, estimated as $WL = (t|_{back,-40mV} - t|_{wavefront}) \times CV$) and CV restitution curves are presented in **Figures 10B,C**.

Spiral Waves in the Pig Atria

Spiral Initiation

Using the reported parameter set in our 2D model, we produced a spiral wave that survived for more than 40 s of simulation time. To initiate a spiral wave in a domain containing 512× 512 grid points, we used the S1–S2 cross field protocol. We applied a line stimulus along the left edge of the domain to initiate a plane wave (S1) propagating toward the right (**Figure 10A**). As the waveback of the S1 wave crossed $x = 256$, a second stimulus (S2) is applied in the region $y \leq 256$ (**Figure 11A**, $t = 240$ ms). This leads to propagation of the S2 wave in the region that has recovered from excitation. With time, as the wave S1 wave moves out of the domain, more excitable tissue becomes available and a spiral prototype is formed (**Figure 11A**, $t = 280$ ms). **Figure 11A** shows the spatiotemporal formation and evolution of the spiral.

Spiral Characterization

The spiral wave in the pig atrial tissue model meanders with a shifting hypocycloidal trajectory. The trajectory of the tip of the spiral was traced by connecting the points of intersection of the isopotential line V = −35 mV and the line dV/dt = 0 at each snapshot, spaced 10 ms apart in time. An analysis of the tip trajectory shows that the basic pattern contains 5 outward petals enclosing a center (see **Figure 11B**), which shifts in space at the end of every 5 rotational cycles. A Fourier analysis of the tip trajectory reveals the existence of 4 fundamental frequencies (see **Figure 11C**), of which $f_0 = 5.426\,Hz$ and $f_1 = -3.548\,Hz$ are the dominant ones. These contribute to the construction of the basic hypocycloidal pattern, through superposition of the two counter-rotating circular orbits at the given frequencies, where the radii of the orbits are proportional to the heights of the peaks obtained from the Fourier Transform of the trajectory.

Alternans

A visual impression of the spatio-temporal distribution of membrane tension during spiral wave evolution (**Supplementary Video S1**) indicated the occurrence of wavelength fluctuations, as opposed to a constant, uniform wavelength observed during plane wave propagation. To quantify this effect, we measured APD_{90} from every 8^{th} node within the simulation domain in X- and Y- directions. We excluded points from the region that was close to the spiral tip.

Figure 12 shows the restitution curves of APD_{90} in the simulated spirals, both with respect to Cycle Length (CL) (**Figure 12A**) and Diastolic Interval (DI) (**Figure 12B**). **Figure 12A** shows the presence of alternans for cycle lengths in the range ≡ 165-215 ms. This is consistent with the restitution curve in **Figure 12B**, which focuses on the region with slope ≃ 1, a known predictor of the presence of alternans (Nolasco and Dailen, 1968). In a previous work Fakuade et al. (2021) demonstrated the occurrence of alternans at low stimulation frequencies in patients suffering from postoperative AF. Thus, our model can be used to develop useful insights into the origin and control of this alternans in pig atria.

To test if the unique current I_{ClCa} is responsible for alternans in the pig atrial model, we followed an approach that was first proposed by Gomis-Tena et al. (2003). Accordingly, we inhibited the I_{ClCa} (by 50 and 90% in two separate cases) in pig atrial model and re-initiated the spiral. However, unlike Gomis-Tena et al. (2003), alternans continued to exist in our model. APs in the simulated spiral have a duration of at most ≃ 225 ms.

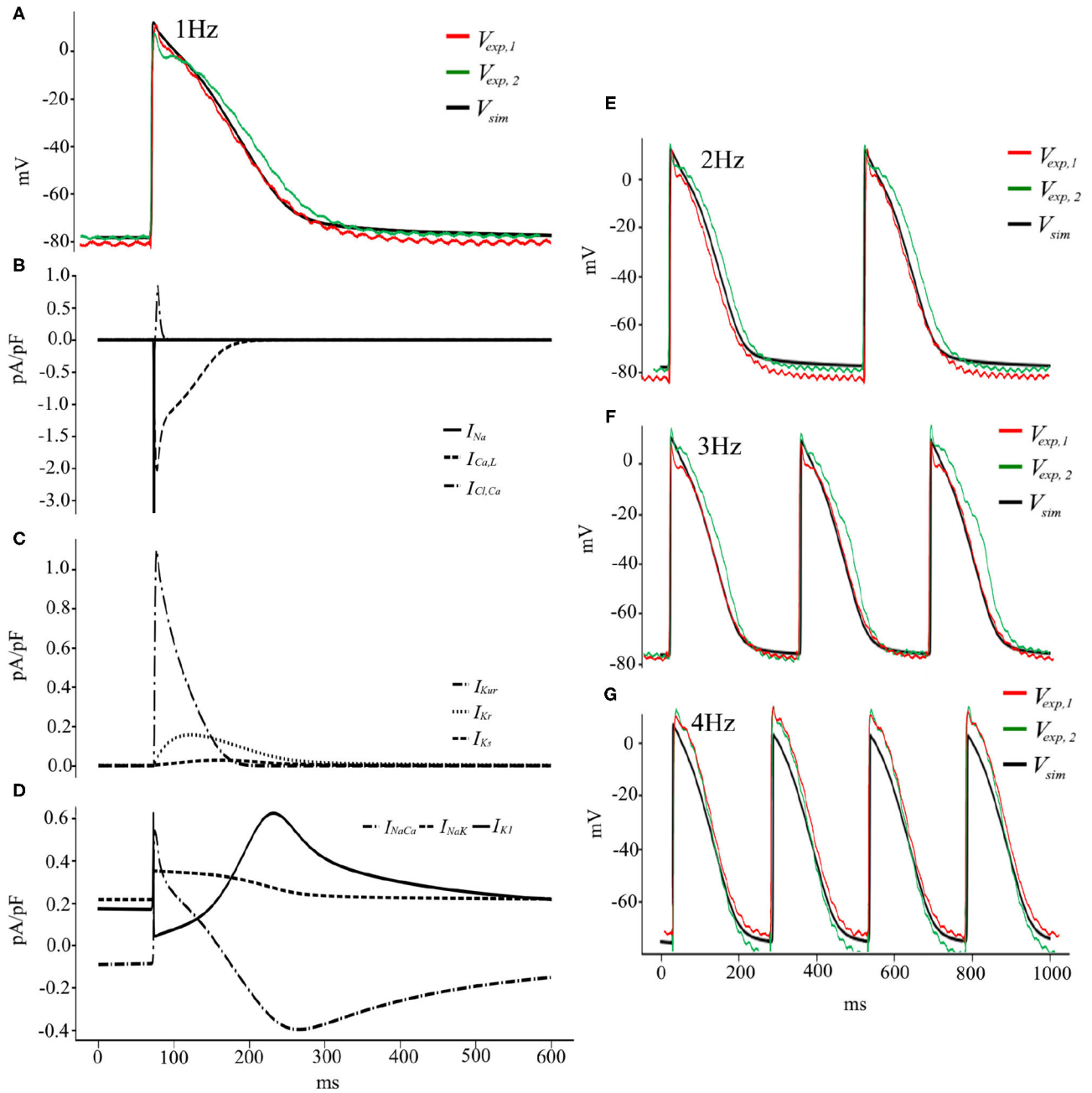

FIGURE 9 | (A) Voltage and Current traces **(B–D)** of a pig atrial action potential at 1 Hz pacing. Simulated (solid black) and experimentally measured (green and red) traces of AP recordings from cardiac tissue. **(E–G)** Voltage traces, both simulated (black) and experimental (green and red), at pacing frequencies of 2, 3, and 4 Hz, respectively.

Referring back to **Figure 8**, we can see that I_{ClCa} is naturally already shut off at such small cycle lengths, and any further inactivation will obviously have a negligible effect on the behavior of the resulting spiral.

Spiral Wave Breakup

Finally, we arrive at the most challenging question. Is it possible to use this model to study atrial fibrillation, with the spiral waves actually breaking up? The answer is, yes. The model does exhibit a state of sustained chaotic electrical activity in an altered parameter regime. Spiral wave breakup could be initiated by suppressing the repolarization reserve. In particular, a reduction of 75% in the value of $g_{Kr,max}$ could lead to a state characterized by more than six spiral waves. The spatiotemporal evolution of the spiral breakup state is demonstrated in **Figure 13** and in **Supplementary Video S2**.

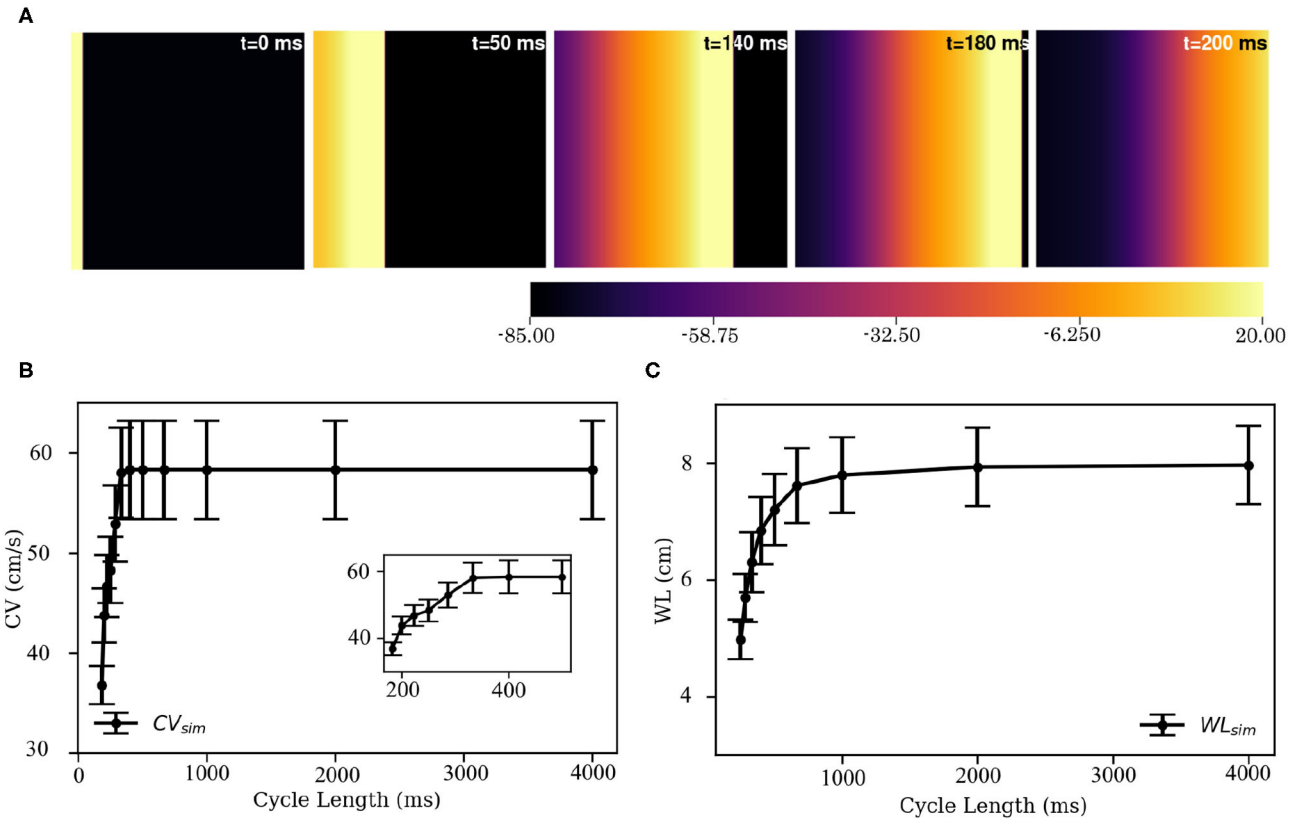

FIGURE 10 | Propagation of a plane wave through simulated 2D pig atrial tissue. **(A)** Shows snapshots of the propagating wave at different times. **(B,C)** Show the conduction velocity (CV) and wavelength (WL) restitution curves, as obtained from simulations.

4. DISCUSSION

In this study, we present the first complete mathematical model of the pig atrial tissue. It is built upon experimental data on pig atria as obtained from literature, and new sharp-electrode data that was produced in our laboratory. The model is numerically stable over long timescales, and is capable of reproducing pig atrial action potentials that can be compared closely with experiments. In particular, the AP characteristics, namely APD, CV, RMP, APA, and $\frac{dV}{dt}_{max}$ show excellent agreement with experiments, not only for a single evoked AP, but also for the full extent of their respective restitution curves. This confirms that our model is capable of reproducing the exact electrical response as can be expected from healthy pig atrial cardiomyocytes.

Our model takes into consideration the uniqueness of the constitution of the transient outward current. In most mammalian tissue, this current is found to be predominantly K^+ based. However, in pig atria, this current is solely Cl^--based and activated by the flow of Ca^{2+} ions. The unique dynamics of this current results in a downward trend of the early repolarization APD restitution curves; a feature that is not observed in most mammalian species. Our model reproduces this experimental trend in early APD restitution curves for large cycle lengths, and attributes the trend to the inactivation of the I_{ClCa} at low cycle lengths (Li et al., 2004).

In 2D, we demonstrate the model's ability to sustain stable spiral waves and spiral wave breakup, which adds to the suitability of the model for *in silico* studies of AF in extended media. To study spiral wave dynamics in the default model representing healthy heart tissue, we used simulation domains that are physically large compared to realistic tissue sizes. Our motivation for choosing such domains is based on the concept presented by Panfilov (2006). He showed that the pattern of stabilization of re-entries in cardiac tissue is not determined by the actual size of the heart *per se*, but by the effective size measured as heart size scaled by the wavelength of electrical activity. This means that in healthy tissue, where the wavelength of electrical activity is relatively large, it is difficult (almost impossible) to obtain self-sustaining spirals. In our default model, the wavelength of the spiral was so large that it was not possible to obtain stable spirals in tissue domains smaller than 8.5 x 8.5 cm. A Fourier analysis of the tip trajectory shows that there are 4 fundamental frequencies responsible for the dynamics of the intact spiral wave. Of these frequencies, one is associated with wave meander at $f_{meander} \simeq 0.1$ Hz, two are associated with the hypocycloid pattern, $f_0 = 5.426$ Hz and $f_1 = 3.548$ Hz, with one of those frequencies also being

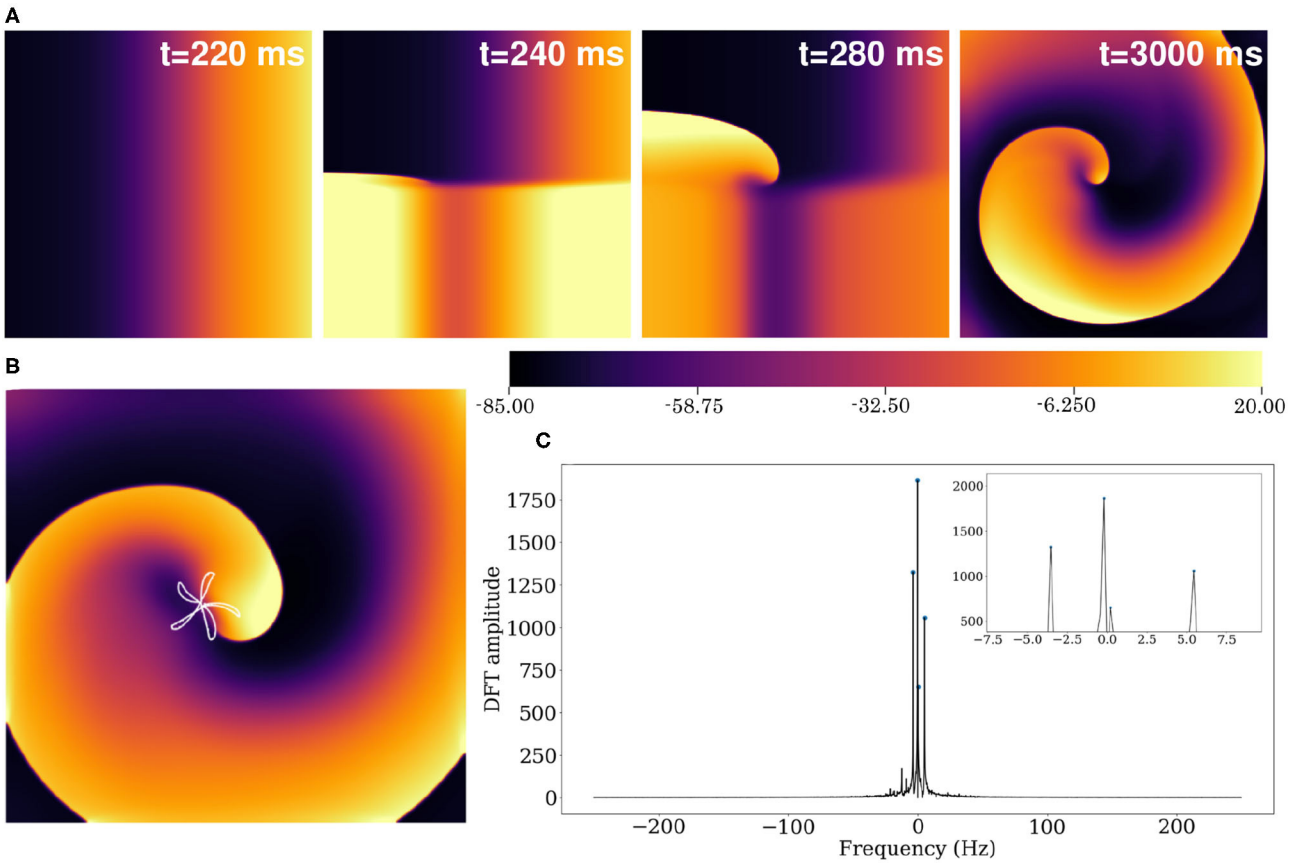

FIGURE 11 | (A) Formation of spiral waves in a 2D pig atrial tissue of size 11.26 × 11.26 cm^2. Here $t = 0$ is considered as the time instant at which the S1 wave is initiated (as in **Figure 10A**). **(B)** Hypocycloid pattern of the spiral tip trajectory. **(C)** Amplitude of the Discrete Fourier Transform (DFT) of the tip trajectory. The sampling frequency is $F_s = 500$ Hz, and the corresponding resolution $\Delta f = 0.2089$ Hz. The inset shows the 4 main peaks of the DFT.

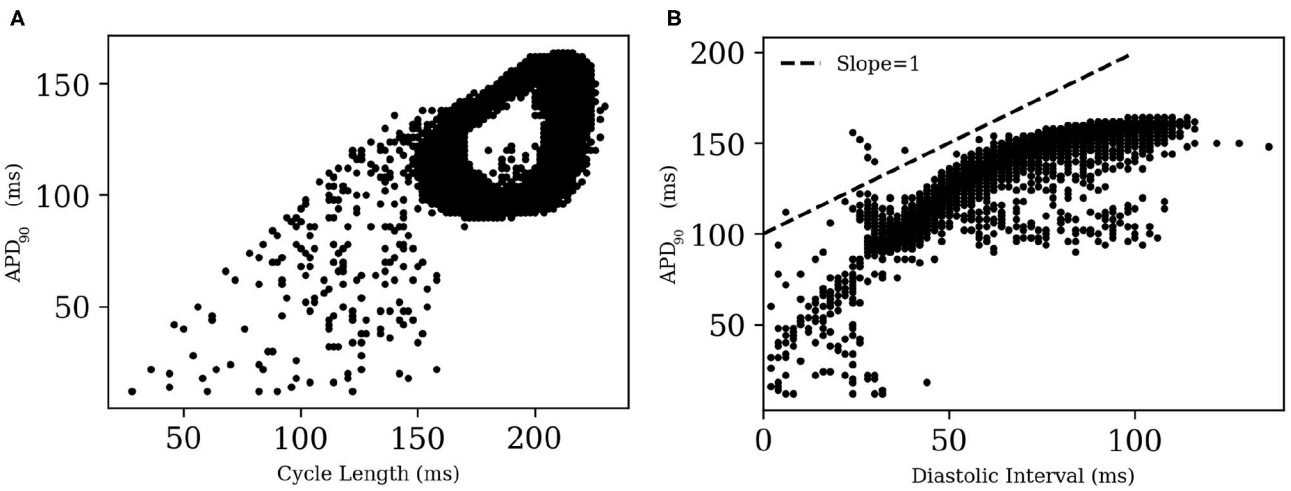

FIGURE 12 | Restitution curves for APD_{90} in **(A)** a simulated spiral with respect to Cycle Length and **(B)** Diastolic Interval. The dashed line in **(B)** indicates the region of slope = 1.

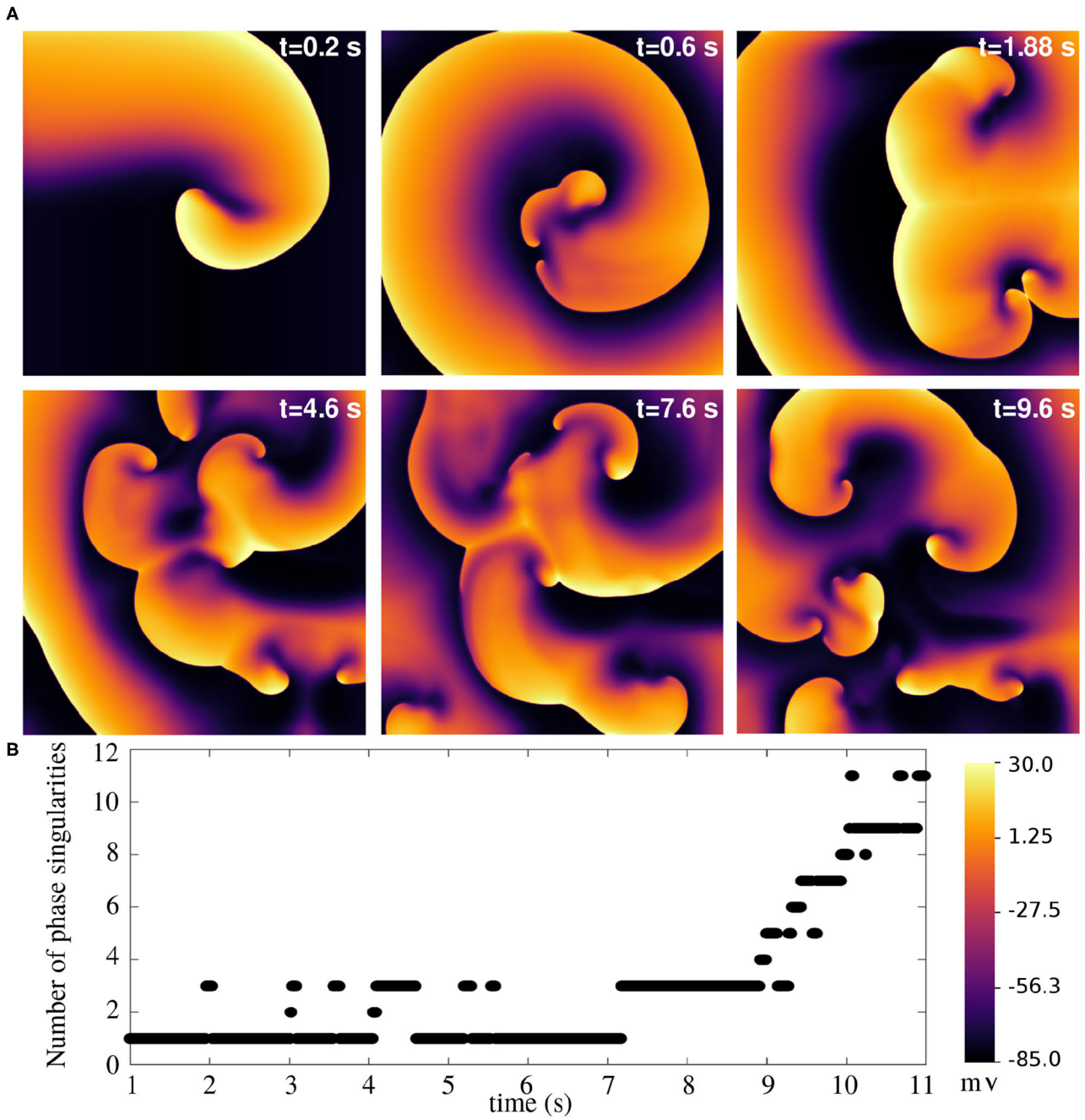

FIGURE 13 | Spiral wave breakup in a 2D pig atrial tissue of size 11.26 × 11.26 cm^2 with $G_{Kr,max}$ reduced to 0.25x its value in the healthy pig model. **(A)** Pseudocolour plots of the membrane voltage distribution at different times demonstrates the occurrence of multiple spiral waves in the domain. **(B)** Quantification of number of spiral waves in the domain at various times, measured as the number of phase singularities (one located at each spiral tip).

the frequency of rotation of the spiral arm (and thus setting the average stimulation frequency). Furthermore, our model points to the occurrence of alternans in 2D in the presence of spiral waves, between the cycle lengths of 165 ms and 215 ms. This may explain the difficulty encountered in experiments with evoking consistent APs at a pacing frequency of 5 Hz. To understand the underlying basis of this alternans, we tested an approach suggested by Gomis-Tena et al. (2003), who inhibited the Ca^{2+}-activated Cl^- current in their canine model to inhibit alternans. Our model, however, failed to show suppression of alternans by similar inhibition of the I_{ClCa}, suggesting that the alternans was not driven by the Cl^- current.

The model presented here has the same general limitations as any other ionically-detailed mathematical model of cardiac electrophysiology. We have tried to incorporate as much porcine specificity to the model as is allowed by the available experimental data. However, there are quite a few currents for which direct validation was not possible, forcing us to resort to indirect methods for model development. In our model, as listed in detail in **Table 1**, experimental data on current voltage characteristics was available for currents like I_{Kur}, I_{Kr}, I_{Ks} and I_{to}. For the remaining currents, we found little or no clear information from literature. For I_{Na}, we had to rely on the APA- and dV/dt_{max} restitution curves for obtaining the correct value of g_{Na}, assuming that the channel kinetics were the same as in the human atrial cell model. For I_{K1} we relied on the RMP restitution curve and the APD restitution curves at 80–90% repolarization to formulate the current. We had no information about the Ca^{2+} dynamics. Therefore, it was adopted in its entirety from the Luo-Rudy dynamic model. Same applied for the pump and exchanger currents, whose maximum values we tuned based on our APD restitution data at 70–90% repolarization. Regarding the L-type Ca^{2+} current, the only information we had was our own data from patch-clamp recordings, which verfied that the maximum conductance used was in line with what we had chosen for the model. As previously discussed by Cherry and Fenton (2007), detailed mathematical models need to be treated with extreme considerations to appreciate their ability to correctly reproduce phenomena outside the general experimental conditions they were modeled after, and their main utility should be in developing new hypotheses in the study of already-known phenomena, rather than for the study of the dynamics of novel, unverified phenomena.

The model falls prey to the natural variability found in cardiac tissue, especially in the atria. The atrial cavities are particularly complex, more so than the ventricles, when it comes to heterogeneity and anisotropy, and the properties of cardiomyocytes are known to be affected by factors like age or sex (Cherry and Fenton, 2007). In the context of this project, this is evidently palpable in the description of I_{Kur} given in the two published papers used as sources in this model, which differ significantly, and it highlights some of the compromises that researchers must make when building a general model. In addition to intrinsic ionic heterogeneities in the heart tissue, structural factors are also known to play an important role in destabilizing reentrant electrical waves in the atria, leading to AF. A recent study by Roy et al. (2018) demonstrates how the gradients in the atrial wall thickness and tissue fibrosis can cause drifting of spiral waves across the left and right atria, resulting in AF. In another study Boyle et al. (2019) report that in patients with persistent AF who develop atrial fibrosis targeted ablation of fibrotic patches can reduce the risk of sustained AF, thereby indicating that structural heterogeneities, such as those introduced by fibrosis, play a major role in stabilizing AF.

Some of the limitations of the model come from the fact that it relies on experiments from literature for the description of individual currents, which sometimes have incomplete data (lack of information of the time dynamics of the currents, for example Li et al., 2004), or which have fundamentally different experimental setups (Li et al., 2004; Ehrlich et al., 2006). However, this model provides a good basis to start, and can be develeoped further, as and when new experimental data become available. Another important limitation of the model lies in its description of the Ca^{2+} dynamics, which is mostly taken from the human atrial model of Courtemanche et al.. The CRN model itself adapts the description of the Ca^{2+} dynamics from the Luo-Rudy model for guinea pig ventricular cardiomyocytes (Courtemanche et al., 1998). Thus the Ca^{2+}-dynamics cannot be called state-of-the-art. Although it does give rise to physiologically relevant pig atrial action potentials, the model does not provide any significant insight to the fundamental role that Ca^{2+} plays in mediating I_{ClCa} (I_{to}) and early AP repolarization. It would therefore be of great interest to make detailed experimental measurements on Ca^{2+} dynamics specific for the pig atria, with the aim of building a more accurate mathematical description to elucidate the mechanisms underlying the dynamics of I_{ClCa} and to make more accurate predictions of its behavior in arrhythmias.

Proposing the single cell model is just the first step. We have taken one step further to extend the model to 2D, where at least we can expect it to reproduce electrophysiological behavior of monolayer cell cultures. The next steps would include incorporation of natural cellular heterogeneity of cardiac tissue, together with structural heterogeneity, such as fibrosis. These are currently not addressed in our paper. Furthermore, we are trying to develop an anatomically detailed 3D atrial model of the pic heart, based on DTMRI data, which would describe the intrinsic fiber anisotropy. A study of AF in such anisotropic, realistic heart geometries would have a huge impact on the advancement of arrhythmia research.

DATA AVAILABILITY STATEMENT

The original contributions presented in the study are included in the article/**Supplementary Material**, further inquiries can be directed to the corresponding author/s.

ETHICS STATEMENT

The animal study was reviewed and approved by Federation of European Laboratory Animal Science Associations (FELASA). All scientists and technicians involved have been accredited by the responsible Ethics Committee (Lower Saxony State Office for Consumer Protection and Food Safety-LAVES).

AUTHOR CONTRIBUTIONS

VP-Y and RM: designed and developed the model and wrote the article. TR, FF, and NV: conceived and carried out the restitution experiments. VP-Y, RM, SL, TR, FF, and NV: read and reviewed

the manuscript. SL and NV: acquired funding. All authors contributed to the article and approved the submitted version.

FUNDING

This work was supported by research grants from the DZHK to NV (81X4300102 and SE181) and from the Deutsche Forschungsgemeinschaft (DFG) to NV (VO 1568/3-1, VO 1568/4-1, IRTG1816, SFB1002, and under Germany's Excellence Strategy—EXC 2067/1—390729940), and to SL [German Center for Cardiovascular Research (DZHK), Project MD 28 grant no. 81Z0300403/81Z0300114 and German Research Foundation (Research Centre SFB 1002, Project C3)]. The funders had no role in study design, data collection and analysis, decision to publish, or preparation of the manuscript.

ACKNOWLEDGMENTS

VP-Y would like to thank Prof. Blas Echebarria for useful discussions.

SUPPLEMENTARY MATERIAL

The Supplementary Material for this article can be found online at: https://www.frontiersin.org/articles/10.3389/fphys.2022.812535/full#supplementary-material

REFERENCES

Aguilar, M., Feng, J., Vigmond, E., Comtois, P., and Nattel, S. (2017). Rate-dependent role of ikur in human atrial repolarization and atrial fibrillation maintenance. *Biophys. J.* 112, 1997–2010. doi: 10.1016/j.bpj.2017.03.022

Bondarenko, V., Szigeti, G., Bett, G., Kim, S., and Rasmusson, R. (2004). Computer model of action potential of mouse ventricular myocytes. *Am. J. Physiol. Heart Circ. Physiol.* 287, H1378–H1403. doi: 10.1152/ajpheart.00185.2003

Boyle, P., Zghaib, T., Zahid, S., Ali, R., Deng, D., Franceschi, W., et al. (2019). Computationally guided personalized targeted ablation of persistent atrial fibrillation. *Nat. Biomed. Eng.* 3, 870–879. doi: 10.1038/s41551-019-0437-9

Butters, T. D., Aslanidi, O. V., Zhao, J., Smaill, B., and Zhang, H. (2013). A novel computational sheep atria model for the study of atrial fibrillation. *Interface Focus* 3, 20120067. doi: 10.1098/rsfs.2012.0067

Cherry, E. M., and Fenton, F. H. (2007). A tale of two dogs: analyzing two models of canine ventricular electrophysiology. *Am. J. Physiol. Heart Circ. Physiol.* 292, H43–H55. doi: 10.1152/ajpheart.00955.2006

Clauss, S., Schüttler, D., Bleyer, C., Vlcek, J., Shakarami, M., Tomsits, P., et al. (2020). Characterization of a porcine model of atrial arrhythmogenicity in the context of ischaemic heart failure. *PLoS ONE* 15, e0232374. doi: 10.1371/journal.pone.0232374

Courtemanche, M., Ramirez, R., and Nattel, S. (1998). Ionic mechanisms underlying human atrial action potential properties: insights from a mathematical model. *Am. J. Physiol. Heart Circ. Physiol.* 275, H301–H321. doi: 10.1152/ajpheart.1998.275.1.H301

Ehrlich, J. R., Hoche, C., Coutu, P., Metz-Wiedmann, C., Dittrich, W., Hohnloser, S. H., et al. (2006). Properties of a time-dependent potassium current in pig atrium-evidence for a role of kv1.5 in repolarization. *J. Pharmacol. Exp. Ther.* 319, 898–906. doi: 10.1124/jpet.106.110080

Fakuade, F., Steckmeister, V., Seibertz, F., Gronwald, J., Kestel, S., Menzel, J., et al. (2021). Altered atrial cytosolic calcium handling contributes to the development of postoperative atrial fibrillation. *Cardiovasc. Res.* 117, 1790–1801. doi: 10.1093/cvr/cvaa162

Gomis-Tena, J., and Saiz, J. (1998). Role of ca-activated cl currents in the heart: a computer model. *Comput. Cardiol.* 26, 109–112.

Gomis-Tena, J., Saiz, J., and Ferrero, J. (2003). Inhibition of atrial action potentials alternans by calcium-activated chloride current blockade - simulation study. *Comput. Cardiol.* 30, 421–424. doi: 10.1109/CIC.2003.1291182

Hiraoka, M., Kawano, S., Hirano, Y., and Furukawa, T. (1998). Role of cardiac chloride currents in changes in action potential characteristics and arrhythmias. *Cardiovasc. Res.* 40, 23–33. doi: 10.1016/S0008-6363(98)00173-4

Jang, J., Whitaker, J., Leshem, E., Ngo, L. H., Neisius, U., Nakamori, S., et al. (2019). Local conduction velocity in the presence of late fadolinium enhancement and myocardial wall thinning. *Circ. Arrhythm. Electrophysiol.* 12, e007175. doi: 10.1161/CIRCEP.119.007175

Lee, A., Miller, J., Voeller, R., Zierer, A., Lall, S., Schuessler, R. Jr, R. D., et al. (2016). A simple porcine model of inducible sustained atrial fibrillation. *Innovations (Phila)* 11, 76–78. doi: 10.1097/imi.0000000000000230

Li, G.-R., Du, X.-L., Siow, Y. L., Karmin, O., Tse, H.-F., and Lau, C.-P. (2003). Calcium-activated transient outward chloride current and phase 1 repolarization of swine ventricular action potential. *Cardiovasc. Res.* 58, 89–98. doi: 10.1016/S0008-6363(02)00859-3

Li, G.-R., Sun, H., To, J., Tse, H.-F., and Lau, C.-P. (2004). Demonstration of calcium-activated transient outward chloride current and delayed rectifier potassium currents in swine atrial myocytes. *J. Mol. Cell Cardiol.* 36, 495–504. doi: 10.1016/j.yjmcc.2004.01.005

Luo, C., and Rudy, Y. (1994). A dynamic model of the cardiac ventricular action potential. *Circ. Res.* 74, 1071–1096. doi: 10.1161/01.RES.74.6.1071

Majumder, R., Jangsangthong, W., Feola, I., Ypey, D. L., Pijnappels, D. A., and Panfilov, A. V. (2016). A mathematical model of neonatal rat atrial monolayers with constitutively active acetylcholine-mediated k+ current. *PLoS Comput. Biol.* 12, e1004946. doi: 10.1371/journal.pcbi.1004946

Nolasco, J., and Dailen, R. W. (1968). A graphic method for the study of alternation in cardiac action potentials. *J. Appl. Physiol.* 25, 191–196. doi: 10.1152/jappl.1968.25.2.191

Pandit, S., Clark, R., Gile, W., and Demir, S. (2001). A mathematical model of action potential heterogeneity in adult rat left ventricular myocytes. *Biophys. J.* 81, 3029–3051. doi: 10.1016/S0006-3495(01)75943-7

Pandit, S. V., Zlochiver, S., Filgueiras-Rama, D., Mironov, S., Yamazaki, M., Ennis, S. R., et al. (2011). Targeting atrioventricular differences in ion channel properties for terminating acute atrial fibrillation in pigs. *Cardiovasc. Res.* 89, 843–851. doi: 10.1093/cvr/cvq359

Panfilov, A. V. (2006). Is heart size a factor in ventricular fibrillation? or how close are rabbit and human hearts? *Heart Rhythm.* 3, 862–864. doi: 10.1016/j.hrthm.2005.12.022

Ramirez, R., Nattel, S., and Courtemanche, M. (2000). Mathematical analysis of canine atrial action potentials: rate, regional factors, and electrical remodeling. *Ame. J. Physiol. Heart Circ. Physiol.* 279, H1767–H1785. doi: 10.1152/ajpheart.2000.279.4.H1767

Roy, A., Varela, M., and Aslanidi, O. (2018). Image-based computational evaluation of the effects of atrial wall thickness and fibrosis on re-entrant drivers for atrial fibrillation. *Front. Physiol.* 9, 1352. doi: 10.3389/fphys.2018.01352

Schultz, J.-H., Volk, T., Bassalaý, P., Hennings, C. J., Hübner, C. A., and Ehmke, H. (2007). Molecular and functional characterization of kv4.2 and kchip2 expressed in the porcine left ventricle. *Eur. J. Physiol.* 454, 195–207. doi: 10.1007/s00424-006-0203-1

Tseng, G.-N., and Hoffman, B. F. (1989). Two components of transient outward current in canine ventricular myocytes. *Circ. Res.* 64, 633–647. doi: 10.1161/01.RES.64.4.633

Virtanen, P., Gommers, R., Oliphant, T. E., Haberland, M., Reddy, T., Cournapeau, D., et al. (2020). SciPy 1.0: fundamental algorithms for scientific computing in python. *Nat. Methods* 17, 261–272. doi: 10.1038/s41592-020-0772-5

Wang, L. J., and Sobie, E. A. (2008). Mathematical model of the neonatal mouse ventricular action potential. *Am. J. Physiol. Heart Circ. Phisiol.* 294, H2565–H2575. doi: 10.1152/ajpheart.01376.2007

Wang, Z., Fermini, B., and Nattel, S. (1987). Two types of transient outward currents in adult human atrial cells. *Am. J. Physiol.* 252, H142–H148. doi: 10.1152/ajpheart.1987.252.1.H142

Wang, Z., Fermini, B., and Nattel, S. (1993). Delayed rectifier outward current and repolarization in human atrial myocytes. *Circ. Res.* 73, 276–285. doi: 10.1161/01.RES.73.2.276

Xu, Y., Dong, P.-H., Zhang, Z., Ahmmed, G. U., and Chiamvimonvat, N. (2002). Presence of a calcium-activated chloride current in mouse ventricular myocytes. *Am. J. Physiol. Heart Circ. Physiol.* 283, H302–H314. doi: 10.1152/ajpheart.00044.2002

Zygmunt, A. C., and Gibbons, W. R. (1991). Calcium-activated chloride current in rabbit ventricular myocytes. *Circ. Res.* 68, 424–437. doi: 10.1161/01.RES.68.2.424

Conflict of Interest: The authors declare that the research was conducted in the absence of any commercial or financial relationships that could be construed as a potential conflict of interest.

frontiers | Frontiers in Physiology

ORIGINAL RESEARCH
published: 26 April 2022
doi: 10.3389/fphys.2022.879035

A Parameter Representing Missing Charge Should Be Considered when Calibrating Action Potential Models

*Yann-Stanislas H. M. Barral[1,2], Joseph G. Shuttleworth[3], Michael Clerx[3], Dominic G. Whittaker[3], Ken Wang[1], Liudmila Polonchuk[1], David J. Gavaghan[2] and Gary R. Mirams[3]**

[1]Roche Pharma Research and Early Development, Pharmaceutical Sciences, Roche Innovation Center Basel, F. Hoffmann-La Roche Ltd., Basel, Switzerland, [2]Department of Computer Science, University of Oxford, Oxford, United Kingdom, [3]Centre for Mathematical Medicine and Biology, School of Mathematical Sciences, University of Nottingham, Nottingham, United Kingdom

Computational models of the electrical potential across a cell membrane are longstanding and vital tools in electrophysiology research and applications. These models describe how ionic currents, internal fluxes, and buffering interact to determine membrane voltage and form action potentials (APs). Although this relationship is usually expressed as a differential equation, previous studies have shown it can be rewritten in an algebraic form, allowing direct calculation of membrane voltage. Rewriting in this form requires the introduction of a new parameter, called Γ_0 in this manuscript, which represents the net concentration of all charges that influence membrane voltage but are not considered in the model. Although several studies have examined the impact of Γ_0 on long-term stability and drift in model predictions, there has been little examination of its effects on model predictions, particularly when a model is refit to new data. In this study, we illustrate how Γ_0 affects important physiological properties such as action potential duration restitution, and examine the effects of (in)correctly specifying Γ_0 during model calibration. We show that, although physiologically plausible, the range of concentrations used in popular models leads to orders of magnitude differences in Γ_0, which can lead to very different model predictions. In model calibration, we find that using an incorrect value of Γ_0 can lead to biased estimates of the inferred parameters, but that the predictive power of these models can be restored by fitting Γ_0 as a separate parameter. These results show the value of making Γ_0 explicit in model formulations, as it forces modellers and experimenters to consider the effects of uncertainty and potential discrepancy in initial concentrations upon model predictions.

Keywords: action potential, electrophysiology, mathematical model, conservation of charge, parameter fitting, calibration

OPEN ACCESS

Edited by:
Gernot Plank,
Medical University of Graz, Austria

Reviewed by:
Richard A. Gray,
United States Food and Drug Administration, United States
Sanjay Ram Kharche,
Western University, Canada

****Correspondence:***
Gary R. Mirams
gary.mirams@nottingham.ac.uk

Specialty section:
This article was submitted to Cardiac Electrophysiology, a section of the journal Frontiers in Physiology

Received: *18 February 2022*
Accepted: *16 March 2022*
Published: *26 April 2022*

Citation:
Barral Y-SHM, Shuttleworth JG, Clerx M, Whittaker DG, Wang K, Polonchuk L, Gavaghan DJ and Mirams GR (2022) A Parameter Representing Missing Charge Should Be Considered when Calibrating Action Potential Models. Front. Physiol. 13:879035. doi: 10.3389/fphys.2022.879035

1 INTRODUCTION

Since the seminal work by Hodgkin and Huxley (1952), mathematical models of electrophysiology have been developed for many different cell types, including neurons, cardiomyocytes, gastric smooth muscle cells, and many more (Noble, 1962; Dodge and Cooley, 1973; Corrias and Buist, 2007). Differences in ionic concentrations across cell membranes lead to a transmembrane voltage (V_m). Its evolution over time is usually calculated in mathematical models by numerically integrating the effects of the ionic currents passing through the membrane. Since the late 90s, several authors

have showed that V_m can also be computed directly from intra- and extracellular concentrations of charges, due to a conservation principle in the models (Guan et al., 1997; Varghese and Sell, 1997; Endresen et al., 2000; Hund et al., 2001; Jacquemet, 2007; Livshitz and Rudy, 2009; Pan et al., 2018). In this work, we investigate further the implications of using this second expression for V_m in terms of numerical stability, we highlight its impact on electrophysiological predictions, and we discuss the benefits to using this approach in model calibration.

First, in this section we present a brief overview of relevant work that leads to different ways of computing the voltage in AP models, based on a conservation of charge principle hidden in the equations, as well as how this conservation of charge relates to the steady state of the AP models. **Section 2** then highlights how the accuracy of solutions is improved by the algebraic expression for voltage. In **Section 3**, we show that model outputs are sensitive to the net concentration of charge across the cell membrane, which varies because of high variability and/or uncertainty in initial concentrations. We finally show in **Section 4** that Γ_0, a parameter characterising the relationship between V_m and the intra- and extracellular concentrations of charges, can be inferred from experimental data to produce the desired steady-state behaviour of the AP model, despite being challenging to estimate experimentally.

In this study, we explore the consequences of writing V_m algebraically using the Ten Tusscher-Panfilov model of human ventricular cells (TTP06) (Ten Tusscher and Panfilov, 2006) and the CiPA version of the O'Hara-Rudy model by Dutta et al. (2017) (ORd-CiPA). Beyond these two models, our findings apply to any model tracking the intracellular concentrations of all charge-carriers, which make up the majority of modern electrophysiology models.

1.1 Membrane Voltage and Ionic Concentrations in AP Models

Major variables in AP models include V_m, channel and pump/transporter state variables and, in later models, concentrations of ions, buffers, and signalling molecules. The relationship between these variables, grouped together in a vector $\mathbf{X}$, is expressed as a system of ordinary differential equations (ODEs) of the form

$$\frac{d\mathbf{X}}{dt} = f(\mathbf{X}),$$
$$\mathbf{X} = \{V_m, \mathbf{C}, \mathbf{g}\},$$

where the vector function $f(\mathbf{X})$ describes the rate of change of $\mathbf{X}$, which can be subdivided into V_m, the ionic concentrations $\mathbf{C}$ and all other variables $\mathbf{g}$. The first equation in f is usually the one that defines the rate of change in V_m, using an ideal capacitor equation:

$$\frac{dV_m}{dt} = -\frac{1}{C_m}\sum_{j=1}^{N} I_j(\mathbf{X}), \tag{1}$$

where C_m is the membrane capacitance (usually in pF), and I_j are the N different ionic currents flowing across the cell membrane (in pA). Note that the currents depend non-linearly on voltage, concentration, and time, so that all the state variables are coupled together in a non-linear system.

The earliest AP models (e.g. Hodgkin and Huxley, 1952; Noble, 1962; McAllister et al., 1975) approximated intracellular concentrations as constants, arguing that the relatively small ionic currents would not alter concentrations significantly. This assumption holds well for the K^+ and Na^+ currents included in these models, which have relatively large internal concentrations which do not show significant variations during a single AP. In addition, simulating longer time spans during which these small changes could build up, was computationally infeasible at the time. But after the discovery of Ca^{2+} currents in the 60s, it was quickly realised that $[Ca^{2+}]_i$ could vary by orders of magnitude during a single AP, necessitating the inclusion of a time-varying $[Ca^{2+}]_i$ in models as early as the Beeler and Reuter (1977) model.

Later, DiFrancesco and Noble (1985) proposed a model where the current-induced changes in $[Ca^{2+}]_i$, $[K^+]_i$, and $[Na^+]_i$ are tracked over time, along with the extracellular concentration of K^+ close to the cell membrane. This revolutionised the understanding of major features of cardiac electrophysiology, as reviewed by Dibb et al. (2015). Most subsequent AP models have retained the dynamic description for *intracellular* concentrations (although $[K^+]_i$ is sometimes held constant) and extended it with concentrations in intracellular compartments such as the sarcoplasmic reticulum (SR, e.g., Noble et al., 1991; Wilders et al., 1991; Luo and Rudy, 1994) and other species (e.g. chloride in Tomek et al., 2020). Variations in extracellular concentrations over the course of the action potential proved less popular but are still present e.g., in some models of atrial (Hilgemann and Noble, 1987; Lindblad et al., 1996; Nygren et al., 1998) and sino-atrial (Demir et al., 1994; Dokos et al., 1996; Lovell et al., 2004; Pohl et al., 2016) action potentials. Even though extracellular concentrations do vary in practice (e.g., under ischemic conditions), their variations due to ionic currents are often neglected in AP models because ions are constantly exchanged with the vascular buffer which limits their temporal variation in the extracellular space (Dokos et al., 1996) and reduces accumulation of ions in the extracellular space.

1.2 Algebraic Expressions for V_m

A study by Varghese and Sell (1997) showed that models in which all membrane currents are assigned to a charge-carrying species, and in which the intracellular ionic concentrations vary accordingly, will implicitly satisfy a *conservation of charge* principle. As a result, V_m can be computed algebraically as a function of the concentrations, so that the ODE for V_m **Eq. 1** is redundant. Applying the approach of Varghese & Sell to the Luo and Rudy (1994) model as an example, we obtain

$$V_m = \frac{\mathcal{V}_i F}{C_m}\left([Na^+]_i + [K^+]_i + 2[Ca^{2+}]_i + 2\frac{\mathcal{V}_{JSR}}{\mathcal{V}_i}[Ca^{2+}]_{JSR} + 2\frac{\mathcal{V}_{NSR}}{\mathcal{V}_i}[Ca^{2+}]_{NSR}\right) + V_0, \tag{2}$$

where V_0 is an integration constant (called C_0 in the original publication), F is the Faraday constant, $\mathcal{V}_i$ is the volume of the

cytosol compartment of the cell, $\mathcal{V}_{JSR}$ and $\mathcal{V}_{NSR}$ are the volumes of the junctional (JSR) and network (NSR) sarcoplasmic reticulum compartments of the cell, respectively, and $[Ca^{2+}]_{JSR}$ and $[Ca^{2+}]_{NSR}$ are the concentrations of Ca^{2+} in these compartments. Hund et al. (2001) used a similar expression for V_m but moved the integration constant within the brackets, thereby turning it into a concentration instead of a voltage. Using C_0 to represent the concentration, the two representations are related by $V_0 = -\frac{\mathcal{V}_i F}{C_m} C_0$.

Endresen et al. (2000) proposed an expression very similar to that of Varghese and Sell but with a strong assumption: that all charges contributing to V_m are carried by K^+, Na^+, and Ca^{2+}. This assumption leads to

$$V_0 = -\frac{\mathcal{V}_i F}{C_m}\left([K^+]_o + [Na^+]_o + 2[Ca^{2+}]_o\right), \tag{3}$$

where $[X]_o$ is the extracellular concentration of species X. In other words, V_m is simply proportional to the difference between total intracellular and extracellular concentrations of these three species. Endresen et al. acknowledged that their approach omitted anions, but justified this with the observation that the total concentrations of anions are approximately the same inside and outside the cell and that most currents are carried by cations. However, this framework needs to be extended for models which include Cl^-, e.g., Hund and Rudy (2004); Grandi et al. (2010); Tomek et al. (2020): **Eqs 2**, **3** can be combined and generalised to any number of modelled species and compartments as follows

$$V_m = \frac{\mathcal{V}_i F}{C_m}\left(\sum_A \sum_k z_A [A]_{total,k} \frac{\mathcal{V}_k}{\mathcal{V}_i} - \sum_A z_A [A]_o\right), \tag{4}$$

where A represents each charged species in the model, z_A its valence, $\mathcal{V}_k$ is the volume of the compartment k and the index k is over all intracellular compartments (e.g. compartment $k = i$ corresponds to the cytosol). **Equation 4** therefore accommodates further electrically charged species such as chloride, provided that the model keeps track of changes in their intracellular concentrations.

Note that the total concentration of any ion A is denoted here as $[A]_{total,k}$. Some models include buffering of ions which alters free ionic concentrations, but as binding to buffers does not cause current flow over the membrane it should not change membrane voltage. So the $[A]_{total}$ notation in **Eq. 4** serves as a reminder that the total concentration carried by A is given by the sum of any buffered and free concentrations. For example, in many models $[Ca^{2+}]_{total,i}$ is not equal to $[Ca^{2+}]_i$. This can make derivation of an algebraic-V_m form more complicated than in the examples above.

However, various other charge-carriers—ions, compounds and charged proteins—are known to be present at different concentrations on either side of the membrane, but are omitted from models. If these omitted charge carriers lead to a net transmembrane voltage, then an extra parameter is needed to account for the contribution of their charge imbalance to V_m. For example, the Hund and Rudy (2004) dog action potential model includes Cl^- ions and an extra offset parameter would be needed to compensate the strong imbalance between intracellular (~ 20 mM) and extracellular (~ 100 mM) concentrations of Cl^-, or there would be huge voltages using **Eq. 4**. In this model, chloride co-transporters change intracellular K^+, Na^+ and Cl^- concentrations but do not induce any ionic current or change voltage as they transport pairs of oppositely charged ions. The balanced effect of these co-transporters does not need special treatment in the equations above as long as both co-transported ionic species are accounted for.

We can modify **Eq. 4** to explicitly allow for transmembrane imbalance of species that are not included in the model:

$$V_m = \frac{\mathcal{V}_i F}{C_m}\left(\sum_A \sum_k z_A [A]_{total,k} \frac{\mathcal{V}_k}{\mathcal{V}_i} - \sum_A z_A [A]_o\right) + \Delta V. \tag{5}$$

Here, ΔV corresponds to the transmembrane potential due to the difference in charge of *all* un-modelled species on either side of the membrane. As the contribution of these species to V_m is not modelled as varying, ΔV remains constant through the simulations. Equivalently, we can express the offset constant as a concentration that we denote Γ_0:

$$V_m = \frac{\mathcal{V}_i F}{C_m}\left(\sum_A \sum_k z_A [A]_{tot,k} \frac{\mathcal{V}_k}{\mathcal{V}_i} - \sum_A z_A [A]_o + \Gamma_0\right), \tag{6}$$

where $\Gamma_0 = \mathcal{V}_i F \Delta V / C_m$.

Expressing the offset as a concentration rather than voltage may help in assessing whether the values implicitly attributed to Γ_0 by ODE models could be realistic. If positive, Γ_0 could be interpreted as the net concentration of 1 + charged intracellular ions carried by species omitted in the model (or equivalently the net extracellular concentration of 1 − charged ions), and if negative it could be interpreted as a net intracellular concentration of 1 − charged omitted ions—but in reality it will reflect the sum of concentrations of a wide range of intra and extracellular un-modelled charged species. The smaller the magnitude of Γ_0, the smaller the transmembrane imbalance of charge carried by un-modelled species. As a consequence, a value of $\Gamma_0 = 0$ mM does not necessarily imply that no charge is missing in the model; but it does imply that any external missing charge is balanced exactly by an internal missing charge. Thus, the value of Γ_0 must be interpreted in the light of which charged species are included in each model. Throughout this manuscript, we will use the Γ_0 symbol to represent these missing charges, but the results hold equally well for its mathematically equivalent representation as voltage (Endresen et al., 2000), concentration of charge (Hund et al., 2001), or electrical charge (Jacquemet, 2007). Further detail on these expressions and their interpretation is provided in **Supplementary Material Section S1-2**.

A value for Γ_0 can be found by substituting in the initial conditions for the concentrations and the initial value of V_m from the ODE formulation. This highlights an important point: models that express V_m in ODE form "hide" the value of this model parameter within their initial conditions. So when a set of initial conditions is chosen, perhaps arbitrarily from within the bounds of physiological realism, a hidden assumption is being made about the (im)balance of un-modelled charges in the cell. As we

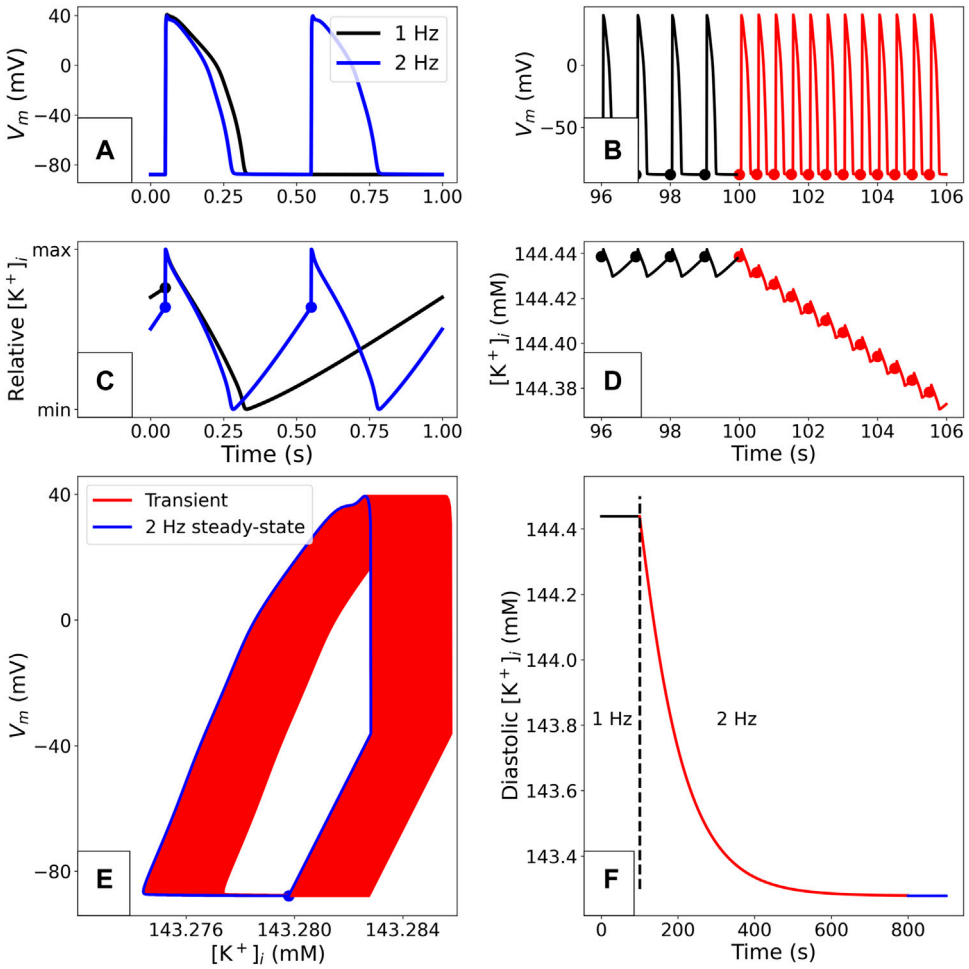

FIGURE 1 | Example of a limit cycle in the O'Hara-Rudy CiPA 2017 model (Dutta et al., 2017), using the initial conditions from the published CellML model. The simulation methods are detailed in "Simulation". **(A)**: Comparison of paced steady-state APs with 1 and 2 Hz pacing. **(B)**: Adaptation of the voltage profile when the pacing rate is suddenly changed from 1 to 2 Hz. The dots plotted on the traces correspond to the end of the diastolic phase in each AP. **(C)**: Comparison of periodic steady-state $[K^+]_i$ variations during the AP with 1 and 2 Hz pacing. The values are normalised for easier comparison. **(D)**: Adaptation of $[K^+]_i$ after the sudden change to 2 Hz shown in panel **(B)**. **(E)**: V_m and $[K^+]_i$ during the transient adaptation phase where the model converges towards its periodic steady state. Data is shown from the 500th pace onward. After a slow drift of $[K^+]_i$ over time, a limit cycle (in blue) is reached where the patterns from consecutive APs overlap. **(F)**: Evolution of diastolic intracellular potassium (measured at the time points denoted with dots in B and D) after a change in pacing rate. A limit cycle is reached after approximately 700 2 Hz paces.

will show in this study, this net imbalance in un-modelled charge, captured by Γ_0, is a key parameter in determining the behaviour of AP models.

1.3 Γ_0 and Stable Behaviour

In **Figure 1** we show the stable behaviour of the O'Hara-Rudy CiPA model when paced for a long time at 1 Hz. The solution converges to a pattern under which all variables in the system take the same trajectory (to within numerical simulation tolerances) every time a stimulus is applied. The resulting periodic orbit in the state variable space (as shown in **Figure 1E**) is called a "stable limit cycle" in the study of dynamical systems, but is often referred to as a "steady state" for shorthand in electrophysiology modelling. **Figure 1** also shows how a change in pacing to 2 Hz results in a transient shift to a new limit cycle. Similar transients to different limit cycles will also occur when other parameters in the model are changed (e.g., those representing maximal ion channel conductances being altered by drug block, or a change in extracellular concentrations). A model at a limit cycle has settled to a stable behaviour where each ionic concentration is in a dynamic equilibrium—any depletion/accumulation due to ions flowing down concentration gradients is restored before the next pace by pumps and exchangers (see **Figure 1C**).

Convergence to a stable limit cycle of the same period as the pacing (a "period-1" orbit) is not guaranteed: some models' variables/concentrations may simply keep drifting (perhaps reaching unrealistic levels); exhibit more complex behaviour such as alternans (a stable "period-2" limit cycle in which we arrive back at the same state after two stimuli periods rather than

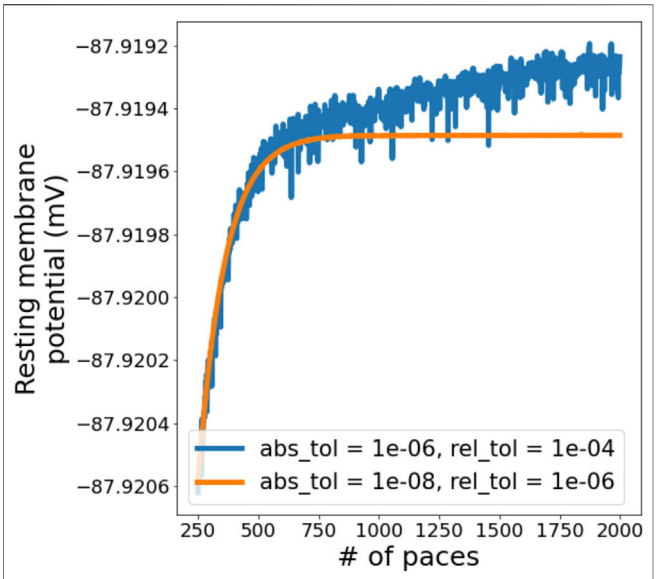

FIGURE 2 | Evolution of resting membrane potential (RMP) in a simulation with the derivative-V_m ORd-CiPA model, starting from the published initial conditions. 2000 paces were simulated, we are showing paces 250 onwards to examine the behaviour close to periodic steady state. A slight drift is observed when using a coarse solver tolerance, but this disappears when tolerances are tightened.

one); or even chaotic behaviour (Qu, 2011). If pacing is stopped altogether, model variables may converge to stable values—a "stable steady state". In models that exhibit automaticity, a limit cycle can be reached without any periodic forcing applied by a stimulus current. In this manuscript, we will use either "limit cycle" or "periodic steady state" when referring to stable limit cycles, and "quiescent steady state" when referring to stable steady states without any periodic forcing by a stimulus current.

Many published models do not exhibit a periodic steady state. Hund et al. (2001); Jacquemet (2007) showed that models where variables drift can often be 'fixed' to produce periodic steady states by ensuring that all currents through the membrane, including the stimulus current, are taken into account in the concentration updates, i.e. by ensuring that charge is conserved (as well as other conservation laws, see Pan et al., 2018).

Even when a model does have a periodic steady state, for any models where V_m is written as a redundant ODE, the charge represented by Γ_0 is defined by the initial conditions. As a result, arbitrarily varying initial conditions in the presence of this redundant ODE alters the parameterisation of the model (changes the amount of charge in the system), and any quiescent steady states or limit cycles can alter accordingly. Or in other words, when a redundant ODE is included there can be no unique periodic steady state, it will vary depending on the initial conditions. Conversely, when the redundant ODE is removed there is often a unique stable limit cycle or quiescent steady state; that is, the same quiescent steady state or limit cycle is reached for *any* initial conditions.

Some authors such as Livshitz and Rudy (2009) have gone a step further, and suggested that uniqueness of limit cycles/quiescent steady states is guaranteed once conservation of charge is met. An analysis by Jacquemet (2007), however, shows that more than one stable quiescent steady state can exist for a charge-conserving model with a given value of Γ_0. Examining the atrial model by Nygren et al. (1998), Jacquemet found that for some values of Γ_0 the model had a stable steady state where V_m is polarised at rest (−60 to −90 mV), a stable steady state where the cell is depolarised to about −30 mV, and an unstable periodic steady state where the model displays automaticity. In the course of this study we also found examples of more than one stable limit cycle in other analytic-V_m models, which are discussed below.

Although undoubtedly important for reproducible modelling, it is reasonable to question the physiological relevance of quiescent steady states and limit cycles. Convergence to a perfect limit cycle seems unlikely to occur in real cells, as channel activity and other chemical processes are inherently stochastic and will perturb each orbit differently. The idea of a limit cycle, however, overlaps well with biological concepts of homeostasis and robustness. Even though the cell's environment is constantly altering to some degree, it would be ideal for a cell to exist in close proximity to a stable limit cycle such that small stochastic perturbations converge back to the same behaviour—at least while energetic demands are met.

2 IMPACT OF THE ALGEBRAIC VOLTAGE FORMULATION ON NUMERICAL SOLUTIONS

2.1 Models and Simulation

CellML files for the TTP06 and ORd-CiPA models were obtained from the Physiome Model Repository (Yu et al., 2011). The TTP06 model has epi-, endo- and mid-myocardial variants; where not stated otherwise we used the epicardial variant in this study. The units in the obtained CellML files for TTP06 had to be corrected before the algebraic-V_m form could be applied, as described in **Supplementary Material Section S1.1**. The algebraic-V_m forms of the TTP06 and ORd-CiPA models were derived, and model variants that employ this form were created for comparison with the original derivative-V_m form. A detailed overview of the conversion of a model to its algebraic-V_m form is given in **Supplementary Material Section S1.3**, along with a guide to performing this translation in other models.

Simulations were performed using Myokit (Clerx et al., 2016) which imported the CellML models, and using solver tolerances stated in the section below. Unless stated otherwise, figures were created after 2000 pre-pacing stimuli at a frequency of 1 Hz. In the TTP06 model, the stimulus current was modelled as a K^+ current of amplitude −52 A/F lasting 0.5 ms. In the ORd-CiPA model, the stimulus current was also attributed to K^+ ions and its amplitude was set at −50 A/F and its duration at 1 ms.

All code used for this article is publicly available and open source (see *Data Availability* at the end of the article).

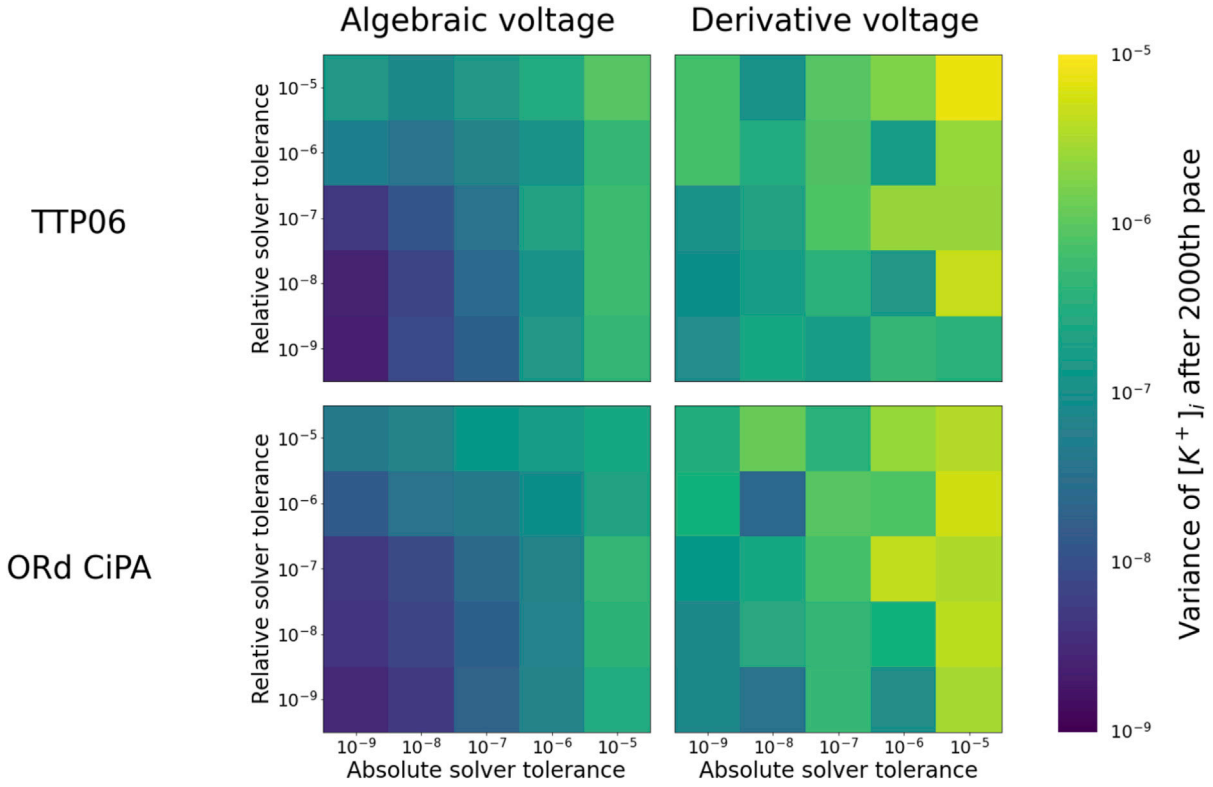

FIGURE 3 | Numerical stability of $[K^+]_i$ in the TTP06 and ORd-CiPA models, comparing the derivative and algebraic-V_m forms. The colour map corresponds to the standard deviation of $[K^+]_i$ between the 2000th and 3000th pace. The darker the map, the lower the variance, and the more stable the simulation.

2.2 Accuracy of Solutions

Simulations in Myokit are performed using the CVODES software package (Hindmarsh et al., 2005) to numerically integrate the differential equations. CVODES has two "tolerance" settings that control the accuracy of the numerical solutions (Cohen et al., 1996). To visualise the influence of solver tolerance on AP simulations and find suitable tolerances to use in this study, simulations were run for 2000 paces with the ORd-CiPA model in its derivative-V_m form, using a coarse setting (10^{-6} and 10^{-4} for absolute and relative tolerance, respectively) and a fine setting (10^{-8} and 10^{-6}). The resting membrane potential (RMP) was measured as the V_m 1 ms before application of the stimulus, and plotted for the final 1750 paces in **Figure 2**.

As expected, using coarse tolerances results in (a small) numerical error in the solution, but the figure also shows a slight drift in V_m, even after 1,000 paces. When tightening the solver tolerance, the numerical noise is significantly reduced, and V_m stabilises after around 700 paces. The other state variables show a similar pattern, as can be seen for $[K^+]_i$ in **Supplementary Material Section S1.4**.

To further investigate the long term stability of the solutions, 3,000 paces were simulated with the ORd-CiPA and TTP06 models, in both the derivative and the algebraic-V_m forms. Since, with fine tolerances, the system had stabilised after 2000 paces (see **Figure 2**), the variation in the state variables after 2000 paces could safely be attributed to numerical error and not to electrophysiological phenomena. We quantified this variation by measuring the standard deviation in the final 1,000 paces in $[K^+]_i$ (the state variable that had the highest absolute value and largest variations over successive paces, see **Supplementary Material Section S1.4**). This standard deviation was evaluated for several solver tolerances, in both the derivative and algebraic-V_m forms of the models, and plotted in **Figure 3** to create a "map of stability".

For both models, numerical solutions appear less stable when using the derivative-V_m form **Eq. 1**. We believe this is because the intracellular ionic concentrations and V_m are updated without the numerical method having any knowledge of Γ_0. This can lead to numerical errors that break conservation of charge, effectively introducing variations in Γ_0, and allowing the periodic steady state of the system to change. By contrast, when explicitly incorporating the algebraic constraint on V_m (**Eq. 6**) and fixing Γ_0, conservation of charge is guaranteed, so that the periodic steady state stays the same and the stability of the solution is improved.

For the remainder of this manuscript, we therefore used the algebraic-V_m form and absolute and relative solver tolerances of 10^{-8} and 10^{-6}, respectively.

2.3 Computation Time

We also investigated whether computation time was affected by switching to the algebraic-V_m form of the model. One might have

TABLE 1 | The integration constant for a range of human AP models, written as C_0 (Hund et al., 2001)—see **Section 1.2**—, net un-modelled species concentration Γ_0 **Eq. 6**, and voltage offset ΔV **Eq. 5**. The Trovato et al. (2020) and Stewart et al. (2009) models are Purkinje fibre models, while the remaining models represent ventricular cells.

Model	C_0 (mM)	Γ_0 (mM)	ΔV (mV)	Included ions
Trovato et al. (2020)	195.3377	−46.3377	-1.0605×10^6	K^+, Na^+, Ca^{2+}
Stewart et al. (2009)	147.2641	2.1359	1.8273×10^4	K^+, Na^+, Ca^{2+}
Ten Tusscher et al. (2004) Epi/Endo	150.5207	−1.1207	-9.5878×10^3	K^+, Na^+, Ca^{2+}
Ten Tusscher and Panfilov (2006) Epi	147.2683	2.1317	1.8237×10^4	K^+, Na^+, Ca^{2+}
Ten Tusscher and Panfilov (2006) Endo	150.5427	−1.1427	-9.776×10^3	K^+, Na^+, Ca^{2+}
Iyer et al. (2004)	135.7501	10.2499	1.6659, ×, 10^5	K^+, Na^+, Ca^{2+}
O'Hara et al. (2011) Endo	156.8010	−7.8010	−1.2680, ×, 10^5	K^+, Na^+, Ca^{2+}
O'Hara et al. (2011) Epi	156.8022	−7.8022	-1.2682×10^5	K^+, Na^+, Ca^{2+}
Dutta et al. (2017) (ORd-CiPA) Endo	156.8011	−7.8011	-1.2680×10^5	K^+, Na^+, Ca^{2+}
Tomek et al. (2020) Epi	135.7563	−137.1563	-2.2294×10^6	K^+, Na^+, Ca^{2+}, Cl^-
Tomek et al. (2020) Endo	135.7555	−137.1555	-2.2294×10^6	K^+, Na^+, Ca^{2+}, Cl^-

expected an improvement in simulation time due to a smaller and better conditioned system with the redundant ODE removed (avoiding a singular Jacobian as Varghese and Sell (1997) suggested), but there was no significant (if any) change in computation time, see **Supplementary Figure S5** in the Supplementary Material.

3 PHYSIOLOGICAL IMPACT OF Γ_0

3.1 Γ_0, $[K^+]_i$ and $[Na^+]_i$ in Human Ventricular AP Models

The algebraic-V_m form of the model (**Eq. 6**) gives the voltage in terms of the total intra- and extra-cellular ionic concentrations. The impact of variations in these parameters and variables across ventricular models was investigated by computing Γ_0 for several literature models using the published initial conditions. This work could be carried out only for models which obey the conservation of charge principle. The results are shown in **Table 1** which reports Γ_0 (**Eq. 6**), the corresponding C_0 as defined by Endresen et al., and the corresponding voltage offset ΔV for each of the investigated models.

These parameters contain information about the difference between the un-modelled intra- and extracellular charged species (e.g. H^+, Mg^{2+}, cations, phosphates, proteins). In the TTP06 Epi model, for example, the intra- and extra-cellular charges of these missing species are responsible for a voltage offset of 18.2 V. In the ORd-CiPA model, the voltage offset is of −126.8 V.

The Tomek et al. (2020) model (an update of the 2019 version to conserve charge) has a very high Γ_0 constant due to the inclusion of chloride ions, for which there is a very large difference between intra- and extracellular concentrations. In the Ten Tusscher et al. (2004) model, the epicardial and endocardial versions were assumed to have the same initial conditions, so their missing charge concentrations are the same. The 2006 epi/endo variants of the Ten Tusscher model (Ten Tusscher and Panfilov, 2006) have minor differences in the initial conditions and buffered Ca^{2+} concentrations. As a result, there are slight differences in Γ_0 between the various versions of the Ten Tusscher et al. model.

It remains to be seen whether the Γ_0 value (net concentration of un-modelled charge) is biologically as variable as the values it has been implicitly assigned within models, or whether this simply reflects lack of information on real concentrations and subsequent uncertainty in what initial conditions should be used.

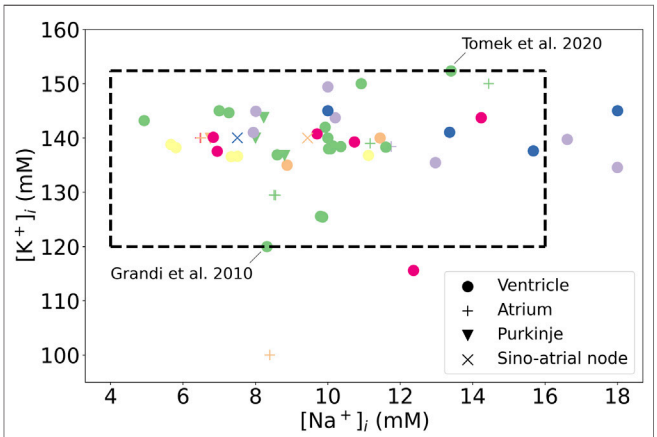

FIGURE 4 | Initial concentrations published for cardiac AP models, for a range of species and tissues. Green: human, Purple: canine, Orange: rabbit, Yellow: Guinea pig, Blue: mammalian, Pink: murine. The dotted box highlights the extreme values of intracellular concentrations, estimated from the work of Bers et al. (2003) for Na^+ and from the Grandi et al. (2010) and the Tomek et al. (2020) models for K^+.

Comparing the magnitudes of Γ_0 and ΔV in **Table 1** shows that a 20 mV variation one might observe in resting potential between models corresponds to Γ_0 variations of approximately 0.002 mM, much smaller than the variation in the offset constants between models. So what we observe is not influenced much by the precise value of the initial condition for the RMP (this is the same reason initial gating variable values have negligible effects) but instead by how the various possible initial concentrations cause longer term system behaviour to change *via* altered Nernst potential (or GHK flux equations) and resulting currents, as well as any explicit concentration-dependence in gating kinetics. So the impact of initial RMP on Γ_0 can be neglected in comparison to that of initial concentrations (RMP is also much easier to measure to within a few millivolts in experiments). As a consequence, variation of

the initial voltage used to compute Γ_0 from **Eq. 6** was neglected in this study and the initial voltage as published in the original models was used to compute Γ_0 in simulations of the sections below.

3.2 Γ_0 and Ranges of K^+ and Na^+

In this section, we estimate the variability of Γ_0 from literature and observe how this variability might impact the AP predicted by the model. The values that can be taken by Γ_0 are, for a large part, dictated by the uncertainty in intracellular concentrations in intact myocytes. Extracellular concentrations are fixed parameters in most AP models that are more reliably estimated (at least in *in vitro* experiments); we therefore investigate the effect of only the initial conditions of intracellular state variables on long-term model behaviour.

A literature search was carried out to find the range of intracellular K^+ and Na^+ concentrations observed experimentally in human cardiomyocytes and/or used in simulations. The contribution of Ca^{2+} to total intracellular charge at the end of the resting phase of the AP is much smaller, so its variation can be neglected compared to K^+ and Na^+, and Γ_0 variation between the models is mainly due to different intra- and extra-cellular K^+ and Na^+. The concentrations of $[K^+]_i$ and $[Na^+]_i$ used in previous cardiac AP models are reported in **Figure 4**, for a range of tissues and species based on the annotated CellML models at https://github.com/Chaste/cellml that were studied in Cooper et al. (2015).

In human ventricular cardiomyocytes the intracellular sodium concentration ($[Na^+]_i$) was found to range experimentally from 4 to 16 mM (Bers et al., 2003). Fry et al. (1986) determined experimentally that the intracellular potassium concentration ($[K^+]_i$) is 113 ± 6 mM in rat cardiomyocytes. We did not find direct experimental measurements of $[K^+]_i$ in ventricular human cardiomyocytes in the literature. Also, experimental measurements of intracellular ionic concentrations in intact cardiomyocytes were all performed in the quiescent configuration. We therefore used initial values for $[K^+]_i$ from human ventricular AP models as a measure of uncertainty in $[K^+]_i$, which ranged from 120 mM in the Grandi et al. (2010) model to 152 mM in the Tomek et al. (2020) model. With these estimated ranges for $[K^+]_i$ and $[Na^+]_i$, the range for their sum varies by 44 mM. Such uncertainty in intracellular concentrations produces the high variability of Γ_0 between models that is observed in **Table 1**.

The extreme K^+ and Na^+ concentrations from **Figure 4** were used to initialise $[K^+]_i$ and $[Na^+]_i$ in simulations to observe the effect of such variations on the limit cycle AP. The K^+ concentration was initialised to 120 mM and to 152 mM in the two models, whilst the initial Na^+ concentration was initialised to 4 mM and to 16 mM, respectively. Γ_0 was computed from **Eq. 6** for these intracellular concentrations and initial voltage set to its published value (−84.9 mV for the TTP06 model, − 88 mV for the ORd-CiPA model). The high total concentration of intracellular ions yielded $\Gamma_0 = -20.4$ mM and $\Gamma_0 = -24.4$ mM in the TTP06 and the ORd-CiPA models, respectively. The low total concentration of intracellular ions yielded $\Gamma_0 = 23.6$ mM and $\Gamma_0 = 20.9$ mM in the TTP06 and the ORd-CiPA models, respectively.

In simulations in sections below where the value of Γ_0 is imposed by the user, the initial intracellular concentrations must be changed to satisfy the algebraic constraint of **Eq. 6** and leave the initial voltage unchanged. Otherwise, the high variations of Γ_0 reported in **Table 1** would lead to voltage offsets of up to several kilovolts. The intracellular concentration of K^+ was therefore adjusted with **Eq. 6** so that the initial voltage remains untouched and consistent with the required value of Γ_0. Alternatively, Na^+ could be adjusted; but the degree of variation of Γ_0 could lead to negative values of $[Na^+]_i$ so we adjust K^+ instead.

The ORd-CiPA model has extra ionic variables compared to the TTP06 model: variables were added for the concentrations of sodium and potassium in the subspace domain, denoted by $[Na^+]_{SS}$ and $[K^+]_{SS}$. At the limit cycle, the difference between diastolic concentrations of ions in the subspace and in the intracellular compartment were observed to be smaller than 0.1 mM, even when initial conditions were set to very different values (results not shown). Furthermore, there is no physical structure delimiting the subspace from the bulk intracellular space. Thus, K^+ and Na^+ concentrations in the subspace are very close to concentrations in the main intracellular compartments at the end of the resting phase of the AP, i.e., when state variables are initialised in simulations. To avoid introducing big differentials in K^+ and Na^+ concentrations between the subspace and the bulk cytosol compartment in simulations where the user introduced changes to initial conditions for $[K^+]_i$ and $[Na^+]_i$, the initial conditions of $[Na^+]_{SS}$ and $[K^+]_{SS}$ were set to the same values as $[Na^+]_i$ and $[K^+]_i$ respectively.

The limit cycle APs, observed after 2,000 paces, are plotted in **Figure 5**. The difference in Γ_0 induces important changes in the limit cycle AP, especially for the TTP06 model. For instance, the TTP06 model does not have a physiological AP when simulated with a very low Γ_0 value, the cell does not depolarise. In the ORd-CiPA model, the RMP is particularly impacted, decreasing from −82 mV for $\Gamma_0 = -24.4$ mM to −88 mV for $\Gamma_0 = 20.9$ mM. This shows that Γ_0 variations have a strong impact on the model output, which is investigated further below.

3.3 Effect of Γ_0 on Steady States

Several authors have asserted that Γ_0 (or its equivalents from the literature) defines the steady states of various models, both under paced and unpaced conditions (Hund et al., 2001; Jacquemet, 2007; Livshitz and Rudy, 2009; Pan et al., 2018). Here we investigate the steady states and limit cycles reached by the TTP06 and ORd-CiPA models for initial conditions that sample the range of physiologically-plausible Γ_0 values (**Section 3.2**).

The range of experimental concentrations determined in the previous section was sampled at 10 linearly spaced Γ_0 values. For each Γ_0 value, the $[Na^+]_i$ range was sampled linearly at 10 points. The initial $[Ca^{2+}]_i$ was taken to range from 0.5 to 1.5 times its originally published value, also with 10 sampling points, giving a total of 100 samples for each Γ_0 value. The remaining Ca^{2+} concentrations were initialised to a random value ranging from 0.5 to 1.5 times their published initial value. The initial value for $[K^+]_i$ was computed using **Eq. 6** to match with the initial

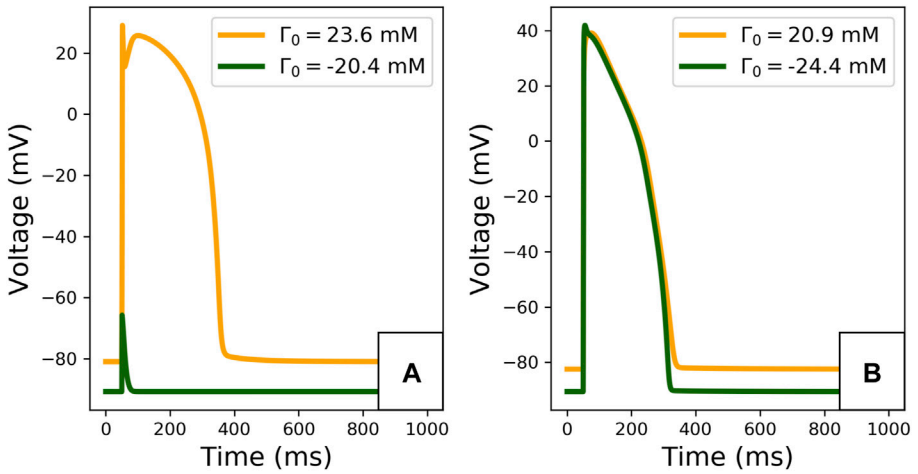

FIGURE 5 | Limit cycle APs for extreme initial conditions for the TTP06 model **(A)** and for the ORd-CiPA model **(B)**. Extreme Γ_0 values covering approximately 44 mM are computed from the extreme $[K^+]_i$ and $[Na^+]_i$ observed in human ventricular models, as reported in **Figure 4**.

voltage of the published model. Due to the linear relationship between the ionic concentrations in **Eq. 6**, a hyperplane in the state variable space can be associated to each Γ_0 value. The initial values of the remaining state variables (gating variables) were taken randomly within the range 0–1, and the sum of the Markov states in the I_{Kr} compartment of the ORd-CiPA model was maintained equal to 1. The quiescent steady state was reached after 4000 s without pacing and the limit cycle was recorded after 2000 s of steady 1 Hz pacing, and the values of the state variables at the end of the diastole were recorded.

The quiescent steady state and the 1 Hz limit cycle diastolic intracellular concentrations are shown in **Figure 6**. For each Γ_0 value, all the simulations converged to the same quiescent or periodic steady state. The steady states that can be reached by the models for the various Γ_0 values align on these plots.

Note how some of the points in **Figure 6A** appear to move outside the Γ_0 plane. Only $[K^+]_i$, $[Na^+]_i$, and $[Ca^{2+}]_i$ are plotted to allow a 3D visualisation of the quiescent steady states and limit cycles. Thus, major changes in other concentrations, which are not plotted in the figure, shift the steady states. Although the steady state variables appear outside of the initial Γ_0 plane in this lower dimensional representation, Γ_0 was correctly preserved throughout the simulations.

For both models, regardless of the initial conditions used for the state variables, a unique quiescent steady state and a unique 1 Hz limit cycle were observed for each value of Γ_0. Thus, the solution of the model under quiescence and for prolonged regular pacing is defined by the value of Γ_0. This observation is consistent with the studies mentioned previously, with constants equivalent to Γ_0. As a conclusion, Γ_0 can be used as a single model parameter to summarise the intracellular concentrations in these models at these pacing conditions and parameter values. Moreover, the initial conditions for the gating variables did not impact the limit cycle or steady-state outputs, so their initial conditions were not altered in further simulations. When calibrating an AP model based on its limit cycle or steady state outputs, it appears sufficient to establish the correct value of Γ_0, regardless of how K^+, Na^+ and Ca^{2+} concentrations and gating variables are individually initialised as long as they remain physiologically plausible. Thus, when exploring values of Γ_0 in a derivative-V_m model the changes could be attributed to a single intracellular concentration (K^+ for example) without loss of generality.

3.4 Model Predictions Are Sensitive to Γ_0

The influence of Γ_0 on the limit cycle outputs and on the APD restitution portrait was evaluated in the TTP06 and ORd-CiPA models. The models' outputs were recorded with Γ_0 values varying by 30 mM. Intracellular concentrations were initialised so that **Eq. 6** is satisfied with the initial voltage set to its published value. The state variables other than intracellular concentrations were initialised to their originally published initial values. 2000 paces were simulated to approach the limit cycle. The inward rectifier potassium current (I_{K1}) and the sodium potassium exchanger current (I_{NaK}), the currents which showed the highest sensitivity to Γ_0 change, were recorded at 1 Hz pacing, together with V_m.

The AP duration restitution portrait at limit cycle was investigated using the Cardiac Electrophysiology Web Lab (https://chaste.cs.ox.ac.uk/WebLab) (Cooper et al., 2016; Daly et al., 2018). There, the models were loaded as CellML files, using the public protocol "Steady State Restitution". In this protocol, 2000 paces are applied (bringing models close to their limit cycles) at various pacing periods ranging from 250 to 2000 ms. Two consecutive APs are then recorded, and their APD_{90}s measured. The limit cycle outputs at 1 Hz and the restitution plots are shown in **Figure 7**.

Γ_0 variations impacted the I_{K1} current particularly strongly in both models, with faster I_{K1} activation kinetics for lower Γ_0 values, see **Figures 7A,E**. In addition, peak I_{K1} is decreased by 45% when increasing Γ_0 by 30 mM in the ORd-CiPA model. I_{NaK} is also shown to be sensitive to Γ_0, see **Figures 7B,F**. When using a low Γ_0

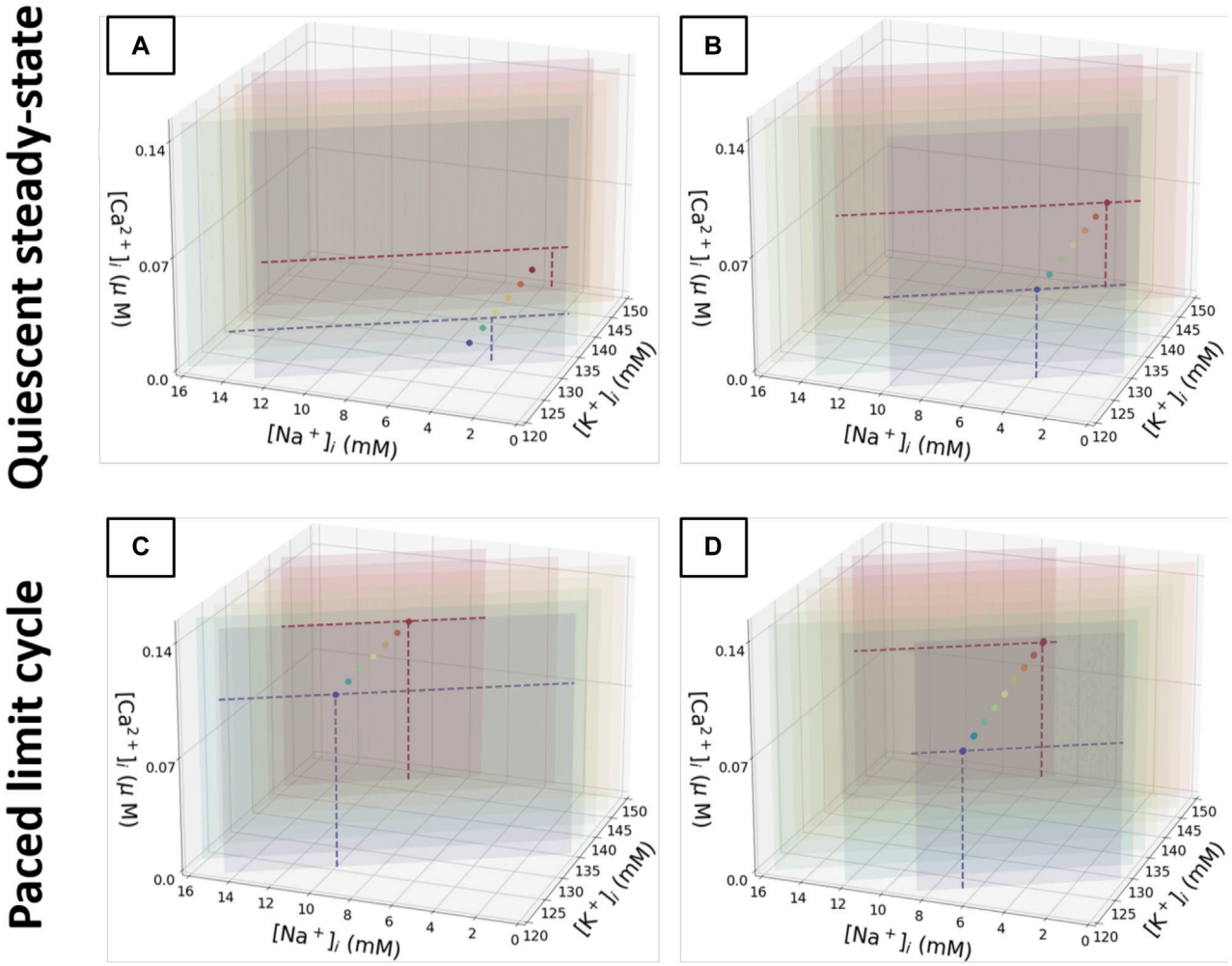

FIGURE 6 | Plot of the quiescent steady state and limit cycle values for $[Na^+]_i$, $[K^+]_i$ and $[Ca^{2+}]_i$. **(A)**: TTP06 model at a quiescent steady state. **(B)**: ORd-CiPA model at a quiescent steady state. **(C)**: TTP06 model in a limit cycle. **(D)**: ORd-CiPA model in a limit cycle. Each plane has initial conditions satisfying **Eq. 6** with the same fixed Γ_0 value. 100 combinations of initial conditions are sampled from each plane to cover the physiological range of concentrations. These initial conditions are used in simulations to reach the (top row) quiescent steady state and the (bottom row) paced limit cycle. The steady state and limit cycle concentrations are plotted as points (with dashed projections along the associated Γ_0 plane), with the colour matching the plane from which the initial conditions were sampled. For clarity, the planes for which the quiescent steady state is out of the range reported in **Section 3.2**, are not shown.

value, I_{NaK} is reduced by approximately 15% in both the TTP06 and the ORd-CiPA models. The consequences for the simulated AP are important, see **Figures 7C,G**. When looking at the resting membrane potential (RMP) and the APD at 90% repolarisation (APD_{90}) for example, RMP is increased from −88 mV to −82 mV for the TTP06 model, and from −88 mV to −83 mV in the ORd-CiPA model when increasing Γ_0 by 30 mM. APD_{90} is increased from 299 to 306 ms for the TTP06 model, and is increased from 265 to 273 ms in the TTP06 ORd-CiPA model, when increasing Γ_0 by 30 mM.

Figures 7D,H show that Γ_0 has an effect on the APD_{90} steady state restitution portraits. The bifurcation of APD_{90} in the restitution portrait is particularly important as it is characteristic of *alternans*, when two consecutive APs do not have the same APD_{90} but the model outputs are still periodic. Note that when stable alternans occurs, the limit cycle no longer follows the trajectory of the state variables over a single pacing period, but over two consecutive pacing periods.

There is a bifurcation of APD_{90} for pacing periods at 700 ms for the TTP06 model and at 400 ms for the ORd-CiPA model. The pacing periods generating this bifurcation appear to be independent of Γ_0. However, the steepness of the restitution slope as well as the size of the bifurcation depend on Γ_0 used for the simulation, especially for the ORd-CiPA model. In the

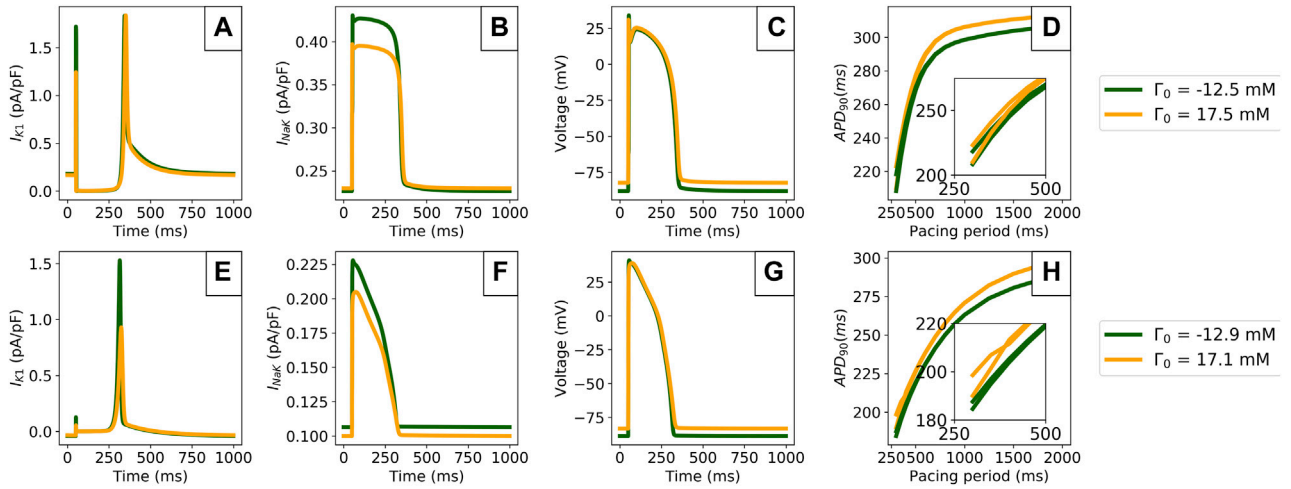

FIGURE 7 | Comparison of model predictions in the periodic steady state outputs for the extreme values of Γ_0 computed from **Section 3.2**. Data is shown for the TTP06 (top row) and ORd-CiPA models (bottom row). **(A,E)**: I_{K1} current. **(B,F)**: Sodium-Potassium exchanger (I_{NaK}) current. **(C,G)**: AP. **(D,H)**: Limit cycle restitution portraits showing APD_{90} variation with the pacing period. The insets show pacing cycle lengths of 500 ms and shorter.

studied models, higher values of Γ_0 generate wider bifurcations in the APD_{90} restitution portrait. The impact of Γ_0 on characteristics of the alternans predicted by the TTP06 and ORd-CiPA models stresses the need to carefully consider the value of Γ_0 used in AP models.

4 CALIBRATION OF AP MODELS AND Γ_0

The dependency of model outputs to Γ_0 observed in **Figure 7** is also expected have an impact when fitting parameter values to whole traces of V_m, or their derived biomarkers. Indeed, if Γ_0 is fixed to a value that incorrectly summarises the experimental concentrations under which the data were generated, we might expect a fitting process to return parameter values which are skewed away from their correct values. A fitting of the ORd-CiPA model to synthetic (simulated) data was performed to examine this effect.

The synthetic datasets used in model training were generated by running the ORd-CiPA model for 2000 pre-paces (1 Hz pacing), and recording the 2001th AP, with one data point per 0.05 ms, no noise was added. The "true" scaling parameters for conductances were then "forgotten" and re-calibrated to the synthetic AP data, as in Johnstone et al. (2016). The parameters used for the simulations are expressed as: $g_{\text{simulation}} = \theta \times g_{\text{original}}$, with $g_{\text{simulation}}$ the value of the conductance used for the simulation, θ the scaling factor, and g_{original} the original value of the conductance parameter. Thus, a scaling factor of $\theta = 1$ corresponds to the conductance used in the original published model (the "*true*" value in this synthetic study).

Three cases were explored to assess the influence of Γ_0 in the fitting process. In the first case, the initial conditions were unaltered (assumed to be known/exactly correct), therefore the value of Γ_0 during the fitting was set to the "true" value, i.e. the one used for synthetic data generation. In the second case, the model was fitted with a fixed and incorrect Γ_0 value computed from initial concentrations and voltage published for the TTP06 model, a different but still plausible value. The third fitting is the same as the second case, but Γ_0 was added to the set of parameters to be fitted, to allow compensation for discrepancy in the initial intracellular ion concentrations provided by the user (in terms of **Figure 6** this allows flexibility in the plane upon which intracellular concentrations will settle). The initial conditions used for the fittings are reported in the **Table 2**.

When using initial concentrations from the TTP06 model, calcium concentrations, $[Na^+]_i$ and $[K^+]_i$ were set to the values published by Ten Tusscher and Panfilov (2006) $[K^+]_{SS}$ and $[Na^+]_{SS}$ were initialised to the same value as $[K^+]_i$ and $[Na^+]_i$. In the ORd-CiPA model, the SR is split into two sub-compartments while the TTP06 model has only one SR compartment. Therefore $[Ca^{2+}]_{NSR}$ and $[Ca^{2+}]_{JSR}$ were initialised at the same concentration published by Ten Tusscher et al. for $[Ca^{2+}]_{SR}$.

The optimisation problem was defined as the minimisation of the sum of square errors between the synthetic data and the fitted model AP. The fitting algorithm uses the PINTS Python package (https://github.com/pints-team/pints) (Clerx et al., 2019), to run the Covariance Matrix Adaptation-Evolution Strategy (CMA-ES) (Hansen et al., 2003). The scaling factor parameters θ_{CaL}, θ_{Kr}, θ_{Ks}, θ_{Na}, θ_{NaL} of the ORd-CiPA model were fitted. The initial guesses for scaling factors were taken from the range 0.2–5, while the boundaries were set to 0.1 to 10. The CMA-ES hyper-parameter Σ_0, the initial proposal covariance for new parameter samples, was set to 0.1 along the diagonal for all parameters and zero otherwise.

The value of scaling parameters retrieved by the three fittings are compared in **Table 3**, and the corresponding APs are plotted in **Figure 8**. In the case of the first fitting with the correct Γ_0, the true parameter values are retrieved as expected due to these model parameters being identifiable. In the case of the second

TABLE 2 | Initial conditions used in the various fittings of the ORd-CiPA model to synthetic data.

Case	Γ_0	Initial conditions for $[K^+]_i$	Initial conditions for other concentrations
Data generation	– 7.801	144.6 mM	ORd-CiPA
#1 Fixed & 'correct' Γ_0	– 7.801	144.6 mM	ORd-CiPA
#2 Fixed & 'wrong' Γ_0	– 1.562	135.4 mM	TTP06
#3 Fitted Γ_0	Fitted	135.4 mM	TTP06

TABLE 3 | Parameters retrieved from fittings in the investigated cases. The fitting process with an incorrect Γ_0 value yields incorrect values for model parameters. Such a model suffers from poor predictive power, this can be corrected by fitting Γ_0 together with the other model parameters.

Case	Γ_0 (mM)	Diastolic $[K+]_i$ atlimitcycle	θ_{CaL}	θ_{Kr}	θ_{Ks}	θ_{Na}	θ_{NaL}	APD_{90} baseline	APD_{90} with 50% I_{Kr} block
Data generation	**−7.801**	**144.4**	**1**	**1**	**1**	**1**	**1**	**266** ms	**369** ms
#1 Fixed & "correct" Γ_0	−7.801	144.4	1.000	1.000	1.000	1.000	1.000	266 ms	369 ms
#2 Fixed & "wrong" Γ_0	−1.562	138.6	0.760	1.187	0.522	1.129	1.585	265 ms	383 ms
#3 Fitted Γ_0	−7.801	144.4	1.000	1.000	1.000	1.000	1.000	266 ms	369 ms

Values associated with the synthetic (simulated) data generation are written in bold font.

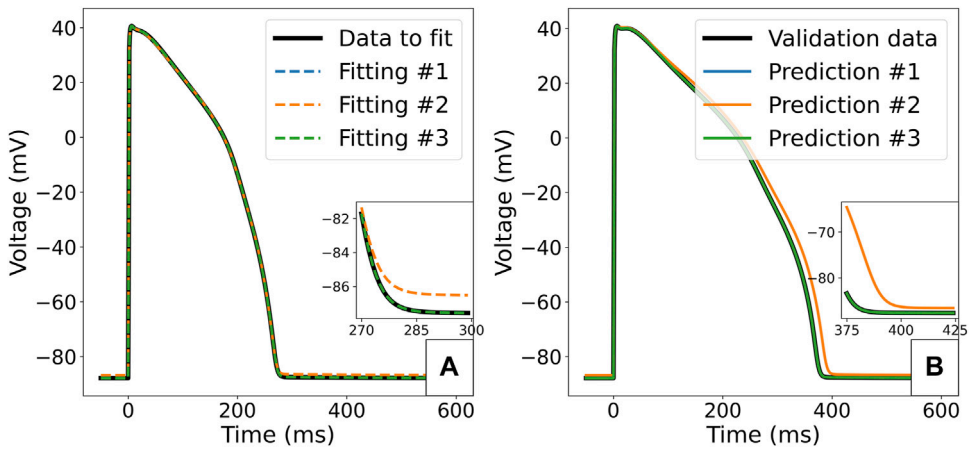

FIGURE 8 | Predicted APs for the ORd-CiPA model fitted to synthetic data. **(A)** Comparison of the synthetic data with APs obtained from optimal parameterisations in the different fitting cases. **(B)** Prediction of response of the model to 50% block of I_{Kr}. Predictions of model with parameter fittings #1, #3 and the true parameters set overlay.

fitting with a discrepancy in Γ_0, the model cannot converge to the right limit cycle. The optimal AP is still very similar to the synthetic data, the only difference being a small shift in the resting membrane potential, as seen in **Figure 8A**. However, the discrepancy in ionic concentrations is compensated by a dramatic shift in the retrieved scaling parameters, especially for g_{Ks} (0.522) and g_{NaL} (1.585). This impacts the response of the model to perturbation: for example 50% block of I_{Kr} as shown in **Figure 8B**, where we see a 14 ms difference in the predicted APD_{90} which would be significant in many drug effect prediction settings.

In the case of the third fitting with Γ_0 as an inferred parameter, the true values for all scaling parameters could be recovered. The fact that the value of Γ_0 could also be accurately retrieved from fitting supports its identifiability as a model parameter, at least in the absence of model misspecification/discrepancy.

4.1 Calibration When Multiple Stable Limit Cycles Exist for a Single Γ_0 Value

It was shown in **Section 3.3** that the ORd-CiPA model, with published parameters, has a unique limit cycle for any particular

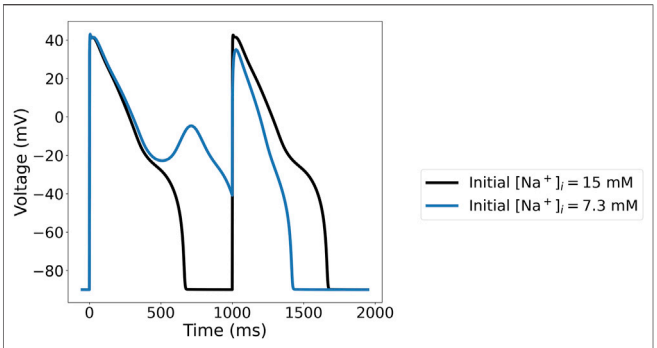

FIGURE 9 | Limit cycle APs for the ORd-CiPA model under 95% of I_{Kr} reduction, generated with the same value for Γ_0=−20 mM, but different initial Na^+ concentrations. With the initial Na^+ concentration set to 15 mM (Black), the limit cycle AP shows no early after-depolarisation (EAD). With a lower initial Na^+ concentration of 7.3 mM (Blue), the limit cycle AP exhibits alternans with an EAD.

value of Γ_0 that has been used (implicitly) in previous models. As shown by previous studies, under certain conditions there are possibly multiple quiescent steady state (Guan et al., 1997; Jacquemet, 2007) and/or limit cycle (Surovyatkina et al., 2010) solutions for the same value of Γ_0.

For instance, with 95% reduction of I_{Kr}, $\Gamma_0 = -20$ mM, and 1 Hz pacing, the ORd-CiPA model has two stable limit cycle APs, shown in **Figure 9**. With the initial Na^+ concentration as originally published in the ORd-CiPA model, the limit cycle AP has an early after-depolarisation (EAD), whereas the limit cycle AP with higher initial Na^+ concentration exhibits alternans and an EAD. This is characteristic of a bifurcation of the limit cycle for the same value of Γ_0, which is investigated further in this section.

Various conditions of I_{Kr} block (0, 90 and 95%) were applied to the ORd-CiPA model to test for the presence of multiple limit cycles for a single value of Γ_0. As in **Section 3.3**, the ORd-CiPA model was paced to its limit cycle for various initial conditions that sample the physiological range of concentrations reported in **Section 3.2**, but variations of initial conditions were considered only for $[K^+]_i$ and $[Na^+]_i$ this time. Given the low influence of $[Ca^{2+}]$ variations on Γ_0 value, its influence on the model outputs were neglected. **Eq. 6** defines a linear relationship between $[Na^+]_i$ and $[K^+]_i$ and Γ_0, and therefore for a fixed value of Γ_0, the intracellular concentrations follow a line in the ($[Na^+]_i$, $[K^+]_i$) plane, if the other ionic concentrations are not changed. Ten different initial conditions were sampled for each of the 15 values of Γ_0 covering the physiological range of concentrations ($[K^+]_i$ between 120 and 152 mM and $[Na^+]_i$ between 4 and 16 mM). In case there is alternans, diastolic concentrations are read out at the end of the longer AP.

The limit cycle diastolic concentrations reached for the various Γ_0 values with various I_{Kr} block conditions are represented in **Figure 10**. For I_{Kr} block lower than 90% across the range of initial conditions we studied, the limit cycle is unique for a given value of Γ_0. In such situations, fitting Γ_0 would be sufficient to fully inform the intracellular concentrations.

In the extreme case of 95% of I_{Kr} block, a bifurcation is observed for the ORd-CiPA model—see **Figure 10C**. A second stable limit cycle appears, and intracellular concentrations converge to one or the other limit cycle value depending on their initial conditions, despite corresponding to the same Γ_0 value. The multiple limit cycles at a fixed Γ_0 value are observed for Γ_0 values ranging from −13 to 2 mM—see **Figure 10C**. In such cases, Γ_0 does not solely determine which limit cycle will be reached, and one needs to consider $[K^+]_i$ and $[Na^+]_i$ initial conditions.

As observed in **Figure 10**, multiple stable limit cycles can be found for the same value of Γ_0 under particular conditions. In this section, we investigate how the bifurcations of the limit cycle can impact the fitting process. Under 95% of I_{Kr} reduction, there are two stable limit cycle APs for the ORd-CiPA model for the same value of Γ_0: one with early after-depolarisation (EAD) generated with low initial $[Na^+]_i$, and one without EAD when simulating the limit cycle AP from high initial $[Na^+]_i$—see **Figure 9**.

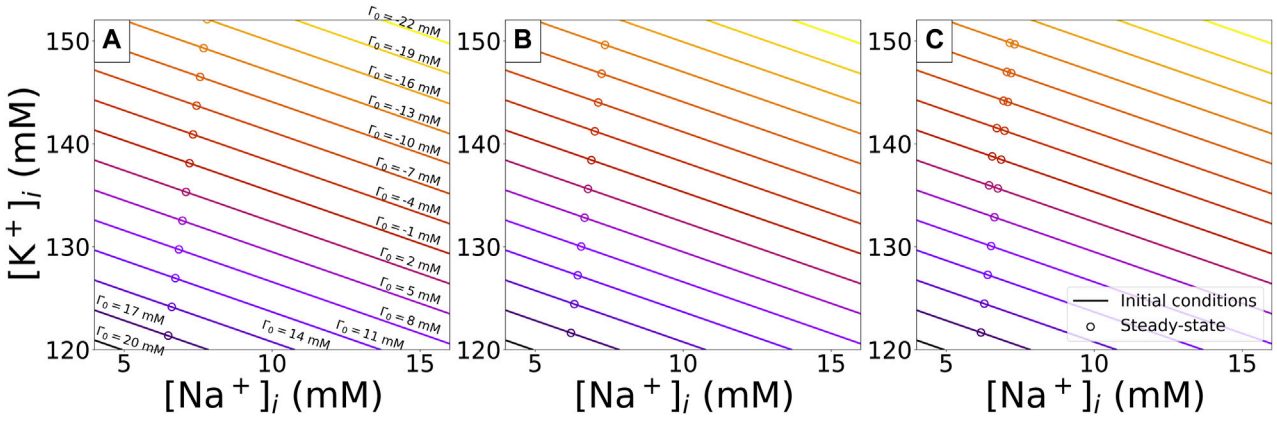

FIGURE 10 | Limit cycle concentrations of $[K^+]_i$ and $[Na^+]_i$ for simulations with ORd-CiPA model starting from different initial conditions. Each line corresponds to combinations of intracellular concentrations bound by a single Γ_0 value. For each value of Γ_0, 10 combinations of $[K^+]_i$ and $[Na^+]_i$ are used to sample the whole physiological range reported in **Section 3.2**. Limit cycle concentrations of the 10 combinations are marked by circles, with colour matching the initial conditions. For I_{Kr} reduction up to 90%, a unique limit cycle can be reached per value of Γ_0. In the case of 95% of I_{Kr} reduction, two distinct limit cycles can be observed for higher intracellular concentrations. **(A)**: With no I_{Kr} reduction. **(B)**: With 90% I_{Kr} reduction. **(C)**: With 95% I_{Kr} reduction.

TABLE 4 | Rescaling factors for conductance parameters retrieved from fitting to data generated under conditions where several stable limit cycles coexist for the same value of $\Gamma_0 = -20$ mM.

	Γ_0 (mM)	Diastolic $[K+]_i$ (mM)	θ_{CaL}	θ_{Kr}	θ_{Ks}	θ_{Na}	θ_{NaL}	APD_{90} with 95% I_{Kr} block	APD_{90} baseline
Data generation	**−20.0**	**156.18**	**1**	**1**	**1**	**1**	**1**	**663 ms**	**264 ms**
Fitted values	−19.7	155.73	0.863	0.933	1.263	0.936	1.574	663 ms	294 ms

Values associated with the synthetic (simulated) data generation are written in bold font.

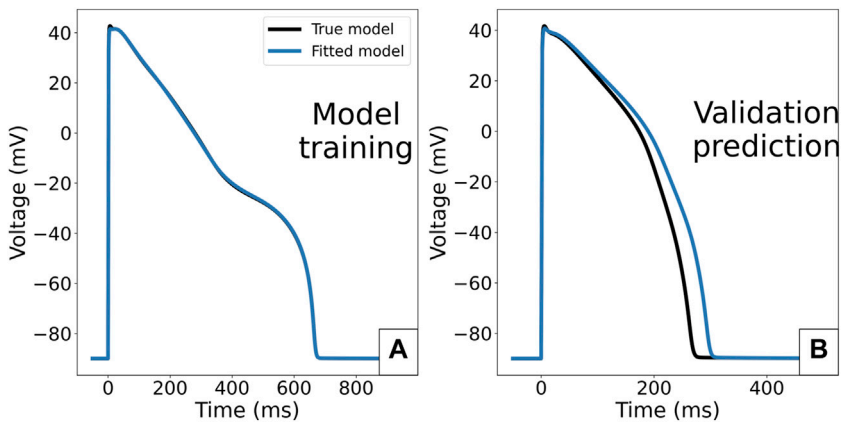

FIGURE 11 | Consequence of fitting the ORd-CiPA model in case of multiple stable limit cycles for the same Γ_0 value. **(A)**: ORd-CiPA fitted with initial $[Na^+]_i$ = 7.3 mM under 95% of I_{Kr} block is able to reproduce the synthetic data generated with initial $[Na^+]_i$ = 15 mM (APs superposed). **(B)**: predictions for no I_{Kr} block. Despite the good fit to I_{Kr} block data in panel **(A)**, incorrect parameter values are retrieved from fitting, and the prediction of the calibrated model is erroneous.

The synthetic data was generated with the ORd-CiPA model under 95% of I_{Kr} block, with intracellular concentrations initialised at $[Na^+]_i$ = 15 mM and $[K^+]_i$ = 149 mM, corresponding to $\Gamma_0 = -20$ mM. Synthetic data showed no EAD. As seen in **Figure 9**, there is a second stable limit cycle AP, with EAD, in this configuration of the ORd-CiPA model with lower initial Na^+ concentration.

During the fitting process, the initial concentration of Na^+ was fixed to its published value $[Na^+]_i$ = 7.3 mM, and when a new value of Γ_0 was proposed by the fitting algorithm, the changes in Γ_0 were attributed to K^+ ions. As a consequence, when the "true parameters" were evaluated during the fitting process, an EAD was observed. The fitting of the ORd-CiPA model to synthetic data from the same model was performed with the same methods as in **Section 4**. The same parameters as previously were fitted (θ_{CaL}, θ_{Kr}, θ_{Ks}, θ_{Na}, θ_{NaL}, Γ_0).

Note that for $\Gamma_0 = -20$ mM, $[Na^+]_i$ can take only values between 14 and 16 mM for $[K^+]_i$ to remain in the physiological range (**Figure 10**). This bifurcation was selected despite the initial and limit cycle concentrations being outside the physiological range, because of the dramatic changes between the two limit cycle APs that make more visual the potential impact of multiple stable limit cycles on the parameters retrieved from model calibration.

The parameters retrieved from the fitting are reported in **Table 4**. The limit cycle AP under 95% I_{Kr} reduction for the calibrated model is compared to the synthetic data (**Figure 11A**) and its prediction of AP without I_{Kr} block is compared to that of the true model that generated the synthetic data in the validation case of **Figure 11B**.

The optimal values of θ_{Kr} and θ_{Na} are close to their true values, but θ_{NaL} and θ_{Ks} have considerable differences to their true values, 57 and 26% too large respectively. This explains why even though the synthetic data AP is well reproduced (**Figure 11A**), the fitted model makes an incorrect prediction in the validation case with no I_{Kr} block (**Figure 11B**). The optimal value of Γ_0 is interestingly close to its true value. However, one cannot conclude from this example alone that Γ_0 value will still be correctly recovered in the case of bifurcation.

In this case with bifurcation, fitting initial conditions for both $[Na^+]_i$ and $[K^+]_i$ would be necessary to reach the correct limit cycle and obtain a correct optimal model. However, we would not recommend fitting both $[Na^+]_i$ and $[K^+]_i$ simultaneously as a standard. In most cases, there is only one limit cycle solution for a given value of Γ_0, so that the two parameters would be unidentifiable (see Whittaker et al., 2020).

5 DISCUSSION

We investigated the consequences of computing voltage in AP models directly from concentrations, using an algebraic-V_m formulation (**Eq. 6**). This method for computing voltage increases the numerical accuracy of solutions, compared to the canonical derivative-V_m method of integrating the sum of trans-

membrane currents. The computation time of simulations is not impacted significantly by the choice of expression for the voltage. Changing to the algebraic-V_m form of the model did not reduce the computational time required for AP simulations, as it does not change the stiffness of the model (the main driver for the computational cost).

Γ_0 is a constant representing the net concentration of unmodelled charge present in the model, needed to ensure the consistency of initial values for concentrations and voltage. In most cases, the value of Γ_0 defines the steady-state behaviour of the model, regardless of the combination of initial values for state variables such as concentrations in the simulations. Given the high variability of intracellular concentrations that have been used in action potential models, with less variability in extracellular concentrations, Γ_0 is also highly variable. Extreme variations of Γ_0 lead to very different steady-state behaviours and substantially impact their outputs, making it important to establish the value of Γ_0 as accurately as possible.

Measurements of intracellular ionic concentrations in intact myocytes are not generally available alongside recordings of electrophysiological activity used to calibrate AP models. We showed that this issue could potentially be addressed by inferring Γ_0 from the data, along with other parameters of the AP model.

With the algebraic-V_m form of the model, the algebraic constraint on the variables appears explicitly. At each time-step, this constraint is therefore rigorously applied to the system. With the derivative-V_m form of the model, the constraint is mathematically satisfied by the system—by design in AP models which satisfy the conservation of charge principle—but during the numerical integration of the equations, the constraint is not verified at each time step. Therefore, the numerical errors that appear during the integration allow the constraint to be violated. This violation of conservation of charge explains that with a coarse solver tolerance, the model does not properly converge to a limit cycle—see **Figure 2**. Livshitz & Rudy noted that AP models are often mistaken as Ordinary Differential Equation (ODE) systems when they are actually Differential-Algebraic Equation (DAE) systems—ODE systems with algebraic constraints. With the algebraic-V_m form of the model, all constraints of the DAEs appear explicitly, which is best practice (Livshitz and Rudy, 2009). In theory, the differential and algebraic representations of the membrane voltage are still mathematically equivalent, so modellers could use either of them as preferred (Hund et al., 2001). In practice, we recommend to use the algebraic-V_m formulation.

Using the algebraic-V_m form of the model makes also Γ_0 appear as a model parameter, highlighting the need to consider its value explicitly. We propose to infer Γ_0 from the experimental data on which the model is calibrated. Endresen et al. (2000) reported with the derivative-V_m form of the model that "the observer tracks only the variations in the number of ions, but then an initial concentration must be guessed". Livshitz & Rudy proposed criteria for validation against experimental data and adequate comparison between dynamic models (Livshitz and Rudy, 2009). Among these criteria, the use of "a consistent set of initial conditions for state variables (V_m, intracellular ion concentrations)" is recommended. Smirnov et al. (2020) also noted that the question of initial conditions for ionic concentrations is often overlooked when fitting AP models, when they fitted the O'Hara Rudy model (O'Hara et al., 2011) to AP recordings from optical mapping experiments in human ventricular wedges.

The errors induced in conductance fits when using a fixed but incorrect Γ_0—see **Section 4**—emphasise the importance of using the correct initial conditions for concentrations when fitting to AP data. An AP model calibrated using an incorrect representation of concentrations (i.e. an incorrect but plausible value for Γ_0) is badly parameterised with up to ±50% error in some maximal conductance parameters, and has a reduced predictive power.

Our results show that Γ_0 can be fitted to compensate for errors in assumed intracellular concentrations, at least when fitting to synthetic (simulated) AP data. So we recommend inferring Γ_0 from the training data during model calibration, following the methods of **Section 4**. When using real data, discrepancy in the AP model may cause additional problems, but still the possibility for uncertainty in Γ_0 should be explicitly considered.

In our study, we show that due to the conservation law: 1) a consistent Γ_0 value should be used throughout the model calibration, and 2) it is sufficient to fit the value of Γ_0 to capture the input of intracellular concentrations on steady state outputs, unless bifurcations are present. The second point is supported by observations on other models reported in the literature (Hund et al., 2001; Jacquemet, 2007; Livshitz and Rudy, 2009; Pan et al., 2018). For example, Smirnov et al. (2020) have included initial values for $[Na^+]_i$ and $[Ca^{2+}]_{SR}$ in their set of parameters to calibrate, which is similar to fitting Γ_0. However, they fitted their initial conditions independently at each pacing rate, thus changing the value of Γ_0 from one pacing rate to another.

It remains important to consider that the uniqueness of the limit cycle for a single Γ_0 value cannot be always guaranteed (Guan et al., 1997; Jacquemet, 2007). The methods presented in **Section 3.3** can be reused to verify that Γ_0 solely defines the limit cycle for a model under a given set of studied experimental conditions. If the uniqueness of a limit cycle is verified, it is reasonable to fit Γ_0 alone to summarise the initial conditions of intracellular ionic concentrations. Otherwise, in case of bifurcation of the limit cycle, we would recommend fitting Γ_0 and the initial condition of $[Na^+]_i$. Alternatively, initial conditions for two intracellular concentrations could be inferred, for instance $[K^+]_i$ and $[Na^+]_i$ which have the highest contribution to the value of Γ_0.

5.1 Limitations

As mentioned above and in the literature (Guan et al., 1997; Jacquemet, 2007), the uniqueness of the steady states for a single Γ_0 value is not always guaranteed. In cases of bifurcation, where several stable solutions exist for the model with a single value of Γ_0, Γ_0 (as well as other parameters) can be incorrectly determined. We observed in this study that for the ORd-CiPA model, the limit cycle is unique in most physiologically-plausible cases. However, this property does not always hold if parameters are changed. A

method to investigate thoroughly the uniqueness of the limit cycle for a given value of Γ_0 for all parameterisations of an AP model could be extremely costly computationally. Still, we have demonstrated for the ORd-CiPA model, as originally published, that Γ_0 is identifiable and could be correctly estimated. We observed consistent findings for Γ_0 in the TTP06 model, which has a very different model structure to the ORd-CiPA model—data not shown. We therefore expect this behaviour to be replicated for all AP models that conserve charge. Hence we recommend to consider calibrating Γ_0 as a parameter that usually encapsulates both the initial conditions of the modelled ionic species and the un-modelled charge. In the cases where there are multiple steady states for the same Γ_0, the unidentifiability could be resolved by fitting initial conditions for ionic concentrations as well.

To define the physiologically-plausible range of concentrations, we used the extreme values of $[K^+]_i$ reported in previous human ventricular AP models. Direct experimental measurements of $[K^+]_i$ would help refining this range. Moreover, $[Na^+]_i$ and $[K^+]_i$ were considered separately in our study. Simultaneous experimental measurements of $[Na^+]_i$ and $[K^+]_i$ in human ventricular cardiomyocytes would give better understanding of correlation between these concentrations, which may further restrict the range of physiologically-plausible Γ_0 values.

When AP models are used to investigate changes in extracellular concentrations (e.g. when simulating hypo/er-kalemia or ischaemia—pathological changes to extracellular concentrations such as $[K^+]$) care is needed with **Eq. 6**. In such situations, as the extracellular ion of interest changes concentration, opposite charges will be introduced into the same solution to maintain electrical neutrality (e.g. if we experimentally use the salt KCl to change $[K^+]_o$ we also change $[Cl^-]_o$); if one ion is accounted for in **Eq. 6** but the 'opposite ion' is not (e.g. the model does include $[K^+]_o$ but does not explicitly consider $[Cl^-]_o$) then Γ_0 will need to be adjusted by the same amount to account for this extra "opposite" charge. For models where external concentrations are fixed as constants, an equation of the form of **Eq. 2** with V_0 or C_0 can then be used equivalently, and would simplify simulation procedures when extracellular concentrations are changed by the user, but the interpretation of Γ_0 as "net un-modelled charge" is clearer.

5.2 Possible Extensions to This Study

Although this study was focused on ventricular AP models, the conservation law that binds together the voltage and intracellular ionic concentrations applies to all cellular electrophysiology models: other cardiac cell types, neural, gastric, skeletal muscle etc.

The improvement in numerical accuracy enabled by the algebraic-V_m form of the model was shown to reduce the numerical error that can lead to deviation of state variables after reaching the periodic steady state—see **Figure 3** and **Supplementary Material Section S1.4**. The computational efficiency was similar with the algebraic-V_m form of the model when using the same solver tolerance.

The extent to which intracellular concentrations are well established has been somewhat overlooked (Smirnov et al., 2020). Our study, showed the importance of the correct estimation of Γ_0 in specifying concentrations. In literature models, there is significant variation between the assumed initial concentrations, and therefore variation in Γ_0, as shown in **Section 3.2**. In papers on action potential model development, we have not found any discussion of the choice of Γ_0, or equivalently the choice of the offset between concentrations and voltage in initial conditions, perhaps suggesting somewhat arbitrary choices. It remains to be seen whether Γ_0 exhibits significant physiological variation to contribute to inter-cell and/or inter-individual differences in electrophysiology, or whether it is a well-constrained biological quantity—which would be the case if the un-modelled missing ions that Γ_0 represents do not vary significantly between cells or individuals. In either case, Γ_0 strongly influences model behaviour and a concerted effort should be made to identify its value alongside other key model parameters. The recent emergence of cell-specific models (Groenendaal et al., 2015) may offer an approach to quantify Γ_0 more accurately.

6 CONCLUSION

We advocate here for the use of the algebraic-voltage form of AP models, as it improves the stability of numerical solutions by enforcing a hidden algebraic constraint in the models. Furthermore, the algebraic-voltage form ensures that the model conserves charge. It also requires the modeller to think carefully about initial conditions for intracellular concentrations and to acknowledge their effects on the model output. We recommend consideration of the potential discrepancy and uncertainty in intra- and extracellular concentrations of ions, as model outputs and model fitting are dependent on these. The Γ_0 value summarises these factors into one parameter which can be fitted alongside the rest of a model.

DATA AVAILABILITY STATEMENT

The datasets presented in this study can be found in online repositories. The names of the repository/repositories can be found below: Github: https://github.com/CardiacModelling/Gamma_0. Zenodo (permanent archive of Github): http://dx.doi.org/10.5281/zenodo.6423387.

AUTHOR CONTRIBUTIONS

Y-SB, JS, DW, MC, DG, and GM designed the investigation. Y-SB wrote the codes and performed the simulations under the supervision of MC, KW, LP, DG, and GM. Y-SB, MC, DG, and GM wrote the manuscript. All authors read and approved the final version of the manuscript.

FUNDING

This work was supported by the UK Engineering and Physical Sciences Research Council (grant number EP/S024093/1); the Biotechnology and Biological Sciences Research Council (grant number BB/P010008/1); and the Wellcome Trust (grant number 212203/Z/18/Z). Y-SB. acknowledges support from F. Hoffmann-La Roche Ltd. for studentship support *via* the EPSRC and MRC Centre for Doctoral Training in Systems Approaches to Biomedical Science. GM, JS, MC, and DW acknowledge support from the Wellcome Trust *via* a Wellcome Trust Senior Research Fellowship to GM, MC, and GM acknowledge support from a BBSRC project grant. DG. gratefully acknowledges support from the EPSRC Centres for Doctoral Training Programme. This research was funded in whole, or in part, by the Wellcome Trust (212203/Z/18/Z). For the purpose of open access, the author has applied a CC-BY public copyright licence to any Author Accepted Manuscript version arising from this submission.

SUPPLEMENTARY MATERIAL

The Supplementary Material for this article can be found online at: https://www.frontiersin.org/articles/10.3389/fphys.2022.879035/full#supplementary-material

REFERENCES

Beeler, G. W., and Reuter, H. (1977). Reconstruction of the Action Potential of Ventricular Myocardial Fibres. *J. Physiol.* 268, 177–210. doi:10.1113/jphysiol.1977.sp011853

Bers, D., Barry, W., and Despa, S. (2003). Intracellular Na^+ Regulation in Cardiac Myocytes. *Cardiovasc. Res.* 57, 897–912. doi:10.1016/S0008-6363(02)00656-9

Clerx, M., Collins, P., de Lange, E., and Volders, P. G. A. (2016). Myokit: A Simple Interface to Cardiac Cellular Electrophysiology. *Prog. Biophys. Mol. Biol.* 120, 100–114. doi:10.1016/j.pbiomolbio.2015.12.008

Clerx, M., Robinson, M., Lambert, B., Lei, C. L., Ghosh, S., Mirams, G. R., et al. (2019). Probabilistic Inference on Noisy Time Series (PINTS). *J. Open Res. Softw.*. doi:10.5334/jors.252

Cohen, S. D., Hindmarsh, A. C., and Dubois, P. F. (1996). CVODE, a Stiff/nonstiff ODE Solver in C. *Comput. Phys.* 10, 138–143. doi:10.1063/1.4822377

Cooper, J., Scharm, M., and Mirams, G. R. (2016). The Cardiac Electrophysiology Web Lab. *Biophysical J.* 110, 292–300. doi:10.1016/j.bpj.2015.12.012

Cooper, J., Spiteri, R. J., and Mirams, G. R. (2015). Cellular Cardiac Electrophysiology Modeling with Chaste and Cellml. *Front. Physiol.* 5, 511. doi:10.3389/fphys.2014.00511

Corrias, A., and Buist, M. L. (2007). A Quantitative Model of Gastric Smooth Muscle Cellular Activation. *Ann. Biomed. Eng.* 35, 1595–1607. doi:10.1007/s10439-007-9324-8

Daly, A. C., Clerx, M., Beattie, K. A., Cooper, J., Gavaghan, D. J., and Mirams, G. R. (2018). Reproducible Model Development in the Cardiac Electrophysiology Web Lab. *Prog. Biophys. Mol. Biol.* 139, 3–14. doi:10.1016/j.pbiomolbio.2018.05.011

Demir, S. S., Clark, J. W., Murphey, C. R., and Giles, W. R. (1994). A Mathematical Model of a Rabbit Sinoatrial Node Cell. *Am. J. Physiology-Cell Physiol.* 266, C832–C852. doi:10.1152/ajpcell.1994.266.3.c832

Dibb, K., Trafford, A., Zhang, H., and Eisner, D. (2015). A Model Model: A Commentary on DiFrancesco and Noble (1985) 'A Model of Cardiac Electrical Activity Incorporating Ionic Pumps and Concentration Changes'. *Phil. Trans. R. Soc. B* 370, 20140316. doi:10.1098/rstb.2014.0316

DiFrancesco, D., and Noble, D. (1985). A Model of Cardiac Electrical Activity Incorporating Ionic Pumps and Concentration Changes. *Philos. Trans. R. Soc. Lond. B Biol. Sci.* 307, 353–398. doi:10.1098/rstb.1985.0001

Dodge, F. A., and Cooley, J. W. (1973). Action Potential of the Motorneuron. *IBM J. Res. Dev.* 17, 219–229. doi:10.1147/rd.173.0219

Dokos, S., Celler, B., and Lovell, N. (1996). Ion Currents Underlying Sinoatrial Node Pacemaker Activity: A New Single Cell Mathematical Model. *J. Theor. Biol.* 181, 245–272. doi:10.1006/jtbi.1996.0129

Dutta, S., Chang, K. C., Beattie, K. A., Sheng, J., Tran, P. N., Wu, W. W., et al. (2017). Optimization of an In Silico Cardiac Cell Model for Proarrhythmia Risk Assessment. *Front. Physiol.* 8, 616. doi:10.3389/fphys.2017.00616

Endresen, L. P., Hall, K., Høye, J. S., and Myrheim, J. (2000). A Theory for the Membrane Potential of Living Cells. *Eur. Biophys. J.* 29, 90–103. doi:10.1007/s002490050254

Fry, C. H., Ward, J. P. T., Twist, V. W., and Powell, T. (1986). Determination of Intracellular Potassium Ion Concentration in Isolated Rat Ventricular Myocytes. *Biochem. Biophysical Res. Commun.* 137, 573–578. doi:10.1016/0006-291X(86)91249-0

Grandi, E., Pasqualini, F. S., and Bers, D. M. (2010). A Novel Computational Model of the Human Ventricular Action Potential and Ca Transient. *J. Mol. Cell Cardiol.* 48, 112–121. doi:10.1016/j.yjmcc.2009.09.019

Groenendaal, W., Ortega, F. A., Kherlopian, A. R., Zygmunt, A. C., Krogh-Madsen, T., and Christini, D. J. (2015). Cell-Specific Cardiac Electrophysiology Models. *Plos Comput. Biol.* 11, e1004242. doi:10.1371/journal.pcbi.1004242

Guan, S., Lu, Q., and Huang, K. (1997). A Discussion about the DiFrancesco-Noble Model. *J. Theor. Biol.* 189, 27–32. doi:10.1006/jtbi.1997.0486

Hansen, N., Müller, S. D., and Koumoutsakos, P. (2003). Reducing the Time Complexity of the Derandomized Evolution Strategy with Covariance Matrix Adaptation (CMA-ES). *Evol. Comput.* 11, 1–18. doi:10.1162/106365603321828970

Hilgemann, D., and Noble, D. (1987). Excitation-Contraction Coupling and Extracellular Calcium Transients in Rabbit Atrium: Reconstruction of Basic Cellular Mechanisms. *Proc. R. Soc. Lond. B.* 230, 163–205. doi:10.1098/rspb.1987.0015

Hindmarsh, A. C., Brown, P. N., Grant, K. E., Lee, S. L., Serban, R., Shumaker, D. E., et al. (2005). SUNDIALS: Suite of Nonlinear and Differential/Algebraic Equation Solvers. *ACM Trans. Math. Softw.* 31, 363–396. doi:10.1145/1089014.1089020

Hodgkin, A. L., and Huxley, A. F. (1952). A Quantitative Description of Membrane Current and its Application to Conduction and Excitation in Nerve. *J. Physiol.* 117, 500–544. doi:10.1113/jphysiol.1952.sp004764

Hund, T. J., Kucera, J. P., Otani, N. F., and Rudy, Y. (2001). Ionic Charge Conservation and Long-Term Steady State in the Luo-Rudy Dynamic Cell Model. *Biophysical J.* 81, 3324–3331. doi:10.1016/S0006-3495(01)75965-6

Hund, T. J., and Rudy, Y. (2004). Rate Dependence and Regulation of Action Potential and Calcium Transient in a Canine Cardiac Ventricular Cell Model. *Circulation* 110, 3168–3174. doi:10.1161/01.CIR.0000147231.69595.D3

Iyer, V., Mazhari, R., and Winslow, R. L. (2004). A Computational Model of the Human Left-Ventricular Epicardial Myocyte. *Biophysical J.* 87, 1507–1525. doi:10.1529/biophysj.104.043299

Jacquemet, V. (2007). Steady-State Solutions in Mathematical Models of Atrial Cell Electrophysiology and Their Stability. *Math. Biosciences* 208, 241–269. doi:10.1016/j.mbs.2006.10.007

Johnstone, R. H., Chang, E. T. Y., Bardenet, R., De Boer, T. P., Gavaghan, D. J., Pathmanathan, P., et al. (2016). Uncertainty and Variability in Models of the Cardiac Action Potential: Can We Build Trustworthy Models? *J. Mol. Cell Cardiol.* 96, 49–62. doi:10.1016/j.yjmcc.2015.11.018

Lindblad, D. S., Murphey, C. R., Clark, J. W., and Giles, W. R. (1996). A Model of the Action Potential and Underlying Membrane Currents in a Rabbit Atrial Cell. *Am. J. Physiology-Heart Circulatory Physiol.* 271, H1666–H1696. doi:10.1152/ajpheart.1996.271.4.H1666

Livshitz, L., and Rudy, Y. (2009). Uniqueness and Stability of Action Potential Models during Rest, Pacing, and Conduction Using Problem-Solving Environment. *Biophysical J.* 97, 1265–1276. doi:10.1016/j.bpj.2009.05.062

Lovell, N. H., Cloherty, S. L., Celler, B. G., and Dokos, S. (2004). A Gradient Model of Cardiac Pacemaker Myocytes. *Prog. Biophys. Mol. Biol.* 85, 301–323. doi:10.1016/j.pbiomolbio.2003.12.001

Luo, C. H., and Rudy, Y. (1994). A Dynamic Model of the Cardiac Ventricular Action Potential. I. Simulations of Ionic Currents and Concentration Changes. *Circ. Res.* 74, 1071–1096. doi:10.1161/01.RES.74.6.1071

McAllister, R. E., Noble, D., and Tsien, R. W. (1975). Reconstruction of the Electrical Activity of Cardiac Purkinje Fibres. *J. Physiol.* 251, 1–59. doi:10.1113/jphysiol.1975.sp011080

Noble, D. (1962). A Modification of the Hodgkin-Huxley Equations Applicable to Purkinje Fibre Action and Pacemaker Potentials. *J. Physiol.* 160, 317–352. doi:10.1113/jphysiol.1962.sp006849

Noble, D., Noble, S. J., Bett, G. C. L., Earm, Y. E., Ho, W. K., and So, I. K. (1991). The Role of Sodium - Calcium Exchange during the Cardiac Action Potential. *Ann. NY Acad. Sci.* 639, 334–353. doi:10.1111/j.1749-6632.1991.tb17323.x

Nygren, A., Fiset, C., Firek, L., Clark, J. W., Lindblad, D. S., Clark, R. B., et al. (1998). Mathematical Model of an Adult Human Atrial Cell: the Role of K^+ Currents in Repolarization. *Circ. Res.* 82, 63–81. doi:10.1161/01.RES.82.1.63

O'Hara, T., Virág, L., Varró, A., and Rudy, Y. (2011). Simulation of the Undiseased Human Cardiac Ventricular Action Potential: Model Formulation and Experimental Validation. *Plos Comput. Biol.* 7, e1002061. doi:10.1371/journal.pcbi.1002061

Pan, M., Gawthrop, P. J., Tran, K., Cursons, J., and Crampin, E. J. (2018). Bond Graph Modelling of the Cardiac Action Potential: Implications for Drift and Non-Unique Steady States. *Proc. R. Soc. A.* 474, 20180106. doi:10.1098/rspa.2018.0106

Pohl, A., Wachter, A., Hatam, N., and Leonhardt, S. (2016). A Computational Model of a Human Single Sinoatrial Node Cell. *Biomed. Phys. Eng. Express* 2, 035006. doi:10.1088/2057-1976/2/3/035006

Qu, Z. (2011). Chaos in the Genesis and Maintenance of Cardiac Arrhythmias. *Prog. Biophys. Mol. Biol.* 105, 247–257. doi:10.1016/j.pbiomolbio.2010.11.001

Smirnov, D., Pikunov, A., Syunyaev, R., Deviatiiarov, R., Gusev, O., Aras, K., et al. (2020). Genetic Algorithm-Based Personalized Models of Human Cardiac Action Potential. *PLoS ONE* 15, e0231695. doi:10.1371/journal.pone.0231695

Stewart, P., Aslanidi, O. V., Noble, D., Noble, P. J., Boyett, M. R., and Zhang, H. (2009). Mathematical Models of the Electrical Action Potential of Purkinje Fibre Cells. *Phil. Trans. R. Soc. A.* 367, 2225–2255. doi:10.1098/rsta.2008.0283

Surovyatkina, E., Noble, D., Gavaghan, D., and Sher, A. (2010). Multistability Property in Cardiac Ionic Models of Mammalian and Human Ventricular Cells. *Prog. Biophys. Mol. Biol.* 103, 131–141. doi:10.1016/j.pbiomolbio.2010.01.004

Ten Tusscher, K. H. W. J., Noble, D., Noble, P. J., and Panfilov, A. V. (2004). A Model for Human Ventricular Tissue. *Am. J. Physiology-Heart Circulatory Physiol.* 286, H1573–H1589. doi:10.1152/ajpheart.00794.2003

Ten Tusscher, K. H. W. J., and Panfilov, A. V. (2006). Alternans and Spiral Breakup in a Human Ventricular Tissue Model. *Am. J. Physiology-Heart Circulatory Physiol.* 291, H1088–H1100. doi:10.1152/ajpheart.00109.2006

Tomek, J., Bueno-Orovio, A., and Rodriguez, B. (2020). ToR-ORd-dynCl: An Update of the ToR-ORd Model of Human Ventricular Cardiomyocyte with Dynamic Intracellular Chloride. BioRxiv. doi:10.1101/2020.06.01.127043

Trovato, C., Passini, E., Nagy, N., Varró, A., Abi-Gerges, N., Severi, S., et al. (2020). Human Purkinje In Silico Model Enables Mechanistic Investigations into Automaticity and Pro-Arrhythmic Abnormalities. *J. Mol. Cell Cardiol.* 142, 24–38. doi:10.1016/j.yjmcc.2020.04.001

Varghese, A., and Sell, G. R. (1997). A Conservation Principle and its Effect on the Formulation of Na-Ca Exchanger Current in Cardiac Cells. *J. Theor. Biol.* 189, 33–40. doi:10.1006/jtbi.1997.0487

Whittaker, D. G., Clerx, M., Lei, C. L., Christini, D. J., and Mirams, G. R. (2020). Calibration of Ionic and Cellular Cardiac Electrophysiology Models. *Wires Syst. Biol. Med.* 12, e1482. doi:10.1002/wsbm.1482

Wilders, R., Jongsma, H. J., and Van Ginneken, A. C. (1991). Pacemaker Activity of the Rabbit Sinoatrial Node. A Comparison of Mathematical Models. *Biophysical J.* 60, 1202–1216. doi:10.1016/s0006-3495(91)82155-5

Yu, T., Lloyd, C. M., Nickerson, D. P., Cooling, M. T., Miller, A. K., Garny, A., et al. (2011). The Physiome Model Repository 2. *Bioinformatics* 27, 743–744. doi:10.1093/bioinformatics/btq723

Conflict of Interest: Authors KW and LP were employees of F. Hoffmann-La Roche Ltd. and KW is a shareholder.

The remaining authors declare that the research was conducted in the absence of any commercial or financial relationships that could be construed as a potential conflict of interest.

Publisher's Note: All claims expressed in this article are solely those of the authors and do not necessarily represent those of their affiliated organizations, or those of the publisher, the editors and the reviewers. Any product that may be evaluated in this article, or claim that may be made by its manufacturer, is not guaranteed or endorsed by the publisher.

frontiers | Frontiers in Physiology

REVIEW
published: 10 May 2022
doi: 10.3389/fphys.2022.908069

A Review of Healthy and Fibrotic Myocardium Microstructure Modeling and Corresponding Intracardiac Electrograms

Jorge Sánchez and Axel Loewe*

Institute of Biomedical Engineering, Karlsruhe Institute of Technology (KIT), Karlsruhe, Germany

Computational simulations of cardiac electrophysiology provide detailed information on the depolarization phenomena at different spatial and temporal scales. With the development of new hardware and software, *in silico* experiments have gained more importance in cardiac electrophysiology research. For plane waves in healthy tissue, *in vivo* and *in silico* electrograms at the surface of the tissue demonstrate symmetric morphology and high peak-to-peak amplitude. Simulations provided insight into the factors that alter the morphology and amplitude of the electrograms. The situation is more complex in remodeled tissue with fibrotic infiltrations. Clinically, different changes including fractionation of the signal, extended duration and reduced amplitude have been described. *In silico*, numerous approaches have been proposed to represent the pathological changes on different spatial and functional scales. Different modeling approaches can reproduce distinct subsets of the clinically observed electrogram phenomena. This review provides an overview of how different modeling approaches to incorporate fibrotic and structural remodeling affect the electrogram and highlights open challenges to be addressed in future research.

Keywords: cardiac modeling, fibrosis, electrogram, multiscale, microstructure

OPEN ACCESS

Edited by:
Matthijs Cluitmans,
Maastricht University, Netherlands

Reviewed by:
Jason D. Bayer,
Université de Bordeaux, France
Marianna Meo,
EPD Solutions, A Philips Company, Netherlands

****Correspondence:***
Jorge Sánchez
publications@ibt.kit.edu

Specialty section:
This article was submitted to Cardiac Electrophysiology, a section of the journal Frontiers in Physiology

Received: *30 March 2022*
Accepted: *21 April 2022*
Published: *10 May 2022*

Citation:
Sánchez J and Loewe A (2022) A Review of Healthy and Fibrotic Myocardium Microstructure Modeling and Corresponding Intracardiac Electrograms. Front. Physiol. 13:908069. doi: 10.3389/fphys.2022.908069

1 INTRODUCTION

Patients with cardiac arrhythmias are often treated with ablation therapy. Substrate-based ablation therapy is guided by intracardiac measurements acquired from catheters inserted into the cardiac chamber that record the extracellular potential.

The signal recorded by an electrode with respect to a distant reference is called unipolar electrogram (uEGM). EGMs of several electrodes on a catheter and/or multiple catheter locations are used to understand the dynamics of the cardiac arrhythmia. However, the recorded uEGMs are affected by different artifacts such as contraction of the heart, breathing of the patient, far-field signals from distant parts of the heart and noise from different hardware components. To alleviate these issues, bipolar electrograms (biEGM) are most frequently used, which subtract the uEGMs of two close-by electrodes. In this way, artifacts that affect both electrodes in the same way are cancelled. The difference between two potentials is called voltage and we should keep in mind that we can only measure voltages. Therefore, uEGMs always have to be considered with respect to their (distant) reference electrode. In clinical literature, also the peak-to-peak amplitude of an electrogram signal (i.e., a voltage time course) is often called “voltage”.

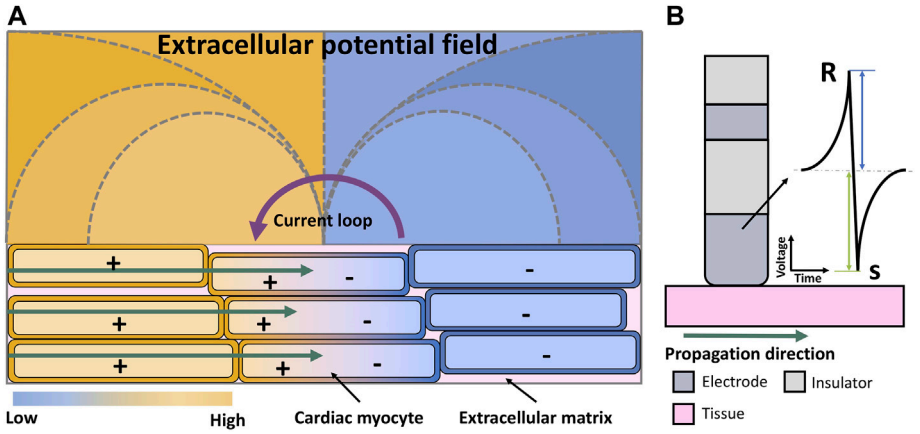

FIGURE 1 | Electrical propagation in healthy cardiac tissue. **(A)** Extracellular field caused by the depolarization of cardiomyocytes when an excitation propagates from left to right (green arrows). **(B)** Symmetric unipolar electrogram measured at the surface of the cardiac tissue (pink). The initial positive wave (R-peak) is caused by the wavefront approaching the electrode (dark gray), the polarity changes when the wavefront passes underneath the electrode, and the S-peak is caused by the wavefront traveling away from the measuring electrode.

The mathematical model of an excitable cell proposed by Hodgkin and Huxley, (1952), the tissue homogenization approach proposed by Schmitt, (1969), and the set of bidomain equations first applied by Tung, (1978) in 1978 is the most complete and accurate model that describes the spread of electrical depolarization across the myocardium and its cells.

Computational simulations based on this mathematical model have been used to understand the phenomena of the depolarization spread in cardiac tissue and their effects on electrogram genesis and morphology (Bishop and Plank, 2011b; Oesterlein et al., 2016; Roney et al., 2016; Pollnow et al., 2017; Beheshti et al., 2018; Hwang et al., 2019). While EGMs can be extracted from the extracellular medium in a bidomain simulation, this approach is computationally expensive. Thus, different methods based on excitation propagation simulations in the monodomain model have been proposed. Another modeling approach to accelerate the computation is the so-called reaction-eikonal model Neic et al. (2017), which can simulate physiological propagation using a coarser mesh (element average length 400 µm). In the monodomain model and the reaction-eikonal model, the extracellular potential is not calculated directly. However, it can be approximated with the pseudo-bidomain approach or the infinite homogeneous volume conductor method to obtain EGMs as detailed below. The infinite homogeneous volume conductor method approximates the extracellular potential caused by a group of cells spatially distributed in space and acting as sources of the electric field (Malmivuo and Plonsey, 1995).

In this review, we give an overview of the biophysical phenomena governing wave propagation in cardiac tissue and the corresponding extracellular potentials measured as electrograms. We will particularly focus on different approaches used to model fibrotic remodelling and simulate the corresponding electrograms to reproduce and understand the clinically observed changes in electrogram amplitude and morphology.

2 INTRACARDIAC ELECTROGRAMS

The electrical activity in the myocardium originates from the coordinated opening and closing of the ion channels in the cell membrane. The time course of the difference between the potential in the intracellular and in the extracellular medium is known as the action potential. In cardiac tissue, the cells are interconnected through gap junctions that will start a cascade effect of cellular activation along the major axis in which myocytes are aligned locally (also known as fiber direction), resulting in excitation propagation across the myocardium.

The extracellular field is a consequence of the spatial distribution of the transmembrane voltage of the cells in the myocardium (**Figure 1A**). An advancing depolarization wave in the cardiac tissue changes the spatial distribution of the extracellular potential. The extracellular potential can be measured as the uEGM at one electrode (technically the voltage between the extracellular potential at the measuring electrode with reference to for example, Wilson central terminal). The unipolar electrogram morphology is characterized by a biphasic symmetric shape (**Figure 1B**) where the positive phase (R-peak) indicates the approaching of the wavefront to the measuring electrode and the fast downslope indicates the moment that the wavefront is underneath the electrode. The opposing negative phase (S-peak) indicates the movement of the wavefront away from the measuring electrode. The peak-to-peak amplitude of the signal is also called "voltage" in the clinical literature. Peak-to-peak voltage is used as a marker to distinguish healthy from pathological tissue both for biEGMs (Jadidi et al., 2020) and uEGMs (Nairn et al., 2020b). However, biEGM amplitude can be affected by to several factors (Hwang et al., 2019) such as the orientation of the catheter (Schuler et al., 2013; Gaeta et al., 2020), the electrode spacing and size (Beheshti et al., 2018; Abdi et al., 2020; Nairn et al., 2020a; Takigawa et al., 2022), depolarization patterns (Jacquemet et al., 2003), substrate remodeling (Jacquemet et al., 2003; McDowell et al., 2012;

Campos et al., 2013; Mendonca Costa et al., 2014; Roney et al., 2016; Sánchez et al., 2021b) and signal filter settings (Starreveld et al., 2020).

3 MODELLING INTRACARDIAC SIGNALS

Computational cardiac modeling has advanced rapidly in the last years and different numerical methods to simulate the propagation of the cardiac depolarization have been proposed over the years. Finite difference approaches have been widely used (Potse et al., 2006) and can be generalized for grids with distinct spacing (Trew et al., 2005; Sánchez et al., 2019a). Also the finite element method has been used to discretize complex geometries such as the cardiac chambers to simulate cardiac electrophysiology (Vigmond et al., 2003; Cooper et al., 2015; Neic et al., 2017; Plank et al., 2021).

The bidomain model represents cardiac tissue as a homogenized medium composed of the intracellular and the extracellular domains. The two computational domains coexist in the bidomain model and occupy the same geometrical space:

$$\nabla \cdot (\sigma_i \nabla \phi_i)) = \beta I_m \tag{1}$$

$$\nabla \cdot (\sigma_e \nabla \phi_e)) = -\beta I_m - I_{extra} \tag{2}$$

$$I_m = C_m \frac{\partial V_m}{\partial t} + I_{ion}(V_m, v) - I_{intra} \tag{3}$$

$$V_m = \phi_i - \phi_e \ , \tag{4}$$

where ϕ represents the electrical potential, the indices i and e refer to the intracellular and extracellular spaces, respectively. σ is the conductivity tensor, β is the surface to volume ratio of the myocytes and I_{ion} the total transmembrane ionic current density defined by the cellular model. The latter is dependent on V_m and a vector v of further state variables. I_{intra} (a transmembrane current density) and I_{extra} (an extracellular current density) describe external stimuli. If a bath surrounds the tissue, it is treated as an extension of the extracellular space.

Adding **Eqs 1**, **2** and incorporating it into **Eq. 4** yields:

$$\nabla \cdot (\sigma_i + \sigma_e) \nabla \phi_e = -\nabla \cdot (\sigma_i \nabla V_m) - I_{extra} \tag{5}$$

$$\nabla \cdot (\sigma_i \nabla V_m) = -\nabla \cdot (\sigma_i \nabla \phi_e) + \beta I_m \ . \tag{6}$$

As mentioned before, the reference potential during an electro-anatomical mapping procedure is usually a potential in a remote site or an average of potential values such as Wilson's central terminal. For a bidomain model, when calculating uEGMs, the reference potential can, for example, be considered as an average of the extracellular potential of the furthest surface with respect to the tissue (Colli Franzone et al., 2007; Keller et al., 2014), which is not a perfect approximation of a remote reference electrode (e.g., a surface patch on the back of the patient) but markedly reduces drift of the reference potential. The further away the reference is from the myocardial tissue in the model, the better the representation of the reference potential but also the higher the computational cost due to the extended computational domain. Considering the average potential in a remote surface or volume is numerically advantageous compared to defining a fixed reference potential as a Dirichlet boundary condition.

The monodomain model is an approximation that assumes that the anisotropy of the extracellular and intracellular conductivity are aligned. Therefore, under the assumption of equal anisotropy ratios, one needs to solve only the parabolic partial differential equation above with the monodomain conductivity set appropriately:

$$\nabla \cdot (\sigma_m \nabla V_m) = \beta I_m + \beta I_t r \ , \tag{7}$$

where the bidomain equivalent monodomain conductivity σ_m is given as

$$\sigma_m = \sigma_i \sigma_e (\sigma_i + \sigma_e)^{-1} \ . \tag{8}$$

Potse et al. (2006) performed a thorough comparison between the results of the bidomain model and monodomain model. The authors conclude that the monodomain model, although being a simplification of the bidomain model, is sufficient to study and understand the electrical propagation in the cardiac tissue under physiological conditions as well as for electrically remodeled tissue (ionic current abnormalities). The acceleration of the wavefront at the tissue-to-blood interface due to the bath-loading effect can be represented with the augmented bidomain approach (Bishop and Plank, 2011b). One of the biggest disadvantages of the bidomain model is the long computation time that it requires. Therefore, a common modeling approach is to combine the monodomain model with independent forward calculation of extracellular potentials. The most simplistic approach is the infinite volume conductor assumption, which assumes that the cardiac tissue is immersed in a homogeneous extracellular medium with infinite extent. This approach was for example, used to study the relation of the spread of depolarization in the cardiac tissue to the genesis and morphology of the unipolar electrogram (Gima and Rudy, 2002; Ganesan et al., 2013; Ugarte et al., 2014; Cabrera-Lozoya et al., 2017; Hwang et al., 2019) but neglects the influence of the heterogeneous surrounding tissue like other cardiac chambers, the lungs or the liver.

Briefly, the source and the measuring point (electrode) for a dipole are assumed to be immersed in an unbounded (infinite) volume conductor with homogeneous properties. The time course of the potential of the dipole corresponds to the uEGM electrogram measured at a location x in a certain distance to the source located in the cardiac tissue (x_{src}) with respect to a reference electrode in infinite distance using the integral solution to Poisson's equation:

$$\phi_e = \frac{1}{4\pi\sigma} \iiint_V \frac{I_{src}}{\|x - x_{src}\|} \, dV \ , \tag{9}$$

where ϕ_e is the extracellular potential, σ is the conductivity of the volume conductor, I_{src} is the source current density and $\|x - x_{src}\|$ is the Euclidean distance from the source point to the measuring point.

Bishop and Plank (2011a) proposed a combined bidomain and monodomain model (pseudo-bidomain) to calculate the extracellular potential. The proposed pseudo-bidomain

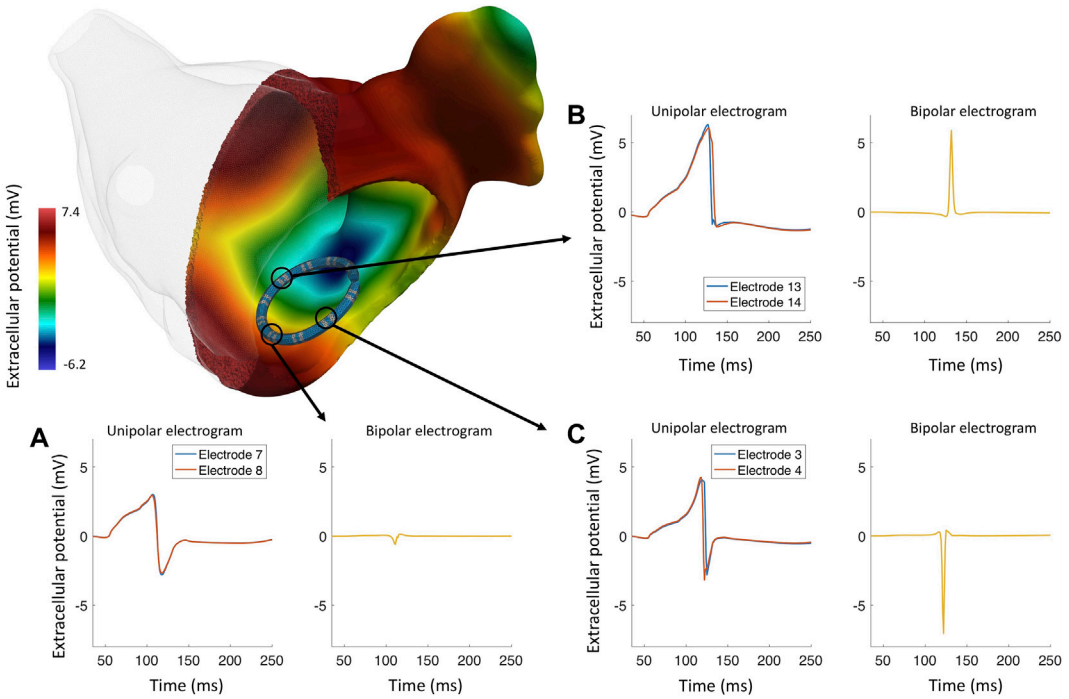

FIGURE 2 | Bidomain simulation of a realistically deformed LASSO™ (Biosense Webster) catheter in a left atrium to study the genesis of different EGM morphologies in healthy myocardium. **(A)** The wavefront approaches the electrode pair 7–8 and activates both electrodes at the same time, the resulting bipolar electrogram with a reduced peak-to-peak amplitude (0.42 mV). **(B)** Several wavefronts approaching electrode pair 13–14, both unipolar electrograms are asymmetrical, lacking an S-peak; the resulting bipolar electrogram has a high peak-to-peak amplitude and a positive polarity. **(C)** The wavefront travels almost perpendicular to electrode pair 3–4; the electrodes are activated at different times, the resulting bipolar electrogram has negative polarity and a high peak-to-peak amplitude (7.45 mV).

approach computes the elliptic bidomain equation for a given transmembrane voltage distribution only at the time instants for which the extracellular potential is sampled. This approach is suitable to reproduce extracellular signals [EGM (Keller et al., 2012) and ECG (Nagel et al., 2022)] for a finite surrounding conductive medium (bath, potentially inhomogeneous) and is computationally efficient.

3.1 Factors Affecting the Intracardiac Signals

Using the bidomain model and realistic geometries of commercially available catheters can help to better understand EGM morphology (Schuler et al., 2013; Pollnow et al., 2017; Sánchez et al., 2021a). Schuler et al. (2013) modeled a realistic 7F catheter with two electrodes such that the tip was at the center of the tissue and in direct contact with the tissue patch surface. The catheter angle was changed with respect to the surface of the tissue (elevation) and to the wavefront propagation direction (rotation). Additionally, the authors explored the impact of the tissue thickness and conduction velocity on biEGM amplitude and duration. One of their main findings was that catheter orientation greatly affects the height and ratio of the positive and negative bipolar signal amplitude, which can be traced back to changes in the proximal signal. Moreover, the authors pointed out that the substrate characteristics (thickness and conduction velocity) mainly affect the biEGM peak-to-peak amplitude.

In new highly detailed bidomain simulations for this review, we show the biophysical phenomena of the spread of depolarization in the left atrium and the EGMs from a 7F LASSO™ (Biosense Webster) catheter in a healthy left atrium. **Figure 2** shows that local activation time is the main factor that impacts the biEGM amplitude and that it is less sensitive to the wavefront direction. Additionally, bidomain simulations showed that biEGMs from electrodes that are not in direct contact with the tissue have the same activation time resulting in a small biEGM amplitude, which confirms the results previously shown (Gaeta et al., 2020). In brief, the atrial anatomical model (Roney et al., 2021) has a realistic wall thickness and an average edge length of 100 µm. Tissue conductivity was tune to achieved a conduction velocity of 40 cm/s (McDowell et al., 2013). The value of conductivity of the blood were as reported by Clerc (1976), the electrode conductivity was set to 1×10^{12} S/m to represent a good conductor that yields an isopotential volume, the conductivity of the catheter insulator was set close to zero (1×10^{6} S/m).

The amplitude of uEGMs is affected by the geometrical properties of the electrode, such as the size of the electrode. Nairn et al. (2020a) performed a series of *in silico* experiments to understand the effect of the electrode size on the amplitude of the measured EGM. uEGM amplitude was shown to be inversely

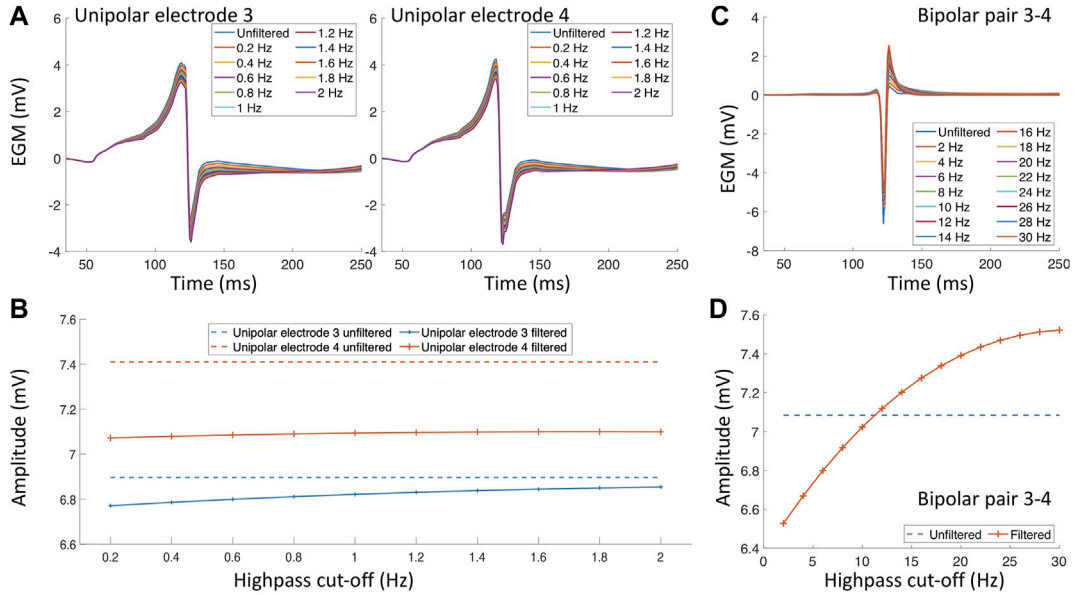

FIGURE 3 | Filter effects on electrograms measured in healthy myocardium. **(A)** Unipolar electrograms with different highpass filter values. **(B)** Effect of different highpass cut-off values on the unipolar electrogram amplitude. **(C)** Bipolar electrogram with different highpass cut-off values. **(D)** Effect of different highpass cut-off values on the bipolar electrogram amplitude.

related to the size of the electrode. biEGM amplitude is additionally affected by the electrode pair spacing. Beheshti et al. (2018) showed that biEGM amplitude was increased when the electrode spacing increased. Assuming a plane wave and a perfectly symmetric uEGM in a simple thought experiment, the biEGM amplitude is zero for electrodes that are activated at exactly the same time. When increasing the distance between the electrodes, the peak-to-peak biEGM amplitude increases up to two times the uEGM amplitude. When further increasing the interelectrode distance, the biEGM amplitude decreases again until there is no more temporal overlap between the two uEGMs and the biEGM amplitude plateaus at the uEGM amplitude.

An additional factor that impacts the EGM amplitude and morphology are the filter settings (Schneider et al., 2004; Lin et al., 2007; Starreveld et al., 2020). In clinical practice, a bandpass filter is commonly used. However, the cut-off values of the bandpass filter differs for different mapping systems, catheters or due to the noise environment present in the specific electrophysiology laboratory. During an electroanatomical mapping procedure, uEGMs are typically filtered with a highpass of 0.5–2 Hz and a lowpass filter of 300–600 Hz biEGMs are typically bandpass filtered with a highpass of 1–30 Hz and a lowpass of 300–500 Hz. Both EGM types are also filtered at the frequency of the powerline with a notch filter (50 or 60 Hz). **Figure 3** depicts the effect of the filter settings on both uEGMs (panel A) and biEGMs (panel C). In particular for biEGMs, the highpass filter cut-off value affects the measure voltage (**Figure 3D**). The higher amplitude of these simulated EGMs compared to clinical EGMs is likely due to the chosen extracellular conductivity, perfect contact of the electrode with the tissue and absence of losses along the signal chain.

Considering the numerous factors that affect the uEGM and biEGM amplitude and morphology, standardized mapping modality (uEGM or biEGM), electrode size, electrode spacing and filter settings could increase comparability between studies. For modeling the healthy myocardium and electrograms, bidomain models provide the most accurate representation of the biophysical phenomena of depolarization and the influence of the catheter inside the cardiac cavity. Monodomain models and reaction-eikonal models in combination with forward calculation approaches to obtain the EGMs provide sufficient information about the propagation in the cardiac tissue in most scenarios. After reviewing the factors that influence the EGMs in the healthy myocardium, the next section covers factors that increase the complexity of the signals due to heterogeneities of the tissue and different patterns of propagation.

4 MYOCARDIAL STRUCTURAL REMODELING AND INTRACARDIAC SIGNALS

Structural remodeling alters the cardiac substrate, and the depolarization wavefront often has to follow a zig-zag pattern (**Figure 4** white arrows). The zig-zag pattern of the propagation is reflected in uEGM and biEGM as fractionation in the signal due to constantly changing orientation of the wavefront. Fractionation is defined as an increase of deflections, thus an increase in complexity of the signal as well as a prolongation of the EGM (Jacquemet and Henriquez, 2009; Verheule and Schotten, 2021). As previously mentioned, the highpass filter cut-off value affects the signal amplitude. In

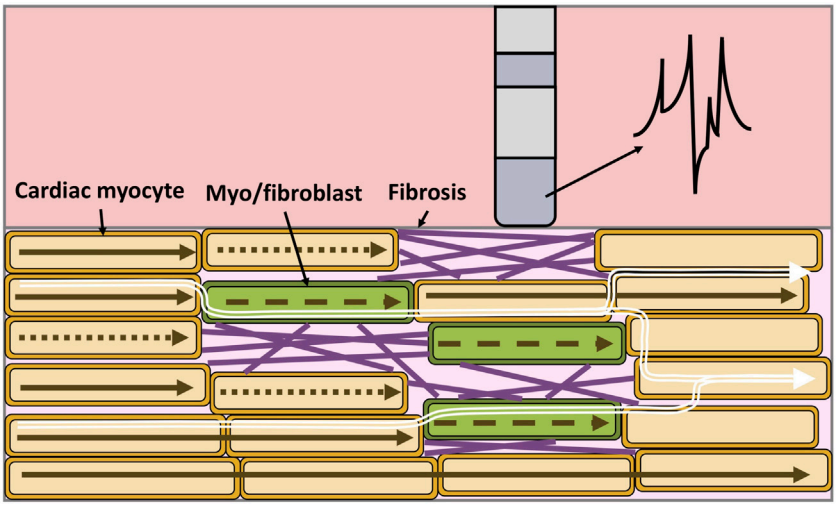

FIGURE 4 | Electrical propagation in fibrotic cardiac tissue, the composition is heterogeneous and includes cardiac myocytes (orange), myofibroblasts/fibroblasts (green) and collagen fibers (purple). Depolarization of cardiomyocytes when an excitation propagates from left to right (brown arrows). Dotted arrows represent a conduction block, while dashed arrows represent slowed conduction. As a result of the zig-zag propagation of the wavefront (white arrows), the unipolar electrogram morphology is not symmetric, is prolonged and shows multiple deflections.

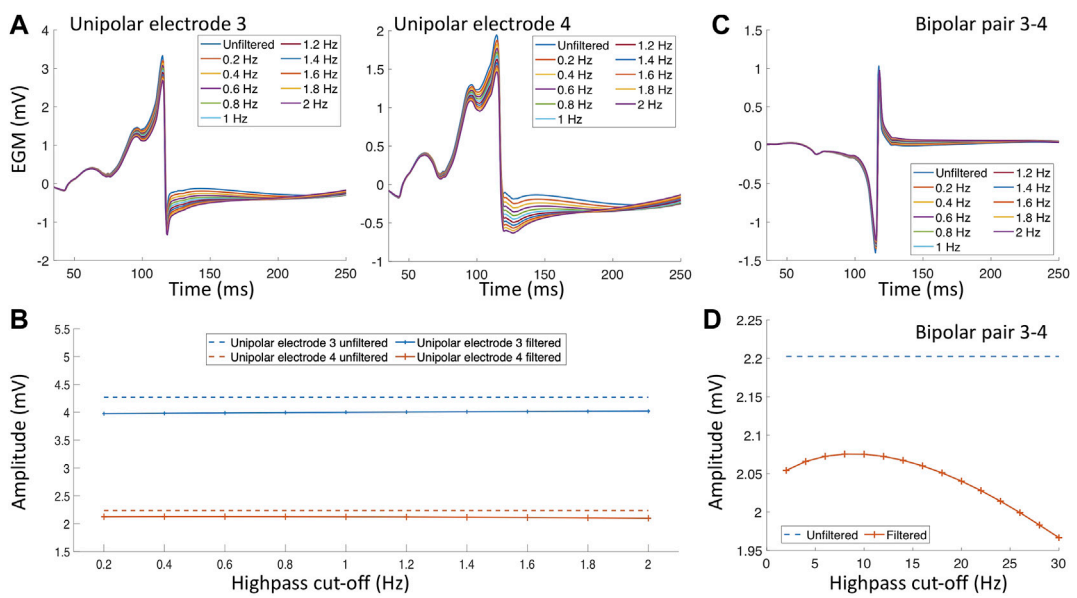

FIGURE 5 | Filter effect on electrograms measured in the proximity of a fibrotic area. **(A)** Unipolar electrograms with different highpass filter values. **(B)** Effect of different highpass cut-off values on the unipolar electrogram amplitude. **(C)** Bipolar electrogram with different highpass cut-off values. **(D)** Effect of different highpass cut-off values on the bipolar electrogram amplitude.

the presence of fibrotic tissue, uEGMs and biEGMs have a different frequency spectrum and are affected in a different manner. **Figure 5D** shows that there is no optimal cut-off frequency as previously reported by Starreveld et al. (2020). The filtered biEGM amplitude (orange line) drops due to the highpass cut-off but does not intersect the unfiltered amplitude (blue dashed line) as is the case for healthy myocardium (**Figure 3D**).

Many approaches have been proposed to model fibrotic cardiac tissue (**Table 1**) to understand the effect on the wavefront propagation and the corresponding electrograms (Ashihara et al., 2012; McDowell et al., 2013; Roney et al., 2016).

Creating a model of cardiac fibrotic tissue is not an easy task as fibrosis formation has been associated with different diseases (myocardial infarction (Liu et al., 2017), diabetes (Russo and Frangogiannis, 2016), autoimmune diseases

TABLE 1 | Different modeling approaches to represent fibrotic tissue in computational models and their effect on simulated EGMs.

Modeling approach	Effect on EGMs	References
Myofibroblasts/fibroblasts coupled to myocytes	longer duration due conduction slowing in the fibrotic area	MacCannell et al. (2007), Ashihara et al. (2012), McDowell et al. (2013), Morgan et al. (2016), Roney et al. (2016), Zahid et al. (2016), Sánchez et al. (2019b)
Reduced conductivity in fibrotic region, potentially with gradient to surrounding tissue	peak-to-peak amplitude reduced and duration prolonged due to slow propagation of the wavefront	Krueger et al. (2014), Caixal et al. (2020), Lim et al. (2020), Beach et al. (2021)
Severely reduced conductivity in some elements in the fibrotic region	reduced peak-to-peak amplitude in the fibrotic area	Alonso and Bär, (2013), ten Tusscher and Panfilov, (2007), Clayton, (2018)
Removing some elements in the fibrotic region	fractionation and reduced peak-to-peak amplitude	Roney et al. (2016), Vigmond et al. (2016)
Edge splitting	fractionation depending on the length of the path	Jacquemet and Henriquez, (2009), McDowell et al. (2013), Mendonca Costa et al. (2014), Roney et al. (2016)
Reduction of conductivity in the transversal fiber direction	increased anisotropy of excitation propagation, effect on EGMs not yet studied	McDowell et al. (2012)
Reduction of conductivity in the transmural direction	excitation propagation dissociation between transmural layers, effect on EGMs not yet studied	Gharaviri et al. (2016), Irakoze and Jacquemet, (2020)

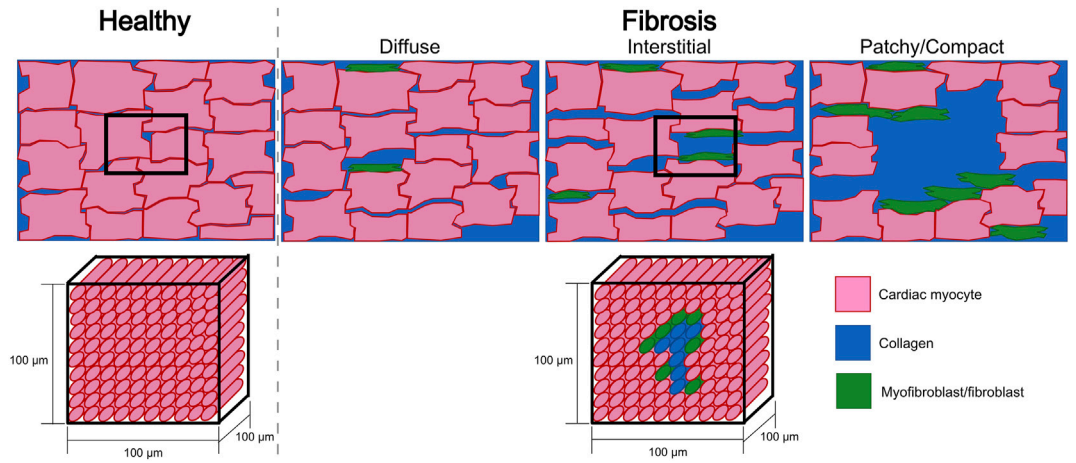

FIGURE 6 | Sketches of a tissue cut for healthy and fibrotic tissue (top row). Fibrotic sketches represent different fibrotic patterns (diffuse, interstitial, patchy or compact). The bottom row depicts the homogenization assumption where a hexahedral mesh element of 100 µm × 100 µm × 100 µm represents several cardiac myocytes and has to assume one average set of properties that describes the electrophysiology of this group of cells. For fibrotic tissue, homogenization implies that one element contains different types of cells (cardiac myocytes and fibroblasts/myofibroblasts) and collagen. Also the electrophysiological characteristics of this piece of tissue has to be represented by one set of effective parameters.

(Tschöpe et al., 2021) and others), which produce different patterns of structural remodeling (interstitial, compact, diffuse, and patchy) (Nguyen et al., 2014). For example, it has been described that during an ischemic episode in the ventricle, the myocardium undergoes electrical remodeling (Mendonca Costa et al., 2018). From a macroscopic view, conduction velocity is reduced in the scar area, which can be modeled by decreasing the conductivity or by including isolating barriers (Balaban et al., 2018). Additionally, at a cellular scale the cardiac myocytes undergo electrical remodeling (Mendonca Costa et al., 2018). At the border zone of the ischemic area, cardiomyocytes lack oxygen which impacts their metabolism and increase acidity. This triggers a series of effects in the cell's ion channels. To model these effects, the maximum conductance (Rodriguez et al., 2006; Loewe et al., 2018) of certain ionic channels are modified including an ATP-sensitive potassium channel (I_{KATP}), which has a major contribution during ischemic episodes (Dutta et al., 2017).

Moreover, computational models of pathological tissue need to include fibrosis at the tissue scale. Fibrosis patterns (**Figure 6**) can be modeled using different approaches by assigning different properties to the mesh using for example, a random distribution (e.g., uniform or Gaussian) (Sánchez et al., 2019b; ten Tusscher and Panfilov, 2007; Alonso and Bär, 2013; Vigmond et al., 2016), by extracting the scar area from MRI (McDowell et al., 2012; Krueger et al., 2014; Morgan et al., 2016; Beach et al., 2021) or by using algorithms that synthetically generate similar patterns as

observed in histological cuts of fibrotic tissue (Jakes et al., 2019; Pezzuto et al., 2019; Sutanto et al., 2020; Sánchez et al., 2021b).

Fibrosis can be modeled differently and many studies reduce the tissue conductivity such as for example, informed by microstructural modeling in Gokhale et al. (2017). The conductivity of the fibrotic areas can also be reduced in the transversal direction (McDowell et al., 2012) to represent lateralization of gap junctions, close to zero in all directions (Clayton, 2018) or affected by a no flux boundary condition (ten Tusscher and Panfilov, 2007; Alonso and Bär, 2013) to represent replacement fibrosis. The specific spatial distribution of conductivities or conduction velocity can be informed by fibrosis imaging such as the pixel intensity in late gadolinium enhanced magnetic resonance images (Krueger et al., 2014; Morgan et al., 2016; Caixal et al., 2020; Beach et al., 2021) or using a mathematical function determined from EGM amplitude (Lim et al., 2020). Within the regions, either uniform conductivities can be assumed or a gradient from the center of the fibrotic area to the healthy surrounding tissue is assumed.

Furthermore, the edge splitting method has been proposed to separate the computational mesh along its edges with the aim to reproduce the effect of collagen deposition in fibrotic tissue that separates the cardiac myocytes (Mendonca Costa et al., 2014). Edge splitting consists of splitting the nodes along and edge to disconnect adjacent elements creating an alternative path for the wavefront propagation in the cardiac tissue. However, reducing the conductivity or splitting the edges of the mesh does not capture the effect of increased cellular heterogeneity in the cardiac tissue (fibroblast-myocyte coupling) and the inflammatory response. To model cellular heterogeneity, myofibroblast or fibroblast models have been introduced (MacCannell et al., 2007; Ashihara et al., 2012; Morgan et al., 2016; Roney et al., 2016; Sánchez et al., 2021b). Myofibroblasts or fibroblasts were electrically connected to the myocytes by gap junctions. There are equivocal data about the exact conductance of these gap junctions and the number of fibroblasts that a myocyte couples to. In computational models, the value of conductance ranges between 0.5 nS to 2 nS and up to 9 fibroblasts are considered Morgan et al. (2016), MacCannell et al. (2007), Maleckar et al. (2009), Rook et al. (1992), Sánchez et al. (2019a), Seemann et al. (2017). The inflammatory response (myocyte-fibroblast paracrine interactions) has been modeled by altering the maximum conductance of the sodium ion channel (reduced by 50%), the maximum conductance of the L-type calcium ion channel (reduced by 50%), and the maximum conductance of the inward potassium rectifier ion channel (reduced by 40%) (Zahid et al., 2016), as reported by *in vitro* experiments (Avila et al., 2007; Ramos-Mondragón et al., 2011).

Lately, Vigmond et al. (2016) proposed to represent fibrotic tissue in a monodomain model by removing the elements of the mesh to capture the effect of the low conductive extracellular medium and the absence of an intracellular current path. One advantage of the proposed modeling approach, is that there is no flux of current towards the fibrotic tissue; therefore, there are no source elements that will contribute to the calculated extracellular potential. Using this modeling approach, the authors observed that at the percolation threshold (Alonso and Bär, 2013) the fibrotic tissue was be able to trigger and maintain an arrhythmia. The EGMs calculated over the fibrotic tissue exhibit fractionation due to the zig-zag patterns of depolarization in the cardiac tissue in this modeling approach. Moreover, the study also looked at the impact of the mesh resolution when modeling fibrotic tissue and showed that in meshes with a resolution of 300 μm conduction block was reached at lower degrees of fibrosis than in meshes with finer resolution (< 100 μm).

Using a realistic geometry Jacquemet et al. (2003) studied the morphology of uEGMs during different atrial fibrillation propagation patterns. The authors showed that different propagation patterns (plane waves, spiral waves, and wavefront collision) lead to different uEGM morphology (symmetry and amplitude) and that asymmetric signals (**Figure 2B**) occurred in less than 2% of the cases in homogeneous substrate. However, the increase of heterogeneities in the cardiac tissue also increases the asymmetry and reduces the amplitude of the EGM(van der Does and de Groot, 2017). Frontera et al. (2018) showed how different depolarization patterns affected the biEGM morphology. High peak-to-peak amplitude and short duration of biEGMs are wavefront collisions or pivotal points, low peak-to-peak amplitude and EGM prolongation are associated with slow conduction areas. The authors remarked how understanding the genesis of the electrograms is a key factor to improving the arrhythmia treatments.

Including heterogeneous tissue composition in the model changes the wavefront propagation in the cardiac tissue (McDowell et al., 2012; Campos et al., 2013; Mendonca Costa et al., 2014; Roney et al., 2016) (**Figure 7**). Roney et al. (2016) showed how different modeling approaches of cardiac fibrosis can change the propagation in the cardiac tissue and affect the morphology of EGMs. In that study, Roney et al. (2016) modeled fibrosis as conduction disturbances (lower conductivity, edge splitting, or removing elements). They included electrical remodeling of the cardiac myocyte due to inflammatory processes mediated by transforming growth factor-β1, myocyte-fibroblast coupling and combinations of the preceding. EGM morphology was mostly affected when fibrosis was modeled by edge splitting or removing the elements (**Figure 7**) as also shown previously. In addition, including fibroblast coupling has an organizing effect on rotor dynamics, also shown by other studies (McDowell et al., 2012; Sánchez et al., 2019b).

The amplitude of the EGMs can also be affected by conduction impairment along certain axes (McDowell et al., 2012; Gharaviri et al., 2016; Irakoze and Jacquemet, 2020). Gharaviri et al. (2016) created a model of the cardiac tissue that enables the study of dissociation between transmural layers, for example, dissociation between the subendocardial and the subepicardial myocardium as can be caused by endomysial fibrosis. Moreover, Saba et al. (2009) described how the epicardial EGM amplitude varies in the ventricle with the thickness of the epicardial fat layer. The authors showed that biEGM amplitude was inversely related to epicardial fat

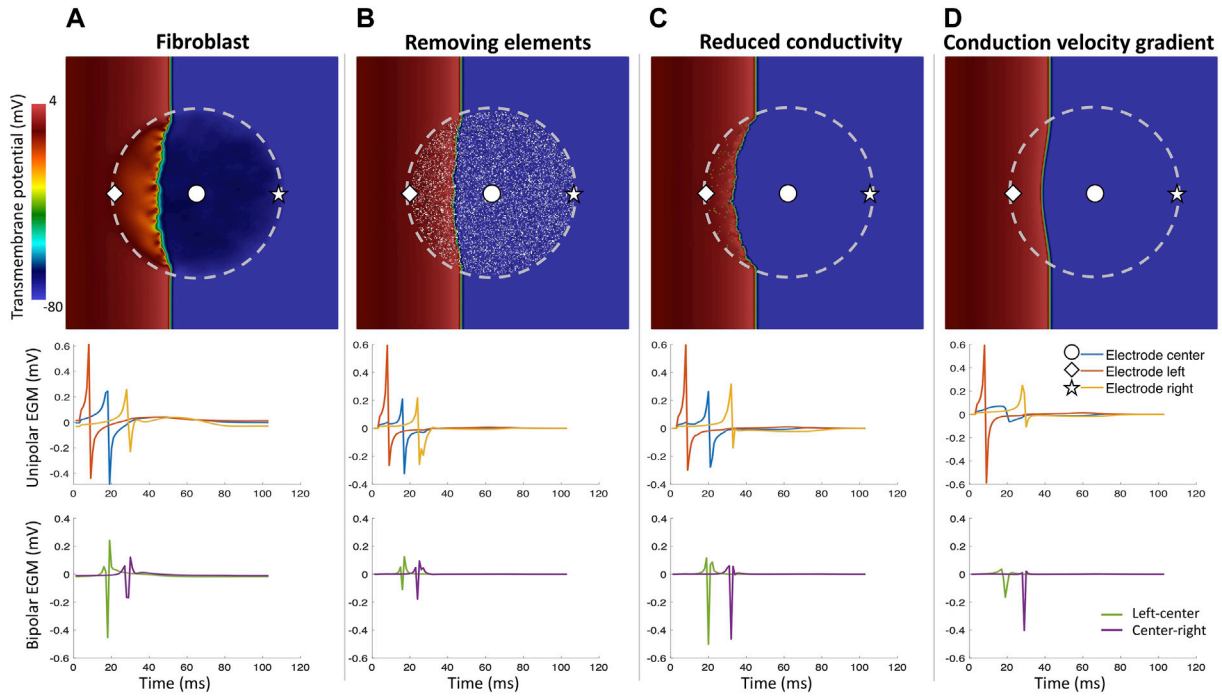

FIGURE 7 | Different fibrosis modeling methodologies and their corresponding unipolar and bipolar electrograms. Central fibrotic area (dashed line), the choice of the modeling approach affects the resulting uEGMs and biEGMs. **(A)** fibroblasts coupled to myocytes in the fibrotic region; **(B)** removing a share of elements in the fibrotic region from the computational domain; **(C)** severely reducing conductivity in a share of elements in the fibrotic region but the spatial transmembrane voltage gradients of fibrotic elements still contribute to the EGMs; **(D)** conductivity gradient from center of the fibrotic region to the surrounding healthy tissue. Absolute EGM amplitudes are smaller than *in vivo* due to the small size of the tissue patch.

thickness. Thus, using a voltage cut-off of 0.5 mV to define scar tissue would lead to identifying also healthy areas with overlaying fat and more information needs to be used to define epicardial tissue characteristics.

5 OTHER FACTORS IMPACTING INTRACARDIAC SIGNALS

EGM morphology and amplitude are also affected by electrode polarization, excessive contact pressure, catheter motion (Oesterlein et al., 2016), electromagnetic interference (Unger et al., 2019), near field and far field effects (Schicketanz et al., 2021), and poor grounding. However, most *in silico* experiments do not consider these factors, which might alter the EGM characteristics. Simulation studies have created a model of clinical noise which covers the electromagnetic interference (Sánchez et al., 2021a; Nothstein et al., 2021). However, further aspects likely need to be considered explicitly if their influence is relevant for the intended use of the model.

6 RESEARCH GAPS AND POTENTIAL FUTURE DEVELOPMENTS

Modeling of the cardiac tissue has significantly advanced understanding of the electrical propagation and the measured intracardiac EGMs. There is consensus on how to assign the properties of the computational model to represent healthy myocardium and the advantages and limitations of the different approaches to compute the extracellular potentials are mostly characterized. However, the question how to model fibrosis is far from being ultimately answered and will most likely continue to depend on the question of interest to be answered with a specific model. Additionally, the mesh resolution used in most of the studies of ≈300 µm determines the degree of homogenization (**Figure 6**). Spatial discretization of the mesh at the cellular level should be considered to study the influence of microstructural heterogeneity in the tissue (e.g., fibrosis) on EGMs (**Figure 4**). In addition, such models with subcellular resolution would enable to investigate to which degree discontinuous propagation within a cell vs. between cells leads to fractionation in healthy tissue. Here, we presented an overview of the commonly used methods and their corresponding EGMs.

Over the last years, the human cardiac digital twin has been under development to suggest personalized treatments for cardiac arrhythmias. Gillette et al. (2021) proposed an automated framework to generate a patient's digital twin from clinical data and Nagel et al. (2021) proposed a statistical approach to generate a population of anatomical models. While the anatomical model can be accurately generated from magnetic resonance images or statistical shape models, functional twinning can be achieved by tuning a phenomenological model or using generalized global properties for the cardiac tissue. Functional information will

impact the morphology and amplitude of the EGM. However, over the years, different studies proposed distinct methodologies to extract structural and functional information from the EGM signals. One open question is still the possibility of obtaining repolarization times from EGMs as repolarization of the cardiac tissue plays a pivotal role for the initiation of arrhythmias (Rivaud et al., 2021). From simulations of atrial electrophysiology, Celotto et al. (2021) proposed a method to detect areas of parasympathetic innervation from the amplitude of the repolarization EGM. Verrier et al. (2016) showed that repolarization times can be recovered from EGMs for both the atrium and the ventricle in a controlled clinical environment. However, initial experience in other groups including our own suggest that reliably obtaining atrial repolarization information from EGMs remains a challenge.

Different studies demonstrated discrepancies when using the same voltage threshold (for example, 0.5 mV) to distinguish healthy from pathological tissue when mapping during different rhythms (sinus rhythm and AF) (Rodríguez-Mañero et al., 2018; Nairn et al., 2020b; Nairn et al., 2022). Nairn et al. (2022) looked at how the amplitude of EGMs changed when electroanatomical mapping was performed under three different rhythms (sinus rhythm, native AF, and induced AF). The authors proposed not only one single cut-off voltage value for the entire atrium but regional voltage thresholds to minimize the discrepancies between different mapping rhythms. Computer models could help to further characterize the voltage relations during different rhythms and to overcome the use of a voltage threshold to distinguish the cardiac substrate (healthy and fibrotic) by combining *in vivo* data and *in silico* data to fully exploit the information contained in EGMs (Sánchez et al., 2021a). Additionally, computer models of cardiac electrophysiology could aid the design of medical devices helping in understanding the factors that affect EGMs to raise awareness for them (Oesterlein et al., 2016; Pollnow et al., 2017; Beheshti et al., 2018; Hwang et al., 2019) as well as to inform the choice of parameters to improve the technologies as proposed for cardiac resynchronization therapy (Jolley et al., 2010).

Understanding the functional relationship between the discrete structure and continuum behaviour of cardiac tissue at microscopic and macroscopic levels is a significant challenge (Gokhale et al., 2017). At the microscopic level, Tveito et al. (2017) and Bécue et al. (2017) proposed a cell-by-cell approach that explicitly models the extracellular, membrane and intracellular domain. However, cell-by-cell models are computationally expensive and will require an increase of computational resources such that finer meshes up to cellular resolution can be handled efficiently (Potse et al., 2020). At the macroscopic level, reduced order models (Fresca et al., 2020) could help to reproduce in detail the electrophysiology of the cardiac tissue without losing important details that will determine the vulnerability of the tissue to arrhythmia. Recently, (Herrero Martin et al., 2022) explored the use of Physics Informed Neural Networks (PINN) to model the electrical propagation in the cardiac tissue. The authors introduced electrophysiology models to the neural network and were able to reconstruct the spatial-temporal dynamics of the action potential and its propagation. One of the big drawbacks of these approaches is the amount of data needed to train the network in order to predict different possible propagations patterns.

Software plays a fundamental role in cardiac modeling. Recent work demonstrated significant speedup of simulations of cardiac electrophysiology (Sundnes et al., 2006; Seemann et al., 2010; Cooper et al., 2015; Quarteroni et al., 2017; Sánchez et al., 2020; Plank et al., 2021). However, it remains to be seen how effectively GPUs can be integrated into large-scale cardiac simulations. Regardless, several numerical libraries are currently available, opening the door to accelerate cardiac electrophysiology simulations (Anzt et al., 2020; Mills et al., 2021).

7 CONCLUSION

Models of cardiac tissue electrophysiology have played an essential role in advancing our understanding of action potential propagation in the heart and the genesis of EGMs. Despite the significant progress of different modeling approaches and efficient numerical software, there are substantial challenges, such as modeling of the microstructure at a close-to-cellular scale, modeling the different aspects of fibrosis, electrophysiological heterogeneity as well as realistic electrode configurations. Dedicated simulation studies with refined models will help to further elucidate the different factors that contribute to EGM genesis and impact their morphology.

AUTHOR CONTRIBUTIONS

JS and AL contributed to conception and design of the study. JS drafted the manuscript. All authors contributed to manuscript revision, read and approved the submitted version.

FUNDING

This work was supported by the European High-Performance Computing Joint Undertaking EuroHPC under grant agreement No 955495 (MICROCARD) co-funded by the Horizon 2020 programme of the European Union (EU), the French National Research Agency ANR, the German Federal Ministry of Education and Research, the Italian ministry of economic development, the Swiss State Secretariat for Education, Research and Innovation, the Austrian Research Promotion Agency FFG, and the Research Council of Norway.

ACKNOWLEDGMENTS

We gratefully acknowledge the state of Baden-Württemberg through bwHPC and the KIT-Publication Fund of the Karlsruhe Institute of Technology. In addition, the authors thank Deborah Nairn, Joshua Frederic Steyer, and Mark Potse for their valuable suggestions.

REFERENCES

Abdi, B., Hendriks, R. C., van der Veen, A.-J., and de Groot, N. M. S. (2020). Improved Local Activation Time Annotation of Fractionated Atrial Electrograms for Atrial Mapping. *Comput. Biol. Med.* 117, 103590. doi:10.1016/j.compbiomed.2019.103590

Alonso, S., and Bär, M. (2013). Reentry Near the Percolation Threshold in a Heterogeneous Discrete Model for Cardiac Tissue. *Phys. Rev. Lett.* 110, 158101. doi:10.1103/PhysRevLett.110.158101

Anzt, H., Cojean, T., Flegar, G., Göbel, F., Grützmacher, T., Nayak, P., et al. (2020). *Ginkgo: A Modern Linear Operator Algebra Framework for High Performance Computing*. Available at: https://arxiv.org/abs/2006.16852

Ashihara, T., Haraguchi, R., Nakazawa, K., Namba, T., Ikeda, T., Nakazawa, Y., et al. (2012). The Role of Fibroblasts in Complex Fractionated Electrograms During Persistent/Permanent Atrial Fibrillation. *Circ. Res.* 110, 275–284. doi:10.1161/CIRCRESAHA.111.255026

Avila, G., Medina, I. M., Jiménez, E., Elizondo, G., and Aguilar, C. I. (2007). Transforming Growth Factor-B1 Decreases Cardiac Muscle L-type Ca^{2+} Current and Charge Movement by Acting on the $Ca_v1.2$ mRNA. *Am. J. Physiology-Heart Circulatory Physiology* 292, H622–H631. doi:10.1152/ajpheart.00781.2006

Bécue, P.-E., Potse, M., and Coudière, Y. (2017). A Three-Dimensional Computational Model of Action Potential Propagation through a Network of Individual Cells. *Computing in Cardiology (CinC)*, 1–4. doi:10.22489/CinC.2017.022-271

Balaban, G., Halliday, B. P., Mendonca Costa, C., Bai, W., Porter, B., Rinaldi, C. A., et al. (2018). Fibrosis Microstructure Modulates Reentry in Non-Ischemic Dilated Cardiomyopathy: Insights From Imaged Guided 2D Computational Modeling. *Front. Physiol.* 9, 1–13. doi:10.3389/fphys.2018.01832

Beach, M., Sim, I., Mehta, A., Kotadia, I., O'Hare, D., Whitaker, J., et al. (2021). Using the Universal Atrial Coordinate System for MRI and Electroanatomic Data Registration in Patient-Specific Left Atrial Model Construction and Simulation. 11th International Conference on Functional Imaging and Modeling of the Heart. 629–638. doi:10.1007/978-3-030-78710-3_60

Beheshti, M., Magtibay, K., Massé, S., Porta-Sanchez, A., Haldar, S., Bhaskaran, A., et al. (2018). Determinants of Atrial Bipolar Voltage: Inter Electrode Distance and Wavefront Angle. *Comput. Biol. Med.* 102, 449–457. doi:10.1016/j.compbiomed.2018.07.011

Bishop, M. J., and Plank, G. (2011a). Bidomain ECG Simulations Using an Augmented Monodomain Model for the Cardiac Source. *IEEE Trans. Biomed. Eng.* 58, 2297–2307. doi:10.1109/TBME.2011.2148718

Bishop, M. J., and Plank, G. (2011b). Representing Cardiac Bidomain Bath-Loading Effects by an Augmented Monodomain Approach: Application to Complex Ventricular Models. *IEEE Trans. Biomed. Eng.* 58, 1066–1075. doi:10.1109/TBME.2010.2096425

Cabrera-Lozoya, R., Berte, B., Cochet, H., Jais, P., Ayache, N., and Sermesant, M. (2017). Image-Based Biophysical Simulation of Intracardiac Abnormal Ventricular Electrograms. *IEEE Trans. Biomed. Eng.* 64, 1446–1454. doi:10.1109/TBME.2016.2562918

Caixal, G., Alarcón, F., Althoff, T. F., Nuñez-Garcia, M., Benito, E. M., Borràs, R., et al. (2020). Accuracy of Left Atrial Fibrosis Detection with Cardiac Magnetic Resonance: Correlation of Late Gadolinium Enhancement with Endocardial Voltage and Conduction Velocity. *EP Eur.* 23, 380–388. doi:10.1093/europace/euaa313

Campos, F. O., Wiener, T., Prassl, A. J., Weber dos Santos, R., Sanchez-Quintana, D., Ahammer, H., et al. (2013). Electroanatomical Characterization of Atrial Microfibrosis in a Histologically Detailed Computer Model. *IEEE Trans. Biomed. Eng.* 60, 2339–2349. doi:10.1109/TBME.2013.2256359

Celotto, C., Sánchez, C., Mountris, K. A., Laguna, P., and Pueyo, E. (2021). Location of Parasympathetic Innervation Regions From Electrograms to Guide Atrial Fibrillation Ablation Therapy: An In Silico Modeling Study. *Front. Physiol.* 12. Available at: https://www.frontiersin.org/articles/10.3389/fphys.2021.674197/full. doi:10.3389/fphys.2021.674197

Clayton, R. H. (2018). Dispersion of Recovery and Vulnerability to Re-Entry in a Model of Human Atrial Tissue with Simulated Diffuse and Focal Patterns of Fibrosis. *Front. Physiol.* 9, 1052. doi:10.3389/fphys.2018.01052

Clerc, L. (1976). Directional Differences of Impulse Spread in Trabecular Muscle from Mammalian Heart. *J. Physiology* 255, 335–346. doi:10.1113/jphysiol.1976.sp011283

Colli Franzone, P., Pavarino, L. F., Scacchi, S., and Taccardi, B. (2007). Monophasic Action Potentials Generated by Bidomain Modeling as a Tool for Detecting Cardiac Repolarization Times. *Am. J. Physiology-Heart Circulatory Physiology* 293, H2771–H2785. doi:10.1152/ajpheart.00651.2007

Cooper, J., Spiteri, R. J., and Mirams, G. R. (2015). Cellular Cardiac Electrophysiology Modeling with Chaste and CellML. *Front. Physiol.* 5, 511. doi:10.3389/fphys.2014.00511

Dutta, S., Mincholé, A., Quinn, T. A., and Rodriguez, B. (2017). Electrophysiological Properties of Computational Human Ventricular Cell Action Potential Models under Acute Ischemic Conditions. *Prog. Biophysics Mol. Biol.* 129, 40–52. doi:10.1016/j.pbiomolbio.2017.02.007

Fresca, S., Manzoni, A., Dedè, L., and Quarteroni, A. (2020). Deep Learning-Based Reduced Order Models in Cardiac Electrophysiology. *Plos One* 15, e0239416. doi:10.1371/journal.pone.0239416

Frontera, A., Takigawa, M., Martin, R., Thompson, N., Cheniti, G., Massoullié, G., et al. (2018). Electrogram Signature of Specific Activation Patterns: Analysis of Atrial Tachycardias at High-Density Endocardial Mapping. *Heart rhythm.* 15, 28–37. doi:10.1016/j.hrthm.2017.08.001

Gaeta, S., Bahnson, T. D., and Henriquez, C. (2020). Mechanism and Magnitude of Bipolar Electrogram Directional Sensitivity: Characterizing Underlying Determinants of Bipolar Amplitude. *Heart rhythm.* 17, 777–785. doi:10.1016/j.hrthm.2019.12.010

Ganesan, A. N., Kuklik, P., Lau, D. H., Brooks, A. G., Baumert, M., Lim, W. W., et al. (2013). Bipolar Electrogram Shannon Entropy at Sites of Rotational Activation. *Circ Arrhythmia Electrophysiol.* 6, 48–57. doi:10.1161/CIRCEP.112.976654

Gharaviri, A., Verheule, S., Eckstein, J., Potse, M., Kuklik, P., Kuijpers, N. H., et al. (2016). How Disruption of Endo-Epicardial Electrical Connections Enhances Endo-Epicardial Conduction during Atrial Fibrillation. *Europace* 19 (2), 308–318. doi:10.1093/europace/euv445

Gillette, K., Gsell, M. A. F., Prassl, A. J., Karabelas, E., Reiter, U., Reiter, G., et al. (2021). A Framework for the Generation of Digital Twins of Cardiac Electrophysiology from Clinical 12-leads ECGs. *Med. Image Anal.* 71, 102080. doi:10.1016/j.media.2021.102080

Gima, K., and Rudy, Y. (2002). Ionic Current Basis of Electrocardiographic Waveforms. *Circulation Res.* 90, 889–896. doi:10.1161/01.RES.0000016960.61087.86

Gokhale, T. A., Medvescek, E., and Henriquez, C. S. (2017). Modeling Dynamics in Diseased Cardiac Tissue: Impact of Model Choice. *Chaos* 27, 093909. doi:10.1063/1.4999605

Herrero Martin, C., Oved, A., Chowdhury, R. A., Ullmann, E., Peters, N. S., Bharath, A. A., et al. (2022). EP-PINNs: Cardiac Electrophysiology Characterisation Using Physics-Informed Neural Networks. *Front. Cardiovasc. Med.* 8. doi:10.3389/fcvm.2021.768419

Hodgkin, A. L., and Huxley, A. F. (1952). A Quantitative Description of Membrane Current and its Application to Conduction and Excitation in Nerve. *J. Physiology* 117, 500–544. doi:10.1113/jphysiol.1952.sp004764

Hwang, M., Kim, J., Lim, B., Song, J.-S., Joung, B., Shim, E. B., et al. (2019). Multiple Factors Influence the Morphology of the Bipolar Electrogram: An In Silico Modeling Study. *PLoS Comput. Biol.* 15, e1006765. doi:10.1371/journal.pcbi.1006765

Irakoze, É., and Jacquemet, V. (2020). Breakthrough Wave Detection in a 3D Computer Model of Atrial Endo-Epicardial Dissociation. 2020 Computing in Cardiology Conference. doi:10.22489/CinC.2020.425

Jacquemet, V., and Henriquez, C. S. (2009). Genesis of Complex Fractionated Atrial Electrograms in Zones of Slow Conduction: A Computer Model of Microfibrosis. *Heart rhythm.* 6, 803–810. doi:10.1016/j.hrthm.2009.02.026

Jacquemet, V., Virag, N., Ihara, Z., Dang, L., Blanc, O., Zozor, S., et al. (2003). Study of Unipolar Electrogram Morphology in a Computer Model of Atrial Fibrillation. *J. Cardiovasc. Electrophysiol.* 14, S172–S179. doi:10.1046/j.1540.8167.90308.x

Jadidi, A., Nothstein, M., Chen, J., Lehrmann, H., Dössel, O., Allgeier, J., et al. (2020). Specific Electrogram Characteristics Identify the Extra-pulmonary Vein Arrhythmogenic Sources of Persistent Atrial Fibrillation -

Characterization of the Arrhythmogenic Electrogram Patterns During Atrial Fibrillation and Sinus Rhythm. *Sci. Rep.* 10, 9147. doi:10.1038/s41598-020-65564-2

Jakes, D., Burrage, K., Drovandi, C. C., Burrage, P., Bueno-Orovio, A., Santos, R. W. d., et al. (2019). Perlin noise generation of physiologically realistic patterns of fibrosis. *bioRxiv*. doi:10.1101/668848

Jolley, M., Stinstra, J., Tate, J., Pieper, S., MacLeod, R., Chu, L., et al. (2010). Finite Element Modeling of Subcutaneous Implantable Defibrillator Electrodes in an Adult Torso. *Heart rhythm.* 7, 692–698. doi:10.1016/j.hrthm.2010.01.030

Keller, M. W., Schuler, S., Seemann, G., and Dössel, O. (2012). Differences in Intracardiac Signals on a Realistic Catheter Geometry Using Mono- and Bidomain Models. *Comput. Cardiol.*, 305–308. Available at: http://cinc.mit.edu/archives/2012/pdf/0305.pdf

Keller, M. W., Schuler, S., Wilhelms, M., Lenis, G., Seemann, G., Schmitt, C., et al. (2014). Characterization of Radiofrequency Ablation Lesion Development Based on Simulated and Measured Intracardiac Electrograms. *IEEE Trans. Biomed. Eng.* 61, 2467–2478. doi:10.1109/TBME.2014.2322515

Krueger, M. W., Rhode, K. S., O'Neill, M. D., Rinaldi, C. A., Gill, J., Razavi, R., et al. (2014). Patient-specific Modeling of Atrial Fibrosis Increases the Accuracy of Sinus Rhythm Simulations and May Explain Maintenance of Atrial Fibrillation. *J. Electrocardiol.* 47, 324–328. doi:10.1016/j.jelectrocard.2013.11.003

Lim, B., Kim, J., Hwang, M., Song, J.-S., Lee, J. K., Yu, H.-T., et al. (2020). *In Situ* procedure for High-Efficiency Computational Modeling of Atrial Fibrillation Reflecting Personal Anatomy, Fiber Orientation, Fibrosis, and Electrophysiology. *Sci. Rep.* 10, 2417. doi:10.1038/s41598-020-59372-x

Lin, Y.-J., Tai, C.-T., Lo, L.-W., Udyavar, A. R., Chang, S.-L., Wongcharoen, W., et al. (2007). Optimal Electrogram Voltage Recording Technique for Detecting the Acute Ablative Tissue Injury in the Human Right Atrium. *J. Cardiovasc Electrophysiol.* 18, 617–622. doi:10.1111/j.1540-8167.2007.00803.x

Liu, T., Song, D., Dong, J., Zhu, P., Liu, J., Liu, W., et al. (2017). Current Understanding of the Pathophysiology of Myocardial Fibrosis and its Quantitative Assessment in Heart Failure. *Front. Physiol.* 8, 238. doi:10.3389/fphys.2017.00238

Loewe, A., Wülfers, E. M., and Seemann, G. (2018). Cardiac Ischemia-Insights from Computational Models. *Herzschr Elektrophys* 29, 48–56. doi:10.1007/s00399-017-0539-6

MacCannell, K., Bazzazi, H., Chilton, L., Shibukawa, Y., Clark, R. B., and Giles, W. R. (2007). A Mathematical Model of Electrotonic Interactions Between Ventricular Myocytes and Fibroblasts. *Biophysical J.* 92, 4121–4132. doi:10.1529/biophysj.106.101410

Maleckar, M. M., Greenstein, J. L., Giles, W. R., and Trayanova, N. A. (2009). Electrotonic Coupling between Human Atrial Myocytes and Fibroblasts Alters Myocyte Excitability and Repolarization. *Biophysical J.* 97, 2179–2190. doi:10.1016/j.bpj.2009.07.054

Malmivuo, J., and Plonsey, R. (1995). *BioelectromagnetismPrinciples and Applications of Bioelectric and Biomagnetic Fields*. Oxford: Oxford University Press.

McDowell, K. S., Vadakkumpadan, F., Blake, R., Blauer, J., Plank, G., Macleod, R. S., et al. (2013). Mechanistic Inquiry into the Role of Tissue Remodeling in Fibrotic Lesions in Human Atrial Fibrillation. *Biophysical J.* 104, 2764–2773. doi:10.1016/j.bpj.2013.05.025

McDowell, K. S., Vadakkumpadan, F., Blake, R., Blauer, J., Plank, G., MacLeod, R. S., et al. (2012). Methodology for Patient-Specific Modeling of Atrial Fibrosis as a Substrate for Atrial Fibrillation. *J. Electrocardiol.* 45, 640–645. doi:10.1016/j.jelectrocard.2012.08.005

Mendonca Costa, C., Campos, F. O., Prassl, A. J., Weber dos Santos, R., Sanchez-Quintana, D., Ahammer, H., et al. (2014). An Efficient Finite Element Approach for Modeling Fibrotic Clefts in the Heart. *IEEE Trans. Biomed. Eng.* 61, 900–910. doi:10.1109/TBME.2013.2292320

Mendonca Costa, C., Plank, G., Rinaldi, C. A., Niederer, S. A., and Bishop, M. J. (2018). Modeling the Electrophysiological Properties of the Infarct Border Zone. *Front. Physiol.* 9, 356. doi:10.3389/fphys.2018.00356

Mills, R. T., Adams, M. F., Balay, S., Brown, J., Dener, A., Knepley, M., et al. (2021). Toward Performance-Portable PETSc for GPU-Based Exascale Systems. *Parallel Comput.* 108, 102831. doi:10.1016/j.parco.2021.102831

Morgan, R., Colman, M. A., Chubb, H., Seemann, G., and Aslanidi, O. V. (2016). Slow Conduction in the Border Zones of Patchy Fibrosis Stabilizes the Drivers for Atrial Fibrillation: Insights from Multi-Scale Human Atrial Modeling. *Front. Physiol.* 7, 1–15. doi:10.3389/fphys.2016.00474

Nagel, C., Espinosa, C. B., Gillette, K., Gsell, M. A. F., Sánchez, J., Plank, G., et al. (2022). *Comparison of Propagation Models and Forward Calculation Methods on Cellular, Tissue and Organ Scale Atrial Electrophysiology*. Available at: https://arxiv.org/abs/2203.07776

Nagel, C., Schuler, S., Dössel, O., and Loewe, A. (2021). A Bi-atrial Statistical Shape Model for Large-Scale In Silico Studies of Human Atria: Model Development and Application to ECG Simulations. *Med. Image Anal.* 74, 102210. doi:10.1016/j.media.2021.102210

Nairn, D., Eichenlaub, M., Lehrmann, H., Müller-Edenborn, B., Chen, J., Huang, T., et al. (2022). Spatial Correlation of Left Atrial Low Voltage Substrate in Sinus Rhythm versus Atrial Fibrillation: Identifying the Pathological Substrate Irrespective of the Rhythm. *medRxiv*. doi:10.1101/2022.02.18.22271172

Nairn, D., Hunyar, D., Sánchez, J., Doessel, O., and Loewe, A. (2020a). Impact of Electrode Size on Electrogram Voltage in Healthy and Diseased Tissue. 2020 Computing in Cardiology Conference. doi:10.22489/CinC.2020.146

Nairn, D., Lehrmann, H., Müller-Edenborn, B., Schuler, S., Arentz, T., Dössel, O., et al. (2020b). Comparison of Unipolar and Bipolar Voltage Mapping for Localization of Left Atrial Arrhythmogenic Substrate in Patients with Atrial Fibrillation. *Front. Physiol.* 11, 575846. doi:10.3389/fphys.2020.575846

Neic, A., Campos, F. O., Prassl, A. J., Niederer, S. A., Bishop, M. J., Vigmond, E. J., et al. (2017). Efficient Computation of Electrograms and ECGs in Human Whole Heart Simulations Using a Reaction-Eikonal Model. *J. Comput. Phys.* 346, 191–211. doi:10.1016/j.jcp.2017.06.020

Nguyen, T. P., Qu, Z., and Weiss, J. N. (2014). Cardiac Fibrosis and Arrhythmogenesis: The Road to Repair Is Paved with Perils. *J. Mol. Cell. Cardiol.* 70, 83–91. doi:10.1016/j.yjmcc.2013.10.018

Nothstein, M., Luik, A., Jadidi, A., Sánchez, J., Unger, L. A., Wülfers, E. M., et al. (2021). CVAR-Seg: An Automated Signal Segmentation Pipeline for Conduction Velocity and Amplitude Restitution. *Front. Physiol.* 12, 673047. doi:10.3389/fphys.2021.673047

Oesterlein, T., Frisch, D., Loewe, A., Seemann, G., Schmitt, C., Dössel, O., et al. (2016). Basket-Type Catheters: Diagnostic Pitfalls Caused by Deformation and Limited Coverage. *BioMed Res. Int.* 2016, 1–13. doi:10.1155/2016/5340574

Pezzuto, S., Quaglino, A., and Potse, M. (2019). "On Sampling Spatially-Correlated Random Fields for Complex Geometries," in *Functional Imaging and Modeling of the Heart* (Cham: Springer International Publishing). doi:10.1007/978-3-030-21949-9_12

Plank, G., Loewe, A., Neic, A., Augustin, C., Huang, Y. L., Gsell, M. A. F., et al. (2021). The openCARP Simulation Environment for Cardiac Electrophysiology. *Comput. Methods Programs Biomed.* 208, 106223. doi:10.1016/j.cmpb.2021.106223

Pollnow, S., Greiner, J., Oesterlein, T., Wülfers, E. M., Loewe, A., and Dössel, O. (2017). Mini Electrodes on Ablation Catheters: Valuable Addition or Redundant Information?-Insights from a Computational Study. *Comput. Math. Methods Med.* 2017, 1–13. doi:10.1155/2017/1686290

Potse, M., Dube, B., Vinet, A., and Cardinal, R. (2006). "A Comparison of Monodomain and Bidomain Propagation Models for the Human Heart," in 2006 International Conference of the IEEE Engineering in Medicine and Biology Society (IEEE), 3895–3898. doi:10.1109/IEMBS.2006.259484

Potse, M., Saillard, E., Barthou, D., and Coudière, Y. (2020). Feasibility of Whole-Heart Electrophysiological Models with Near-Cellular Resolution. 2020 Computing in Cardiology. doi:10.22489/CinC.2020.126

Quarteroni, A., Manzoni, A., and Vergara, C. (2017). The Cardiovascular System: Mathematical Modelling, Numerical Algorithms and Clinical Applications. *Acta Numer.* 26, 365–590. doi:10.1017/S0962492917000046

Ramos-Mondragón, R., Vega, A. V., and Avila, G. (2011). Long-term Modulation of Na+ and K+ Channels by TGF-B1 in Neonatal Rat Cardiac Myocytes. *Pflugers Arch. - Eur. J. Physiol.* 461, 235–247. doi:10.1007/s00424-010-0912-3

Rivaud, M. R., Bayer, J. D., Cluitmans, M., van der Waal, J., Bear, L. R., Boukens, B. J., et al. (2021). Critical repolarization gradients determine the induction of reentry-based torsades de pointes arrhythmia in models of long QT syndrome. *Heart rhythm* 18, 278–287. doi:10.1016/j.hrthm.2020.09.020

Rodriguez, B., Trayanova, N., and Noble, D. (2006). Modeling Cardiac Ischemia. *Ann. N. Y. Acad. Sci.* 1080, 395–414. doi:10.1196/annals.1380.029

Rodríguez-Mañero, M., Valderrábano, M., Baluja, A., Kreidieh, O., Martínez-Sande, J. L., García-Seara, J., et al. (2018). Validating Left Atrial Low Voltage Areas During Atrial Fibrillation and Atrial Flutter Using Multielectrode

Automated Electroanatomic Mapping. *JACC Clin. Electrophysiol.* 4, 1541–1552. doi:10.1016/j.jacep.2018.08.015

Roney, C. H., Bayer, J. D., Zahid, S., Meo, M., Boyle, P. M. J., Trayanova, N. A., et al. (2016). Modelling Methodology of Atrial Fibrosis Affects Rotor Dynamics and Electrograms. *EP Eur.* 18, iv146–iv155. doi:10.1093/europace/euw365

Roney, C. H., Bendikas, R., Pashakhanloo, F., Corrado, C., Vigmond, E. J., McVeigh, E. R., et al. (2021). Constructing a Human Atrial Fibre Atlas. *Ann. Biomed. Eng.* 49, 233–250. doi:10.1007/s10439-020-02525-w

Rook, M. B., Van Ginneken, A. C., de Jonge, B., el Aoumari, A., Gros, D., Jongsma, H. J., et al. (1992). Differences in Gap Junction Channels between Cardiac Myocytes, Fibroblasts, and Heterologous Pairs. *Am. J. Physiology-Cell Physiology* 263, C959–C977. doi:10.1152/ajpcell.1992.263.5.C959

Russo, I., and Frangogiannis, N. G. (2016). Diabetes-associated Cardiac Fibrosis: Cellular Effectors, Molecular Mechanisms and Therapeutic Opportunities. *J. Mol. Cell. Cardiol.* 90, 84–93. doi:10.1016/j.yjmcc.2015.12.011

Saba, M. M., Akella, J., Gammie, J., Poston, R., Johnson, A., Hood, R. E., et al. (2009). The Influence of Fat Thickness on the Human Epicardial Bipolar Electrogram Characteristics: Measurements on Patients Undergoing Open-Heart Surgery. *Europace* 11, 949–953. doi:10.1093/europace/eup156

Sánchez, J., Gomez, J. F., Martinez-Mateu, L., Romero, L., Saiz, J., and Trenor, B. (2019a). Heterogeneous Effects of Fibroblast-Myocyte Coupling in Different Regions of the Human Atria under Conditions of Atrial Fibrillation. *Front. Physiol.* 10, 847. doi:10.3389/fphys.2019.00847

Sánchez, J., Nothstein, M., Unger, L., Saiz, J., Trénor, B., Dössel, O., et al. (2019b). "Influence of Fibrotic Tissue Arrangement on Intracardiac Electrograms During Persistent Atrial Fibrillation," in 2019 Computing in Cardiology (CinC), 1. doi:10.22489/cinc.2019.342

Sánchez, J., Luongo, G., Nothstein, M., Unger, L. A., Saiz, J., Trenor, B., et al. (2021a). Using Machine Learning to Characterize Atrial Fibrotic Substrate From Intracardiac Signals with a Hybrid In Silico and *In Vivo* Dataset. *Front. Physiol.* 12, 699291. doi:10.3389/fphys.2021.699291

Sánchez, J., Trenor, B., Saiz, J., Dössel, O., and Loewe, A. (2021b). Fibrotic Remodeling during Persistent Atrial Fibrillation: In Silico Investigation of the Role of Calcium for Human Atrial Myofibroblast Electrophysiology. *Cells* 10, 2852. doi:10.3390/cells10112852

Sánchez, J., Nothstein, M., Neic, A., Huang, Y.-L., J. Prassl, A., Ulrich, R., et al. (2020). "openCARP: An Open Sustainable Framework for In-Silico Cardiac Electrophysiology Research," in 2020 Computing in Cardiology Conference (CinC). doi:10.22489/CinC.2020.111

Schicketanz, L., Unger, L. A., Sánchez, J., Dössel, O., and Loewe, A. (2021). Separating Atrial Near Fields and Atrial Far Fields in Simulated Intra-atrial Electrograms. *Curr. Dir. Biomed. Eng.* 7, 175–178. doi:10.1515/cdbme-2021-2045

Schmitt, O. H. (1969). "Biological Information Processing Using the Concept of Interpenetrating Domains," in Information Processing in The Nervous System: Proceedings of a Symposium held at the State University of New York at Buffalo. Editor K. N. Leibovic (Berlin, Heidelberg: Springer Berlin Heidelberg), 325–331. doi:10.1007/978-3-642-87086-6_18

Schneider, M. A. E., Ndrepepa, G., Weber, S., Deisenhofer, I., Schomig, A., and Schmitt, C. (2004). Influence of High-Pass Filtering on Noncontact Mapping and Ablation of Atrial Tachycardias. *Pacing Clin. Electrophysiol.* 27, 38–46. doi:10.1111/j.1540-8159.2004.00383.x

Schuler, S., Keller, M. W., Oesterlein, T., Seemann, G., and Dössel, O. (2013). Influence of Catheter Orientation, Tissue Thickness and Conduction Velocity on the Intracardiac Electrogram. *Biomed. Eng./Biomed. Tech.* doi:10.1515/bmt-2013-4334

Seemann, G., Bustamante, P., Ponto, S., Wilhelms, M., Scholz, E., and Dossel, O. (2010). "Atrial Fibrillation-Based Electrical Remodeling in a Computer Model of the Human Atrium," in 2010 Computers in Cardiology, 417–420.

Seemann, G., Loewe, A., and Wülfers, E. M. (2017). "Effects of Fibroblasts Coupling on the Electrophysiology of Cardiomyocytes from Different Regions of the Human Atrium: a Simulation Study," in 2017 Computing in Cardiology (CinC). doi:10.22489/CinC.2017.380-451

Starreveld, R., Knops, P., Roos-Serote, M., Kik, C., Bogers, A. J. J. C., Brundel, B. J. J. M., et al. (2020). The Impact of Filter Settings on Morphology of Unipolar Fibrillation Potentials. *J. Cardiovasc. Trans. Res.* 13, 953–964. doi:10.1007/s12265-020-10011-w

Sundnes, J., Nielsen, B. F., Mardal, K. A., Cai, X., Lines, G. T., and Tveito, A. (2006). On the Computational Complexity of the Bidomain and the Monodomain Models of Electrophysiology. *Ann. Biomed. Eng.* 34, 1088–1097. doi:10.1007/s10439-006-9082-z

Sutanto, H., Cluitmans, M. J. M., Dobrev, D., Volders, P. G. A., Bébarová, M., and Heijman, J. (2020). Acute Effects of Alcohol on Cardiac Electrophysiology and Arrhythmogenesis: Insights from Multiscale In Silico Analyses. *J. Mol. Cell. Cardiol.* 146, 69–83. doi:10.1016/j.yjmcc.2020.07.007

Takigawa, M., Kitamura, T., Basu, S., Bartal, M., Martin, C. A., Martin, R., et al. (2022). Effect of Electrode Size and Spacing on Electrograms: Optimized Electrode Configuration for Near-Field Electrogram Characterization. *Heart rhythm.* 19, 102–112. doi:10.1016/j.hrthm.2021.09.011

ten Tusscher, K. H. W. J., and Panfilov, A. V. (2007). Influence of Diffuse Fibrosis on Wave Propagation in Human Ventricular Tissue. *EP Eur.* 9, vi38–vi45. doi:10.1093/europace/eum206

Trew, M. L., Smaill, B. H., Bullivant, D. P., Hunter, P. J., and Pullan, A. J. (2005). A Generalized Finite Difference Method for Modeling Cardiac Electrical Activation on Arbitrary, Irregular Computational Meshes. *Math. Biosci.* 198, 169–189. doi:10.1016/j.mbs.2005.07.007

Tschöpe, C., Ammirati, E., Bozkurt, B., Caforio, A. L. P., Cooper, L. T., Felix, S. B., et al. (2021). Myocarditis and Inflammatory Cardiomyopathy: Current Evidence and Future Directions. *Nat. Rev. Cardiol.* 18, 169–193. doi:10.1038/s41569-020-00435-x

Tung, L. (1978). *A Bidomain Model for Describing Ischemic Myocardial D-C Potentials*. Massachusetts: Ph.D. thesis.

Tveito, A., Jæger, K. H., Kuchta, M., Mardal, K.-A., and Rognes, M. E. (2017). A Cell-Based Framework for Numerical Modeling of Electrical Conduction in Cardiac Tissue. *Front. Phys.* 5, 48. doi:10.3389/fphy.2017.00048

Ugarte, J. P., Orozco-Duque, A., Tobón, V., Novak, D., Saiz, J., Oesterlein, T., et al. (2014). Dynamic Approximate Entropy Electroanatomic Maps Detect Rotors in a Simulated Atrial Fibrillation Model. *Plos One* 9, e114577–19. doi:10.1371/journal.pone.0114577

Unger, L. A., Oesterlein, T. G., Loewe, A., and Dössel, O. (2019). "Noise Quantification and Noise Reduction for Unipolar and Bipolar Electrograms," in 2019 Computing in Cardiology (CinC). doi:10.22489/cinc.2019.288

van der Does, L. J. M. E., and de Groot, N. M. S. (2017). Inhomogeneity and Complexity in Defining Fractionated Electrograms. *Heart rhythm.* 14, 616–624. doi:10.1016/j.hrthm.2017.01.021

Verheule, S., and Schotten, U. (2021). Electrophysiological Consequences of Cardiac Fibrosis. *Cells* 10, 3220. doi:10.3390/cells10113220

Verrier, R. L., Fuller, H., Justo, F., Nearing, B. D., Rajamani, S., and Belardinelli, L. (2016). Unmasking Atrial Repolarization to Assess Alternans, Spatiotemporal Heterogeneity, and Susceptibility to Atrial Fibrillation. *Heart rhythm.* 13, 953–961. doi:10.1016/j.hrthm.2015.11.019

Vigmond, E. J., Hughes, M., Plank, G., and Leon, L. J. (2003). Computational Tools for Modeling Electrical Activity in Cardiac Tissue. *J. Electrocardiol.* 36, 69–74. doi:10.1016/j.jelectrocard.2003.09.017

Vigmond, E., Pashaei, A., Amraoui, S., Cochet, H., and Hassaguerre, M. (2016). Percolation as a Mechanism to Explain Atrial Fractionated Electrograms and Reentry in a Fibrosis Model Based on Imaging Data. *Heart rhythm.* 13, 1536–1543. doi:10.1016/j.hrthm.2016.03.019

Zahid, S., Cochet, H., Boyle, P. M., Schwarz, E. L., Whyte, K. N., Vigmond, E. J., et al. (2016). Patient-derived Models Link Re-entrant Driver Localization in Atrial Fibrillation to Fibrosis Spatial Pattern. *Cardiovasc Res.* 110, 443–454. doi:10.1093/cvr/cvw073

Conflict of Interest: The authors declare that the research was conducted in the absence of any commercial or financial relationships that could be construed as a potential conflict of interest.

Publisher's Note: All claims expressed in this article are solely those of the authors and do not necessarily represent those of their affiliated organizations, or those of the publisher, the editors and the reviewers. Any product that may be evaluated in this article, or claim that may be made by its manufacturer, is not guaranteed or endorsed by the publisher.

frontiers | Frontiers in Physiology

ORIGINAL RESEARCH
published: 16 May 2022
doi: 10.3389/fphys.2022.873049

Intracardiac Inverse Potential Mapping Using the Method of Fundamental Solutions

*Shu Meng[1], Nicholas Sunderland[1,2], Judit Chamorro-Servent[3], Laura R. Bear[4,5,6], Nigel A. Lever[1,7,8], Gregory B. Sands[1], Ian J. LeGrice[1,9], Anne M. Gillis[10], Jichao Zhao[1], David M. Budgett[1] and Bruce H. Smaill[1]**

[1]Auckland Bioengineering Institute, University of Auckland, Auckland, New Zealand, [2]Bristol Heart Institute, University of Bristol, Bristol, United Kingdom, [3]Department of Mathematics, Universitat Autònoma de Barcelona, Bellaterra, Spain, [4]IHU Liryc, Electrophysiology and Heart Modeling Institute, Fondation Bordeaux Université, Bordeaux, France, [5]Centre de Recherche Cardio-Thoracique de Bordeaux, Univ. Bordeaux, Bordeaux, France, [6]Centre de Recherche Cardio-Thoracique de Bordeaux, INSERM, Bordeaux, France, [7]Auckland City Hospital, Auckland, New Zealand, [8]Department of Medicine, University of Auckland, Auckland, New Zealand, [9]Department of Physiology, University of Auckland, Auckland, New Zealand, [10]Libin Cardiovascular Research Institute, Calgary University, Calgary, AB, Canada

OPEN ACCESS

Edited by:
Gernot Plank,
Medical University of Graz, Austria

Reviewed by:
Vincent Jacquemet,
Université de Montréal, Canada
Peter Michael Van Dam,
University Medical Center Utrecht, Netherlands
Edward Joseph Vigmond,
Université de Bordeaux, France

***Correspondence:**
Bruce H. Smaill
b.smaill@auckland.ac.nz

Specialty section:
This article was submitted to Cardiac Electrophysiology, a section of the journal Frontiers in Physiology

Received: 10 February 2022
Accepted: 19 April 2022
Published: 16 May 2022

Citation:
Meng S, Sunderland N, Chamorro-Servent J, Bear LR, Lever NA, Sands GB, LeGrice IJ, Gillis AM, Zhao J, Budgett DM and Smaill BH (2022) Intracardiac Inverse Potential Mapping Using the Method of Fundamental Solutions. Front. Physiol. 13:873049. doi: 10.3389/fphys.2022.873049

Introduction: Atrial fibrillation (AF) is the most prevalent cardiac dysrhythmia and percutaneous catheter ablation is widely used to treat it. Panoramic mapping with multi-electrode catheters can identify ablation targets in persistent AF, but is limited by poor contact and inadequate coverage.

Objective: To investigate the accuracy of inverse mapping of endocardial surface potentials from electrograms sampled with noncontact basket catheters.

Methods: Our group has developed a computationally efficient inverse 3D mapping technique using a meshless method that employs the Method of Fundamental Solutions (MFS). An *in-silico* test bed was used to compare ground-truth surface potentials with corresponding inverse maps reconstructed from noncontact potentials sampled with virtual catheters. Ground-truth surface potentials were derived from high-density clinical contact mapping data and computer models.

Results: Solutions of the intracardiac potential inverse problem with the MFS are robust, fast and accurate. Endocardial surface potentials can be faithfully reconstructed from noncontact recordings in real-time if the geometry of cardiac surface and the location of electrodes relative to it are known. Larger catheters with appropriate electrode density are needed to resolve complex reentrant atrial rhythms.

Conclusion: Real-time panoramic potential mapping is feasible with noncontact intracardiac catheters using the MFS.

Significance: Accurate endocardial potential maps can be reconstructed in AF with appropriately designed noncontact multi-electrode catheters.

Keywords: atrial arrhythmia, multi-electrode basket catheters, method of fundamental solutions, inverse mapping, endocardial potentials

INTRODUCTION

Accurate identification of regions in the heart which trigger ectopic activation and sustain reentrant arrhythmia is a critical step in effective interventional treatment of heart rhythm disturbance. Sequential contact mapping with catheters introduced percutaneously into one or more heart chambers is widely used for this purpose (Issa et al., 2019), but it can be time-consuming and works poorly in atrial fibrillation (AF) where rhythm is non-stationary. While multi-electrode basket catheters have been used for panoramic mapping in AF (Narayan et al., 2012; Pathik et al., 2018), it is difficult to position them so that the electrodes are uniformly distributed across the atrial surface and in contact with it (Oesterlein et al., 2016; Martinez- Mateu et al., 2018; Pathik et al., 2018).

In principle, inverse methods can be used to reconstruct potentials on the endocardial surface of a cardiac chamber from electrograms recorded at electrodes that are not in contact with it if three-dimensional (3D) chamber geometry is specified, the locations of electrodes are known and the forward problem, which describes the transfer relationship between measured and endocardial surface potentials, is specified accurately. However, the boundary mesh-based solution methods used previously to solve the intracardiac potential inverse problem have shortcomings that are discussed in detail elsewhere (Meng et al., 2017; Meng et al., 2022). With the finite element method (FEM), the transfer matrix is sparse, inherently ill-conditioned and time-consuming to evaluate (Pullan et al., 2005). On the other hand, boundary elements (BEMs) are not robust for measurement points near the heart wall, particularly when surface topology is complex as is commonly the case with the atria. (Pullan et al., 2005).

Meshless methods (MMs) employing the Method of Fundamental Solutions (MFS) (Fairweather and Karageorghis, 1998) have been successfully used to solve the body surface potential inverse problem (Wang and Rudy, 2006). This approach is computationally efficient and robust in a uniform, isotropic domain, an assumption that is realistic for the intracardiac problem. In this case, the MFS provides an inherently simpler representation of the forward problem than boundary mesh-based methods.

While there have been numerous systematic analyses of the efficacy of inverse body surface potential mapping (Ramanathan and Rudy, 2001; Cluitmans et al., 2017; Bear et al., 2018), there have been very few equivalent studies of intracardiac potential mapping (Meng et al., 2022) and no attempt to use the MFS in this setting. In the research reported here, we have used the MFS to address the accuracy with which time-varying potentials on the endocardial surface of the left atrium (LA) can be reconstructed from electrograms recorded inside the chamber with basket catheters where the electrodes may or may not be in contact with the atrial wall. We conclude that accurate real-time panoramic potential mapping and 3D phase mapping are feasible with noncontact intracardiac catheters using the MFS. However, to faithfully recover complex potential fields, such as those seen in AF on the endocardial surfaces of the atria, it is necessary to use catheters that are sufficiently large to capture characteristic features of surface potential variation with an electrode distribution appropriate to resolve it spatially (Meng et al., 2022). We argue that the sampling constraints identified in this study apply to noncontact intracardiac mapping in general.

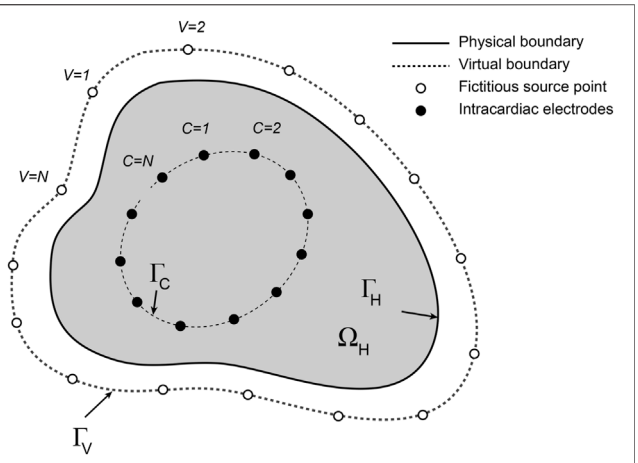

FIGURE 1 | Schematic representation of the intracardiac forward problem. Fictitious electrical sources (open circles) distributed around a virtual boundary Γ_V outside the surface Γ_H that bounds a heart cavity Ω_H generate current flux within the domain. This contributes to potentials recorded with electrodes (closed circles) on a basket catheter. The electrodes lie on the open surface Γ_C.

MATHEMATICAL BACKGROUND

Noncontact intracardiac potential mapping seeks to reconstruct the potential distribution on the inner surface of a heart chamber from a discrete set of potentials recorded at known points inside the chamber with a multi-electrode catheter. To solve this inverse problem, it is first necessary to formulate the corresponding forward problem. Here, we extend an approach followed by Wang and Rudy (Wang and Rudy, 2006), in which the MFS was applied to inverse body surface potential mapping.

The formulation of the intracardiac forward problem is shown in **Figure 1**. Potentials $\phi(\mathbf{x}_c)$ are recorded at M points $\mathbf{x}_c$ on the surface Γ_C that bounds the electrodes. A set of N fictitious sources is positioned at locations $\{\xi_i\}_{i=1}^N$ along a virtual 3D boundary Γ_V that lies outside the endocardial surface of the cardiac chamber. The linear combination of the Laplace fundamental solution over the sources on $\{\xi_i\}_{i=1}^N$ allows us to have an expression of the potentials in the source free volume Ω_H contained in the cardiac chamber. It is assumed that 1) there are no electrical sources or sinks within the heart cavity, 2) conductivity throughout the domain is uniform and isotropic, 3) the electrical properties of the basket catheter can be neglected, and 4) bioelectric processes are quasi-static.

At any instant, the potential $\phi(\mathrm{x})$ at any point $\mathbf{x}$ in Ω_H due to fictitious sources located on the virtual external boundary Γ_V is

$$\phi(\boldsymbol{x}) = a_0 + \sum_{i=1}^{N} a_i G(\xi_i, \boldsymbol{x}) \tag{1}$$

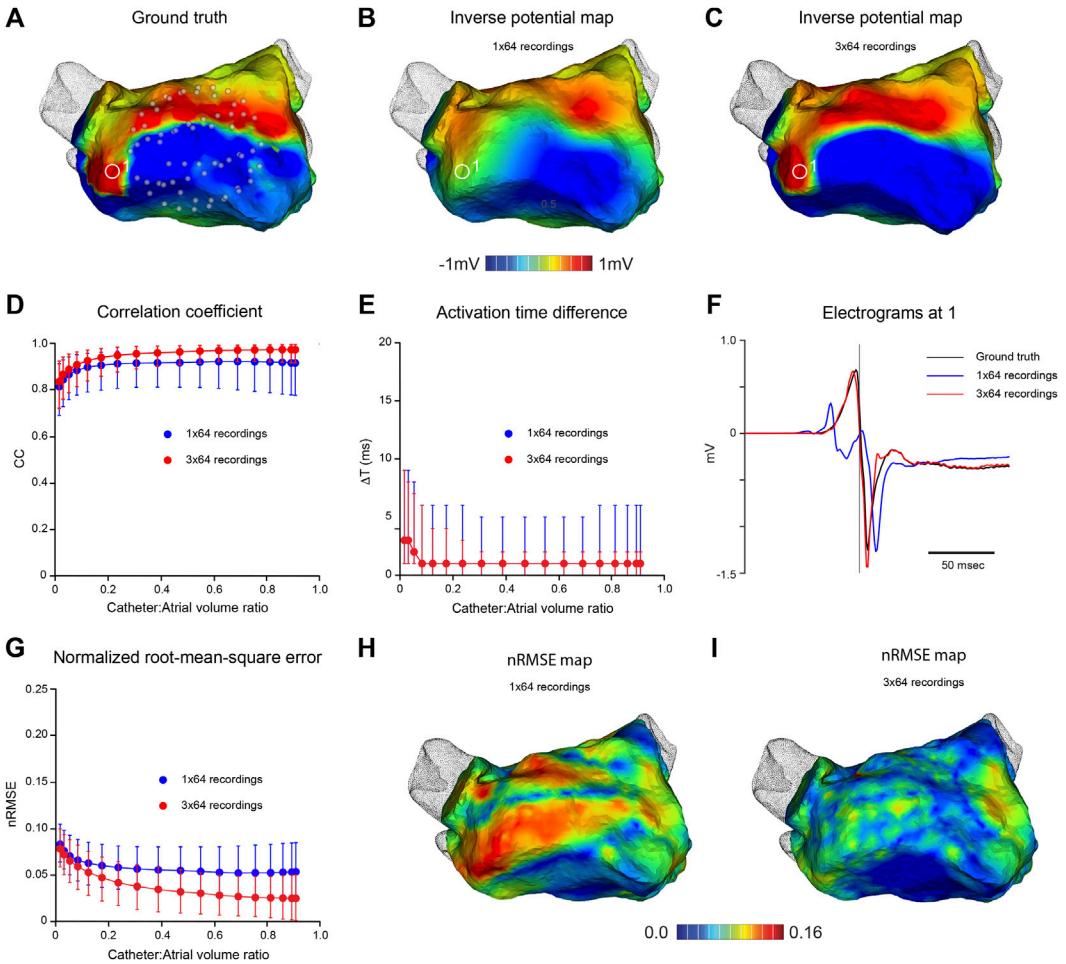

FIGURE 2 | *In silico* analysis of the effects of mapping catheter dimension and electrode distribution on MFS inverse solutions during pacing from distal coronary sinus. Ground-truth LA surface potential distributions during atrial activation are constructed from pace-synchronized contact recordings acquired with a high density electrode array. Corresponding potential fields in the LA cavity are estimated throughout the atrial activation cycle and "sampled" at locations of virtual basket catheter electrodes. Inverse surface potential maps are then reconstructed from these data and compared with ground truth maps. **(A)** Ground-truth LA surface potential distribution at one instant during activation - see red line in **(C)**. Corresponding inverse potential map **(B)** reconstructed from potentials sampled with virtual 64-electrode basket catheter with 0.67 volume fraction relative to LA. Electrodes are distributed uniformly along 8 splines as indicated in **(A)**. **(C)** Ground truth and reconstructed electrograms at 1 in **(A,B)**. In the middle panel, CC **(D)**, nRMSE **(E)** and ΔT **(F)** are presented as functions of relative catheter volume for inverse solutions over one activation cycle. Median values and IQR are given for inverse maps constructed from "recordings" at 64 sites (blue) and 3 sequential "recordings" at 64 sites following stepwise rotation of the catheter through 15° around its axis (red). Both maps in the lower panel relate to the same time as in **(A,B)**. In **(G)**, the distribution of nRMSE on the LA surface is compared with spline location for a potential map constructed from 64 full or near-contact "recordings", while **(H)** corresponds to **(B)**. Here, the inverse map was constructed from 3 sequential "recordings" at 64 sites with a relative catheter volume fraction of 0.67. **(I)** Ground truth and inverse electrograms at 2) in **(H)**. Abbreviations: MFS, Method of Fundamental Solutions; LA, left atrium; CC, correlation coefficient; nRMSE, normalized root-mean-squared error; ΔT, activation time difference; IQR, interquartile range.

where a_0 is a constant and $a = (a_1, \ldots, a_N)$ is the instantaneous source current at a source $\{\xi_i\}_{i=1}^N$. G is the fundamental solution of the Laplace operator in 3D

$$G(\xi, \boldsymbol{x}) = \frac{1}{4\pi|\xi - \boldsymbol{x}|} \tag{2}$$

and $\{\xi_i\}_{i=1}^N$ are the 3D locations of the fictious sources and $|\xi - \boldsymbol{x}|$ is the Euclidean distance between $\mathbf{x}$ and ξ. Note that $a_i = \sigma l_i$ for $i = 1, N$ where l_i is the source current at ξ_i and σ is conductivity.

Potentials at $\mathbf{x}_c$ on the surface Γ_C that bounds the electrodes therefore can be estimated by using **Eq. 1** for $x \in \Gamma_c$. This results in a linear system of equations when they are equated to the measured potentials on the M electrodes of the catheter. It should be noted that while the forward problem has been set up here for the continuous surfaces Γ_C and Γ_H, this is not a requirement of the MFS.

Solution of this system yields the associated current source densities on the fictitious external boundary Γ_V and corresponding potentials on the endocardial surface Γ_H are then estimated by using **Eq. 1** again for $x \in \Gamma_H$. This system is inherently under-determined because the number of electrodes M is generally less than N, the number of fictitious sources needed to map potentials faithfully onto Γ_H.

METHODS

An established computational approach (Ramanathan and Rudy, 2001) was used to quantify the accuracy of inverse potential mapping and key steps are illustrated in **Figure 2**. First, ground-truth potential distributions were specified on the endocardial surface of the left atrium (LA). The associated field throughout the LA was determined by numerical solution of Laplace's equation and potentials were sampled at points corresponding to electrode locations on open basket catheters with different electrode distributions across a range of dimensions (**Figure 2A**). Endocardial surface potentials were then reconstructed from the sampled potentials using the MFS (**Figure 2B**) and compared with ground-truth potential distributions. This process was continued through a complete atrial activation cycle for stationary rhythms or over several cycles of reentrant activity. Ground-truth electrograms were also compared with corresponding inverse estimates at points across the endocardial surface (**Figure 2F**) to assess the accuracy with which local activation timing information is reconstructed.

Clinical ground truth data used in this study were acquired as follows. CT imaging was performed in one patient undergoing catheter ablation to treat atrial flutter. The patient gave written informed consent and the study protocol was approved by the Melbourne Health Research and Human Ethics Committee. LA geometry was segmented with the Ensite Verismo^{TM} tool and registered with respect to the mapping system (Ensite Precision, Abbott). A decapolar pacing catheter was positioned in the coronary sinus (CS). A 20-pole Lasso^{TM} catheter was introduced into the LA *via* trans-septal puncture and used to collect 3,200 time-referenced, spatially-registered contact unipolar electrograms across the LA during pacing (300 ms interval) from the distal CS at a sampling rate of 1 kHz. The LA shell was refined to 5,000 vertices and potentials were interpolated by Dirichlet energy minimization (Botsch et al., 2010).

Ground truth data representing polymorphic reentrant atrial activation were simulated. Atrial surface geometry was reconstructed in an anaesthetized sheep (crossbred female, 53 Kg). All procedures were approved by the Animal Ethics Committee of the University of Auckland and conform to the Guide for the Care and Use of Laboratory Animals (National Institutes of Health publication no. 85-23). Gadolinium-enhanced ECG-gated MRI images of the atria ($1.0 \times 1.0\ mm^2$ in-plane resolution approximately parallel to the atrio-ventricular valve plane and 1.6 mm between slices) were acquired with a 3T Siemens Magnetom Skyra^{TM} scanner. LA endocardial surface geometry was segmented using Amira (Thermo Fisher Scientific) and a 3D triangular surface mesh (1,529 nodes) was fitted to the LA with pulmonary veins and left atrial appendage truncated. Ground-truth potential distributions representing polymorphic reentrant atrial activation were modeled on this geometry as follows. Meandering spiral wave reentry was simulated on an isotropic 2D monodomain with Fenton Karma activation kinetics (Fenton and Karma, 1998) using a standard cross-field S1-S2 stimulus protocol (Pandit et al., 2005). Points on the 2D domain were sampled and mapped onto the 3D surface mesh so that surface area was similar in both, with a contour adjacent to the boundary in the former assigned to the mitral valve orifice. Extracellular potentials were approximated from the transmembrane currents computed at each 3D point at a sampling rate of 1 kHz (**Supplementary Video S1**—Simulated ground truth data—in the **Supplementary Material**).

The open-source software environment SCIRun (http://www.sci.utah.edu/cibc-software/scirun.html) was used for FEM solutions of the 3D forward problem. (Burton et al., 2011). Intracardiac potential fields were computed from the ground-truth surface potential distributions at successive time instants by solving Laplace's equation throughout Ω_H. The intracardiac field was sampled at points corresponding to electrodes on two basket catheter configurations with 1) 64 channels with 8 equally spaced electrodes along 8 splines at equal radial angles, and 2) 130 channels with 8 equally spaced electrodes along 16 splines at equal radial angles and electrodes at upper and lower poles. Basket dimensions were uniformly scaled to vary catheter: atrial volume ratio. The centroids of catheters and the LA chamber were aligned to allow maximum catheter expansion and to ensure reproducibility between results. Noise was imposed by adding Gaussian noise independently to the electrograms recorded at each electrode with power set at realistic levels. Signal-to-noise ratio (SNR) is quantified as the ratio of root-mean-squared (RMS) voltages of reconstructed electrograms and noise.

Inverse solutions with the MFS were run with purpose-written code. The fictitious boundary was formed by uniform scaling of the atrial surface mesh and sources were associated with each node. Inflation was quantified as the relative volume difference between Γ_V and Γ_H. Solutions were stable across the inflation range 2–10% (**Supplementary Figure S1**) and the value 6% was selected as optimal in the results presented here. Inverse endocardial potential distributions for intracardiac potentials "sampled" with virtual catheters were obtained using zero-order Tikhonov regularization (Tikhonov and Arsenin, 1977) employing the L-curve method to calculate the regularization parameter (Hansen, 2010).

Phase maps were constructed using the approach outlined by Kuklik et al. (Kuklik et al., 2017) Sinusoidal recomposition was applied to electrograms at each LA surface node and the Hilbert transformation was then used to estimate instantaneous phase at these points.

Correspondence between ground-truth and reconstructed potential maps were quantified by evaluating normalized RMS error (nRMSE) and correlation coefficient (CC).

$$nRMSE = \sqrt{\frac{\sum_{i=1}^{N}\left(\varnothing_{GT}^{i} - \varnothing_{R}^{i}\right)^2}{\sum_{i=1}^{N}\left(\varnothing_{GT}^{i}\right)^2}} \text{ and } CC = \frac{\sum_{i=1}^{N}\left(\varnothing_{GT}^{i} - \mu_{GT}\right)\sum_{i=1}^{N}\left(\varnothing_{R}^{i} - \mu_{R}\right)}{\sqrt{\sum_{i=1}^{N}\left(\varnothing_{GT}^{i} - \mu_{GT}\right)^2}\sqrt{\sum_{i=1}^{N}\left(\varnothing_{R}^{i} - \mu_{R}\right)^2}} \quad (3)$$

where N is the number of surface points compared, $\varnothing_{GT}^{i}$ and $\varnothing_{R}^{i}$ are ground-truth and reconstructed potentials at surface point i, and μ_{GT} and μ_{R} are mean values for ground-truth and reconstructed potentials, respectively, across the surface.

Activation times (ATs) for ground-truth (AT_{GT}) and reconstructed electrograms (AT_R) were estimated as maximum negative rate of potential change and the activation time difference ΔT at each surface point was evaluated as

$$\Delta T = |AT_{GT} - AT_R| \quad (4)$$

Programs were written in C or in the MATLAB programming language (The Mathworks, Natick, Massachusetts).

RESULTS

Inverse Potential Mapping in Stationary Rhythm

Figure 2 indicates the accuracy with which high-density potential maps can be reconstructed from clinical ground truth electrograms recorded during the relatively uniform spread of LA activation in coronary sinus pacing. Key features of activation were reconstructed from intra-atrial potentials sampled with a virtual 64-electrode noncontact catheter that occupied ~67% of atrial cavity volume (**Figure 2A**). However, neither high resolution features of instantaneous potential maps (**Figure 2B**) nor high frequency components of regional electrograms (**Figure 2F**) were captured faithfully. Despite this, accuracy measures were high and surprisingly stable across a wide range of catheter dimensions with median CC = 0.92, nRMSE = 0.054 and ΔT = 1 ms for catheter:atrial volume ratios >0.3 with a 64-electrode basket catheter (**Figures 2D–F**). None of these measures improved with full or near contact between electrodes and endocardial surface, and nRMSE was highest between splines where the spacing of adjacent electrodes was greatest (**Figure 2H**), indicating that spatial distribution of electrodes on the surface that bounds the catheter is the problem here. Sampling density was increased by moving the catheter and synchronizing the electrograms acquired. The instantaneous potential map in **Figure 2C** was reconstructed from 192 electrograms "recorded" in 3 sequential steps by rotating the virtual 64-electrode catheter (relative volume ratio 0.67) around its axis in increments of 15°. This markedly improved the match between high-density ground truth and inverse maps (compare **Figures 2A,C**). The nRMSE between electrodes was substantially reduced (compare **Figures 2H,I**) and high frequency components of complex local electrograms were reconstructed accurately (**Figure 2F**). Median CC increased to ~0.97 and median nRMSE halved across a wide range of catheter dimensions (**Figure 2G**).

Inverse Potential Mapping in Reentrant Rhythm

In **Figure 3**, we present the effects of catheter dimension and electrode distribution on inverse solutions obtained with the MFS in simulated macroscopic reentrant activation of the LA that replicates features of atrial flutter. Catheter designs considered are a 64-electrode catheter with 8 uniformly spaced electrodes along 8 splines and a 130-electrode catheter that has 8 uniformly distributed electrodes on 16 splines with 2 additional polar electrodes. Once again, the centroids of catheters and LA chamber were aligned.

In the upper panel of **Figure 3**, an instantaneous ground-truth potential map (**Figure 3A**) is compared with corresponding inverse maps constructed from potentials sampled with a 64-electrode catheter (**Figure 3B**) and a 130-electrode catheter (**Figure 3C**). Endocardial potentials were poorly reconstructed in some regions of the LA with an 8 spline 64-electrode basket catheter but recovered more faithfully with a 16 spline 130-electrode catheter where electrode distribution is more uniform, spatially. As might be expected, errors with the 64-electrode catheter were greatest between splines near the equator where inter-electrode spacing was largest.

The correspondence between ground-truth and reconstructed surface electrograms was quantified for these two catheters over 3 consecutive activation cycles for a range of catheter dimensions, and results are presented in the lower panel of **Figure 3**. The accuracy with which unanchored reentrant rhythm could be reconstructed was consistently less than for more stable paced rhythms (compare **Figure 3** with **Figure 2**) and it was affected more markedly by relative catheter dimensions. For each of the 3 metrics considered, performance was better at all catheter dimensions with 130-electrode catheters than with the 64-electrode catheters. For example, with 130-electrode catheters, CC approached a median of 0.97 [IQR 0.07] as catheter dimensions were increased, compared with corresponding values around 0.9 [IQR 0.19] with 64-electrode catheters (**Figure 3D**). Consistent with these results, nRMSE was reduced with increased catheter dimension reaching a median of 0.042 [IQR 0.055] for the 130-electrode catheter compared with 0.083 [IQR 0.099] for 64-electrode catheters (**Figure 3E**). Finally, ΔT was reduced to a median of 1 ms with a 130-electrode catheter compared with 2 ms for 64-electrode catheters (**Figure 3F**). All three metrics were relatively stable for catheter volumes >0.6 relative to LA volume.

Effects of Noise on Inverse Potential Mapping

The effects of noise on the accuracy of inverse endocardial potentials reconstructed with the MFS are summarized in **Figure 4**. Intra-atrial electrograms were "sampled" with 130-channel catheters during simulated macro-reentry with superimposed Gaussian noise at RMS voltages of 18, 56 and 178 μV. In general, addition of noise had little effect for catheter: LA volume ratios >0.5. However, inverse solutions were progressively degraded by noise at catheter volumes less than this (**Figures 4B–D**). Comparison of the representative electrograms in **Figure 4A** provides further insight into this finding. While SNR in reconstructed electrograms scales inversely with added noise, it is much worse for the smaller of the two catheters (6.54, 4.23 and 1.91 for RMS noise voltages of 18, 56 and 178 μV, respectively, compared with 69.56, 22.85 and 6.83 for the larger catheter). It is also noteworthy that while our inverse solutions do not recover higher frequency components in the ground truth electrograms when the catheter is small this is not systematically altered by noise.

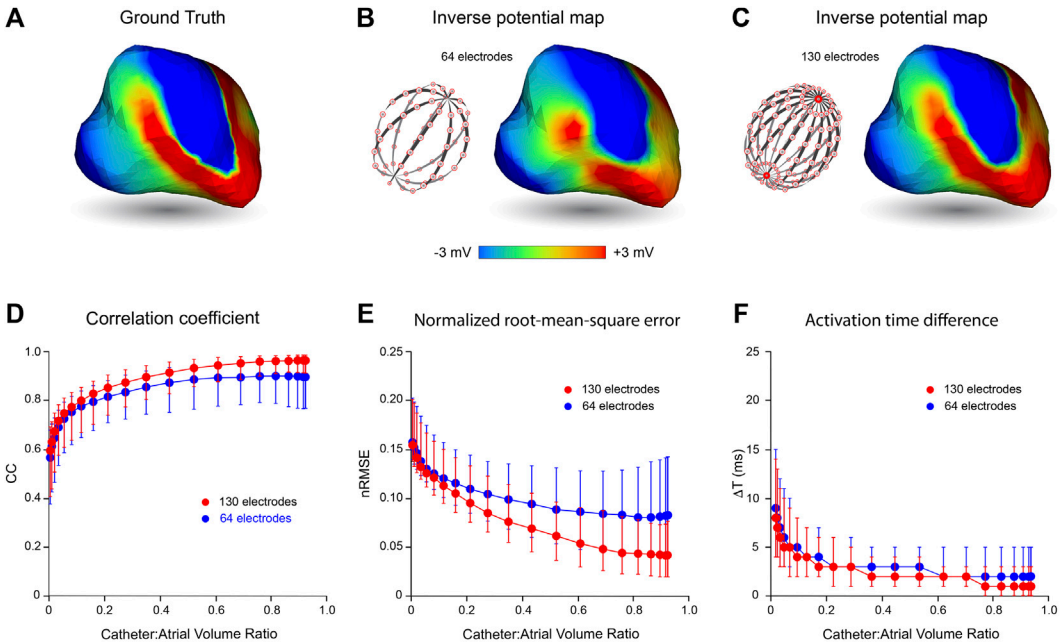

FIGURE 3 | Effects of mapping catheter electrode distribution on inverse solutions with MFS during macro reentry. LA surface potentials throughout 3 activation cycles in simulated atrial flutter are reconstructed from electrograms sampled inside the LA cavity with 64- and 130-electrode basket catheters and compared with ground-truth surface potentials. The upper panel presents typical results for catheters that bound a volume fraction of 0.67 relative to LA volume. These include **(A)** the ground-truth surface potential distribution at one instant during reentrant activation and corresponding potential maps reconstructed using electrograms sampled with **(B)** a 64- electrode basket catheter, and **(C)** a 130-electrode basket catheter. In the lower panel CC **(D)**, nRMSE **(E)** and ΔT **(F)** are presented as functions of relative catheter volume for the 64-electrode catheter (blue) and 130-electrode catheter (red). Median values and IQR are given. Abbreviations: MFS, Method of Fundamental Solutions; LA, left atrium; CC, correlation coefficient; nRMSE, normalized root-mean-squared error; ΔT, activation time difference; IQR, interquartile range.

Inverse Phase Mapping in Macroscopic Reentry

While potential maps during macro reentrant activity were reconstructed more faithfully using a 130-electrode catheter than a 64-electrode catheter with the same dimension, corresponding phase maps in **Figure 5A** appear to carry very similar information about the history of activation across the LA surface. This similarity in phase distribution was preserved throughout an extended sequence of simulated electrical activity (**Supplementary Video S1**), where phase singularities identified recovered with 64- and 130-electrode catheters are also collocated. The correspondence with ground truth for phase maps obtained with noncontact catheters was maintained for a wider range of relative catheter volumes than for the potential maps in **Figure 3** above. However, CC was increased and nRMSE reduced with a 130-electrode catheter compared to a 64-electrode catheter (**Figure 5B**). This indicates that phase maps with the latter capture key features of wave front propagation in macro reentrant arrhythmia, but aspects of the fine structure of the phase distribution are lost.

Region-Of-Interest Potential Mapping

With region-of-interest (RoI) mapping, a small catheter is positioned close to a region of the endocardial surface to reconstruct local electrical activity. In **Figure 6**, we consider the accuracy with which regional electrical activity can be recovered using non-contact catheters. This analysis was completed without adding Gaussian noise. An 8-spline 64-electrode basket catheter (major and minor axes 25 and 23 mm, respectively) was initially located close to the origin of a simulated macro-reentrant circuit in the LA (**Figure 6A**). The inverse solution (**Figure 6B**) was good near the catheter, but much poorer over the rest of the LA. This is demonstrated in **Figure 6C** where CC is rendered on the LA surface; median CC is >0.9 in the RoI, but falls off rapidly with distance from this region. In the lower panel we present CC (**Figure 6D**), nRMSE (**Figure 6E**) and ΔT (**Figure 6F**) in the RoI (red) and across the full endocardial surface (blue) for inverse solutions constructed as the catheter was moved progressively along a line from the origin of the LAA to the inter-atrial septum (**Figure 6A**). These figures demonstrate that regional mapping performance was excellent when the catheter was in or adjacent to the RoI, but poor when the catheter was most distant from it. Global mapping performance was best when the catheter was located centrally, but significantly poorer in this case in the RoI. Of particular interest, RoI performance was optimal when the catheter was ~10 mm from its initial position with electrodes 9–20 mm from the LA wall; median CC was 0.96 [IQR 0.072], median nRMSE 0.09 [IQR 0.05] and median ΔT 0.89 ms [IQR 1.97 ms].

DISCUSSION

Summary

This analysis of noncontact intracardiac potential mapping extends an *in-silico* boundary mesh-based study previously

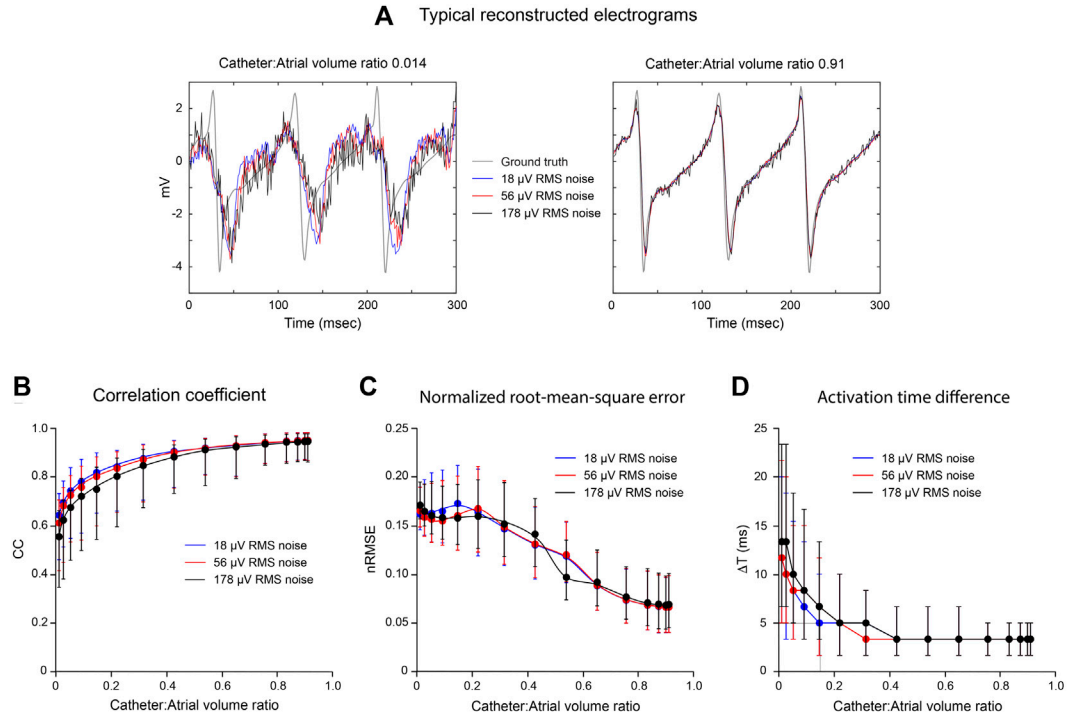

FIGURE 4 | Effects of noise on inverse solutions with the MFS during macro reentry. LA surface potentials throughout activation cycle in simulated atrial flutter are reconstructed from electrograms sampled inside the LA cavity using 130-electrode basket catheters with added Gaussian noise at different mean power levels. All data are compared with ground-truth endocardial potentials. In the upper panel **(A)** electrograms reconstructed from records acquired from a very small and a large basket catheter with 18, 56 and 178 μV of added noise are presented with the corresponding ground-truth electrogram. Catheter volumes relative to LA volume are 0.014 and 0.91, respectively. In the lower panel, CC **(B)**, nRMSE **(C)** and ΔT **(D)** are presented as functions of relative catheter volume for the three noise levels. Median values and IQR are given. Abbreviations: LA, left atrium; CC, correlation coefficient; nRMSE, normalized root-mean-squared error; ΔT, activation time difference.

reported by our laboratory (Meng et al., 2017; Meng et al., 2022). Here we have investigated the accuracy with which endocardial potential maps can be reconstructed from noncontact electrograms recorded with a multi-electrode basket catheter using meshless methods that use the MFS, the first time that this has been done as far as we are aware. We demonstrate that fast, accurate noncontact potential mapping and phase mapping are possible using this approach. However, the spatial frequency of the electrical activity captured is determined by the distribution of electrodes and in order to recover complex non-stationary rhythms, such as AF, the mapping catheter must address a representative subvolume of the cardiac chamber.

Effects of Catheter Dimension

We have reported that noncontact mapping performance deteriorates progressively as catheter dimensions are reduced relative to those of the cardiac chamber and that this degradation becomes more marked when activation is complex. Neither of these findings is surprising. With increasing distance from the heart surface, intracardiac potentials associated with local activation are progressively attenuated and blurred, and information lost in this process cannot be recovered fully. Furthermore, as catheter dimension is reduced, information is captured from a decreasing subset of the cavity volume which may not fully reflect local activity. More striking, perhaps, is the finding that surface electrograms can be reconstructed with acceptable accuracy (CC > 0.9, nRMSE ≤0.06 and ΔT ≤ 2 ms) during reentrant rhythm with basket catheters that fill only half of the cavity. A supplementary point that needs to be made here, is that while relative catheter volume is an accessible measure of dimension, it scales with the third power of radius for a spherical basket catheter. Therefore, catheter volume increases by 112.5% when its diameter changes from 35 to 45 mm. While there was no contact between electrodes and LA wall for the centrally located catheter in **Figure 3A** (Catheter:Atrial volume ratio = 0.67), there was increasing (though incomplete) contact between them as relative volume expanded to ~0.9.

Effects of Noise

Median CC was decreased and median ΔT was increased with reduced catheter dimension (**Figures 4B,D**) when Gaussian noise was added but there was no corresponding effect on median nRMSE (**Figure 4C**). The reconstructed electrograms in **Figure 4A** provide explanation for these results. Because electrograms recorded toward the centre of the LA cavity with a small central catheter are attenuated, the noise added to them markedly reduces SNR. This is reflected in the reconstructed surface electrograms presented in the left-hand panel of **Figure 4A**, where SNR is low and is reduced progressively as noise amplitude increases. The recorded electrograms are also

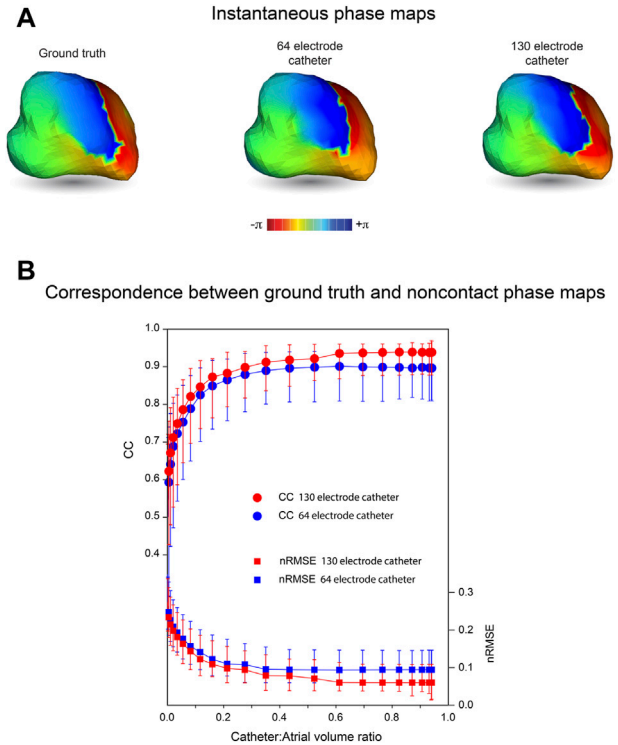

FIGURE 5 | Phase maps of inverse solutions with MFS during macro-reentry. LA surface potentials throughout activation cycle in simulated atrial flutter are reconstructed from electrograms sampled inside the LA cavity using 64- and 130-electrode basket catheters. The centrally located catheters occupy 67% of LA volume. **(A)** Ground truth phase map at one instant during activation compared with corresponding phase maps for surface potentials reconstructed from electrograms recorded with 64-electrode and 130-electrode basket catheters. **(B)** CC and nRMSE presented as functions of relative catheter volume for the 64-electrode catheter (blue) and 130-electrode catheter (red). Median values and IQR are given. Abbreviations: MFS, Method of Fundamental Solutions; LA, left atrium; CC, correlation coefficient; nRMSE, normalized root-mean-squared error; IQR, interquartile range.

smoothed in this case and the frequency content of the ground-truth surface electrograms is not recovered by inverse mapping. However, the overlap between ground-truth and reconstructed electrograms is affected less by noise than might have been expected. With increased noise power, the deviation between reconstructed and ground-truth electrograms can increase, but there is also greater instantaneous overlap between the two. With a large catheter (right-hand panel in **Figure 4A**), the magnitudes of recorded electrograms are substantially greater and there is much less smoothing. As a result, surface electrograms are recovered more faithfully with much less impact of added noise.

Inverse methods are prone to instability and error in the presence of noise. The fact that this is not the case here further reinforces the fact that the transfer matrix used is inherently well-conditioned and the regularization procedures adopted are appropriate. However, the Gaussian noise introduced here is a very narrow representation of the problems faced in practice with inverse potential mapping. Artifacts in the unipolar signals used for this purpose include common-mode electrical noise, far-field activity due to electrical activation of the ventricles which can mask local activity completely in AF and complexity in atrial electrograms that may be due to far-field atrial activity, inadequate spatial sampling or non-uniform electrical properties in the underlying substrate. That said there are many ways that more robust regional information can be extracted from these channels using signal processing methods that exploit temporal and spatial correlation among adjacent electrograms and wavelet-based methods which identify characteristic differences in the instantaneous frequency content of recorded electrograms (Zhao et al., 2013).

Electrode Distribution and Recovery of Complex Activation Patterns

Our data show that ground truth potential maps based on simulated macro-reentrant activity were reconstructed more faithfully using a 130-electrode catheter than a 64-electrode catheter with the same dimension (**Figure 3**). Furthermore, when noncontact electrodes were within a few mm of the cavity surface, dimension had no effect on the efficacy of the inverse solution, which was wholly dependent on electrode distribution. This reflects the fact that the accuracy with which surface potentials can be reconstructed depends on whether the sampled potentials provide a faithful representation of the field addressed. If the electrode distribution is not sufficiently dense, high spatial frequencies cannot be recovered and low frequency artifacts (aliasing) may occur (Shannon, 1949). An example of this is provided in **Figure 2** where apparent fractionation of the electrogram reconstructed between adjacent splines with a 64 electrode basket catheter (see blue trace in **Figure 2F**) disappears with more dense sampling in that region (compare red trace with ground truth electrogram in **Figure 2F**). While compressed sensing approaches can collect and represent sparse signals with many fewer sampling points than indicated by the Nyquist (Shannon, 1949) theorem, optimal sampling strategies are determined by regional spatial and temporal correlation (Long et al., 2011). Specialized regularization techniques are also needed for inverse reconstruction of higher frequencies from sparsely sampled signals without introducing excessive noise.

It should be noted that metrics such as CC and nRMSE used here to quantify the correspondence between ground-truth and reconstructed potentials do not take the time-history of the electrograms into account. This provides additional information about the spread of electrical activation across the heart surface as illustrated by the phase maps in **Figure 5**. The phase map shown here for a 64-electrode catheter is very similar to that presented for a 130-electrode catheter. Both correspond closely to ground truth phase maps throughout the activation sequence (**Supplementary Video S1**). Because phase mapping identifies local activation as an abrupt standardized transition from $+\pi$ to $-\pi$ and imposes relatively uniform spatio-temporal variation around this, confounding effects of local variation in potential magnitude are removed.

It is also important to acknowledge that sampling density is affected by catheter dimensions. For instance, for a 64-electrode 25-mm diameter spherical catheter, inter-electrode spacing along

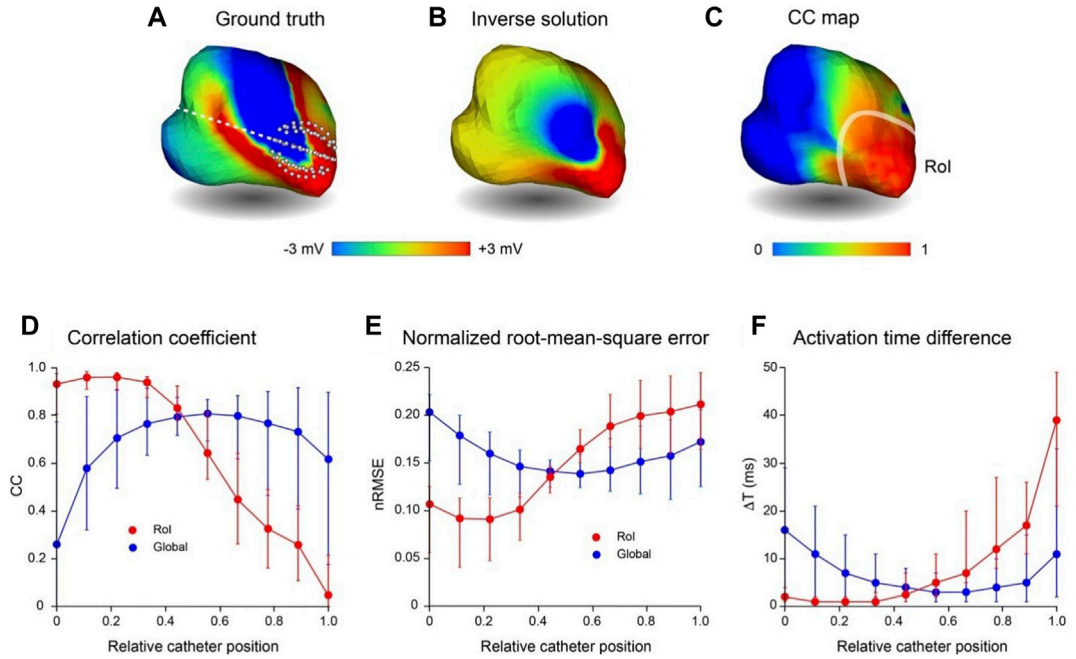

FIGURE 6 | Comparison of region-of-interest inverse potential mapping with global mapping. LA surface potentials during 3 activation cycles of simulated macroscopic reentry were reconstructed from electrograms sampled inside the LA cavity with a small 64-electrode basket catheter. The catheter was initially positioned with some electrodes touching the wall at the junction with the LAA and then moved rightward until electrodes made contact with the inter-atrial septum. **(A)** Representative ground truth potentials on cavity surface also showing broken white line along which catheter is moved from origin of LAA (relative catheter position 0) to inter-atrial septum (relative catheter position 1). **(B)** Inverse solution reconstructed from potentials sampled at relative catheter position 0. **(C)** Correlation coefficient map for ground-truth and inverse solutions in this case. The RoI indicated is the smoothed boundary of the surface in **(C)** where CC ≥ 0.9. In the lower panel **(D–F)** present CC, nRMSE and ΔT, respectively, in the RoI (red) and across the complete LA surface (blue) for inverse solutions with the catheter at equi-spaced locations along the line in **(A)**; catheter locations 0 and 1 are indicated in **(A)**. Median values and interquartile range (IQR) are given in lower panel. Abbreviations: RoI, region of interest; LA, left atrium; LAA, left atrial appendage; CC, correlation coefficient; nRMSE, normalized.

splines is ~5 mm, while the curvilinear distance between splines at the equator is ~10 mm. These measurements are doubled with a 50-mm diameter catheter. This explains the apparent reduction in median CC and the increase in median nRMSE and its interquartile range for 64-electrode catheters when relative catheter volume increases from 0.8–0.91 (**Figures 3D,E**, respectively). Here any improvement in accuracy associated with proximity to the wall is offset by reduced electrode density. In the clinical setting, attempts to achieve direct contact between electrodes and the heart surface can introduce additional error by deforming catheter splines and increasing the nonuniformity of sampling. (Oesterlein et al., 2016; Pathik et al., 2018). It follows that global mapping with multi-electrode basket catheters is more likely to produce reliable results when electrodes are not in contact with the heart wall than when attempts are made to achieve close contact.

The results for RoI mapping are consistent with these observations. The relatively small 64-electrode catheter in **Figure 6** recovered local electrical activity with a high level of accuracy. Moreover, regional mapping produced best results when electrodes were not in contact with the wall (median CC, nRMSE and ΔT: 0.96, 0.09 and 0.89 ms, respectively). Global performance was much poorer, but it would be straightforward to quantify the uncertainty of reconstructed maps based on the distance of electrodes from surface nodes and the results of analyses such as those outlined here.

Potential Clinical Impact of These Findings

The results of this study indicate that global electroanatomic maps can be recovered faithfully in real-time from electrograms recorded with noncontact multi-electrode basket catheters using meshless methods that use the MFS. Accurate specification of 3D electrode locations with respect to cardiac anatomy is required for inverse intracardiac mapping, but this is readily achieved with current hybrid navigation technologies (Issa et al., 2019). Our findings indicate that, for optimal performance, catheters should be located centrally within the cardiac chamber and address a representative subvolume of the cavity (>50% in the data presented here) with minimum contact between electrodes and endocardial surface. The capacity to reconstruct spatially complex activation patterns is limited by electrode distribution, but when heart rhythm is stable and repeated, more detailed maps can be reconstructed with sequential alteration of electrode locations, for instance by catheter rotation/translation. Potentially, this could be more efficient than sequential contact mapping with high density contact arrays because complete maps can be developed with relatively few iterations. For nonstationary heart rhythms such as AF,

however, the accuracy with which endocardial surface activation can be reconstructed is constrained by the spatial distribution of electrodes on the catheter for both contact and noncontact mapping. Sparse sampling can lead to repeating artifact in reconstructed activation patterns that is incorrectly identified as rotors (Roney et al., 2017; Martinez- Mateu et al., 2018). Williams et al. (Williams et al., 2018) reported that >1.0–1.5 points/cm^2 were needed on the endocardial surface to resolve spiral wave activity and this corresponds to an inter-electrode spacing of 2–3 mm - much denser than is the case for 64-electrode basket catheters, particularly for equatorial electrodes on adjacent splines. As demonstrated here, more optimal electrode distribution is achieved with catheters that have 16 rather than 8 splines. While phase mapping may relax sampling requirements to some extent, it seems evident that improved catheter design is necessary for accurate panoramic mapping in AF.

Inverse methods have been used for noncontact intracardiac electrical mapping in two commercial systems. (Schilling et al., 1999; Grace et al., 2019). The Ensite multi-electrode array (Abbott) is used for noncontact potential mapping and consists of 64 electrodes mounted on an inflatable balloon. Consistent with the results reported here, validation studies have shown that accuracy is inversely related to the distance between the array and the heart wall with poor recovery of endocardial surface potentials when this distance is >25 mm (Earley et al., 2006). More recently, instantaneous charge density distributions associated with atrial electrical activation have been constructed from electrograms recorded with noncontact 48-electrode basket catheters (Acutus/Biotronik) (Grace et al., 2019). This is based on a forward model that relates intracardiac potential fields to secondary cellular sources associated with distributed membrane charge dipoles (Plonsey, 1982; Grace et al., 2019; Willems et al., 2019). Our analysis makes no assumptions about the cellular basis of electrical activation. Instead, we address how well endocardial surface potentials can be recovered from a limited number of electrograms recorded inside the heart cavity. We found that information is lost with noncontact mapping if the basket catheters used are too small and with both contact and noncontact mapping if the sampling density is not sufficient. These factors would be expected to impact the spatial resolution with which surface charge distributions can be recovered from noncontact electrograms also.

Limitations

A limitation of this study is that error introduced by uncertainty of the 3D geometry of the heart surface relative to 3D electrode locations has not been explicitly considered. While this would be expected to amplify uncertainty associated with relative catheter size, electrode distribution and noise, we note that our formulation of the intracardiac inverse problem is surprisingly robust. A further limitation is that although our ground-truth data represent atrial rhythms of increasing complexity, they do not fully replicate the spatio-temporal disorder which characterizes AF. However, the analysis presented here demonstrates that the performance of contact mapping is matched by this inverse approach and that spatial resolution in both cases is limited by electrode distribution. Finally, while ground-truth data are based in part on clinical and simulated data, the accuracy of inverse intracardiac mapping has been confirmed computationally. While many of the assumptions made in specifying the forward problem are entirely reasonable, other are not. The electrical properties of the blood in the cardiac chambers are isotropic and uniform but they are certainly not the same as those in the myocardium adjacent to the endocardial surface where the fictitious sources are located. More detailed experimental characterization of the accuracy with which endocardial potentials can be reconstructed using inverse mapping is therefore needed to confirm the analyses presented here.

CONCLUSION

This study demonstrates that atrial endocardial potentials can be reconstructed accurately from electrograms recorded with noncontact multi-electrode basket catheters using a fast robust inverse mapping approach that employs the MFS. This enables efficient and potentially more precise capture of global and region-of-interest potential maps than comparable contact mapping methods. Because data for all electrodes are used, it is not necessary to maximize contact between catheter and the heart wall. This reduces the deformation of catheter splines which occurs when direct contact is sought, thereby preserving a more uniform electrode distribution. However, we demonstrate that conventional 8 spline catheters are suboptimal for instantaneous contact or noncontact mapping of complex rhythms, such as AF.

DATA AVAILABILITY STATEMENT

The raw data supporting the conclusion of this article will be made available by the authors, without undue reservation.

ETHICS STATEMENT

The studies involving human participants were reviewed and approved by the Melbourne Health Rseearch and Human Ethics Committee. The patients/participants provided their written informed consent to participate in this study. The animal study was reviewed and approved by the Animal Ethics Committee of the University of Auckland.

AUTHOR CONTRIBUTIONS

SM and NS jointly completed all aspects of the *in silico* analysis presented here and developed the computational pipeline used. JC-S is responsible for our use of the Method of Fundamental Solutions (MFS), completed 2D prototype studies using this approach and was influential in the direction taken in this work. LB wrote our initial 3D MFS code. SM, BS, IL, NL, AG, GS, and JZ designed, performed and analyzed animal

experiments which provided data for this study. JZ contributed to the simulation of reentrant arrhythmia and provided phase mapping code. SM, NS, and BS generated the figures. SM, NS, GS, and BS wrote the manuscript. BS and DB were responsible for funding and direction of the project. All authors contributed to manuscript revision, read, and approved the version submitted.

FUNDING

This study received financial support from the Health Research Council of New Zealand Programme Grant 13/77 and New Zealand Ministry of Business and Innovation Project Grant UOAX1717.

ACKNOWLEDGMENTS

We gratefully acknowledge the input of JM Kalman, Royal Melbourne Hospital, Parkville, Australia and University of Melbourne, Parkville, Australia who provided high resolution mapping data from one patient (identity protected). We also thank Linley Nisbet for her expert assistance with animal studies carried out in Auckland.

SUPPLEMENTARY MATERIAL

The Supplementary Material for this article can be found online at: https://www.frontiersin.org/articles/10.3389/fphys.2022.873049/full#supplementary-material

REFERENCES

Bear, L. R., LeGrice, I. J., Sands, G. B., Lever, N. A., Loiselle, D. S., Paterson, D. J., et al. (2018). How Accurate Is Inverse Electrocardiographic Mapping? A Systematic *In Vivo* Evaluation. *Circ. Arrhythm. Electrophysiol.* 11, e006108. doi:10.1161/CIRCEP.117.006108

Botsch, M., Kobbelt, L., Pauly, M., Alliez, P., and Lévy, B. (2010). in *Polygon Mesh Processing*. Editor A. K. Peters (Boca Raton, FL: CRC Press).

Burton, B. M., Tate, J. D., Erem, B., Swenson, D. J., Wang, D. F., Steffen, M., et al. (2011). A Toolkit for Forward/inverse Problems in Electrocardiography within the SCIRun Problem Solving Environment. *Annu. Int. Conf. IEEE Eng. Med. Biol. Soc.* 2011, 267–270. doi:10.1109/IEMBS.2011.6090052

Cluitmans, M. J. M., Bonizzi, P., Karel, J. M. H., Das, M., Kietselaer, B. L. J. H., de Jong, M. M. J., et al. (2017). *In Vivo* Validation of Electrocardiographic Imaging. *JACC Clin. Electrophysiol.* 3, 232–242. doi:10.1016/j.jacep.2016.11.012

Earley, M. J., Abrams, D. J. R., Sporton, S. C., and Schilling, R. J. (2006). Validation of the Noncontact Mapping System in the Left Atrium during Permanent Atrial Fibrillation and Sinus Rhythm. *J. Am. Coll. Cardiol.* 48, 485–491. doi:10.1016/j.jacc.2006.04.069

Fairweather, G., and Karageorghis, A. (1998). The Method of Fundamental Solutions for Elliptic Boundary Value Problems. *Adv. Comput. Math.* 9, 69–95.

Fenton, F., and Karma, A. (1998). Vortex Dynamics in Three-Dimensional Continuous Myocardium with Fiber Rotation: Filament Instability and Fibrillation. *Chaos* 8, 20–47. doi:10.1063/1.166311

Grace, A., Willems, S., Meyer, C., Verma, A., Heck, P., Zhu, M., et al. (2019). High-resolution Noncontact Charge-Density Mapping of Endocardial Activation. *JCI Insight* 4, e126422. doi:10.1172/jci.insight.126422

Hansen, P. (2010). *Discrete Inverse Problems*. Philadelphia: SIAM.

Issa, Z. F., Miller, J. M., and Zipes, D. P. (2019). "Advanced Mapping and Navigation Modalities," in *Clinical Arrhythmology and Electrophysiology: A Companion to Braunwald's Heart Disease*. 3rd Edition. (Elsevier), 155–205. Chapter 6 In. doi:10.1016/b978-0-323-52356-1.00006-2

Kuklik, P., Zeemering, S., van Hunnik, A., Maesen, B., Pison, L., Lau, D. H., et al. (2017). Identification of Rotors during Human Atrial Fibrillation Using Contact Mapping and Phase Singularity Detection: Technical Considerations. *IEEE Trans. Biomed. Eng.* 64, 310–318. doi:10.1109/TBME.2016.2554660

Long, C. J., Purdon, P. L., Temereanca, S., Desai, N. U., Hämäläinen, M. S., and Brown, E. N. (2011). State-space Solutions to the Dynamic Magnetoencephalography Inverse Problem Using High Performance Computing. *Ann. Appl. Stat.* 5, 1207–1228. doi:10.1214/11-AOAS483

Martinez-Mateu, L., Romero, L., Ferrer-Albero, A., Sebastian, R., Rodríguez Matas, J. F., Jalife, J., et al. (2018). Factors Affecting Basket Catheter Detection of Real and Phantom Rotors in the Atria: A Computational Study. *PLoS Comput. Biol.* 14, e1006017. doi:10.1371/journal.pcbi.1006017

Meng, S., Zhao, J., LeGrice, I., Lever, N., Sands, G., Bear, L., et al. (2017). Atrial Electro-Anatomic Mapping with a Novel Noncontact Approach. *Comput. Cardiol.* 44, 1–4. doi:10.22489/cinc.2017.105-291

Meng, S., Chamorro-Servent, J., Sunderland, N., Zhao, J., Bear, L. R., Sands, G. B., et al. (2022). *Noncontact Intracardiac Potential Mapping: A Comparison of Boundary Mesh-based and Meshless Inverse Solvers. Front. Physiol.*. (In Review).

Narayan, S. M., Krummen, D. E., and Rappel, W.-J. (2012). Clinical Mapping Approach to Diagnose Electrical Rotors and Focal Impulse Sources for Human Atrial Fibrillation. *J. Cardiovasc. Electrophysiol.* 23 (5), 447–454. doi:10.1111/j.1540-8167.2012.02332.x

Oesterlein, T., Frisch, D., Loewe, A., Seemann, G., Schmitt, C., Dössel, O., et al. (2016). Basket-type Catheters: Diagnostic Pitfalls Caused by Deformation and Limited Coverage. *Biomed. Res. Int.* 2016, 5340574. doi:10.1155/2016/5340574

Pandit, S. V., Berenfeld, O., Anumonwo, J. M. B., Zaritski, R. M., Kneller, J., Nattel, S., et al. (2005). Ionic Determinants of Functional Reentry in a 2-D Model of Human Atrial Cells during Simulated Chronic Atrial Fibrillation. *Biophys. J.* 88, 3806–3821. doi:10.1529/biophysj.105.060459

Pathik, B., Kalman, J. M., Walters, T., Kuklik, P., Zhao, J., Madry, A., et al. (2018). Transient Rotor Activity during Prolonged 3-dimensional Phase Mapping in Human Persistent Atrial Fibrillation. *JACC Clin. Electrophysiol.* 4, 72–83. doi:10.1016/j.jacep.2017.06.005

Plonsey, R. (1982). The Nature of Sources of Bioelectric and Biomagnetic Fields. *Biophysical J.* 39, 309–312. doi:10.1016/s0006-3495(82)84521-9

Pullan, A. J., Buist, M. L., and Cheng, L. K. (2005). *Mathematically Modelling the Electrical Activity of the Heart: From Cell to Body Surface and Back Again*. Singapore: World Scientific Publishing.

Ramanathan, C., and Rudy, Y. (2001). Electrocardiographic Imaging: I. Effect of Torso Inhomogeneities on Body Surface Electrocardiographic Potentials. *J. Cardiovasc Electrophysiol.* 12, 229–240. doi:10.1046/j.1540-8167.2001.00229.x

Roney, C. H., Cantwell, C. D., Bayer, J. D., Qureshi, N. A., Lim, P. B., Tweedy, J. H., et al. (2017). Spatial Resolution Requirements for Accurate Identification of Drivers of Atrial Fibrillation. *Circ. Arrhythm. Electrophysiol.* 10, e004899. doi:10.1161/CIRCEP.116.004899

Schilling, R. J., Peters, N. S., and Davies, D. W. (1999). Feasibility of a Noncontact Catheter for Endocardial Mapping of Human Ventricular Tachycardia. *Circulation* 99, 2543–2552. doi:10.1161/01.cir.99.19.2543

Shannon, C. E. (1949). Communication in the Presence of Noise. *Proc. IRE* 37, 10–21. doi:10.1109/jrproc.1949.232969

Tikhonov, A. N., and Arsenin, V. Y. (1977). *Solutions of Ill-Posed Problems*. Washington DC: Winston and Sons.

Wang, Y., and Rudy, Y. (2006). Application of the Method of Fundamental Solutions to Potential-Based Inverse Electrocardiography. *Ann. Biomed. Eng.* 34, 1272–1288. doi:10.1007/s10439-006-9131-7

Willems, S., Verma, A., Betts, T. R., Murray, S., Neuzil, P., Ince, H., et al. (2019). Targeting Nonpulmonary Vein Sources in Persistent Atrial

Fibrillation Identified by Noncontact Charge Density Mapping: UNCOVER AF Trial. *Circ. Arrhythm. Electrophysiol.* 12, e007233. doi:10.1161/CIRCEP.119.007233

Williams, S. E., Harrison, J. L., Chubb, H., Whitaker, J., Kiedrowicz, R., Rinaldi, C. A., et al. (2018). Local Activation Time Sampling Density for Atrial Tachycardia Contact Mapping: How Much Is Enough? *Europace* 20, e11–e20. doi:10.1093/europace/eux037

Zhao, J., Yao, Y., Huang, W., Shi, R., Zhang, S., LeGrice, I. J., et al. (2013). Novel Methods for Characterization of Paroxysmal Atrial Fibrillation in Human Left Atria. *Tobej* 7, 29–40. doi:10.2174/1874120701307010029

Conflict of Interest: The authors declare that the research was conducted in the absence of any commercial or financial relationships that could be construed as a potential conflict of interest.

The reviewer EJV declared a shared affiliation with one of the authors LRB at the time of review.

Publisher's Note: All claims expressed in this article are solely those of the authors and do not necessarily represent those of their affiliated organizations, or those of the publisher, the editors and the reviewers. Any product that may be evaluated in this article, or claim that may be made by its manufacturer, is not guaranteed or endorsed by the publisher.

frontiers | Frontiers in Physiology

ORIGINAL RESEARCH
published: 30 May 2022
doi: 10.3389/fphys.2022.843292

Mechanistic Insights Into Inflammation-Induced Arrhythmias: A Simulation Study

Xiangpeng Bi[1], Shugang Zhang[1], Huasen Jiang[1], Wenjian Ma[1], Yuanfei Li[1], Weigang Lu[2], Fei Yang[3] and Zhiqiang Wei[1]*

[1]College of Computer Science and Technology, Ocean University of China, Qingdao, China, [2]Department of Educational Technology, Ocean University of China, Qingdao, China, [3]School of Mechanical, Electrical and Information Engineering, Shandong University, Weihai, China

Cardiovascular diseases are the primary cause of death of humans, and among these, ventricular arrhythmias are the most common cause of death. There is plausible evidence implicating inflammation in the etiology of ventricular fibrillation (VF). In the case of systemic inflammation caused by an overactive immune response, the induced inflammatory cytokines directly affect the function of ion channels in cardiomyocytes, leading to a prolonged action potential duration (APD). However, the mechanistic links between inflammatory cytokine-induced molecular and cellular influences and inflammation-associated ventricular arrhythmias need to be elucidated. The present study aimed to determine the potential impact of systemic inflammation on ventricular electrophysiology by means of multiscale virtual heart models. The experimental data on the ionic current of three major cytokines [i.e., tumor necrosis factor-α (TNF-α), interleukin-1 (IL-1β), and interleukin-6 (IL-6)] were incorporated into the cell model, and the effects of each cytokine and their combined effect on the cell action potential (AP) were evaluated. Moreover, the integral effect of these cytokines on the conduction of excitation waves was also investigated in a tissue model. The simulation results suggested that inflammatory cytokines significantly prolonged APD, enhanced the transmural and regional repolarization heterogeneities that predispose to arrhythmias, and reduced the adaptability of ventricular tissue to fast heart rates. In addition, simulated pseudo-ECGs showed a prolonged QT interval—a manifestation consistent with clinical observations. In summary, the present study provides new insights into ventricular arrhythmias associated with inflammation.

Keywords: inflammation, COVID-19, cardiac simulation, ventricular arrhythmia, rat ventricle

OPEN ACCESS

Edited by:
Gernot Plank,
Medical University of Graz, Austria

Reviewed by:
Jordi Heijman,
Maastricht University, Netherlands
Matthijs Cluitmans,
Maastricht University, Netherlands

****Correspondence:***
Shugang Zhang
zsg@ouc.edu.cn

Specialty section:
This article was submitted to Cardiac Electrophysiology, a section of the journal Frontiers in Physiology

Received: *25 December 2021*
Accepted: *25 April 2022*
Published: *30 May 2022*

Citation:
Bi X, Zhang S, Jiang H, Ma W, Li Y, Lu W, Yang F and Wei Z (2022) Mechanistic Insights Into Inflammation-Induced Arrhythmias: A Simulation Study. Front. Physiol. 13:843292. doi: 10.3389/fphys.2022.843292

Abbreviations: VF, ventricular fibrillation; TNF-α, tumor necrosis factor-α; IL-1β, interleukin-1β; IL-6, interleukin-6; CVDs, cardiovascular diseases; COVID-19, coronavirus disease 2019; ECG, electrocardiogram; BCL, basic cycle length; AP, action potential; APD, action potential duration; ENDO, endocardial; EPI, epicardial; MID, middle; SR, sarcoplasmic reticulum; CV, conduction velocity; VW, vulnerable window; PCL, pacing cycle length; SERCA, sarco/endoplasmic reticulum Ca^{2+}-ATPase; EAD, early-afterdepolarizations; DAD, delayed afterdepolarizations; POAF, post-operative atrial fibrillation; TdP, torsade de pointes; TRIaD, triangulation, reverse use dependence, instability and dispersion.

1 INTRODUCTION

Inflammation is a part of the complex biological response of body tissues to harmful stimuli, such as pathogens, damaged cells, toxic compounds, or irradiation (Chen et al., 2018). These harmful stimuli trigger a cascade that releases inflammatory biomarkers and recruits immune cells, which contribute to eliminating the initial cause of cell injury and initiating tissue repair. However, an excessive immune response could potentially lead to multiorgan dysfunction by triggering a cytokine storm.

According to World Health Organization statistics, cardiovascular diseases (CVDs) are the number one cause of death globally, accounting for an estimated 17.9 million lives each year (Kaptoge et al., 2019). In some recent studies, accumulating data suggest increased CVD morbidity and mortality in patients infected with coronavirus disease 2019 (COVID-19), among which there may be an arrhythmia effect (Lazzerini et al., 2020a, 2020b; O'Shea et al., 2021). The mechanisms underlying COVID-19-related arrhythmia events are complicated. For example, CVDs in these patients can be caused by immune cell tissue invasion associated with pulmonary or cardiogenic myocardial injury (Agricola et al., 2020; Jaffe et al., 2020; Magadum and Kishore, 2020). Recently, clinical research by Lazzerini et al. reported that the QT interval was prolonged in patients with COVID-19, and this electrocardiogram (ECG) abnormality was accompanied by high levels of inflammatory cytokines in serum, suggesting a potential link between systematic inflammation and cardiac arrhythmias (Lazzerini et al., 2020a).

There is increasing experimental evidence supporting the effects of inflammatory cytokines (mainly tumor necrosis factor-α (TNF-α), interleukin-1β (IL-1β), and interleukin-6 (IL-6)) on cardiac ion channels, and this specific type of channelopathy is termed *inflammatory cardiac channelopathy* (Lazzerini et al., 2018, 2019). Existing studies have found that inflammatory cytokines can affect multiple ion channels, including transient outward potassium current (I_{to}) (Kawada et al., 2006; Fernández-Velasco et al., 2007; Grandy and Fiset, 2009; Monnerat et al., 2016), rapid delayed-rectifier potassium channel (I_{Kr}) (Wang et al., 2004; Aromolaran et al., 2018), and L-type calcium current (Hagiwara et al., 2007). There are also studies suggesting the effects of inflammatory cytokines on calcium handling. For example, IL-6 was reported to inhibit the gene expression of sarco/endoplasmic reticulum Ca^{2+}-ATPase (SERCA) (Villegas et al., 2000; Tanaka et al., 2004), and IL-1β was observed to increase sarcoplasmic reticulum (SR) calcium leakage (Monnerat et al., 2016). Although the effects of inflammatory cytokines on individual ion channels have been investigated in these studies, its integral effect on ventricular cellular action potential (AP) and its conduction properties remain unclear. In recent years, emerging cardiac simulations have provided powerful tools for exploring the pathogenesis of cardiovascular diseases (Xie et al., 2004; Arevalo et al., 2016; Zhang et al., 2019, 2020). In our recent work, we constructed a multiscale ventricle model that is able to reproduce both physiological and pathological phenomena on different scales (Bi et al., 2021). Based on this multiscale model, we investigated and evaluated the effects of inflammatory cytokines on ventricular electrophysiology.

The present study aimed to determine the potential impact of systemic inflammation on ventricular electrophysiology. Several simulations were conducted in this work. First, available experimental data regarding the effects of several inflammatory cytokines on multiple cardiac targets were incorporated into rat and human ventricular myocyte models so that the inflammation-induced electrophysiological alterations at the cellular level could be simulated. Next, we constructed a 1-D strand model and quantitatively evaluated the temporal susceptibility of inflammatory tissue to unidirectional conduction blocks. Finally, inflammatory cells were coupled to form a local inflammatory area, which was then incorporated into a ventricular slice model to explore the potential proarrhythmic factors under local inflammatory conditions. As a parallel experiment, we also simulated the electrical activities under global inflammatory conditions by setting all of the cells on the slice as inflammatory cells.

2 METHODS

2.1 Effects of Inflammatory Cytokines

Evidence from several *in vitro* and animal studies indicated that an overactive immune response might lead to a storm of inflammatory cytokines, and some of these inflammatory cytokines directly affect the function of ion channels in cardiomyocytes. In this research, we mainly evaluated the effects of three cytokines (i.e., TNF-α, IL-1β, and IL-6) on cardiomyocytes and their possible proarrhythmic effects. It has been demonstrated that these cytokines can prolong the ventricular action potential duration (APD) by modulating several targets in cardiomyocytes, specifically the transient outward K^+ channel (I_{to}), the rapid delayed-rectifier K^+ current (I_{Kr}), and some targets involved in calcium handling. Focusing on *acute* inflammation, we screened out the experimental data based on the duration of the experimental treatment (less than 48 h), which are listed in **Table 1**, **Table 2**, and **Table 3**.

2.2 Single-Cell Simulations

The rat ventricular cell model by Terkildsen et al. (referred to as the Terk model) (Terkildsen et al., 2008) and the human ventricular cell model by Ten Tusscher et al. (referred to as the TP06 model) (Ten Tusscher et al., 2006) were adopted in this study. Due to the lack of heterogeneity in the Terk model, AP heterogeneities, including transmural heterogeneity and interventricular heterogeneity, were incorporated according to our previous study (Bi et al., 2021) and experimental observations (Clark et al., 1993; Shimoni et al., 1995; Casis et al., 1998; MacDonell et al., 1998; Kaprielian et al., 1999; Ashamalla et al., 2001).

In the single-cell simulation, the rat model was paced with a series of 1000 stimuli with an amplitude of 6 pA/pF and a duration of 5.0 ms (80 pA/PF, 0.5 ms in the TP06 model) to reach the steady-state. To investigate the effects of a single cytokine and the combined influences of multiple cytokines on the cardiomyocytes, we adjusted the conductance of the related channel or ion flux of the related calcium handling process in the cell models according to the

TABLE 1 | The effects of TNF-α on cellular targets.

Targets	Experimental observations				References
	Effects	Time of treatment	Concentration	Type of cell tested	—
I_{to}	Current density: −23.4–65% Inactivation curve: Approximately 5.7 mV shift to the left	48 h	1–5 ng/ml	Ventricular myocyte (rat)	Fernández-Velasco et al. (2007)
I_{Kr}	Current density: −33%	10 h	1 ng/ml	HEK293	Wang et al. (2004)

TABLE 2 | The effects of IL-6 on cellular targets.

Targets	Experimental observations				References
	Effects	Time of treatment	Concentration	Type of cell tested	—
I_{Kr}	Current density: −29.6% Activation curve: 5 mV shift to the left	40 min	20 ng/ml	HEK293	Aromolaran et al. (2018)
I_{CaL}	Current density: +27%	30 min	20 ng/ml	Ventricular myocyte (mice)	Hagiwara et al. (2007)
J_{up}	Expression of SERCA gene: −21%~−50%	48 h	10 ng/ml	Ventricular myocyte (rat)	Villegas et al. (2000)

TABLE 3 | The effects of IL-1β on cellular targets.

Targets	Experimental observations				References
	Effects	Time of treatment	Concentration	Type of cell tested	—
I_{to}	Current density: −36.8%	24 h	60 pg/ml	Ventricular myocyte (rat)	Monnerat et al. (2016)
J_{leak}	SR Ca^{2+} leak: +63.6%	24 h	60 pg/ml	Ventricular myocyte (rat)	Monnerat et al. (2016)

previous experimental recordings (**Table 1**, **Table 2**, **Table 3**). Note that the combined effects of the three cytokines were assumed to be an accumulation of each cytokine. The AP traces, APD_{90}, and current density traces of the different types of cells under various conditions were recorded for later analysis.

In addition, the data used in this study were obtained from bioexperiments in which the preparation concentrations of the cytokines were higher than the clinically measured cytokine levels in patients (Liu and Zhao, 1999; Monnerat et al., 2016; Liu et al., 2021). Therefore, we also considered another 'mild' type of inflammation (referred to as *mild inflammation* in this study) by halving the reported effects of cytokines as shown in **Table 1**, **Table 2**, **Table 3**.

2.3 One-Dimensional (1-D) Simulations Using Transmural Tissue Strand Models

2.3.1 Numerical Details

A 15-mm-long 1-D transmural tissue strand model of humans was constructed using the monodomain equation:

$$\frac{\partial V_m}{\partial t} = \nabla \cdot \mathbf{D} \nabla V_m - \frac{I_{ion}}{C_m} \quad (1)$$

where V_m is the membrane voltage, I_{ion} is the sum of the currents that flow through the membrane, and C_m is the membrane capacitance. The 1-D model was discretized by a spatial resolution of 0.15 mm to form 100 interconnected nodes. The proportions for the transmural cell types were set to 25:35:40 for endocardial (ENDO), middle (MID), and epicardial (EPI) cells to produce a positive going T-wave, in accordance with our previous work (Jiang et al., 2022). The diffusion coefficient D was set to 0.154 mm^2/ms, and the corresponding conduction velocity (CV) was 0.74 m/s through the strand. In addition, there is evidence suggesting that cell-to-cell coupling in tissue is reduced under inflammation (Baum et al., 2012). Therefore, the conduction coefficient in the inflammatory area was set to 0.1 mm^2/ms (CV: 0.6 m/s) to simulate cell coupling under inflammation.

2.3.2 Measurements of the Vulnerable Window

A *vulnerable window* (VW) is a certain time period in which a unidirectional conduction block occurs. A standard S1–S2 protocol was used to measure the VWs across the whole tissue strand. Specifically, a series of supra-threshold stimuli (S1) were applied to the first three cells at the ENDO end with a frequency of 1 Hz. After an interval (Δt), a premature stimulus was applied to a 0.45 mm segment centered on the location currently being measured. Due to the different refractory durations, different Δt would correspond to different results: bidirectional conduction block, unidirectional conduction block, and bidirectional conduction. The width of the VWs across the strand was averaged by the cell number, which acted as a metric for the temporal vulnerability to arrhythmias.

2.4 Two-Dimensional (2-D) Simulations Using Realistic Ventricular Slice Models

2.4.1 Model Geometries and Numerical Details

Two geometries of 2-D realistic ventricular tissue for rats and humans were employed in this study. Preprocessing of geometries, including transmural layer segmentation, was conducted according to our previous work (Bi et al., 2021). The proportions of transmural layers in humans were consistent with the aforementioned transmural settings in the 1-D strand model and were 2:1 for ENDO:EPI in rats.

Similar to the 1-D model, the monodomain equation (**Eq. 1**) was adopted to describe the propagation of excitation waves in the ventricular slice. Isotropic propagation was assumed, and the diffusion coefficient D was set to 0.08 mm^2/ms and 0.154 mm^2/ms in rats and humans, respectively, to produce CVs of 0.42 m/s for rats (Sedmera et al., 2016) and 0.74 m/s for humans (Taggart et al., 2000). It should be noted that there is evidence suggesting that cell-to-cell coupling is reduced by 30–55% in inflammatory tissue (Baum et al., 2012); therefore, the conductivity coefficient was reduced by 35% in the model for inflammation to reflect this reduction. The spatial step was set to 0.1 mm in rats and 0.15 mm in humans to be consistent with the reported cell length (i.e., 80–150 μm (Hinrichs et al., 2011)). To mimic the physiological characteristics of the Purkinje fibers, a series of supra-threshold stimuli were applied to several pacing sites on the endocardium of the slice.

2.4.2 Model Settings for the Inflammatory Conditions

Two inflammatory conditions, namely, local inflammation and global inflammation, were discussed in this study. Specifically, cells that incorporated the effects of the inflammatory cytokines were regarded as 'inflammatory cells'. In the local inflammatory condition, a group of normal cells within a local area on the free wall of the left ventricle were replaced by inflammatory cells (**Supplementary Figure S1**), whereas all cells were set as inflammatory cells under the global inflammatory condition.

2.4.3 Initiation of Reentry Arrhythmias in 2-D Ventricular Slices

A typical S1–S2 protocol (Sutanto et al., 2020; Cluitmans et al., 2021) was used to induce reentry arrhythmias in 2-D slice models. Specifically, under physiological conditions, the premature S2 stimulus was applied to a local region of the epicardium within the VW caused by transmural repolarization heterogeneity. In contrast, due to the presence of pathological heterogeneity in the local inflammatory condition, S2 was applied to the boundary between the normal and inflammatory areas. The above process of applying S2 stimulation may be repeated several times until S2 falls within the VW, thus producing a unidirectional conduction block.

2.4.4 Measurements of the Critical Pacing Cycle Length

The critical pacing cycle length (PCL) was defined as the minimum pacing cycle length for maintaining a normal 1:1 conduction in 2-D ventricular slices. In this study, we tested the critical PCL under control and global inflammatory conditions. For both cases, we gradually decreased the PCL until reaching a critical value under which the tissue failed to maintain a normal 1:1 conduction.

2.4.5 Generation of the Pseudo-ECG

The pseudo-ECG was calculated from the 2-D ventricular slice by the following equation:

$$\phi\left(x', y'\right) = \frac{a^2\sigma_i}{4\sigma_e}\int\left(-\nabla V_m\right)\cdot\left[\nabla\frac{1}{r}\right]d\Omega \tag{2}$$

where V_m is the membrane potential, ϕ is a unipolar potential generated by the tissue, r is the distance between a source point and the virtual electrode, σ_i and σ_e are the extracellular and intracellular conductivities, respectively, and $\int$ is the domain of integration. The models were paced to their steady states at 1 Hz before being used to calculate ECGs.

3 RESULTS

3.1 Effects of Inflammatory Cytokines at the Cellular Level

The individual effect of each inflammatory cytokine and their combined effects (called "inflammation" in this study) on APs (1 Hz) are shown in **Figure 1**. First, for the rat cell model, it can be observed that except for IL-6 causing a negligible influence on EPI AP, all of these cytokines caused obvious AP prolongations in the ENDO/EPI cells. In terms of APD_{90}, both EPI and ENDO cells exhibited a significant increase compared with their control levels, which hinted at the presence of severe pathological repolarization heterogeneity between normal and inflammatory tissue. Next, in the human cell model, the simulation results (**Figure 1B**) showed that the APs in the IL-6 and TNF-α groups were prolonged in all three types of cells, but there was little change in AP in the IL-1β group. Moreover, as **Figure 1Biv** shows, the ΔAPD between MID and ENDO/EPI exhibited an obvious augmentation (from 97 to 150 ms) under inflammatory conditions, leading to a larger transmural repolarization heterogeneity compared with the control level.

In addition to the influences on AP, we also investigated the alteration of calcium handling using the TP06 model, as shown in **Figure 2**. In this regard, the reported reduced systolic $[Ca^{2+}]_i$ (Sugishita et al., 1999) and elevated diastolic $[Ca^{2+}]_i$ (London et al., 2003) under inflammatory conditions were successfully reproduced (**Figure 2B**). This observation might be attributed to the reduced SERCA activity and the increased SR Ca^{2+} leakage, which also caused a decreased SR Ca^{2+} content (**Figure 2C**). Moreover, the greatly decreased peak Ca^{2+} concentration in the cytoplasm exactly reflected the negative inotropic effect (Weisensee et al., 1993; Sugishita et al., 1999; Duncan et al., 2010) under inflammatory conditions.

The above simulation results were based on experimental data using high doses of cytokines. In this study, we also tested a type of *mild* inflammation by downregulating the reported effects in

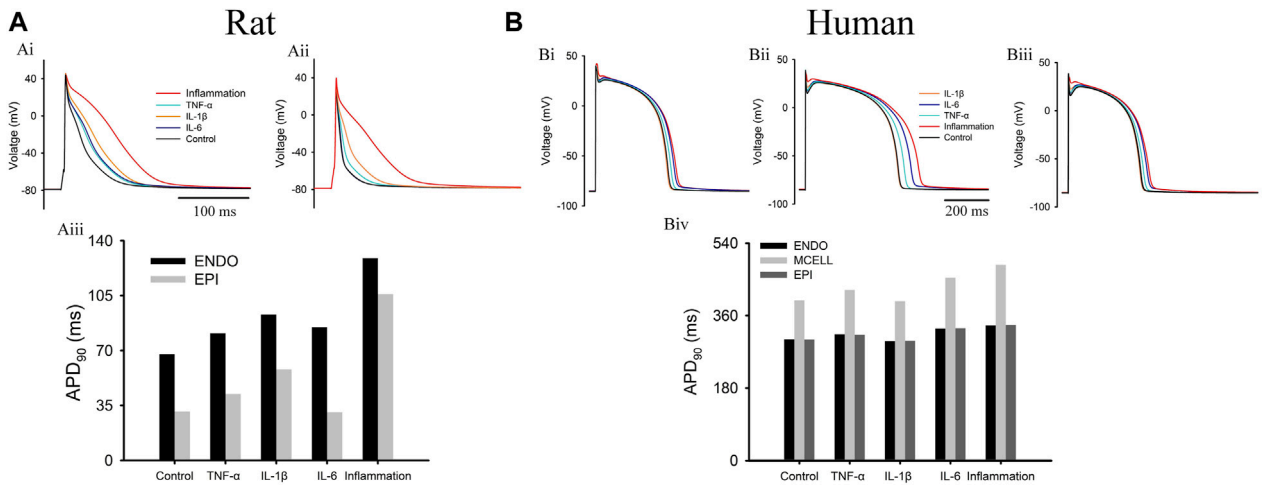

FIGURE 1 | Effects of different inflammatory cytokines on action potentials in **(A)** rat and **(B)** human models. Top panels plot the APs in **(Ai)** rat ENDO **(Aii)** rat EPI, **(Bi)** human ENDO, **(Bii)** human MID, and **(Biii)** human EPI cells. The bottom panels are the APD_{90} of different cells for **(Aiii)** rats and **(Biv)** humans. Note: "inflammation" represents the combined effects of three cytokines.

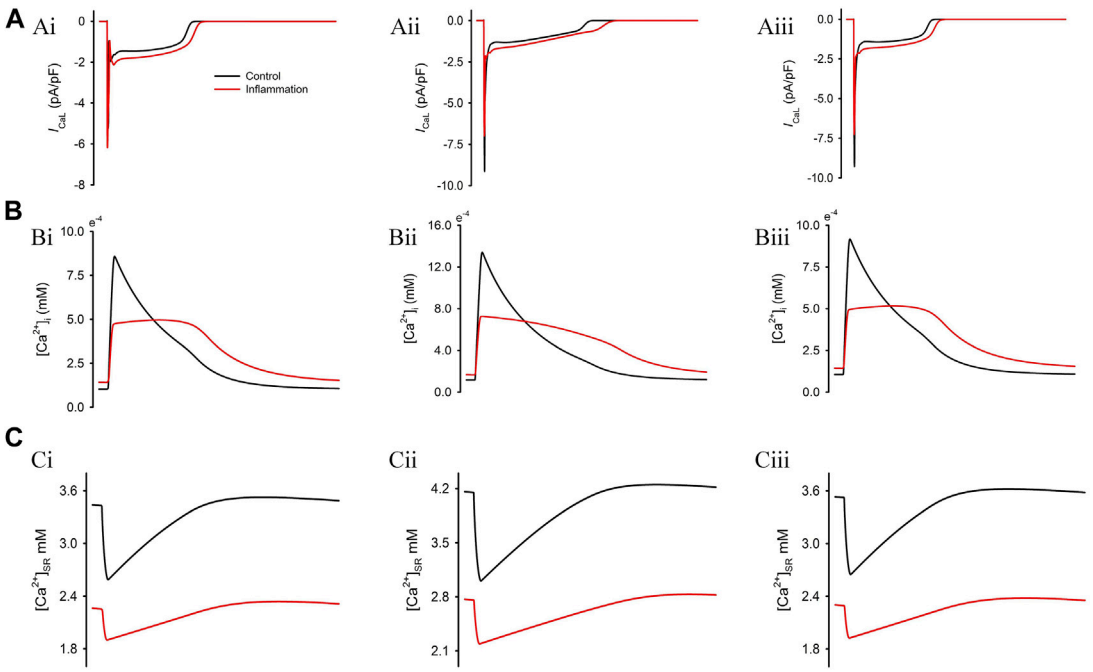

FIGURE 2 | Simulation results of the combined effects of three inflammatory cytokines on calcium handling. Corresponding profiles for I_{CaL} **(A)** and the concentration of Ca^{2+} in the cytosol **(B)** and sarcoplasmic reticulum **(C)**.

the TP06 model. The simulation results are shown in **Figure 3**. We can see that APD varied with the degree of inflammation, and in the case of mild inflammation, the ΔAPD between MID and ENDO/EPI cells showed a slight increase (from 97 to 119 ms) compared with the control group.

The other ionic current traces in the rat and human cell models under different cytokines can be found in **Supplementary Figures S2,S3**.

3.2 Evaluation of the Temporal Vulnerability to Unidirectional Conduction Blocks Under Inflammatory Conditions

Unidirectional conduction blocks are an important pathological phenomenon in 1-D tissue, as the unidirectionally propagated excitation wave can evolve into reentrant spiral/scroll waves in 2-D slices and 3-D organs. The time window within which

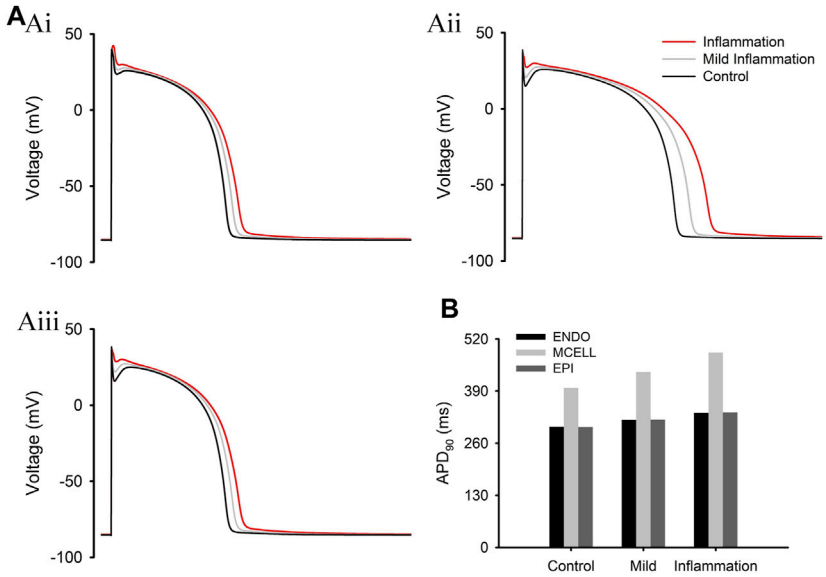

FIGURE 3 | Simulation results under different levels of inflammation. **(A)** APs of ENDO **(Ai)**, MID **(Aii)**, and EPI **(Aiii)** cells at different levels of inflammation. **(B)** APD_{90} of three types of cells under normal and inflammatory conditions.

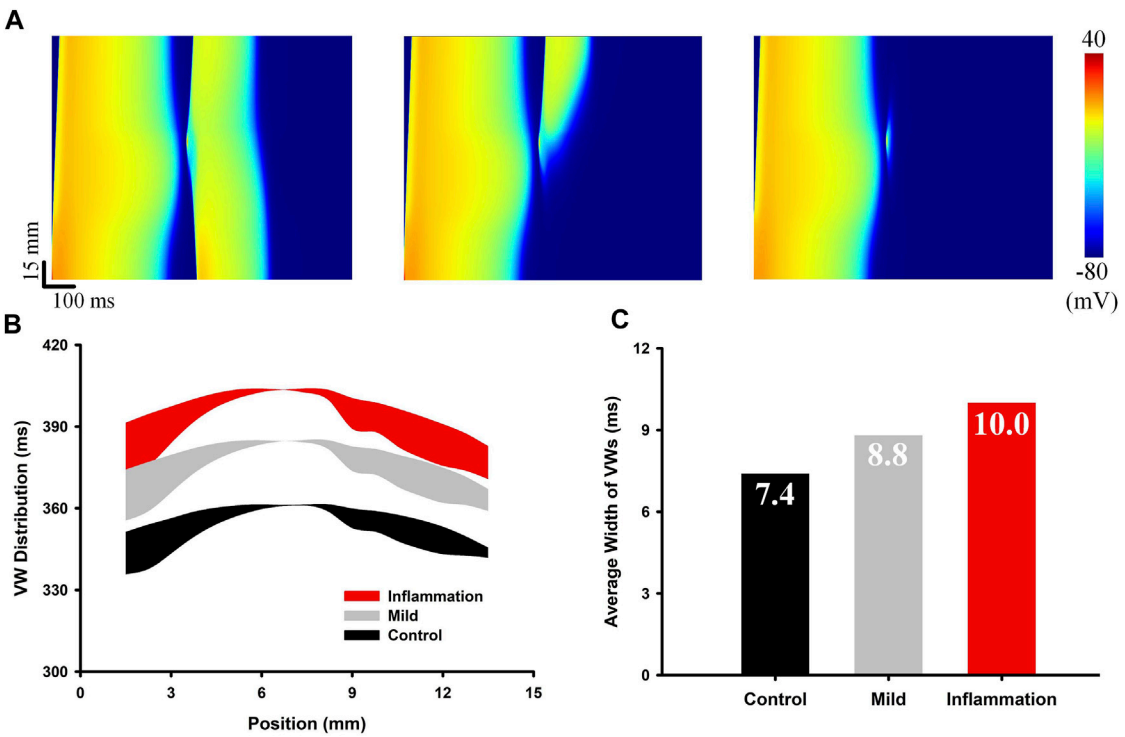

FIGURE 4 | Measurement of the VW in the 1-D strand model under normal, mild inflammatory, and extreme inflammatory conditions. **(A)** The three subplots from left to right show the bidirectional conduction, the unidirectional conduction block, and the bidirectional conduction block. **(B)** Distributions of VWs across the strand. Black and red belts represent the control and inflammatory conditions, respectively. **(C)** Comparison of the average width of the VWs in the three groups.

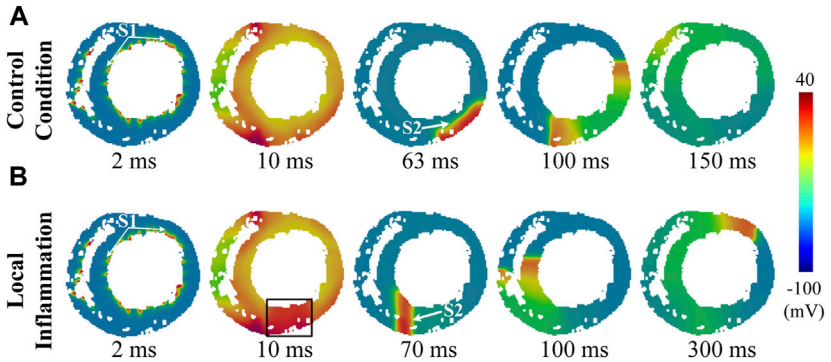

FIGURE 5 | Induced reentry arrhythmias in rat ventricular slices under conditions of **(A)** control and **(B)** local inflammation. The S1 and S2 stimuli are marked by white arrows, while the inflammatory region is indicated by a black rectangle.

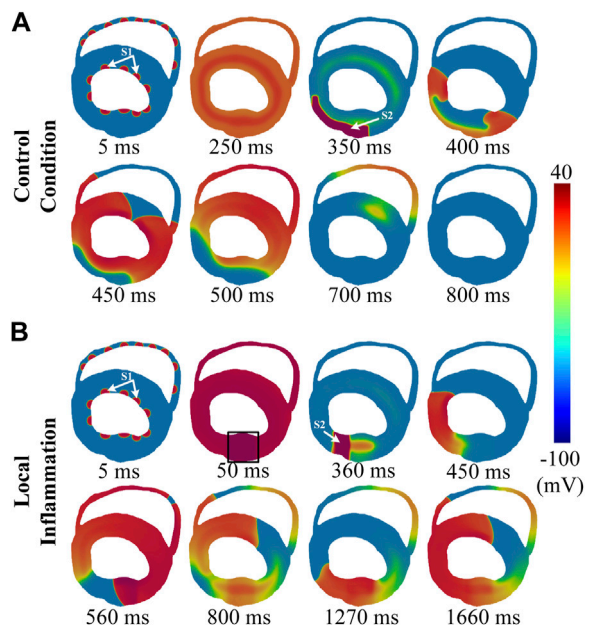

FIGURE 6 | Induced reentry arrhythmias in rat ventricular slices under conditions of **(A)** control and **(B)** local inflammation. The S1 and S2 stimuli are marked by white arrows, while the inflammatory region is indicated by a black rectangle.

unidirectional conduction blocks occur, termed the *vulnerable window*, is a commonly used metric for measuring the temporal susceptibility of tissue to arrhythmias. In this section, we quantified the influence of inflammation on temporal vulnerability by measuring the VW across the 1-D transmural strand. Different degrees of inflammation, i.e., an extreme level of inflammation (e.g., sepsis) and a mild level of inflammation, were evaluated individually. The simulation results are shown in **Figure 4**. Specifically, **Figure 4A** shows different responses to the premature S2 stimulus, including bidirectional conduction (S2 too early), unidirectional conduction block (VW), and bidirectional conduction block (S2 too late). The distribution of the time window when unidirectional conduction blocks occurred (i.e., the distribution of VW) is plotted in **Figure 4B**. Both mild inflammation and inflammation delayed the occurrence of VW, and the average width of the VWs increased gradually from 7.4 to 8.8 and 10.0 ms depending on the degree of inflammation. As a wider VW signifies a higher chance of a unidirectional conduction block, the above simulation results implied an increased temporal susceptibility to reentry arrhythmias under inflammatory conditions.

3.3 Evaluation of the Proarrhythmic Effects of Pathological Heterogeneity Under Local Inflammatory Conditions

Inflammation may initially occur in a specific area in the heart. This type of inflammation, termed *local inflammation* in this study, may result in the presence of pathological heterogeneity in ventricular tissue due to the prolonged APD of the affected cells, which predisposes to ventricular arrhythmias. In this section, we mimicked this condition by setting a local region of inflammation on the free wall of the left ventricle, and a typical S1-S2 protocol was used to evaluate the inducibility of reentry arrhythmias in this condition (see *Methods* for more details). The simulation results are shown in **Figure 5** (rat) and **Figure 6** (human).

First, for the control condition (**Supplementary Video S1**), it can be observed that, due to the limited size of rat hearts, the evoked unidirectional conduction was not able to turn back to form a functional reentry, and the subsequent two waves propagating along the ventricular wall collided and failed to form anatomical reentry (snapshots in **Figure 5A**). The whole process lasted only approximately 90 ms. For the human ventricular slice (**Supplementary Video S2**), although the evoked unidirectional conduction could turn back to form a functional reentry, such a process was unsustainable, and the spiral waves terminated shortly after the first cycle with a brief lifetime of approximately 350 ms (snapshots in **Figure 6A**).

Simulation results of local inflammatory conditions are shown in **Figure 5B** (rat) and **Figure 6B** (human). Due to the

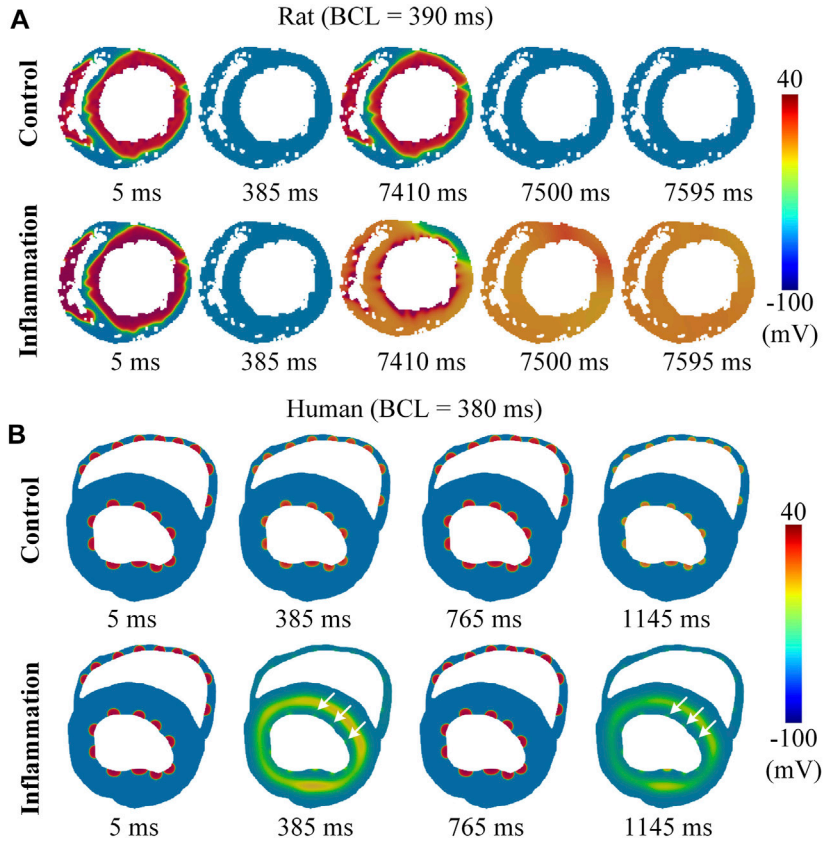

FIGURE 7 | The performance of the model at high frequency. Conduction waves under physiological and inflammatory conditions at high frequency **(A)** for rats and **(B)** for humans. The white arrow represents stimulus S1, which failed to pace.

asynchronous repolarization caused by the prolonged APD of inflammatory cells, extra S2 stimulation applied to the border area would encounter the refractory tail on the inflammatory side. Therefore, S2 would generate a unidirectional conduction block, which in turn would evolve gradually into an anatomical spiral wave circling around the ventricular ring structure (**Supplementary Video S3,S4**). In brief, the pathological heterogeneity caused by inflammatory cytokines provided extra substrates for unidirectional conduction block and reentry arrhythmias.

3.4 Evaluation of the Adaptability of Tissue to High Stimulating Frequencies Under Global Inflammatory Conditions

Another type of inflammatory condition, as opposed to local inflammation, is *global inflammation*. It reflects a globally affected condition in which the whole ventricle is influenced by inflammatory cytokines. Compared to its counterpart, global inflammation does not create additional pathological heterogeneity; however, the prolonged wavelength may impair the tissue's adaptability to fast heart rates. In this study, we mimicked the global inflammatory condition by setting all cells as inflammatory cells and tested the influences of global inflammation on the critical PCL using rat and human ventricular models (see *Methods* for more details). In the rat model, the measured critical PCL was 101 ms (9.9 Hz) in control conditions, while in global inflammation, it increased to 390 ms (2.56 Hz), and stimuli with cycle lengths below 390 ms led to complete repolarization failure (see **Figure 7A** or **Supplementary Video S5**). The critical PCL of 390 ms corresponds to a heart rate of 154 bpm, which is significantly lower than the physiological range of approximately 300–500 bpm in rats. Such simulation results showed a decreased adaptability of tissue to fast heart rates under global inflammation conditions and suggested a strong proarrhythmic effect. However, considering that the heart rate of rats is much faster than that of humans, this result might be species dependent. In addition, the atypical phenomenon of complete repolarization failure might also depend on the specific model (**Supplementary Figure S6**). To further clarify these questions, we performed parallel simulations using human tissue models. The simulation results showed that complete repolarization failure did not occur even at very high frequencies; however, there was still a critical PCL below which the 1:1 conduction could not be maintained and was replaced by 2:1 conduction (see **Figure 7B** or **Supplementary Video S6**). In this setting, the critical PCL was increased from

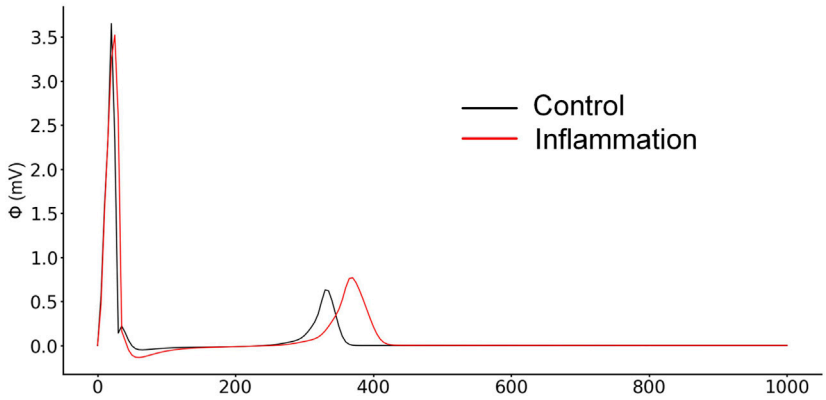

FIGURE 8 | Comparison of pseudo-ECGs between normal and inflammatory conditions.

319 ms in the control condition to 380 ms in the global inflammatory condition. Notably, the BCL of 380 ms, which corresponds to a heart rate of approximately 157 bpm, was physiologically relevant and therefore might lead to arrhythmogenesis.

3.5 Pseudo-ECGs in 2-D Simulation

The generated pseudo-ECG of the human ventricular 2-D slice model under physiological and inflammatory conditions is shown in **Figure 8**. As some available studies concerning systemic inflammation have reported (Adlan et al., 2015; Lazzerini et al., 2020a; Armbruster et al., 2022), prolonged QT intervals were also reproduced in our simulation results.

4 DISCUSSION

4.1 Main Findings

In recent years, accumulating evidence has shown an association between systemic inflammation and cardiovascular disease. Inflammatory cytokines, a type of signaling molecule secreted from immune cells, were proven to be able to affect membrane ion channels and might therefore lead to ventricular arrhythmias. In this study, we selected three of these major cytokines and evaluated their proarrhythmic effects using a multiscale virtual heart. The main findings are as follows: 1) at the cellular level, inflammatory cytokines caused a prolongation of APD by affecting multiple ion channels, and heterogeneously prolonged APDs led to augmented transmural heterogeneities; 2) simulation results of the VW using the 1-D strand suggested that inflammation increased the temporal vulnerability to arrhythmias; 3) in the case of local inflammation, the repolarization of the inflammatory area was delayed due to the cytokine-induced APD prolongation, leading to the presence of pathological heterogeneities around the local inflammatory area. Such regional differences in repolarization provided extra substrates for the unidirectional conduction block and increased the chance of the development of anatomical reentry arrhythmias; 4) In the global inflammatory condition, the generated pseudo-ECG exhibited a prolonged QT interval that was in accordance with the clinical observations. Furthermore, the globally prolonged APD impaired the tissue adaptability to high frequencies and caused 2:1 conduction at physiologically relevant heart rates.

APD prolongation has been observed in many pathological conditions and has been shown to be proarrhythmic (Antoniou et al., 2017; Dietrichs et al., 2019; Shimaoka et al., 2020). For example, APD prolongation and changes in electrophysiological characteristics caused by the downregulation of outward potassium currents, alterations of calcium channel kinetics and increases in late sodium currents create a substrate for ventricular arrhythmias in the case of heart failure (Zhang et al., 2018). A study on hypokalemia showed that APD prolongation could predispose patients to early afterdepolarizations, which in turn act as triggers for ventricular arrhythmias (Tse et al., 2021). APD prolongation is also the main factor responsible for the proarrhythmic influences of drugs with cardiotoxicity. A prolonged APD and, consequently, a prolonged QT interval, are considered important biomarkers of drug cardiotoxicity in drug discovery (Schrickel et al., 2006; Hondeghem et al., 2011). For example, the antihistamine drug terfenadine, which was previously used for the treatment of allergic conditions, was proven to be able to prolong APD due to its effects of blocking hERG currents (I_{Kr}), causing QT prolongation and torsade de pointes (TdP). Despite the tight association between APD/QT prolongation and ventricular arrhythmia, prolonged QT does not always lead to arrhythmogenesis events. Some new evaluation criteria, such as TRIaD (Triangulation, Reverse use dependence, Instability and Dispersion), have been suggested to identify false-positive cases. On the other hand, it should also be noted here that APD prolongation can also exert antiarrhythmic effects by extending the effective refractory period, which is also the major pharmaceutical mechanism of class III antiarrhythmic drugs. In particular, homogeneous APD prolongation in the absence of early afterdepolarizations (EADs) commonly exerts antiarrhythmic effects, whereas EADs or repolarization

heterogeneities induced by inhibition of repolarization are proarrhythmic. For the case in this study, the simulation results demonstrated a double-sided nature, especially in a condition of global inflammation: the prolonged refractory period in ventricles tends to be antiarrhythmic, but it also reduces the adaptability of the tissue to high heart rates. For the local inflammatory condition, although we did not observe EADs, the presence of both pathological heterogeneities and augmented transmural heterogeneity increased the vulnerability to arrhythmogenesis in terms of both spatial and temporal aspects.

Accumulating studies have demonstrated that augmented electrophysiological heterogeneity provides proarrhythmic substrates (Laurita and Rosenbaum, 2000; Pak et al., 2004; Antzelevitch, 2007; Boukens et al., 2009). Intrinsic heterogeneity within normal hearts contributes to the development of arrhythmias under certain conditions (Bishop et al., 2013). Premature beats in the heterogeneous area that occurred during a certain time duration (i.e., VW) would lead to unidirectional conduction block and reentry arrhythmias. In most cases, the VW is rather small; however, it can be significantly enlarged in some pathological conditions due to augmented regional heterogeneity, such as ischemia (De Bakker et al., 1988; Yuuki et al., 2004) and heart failure (Roden, 2003; Coronel et al., 2013). For the local inflammatory condition, our simulation results suggested that the repolarization of the tissue developing inflammation was significantly delayed, which in turn contributed to an apparent electrical heterogeneity around the local area. Such regional dispersion of repolarization, as an arrhythmogenic substrate, will be further amplified in higher but physiologically relevant pacing frequencies and eventually lead to arrhythmia. Regarding interspecies differences, the simulation results suggested that inflammation weakened the repolarization ability of both rat and human myocytes, but there were obvious interspecies variances behind it, as repolarization is notably different in rodents compared to large mammals. In particular, the cytokine-induced APD prolongation in rat myocytes was mainly attributed to the decreased I_{to}; in contrast, the APD prolongation in human ventricular cells resulted mainly from the reduced I_{Kr}. It has been demonstrated that I_{to} is the major repolarization current in rat myocytes (Zhao et al., 2012), but for humans, I_{to} is only one of various repolarizing currents and is mainly involved in repolarizing phase 1 of cardiac AP. In comparison, hERG (the gene that codes for the alpha subunit of I_{Kr}) is abundantly expressed in human ventricles, and I_{Kr} plays a critical role in repolarizing during cardiac AP (Ledford et al., 2022; Cheng and Kodama, 2004). This interspecies variation has also been widely observed in other studies. For instance, when used to treat carbon monoxide (CO)-induced arrhythmias, ranolazine was shown to be effective in inhibiting CO-induced EAD in rat cells (Dallas et al., 2012), but it exacerbated EADs and even caused oscillation in guinea pigs (which have wide APs similar to those in humans). In a recent study (Morotti et al., 2021), Morotti et al. examined the influences of interspecies differences on animal experimentation and drug efficacy assessment, and they created cross-species translators of electrophysiological responses to translate the drug-induced effects experimentally observed in myocytes from animal models to predict the effects that these perturbations would cause in humans. In summary, although our simulations demonstrated that inflammation caused similar reentry arrhythmias in rats and humans, the underlying mechanisms were different among various species and this needs to be taken into account, especially when translating experimental findings regarding drug efficacy and safety from animal models to clinical use.

4.2 Limitations

It should be noted that the combined effect of three cytokines was assumed to be an additive effect of each cytokine in the present work. Kumar et al. (Kumar et al., 1996) reported a synergistic inhibitory effect of TNF-α and IL-1β on ventricular contractility, where the concentration of each cytokine under conditions of a combination was much lower than those acting alone. Such synergistic effects and the potential antagonistic effects among cytokines were not considered in this study.

Although the present study followed the experimental setup in the original reports exactly, the concentrations of inflammatory cytokines used in previous experiments were generally higher than those observed under pathophysiological conditions. Specifically, Liu et al. reported a median IL-6 serum level of 4809 pg/ml in a nonsurvivor group of patients with sepsis (Liu et al., 2021). Liu et al. reported that the pathophysiological level of TNF-alpha was approximately 0.15 ng/ml in the serum of heart failure patients (Liu and Zhao, 1999). Monnerat et al. reported a serum IL-1β level of 60 pg/ml in diabetic mice (Monnerat et al., 2016). Therefore, our simulation results reflected an extreme condition of inflammation (i.e., sepsis). To account for this, we have considered another 'mild' inflammatory condition by halving the concentrations of the inflammatory cytokines; however, caution should still be taken when translating these findings to clinical use.

The effects of inflammatory cytokines on ion channels were assumed to be consistent by setting specific constant change ratios to the conductance of the involved ion channels. However, inflammation is a dynamic process with complicated mechanisms. For example, there have been studies showing that inflammatory cytokines could increase sympathetic activity to inhibit cytokine production; however, it also deserves to be noted that hyperactive sympathetic nerves could directly influence the function of ion channels by phosphorylation in myocardial cells and may induce arrhythmias (Lazzerini et al., 2017). The above dynamic process, as a kind of negative feedback mechanism, could change the concentrations of inflammatory cytokines in serum, which was not incorporated in our simulations. In addition, inflammatory cytokines could also affect the electrophysiological function via complicated indirect pathways in addition to the introduced direct modulations of ion channels and calcium handling. These indirect pathways include, but are not limited to, the following two aspects: 1) inflammatory cytokines could cause chronic remodeling and myocardial

fibrosis, thus increasing the susceptibility of cardiac tissue to arrhythmias in chronic heart failure patients (Dick and Epelman, 2016); 2) current evidence suggests that TNF-α may promote the formation of atherosclerotic plaques by upregulating the expression of multiple protein molecules (e.g., adhesion molecule-1) in the vascular wall (Ohta et al., 2005), which would exacerbate the ischemic condition of hearts and lead to ischemic-related arrhythmias. As we mentioned above, inflammation has complex mechanisms and effects that require further simulation studies. Above all, these indirect pathways play critical roles in inflammation-mediated arrhythmias but they were not investigated in this study.

Limited to the sources of the experimental data, the proarrhythmic mechanisms investigated in this study focused mainly on ventricular arrhythmia. In fact, accumulating evidence has shown that there is a strong link between inflammation and postoperative atrial fibrillation. Maesen et al. reported an overlapping time course of atrial fibrillation occurrence after cardiac surgery and the activation of the complement system with the release of proinflammatory cytokines, suggesting potential roles of inflammation in triggering postoperative atrial fibrillation (POAF) (Maesen et al., 2012). Heijman et al. observed that postoperative inflammation along with preexisting Ca^{2+}-handling abnormalities contributed to the formation of DADs and thus led to POAF (Heijman et al., 2020). The above postoperative atrial fibrillation, as a widely accepted form of inflammation-induced arrhythmia, warrants further research.

5 CONCLUSION

In this study, we conducted an in silico investigation using a multiscale virtual heart to explore the proarrhythmic mechanisms of inflammation. Inflammatory cytokines directly affect the function of ion channels and thus cause prolongation of AP and augmentation of transmural dispersion. The augmentation of the transmural dispersion would increase the vulnerability to arrhythmia (e.g., the greater VWs). In addition, the prolongation of AP contributes to significant pathological heterogeneity and provides extra substrates for inducing arrhythmia under conditions of local inflammation. In the case of global inflammation, the QT interval and the minimum PCL for normal 1:1 conduction are both enhanced, indicating a greater proarrhythmic effect. In summary, the present study provides new insights into the underlying mechanisms of the systemic inflammatory response to arrhythmia.

DATA AVAILABILITY STATEMENT

The original contributions presented in the study are included in the article/**Supplementary Material**, further inquiries can be directed to the corresponding author.

AUTHOR CONTRIBUTIONS

Conceptualization, SZ; Methodology, XB and HJ; Software, XB, SZ, WM, and WL; Validation, XB, SZ, YL, and FY; Formal analysis, XB, SZ, and WM; Investigation, XB and SZ; Resources, WL, and ZW; Data curation, XB, HJ, and WM; Writing-original draft, XB; Writing-Review and editing, SZ and ZW; Visualization, YL, FY, and WL; Supervision, SZ and ZW; Project administration, ZW; Funding acquisition, SZ and ZW. All authors have read and agreed to the published version of the manuscript.

FUNDING

This work was supported by the Natural Science Foundation of Shandong Province (NO. ZR2021MF011) and the Shandong Provincial Postdoctoral Program for Innovative Talents (grantee SZ).

SUPPLEMENTARY MATERIAL

The Supplementary Material for this article can be found online at: https://www.frontiersin.org/articles/10.3389/fphys.2022.843292/full#supplementary-material

REFERENCES

Adlan, A. M., Panoulas, V. F., Smith, J. P., Fisher, J. P., and Kitas, G. D. (2015). Association between Corrected QT Interval and Inflammatory Cytokines in Rheumatoid Arthritis. *J. Rheumatol.* 42, 421–428. doi:10.3899/jrheum.140861

Agricola, E., Beneduce, A., Esposito, A., Ingallina, G., Palumbo, D., Palmisano, A., et al. (2020). Heart and Lung Multimodality Imaging in COVID-19. *JACC Cardiovasc. Imaging* 13, 1792–1808. doi:10.1016/j.jcmg.2020.05.017

Antoniou, C.-K., Dilaveris, P., Manolakou, P., Galanakos, S., Galanakos, N., Gatzoulis, K., et al. (2017). QT Prolongation and Malignant Arrhythmia: How Serious a Problem? *Eur. Cardiol. Rev.* 1216, 112–120. doi:10.15420/ecr10.15420/ecr.2017:16:1

Antzelevitch, C. (2007). Heterogeneity and Cardiac Arrhythmias: An Overview. *Heart rhythm.* 4, 964–972. doi:10.1016/j.hrthm.2007.03.036

Arevalo, H. J., Vadakkumpadan, F., Guallar, E., Jebb, A., Malamas, P., Wu, K. C., et al. (2016). Arrhythmia Risk Stratification of Patients after Myocardial Infarction Using Personalized Heart Models. *Nat. Commun.* 7, 11437–11438. doi:10.1038/ncomms11437

Armbruster, A. L., Campbell, K. B., Kahanda, M. G., and Cuculich, P. S. (2022). The Role of Inflammation in the Pathogenesis and Treatment of Arrhythmias. *Pharmacotherapy* 42, 250–262. doi:10.1002/phar.2663

Aromolaran, A. S., Srivastava, U., Alí, A., Chahine, M., Lazaro, D., El-Sherif, N., et al. (2018). Interleukin-6 Inhibition of hERG Underlies Risk for Acquired Long QT in Cardiac and Systemic Inflammation. *PLoS One* 13, e0208321. doi:10.1371/journal.pone.0208321

Ashamalla, S. M., Navarro, D., and Ward, C. A. (2001). Gradient of Sodium Current across the Left Ventricular Wall of Adult Rat Hearts. *J. Physiology* 536, 439–443. doi:10.1111/j.1469-7793.2001.0439c.xd

Baum, J. R., Dolmatova, E., Tan, A., and Duffy, H. S. (2012). Omega 3 Fatty Acid Inhibition of Inflammatory Cytokine-Mediated Connexin43 Regulation in the Heart. *Front. Physio.* 3 (JUL), 272. doi:10.3389/fphys.2012.00272

Bi, X., Zhang, S., Jiang, H., and Wei, Z. (2021). A Multi-Scale Computational Model for the Rat Ventricle: Construction, Parallelization, and Applications. *Comput. Methods Programs Biomed.* 208, 106289. doi:10.1016/j.cmpb.2021.106289

Bishop, M. J., Vigmond, E. J., and Plank, G. (2013). The Functional Role of Electrophysiological Heterogeneity in the Rabbit Ventricle during Rapid Pacing and Arrhythmias. *Am. J. Physiology-Heart Circulatory Physiology* 304, H1240–H1252. doi:10.1152/ajpheart.00894.2012

Boukens, B. J. D., Christoffels, V. M., Coronel, R., and Moorman, A. F. M. (2009). Developmental Basis for Electrophysiological Heterogeneity in the Ventricular and Outflow Tract Myocardium as a Substrate for Life-Threatening Ventricular Arrhythmias. *Circulation Res.* 104, 19–31. doi:10.1161/CIRCRESAHA.108.188698

Casis, O., Iriarte, M., Gallego, M., and Sánchez-Chapula, J. A. (1998). Differences in Regional Distribution of K+ Current Densities in Rat Ventricle. *Life Sci.* 63, 391–400. doi:10.1016/s0024-3205(98)00287-2

Chen, L., Deng, H., Cui, H., Fang, J., Zuo, Z., Deng, J., et al. (2018). Inflammatory Responses and Inflammation-Associated Diseases in Organs. *Oncotarget* 9, 7204–7218. doi:10.18632/oncotarget.23208

Cheng, J. H., and Kodama, I. (2004). Two Components of Delayed Rectifier K+ Current in Heart: Molecular Basis, Functional Diversity, and Contribution to Repolarization. *Acta Pharmacol. Sin.* 25, 137

Clark, R. B., Bouchard, R. A., Salinas-Stefanon, E., Sanchez-Chapula, J., and Giles, W. R. (1993). Heterogeneity of Action Potential Waveforms and Potassium Currents in Rat Ventricle. *Cardiovasc. Res.* 27, 1795–1799. doi:10.1093/cvr/27.10.1795

Cluitmans, M. J. M., Bear, L. R., Nguyên, U. C., van Rees, B., Stoks, J., ter Bekke, R. M. A., et al. (2021). Noninvasive Detection of Spatiotemporal Activation-Repolarization Interactions that Prime Idiopathic Ventricular Fibrillation. *Sci. Transl. Med.* 13, 9317. doi:10.1126/scitranslmed.abi9317

Coronel, R., Wilders, R., Verkerk, A. O., Wiegerinck, R. F., Benoist, D., and Bernus, O. (2013). Electrophysiological Changes in Heart Failure and Their Implications for Arrhythmogenesis. *Biochimica Biophysica Acta (BBA) - Mol. Basis Dis.* 1832, 2432–2441. doi:10.1016/j.bbadis.2013.04.002

Dallas, M. L., Yang, Z., Boyle, J. P., Boycott, H. E., Scragg, J. L., Milligan, C. J., et al. (2012). Carbon Monoxide Induces Cardiac Arrhythmia via Induction of the Late Na^+Current. *Am. J. Respir. Crit. Care Med.* 186, 648–656. doi:10.1164/rccm.201204-0688OC

De Bakker, J. M., Van Capelle, F. J., Janse, M. J., Wilde, A. A., Coronel, R., Becker, A. E., et al. (1988). Reentry as a Cause of Ventricular Tachycardia in Patients with Chronic Ischemic Heart Disease: Electrophysiologic and Anatomic Correlation. *Circulation* 77, 589–606. doi:10.1161/01.CIR.77.3.589

Dick, S. A., and Epelman, S. (2016). Chronic Heart Failure and Inflammation: What Do We Really Know? *Circ. Res.* 119, 159–176. doi:10.1161/CIRCRESAHA.116.308030

Dietrichs, E. S., Tveita, T., and Smith, G. (2019). Hypothermia and Cardiac Electrophysiology: A Systematic Review of Clinical and Experimental Data. *Cardiovasc. Res.* 115, 501–509. doi:10.1093/cvr/cvy305

Duncan, D. J., Yang, Z., Hopkins, P. M., Steele, D. S., and Harrison, S. M. (2010). TNF-α and IL-1β Increase $Ca2^+$ Leak from the Sarcoplasmic Reticulum and Susceptibility to Arrhythmia in Rat Ventricular Myocytes. *Cell Calcium* 47, 378–386. doi:10.1016/j.ceca.2010.02.002

Fernández-Velasco, M., Ruiz-Hurtado, G., Hurtado, O., Moro, M. Á., and Delgado, C. (2007). TNF-α Downregulates Transient Outward Potassium Current in Rat Ventricular Myocytes through iNOS Overexpression and Oxidant Species Generation. *Am. J. Physiology-Heart Circulatory Physiology* 293, H238–H245. doi:10.1152/ajpheart.01122.2006

Grandy, S. A., and Fiset, C. (2009). Ventricular K+ Currents Are Reduced in Mice with Elevated Levels of Serum TNFα. *J. Mol. Cell. Cardiol.* 47, 238–246. doi:10.1016/j.yjmcc.2009.02.025

Hagiwara, Y., Miyoshi, S., Fukuda, K., Nishiyama, N., Ikegami, Y., Tanimoto, K., et al. (2007). SHP2-mediated Signaling Cascade through Gp130 Is Essential for LIF-dependent ICaL, [Ca2+]i Transient, and APD Increase in Cardiomyocytes. *J. Mol. Cell. Cardiol.* 43, 710–716. doi:10.1016/j.yjmcc.2007.09.004

Heijman, J., Muna, A. P., Veleva, T., Molina, C. E., Sutanto, H., Tekook, M., et al. (2020). Atrial Myocyte NLRP3/CaMKII Nexus Forms a Substrate for Postoperative Atrial Fibrillation. *Circ. Res.* 127, 1036–1055. doi:10.1161/CIRCRESAHA.120.316710

Hinrichs, S., Heger, J., Schreckenberg, R., Wenzel, S., Euler, G., Arens, C., et al. (2011). Controlling Cardiomyocyte Length: : the Role of Renin and PPAR-{gamma}. *Cardiovasc. Res.* 89, 344–352. doi:10.1093/cvr/cvq313

Hondeghem, L. M., Dujardin, K., Hoffmann, P., Dumotier, B., and De Clerck, F. (2011). Drug-induced QTC Prolongation Dangerously Underestimates Proarrhythmic Potential: Lessons from Terfenadine. *J. Cardiovasc. Pharmacol.* 57, 589–597. doi:10.1097/FJC.0b013e3182135e91

Jaffe, A. S., Cleland, J. G. F., and Katus, H. A. (2020). Myocardial Injury in Severe COVID-19 Infection. *Eur. Heart J.* 41, 2080–2082. doi:10.1093/eurheartj/ehaa447

Jiang, H., Zhang, S., Bi, X., Ma, W., and Wei, Z. (2022). Proarrhythmic Effects of Carbon Monoxide in Human Ventricular Tissue: Insights from Computational Modeling. *Comput. Biol. Med.* 140, 105066. doi:10.1016/j.compbiomed.2021.105066

Kaprielian, R., Wickenden, A. D., Kassiri, Z., Parker, T. G., Liu, P. P., and Backx, P. H. (1999). Relationship between K + Channel Down-Regulation and $[Ca\ 2^+]$ I in Rat Ventricular Myocytes Following Myocardial Infarction. *J. Physiology* 517, 229–245. doi:10.1111/j.1469-7793.1999.0229z.x

Kaptoge, S., Pennells, L., De Bacquer, D., Cooney, M. T., Kavousi, M., Stevens, G., et al. (2019). World Health Organization Cardiovascular Disease Risk Charts: Revised Models to Estimate Risk in 21 Global Regions. *Lancet Glob. Health* 7, e1332–e1345. doi:10.1016/s2214-109x(19)30318-3

Kawada, H., Niwano, S., Niwano, H., Yumoto, Y., Wakisaka, Y., Yuge, M., et al. (2006). Tumor Necrosis Factor-.ALPHA. Downregulates the Voltage Gated Outward K+ Current in Cultured Neonatal Rat Cardiomyocytes A Possible Cause of Electrical Remodeling in Diseased Hearts. *Circ. J.* 70, 605–609. doi:10.1253/circj.70.605

Kumar, A., Thota, V., Dee, L., Olson, J., Uretz, E., and Parrillo, J. E. (1996). Tumor Necrosis Factor Alpha and Interleukin 1beta Are Responsible for *In Vitro* Myocardial Cell Depression Induced by Human Septic Shock Serum. *J. Exp. Med.* 183, 949–958. doi:10.1084/jem.183.3.949

Laurita, K. R., and Rosenbaum, D. S. (2000). Interdependence of Modulated Dispersion and Tissue Structure in the Mechanism of Unidirectional Block. *Circulation Res.* 87, 922–928. doi:10.1161/01.RES.87.10.922

Lazzerini, P. E., Capecchi, P. L., El-Sherif, N., Laghi-Pasini, F., and Boutjdir, M. (2018). Emerging Arrhythmic Risk of Autoimmune and Inflammatory Cardiac Channelopathies. *J. Am. Heart Assoc.* 7, e010595. doi:10.1161/JAHA.118.010595

Lazzerini, P. E., Acampa, M., Laghi-Pasini, F., Bertolozzi, I., Finizola, F., Vanni, F., et al. (2020a). Cardiac Arrest Risk during Acute Infections: Systemic Inflammation Directly Prolongs QTc Interval via Cytokine-Mediated Effects on Potassium Channel Expression. *Circ Arrhythmia Electrophysiol.* 13, e008627. doi:10.1161/CIRCEP.120.008627

Lazzerini, P. E., Boutjdir, M., and Capecchi, P. L. (2020b). COVID-19, Arrhythmic Risk, and Inflammation: Mind the Gap! *Circulation* 142, 7–9. doi:10.1161/CIRCULATIONAHA.120.047293

Lazzerini, P. E., Capecchi, P. L., and Laghi-Pasini, F. (2017). Systemic Inflammation and Arrhythmic Risk: Lessons from Rheumatoid Arthritis. *Eur. Heart J.* 38, ehw208–1727. doi:10.1093/eurheartj/ehw208

Lazzerini, P. E., Laghi-Pasini, F., Boutjdir, M., and Capecchi, P. L. (2019). Cardioimmunology of Arrhythmias: the Role of Autoimmune and Inflammatory Cardiac Channelopathies. *Nat. Rev. Immunol.* 19, 63–64. doi:10.1038/s41577-018-0098-z

Ledford, H. A., Ren, L., Thai, P. N., Park, S., Timofeyev, V., Sirish, P., et al. (2022). Disruption of Protein Quality Control of the Human Ether-À-Go-Go Related Gene K+ Channel Results in Profound Long QT Syndrome. *Heart rhythm.* 19, 281–292. doi:10.1016/j.hrthm.2021.10.005

Liu, J., Bai, C., Li, B., Shan, A., Shi, F., Yao, C., et al. (2021). Mortality Prediction Using a Novel Combination of Biomarkers in the First Day of Sepsis in Intensive Care Units. *Sci. Rep.* 11, 79843. doi:10.1038/s41598-020-79843-5

Liu, L., and Zhao, S.-P. (1999). The Changes of Circulating Tumor Necrosis Factor Levels in Patients with Congestive Heart Failure Influenced by Therapy. *Int. J. Cardiol.* 69, 77–82. doi:10.1016/S0167-5273(99)00008-X

London, B., Baker, L. C., Lee, J. S., Shusterman, V., Choi, B.-R., Kubota, T., et al. (2003). Calcium-dependent Arrhythmias in Transgenic Mice with Heart Failure. *Am. J. Physiology-Heart Circulatory Physiology* 284, H431–H441. doi:10.1152/ajpheart.00431.2002

MacDonell, K. L., Severson, D. L., and Giles, W. R. (1998). Depression of Excitability by Sphingosine 1-phosphate in Rat Ventricular Myocytes. *Am. J. Physiology-Heart Circulatory Physiology* 275, H2291–H2299. doi:10.1152/ajpheart.1998.275.6.h2291

Maesen, B., Nijs, J., Maessen, J., Allessie, M., and Schotten, U. (2012). Post-operative Atrial Fibrillation: A Maze of Mechanisms. *Europace* 14, 159–174. doi:10.1093/europace/eur208

Magadum, A., and Kishore, R. (2020). Cardiovascular Manifestations of COVID-19 Infection. *Cells* 9, 2508. doi:10.3390/cells9112508

Monnerat, G., Alarcón, M. L., Vasconcellos, L. R., Hochman-Mendez, C., Brasil, G., Bassani, R. A., et al. (2016). Macrophage-dependent IL-1β Production Induces Cardiac Arrhythmias in Diabetic Mice. *Nat. Commun.* 7, 13344. doi:10.1038/ncomms13344

Morotti, S., Liu, C., Hegyi, B., Ni, H., Fogli Iseppe, A., Wang, L., et al. (2021). Quantitative Cross-Species Translators of Cardiac Myocyte Electrophysiology: Model Training, Experimental Validation, and Applications. *Sci. Adv.* 7, abg0927. doi:10.1126/sciadv.abg0927

Ohta, H., Wada, H., Niwa, T., Kirii, H., Iwamoto, N., Fujii, H., et al. (2005). Disruption of Tumor Necrosis Factor-α Gene Diminishes the Development of Atherosclerosis in ApoE-Deficient Mice. *Atherosclerosis* 180, 11–17. doi:10.1016/j.atherosclerosis.2004.11.016

O'Shea, C. J., Middeldorp, M. E., Thomas, G., Harper, C., Elliott, A. D., Ray, N., et al. (2021). Atrial Fibrillation Burden during the Coronavirus Disease 2019 Pandemic. *Europace* 23, 1493–1501. doi:10.1093/europace/euab099

Pak, H. N., Hong, S. J., Hwang, G. S., Lee, H. S., Park, S. W., Ahn, J. C., et al. (2004). Spatial Dispersion of Action Potential Duration Restitution Kinetics Is Associated with Induction of Ventricular Tachycardia/fibrillation in Humans. *J. Cardiovasc. Electrophysiol.* 15, 1357–1363. doi:10.1046/j.1540-8167.2004.03569.x

Roden, D. M. (2003). A Surprising New Arrhythmia Mechanism in Heart Failure. *Circulation Res.* 93, 589–591. doi:10.1161/01.RES.0000095382.50153.7D

Schrickel, J. W., Schwab, J. O., Yang, A., Bielik, H., Bitzen, A., Lüderitz, B., et al. (2006). Pro-arrhythmic Effects of Amiodarone and Concomitant Rate-Control Medication. *Europace* 8, 403–407. doi:10.1093/europace/eul038

Sedmera, D., Neckar, J., Benes, J., Pospisilova, J., Petrak, J., Sedlacek, K., et al. (2016). Changes in Myocardial Composition and Conduction Properties in Rat Heart Failure Model Induced by Chronic Volume Overload. *Front. Physiol.* 7, 367. doi:10.3389/fphys.2016.00367

Shimaoka, T., Wang, Y., Morishima, M., Miyamoto, S., and Ono, K. (2020). Magnesium Deficiency Causes Transcriptional Downregulation of Kir2.1 and Kv4.2 Channels in Cardiomyocytes Resulting in QT Interval Prolongation. *Circ. J.* 84, 1244–1253. doi:10.1253/circj.CJ-20-0310

Shimoni, Y., Severson, D., and Giles, W. (1995). Thyroid Status and Diabetes Modulate Regional Differences in Potassium Currents in Rat Ventricle. *J. Physiol.* 488, 673–688. doi:10.1113/jphysiol.1995.sp020999

Sugishita, K., Kinugawa, K.-i., Shimizu, T., Harada, K., Matsui, H., Takahashi, T., et al. (1999). Cellular Basis for the Acute Inhibitory Effects of IL-6 and TNF- α on Excitation-Contraction Coupling. *J. Mol. Cell. Cardiol.* 31, 1457–1467. doi:10.1006/jmcc.1999.0989

Sutanto, H., Cluitmans, M. J. M., Dobrev, D., Volders, P. G. A., Bébarová, M., and Heijman, J. (2020). Acute Effects of Alcohol on Cardiac Electrophysiology and Arrhythmogenesis: Insights from Multiscale In Silico Analyses. *J. Mol. Cell. Cardiol.* 146, 69–83. doi:10.1016/j.yjmcc.2020.07.007

Taggart, P., Sutton, P. M., Opthof, T., Coronel, R., Trimlett, R., Pugsley, W., et al. (2000). Inhomogeneous Transmural Conduction during Early Ischaemia in Patients with Coronary Artery Disease. *J. Mol. Cell. Cardiol.* 32, 621–630. doi:10.1006/jmcc.2000.1105

Tanaka, T., Kanda, T., Takahashi, T., Saegusa, S., Moriya, J., and Kurabayashi, M. (2004). Interleukin-6-induced Reciprocal Expression of SERCA and Natriuretic Peptides mRNA in Cultured Rat Ventricular Myocytes. *J. Int. Med. Res.* 32, 57–61. doi:10.1177/147323000403200109

Tentusscher, K., Bernus, O., Hren, R., and Panfilov, A. (2006). Comparison of Electrophysiological Models for Human Ventricular Cells and Tissues. *Prog. Biophysics Mol. Biol.* 90, 326–345. doi:10.1016/j.pbiomolbio.2005.05.015

Terkildsen, J. R., Niederer, S., Crampin, E. J., Hunter, P., and Smith, N. P. (2008). Using Physiome Standards to Couple Cellular Functions for Rat Cardiac Excitation-Contraction. *Exp. Physiol.* 93, 919–929. doi:10.1113/expphysiol.2007.041871

Tse, G., Li, K. H. C., Cheung, C. K. Y., Letsas, K. P., Bhardwaj, A., Sawant, A. C., et al. (2021). Arrhythmogenic Mechanisms in Hypokalaemia: Insights from Pre-clinical Models. *Front. Cardiovasc. Med.* 8, 620539. doi:10.3389/fcvm.2021.620539

Villegas, S., Villarreal, F. J., and Dillmann, W. H. (2000). Leukemia Inhibitory Factor and Interleukin-6 Downregulate Sarcoplasmic Reticulum Ca 2^+ ATPase (SERCA2) in Cardiac Myocytes. *Basic Res. Cardiol.* 95, 47–54. doi:10.1007/s003950050007

Wang, J., Wang, H., Zhang, Y., Gao, H., Nattel, S., and Wang, Z. (2004). Impairment of HERG K(+) Channel Function by Tumor Necrosis Factor-α. *J. Biol. Chem.* 279, 13289–13292. doi:10.1074/jbc.c400025200

Weisensee, D., Bereiter-Hahn, J., Schoeppe, W., and Löw-Friedrich, I. (1993). Effects of Cytokines on the Contractility of Cultured Cardiac Myocytes. *Int. J. Immunopharmacol.* 15, 581–587. doi:10.1016/0192-0561(93)90075-A

Xie, F., Qu, Z., Yang, J., Baher, A., Weiss, J. N., Garfinkel, A., et al. (2004). A Simulation Study of the Effects of Cardiac Anatomy in Ventricular Fibrillation. *J. Clin. Invest.* 113, 686–693. doi:10.1172/jci17341

Yuuki, K., Hosoya, Y., Kubota, I., and Yamaki, M. (2004). Dynamic and Not Static Change in Ventricular Repolarization Is a Substrate of Ventricular Arrhythmia on Chronic Ischemic Myocardium. *Cardiovasc. Res.* 63, 645–652. doi:10.1016/j.cardiores.2004.04.017

Zhang, D., Tu, H., Wadman, M. C., and Li, Y.-L. (2018). Substrates and Potential Therapeutics of Ventricular Arrhythmias in Heart Failure. *Eur. J. Pharmacol.* 833, 349–356. doi:10.1016/j.ejphar.2018.06.024

Zhang, S., Lu, W., Li, Z., Wang, S., Jiang, M., Yuan, Q., et al. (2020). "Mechanisms Underlying Sulfur Dioxide Pollution Induced Ventricular Arrhythmia: A Simulation Study," in IEEE International Conference on Bioinformatics and Biomedicine (BIBM), Seoul, South Korea, December 16–19, 2020. 381

Zhang, S., Zhang, S., Fan, X., Wang, W., Li, Z., Jia, D., et al. (2019). Pro-arrhythmic Effects of Hydrogen Sulfide in Healthy and Ischemic Cardiac Tissues: Insight from a Simulation Study. *Front. Physiol.* 10, 1482. doi:10.3389/fphys.2019.01482

Zhao, Z., Xie, Y., Wen, H., Xiao, D., Allen, C., Fefelova, N., et al. (2012). Role of the Transient Outward Potassium Current in the Genesis of Early Afterdepolarizations in Cardiac Cells. *Cardiovasc. Res.* 95, 308–316. doi:10.1093/cvr/cvs183

Conflict of Interest: The authors declare that the research was conducted in the absence of any commercial or financial relationships that could be construed as a potential conflict of interest.

Publisher's Note: All claims expressed in this article are solely those of the authors and do not necessarily represent those of their affiliated organizations, or those of the publisher, the editors and the reviewers. Any product that may be evaluated in this article, or claim that may be made by its manufacturer, is not guaranteed or endorsed by the publisher.

frontiers | Frontiers in Physiology

ORIGINAL RESEARCH
published: 01 June 2022
doi: 10.3389/fphys.2022.906146

A Novel *In Silico* Electromechanical Model of Human Ventricular Cardiomyocyte

Chiara Bartolucci[1]*, *Mohamadamin Forouzandehmehr*[2], *Stefano Severi*[1] and *Michelangelo Paci*[2]

[1]Computational Physiopathology Unit, Department of Electrical, Electronic and Information Engineering "Guglielmo Marconi", University of Bologna, Bologna, Italy, [2]BioMediTech, Faculty of Medicine and Health Technology, Tampere University, Tampere, Finland

Contractility has become one of the main readouts in computational and experimental studies on cardiomyocytes. Following this trend, we propose a novel mathematical model of human ventricular cardiomyocytes electromechanics, BPSLand, by coupling a recent human contractile element to the BPS2020 model of electrophysiology. BPSLand is the result of a hybrid optimization process and it reproduces all the electrophysiology experimental indices captured by its predecessor BPS2020, simultaneously enabling the simulation of realistic human active tension and its potential abnormalities. The transmural heterogeneity in both electrophysiology and contractility departments was simulated consistent with previous computational and *in vitro* studies. Furthermore, our model could capture delayed afterdepolarizations (DADs), early afterdepolarizations (EADs), and contraction abnormalities in terms of aftercontractions triggered by either drug action or special pacing modes. Finally, we further validated the mechanical results of the model against previous experimental and in silico studies, e.g., the contractility dependence on pacing rate. Adding a new level of applicability to the normative models of human cardiomyocytes, BPSLand represents a robust, fully-human in silico model with promising capabilities for translational cardiology.

Keywords: computational modeling, human ventricular cardiomyocyte model, action potential (AP), contractility, aftercontraction

OPEN ACCESS

Edited by:
Matthijs Cluitmans, Maastricht University, Netherlands

Reviewed by:
Steven Alexander Niederer, King's College London, United Kingdom
Aurore Lyon, Maastricht University, Netherlands
Alexander Jung, Medical University of Graz, Austria

***Correspondence:**
Chiara Bartolucci
chiara.bartolucci4@unibo.it

Specialty section:
This article was submitted to Cardiac Electrophysiology, a section of the journal Frontiers in Physiology

Received: *28 March 2022*
Accepted: *10 May 2022*
Published: *01 June 2022*

Citation:
Bartolucci C, Forouzandehmehr M, Severi S and Paci M (2022) A Novel In Silico Electromechanical Model of Human Ventricular Cardiomyocyte. Front. Physiol. 13:906146. doi: 10.3389/fphys.2022.906146

1 INTRODUCTION

The future of diagnosis and treatment in cardiology progressively depends on advanced methods in imaging, gene profiling, and pharmaceutical technologies. Despite the recent advances in health technologies, the current empirical clinical investigations face serious challenges as the complexity of therapeutic interventions, prognosis, and the possibility of classifying the treatments grow. Specifically, identifying the optimal treatment strategy with a degree of statistical significance poses serious challenges to current empirical routes in cardiology (Niederer et al., 2019). Furthermore, as precision medicine emerges (Forouzandehmehr et al., 2022), the proven pathophysiological variability between individuals highly augments the detail in the diagnostic process and data, thus, finding an optimal patient-specific solution becomes increasingly difficult (Niederer et al., 2019). Cardiac computational models, based on established physiological and engineering principles, offer a capable framework that not only can be fed by large datasets but also

enable mechanistic and integrative simulations leading to disclose novel insights in cardiac pathophysiology (Niederer et al., 2019).

Early physiologically constrained computational models of cardiac cells could quantitatively translate the protein functions into developing cellular phenotypes (Niederer et al., 2019). During the past decade, these models have also incorporated functional characteristics of ion channels, cellular pumps, transporters, and buffers making them promising candidates in preclinical studies (O'Hara et al., 2011; Tomek et al., 2019; Bartolucci et al., 2020; Paci et al., 2021). Currently, as the cardiac contractility data become increasingly available, together with new recording techniques (Ahola et al., 2018), mathematical models of cardiomyocytes (CMS) are developed to predict dynamics of contraction combined with simulation of drug effects alongside the electrophysiology. Toward building models of myocyte electromechanics, elements of contractility have been developed with different levels of complexity focusing on animals (Rice et al., 2008; Campbell et al., 2010; Sheikh et al., 2012; Land et al., 2013) and human CMs (Land et al., 2017). Initial efforts on developing reliable models to capture the electromechanics of human adult CMs have been initiated recently (Lyon et al., 2020; Margara et al., 2021). Margara et al., integrated an established human-based developed contractile element (Land et al., 2017) into the gold standard *in silico* model of human ventricular cell electrophysiology (O'Hara et al., 2011) and into their new ToR-ORd model (Tomek et al., 2019) to predict ventricular active tension generation alongside action potential (AP) and calcium transients (CaT). Also Lyon et al. complemented the ORd model with a contractile element: their choice was the MedChem model of sarcomere mechanics (Dupuis et al., 2018), which they used to assess the impact of β-adrenergic stimulation and sarcomere length on CaTs and force (Lyon et al., 2020).

Our recently published BPS2020 model of the human adult ventricular CM electrophysiology (Bartolucci et al., 2020), holds significant improvements compared with the original ORd model (e.g., the simulation of the experiments with the correct extracellular K^+ concentration used *in vitro* or the generation of DADs) and includes specific mechanisms not simulated by ToR-ORd (e.g., the inverse APD_{90}-$[Ca^{2+}]_o$ dependence). Given these improvements in simulating electrophysiology phenomena, it is worth investigating how we can expand the spectrum of BPS2020 simulation, by using it as the basis for a new electromechanical human CM *in silico* model.

We have integrated one of the most recent human contractile machinery (LandCE) (Land et al., 2017) into BPS2020 (Bartolucci et al., 2020). As done in Margara et al. (2021), we chose LandCE as it is a contractile element validated against human data. Our goal was to investigate the capabilities of this newly integrated electromechanical model, BPSLand, by evaluating active tension generation and contractility abnormalities e.g., aftercontractions, that can be activated either by drug action or special pacing conditions. BPSLand is a robust, fully-human, *in silico* model meeting the computational expectations from both departments, the electrophysiology and contractility, with the potential for facilitating the translation of biophysical and pharmacological functions into pre-clinical readouts.

2 METHODS

2.1 *In Vitro* Data

To calibrate the BPSLand model, we used a dataset of isometric active tension (Ta) biomarkers recorded from human isolated ventricular CMs (Land et al., 2017; Margara et al., 2021) and a dataset of action potential (AP) biomarkers from human isolated ventricular endocardial CMs (O'Hara et al., 2011; Bartolucci et al., 2020). The Ta biomarker dataset includes measures from strips of the left ventricular myocardium (Mulieri et al., 1992), left ventricular trabeculae (Pieske et al., 1996) and right ventricular trabeculae (Rossman et al., 2004) (additionally considered by Margara et al., 2021). Both datasets were recorded at 37°C. Ta biomarkers are the peak tension (TaPeak), the relaxation time at 50% and 95% ($TaRT_{50}$, $TaRT_{95}$) and the time-to-peak (TaTTP). AP biomarkers are the duration at 30%, 40%, 50%, 70% and 90% (APD_{30}, APD_{40}, APD_{50}, APD_{70}, APD_{90}), the maximum upstroke velocity (dV/dt_{max}), the peak voltage (VPeak) and the resting membrane potential (RMP). *In silico* biomarkers were computed as in Margara et al. (2021). As we previously reported in Bartolucci et al. (2020), we simulated the AP biomarkers for calibration at $[K^+]_o = 4$ mM. Conversely, as no information was reported on the *in vitro* Ta biomarker ranges, we run our simulations at the standard concentration $[K^+]_o = 5.4$ mM.

To validate BPSLand, we used the following human data: 1) APD rate dependence, restitution and accommodation data in control condition and with current blockers from endocardial CMs (O'Hara et al., 2011) (see **Supplementary Methods** for details and **Supplementary Table S1**); 2) TaPeak, $TaRT_{50}$ and CaT relaxation time at 50% ($CaRT_{50}$) rate adaptation data (Pieske et al., 1995; Janssen and Periasamy, 2007); 3) TaPeak transmural heterogeneity data from sub-epicardial, mid-myocardial, and sub-endocardial specimens (Haynes et al., 2014).

2.2 Integration of the Land Contractile Element Into the BPS2020 Model

The original BPS2020 model (Bartolucci et al., 2020) was based on the seminal O'Hara-Rudy model of the human ventricular AP (O'Hara et al., 2011) and it features two cytosolic compartments, the subspace and the bulk myoplasm, and the sarcoplasmic reticulum (SR) represented with a single compartment. It includes the following ion currents: fast and late Na^+ currents (I_{NaF}, I_{NaL}), transient outward K^+ current (I_{to}), L-type Ca^{2+} current (I_{CaL}), also with its Na^+ and K^+ components (I_{CaNa}, I_{CaK}), the rapid, slow and inward rectifying K^+ currents (I_{Kr}, I_{Ks}, I_{K1}), the Na^+/Ca^{2+} exchanger divided in its cytosolic and subspace components (I_{NCXi}, I_{NCXss}), the Na^+/K^+ pump (I_{NaK}), Na^+, K^+ and Ca^{2+} background currents (I_{Nab}, I_{Kb}, I_{Cab}) and the sarcolemmal Ca^{2+} pump (I_{pCa}). Ca^{2+} fluxes from/to SR are the RyR-sensitive Ca^{2+} release (J_{rel}), the SERCA pump (J_{up}) and a leakage flux (J_{leak}).

TABLE 1 | Contractility and electrophysiology biomarkers used for the BPSLand optimization, with their ranges.

Model	Step	Parameter	Range
LandCE	1	Tropomyosin rate constant k_u (1/ms)	[0.01, 0.2]
		Hill coefficient *ntm*	[3, 7]
		Unbound-to-weak crossbridge transition scaling factor ν	[1, 12]
		Weak-to-strong crossbridge transition scaling factor μ	[1, 12]
		Tropomyosin Ca^{2+} sensitivity ($[Ca^{2+}]_{T50}$) (μM)	[0.5, 0.6]
BPS2020	2	Maximum Ca^{2+} release flux from SR $J_{rel,max}$ (1/ms)	[0.016, 0.024]
		Maximum SERCA pump flux $J_{up,max}$ (mM/ms)	[2.504, 3.756]

We integrated LandCE into BPS2020 following the approach presented in (Margara et al., 2021). Shortly, LandCE takes as input the intracellular Ca^{2+} concentration $[Ca^{2+}]_i$ computed by BPS2020, to update a new state variable CaTRPN, representing the fraction of troponin C units which bound to Ca^{2+}.

$$\frac{dCaTRPN}{dt} = k_{TRPN}\left(\frac{[Ca^{2+}]_i}{[Ca^{2+}]_{T50}}\right)^{n_{TRPN}}(1 - CaTRPN) - CaTRPN\Big)$$

BPS2020 receives as feedback the amount of Ca^{2+} buffered by troponin C, $[Ca^{2+}]_{TRPN}$, to update the intracellular Ca^{2+} concentration.

$$\frac{d[Ca^{2+}]_i}{dt} = \beta_{Cai}\Big(- (I_{pCa} + I_{Cab} - 2I_{NaCa,i})\frac{A_{cap}}{2Fv_{myo}} - J_{up}\frac{v_{sr}}{v_{myo}} + J_{diff,Ca}\frac{v_{ss}}{v_{myo}} - \frac{d[\mathrm{EGTA}]_i}{dt} - \frac{d[Ca^{2+}]_{TRPN}}{dt}\Big)$$

$$\frac{d[Ca^{2+}]_{TRPN}}{dt} = [Ca^{2+}]_{TRPN,max}\frac{dCaTRPN}{dt}$$

where $[Ca^{2+}]_{TRPN,max}$ represents the maximum Ca^{2+} concentration that can bind to troponin C.

2.3 Optimization of the BPSLand Model

The structure of the cost function used for both optimizations is the same as in Paci et al. (2018b)

$$Cost = \sum_{1}^{N_{biom}} w_i * Cost_i$$

$$Cost_i = \frac{(b_{i,sim} < LB_i)(b_{i,sim} - LB_i)^2 + (b_{i,sim} > UB_i)(b_{i,sim} - UB_i)^2}{0.5(LB_i + UB_i)}$$

where $b_{i,sim}$ is the ith simulated biomarker, LB_i the ith experimental lower bound for $b_{i,sim}$, UB_i the ith experimental upper bound for $b_{i,sim}$, w_i the weight for each biomarker's cost (**Supplementary Table S2**) and N_{biom} the number of biomarkers used for optimization. Briefly, if the simulated ith biomarker is smaller than LB_i or greater than UB_i, the error is computed as the squared distance between the simulated biomarker and the bound, normalized by the center of mass of $[LB_i, UB_i]$. Finally, in order to minimize the active tension T_a, we included one additional term to Cost, obtaining the final cost function

TABLE 2 | *In vitro* contractility and electrophysiology biomarkers used in the cost function and their goal ranges.

Biomarker	Range [LB, UB]
Active tension peak TaPeak (kPa)	[15, 25]
Active tension time-to-peak TaTTP (ms)	[109, 125]
Active tension relaxation time to 50% $TaRT_{50}$ (ms)	[147, 172]
Active tension relaxation time to 95% $TaRT_{95}$ (ms)	[291, 377]
Minimum active tension min (Ta) (kPa)	—
Systolic intracellular Ca^{2+} CaSys (mM)	[3.004755, 3.321045]e-4
Diastolic intracellular Ca^{2+} CaDias (mM)	[7.712955, 8.524845]e-4

$$Cost_{TOT} = w_{minTa} * \min(T_a) + Cost$$

with w_{minTa} the weight of the minimun active tension.

2.3.1 Step 1: Hybrid Optimization on the LandCE Parameters

After integrating LandCE into BPS2020, we first optimized the LandCE parameters using a hybrid approach combining first a genetic optimization (Matlab function *ga*), followed by the simplex optimization [Matlab function *fminsearchbnd* (D'Errico, 2022)]. The parameters optimized in this first step are only the LandCE parameters listed in **Table 1**. The optimization ranges for the LandCE parameters are the same as in the original LandCE publication (Land et al., 2017), except for the tropomyosin Ca^{2+} sensitivity ($[Ca^{2+}]_{T50}$), for which we chose [0.5, 0.6] instead of [0.8, 0.9]. As the original range [0.8, 0.9] increased substantially the CaT peak, i.e. the systolic Ca^{2+} (+22%), we decided not to affect the BPS2020 electrophysiology and chose [0.5, 0.6] as it preserved the original BPS2020 CaT peak.

For this first optimization step, we considered five contractility and two electrophysiology biomarkers: active tension peak (TaPeak), time-to-peak (TaTTP), relaxation time to 50% and 95% of the diastolic level ($TaRT_{50}$ and $TaRT_{95}$) and the minimum of the diastolic active tension, systolic and diastolic intracellular free Ca^{2+} (CaSys and CaDiast). The acceptable ranges for these biomarkers were taken from the original Land publication (Land et al., 2017) for TaTTP, $TaRT_{50}$ and $TaRT_{95}$, from Margara et al. (2021) for TaPeak, while we chose to set the ranges for CaSys and CaDias as ±5% of their original values (Bartolucci et al., 2020), in order to keep the electrophysiology the most similar to the original BPS2020 model. At the end of this first step, we obtained an

TABLE 3 | Final BPSLand parameter set.

Parameter	Original value	Optimized value
ku (1/ms)	1	1.5230
Ntm	5	3.0899
N	7	1.002
M	3	2.0779
$[Ca^{2+}]_{T50}$ (μM)	0.805	0.5
$J_{rel,max}$ (1/ms)	20e-3	22e-3
$J_{up,max}$ (mM/ms)	3.13	3

electromechanical model whose electrophysiology biomarkers were not significantly affected by the LandCE and correctly simulated $TaRT_{95}$ while the remaining contractility biomarkers were close to their respective lower bounds.

2.3.2 Step 2: Simplex Only

In order to capture the remaining contractility biomarkers, we then run a second simplex optimization on the Ca^{2+} fluxes of the SERCA pump (J_{up}) and the RyR-sensitive release (J_{rel}), using all the constraints in **Table 2**, and additional constraints on the AP biomarkers. In particular, for resting potential (RMP), peak voltage (VPeak), maximum upstroke velocity (dV/dt_{max}), AP duration at 40%, 50% and 90% (APD_{40}, APD_{50} and APD_{90}), and the triangulation metric (Tri_{9040}), we set the lower and upper bounds as ±5% of their values in the original BPS2020 model, which were fit against the experimental data (O'Hara et al., 2011) at $[K^+]_o$ = 4 mM. We chose these parameters as we did not want to change the ion current parameters of BPS2020, derived from the ORd model and partially fit experimental data in Bartolucci et al. (2020). As ranged for manually tune $J_{rel,max}$ and $J_{up,max}$, we chose ±20% of their original values 20e-3 (1/ms) and 3.13 (mM/ms), respectively. At the end of this second step, the electromechanical model correctly simulated $TaRT_{95}$ and TaPeak while the remaining contractility biomarkers were close to their respective lower bounds. However, we missed one of the key features of BPS2020, i.e., the inverse relationship $[Ca^{2+}]_o$ – APD_{90}, which was otherwise simulated at the end of the first step.

2.3.3 Step 3: Manual Tuning

In order to restore the $[Ca^{2+}]_o$ – APD_{90} relationship, we added one final step to our pipeline, where we did a minor manual re-tuning of $J_{rel,max}$ (0.0240 →0.0220 1/ms) and $J_{up,max}$ (3.1333 → 3 mM/ms), still considering their lower and upper bounds as in **Table 1**. The final model is named BPSLand and its parameter values are reported in **Table 3**. **Supplementary Tables S2–S4** summarize the weights, parameters and biomarkers obtained after each of the three optimizations steps. **Supplementary Table S5** shows the impact of the manual tuning of $J_{rel,max}$ and $J_{up,max}$ on the $[Ca^{2+}]_o$ – APD_{90} relationship.

2.3.4 Rate Dependence

To test the active tension dependence on the applied pacing rate, we paced BPSLand at 0.5, 1, 1.5, 2, 2.5 and 3 Hz for 1,000 beats to reach the steady state, using $[K^+]_o$ = 5.4 mM, $[Ca^{2+}]_o$ = 1.8 mM and $[Na^+]_o$ = 144 mM as extracellular ion concentration. We then compared simulated TaPeak, $TaRT_{50}$ and $CaRT_{50}$ with the *in vitro* data by Pieske et al., (1995) and Janssen and Periasamy (2007).

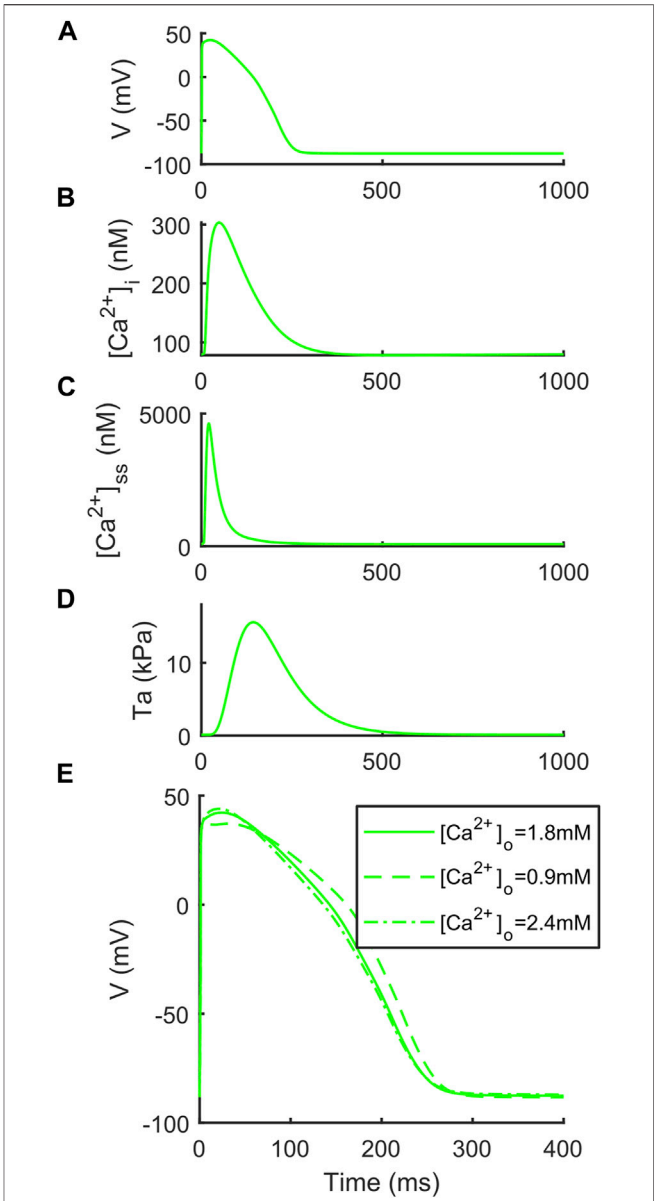

FIGURE 1 | Illustrative traces simulated by BPSLand ($[K^+]_o$ = 5.4 mM). **(A)** Action potential. **(B)** Cytosolic Ca^{2+} concentration. **(C)** Subspace Ca^{2+} concentration. **(D)** Active tension. **(E)** Inverse action potential duration dependence on the extracellular Ca^{2+} concentration.

2.3.5 Heterogeneity

To simulate transmural heterogeneity, i.e., simulating epicardial (EPI) and mid-myocardial (M) CMs in addition to endocardial (ENDO), we used the same scaling factors reported in Bartolucci et al. (2020) for I_{NaL}, I_{to}, I_{CaL}, I_{Kr}, I_{Ks}, I_{K1}, I_{NCX}, I_{NaK}, I_{Kb}, J_{rel} and J_{up} (**Supplementary Table S6**).

TABLE 4 | The electrophysiology and contractility biomarkers simulated by the original BPS2020 and the new BPSLand models, compared to *in vitro* data.

Biomarker	$[K^+]_o$ = 5.4 mM			$[K^+]_o$ = 4 mM		
	BPS2020	BPSLand	*In vitro*	BPS2020	BPSLand	*In vitro*
APD_{90} (ms)	239.9	239.9	—	267.6	268.4	[180, 440]
APD_{50} (ms)	177.1	175.9	—	200.1	200.0	[110, 350]
APD_{40} (ms)	160.1	158.9	—	178.3	177.3	[85, 320]
Tri_{9040}	79.8	81.0	—	89.3	91.1	[50, 150]
dV/dt_{max} (V/s)	248.1	248.8	—	305.3	305.7	[100, 1,000]
VPeak (mV)	42.2	42.2	—	43.7	43.8	[10, 55]
RMP (mV)	-87.6	-87.7	—	-95.6	-95.7	[-103, -88]
CTD_{90} (ms)	247.9	251.3	—	247.6	254.9	—
CTD_{50} (ms)	124.1	138.9	—	125.3	140.3	—
CaSys (nM)	316.3	303.3	—	328.7	311.7	—
CaAmp (nM)	235.1	225.0	—	244.6	230.5	—
CaDias (nM)	81.2	78.2	—	84.1	81.2	—
TaPeak (kPa)	—	15.6	[15, 25]	—	17.4	—
TaTTP (ms)	—	142.9	[147, 172]	—	145.3	—
$TaRT_{95}$ (ms)	—	307.4	[291, 377]	—	308.1	—
$TaRT_{50}$ (ms)	—	108.4	[109, 125]	—	108.2	—
TaMin (kPa)	—	0.100	—	—	0.112	—

2.3.6 EAD and DAD Simulations to Trigger Active Tension Abnormalities

We assessed the occurrence of early-afterdepolarization (EADs) and aftercontractions in the BPSLand following three different protocols. First, we simulated the administration of quinidine considering the drug effects on I_{Na}, I_{Kr}, I_{CaL}, I_{Ks} and I_{to}, using the IC_{50} and Hill's coefficients reported in Passini et al. (2017) and Paci et al. (2018a) and the single pore block model, as in Paci et al. (2021) (**Supplementary Table S7**). We tested three drug concentrations, namely 10, 15 and 20 μM at the standard extracellular ion concentrations ($[K^+]_o$ = 5.4 mM, $[Ca^{2+}]_o$ = 1.8 mM, $[Na^+]_o$ = 144 mM) and cycle length (CL) of 4,000 ms. The second EAD protocol simulated dofetilide, similarly to what we did in Bartolucci et al. (2020). Shortly, we simulated the administration of 0.1 μM dofetilide at CL = 5,000 ms and extracellular concentrations experimentally used by Guo et al. (2011) ($[K^+]_o$ = 5 mM, $[Ca^{2+}]_o$ = 2 mM, $[Na^+]_o$ = 137 mM), using the I_{Kr} drug binding values reported by Dutta et al. (2017). We simulated quinidine and dofetilide effects on the endocardial BPSLand model and we anticipate no EADs nor aftercontractions, despite the remarkable AP prolongation. Conversely, the same tests performed on the M cell version, resulted in EADs and aftercontraction.

To assess the occurrence of delayed afterdepolarizations (DADs) we used the same protocol as in Li and Rudy (2011): we fast paced BPSLand for 1,500 beats (BCL = 275 ms) and then we triggered one long beat (BCL = 10,000 ms).

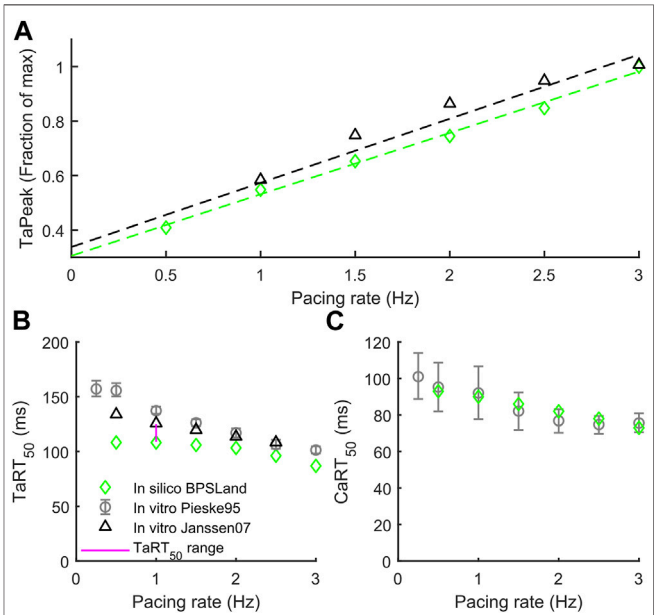

FIGURE 2 | Active tension dependence on pacing rate and comparison with the *in vitro* data from Pieske et al. (1995) and Janssen and Periasamy (2007). **(A)** Normalized active tension peak. **(B)** Active tension relaxation time. **(C)** Ca^{2+} transient relaxation time.

3 RESULTS

3.1 The BPSLand Model

We report the AP, $[Ca^{2+}]_i$, $[Ca^{2+}]_{ss}$ and Ta traces simulated at $[K^+]_o$ = 5.4 mM in **Figure 1**, together with the simulations for variable $[Ca^{2+}]_o$ to highlight the inverse APD_{90}-$[Ca^{2+}]_o$ dependence, which was described first by Severi et al. (2009) and then observed *in vitro* and *in vivo* (Leitch, 1996; Nagy et al., 2013), but failed to be simulated by many *in silico* models, including the original ORd (O'Hara et al., 2011) and ToR-ORd (Tomek et al., 2019). In details, for increasing $[Ca^{2+}]_o$ = 0.9, 1.8 and 2.4 mM, APD_{90} equals to 251.4, 239.9 and 237.1 ms. **Table 4** reports the AP and Ta biomarkers, with the *in vitro* ranges used for the BPSLand calibration, together with additional CaT biomarkers: CaT duration at 50% and 90% (CTD_{50}, CTD_{90}) and amplitude (CaAmp). All the AP biomarkers are within the

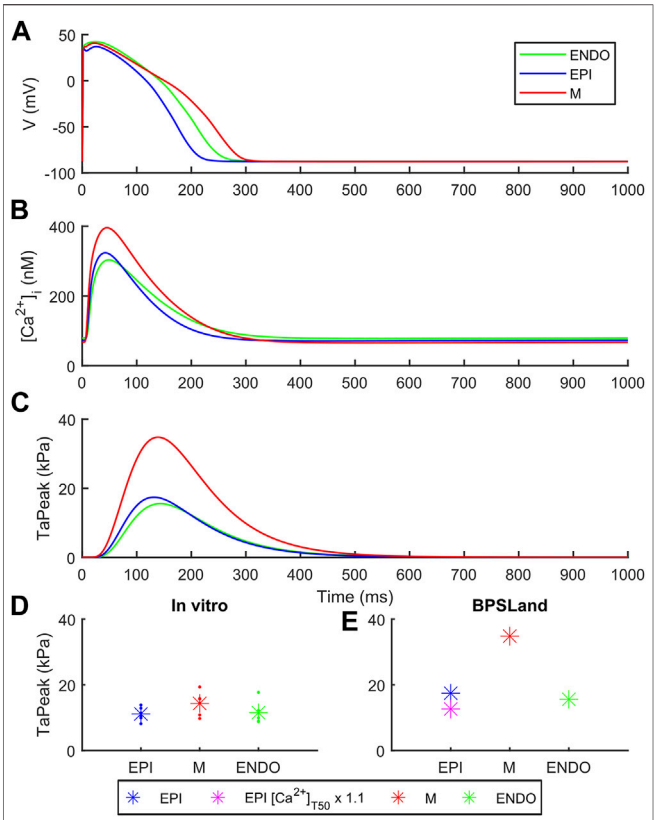

FIGURE 3 | Transmural heterogeneity simulations with BPSLand in endocardial (green), epicardial (blue) and mid-myocardial (red) modes. **(A)** Action potentials. **(B)** Cytosolic Ca^{2+} concentration. **(C)** Active tension. **(D–E)** Comparison of the simulated and experimental active tension peak magnitude across endocardial, epicardial and mid-myocardial cell types. The simulated purple star represents an additional epicardial simulation where we tested a small increments of the calcium sensitivity, ×1.1 the baseline $[Ca^{2+}]_{T50}$ value, to obtain an active tension even closer to the experimental data (Haynes et al., 2014).

experimental ranges, as well as TaPeak and $TaRT_{95}$. Conversely, $TaRT_{50}$ and TaTTP are very close to their respective experimental lower bounds, although out of the *in vitro* ranges. The comparison of AP, Ca^{2+} and Ta traces simulated with $[K^+]_o$ = 4 mM and $[K^+]_o$ = 5.4 mM is presented in **Supplementary Figure S1**.

3.2 Electrophysiology and Contractility Dependence on Pacing Rate

The APD rate adaptation tests reported in Bartolucci et al. (2020) were repeated using BPSLand, to show that introducing LandCE did not affect the capability of the new model in simulating the old data. Briefly, BPSLand simulated the *in vitro* data as satisfactorily as BPS 2020, outperforming the original ORd model (**Supplementary Figures S2, S3**).

In this section we validate BPSLand against two additional *in vitro* datasets of rate adaptation of TaPeak, $TaRT_{50}$ and $CaRT_{50}$, not considered for BPS2020. **Figure 2A** shows the qualitative agreement of our model with the data published by Janssen and Periasamy (2007) in terms of TaPeak-pacing rate dependence. In particular, we successfully simulate the linearity of such dependence. In **Figure 2B**, we considered the rate dependence of $TaRT_{50}$, considering *in vitro* data by Pieske et al., 1995 and Janssen and Periasamy (2007). BPSLand simulations qualitatively agree both with the Janssen07 and the Pieske95 experiments, although $TaRT_{50}$ is lower at the slowest pacing rates. This discrepancy is due to the $TaRT_{50}$ *in vitro* range used to calibrate the BPSLand model at 1 Hz, i.e. [109, 125] ms (purple line). BPSLand is positioned at the interval lower bound (108.4 ms), while Janssen07 data at the upper bound (125 ms) and Pieske95 is out of bound (137.2 ms). Conversely, BPSLand shows quantitative agreement with the Pieske95 $CaRT_{50}$ data (**Figure 2C**). A comparison with the ToR-ORd+Land model is shown in **Supplementary Figure S4**. Furthermore, the length dependence properties of the BPSLand model is presented in **Supplementary Figure S5** and was performed in the same way proposed by Margara et al. (2021) in their original **Supplementary Section S6**.

3.3 Transmural Heterogeneity

Figure 3 shows how BPSLand simulates the transmural heterogeneity in terms of electrophysiology and contractility. Our simulations are in agreement with the ToR-ORd+Land and ORd+Land models presented in Margara et al. (2021). In terms of APD, the M model has the longest APs, followed by the ENDO and EPI models. In terms of CaTs and active tension, the M model shows the highest peaks, followed by EPI and ENDO. Haynes et al. reported transmural heterogeneity data of isometric active tension peaks in human heart preparations, showing similar average active tension in EPI and ENDO preparations (although EPI < ENDO), and greater in M specimens (Haynes et al., 2014). We simulate an EPI TaPeak (17.4 kPa) slightly greater than ENDO (15.6 kPa), while the M model produces greater TaPeak (34.8 kPa). This is the same trend simulated by the ToR-ORd+Land model (TaPeak M > EPI > ENDO), although the absolute TaPeak values are considerably greater in ToR-ORd+Land than in BPSLand. As in (Margara et al., 2021) the authors suggested that the Ca^{2+} sensitivity in ENDO CMs could be higher than in EPI cells, we tested how much upscaling of $[Ca^{2+}]_{T50}$ is required in EPI BPSLand to bring the simulated EPI TaPeak even closer to the experiments (Haynes et al., 2014). In fact, $[Ca^{2+}]_{T50}$ is not considered as one of the parameters to change when switching from ENDO to EPI models. The purple star in **Figure 3E** show that a ×1.1 upscale produces an EPI TaPeak matching the experiments. A comparison of the transmural heterogeneity with the ToR-ORd+Land model is also reported in **Supplementary Figure S6**.

3.4 EADs, DADs and Aftercontractions

The endocardial BPSLand model did not produce EADs just by administering quinidine or dofetilide, despite the extreme APD_{90} prolongation up to +272% with 0.1 μM dofetilide; +398%, +489%, +563% with the three increasing quinidine doses.

Conversely, the M cell version, characterized by smaller I_{Kr} and larger I_{CaL}, reacted to both drugs with EADs and, in some

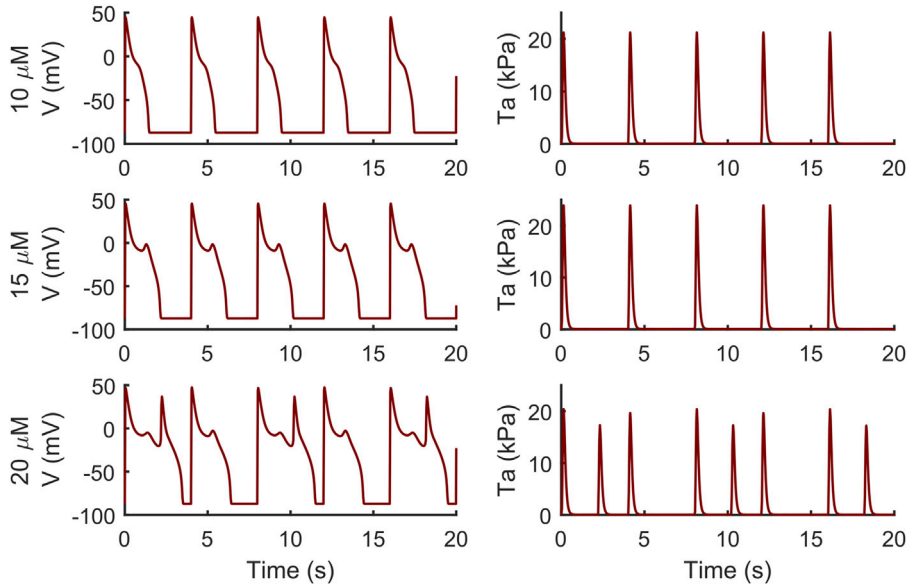

FIGURE 4 | Illustrative traces of the membrane potential (left column) and active tension (right column) simulated by the M cell BPSLand with low (10 μM), intermediate (15 μM) and high (20 μM) quinidine concentrations. The intermediate and high doses trigger early afterdepolarizations and aftercontractions.

cases, aftercontractions. The simulations shown in **Figure 4** are noteworthy: for both the intermediate and high quinidine concentrations (15 μM in the second row and 20 μM in the third row) quinidine triggers EADs, but only some of them have a correspondent aftercontraction. This is due to the different mechanisms underlying each EAD and it is well summarized in case of 20 μM quinidine, reported in more detail in **Figure 5**. The smaller EADs due to I_{CaL} reactivation (I_{CaL}-driven), e.g., $t \sim 1.3$ s or $t \sim 5.3$ s do not have a corresponding aftercontractions. On the other hand, other EADs are triggered by a spontaneous Ca^{2+} release from the SR through J_{rel}, e.g., t ~ 2.2 s or t ~ 10.2 s, which pours into the cytosol enough Ca^{2+} to trigger the contractile element to produce an aftercontraction. Therefore, from this result, we can hypothesize there is not a 1:1 EAD-aftercontraction correspondence, since aftercontractions require enough Ca^{2+} to start, as in the case of J_{rel} intervention.

We observed a similar result with dofetilide in **Figure 6** where the dofetilide simulation resulted in EADs and aftercontractions. Also in this case, the EADs are triggered by spontaneous Ca^{2+} release from the SR through J_{rel}, as shown in the third panel.

Following the DAD Li et al. protocol, BPSLand triggered an unpaced beat further followed by several DADs (**Figure 7**). The fast pacing protocol led to the accumulation of Ca^{2+} in the SR (oscillations in [1.76, 2.12] mM instead of [1.20, 1.47] mM), which was spontaneously released by J_{rel} during the diastolic phase of the last long beat. These unpaced releases of sarcoplasmic Ca^{2+} not only triggered the anticipated AP and DADs (as we already showed in Bartolucci et al., 2020), but it also was enough to trigger aftercontractions (**Figure 7D** inset).

4 DISCUSSION

In this work, we present an updated version of our BPS2020 model of the human ventricular AP (Bartolucci et al., 2020), that we enhanced with the contractility model presented by Land et al. (2017). The potential of *in silico* models is getting more and more recognition both by industry and regulators for specific applications, e.g., cardiac safety pharmacology (Li et al., 2020; Musuamba et al., 2021). However, most of the current cardiac cell models focus mainly on electrophysiology, i.e., AP and Ca^{2+} handling, not considering the fact that the heart behaves like a pump, and therefore the contractile activity of CMs is surely worth of interest. Most of the diseases of interest modelled so far within silico CM models mainly affected specific ion channels [long QT syndrome (Clancy and Rudy, 2002; Paci et al., 2017, 2018a; Kernik et al., 2020)] or Ca^{2+} handling [catecholaminergic polymorphic ventricular tachycardia (CPVT) (Koivumäki et al., 2018)]. Conversely, hypertrophic cardiomyopathy (HCM), the most widespread genetic cardiac disorder, primarily associates with pathogenic variants in protein genes of sarcomere (Santini et al., 2020). In fact, most of pathogenic variants in HCM are hosted by myosin binding protein C and adult cardiac myosin isoforms that are mainly programmed by MYBPS3 and MYH7 genes, respectively, (Toepfer et al., 2020). These variants are responsible for myocardium hypercontractility (Sarkar et al., 2020), impaired contractile relaxation (Toepfer et al., 2020), arrhythmogenesis, diastolic dysfunction and heart failure (Sarkar et al., 2020). Furthermore, the hypoxia-induced lack of oxygenation in ischemia impairs the orchestrate of molecular events leading to normal ventricular contraction (Katz, 1973). Finally, the glycation of myofilaments in diabetes, a major risk factor in heart failure, correlates with significant reduction in

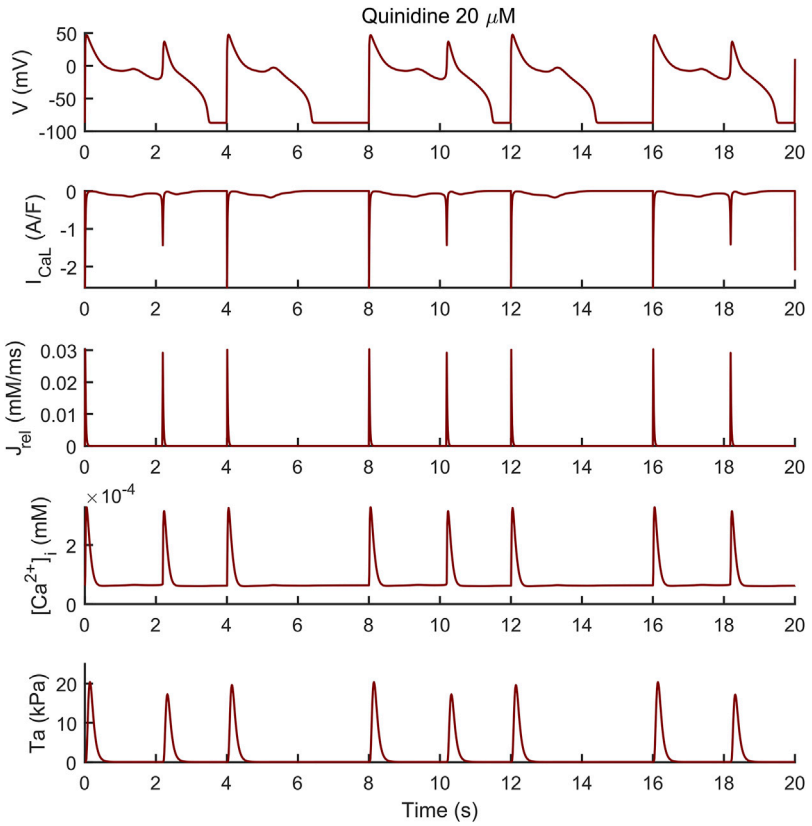

FIGURE 5 | Early afterdepolarizations (EADs) triggered by 20 μM of quinidine and their underlying mechanisms in the M cell BPSLand. The smaller EADs due to I_{CaL} reactivation (I_{CaL}-driven), e.g., *t* ~ 1.3 s or t ~ 5.3 s do not have a corresponding aftercontraction. Conversely, EADs trigger by a spontaneous Ca^{2+} release from the sarcoplasmic reticulum through J_{rel}, e.g., *t* = ~ 2.2 s or *t* = ~ 10.2 s, have a corresponding aftercontraction, since J_{rel} pours into the cytosol enough Ca^{2+} to trigger the contractile element.

calcium sensitivity of the sarcomere (Papadaki et al., 2022) that cannot be captured in electrophysiology-only models. The same applies to new drugs directly targeting sarcomere dynamics, e.g., blebbistatin, omecamtiv mecarbil and mavacamten (Rahman et al., 2018; Awinda et al., 2020; Fülöp et al., 2021): with no *in silico* contractility description, it is not possible to properly simulate them.

Therefore, the goal of our work was to provide the new and validated BPSLand *in silico* model of human adult CMs, combining both electrophysiology and contractility. As the electrophysiology description by BPS2020 carried a few novelties, especially the APD-$[Ca^{2+}]_o$ relationship and an extended and more reliable description of Ca^{2+} handling, including the generation of DADs, it was important to us to create a model able to translate such novelties also to contractility. Of note, we did not aim to simulate here specific pathological conditions affecting contractility, as this will be topic for future works.

4.1 Development of the BPSLand Model

We followed the same strategy published by Margara et al. (2021) for their ToR-ORd+Land model, to integrate the electrophysiology described by BPS2020 and the contractility of LandCE: as forward mechanism, LandCE takes as input the cytosolic Ca^{2+} concentration computed by BPS2020, to compute the fraction of troponin C units bound to Ca^{2+}, and this new flux of Ca^{2+} towards the sarcomere is then included in the equation regulating the BPS2020 cytosolic Ca^{2+} concentration, to close the loop. In terms of mathematical formulation, the process was straightforward, as BPS2020 and ToR-ORd are both based on the original ORd model. For the optimization of the model, we built our cost function with the same biomarkers (TaPeak, TaTTP, $TaRT_{50}$ and $TaRT_{95}$) and experimental ranges as in Land et al. and Margara et al., and we tuned the same parameters (k_u, ntm, ν, μ and $[Ca^{2+}]_{T50}$) within the same ranges, except for the Ca^{2+} sensitivity $[Ca^{2+}]_{T50}$. In both Land et al. and Margara et al., $[Ca^{2+}]_{T50}$ was optimized within [0.8, 0.9]. However, values in that range would have altered too much the CaT amplitude of BPS 2020. Land et al. already reported that such parameter "needs to be fit depending on the calcium transient used to drive the model," as it is not consistent inter-species and also variable in their experiments on skinned human CMs. Therefore, we optimized $[Ca^{2+}]_{T50}$ in the range [0.5, 0.6], which allowed us to keep the same CaT morphology and magnitude of the original BPS 2020. As we reported in **Section 2**, we followed a hybrid optimization approach based on genetic algorithm (Step 1, as in

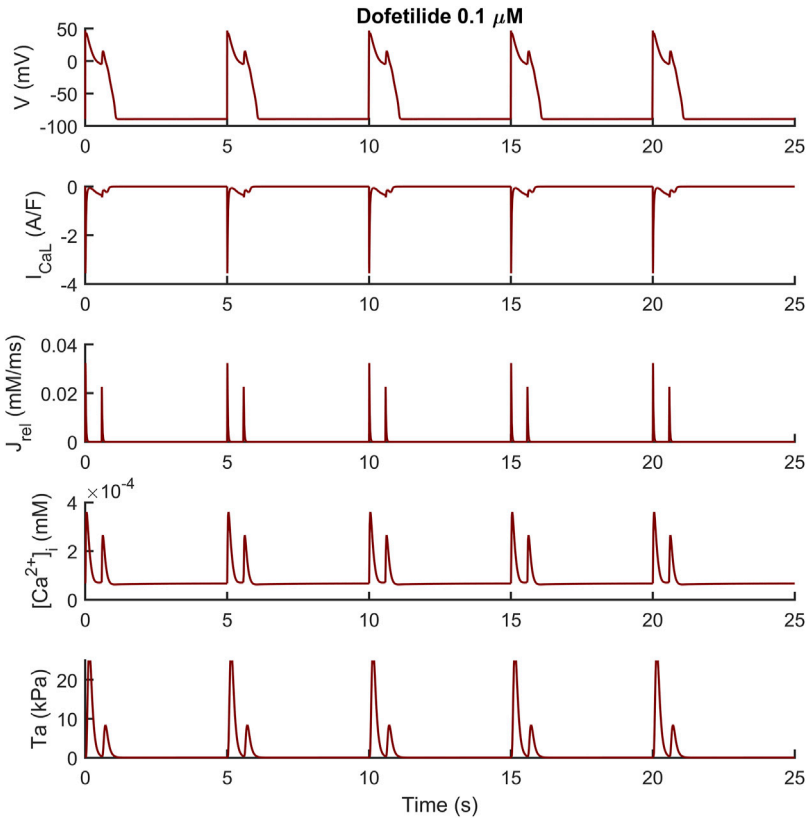

FIGURE 6 | Illustrative early afterdepolarizations and aftercontractions triggered by 0.1 μM of dofetilide in the M cell BPSLand.

Land et al. and Margara et al.) to avoid being stuck in local minima, followed by a simplex (Step 2) on the sarcoplasmic Ca^{2+} fluxes again to keep the BPSLand Ca^{2+} handling the most similar to BPS2020. Already at this stage, the resulting model would have satisfactorily simulated the considered AP and Ta biomarkers. However, it lost the ability to simulate the inverse APD-$[Ca^{2+}]_o$ dependence for high $[Ca^{2+}]_o$ values. Such dependence was one of the key-novelties of BPS2020 (Bartolucci et al., 2020). In order to restore it (**Figure 1**), we added one step of manual tuning on the sarcoplasmic maximal fluxes $J_{rel,max}$ and $J_{up,max}$, applying only minor changes fully consistent with the physiological formulation (Step 3). The final BPSLand model satisfactorily simulates AP and Ta biomarkers, together with the APD-$[Ca^{2+}]_o$ inverse dependence (**Figure 1**; **Table 4**).

4.2 Validation of the Model Against *In Vitro* Data and Comparison With Other *In Silico* Models

We first validated BPSLand against the same AP data (APD rate dependence and restitution in control condition and with current blocker) used to validate BPS2020 and the original ORd model. The rationale is we want BPSLand to work as well as BPS2020 in simulating electrophysiology data. As we already presented in detail those simulations in Bartolucci et al. (2020), here we report our results and the used protocols in the **Supplementary Section S1** and **Supplementary Figures S2, S3**). These results confirm that adding the mechanical model have not altered the behaviour of the model electrophysiology. Nevertheless, it should be taken into account that having a single experimental dataset, including both electrical and mechanical measurements, would be the ideal setting to better calibrate and validate an electromechanical model (same *in vitro* preparations, clearer assessment of the mechanoelectric feedback, etc.). However, to our current knowledge, there is no such kind of data collection.

In terms of contractile properties, we compared BPSLand simulations to *in vitro* experiments performed on human CMs and cardiac preparations (**Section 2.1**). BPSLand successfully simulated the linear force-frequency dependence reported by Janssen and Periasamy (2007) (**Figure 2**). Such dependence was previously simulated by Lyon et al. (2020), although obtaining lower values of normalized force compared to BPSLand and to *in vitro* data in the range [1, 2.5] Hz (see **Figure 2B** in the original Lyon et al. paper). In terms of relaxation time, BPSLand optimally replicated the $CaRT_{50}$ data by Pieske et al., and very well the $TaRT_{50}$ by Pieske et al. (1995) and Janssen and Periasamy (2007). BPSLand $TaRT_{50}$ is lower at the slowest pacing rates (**Figure 2**). We ascribe this discrepancy to the $TaRT_{50}$ interval we used at 1 Hz during the model optimization: BPSLand and Janssen07 $TaRT_{50}$ are positioned at the opposite sides of such interval (purple line in **Figure 2**)

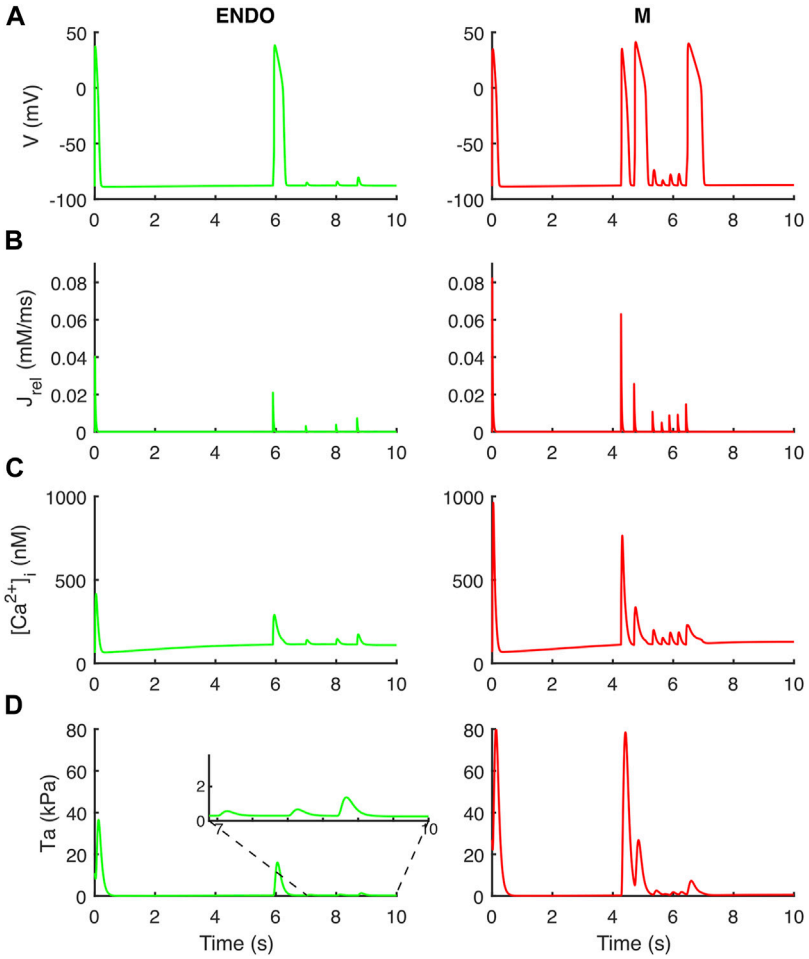

FIGURE 7 | Aftercontractions triggered by anticipated beats and DADs in the endocardial (left column) and M cell (right column) BPS 2020. The action potential at $t = 0$ is the long beat at BCL = 10,000 ms, following 1,500 beats at BCL = 275 ms. The action potential at t ~ 6 s (left) and t ~ 4.2 s/4.7 s/6.4 s (right) is triggered by the spontaneous Ca^{2+} release from the sarcoplasmic reticulum and not by external pacing. **(A)** Membrane potential. **(B)** Ca^{2+} release flux from the sarcoplasmic reticulum. **(C)** Cytosolic Ca^{2+} concentration. **(D)** Active tension with aftercontractions. The zoomed inset on the left column highlights the small aftercontractions corresponding to the DADs following the anticipated action potential.

while Pieske95 is out of bound. In terms of transmural heterogeneity (**Figure 3**), BPSLand simulations are in agreement with the *in silico* results of ToR-ORd+Land in terms of APD (M > ENDO > EPI) and TaPeak (M > EPI > ENDO) sequences, although the TaPeak values are greater in ToR-ORd+Land than in our model (M ~ 60 kPa, EPI ~ 40 kPa, ENDO ~ 20 kPa). In fact, although we used the same TaPeak range as in Margara et al. (2021), i.e., [15, 25] kPa, BPSLand simulates a reference ENDO TaPeak equals to 15.6 kPa, which is more in line with the Haynes et al. (2014) *in vitro* values (**Figure 3**), especially for the small difference we observed in our ENDO vs. EPI TaPeak. As in Margara et al. (2021), we have tested heterogeneities in myofilament calcium sensitivities by acting on the baseline $[Ca^{2+}]_{T50}$ value for the epicardial cell type (**Figure 3E**), showing that a small change of the $[Ca^{2+}]_{T50}$ parameter replicates better the experiments. This result suggests that simulating transmural heterogeneity with electromechanical models may not only require re-calibration of the electrophysiological part but also of the mechanical part of the chosen model (Haynes et al., 2014).

Abnormalities in the ionic regulations of cardiomyocytes e.g., EADs and DADs can trigger the occurrence of a contractile irregularity in form of aftercontractions (Nguyen et al., 2017) the incidence of which has been reported in animal models of heart failure associated with arrhythmogenesis (Pogwizd et al., 2001). We observed that the endocardial BPSLand, as the original BPS2020, reacts to dofetilide and quinidine not producing EADs nor aftercontractions, but with an extreme prolongation of APD. This is not surprising, since we designed BPSLand carefully maintaining the electrophysiology of BPS2020. On the other hand, the M cell model reacted to both drugs with such abnormalities in electrophysiology and contractility. From the modelling point of view, it is not surprising: compared to the endocardial model, the M cell model has smaller G_{Kr} (thus smaller repolarization reserve), larger G_{CaL} (thus being prone to more significant reactivation of I_{CaL} during phase 3 of the AP) and $J_{rel,max}$ (i.e., larger releases, also

spontaneous, of Ca^{2+} from SR). From the *in vitro* point of view, the higher sensitivity of M cells to drugs affecting repolarizing ion currents compared to endocardial and epicardial was reported by Antzelevitch et al. (1999), with a panel of 13 drugs. Nonetheless, we did not observe a 1:1 correspondence between EADs and aftercontractions. We previously observed (see **Figure 6C** in the original BPS2020 paper) EADs triggered by two different mechanisms: I_{CaL} reactivation-driven and RyR spontaneous opening-driven EADs, as we also report here in **Figure 5**. Only in the case of a RyR spontaneous opening-driven EAD, we also have the corresponding aftercontraction, which is not present for I_{CaL}-driven EADs. Similarly to RyR spontaneous opening-driven EADs, also DADs are source of aftercontractions (Desantiago et al., 2008). BPSLand correctly simulated them using a protocol aimed to stress the model. Aftercontractions have been reported *in vitro* following the administration of diverse compounds or in presence of mutations in several cardiac preparations, e.g., cardiac tissues and trabeculae following dofetilide administration (Nguyen et al., 2017), in myocardial slices containing titin and collagen administered with isoproterenol (Watson et al., 2019), or in CPVT human induced pluripotent stem cell-derived CMs (Novak et al., 2012).

4.3 Limitations

The proposed computational model can be used to better understand the electromechanical interactions and the strong relationship between Ca^{2+} regulation and mechanics. Despite this, the experimental *in vitro* human data, taking into account both electrical and mechanical aspects, are still few, and urgently required to ensure better insight in electromechanical coupling and design more accurate models. The BPSLand model itself has some limitations. Preload and afterload conditions contribute to contractility response and should be considered in future model developments by including a mathematical description of dynamic changes in sarcomere length, since now only the isometric condition can be simulated. Other previously published mechanical models, e.g., Rice et al. (2008), Dupuis et al. (2016), and Dupuis et al. (2018), also include a mechanical description of sarcomere lengthening and shortening, thus expanding the range of possible simulations. Our choice to use Land model is based on the fact that it is validated against human experimental data. BPSLand model describes mechano-electric feedback only through the binding of calcium to troponin, but this phenomenon also includes other actors, for example stretch-activated ion channels (Peyronnet et al., 2016), which are modulated by membrane stretch and yield a current acting on the cardiomyocyte membrane potential. Future works should include into the model also these channels. **Figures 2B,C** show another limitation of BPSLand: while the model captures well the $CaRT_{50}$ *in vitro* data, it slightly underestimates the $TaRT_{50}$, as BPSLand simulates very similar $CaRT_{50}$ and $TaRT_{50}$ for each tested rate. One reason could be a slightly too fast relaxation dynamic in the contractile element. However, we replicated the same test with a second *in silico* model (**Supplementary Figure S4**) and an even more different behavior emerges. As cardiomyocyte electromechanical models are not so common yet as electrophysiology only models, it is clear that further iterations of optimization and validation shall be made in the future. Finally, we did not test the application of the model to multiscale simulations (2D or 3D) since it was beyond the scope of the work, although it will be interesting to check BPSLand behaviour also in this field of applicability.

5 CONCLUSION

In this paper, we presented our new electromechanical model of human adult ventricular cardiomyocyte, built and validated using several sets of human *in vitro* experiments. In addition to replicate correctly the results produced by its predecessor BPS2020, BPSLand adds an accurate simulation of active tension and contractility abnormalities, which can be triggered by drugs or specific pacing protocols. Therefore, BPSLand expands the domain of applicability of *in silico* model, which traditionally focus mainly on the simulation of the cardiac cell electrophysiology.

DATA AVAILABILITY STATEMENT

The original contributions presented in the study are included in the article/**Supplementary Material**, further inquiries can be directed to the corresponding author.

AUTHOR CONTRIBUTIONS

CB and MP conceived and designed the study. CB and MP developed and validated the *in silico* model. MF, CB, SS, and MP analysed the *in silico* data, prepared the figures, and drafted the manuscript. All the authors interpreted the results and revised the manuscript.

FUNDING

CB was supported in part by the PRIN (Progetti di Ricerca di Rilevante Interesse Nazionale) 2017, Prot. N.2017AXL54F. MF was supported by the Graduate School of Faculty of Medicine and Health Technology, Tampere University. MP was supported by the Finnish Cultural Foundation, decision 210813, and by Academy of Finland Centre of Excellence in Body-on-Chip Research.

ACKNOWLEDGMENTS

The authors thank the Tampere Center for Scientific Computing for generous computational resources.

SUPPLEMENTARY MATERIAL

The Supplementary Material for this article can be found online at: https://www.frontiersin.org/articles/10.3389/fphys.2022.906146/full#supplementary-material

REFERENCES

Ahola, A., Pölönen, R.-P., Aalto-Setälä, K., and Hyttinen, J. (2018). Simultaneous Measurement of Contraction and Calcium Transients in Stem Cell Derived Cardiomyocytes. *Ann. Biomed. Eng.* 46, 148–158. doi:10.1007/s10439-017-1933-2

Antzelevitch, C., Shimizu, W., Yan, G.-X., Sicouri, S., Weissenburger, J., and Nesterenko, V. V. (1999). The M Cell: Its Contribution to the ECG and to Normal and Abnormal Electrical Function of the Heart. *J. Cardiovasc. Electrophysiol.* 10, 1124–1152. doi:10.1111/j.1540-8167.1999.tb00287.x

Awinda, P. O., Bishaw, Y., Watanabe, M., Guglin, M. A., Campbell, K. S., and Tanner, B. C. W. (2020). Effects of Mavacamten on Ca2+ Sensitivity of Contraction as Sarcomere Length Varied in Human Myocardium. *Br. J. Pharmacol.* 177, 5609–5621. doi:10.1111/bph.15271

Bartolucci, C., Passini, E., Hyttinen, J., Paci, M., and Severi, S. (2020). Simulation of the Effects of Extracellular Calcium Changes Leads to a Novel Computational Model of Human Ventricular Action Potential with a Revised Calcium Handling. *Front. Physiol.* 11, 1–20. doi:10.3389/fphys.2020.00314

Campbell, S. G., Lionetti, F. V., Campbell, K. S., and McCulloch, A. D. (2010). Coupling of Adjacent Tropomyosins Enhances Cross-Bridge-Mediated Cooperative Activation in a Markov Model of the Cardiac Thin Filament. *Biophys. J.* 98, 2254–2264. doi:10.1016/j.bpj.2010.02.010

Clancy, C. E., and Rudy, Y. (2002). Na+ Channel Mutation that Causes Both Brugada and Long-QT Syndrome Phenotypes: A Simulation Study of Mechanism. *Circulation* 105, 1208–1213. doi:10.1161/hc1002.105183

D'Errico, J. (2022). Fminsearchbnd, Fminsearchcon. MATLAB Cent. File Exch. Available at: https://www.mathworks.com/matlabcentral/fileexchange/8277-fminsearchbnd-fminsearchcon.

Desantiago, J., Ai, X., Islam, M., Acuna, G., Ziolo, M. T., Bers, D. M., et al. (2008). Arrhythmogenic Effects of β2-adrenergic Stimulation in the Failing Heart Are Attributable to Enhanced Sarcoplasmic Reticulum Ca Load. *Circ. Res.* 102, 1389–1397. doi:10.1161/CIRCRESAHA.107.169011

Dupuis, L. J., Lumens, J., Arts, T., and Delhaas, T. (2018). High Tension in Sarcomeres Hinders Myocardial Relaxation: A Computational Study. *PLoS One* 13, e0204642. doi:10.1371/journal.pone.0204642

Dupuis, L. J., Lumens, J., Arts, T., and Delhaas, T. (2016). Mechano-chemical Interactions in Cardiac Sarcomere Contraction: A Computational Modeling Study. *PLoS Comput. Biol.* 12, 1–20. doi:10.1371/journal.pcbi.1005126

Dutta, S., Chang, K. C., Beattie, K. A., Sheng, J., Tran, P. N., Wu, W. W., et al. (2017). Optimization of an In Silico Cardiac Cell Model for Proarrhythmia Risk Assessment. *Front. Physiol.* 8, 1–15. doi:10.3389/fphys.2017.00616

Forouzandehmehr, M., Ghoytasi, I., Shamloo, A., and Ghosi, S. (2022). Particles in Coronary Circulation: A Review on Modelling for Drug Carrier Design. *Mat. Des.* 216, 110511. doi:10.1016/j.matdes.2022.110511

Fülöp, G., Oláh, A., Csipo, T., Kovács, Á., Pórszász, R., Veress, R., et al. (2021). Omecamtiv Mecarbil Evokes Diastolic Dysfunction and Leads to Periodic Electromechanical Alternans. *Basic Res. Cardiol.* 116, 1–16. doi:10.1007/s00395-021-00866-8

Guo, D., Liu, Q., Liu, T., Elliott, G., Gingras, M., Kowey, P. R., et al. (2011). Electrophysiological Properties of HBI-3000: A New Antiarrhythmic Agent with Multiple-Channel Blocking Properties in Human Ventricular Myocytes. *J. Cardiovasc. Pharmacol.* 57, 79–85. doi:10.1097/FJC.0b013e3181ffe8b3

Haynes, P., Nava, K. E., Lawson, B. A., Chung, C. S., Mitov, M. I., Campbell, S. G., et al. (2014). Transmural Heterogeneity of Cellular Level Power Output Is Reduced in Human Heart Failure. *J. Mol. Cell. Cardiol.* 72, 1–8. doi:10.1016/j.yjmcc.2014.02.008

Janssen, P. M. L., and Periasamy, M. (2007). Determinants of Frequency-dependent Contraction and Relaxation of Mammalian Myocardium. *J. Mol. Cell. Cardiol.* 43, 523–531. doi:10.1016/j.yjmcc.2007.08.012

Katz, A. M. (1973). Effects of Ischemia on the Contractile Processes of Heart Muscle. *Am. J. Cardiol.* 32, 456–460. doi:10.1016/S0002-9149(73)80036-0

Kernik, D. C., Yang, P.-C., Kurokawa, J., Wu, J. C., and Clancy, C. E. (2020). A Computational Model of Induced Pluripotent Stem-Cell Derived Cardiomyocytes for High Throughput Risk Stratification of KCNQ1 Genetic Variants. *PLOS Comput. Biol.* 16, e1008109. doi:10.1371/journal.pcbi.1008109

Koivumäki, J. T., Naumenko, N., Tuomainen, T., Takalo, J., Oksanen, M., Puttonen, K. A., et al. (2018). Structural Immaturity of Human iPSC-Derived Cardiomyocytes: In Silico Investigation of Effects on Function and Disease Modeling. *Front. Physiol.* 9, 1–17. doi:10.3389/fphys.2018.00080

Land, S., Niederer, S. A., Louch, W. E., Sejersted, O. M., and Smith, N. P. (2013). Integrating Multi-Scale Data to Create a Virtual Physiological Mouse Heart. *Interface Focus* 3. doi:10.1098/rsfs.2012.0076

Land, S., Park-Holohan, S. J., Smith, N. P., dos Remedios, C. G., Kentish, J. C., and Niederer, S. A. (2017). A Model of Cardiac Contraction Based on Novel Measurements of Tension Development in Human Cardiomyocytes. *J. Mol. Cell. Cardiol.* 106, 68–83. doi:10.1016/j.yjmcc.2017.03.008

Leitch, S. (1996). Effect of Raised Extracellular Calcium on Characteristics of the Guinea-pig Ventricular Action Potential. *J. Mol. Cell. Cardiol.* 28, 541–551. doi:10.1006/jmcc.1996.0050

Li, P., and Rudy, Y. (2011). A Model of Canine Purkinje Cell Electrophysiology and Ca 2+ Cycling. *Circ. Res.* 109, 71–79. doi:10.1161/CIRCRESAHA.111.246512

Li, Z., Mirams, G. R., Yoshinaga, T., Ridder, B. J., Han, X., Chen, J. E., et al. (2020). General Principles for the Validation of Proarrhythmia Risk Prediction Models: An Extension of the CiPA In Silico Strategy. *Clin. Pharmacol. Ther.* 107, 102–111. doi:10.1002/cpt.1647

Lyon, A., Dupuis, L. J., Arts, T., Crijns, H. J. G. M., Prinzen, F. W., Delhaas, T., et al. (2020). Differentiating the Effects of β-adrenergic Stimulation and Stretch on Calcium and Force Dynamics Using a Novel Electromechanical Cardiomyocyte Model. *Am. J. Physiol. - Hear. Circ. Physiol.* 319, H519–H530. doi:10.1152/ajpheart.00275.2020

Margara, F., Wang, Z. J., Levrero-Florencio, F., Santiago, A., Vázquez, M., Bueno-Orovio, A., et al. (2021). In-silico Human Electro-Mechanical Ventricular Modelling and Simulation for Drug-Induced Pro-arrhythmia and Inotropic Risk Assessment. *Prog. Biophys. Mol. Biol.* 159, 58–74. doi:10.1016/j.pbiomolbio.2020.06.007

Mulieri, L. A., Hasenfuss, G., Leavitt, B., Allen, P. D., and Alpert, N. R. (1992). Altered Myocardial Force-Frequency Relation in Human Heart Failure. *Circulation* 85, 1743–1750. doi:10.1161/01.CIR.85.5.1743

Musuamba, F. T., Skottheim Rusten, I., Lesage, R., Russo, G., Bursi, R., Emili, L., et al. (2021). Scientific and Regulatory Evaluation of Mechanistic In Silico Drug and Disease Models in Drug Development: Building Model Credibility. *CPT Pharmacometrics Syst. Pharmacol.* 10, 804–825. doi:10.1002/psp4.12669

Nagy, N., Acsai, K., Kormos, A., Sebők, Z., Farkas, A. S., Jost, N., et al. (2013). [Ca2+]i-induced Augmentation of the Inward Rectifier Potassium Current (Ik1) in Canine and Human Ventricular Myocardium. *Pflügers Arch. - Eur. J. Physiol.* 465, 1621–1635. doi:10.1007/s00424-013-1309-x

Nguyen, N., Nguyen, W., Nguyenton, B., Ratchada, P., Page, G., Miller, P. E., et al. (2017). Adult Human Primary Cardiomyocyte-Based Model for the Simultaneous Prediction of Drug-Induced Inotropic and Pro-arrhythmia Risk. *Front. Physiol.* 8, 1–16. doi:10.3389/fphys.2017.01073

Niederer, S. A., Lumens, J., and Trayanova, N. A. (2019). Computational Models in Cardiology. *Nat. Rev. Cardiol.* 16, 100–111. doi:10.1038/s41569-018-0104-y

Novak, A., Barad, L., Zeevi-Levin, N., Shick, R., Shtrichman, R., Lorber, A., et al. (2012). Cardiomyocytes Generated from CPVT D307H Patients Are Arrhythmogenic in Response to β-adrenergic Stimulation. *J. Cell. Mol. Med.* 16, 468–482. doi:10.1111/j.1582-4934.2011.01476.x

O'Hara, T., Virág, L., Varró, A., and Rudy, Y. (2011). Simulation of the Undiseased Human Cardiac Ventricular Action Potential: Model Formulation and Experimental Validation. *PLoS Comput. Biol.* 7, e1002061. doi:10.1371/journal.pcbi.1002061

Paci, M., Casini, S., Bellin, M., Hyttinen, J., and Severi, S. (2018a). Large-Scale Simulation of the Phenotypical Variability Induced by Loss-Of-Function Long QT Mutations in Human Induced Pluripotent Stem Cell Cardiomyocytes. *Int. J. Mol. Sci.* 19, 3583. doi:10.3390/ijms19113583

Paci, M., Koivumäki, J. T., Lu, H. R., Gallacher, D. J., Passini, E., and Rodriguez, B. (2021). Comparison of the Simulated Response of Three In Silico Human Stem Cell-Derived Cardiomyocytes Models and *In Vitro* Data under 15 Drug Actions. *Front. Pharmacol.* 12, 1–16. doi:10.3389/fphar.2021.604713

Paci, M., Passini, E., Klimas, A., Severi, S., Hyttinen, J., Rodriguez, B., et al. (2018b). "In Silico Populations Optimized on Optogenetic Recordings Predict Drug Effects in Human Induced Pluripotent Stem Cell-Derived Cardiomyocytes," in 2018 Computing in Cardiology Conference (CinC),Computing in Cardiology Conference (CinC). doi:10.22489/CinC.2018.086

Paci, M., Passini, E., Severi, S., Hyttinen, J., and Rodriguez, B. (2017). Phenotypic Variability in LQT3 Human Induced Pluripotent Stem Cell-Derived

Cardiomyocytes and Their Response to Antiarrhythmic Pharmacologic Therapy: An In Silico Approach. *Hear. Rhythm* 14, 1704–1712. doi:10.1016/j.hrthm.2017.07.026

Papadaki, M., Kampaengsri, T., Barrick, S. K., Campbell, S. G., von Lewinski, D., Rainer, P. P., et al. (2022). Myofilament Glycation in Diabetes Reduces Contractility by Inhibiting Tropomyosin Movement, Is Rescued by cMyBPC Domains. *J. Mol. Cell. Cardiol.* 162, 1–9. doi:10.1016/j.yjmcc.2021.08.012

Passini, E., Britton, O. J., Lu, H. R., Rohrbacher, J., Hermans, A. N., Gallacher, D. J., et al. (2017). Human In Silico Drug Trials Demonstrate Higher Accuracy Than Animal Models in Predicting Clinical Pro-arrhythmic Cardiotoxicity. *Front. Physiol.* 8, 1–15. doi:10.3389/fphys.2017.00668

Peyronnet, R., Nerbonne, J. M., and Kohl, P. (2016). Cardiac Mechano-Gated Ion Channels and Arrhythmias. *Circ. Res.* 118, 311–329. doi:10.1161/CIRCRESAHA.115.305043

Pieske, B., Kretschmann, B., Meyer, M., Holubarsch, C., Weirich, J., Posival, H., et al. (1995). Alterations in Intracellular Calcium Handling Associated with the Inverse Force-Frequency Relation in Human Dilated Cardiomyopathy. *Circulation* 92, 1169–1178. doi:10.1161/01.CIR.92.5.1169

Pieske, B., Sütterlin, M., Schmidt-Schweda, S., Minami, K., Meyer, M., Olschewski, M., et al. (1996). Diminished Post-rest Potentiation of Contractile Force in Human Dilated Cardiomyopathy: Functional Evidence for Alterations in Intracellular Ca2+ Handling. *J. Clin. Invest.* 98, 764–776. doi:10.1172/JCI118849

Pogwizd, S. M., Schlotthauer, K., Li, L., Yuan, W., and Bers, D. M. (2001). Arrhythmogenesis and Contractile Dysfunction in Heart Failure. *Circ. Res.* 88, 1159–1167. doi:10.1161/hh1101.091193

Rahman, M. A., Ušaj, M., Rassier, D. E., and Månsson, A. (2018). Blebbistatin Effects Expose Hidden Secrets in the Force-Generating Cycle of Actin and Myosin. *Biophys. J.* 115, 386–397. doi:10.1016/j.bpj.2018.05.037

Rice, J. J., Wang, F., Bers, D. M., and De Tombe, P. P. (2008). Approximate Model of Cooperative Activation and Crossbridge Cycling in Cardiac Muscle Using Ordinary Differential Equations. *Biophys. J.* 95, 2368–2390. doi:10.1529/biophysj.107.119487

Rossman, E. I., Petre, R. E., Chaudhary, K. W., Piacentino, V., Janssen, P. M. L., Gaughan, J. P., et al. (2004). Abnormal Frequency-dependent Responses Represent the Pathophysiologic Signature of Contractile Failure in Human Myocardium. *J. Mol. Cell. Cardiol.* 36, 33–42. doi:10.1016/j.yjmcc.2003.09.001

Santini, L., Palandri, C., Nediani, C., Cerbai, E., and Coppini, R. (2020). Modelling Genetic Diseases for Drug Development: Hypertrophic Cardiomyopathy. *Pharmacol. Res.* 160, 105176. doi:10.1016/j.phrs.2020.105176

Sarkar, S. S., Trivedi, D. V., Morck, M. M., Adhikari, A. S., Pasha, S. N., Ruppel, K. M., et al. (2020). The Hypertrophic Cardiomyopathy Mutations R403Q and R663H Increase the Number of Myosin Heads Available to Interact with Actin. *Sci. Adv.* 6, 1–10. doi:10.1126/sciadv.aax0069

Severi, S., Corsi, C., and Cerbai, E. (2009). From *In Vivo* Plasma Composition to *In Vitro* Cardiac Electrophysiology and In Silico Virtual Heart: the Extracellular Calcium Enigma. *Philos. Trans. R. Soc. A Math. Phys. Eng. Sci.* 367, 2203–2223. doi:10.1098/rsta.2009.0032

Sheikh, F., Ouyang, K., Campbell, S. G., Lyon, R. C., Chuang, J., Fitzsimons, D., et al. (2012). Mouse and Computational Models Link Mlc2v Dephosphorylation to Altered Myosin Kinetics in Early Cardiac Disease. *J. Clin. Invest.* 122, 1209–1221. doi:10.1172/JCI61134

Toepfer, C. N., Garfinkel, A. C., Venturini, G., Wakimoto, H., Repetti, G., Alamo, L., et al. (2020). Myosin Sequestration Regulates Sarcomere Function, Cardiomyocyte Energetics, and Metabolism, Informing the Pathogenesis of Hypertrophic Cardiomyopathy. *Circulation* 141, 828–842. doi:10.1161/CIRCULATIONAHA.119.042339

Tomek, J., Bueno-Orovio, A., Passini, E., Zhou, X., Minchole, A., Britton, O., et al. (2019). Development, Calibration, and Validation of a Novel Human Ventricular Myocyte Model in Health, Disease, and Drug Block. *Elife* 8, 1–48. doi:10.7554/eLife.48890

Watson, S. A., Duff, J., Bardi, I., Zabielska, M., Atanur, S. S., Jabbour, R. J., et al. (2019). Biomimetic Electromechanical Stimulation to Maintain Adult Myocardial Slices *In Vitro*. *Nat. Commun.* 10. doi:10.1038/s41467-019-10175-3

Conflict of Interest: The authors declare that the research was conducted in the absence of any commercial or financial relationships that could be construed as a potential conflict of interest.

Publisher's Note: All claims expressed in this article are solely those of the authors and do not necessarily represent those of their affiliated organizations, or those of the publisher, the editors and the reviewers. Any product that may be evaluated in this article, or claim that may be made by its manufacturer, is not guaranteed or endorsed by the publisher.

frontiers | Frontiers in Physiology

ORIGINAL RESEARCH
published: 08 June 2022
doi: 10.3389/fphys.2022.886723

Multi-Domain Variational Autoencoders for Combined Modeling of MRI-Based Biventricular Anatomy and ECG-Based Cardiac Electrophysiology

Marcel Beetz[1]*, *Abhirup Banerjee*[1,2] *and Vicente Grau*[1]

[1]Department of Engineering Science, Institute of Biomedical Engineering (IBME), University of Oxford, Oxford, United Kingdom, [2]Radcliffe Department of Medicine, Division of Cardiovascular Medicine, University of Oxford, Oxford, United Kingdom

Human cardiac function is characterized by a complex interplay of mechanical deformation and electrophysiological conduction. Similar to the underlying cardiac anatomy, these interconnected physiological patterns vary considerably across the human population with important implications for the effectiveness of clinical decision-making and the accuracy of computerized heart models. While many previous works have investigated this variability separately for either cardiac anatomy or physiology, this work aims to combine both aspects in a single data-driven approach and capture their intricate interdependencies in a multi-domain setting. To this end, we propose a novel multi-domain Variational Autoencoder (VAE) network to capture combined Electrocardiogram (ECG) and Magnetic Resonance Imaging (MRI)-based 3D anatomy information in a single model. Each VAE branch is specifically designed to address the particular challenges of the respective input domain, enabling efficient encoding, reconstruction, and synthesis of multi-domain cardiac signals. Our method achieves high reconstruction accuracy on a United Kingdom Biobank dataset, with Chamfer Distances between reconstructed and input anatomies below the underlying image resolution and ECG reconstructions outperforming multiple single-domain benchmarks by a considerable margin. The proposed VAE is capable of generating realistic virtual populations of arbitrary size with good alignment in clinical metrics between the synthesized and gold standard anatomies and Maximum Mean Discrepancy (MMD) scores of generated ECGs below those of comparable single-domain approaches. Furthermore, we observe the latent space of our VAE to be highly interpretable with separate components encoding different aspects of anatomical and ECG variability. Finally, we demonstrate that the combined anatomy and ECG representation improves the performance in a cardiac disease classification task by 3.9% in terms of Area Under the Receiver Operating Characteristic (AUROC) curve over the best corresponding single-domain modeling approach.

Keywords: multi-domain variational autoencoder, combined electrocardiogram and cardiac anatomy generation, cardiac disease classification, point clouds, cine magnetic resonance imaging, cardiac electrophysiology, time series analysis, geometric deep learning

OPEN ACCESS

Edited by:
Gernot Plank,
Medical University of Graz, Austria

Reviewed by:
Karli Gillette,
Medical University of Graz, Austria
Aurore Lyon,
Maastricht University, Netherlands

***Correspondence:**
Marcel Beetz
marcel.beetz@eng.ox.ac.uk

Specialty section:
This article was submitted to Cardiac Electrophysiology, a section of the journal Frontiers in Physiology

Received: *28 February 2022*
Accepted: *02 May 2022*
Published: *08 June 2022*

Citation:
Beetz M, Banerjee A and Grau V (2022) Multi-Domain Variational Autoencoders for Combined Modeling of MRI-Based Biventricular Anatomy and ECG-Based Cardiac Electrophysiology. Front. Physiol. 13:886723. doi: 10.3389/fphys.2022.886723

1 INTRODUCTION

Healthy cardiac function of the human heart consists of complex interactions between anatomical deformations and electrophysiological conduction patterns which vary considerably between individuals in the population. Accounting for this variability is of high importance in clinical practice as it heavily influences the accuracy of cardiovascular disease diagnosis and treatment. Consequently, it is also a core objective of computational modeling approaches of cardiac anatomy and function to correctly represent these inter-person differences and enable more personalized and accurate computer models. Two of the most commonly used modalities in clinical practice to assess healthy cardiac function on both an individual and a population level are, respectively, the cardiac Magnetic Resonance Imaging (MRI) (Stokes and Roberts-Thomson, 2017) and the Electrocardiogram (ECG) (Macfarlane and Lawrie, 2010).

Due to its high soft-tissue contrast and lack of ionizing radiation combined with high temporal resolution, cardiac cine MRI is currently considered the gold-standard for image-based cardiac function analysis (Stokes and Roberts-Thomson, 2017). It has also been extensively used to determine normal cardiac behavior and investigate inter-patient differences. To this end, several image-based atlases of the heart with associated statistical shape models of cardiac anatomy and function have been developed for a variety of different populations and cardiac substructures (Bai et al., 2015; Nagel et al., 2021). In these approaches, a mean template shape is typically created from a distribution of image-derived cardiac shapes, followed by Principal Component Analysis (PCA) to model population variability (Tavakoli and Amini, 2013; Bai et al., 2015; Piazzese et al., 2017). More recently, deep learning approaches based on Variational Autoencoders (VAE) or Generative Adversarial Networks (GAN) have also been explored for this purpose (Litjens et al., 2017; Bello et al., 2019; Biffi et al., 2020; Gilbert et al., 2020; Beetz et al., 2021b; Rezaei, 2021). The resulting statistical models have a variety of use cases, including the prediction of certain cardiac disease events (Acero et al., 2022), the association analysis of cardiac shape and disease risk factors (Mauger et al., 2019), and the generation of virtual populations for physiological simulations (Mincholé et al., 2019; Niederer et al., 2020; Romero et al., 2021).

The ECG offers an easy and non-invasive procedure to capture and visualize the electrical conduction patterns of the heart and is therefore widely used in clinical diagnosis and electrophysiology modeling (Macfarlane and Lawrie, 2010). Similar to cine MRI, considerable research has been focused on capturing population variability in the ECG signals. For example, PCA has been applied to ECG data to derive respiratory signals (Langley et al., 2009), estimate the effect of diabetes on ECG parameters (Kalpana et al., 2013), or classify ECG beats (Martis et al., 2013). GAN and VAE-based approaches have more recently been investigated for the task of virtual ECG generation and to analyze ECG shape variations across the population (Delaney et al., 2019; Zhu et al., 2019; Kuznetsov et al., 2021).

However, in all aforementioned works, inter-subject variability was modeled based on either MRI or ECG information separately in a single-domain setting. This neglects the complex, non-linear relationships between anatomical deformations and electrophysiological conduction, and therefore inhibits a more holistic understanding of cardiac function and its variability across the human population. Hence, the objective of this work is to combine both cine MRI-based cardiac anatomy information and ECG-based electrophysiology information across a whole population in a single data-driven modeling approach and study their variations and interactions in this multi-domain setting. To this end, we propose a multi-domain variational autoencoder framework consisting of multiple domain-specific branches and a latent space shared across all branches for cross-domain information exchange. The design of the individual branches, loss function, and training procedure are specifically tailored to a multi-domain dataset consisting of both MRI-based cardiac anatomy information and ECG-based electrophysiology signals. Anatomical information is represented as high-resolution and multi-class 3D point clouds reconstructed from cine MRI acquisitions and can be efficiently processed by the point cloud-based deep learning branches. Anatomies at both the End-Diastolic (ED) and End-Systolic (ES) phases of the cardiac cycle are used together with the corresponding ECG signals to give the network access to both spatial and temporal information.

Similar to the single-domain shape modeling approaches, the multi-domain VAE has a variety of possible use cases in both clinical and research settings, such as problem-specific dimensionality reduction of high-dimensional data, interpretable shape analysis of both spatial and temporal data, explainable cardiac disease identification and prediction, or the generation of virtual population cohorts for mechanical and electrophysiological computer simulations or to augment datasets for training machine learning or deep learning classifiers or regressors.

To the best of our knowledge, this is the first deep learning method to capture the combined cardiac anatomy and electrophysiology data in a single model. In summary, our contributions are as follows:

- We present a novel multi-domain variational autoencoder capable of modeling combined cardiac anatomy and ECG data.
- We provide a detailed explanation of the preprocessing steps, network architecture, loss function, and training procedure.
- We assess the VAE's ability to reconstruct multi-domain data on a United Kingdom Biobank dataset (Petersen et al., 2015, 2013) of 1,000 cases and compare the reconstruction performance with multiple single-domain benchmarks.
- We evaluate the VAE's capability to generate realistic virtual populations of combined anatomy and ECG data and perform a comparative analysis with the gold standard test set and multiple single-domain benchmarks.
- We investigate the VAE's latent space with regards to its interpretability and degree of disentanglement.

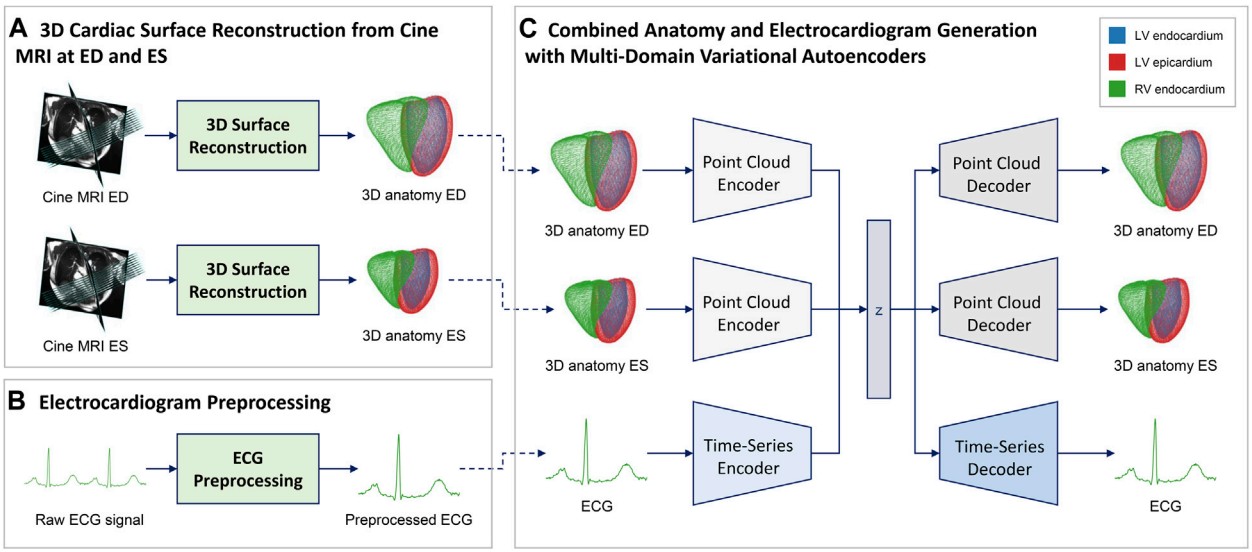

FIGURE 1 | Overview of the proposed combined anatomy and ECG modeling pipeline. We first reconstruct point cloud representations of the 3D biventricular anatomy at the ED and ES phase of the cardiac cycle **(A)** and preprocess the raw ECG acquisitions **(B)** to create a multi-domain dataset. We then use this data to train a multi-domain variational autoencoder **(C)** to capture combined cardiac anatomy and electrophysiology information in a single model. The VAE architecture **(C)** consists of three separate encoder-decoder branches, one for each network input (ED anatomy, ES anatomy, ECG), that share a common latent space for cross-modal information exchange. Each branch architecture is specifically tailored to the requirements of the respective input type, i.e. point clouds for anatomy and time series for ECG processing (**Figure 2**).

- We develop and evaluate a machine learning classifier for cardiac disease prediction from the VAE's latent space.
- We include a detailed discussion of our findings and a pertinent literature review.

A preliminary version of this work was presented in Beetz et al. (2022). This paper provides a more comprehensive explanation of the methodology, additional new experiments including comparisons with various benchmarks and application to 150 pathological cases, and a substantially expanded discussion and literature review.

2 MATERIALS AND METHODS

In this section, we describe the multi-domain dataset used for method development (**Section 2.1**) and explain the required preprocessing steps (**Section 2.2**) as well as our method's architecture (**Section 2.3**, **Section 2.4**, **Section 2.5**), loss function (**Section 2.6**), and training procedure (**Section 2.7**).

2.1 Dataset

We conduct our research work using 1,300 subjects from the United Kingdom Biobank imaging study (Petersen et al., 2013) for which paired cardiac cine Magnetic Resonance (MR) images and electrocardiograms were acquired (Petersen et al., 2015). All cine MR short-axis images had a voxel resolution of $1.8 \times 1.8 \times 8.0\ mm^3$ and typical image dimensions of $208 \times 168–210$, while the cine MR long-axis images had a voxel resolution of $1.8 \times 1.8 \times 6.0\ mm^3$ with typical image dimensions of $208 \times 126–180$ (Petersen et al., 2015). 1,150 subjects were assumed to be healthy individuals, while 150 cases suffered from at least one pathology related to the cardiovascular system. These cardiovascular disease cases were identified following the same procedure outlined in Bai et al. (2020), based on the self-reported disease codes in the United Kingdom Biobank (see **Supplementary Table S1**). We select 1,000 presumably healthy cases for the initial method development and the experiments in **Section 3.2**, **Section 3.3**, **Section 3.4**, and **Section 3.5**. The dataset is randomly split into training, validation, and test sets of sizes ~800, ~50, and ~150, respectively, to give the network access to enough cases for training, while at the same time retaining a sufficiently high number of cases for method evaluation. We use the remaining 150 healthy and 150 diseased cases for our cardiac disease classification experiment described in **Section 3.6**.

2.2 Domain-Specific Data Preprocessing

In order to extract the anatomical and physiological information required for training our multi-domain VAE from the raw cine MRI and ECG signals, we first apply various preprocessing steps to the data from each modality (**Figure 1A,B**). Regarding the imaging data (**Figure 1A**), we first segment both short- and long-axis images of the cine MRI acquisition into four classes that delineate the anatomical substructures of interest (Left Ventricular (LV) cavity, LV myocardium, Right Ventricular (RV) cavity, and background) using the fully convolutional neural networks as detailed in Banerjee et al. (2021) and Bai et al. (2018). Next, we use the obtained segmentation masks from the short-axis images to identify the ED and ES phases of the cine MRI sequence for each case as anatomical representations of the extreme ends of the cardiac cycle (Banerjee et al., 2021). The final

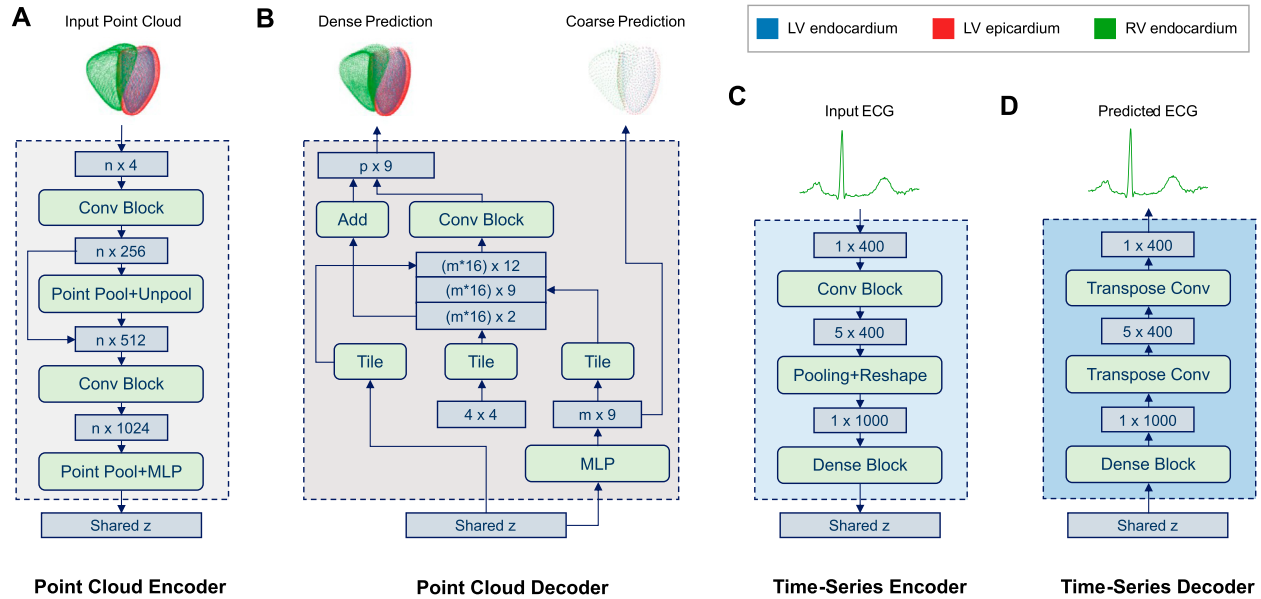

FIGURE 2 | Overview of the encoder and decoder architectures of both the point cloud **(A,B)** and time series **(C,D)** branches of the multi-domain VAE. The input point cloud **(A)** encodes the biventricular anatomy as a set (n = 36,000) of 4D vectors (x,y,z coordinates and the class label of each point), while a separate set of 3D point coordinates is used for each of the three cardiac substructures in the output point cloud **(B)**. The point cloud decoder **(B)** outputs both a coarse, low-dimensional (2,250 points) and a dense, high-dimensional (36,000 points) representation of the cardiac anatomy. The former represents the final output used for further processing, while the latter primarily facilitates the training process in this work (**Eq. 5**) by first focusing on an approximate reconstruction and later putting more emphasis on the dense output. Both input and output ECG time series **(C,D)** are represented as 400-dimensional vectors. Both encoders **(A,C)** are tasked with predicting the shared latent space *z*. The time-series decoder **(D)** follows a symmetric design to its encoder **(C)** and aims to reconstruct the input ECG signal from the latent space during training. (Background colors of architecture blocks are consistent with **Figure 1**)

3D point clouds of the biventricular anatomy are reconstructed at both ED and ES phases from the selected slices using the approach described in Beetz et al. (2021a). For ECG data (**Figure 1B**), the United Kingdom Biobank provides both a raw acquisition consisting of multiple heart beats, as well as a combined ECG signal that averages the information from multiple cardiac cycles into a single one-heartbeat representation for each lead. In this work, we focus on the lead II signals, since they provide a good view of the P and R waves, are predictive of many cardiac arrhythmias, and are also used by previous methods (Delaney et al., 2019; Wang et al., 2019). We choose the average lead II signal in each case as our ECG data and apply the standardization step, i.e. subtracting the mean value from each data instance and dividing by the standard deviation, to each resulting time series. The preprocessed ECG is then combined with the corresponding 3D point cloud reconstructions of the biventricular anatomy at the ED and ES phases of each case to form the multi-domain dataset used for method development.

2.3 Multi-Domain Variational Autoencoder

In order to capture the combined anatomy and ECG data obtained from the preprocessing steps, we propose a multi-domain β-VAE (Higgins et al., 2017) architecture with three branches that share a common latent space for inter-modal information sharing (**Figure 1C**).

Each of the three branches has an encoder-decoder structure and is responsible for processing one of the three inputs, namely the ED anatomy point cloud, the ES anatomy point cloud, and the ECG. The encoder outputs of the three branches are tasked with predicting the mean and standard deviation vectors of the multivariate Gaussian distribution of the latent space following the standard variational autoencoder setting (Kingma and Welling, 2013). A 12-dimensional vector is sampled from this distribution and passed into each decoder of the three branches which aim to reconstruct the input of their corresponding encoder branch. The reparameterization (Kingma and Welling, 2013) trick is applied during training. The architectures of each of the three branches are specifically designed to enable efficient processing of the respective data type (i.e. point clouds and time series) and are described in greater detail in **Section 2.4** and **Section 2.5**. The two anatomy branches share the same network architecture (**Section 2.4**) but maintain separate trainable network parameters, while the ECG branch exhibits a different design (**Section 2.5**).

2.4 Point Cloud Branches

The architecture of the two anatomy branches of the multi-domain VAE (**Figure 2A,B**) follows an extended version of the point completion network (Yuan et al., 2018) and its adaptations to cardiac image analysis (Beetz et al., 2021b).

The network input point clouds are encoded as sets of 36,000 4-dimensional vectors consisting of the 3D coordinates and the class label of each point which indicates its cardiac substructure (LV endocardium, LV epicardium, RV

endocardium). Point clouds are then passed through the encoder (**Figure 2A**), which resembles a multi-class extension of the Pointnet (Qi et al., 2017a) architecture. Similar to (Qi et al., 2017b), it consists of two stacked Pointnets that are connected via a skip connection as well as a pooling and an unpooling step. Furthermore, we add additional fully connected layers before the latent space to enable easier information sharing. The encoder outputs are then concatenated with the respective outputs of the other two branches before the variational sampling step is applied. The sampled latent space vector is then provided as input into the decoder (**Figure 2B**) where a multi-layer perceptron (MLP) is first tasked with creating a low-resolution multi-class point cloud with 2,250 points. This coarse point cloud aims to represent the biventricular anatomy on a global level and is primarily used to stabilize the training process of the network in the early stages. The second step of the decoder follows the design of FoldingNet (Yang et al., 2017) and processes the previous low-resolution output, the sampled latent space vector, and a set of tiled point grids to generate a high-resolution multi-class point cloud with 36,000 points as the final network output. For both the low and high resolution output point clouds, each class is represented by a separate set of 750 and 12,000 3D coordinates, respectively.

2.5 Time-Series Branches

The architecture of the ECG branch combines convolutional, pooling, and dense layers to capture both local and global patterns at different scales (**Figure 2C,D**). The encoder (**Figure 2C**) receives each ECG time series as a 400-dimensional input vector and passes it through two convolutional blocks, each of which consists of a 2D convolution, an Exponential Linear Unit (ELU) activation function, and a batch normalization layer. This is followed by an average pooling layer and two fully connected layers, which output the mean and standard deviation vectors of the multivariate normal distribution of the latent space, respectively. Next, the sampled vector z from the shared latent space distribution of the multi-branch autoencoder is fed through a dense block with two fully connected layers at the beginning of the decoder (**Figure 2D**). Subsequently, two transposed 2D convolutions are applied to obtain the 400-dimensional ECG time series reconstruction as the final network output.

2.6 Loss Function

Following the formulation of the β-VAE (Higgins et al., 2017) framework, our loss function L_{total} is composed of the sum of a reconstruction loss term L_{recon} and a regularizing term L_{KL} weighted by the parameter β, as

$$L_{total} = L_{recon} + \beta * L_{KL}. \tag{1}$$

We use the Kullback-Leibler divergence between the latent space distribution $Q(z|X)$ and the multivariate standard Gaussian prior distribution $P(z)$ as the regularizing loss term L_{KL}, where X refers to the VAE inputs and z to the VAE's latent space. This encourages each latent space component to follow a normal distribution with zero mean and standard deviation of one, which we choose as our prior $P(z)$.

$$L_{KL} = D_{KL}[Q(z|X) \| P(z)] \tag{2}$$

The reconstruction loss L_{recon} consists of three loss terms, one for each of the three branches in the multi-domain autoencoder. It incentivizes the VAE to output anatomy and ECG signals that are as close as possible to the respective inputs, which we consider to be our physiologically accurate gold standard for network training.

$$L_{recon} = L_{ED} + L_{ES} + \gamma * L_{ECG} \tag{3}$$

We introduce a parameter γ to control the importance of the ECG reconstruction during training.

We choose the mean squared error between the reconstructed ECG signals x_n and the gold standard ECG signals y_n across N time steps as our ECG loss term L_{ECG} to put more emphasis on correctly capturing less common values, such as the R-peak of the ECG signal.

$$L_{ECG} = \frac{1}{N} \sum_{n=1}^{N} (x_n - y_n)^2 \tag{4}$$

Each of the two anatomy loss terms L_{ED} and L_{ES} consists of the weighted sum of a coarse and a dense loss term over all three classes C corresponding to the respective cardiac substructures. We consider each part of the anatomy as equally important in the loss function and therefore do not use any class-specific weighting parameter.

$$L_{ED/ES} = \sum_{i=1}^{C} (L_{coarse,i} + \alpha * L_{dense,i}) \tag{5}$$

The coarse loss term measures the difference between the low-density output of the point cloud decoder and the ground truth, while the dense loss term compares the high-density output point cloud with the same ground truth. The weighting parameter α is used during training to first prioritize a good global structure of the coarse prediction and then gradually put increasing emphasis on local accuracy in the dense point cloud prediction.

Both the coarse and dense loss terms are calculated using the Chamfer Distance (CD) between the point cloud predicted by the network P_1 and the ground truth input point cloud P_2.

$$CD(P_1, P_2) = \frac{1}{2} \left(\frac{1}{|P_1|} \sum_{x \in P_1} \min_{y \in P_2} \|x - y\|_2 + \frac{1}{|P_2|} \sum_{y \in P_2} \min_{x \in P_1} \|y - x\|_2 \right) \tag{6}$$

Since the Chamfer Distance aims to find the closest point in the ground truth point cloud for each point in the input point cloud and vice versa, it can be considered as an approximate surface-to-surface distance on point cloud data between the respective anatomical shapes.

2.7 Implementation and Training

Our deep learning experiments are conducted on a GeForce RTX 2070 Graphics Card with 8 GB memory. We use TensorFlow (Abadi et al., 2016) and Scikit-learn (Pedregosa et al., 2011) for our deep learning and machine learning implementations, respectively. All VAEs are trained using the Adam optimizer

(Kingma and Ba, 2014) with a mini-batch size of 4, which we empirically found to provide a good balance between the memory and time constraints of our setup and the improved gradient quality during network training. The training duration is set to 150,000 steps based on the convergence of the loss function in the validation dataset. We set all loss weighting parameters to small values (α and β to 0.01, γ to 0.1) at the start of training to focus on obtaining a good coarse reconstruction of the two anatomy point clouds. We then gradually increase both α and γ to improve local prediction quality in both anatomy and ECG outputs. After both parameters have reached a value of 1, we increase the β parameter using a variation of the monotonic annealing schedule (Bowman et al., 2015) to improve the latent space quality. We stop the β value at 0.25, which we have empirically found to provide a good balance between overall reconstruction quality and latent space quality.

3 EXPERIMENTS AND RESULTS

We evaluate the proposed multi-domain VAE in terms of its performance in multiple tasks. First, we investigate its ability to correctly reconstruct paired input data from all three domains (**Section 3.2**). Second, we assess its ability to generate virtual populations of realistic ECGs and anatomy point clouds, both within and across the different domains (**Section 3.3**, **Section 3.4**). Third, we analyse the effect of certain latent space changes on the reconstructed ECG and anatomy shapes to gain a better understanding of the latent space distribution (**Section 3.5**). Finally, we compare the compressed latent space representation of the proposed multi-domain VAE with its single-domain counterparts in a cardiovascular disease classification task (**Section 3.6**). We propose multiple different metrics for the outlined experiments to account for the different data types and objectives (**Section 3.1**).

3.1 Evaluation Metrics

In order to assess the VAE's ECG reconstruction quality, we follow the metrics suggested by Zhu et al. (2019), which allows us to compare our results with the task of ECG-only generation without any image-based anatomy information. Accordingly, we use the Root Mean Squared Error (RMSE) as our first metric to quantify the distance between predicted ECG time series x and ground truth ECG time series y in our test dataset, each with a length of N time steps.

$$RMSE = \sqrt{\frac{1}{N}\sum_{n=1}^{N}(x_n - y_n)^2} \tag{7}$$

In addition, our second ECG reconstruction metric, Percentage Root Mean Squared Distance (PRD), provides a relative and normalized quantification of the reconstruction performance.

$$PRD = \sqrt{\frac{1}{\sum_{n=1}^{N} x_n^2}\sum_{n=1}^{N}(x_n - y_n)^2} * 100 \tag{8}$$

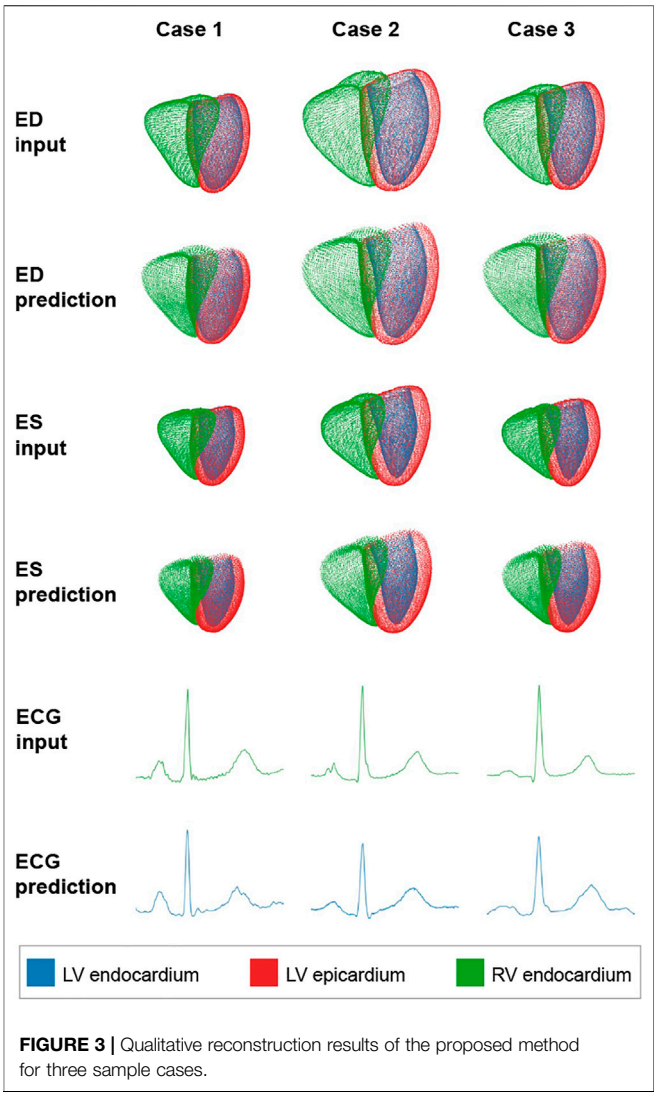

FIGURE 3 | Qualitative reconstruction results of the proposed method for three sample cases.

The anatomy reconstruction quality achieved by our VAE is evaluated using the average Chamfer Distance (**Eq. 6**) between the predicted and ground truth point clouds of the test dataset for both the ED and ES phases.

Similar to work by Delaney et al. (2019) on ECG-only generation, we propose the Maximum Mean Discrepancy (MMD) (Gretton et al., 2012) between two randomly generated distributions as a metric to assess the generative ability of our network. Hereby, K refers to the Gaussian kernel and x and y refer to the two sample distributions of sequences with sizes n and m respectively.

$$MMD = \left[\frac{1}{n(n-1)}\sum_{i=1}^{n}\sum_{j\neq i}^{n}K(x_i, x_j) + \frac{1}{m(m-1)}\sum_{i=1}^{m}\sum_{j\neq i}^{m}K(y_i, y_j) - \frac{2}{nm}\sum_{i=1}^{n}\sum_{j=1}^{m}K(x_i, y_j)\right]^{\frac{1}{2}} \tag{9}$$

In order to evaluate the quality of the generated anatomies at ED and ES separately, we select the widely used clinical evaluation metrics LV volume, RV volume, and myocardial mass. In

TABLE 1 | ECG reconstruction results of multiple methods on different datasets.

Method	Dataset	RMSE	PRD
BiLSTM-CNN GAN *	MIT-BIH	0.22	51.80
BiLSTM-GRU *	MIT-BIH	0.31	74.05
BiLSTM-LSTM *	MIT-BIH	0.35	84.80
BiLSTM-MLP *	MIT-BIH	0.61	147.73
ECG VAE	United Kingdom Biobank	0.16	26.51
Multi-Domain VAE (Proposed)	United Kingdom Biobank	0.17	27.45

**Values obtained directly from Zhu et al. (2019)*

TABLE 2 | ED and ES anatomy reconstruction results of our method on the test dataset.

Phase	Class	Chamfer Distance (mm)
ED	LV endocardium	1.37 (±0.40)
	LV epicardium	1.29 (±0.29)
	RV endocardium	1.42 (±0.29)
ES	LV endocardium	1.11 (±0.39)
	LV epicardium	1.23 (±0.45)
	RV endocardium	1.35 (±0.55)

Values represent mean (±standard deviation)

addition, we choose the Stroke Volume (SV) (**Eq. 10**) and Ejection Fraction (EF) (**Eq. 11**) metrics for both the LV and RV, to assess the correspondence between the generated anatomies at ED and ES.

$$SV = EDV - ESV. \tag{10}$$

$$EF = \frac{SV}{EDV} \times 100. \tag{11}$$

Here, EDV and ESV refer to ED volume and ES volume, respectively. Furthermore, we select the Area Under the Receiver Operating Characteristic (AUROC) curve to evaluate the performance in the binary cardiac disease classification task.

3.2 Reconstruction Ability

We first focus on the network's ability to accurately reconstruct both the two input point clouds and the input electrocardiogram. To this end, we pass the ED point cloud, the ES point cloud, and the ECG time series of each case of the test dataset through the network and compare the network's predicted outputs with the respective inputs. **Figure 3** shows input and prediction data of three such sample cases.

We observe good global and local alignment between inputs and predictions of both point cloud and time series data. Class information in the form of three anatomical substructures is also accurately reconstructed for both ED and ES point clouds. Next, we quantify our method's reconstruction ability on the test dataset using separate metrics for each modality.

For the ECG data, we select the RMSE (**Eq. 7**) and PRD (**Eq. 8**) metrics to determine our method's reconstruction error. We apply min-max normalization to both the input and predicted time series data before calculating the metrics, in order to compare the obtained values with the performance of multiple approaches proposed by Zhu et al. (2019) for single-domain ECG-only generation using the MIT-BIH dataset (Goldberger et al., 2000) (**Table 1**). In addition, we train and evaluate a separate VAE on only the ECG signals of our United Kingdom Biobank dataset as a benchmark method for our multi-domain VAE. It follows the encoder and decoder architecture presented in **Figure 2C,D** and uses the same ECG data and preprocessing steps as our proposed approach, allowing for a direct comparison (**Table 1**).

We find that the proposed multi-domain VAE method achieves lower reconstruction errors than the ones reported by Zhu et al. (2019) for any of their architectures, both in terms of

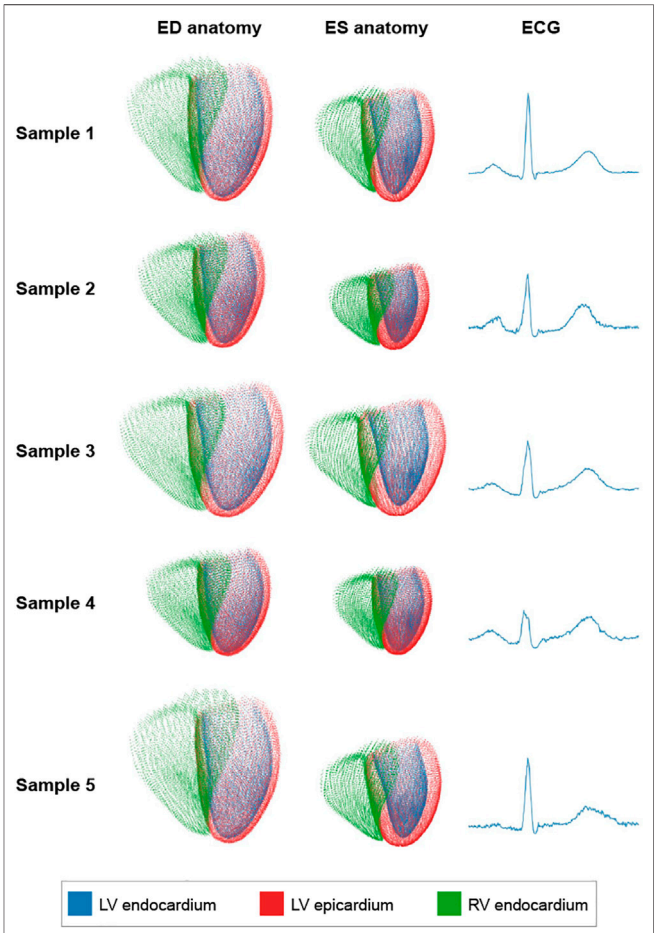

FIGURE 4 | Five randomly generated sample outputs where each row presents one case.

RMSE and PRD, despite the more challenging task of combined anatomy and electrocardiogram generation. However, this result should only be interpreted as an approximate marker of the reconstruction quality of our method instead of a direct outperformance, since different datasets and signal preprocessing steps were used in each analysis. For example, while the proposed approach uses the ECG signals averaged to one cardiac cycle from the United Kingdom Biobank, Zhu et al. (2019) did not mention the usage of averaged signals. Compared

TABLE 3 | ECG generation results of multiple methods based on different datasets.

Method	Dataset	MMD
4CNN GAN (Delaney et al., 2019)*	MIT-BIH	1.03×10^{-3}
4CNN BiLSTM GAN (Delaney et al., 2019)*	MIT-BIH	1.13×10^{-3}
VAE (Kuznetsov et al., 2021)*	LUDB	3.83×10^{-3}
Gold standard (test dataset)	United Kingdom Biobank	1.40×10^{-4}
ECG VAE	United Kingdom Biobank	3.05×10^{-5}
Multi-Domain VAE (Proposed)	United Kingdom Biobank	3.54×10^{-5}

**Values obtained directly from Delaney et al. (2019) or Kuznetsov et al. (2021)*

to the VAE trained on only ECG signals on the same United Kingdom Biobank dataset, our method achieves similar results for both evaluation metrics.

We quantify the reconstruction ability of our method for the point cloud data of the test dataset using the Chamfer Distance (**Eq. 6**). The resulting values for both ED and ES reconstructions, split by the three cardiac substructures, are reported in **Table 2**.

We find low distance values that are smaller than the voxel sizes of the image acquisitions ($1.8 \times 1.8 \times 8.0\,\mathrm{mm}^3$) used to generate the 3D point clouds for both the ED and ES phases as well as for all cardiac substructures. Distances are slightly larger for the right ventricle compared to left ventricular structures and for the ED phase than for the ES phase.

3.3 Generative Ability

In order to assess our network's ability to generate diverse populations with realistic anatomies and ECGs, we randomly sample from the latent space distribution and pass the resulting vectors through the three branches of the decoder. The mean and standard deviation values of the multivariate normal distribution of the latent space are determined based on the averaged encoder outputs of the training data. Hence, every component of the latent space is involved in the sampling step. Five randomly generated decoder outputs, each consisting of an ED anatomy point cloud, an ES anatomy point cloud, and an ECG, are depicted in **Figure 4**.

We observe that all outputs follow realistic shapes and sizes while maintaining a good amount of diversity between different cases. For example, the case in the first row exhibits considerably larger heart sizes at both ED and ES and a noticeably higher R-peak in the electrocardiogram as compared to the case in the fourth row.

Next, we evaluate the multi-domain VAE's capability for ECG generation on a population level. To this end, we synthesize 500 virtual electrocardiogram signals from randomly sampled latent space vectors and calculate their MMD (**Eq. 9**) with respect to the ECGs in our test dataset. We repeat the same procedure for the ECG-only VAE to enable a comparison of our multi-domain approach with a single-domain method on the same dataset. We also randomly split the test dataset into two subsets and determine the MMD between these two subsets to obtain a gold standard benchmark for desired ECG population similarity. The resulting values are reported in **Table 3**, together with MMD scores obtained from different approaches by Delaney et al. (2019) on the MIT-BIH dataset (Goldberger et al., 2000) and by Kuznetsov et al. (2021) on the LUDB dataset (Kalyakulina et al., 2020) for ECG-only generation.

TABLE 4 | Clinical metrics of meshed ED and ES anatomy point clouds generated by our method.

Phase	Clinical Metric	Gold Standard	Ours
ED	LV volume (ml)	141 (±30)	139 (±31)
	RV volume (ml)	170 (±34)	176 (±37)
ES	LV volume (ml)	59 (±15)	58 (±16)
	RV volume (ml)	78 (±20)	80 (±24)
ED/ES	LV mass (g)	102 (±28)	99 (±29)

Values represent mean (±standard deviation) in all cases

Our method achieves lower MMD scores than all other methods by a considerable margin. However, similar to the comparisons of our method's reconstruction performance, it should again be noted that the other approaches utilize different datasets and preprocessing steps. For example, Delaney et al. (2019) generated ECGs with multiple cardiac cycles, while Kuznetsov et al. (2021) focused on ECGs consisting of a single cardiac cycle. Furthermore, we find that the multi-domain VAE achieves a comparable MMD value as the ECG-only VAE. Comparing our method's MMD to the gold standard MMD achieved on the same test dataset, we observe a 74% lower MMD value.

The population quality of the generated ED and ES anatomies is assessed by calculating population-wide cardiac anatomy metrics, which are commonly used in clinical practice, for both the 500 generated point clouds and the point clouds of the test dataset that we consider the gold standard for this analysis. **Table 4** depicts the resulting values for the LV and RV volumes of each phase and the LV mass.

All clinical metrics show high degrees of similarity between generated and gold standard point cloud populations for both ED and ES phases, indicating that the VAE was able to successfully generate realistic virtual anatomies.

3.4 Combined Multi-Domain Generation

While our previous analyses have demonstrated the population quality of the generated ECGs and anatomies separately for each domain, we also want to investigate whether the same holds true for combined distributions of

TABLE 5 | Clinical function metrics of meshed point clouds generated by our method.

Clinical Metric	Gold Standard	Ours
LV EF (%)	58 (±8)	57 (±9)
LV SV (ml)	82 (±21)	81 (±22)
RV EF (%)	55 (±7)	55 (±8)
RV SV (ml)	92 (±19)	96 (±22)

Values represent mean (±standard deviation) in all cases

TABLE 6 | Difference in randomly generated multi-modal distributions combining MRI-based anatomy and ECG-based electrophysiology.

Metric	Gold standard	Ours
MMD	5.02×10^{-4}	4.72×10^{-4}

Values represent mean in all cases

these outputs. To this end, we first calculate common clinical metrics combining ED and ES anatomies (LV SV (**Eq. 10**), RV SV (**Eq. 10**), LV EF (**Eq. 11**), RV EF (**Eq. 11**)) to assess mechanical cardiac function for both our generated and test dataset populations (**Table 5**).

We observe very good alignment between the clinical function metrics from all generated and gold standard meshed point clouds, indicating that our method is capable of synthesizing accurate ED-ES anatomy pairs.

Results presented up to this point demonstrate the ability of our method to produce realistic ECG populations, as well as ED and ES point clouds. In order to evaluate whether the method generates anatomy and electrocardiogram outputs preserving the correspondence between them, we select all cardiac anatomy and function metrics from **Table 4** and **5** and concatenate them with the respective ECG signal to obtain a combined, low-dimensional representation of anatomy and ECG data for each case. We then calculate the MMD between the generated and test datasets consisting of the combined data representations for each case (**Table 6**). Similar to **Table 3**, we also determine the MMD between two random subsets of the test set as our gold standard value.

Our method obtains MMD values close to the gold standard ones, suggesting a good degree of coupling between the generated anatomy and ECG outputs.

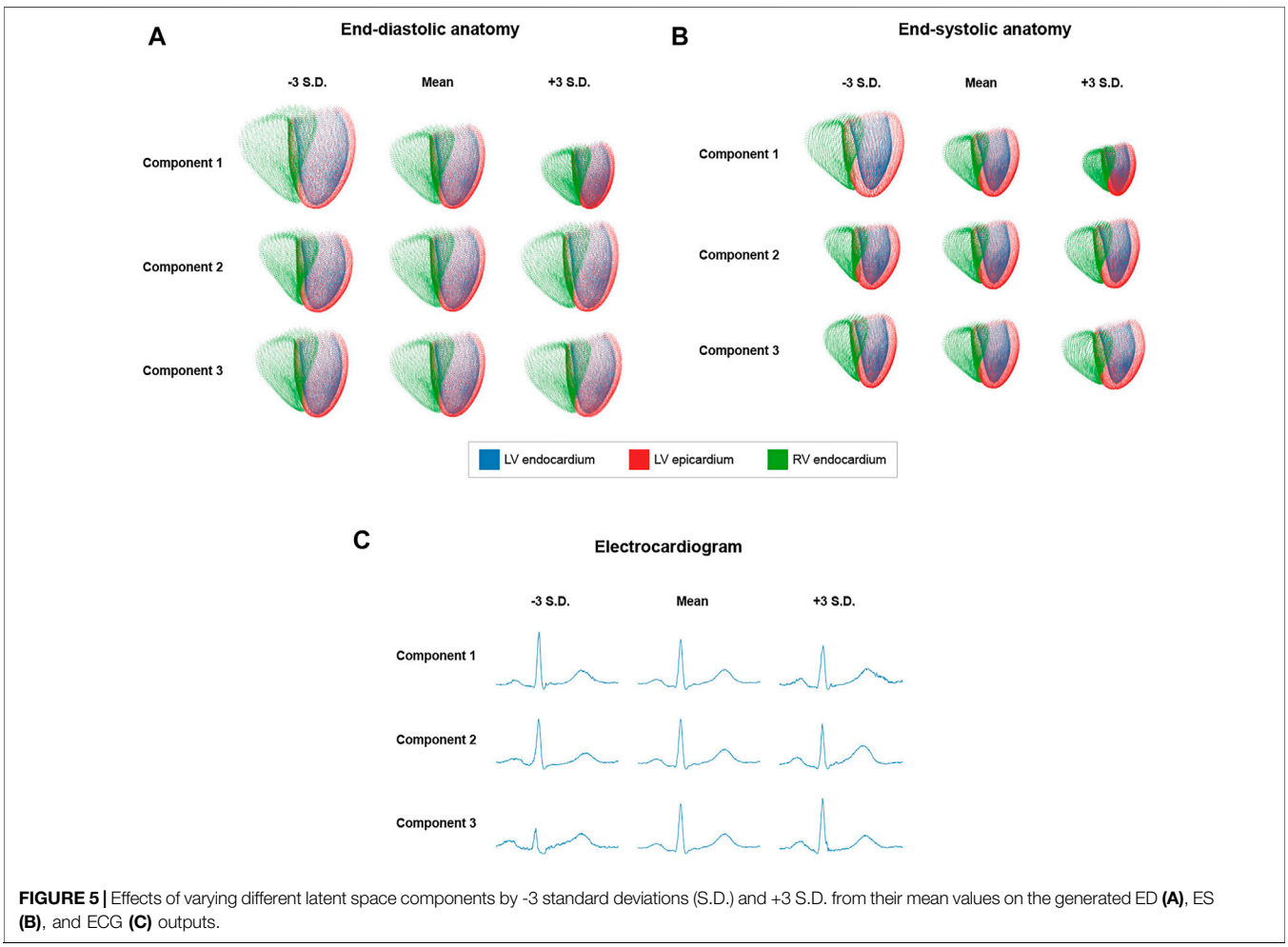

FIGURE 5 | Effects of varying different latent space components by -3 standard deviations (S.D.) and +3 S.D. from their mean values on the generated ED **(A)**, ES **(B)**, and ECG **(C)** outputs.

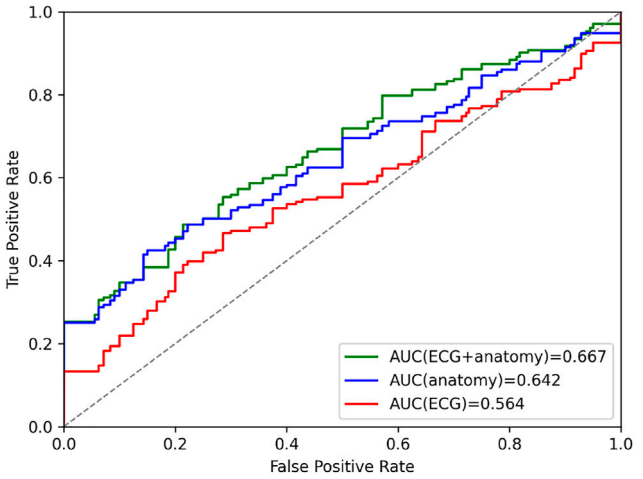

FIGURE 6 | Area under curve (AUC) prediction differences in ROC curves of the cardiac disease classification results based on latent space representations of VAEs trained on combined anatomy and ECG, only anatomy, and only ECG data.

3.5 Latent Space Analysis

A desirable feature of a variational autoencoder is the existence of an interpretable, disentangled latent space, in which different components are responsible for encoding various identifiable structural aspects of the generated output shapes. In order to analyze these characteristics for the proposed multi-domain VAE, we vary the values of each latent space dimension in both positive and negative directions while keeping the mean values for the remaining dimensions the same, and pass the resulting latent space vectors through the decoder to obtain outputs that correspond to the applied latent space changes. Three sample latent space components with easily visible effects on the generated multi-domain outputs are depicted in **Figure 5**.

Regarding the point cloud outputs, each component's variation results in similar changes to the ED (**Figure 5A**) and ES (**Figure 5B**) anatomies, respectively. Component 1 controls the overall size of the point cloud and component 2 causes a tilt in the basal short-axis plane of the heart, while component 3 converts elongated, thin hearts to shorter and wider ones. Regarding the ECG data (**Figure 5C**), component 3 changes both the R-peak height and existence of the S-wave, component 2 increases the height of the P-wave and T-wave, while component 1 has an effect on the height and width of the R-wave as well as the height and sharpness of both the P and T-waves.

3.6 Cardiac Disease Classification

In order to further explore the VAE's latent space, we investigate the utility of its compressed multi-domain representation of cardiac anatomy and physiology information for the task of cardiac disease classification, and compare its performance to similar single-domain representations. To this end, we first select the 150 healthy and 150 pathological United Kingdom Biobank cases described in **Section 2.1** and use them as the basis for our binary disease classification task. We then pass the corresponding bitemporal anatomy and ECG data of each case through their respective encoders in the VAE to obtain the pertinent multi-domain latent space encodings, which serve as input features for the classification. Next, we repeat the same procedure using the point cloud encoders and the time-series encoder separately to calculate the single-domain encodings of bitemporal anatomy and electrophysiology information, respectively, for the same subjects. For each of the three resulting latent space datasets (multi-domain, anatomy-specific, and ECG-specific), we train a logistic regression classifier to identify subjects with cardiac disease. **Figure 6** depicts the binary classification results of the 10-fold cross validation experiments for each combination of latent space datasets in the form of AUROC curves. We find that the multi-domain representation of anatomy and ECG achieves the highest AUROC score.

4 DISCUSSION

In summary, we have demonstrated in our experimental results that the proposed multi-domain VAE can excel at a variety of different tasks despite the challenging multi-domain setting.

4.1 Reconstruction Accuracy

The point cloud branches are able to reconstruct complex 3D anatomical shapes with high accuracy on both a local and global level and for both the ED and ES phases of the cardiac cycle (**Figure 3**) with Chamfer Distances below the underlying image resolution (**Table 2**). This shows the high suitability of the anatomy-specific network architecture. In addition, it is able to accurately maintain class information identifying the different cardiac substructures and cope with anatomies at both the ED and the ES phase of the cardiac cycle. This indicates that an introduction of additional class information about important anatomical substructures or pathological areas (e.g. scar regions in the myocardium) or a further temporal extension is possible. In our experiments, we observe slightly higher distance values for the RV compared to the LV substructures and for the ED phase compared to the ES phase. We hypothesize that this is likely caused by the generally larger heart sizes that are represented by point clouds with the same resolution as the smaller hearts, which in and of itself leads to larger Chamfer Distance values. Therefore, we do not presume this to impede any future applications, as the differences are not due to any anatomical reasons. Furthermore, we find no erroneous overlappings of different anatomical substructures (e.g., at the interventricular septum) despite no loss term specifically enforcing such consistency. From these findings, we conclude that the point cloud branches are flexible and robust with respect to temporal and spatial variations and are able to capture the complexity of part-whole relationships in 3D structures, all of

which are crucial for accurate cardiac anatomy modeling. These results are achieved despite the complex multi-domain setting in which separate point cloud branches for ED and ES as well as another ECG-based branch all share a single latent space and are trained jointly using a weighted combination of several loss function terms. This indicates that the good reconstruction performance of the point cloud-specific deep learning architecture is not limited to the single-domain setting, as in Beetz et al. (2021b), but can be applied effectively in conjunction with data from new domains while still maintaining the more challenging variational setup.

The time-series branches show a similarly good performance in the reconstruction task with a high degree of visual closeness between reconstructed and gold standard signals (**Figure 3**). We also find considerably lower RMSE and PRD scores than multiple benchmarks (**Table 1**). However, we interpret this finding as only an approximate comparison due to the usage of another dataset (MIT-BIH) and preprocessing steps to train and evaluate the benchmark methods. Nevertheless, while the MIT-BIH dataset has some differences compared to the United Kingdom Biobank dataset used in this work (e.g., ambulatory two-channel ECG vs. 12-lead ECG, 47 subjects vs. 1,300 subjects, multiple cardiac cycles vs. single cardiac cycle), they also share many similarities (e.g., both are ECG datasets with normal and pathological subjects, all compared methods focus on single lead ECG signals). In addition, we have applied similar filtering steps as the benchmark approaches (e.g., min-max normalization, same choice of sequence length) to the ECG signals in order to improve comparability between the two datasets. Hence, while a direct comparison with the other methods is limited by the dataset differences, the results still give an indication that the time-series branch architecture is able to successfully encode and decode different temporal patterns of lead II ECG signals. These findings are further corroborated by the similar reconstruction performance of the ECG-only VAE and the proposed multi-domain VAE. Since these results were achieved on the same United Kingdom Biobank dataset, they enable a direct comparison which is not affected by differences in the data or preprocessing steps between the methods. Hence, the similar RMSE and PRD values observed for both methods indicate that the multi-domain VAE was able to capture the ECG-specific information required for the reconstruction task similarly well as a single-domain ECG approach.

4.2 Generation of Virtual Multi-Domain Populations

In addition to the multi-domain VAE's reconstruction ability, we also find it to be capable of generating arbitrarily-sized virtual populations of combined bitemporal anatomies and ECGs with a high degree of realism and correct levels of shape diversity. We are able to observe this visually in **Figure 4**, where typical shape changes in biventricular surfaces (e.g., overall size, basal plane tilt, ventricular thickness) and ECGs (e.g., R-peak height and width, P-wave peakedness, small noise levels in the signal) appear in the generated virtual examples in a similar way as in the real dataset.

The quantitative results further corroborate this finding in multiple ways. First, the generated ECGs from our VAE achieve lower MMD scores than the gold standard real ECGs from our test set (**Table 3**). On the one hand, the generally small values indicate that the distribution of real ECG signals is closely mimicked by the generated ones on both individual and population levels (**Table 3**). On the other hand, we hypothesize that the lower MMD scores for the generated ECGs are likely caused by the VAE's ability to act as a regularizing self-prior and reduce noise. The proposed multi-domain VAE also achieves a comparable MMD score as the ECG-only VAE benchmark on the same United Kingdom Biobank dataset, which indicates that the ECG population was well captured despite the challenging inclusion of additional bitemporal anatomy information. Furthermore, our proposed method obtains lower MMD scores than multiple prior approaches in its ECG generation task. While this particular finding should again (similar to the reconstruction task) only be seen as an approximate comparison due to the usage of different datasets, it does nevertheless provide further evidence that the architectural design of the time-series branches can successfully convert random latent space samples into ECG populations. Second, the clinical volume-based metrics calculated for the population of generated anatomies closely resemble the ones obtained from the true gold standard test dataset, both in terms of their mean and standard deviation values (**Table 4**). This indicates that the point cloud branches are able to synthesize realistic biventricular shapes that accurately represent the morphological variety across the whole population. The network achieves this for both the ED and ES phases showing its architecture's ability to function well with temporally related, but different shape distributions. Third, the clinical function metrics, which combine volume-based anatomical information from ED and ES phases, exhibit high degrees of similarity between the generated and gold standard anatomies in terms of both mean and standard deviation values (**Table 5**). This demonstrates that the synthesized anatomies do not only reflect a realistic population at ED or ES separately but also when considered as a combined bitemporal anatomy population. This correspondence between ED and ES shapes in the generated population is highly beneficial for multiple follow-up tasks (e.g. mechanical deformation modeling (Beetz et al., 2021c)). We also conclude from these results that the ED-ES correspondence information is likely captured in the shared latent space of the VAE and that the respective ED and ES point cloud branches are sufficiently powerful to correctly take into account cross-temporal information during training. Fourth, when combining ECG and bitemporal anatomy information in a unified representation, we find similar MMD values between synthesized and real gold standard populations (**Table 6**). This indicates that good correspondence is present not only between different cardiac phases but also between the generated ECG and anatomy data and that both the decoder branches and latent space information adequately model these inter-domain relationships. We note that while the selected cardiac metrics used to represent the anatomy in the unified representation only act as low-dimensional approximations of the full generated shapes for the MMD calculations, they were weighted accordingly to give the anatomical and ECG-based information a balanced influence in the combined

representation. In general, since the aforementioned results were achieved using real ECG data, we hypothesize that the VAE could also be applied to synthetically-generated ECGs (e.g. via electrophysiology simulations based on mathematical models) for the task of generating personalized models of both normal and pathological data in real-time, which we wish to explore in detail in our future work.

4.3 Latent Space Quality

The positive results in the data generation tasks are likely significantly facilitated by the high quality of the latent space, which we observe to exhibit a good degree of disentanglement and interpretability (**Figure 5**). This can be seen by the clearly distinguishable effects that different individual latent space components have on the reconstructed anatomy and ECG outputs. We also find such latent space changes to cause gradual deformations of the output shapes of all domains while maintaining a realistic overall appearance even in case of larger deviations from the mean values. This indicates that the latent space learnt during training at least approximately resembles a multivariate normal distribution as enforced by the Kullback-Leibler divergence loss, as opposed to a more sparse and disordered representation that might lead to sudden unrealistic outlier shapes in the generated distributions. But compared to the zero mean parameterization of all Gaussians, we achieve better generation results when using the mean values predicted by the encoders on the training dataset to parameterize the latent space normal distributions for sampling. This shows that the actual latent space distribution still exhibits some differences to the target normal distribution. Nevertheless, this slight deviation is to be expected as the overall VAE loss represents a compromise between accurate reconstruction and latent space quality. We find the weighting parameter β to be crucially important for determining the optimal balance for the given dataset empirically, especially considering our highly challenging multi-domain setting. The similar shape changes observed in the ED and ES reconstructions corroborate the good choice of β further and demonstrate that the aforementioned high interpretabiliy of the latent space is retained even in the cross-domain case.

4.4 Cardiovascular Disease Classification

As evidenced by the cardiac disease classification results in **Figure 6**, the multi-domain latent space representation is able to successfully capture shape patterns related to both the healthy hearts and various cardiovascular pathologies in both the ECGs and the bitemporal anatomies. This offers the possibility to discover, visualize, and analyze pathology-specific feature combinations in both ECG and anatomy. One approach to achieve this would be to compare healthy and pathological latent spaces in terms of their respective mean representations or distributions and then reconstruct the corresponding anatomies and ECGs for each group to visualize the differences. Another possibility might be to identify the latent space components that are most predictive during the classification tasks and study what effects the corresponding changes in these latent components have on the reconstructed anatomies. Furthermore, when applying the multi-domain VAE trained on healthy subjects to diseased cases, we observe a slight decrease in reconstruction performance compared to unseen healthy cases, which also indicates that the network has learnt patterns specific to the healthy subpopulation. These results provide further proof of the importance of image-based and ECG shape analysis on both local and global scales for cardiac disease identification, which is in line with other previous findings (Mauger et al., 2019; Acero et al., 2022). One crucial difference to these prior works, however, is the combination of anatomy and ECG information in a compressed format that we observe to be more effective than similar approaches relying on either anatomy or ECG information alone (**Figure 6**). This multi-domain approach is particularly advantageous for the selected cardiovascular disease class containing different pathologies whose diagnoses are usually based on different modalities (e.g., cardiac MRI, ECG). Furthermore, we observe smaller differences in AUROC values between ECG + anatomy and anatomy-only information than between ECG + anatomy and ECG-only information. On the one hand, this might be due to the individual pathologies considered in the classification task that might be more easily predicted based on anatomy information. On the other hand, it could also be caused by our focus on only lead II ECG signals from a single heartbeat. This provides the ECG-only classifier with less information, which is in contrast to the high-dimensional multi-class 3D point cloud data that serves as input to the anatomy-based classifier. We also note that the latent space representation was obtained without any prior explicit training for the task of disease prediction, which outlines the potential for further improvements in directly finding pathology-specific compressed shape representation.

4.5 Architectural Design and Training

We have found the architectural design of our network (**Figure 1C**) to be highly suitable to process combined ECG and anatomy input data. The point cloud branch architectures (**Figure 2A,B**) are able to apply deep learning operations directly on point cloud data, which allows surface data of much higher resolution to be efficiently processed and used for storing anatomical shape information. This is in contrast to the widely-used voxelgrid representations (Çiçek et al., 2016; Bello et al., 2019; Xu et al., 2019), which are considerably less memory-efficient at managing surface-level data leading to lower resolution, longer processing times, and ultimately limit the overall accuracy of the modeled anatomy. Furthermore, each of the high-dimensional point clouds combines both the left and right ventricular anatomy and maintains separate labels for the LV endocardium, LV epicardium, and RV endocardium substructures. This results in a more holistic and accurate representation of the true 3D cardiac anatomy compared to the non-labelled single ventricle approaches and enables a more detailed and effective study of the structure-function interactions between MRI-based cardiac anatomy and ECG-based cardiac electrophysiology information.

As opposed to traditional shape modeling approaches, such as principal component analysis (Mauger et al., 2019; Acero et al., 2022), the deep learning architecture is able to capture

significantly more complex and non-linear shape variations, which is important for the accurate modeling of the intricate interactions of both single-domain ECG and anatomy data, but especially in the multi-domain setting. In addition, no point-to-point correspondence is required in the point cloud dataset and no prior shape registration step needs to be applied, which makes the preprocessing steps considerably simpler, faster, and less error-prone compared to the PCA (**Figure 1A,B**). Another advantage of the VAE framework is its condensed latent space representation of the input data, which is useful for a variety of different tasks as shown in this work. The design of the time-series branches (**Figure 2C,D**) relies on a combination of convolutional, pooling, and fully connected layers, as opposed to recurrent layers such as Long Short-Term Memory (LSTM) or Gated Recurrent Units (GRU), and its good performance is in line with previous findings in ECG modeling (Zhu et al., 2019). For all branches, we hypothesize that the fully connected layers on both sides of the latent space in the encoder and decoder architectures provide the necessary power and flexibility to extract the relevant information for each domain from the shared latent space, while still accounting for inter-domain correspondence. Despite no specifically designed consistency loss between different output branches, we find that a careful empirical choice of weighting parameters in **Eq. 3** and **Eq. 5** in the domain-specific loss function components is sufficient to obtain high quality outputs both intra-domain and inter-domain. Finally, we note that the domain-specific data preprocessing of the proposed approach offers a certain degree of robustness and flexibility with regards to changes in the input data (e.g., different image resolutions in the cine MRI acquisitions), as both the 3D cardiac surface reconstruction and the ECG preprocessing steps can be adjusted as required in order to still be capable of creating 3D anatomy point clouds and ECG time series in a suitable format for the multi-domain VAE. For example, the same point cloud resolution can be maintained by the 3D surface reconstruction method despite changes in the underlying image resolution.

4.6 Limitations

The presented approach to multi-domain cardiac anatomy and physiology modeling also has some limitations. While it has previously been shown that the position and orientation of the heart with respect to the ECG electrodes on the torso significantly affects the ECG shapes (Mincholé et al., 2019), we did not include any torso information in this work. However, since the VAE was trained with paired anatomy and ECG information from real acquisitions, we hypothesize that the network is at least to some extent able to implicitly learn the effect of the torso on the output signals. We also note that since the 3D anatomy models were derived from 2D cine MRI acquisitions, any limitations (e.g., image resolution) or errors (e.g. slice misalignment due to inconsistent breath holds) introduced during the image acquisition or 3D reconstruction will affect the accuracy of the anatomical shapes. Similarly, we also note that the United Kingdom Biobank imaging study uses very established acquisition protocols and certain quality control measures that might not be fully representative of a standard clinical environment. While this makes the results easier to understand, it might also require some adjustments to the proposed methods in case of their application to different settings with a possibly larger variety of acquisition conditions and noise. While this study only focuses on lead II ECGs averaged across multiple cardiac cycles and thereby foregoes additional information from other leads and multi-heartbeat patterns, we believe that the core part of the architecture has the potential to be extended to the full-cycle 12-lead case. This could be achieved by first applying the same preprocessing steps to each of the 12 leads in order to represent each lead signal as a normalized 400-dimensional vector. The resulting vectors could then be concatenated and input into the ECG branch of the VAE. The ECG loss could be easily extended to include multiple leads by summing or averaging over the lead-specific mean squared errors. In addition, adjustments to the ECG branch architecture, training schedule, and possibly the lead-specific weighting terms in the loss function will likely be necessary to accommodate the increased difficulty of processing all 12 leads. Another limitation of the method is that no anatomical information about the atria is included in the model, which plays an important role in modeling electrophysiology. However, as the, to the best of our knowledge, first deep learning approach to combine anatomy and ECG data in a single data-driven model, we found the utilized information sources sufficient to demonstrate the feasibility and show the benefits of a multi-domain cardiac model. Information from other domains can be included into the model in future work, for example, as extra classes in the point cloud inputs, additional time series in the ECG inputs, or as new network branches altogether.

5 CONCLUSION

In this work, we have developed and evaluated a novel multi-domain VAE with the ability to capture combined cardiac anatomy and physiology information and their intricate interconnections in a single data-driven model. We have shown that the network can successfully handle the complex interdependencies of multi-domain datasets by reconstructing existing cardiac data from low-dimensional latent spaces with high accuracy and generating realistic populations of corresponding cardiac anatomies and ECGs. Furthermore, we have found an interpretable latent space in the VAE with each component responsible for a separate morphological change in anatomy and ECG outputs enabling a more localized analysis of cardiac health. Finally, we have observed that combined anatomy and ECG representations improve the identification of cardiovascular disease compared to single-domain approaches. This shows the utility and positive synergies of large-scale data integration from multiple sources in cardiology and opens up promising future research avenues for possible further multi-domain integration.

DATA AVAILABILITY STATEMENT

The data analyzed in this study is subject to the following licenses/restrictions: The United Kingdom Biobank datasets used for network training and evaluation are not allowed to be shared

publicly. Requests to access these datasets should be directed to https://www.ukbiobank.ac.uk. Generated virtual data can be made available upon reasonable request.

AUTHOR CONTRIBUTIONS

MB and VG were involved in the conceptualization and design of the work. AB and MB implemented and executed the data preprocessing steps. MB developed and trained the VAE and machine learning methods. MB conducted the experiments and created a first version of the manuscript. MB, AB, and VG all revised the manuscript and approved its final version.

FUNDING

The work of MB was supported by the Stiftung der Deutschen Wirtschaft (Foundation of German Business). The work of AB and VG was supported by the British Heart Foundation (BHF) Project under Grant HSR01230 and by the CompBioMed 2 Centre of Excellence in Computational Biomedicine (European Commission Horizon 2020 research and innovation programme, grant agreement No. 823712).

ACKNOWLEDGMENTS

This research has been conducted using the United Kingdom Biobank Resource under Application Number "40161". The authors acknowledge the use of the facilities and services of the Institute of Biomedical Engineering (IBME), Department of Engineering Science, University of Oxford.

SUPPLEMENTARY MATERIAL

The Supplementary Material for this article can be found online at: https://www.frontiersin.org/articles/10.3389/fphys.2022.886723/full#supplementary-material

REFERENCES

Abadi, M., Barham, P., Chen, J., Chen, Z., Davis, A., Dean, J., et al. (2016). "Tensorflow: A System for Large-Scale Machine Learning," in 12th USENIX Symposium on Operating Systems Design and Implementation, 265–283.

Acero, J. C., Schuster, A., Zacur, E., Lange, T., Stiermaier, T., Backhaus, S. J., et al. (2022). Understanding and Improving Risk Assessment after Myocardial Infarction Using Automated Left Ventricular Shape Analysis. *JACC Cardiovasc. Imaging*. doi:10.1016/j.jcmg.2021.11.027

Bai, W., Sinclair, M., Tarroni, G., Oktay, O., Rajchl, M., Vaillant, G., et al. (2018). Automated Cardiovascular Magnetic Resonance Image Analysis with Fully Convolutional Networks. *J. Cardiovasc Magn. Reson* 20, 65. doi:10.1186/s12968-018-0471-x

Bai, W., Shi, W., de Marvao, A., Dawes, T. J. W., O'Regan, D. P., Cook, S. A., et al. (2015). A Bi-ventricular Cardiac Atlas Built from 1000+ High Resolution MR Images of Healthy Subjects and an Analysis of Shape and Motion. *Med. Image Anal.* 26, 133–145. doi:10.1016/j.media.2015.08.009

Bai, W., Suzuki, H., Huang, J., Francis, C., Wang, S., Tarroni, G., et al. (2020). A Population-Based Phenome-wide Association Study of Cardiac and Aortic Structure and Function. *Nat. Med.* 26, 1654–1662. doi:10.1038/s41591-020-1009-y

Banerjee, A., Camps, J., Zacur, E., Andrews, C. M., Rudy, Y., Choudhury, R. P., et al. (2021). A Completely Automated Pipeline for 3D Reconstruction of Human Heart from 2D Cine Magnetic Resonance Slices. *Philosophical Trans. R. Soc. A Math. Phys. Eng. Sci.* 379, 20200257. doi:10.1098/rsta.2020.0257

Beetz, M., Banerjee, A., and Grau, V. (2021a). "Biventricular Surface Reconstruction from Cine MRI Contours Using Point Completion Networks," in 2021 IEEE 18th International Symposium on Biomedical Imaging (ISBI), 105–109. doi:10.1109/isbi48211.2021.9434040

Beetz, M., Banerjee, A., and Grau, V. (2021b). "Generating Subpopulation-specific Biventricular Anatomy Models Using Conditional Point Cloud Variational Autoencoders," in International Workshop on Statistical Atlases and Computational Models of the Heart (Springer), 75–83.

Beetz, M., Banerjee, A., Sang, Y., and Grau, V. (2022). "Combined Generation of Electrocardiogram and Cardiac Anatomy Models Using Multi-Modal Variational Autoencoders," in 2022 IEEE 19th International Symposium on Biomedical Imaging (ISBI). doi:10.1109/isbi52829.2022.9761590

Beetz, M., Ossenberg-Engels, J., Banerjee, A., and Grau, V. (2021c). "Predicting 3D Cardiac Deformations with Point Cloud Autoencoders," in International Workshop on Statistical Atlases and Computational Models of the Heart (Springer), 219–228.

Bello, G. A., Dawes, T. J. W., Duan, J., Biffi, C., De Marvao, A., Howard, L. S. G. E., et al. (2019). Deep-learning Cardiac Motion Analysis for Human Survival Prediction. *Nat. Mach. Intell.* 1, 95–104. doi:10.1038/s42256-019-0019-2

Biffi, C., Cerrolaza, J. J., Tarroni, G., Bai, W., de Marvao, A., Oktay, O., et al. (2020). Explainable Anatomical Shape Analysis through Deep Hierarchical Generative Models. *IEEE Trans. Med. Imaging* 39, 2088–2099. doi:10.1109/tmi.2020.2964499

Bowman, S. R., Vilnis, L., Vinyals, O., Dai, A. M., Jozefowicz, R., and Bengio, S. (2015). Generating Sentences from a Continuous Space. *arXiv preprint arXiv:1511.06349*. doi:10.48550/arXiv.1511.06349

Çiçek, Ö., Abdulkadir, A., Lienkamp, S. S., Brox, T., and Ronneberger, O. (2016). "3D U-Net: Learning Dense Volumetric Segmentation from Sparse Annotation," in International Conference on Medical Image Computing and Computer-Assisted Intervention (Springer), 424–432. doi:10.1007/978-3-319-46723-8_49

Delaney, A. M., Brophy, E., and Ward, T. E. (2019). Synthesis of Realistic ECG Using Generative Adversarial Networks. *arXiv preprint arXiv:1909.09150*. doi:10.48550/arXiv.1909.09150

Gilbert, K., Mauger, C., Young, A. A., and Suinesiaputra, A. (2020). Artificial Intelligence in Cardiac Imaging with Statistical Atlases of Cardiac Anatomy. *Front. Cardiovasc. Med.* 7, 102. doi:10.3389/fcvm.2020.00102

Goldberger, A. L., Amaral, L. A., Glass, L., Hausdorff, J. M., Ivanov, P. C., Mark, R. G., et al. (2000). Physiobank, Physiotoolkit, and PhysioNet: Components of a New Research Resource for Complex Physiologic Signals. *Circulation* 101, e215–20. doi:10.1161/01.cir.101.23.e215

Gretton, A., Borgwardt, K. M., Rasch, M. J., Schölkopf, B., and Smola, A. (2012). A Kernel Two-Sample Test. *J. Mach. Learn. Res.* 13, 723–773.

Higgins, I., Matthey, L., Pal, A., Burgess, C., Glorot, X., Botvinick, M., et al. (2017). "Beta-VAE: Learning Basic Visual Concepts with a Constrained Variational Framework," in 5th International Conference on Learning Representations (ICLR), 1–13.

Kalpana, V., Hamde, S. T., and Waghmare, L. M. (2013). ECG Feature Extraction Using Principal Component Analysis for Studying the Effect of Diabetes. *J. Med. Eng. Technol.* 37, 116–126. doi:10.3109/03091902.2012.753126

Kalyakulina, A., Yusipov, I., Moskalenko, V., Nikolskiy, A., Kozlov, A., Kosonogov, K., et al. (2020). Lobachevsky University Electrocardiography Database (Version 1.0.0). *PhysioNet*. doi:10.13026/qweb-sr17

Kingma, D. P., and Ba, J. (2014). Adam: A Method for Stochastic Optimization. *arXiv preprint arXiv:1412.6980*.

Kingma, D. P., and Welling, M. (2013). Auto-encoding Variational Bayes. *arXiv preprint arXiv:1312.6114*. doi:10.48550/arXiv.1312.6114

Kuznetsov, V. V., Moskalenko, V. A., Gribanov, D. V., and Zolotykh, N. Y. (2021). Interpretable Feature Generation in ECG Using a Variational Autoencoder. *Front. Genet.* 12, 638191. doi:10.3389/fgene.2021.638191

Langley, P., Bowers, E. J., and Murray, A. (2009). Principal Component Analysis as a Tool for Analyzing Beat-To-Beat Changes in ECG Features: Application to ECG-Derived Respiration. *IEEE Trans. Biomed. Eng.* 57, 821–829. doi:10.1109/TBME.2009.2018297

Litjens, G., Kooi, T., Bejnordi, B. E., Setio, A. A. A., Ciompi, F., Ghafoorian, M., et al. (2017). A Survey on Deep Learning in Medical Image Analysis. *Med. Image Anal.* 42, 60–88. doi:10.1016/j.media.2017.07.005

Macfarlane, P. W., and Lawrie, T. D. V. (2010). "The Normal Electrocardiogram and Vectorcardiogram," in *Comprehensive Electrocardiology*. Editors P. W. Macfarlane, A. van Oosterom, O. Pahlm, P. Kligfield, M. Janse, and J. Camm (Springer London), 483–546. doi:10.1007/978-1-84882-046-3_13

Martis, R. J., Acharya, U. R., and Min, L. C. (2013). ECG Beat Classification Using PCA, LDA, ICA and Discrete Wavelet Transform. *Biomed. Signal Process. Control* 8, 437–448. doi:10.1016/j.bspc.2013.01.005

Mauger, C., Gilbert, K., Lee, A. M., Sanghvi, M. M., Aung, N., Fung, K., et al. (2019). Right Ventricular Shape and Function: Cardiovascular Magnetic Resonance Reference Morphology and Biventricular Risk Factor Morphometrics in UK Biobank. *J. Cardiovasc Magn. Reson* 21, 41. doi:10.1186/s12968-019-0551-6

Mincholé, A., Zacur, E., Ariga, R., Grau, V., and Rodriguez, B. (2019). MRI-based Computational Torso/biventricular Multiscale Models to Investigate the Impact of Anatomical Variability on the ECG QRS Complex. *Front. Physiol.* 10, 1103. doi:10.3389/fphys.2019.01103

Nagel, C., Schuler, S., Dössel, O., and Loewe, A. (2021). A Bi-atrial Statistical Shape Model for Large-Scale In Silico Studies of Human Atria: Model Development and Application to ECG Simulations. *Med. Image Anal.* 74, 102210. doi:10.1016/j.media.2021.102210

Niederer, S. A., Aboelkassem, Y., Cantwell, C. D., Corrado, C., Coveney, S., Cherry, E. M., et al. (2020). Creation and Application of Virtual Patient Cohorts of Heart Models. *Phil. Trans. R. Soc. A* 378, 20190558. doi:10.1098/rsta.2019.0558

Pedregosa, F., Varoquaux, G., Gramfort, A., Michel, V., Thirion, B., Grisel, O., et al. (2011). Scikit-learn: Machine Learning in python. *J. Mach. Learn. Res.* 12, 2825–2830.

Petersen, S. E., Matthews, P. M., Bamberg, F., Bluemke, D. A., Francis, J. M., Friedrich, M. G., et al. (2013). Imaging in Population Science: Cardiovascular Magnetic Resonance in 100,000 Participants of UK Biobank - Rationale, Challenges and Approaches. *J. Cardiovasc Magn. Reson* 15, 46. doi:10.1186/1532-429X-15-46

Petersen, S. E., Matthews, P. M., Francis, J. M., Robson, M. D., Zemrak, F., Boubertakh, R., et al. (2015). UK Biobank's Cardiovascular Magnetic Resonance Protocol. *J. Cardiovasc Magn. Reson* 18, 8. doi:10.1186/s12968-016-0227-4

Piazzese, C., Carminati, M. C., Pepi, M., and Caiani, E. G. (2017). "Statistical Shape Models of the Heart: Applications to Cardiac Imaging," in *Statistical Shape and Deformation Analysis* (Elsevier), 445–480. doi:10.1016/b978-0-12-810493-4.00019-5

Qi, C. R., Su, H., Mo, K., and Guibas, L. J. (2017a). "Pointnet: Deep Learning on Point Sets for 3D Classification and Segmentation," in Proceedings of the IEEE Conference on Computer Vision and Pattern Recognition, 652–660.

Qi, C. R., Yi, L., Su, H., and Guibas, L. J. (2017b). "Pointnet++: Deep Hierarchical Feature Learning on Point Sets in a Metric Space," in Advances in Neural Information Processing Systems, 5099–5108.

Rezaei, M. (2021). "Generative Adversarial Network for Cardiovascular Imaging," in *Machine Learning in Cardiovascular Medicine*. Editors S. J. Al'Aref, G. Singh, L. Baskaran, and D. Metaxas (Academic Press), 95–121. doi:10.1016/b978-0-12-820273-9.00005-1

Romero, P., Lozano, M., Martínez-Gil, F., Serra, D., Sebastiań, R., Lamata, P., et al. (2021). Clinically Driven Virtual Patient Cohorts Generation: An Application to Aorta. *Front. Physiology* 12, 713118. doi:10.3389/fphys.2021.713118

Stokes, M. B., and Roberts-Thomson, R. (2017). Diagnostic Tests: The Role of Cardiac Imaging in Clinical Practice. *Aust. Prescr.* 40, 151–155. doi:10.18773/austprescr.2017.045

Tavakoli, V., and Amini, A. A. (2013). A Survey of Shaped-Based Registration and Segmentation Techniques for Cardiac Images. *Comput. Vis. Image Underst.* 117, 966–989. doi:10.1016/j.cviu.2012.11.017

Wang, P., Hou, B., Shao, S., and Yan, R. (2019). Ecg Arrhythmias Detection Using Auxiliary Classifier Generative Adversarial Network and Residual Network. *Ieee Access* 7, 100910–100922. doi:10.1109/access.2019.2930882

Xu, H., Zacur, E., Schneider, J. E., and Grau, V. (2019). "Ventricle Surface Reconstruction from Cardiac MR Slices Using Deep Learning," in International Conference on Functional Imaging and Modeling of the Heart (Springer), 342–351. doi:10.1007/978-3-030-21949-9_37

Yang, Y., Feng, C., Shen, Y., and Tian, D. (2017). Foldingnet: Interpretable Unsupervised Learning on 3D Point Clouds. *arXiv preprint arXiv:1712.07262*. doi:10.48550/arXiv.1712.07262

Yuan, W., Khot, T., Held, D., Mertz, C., and Hebert, M. (2018). "PCN: Point Completion Network," in 2018 International Conference on 3D Vision, 728–737. doi:10.1109/3dv.2018.00088

Zhu, F., Ye, F., Fu, Y., Liu, Q., and Shen, B. (2019). Electrocardiogram Generation with a Bidirectional LSTM-CNN Generative Adversarial Network. *Sci. Rep.* 9, 6734. doi:10.1038/s41598-019-42516-z

Conflict of Interest: The authors declare that the research was conducted in the absence of any commercial or financial relationships that could be construed as a potential conflict of interest.

Publisher's Note: All claims expressed in this article are solely those of the authors and do not necessarily represent those of their affiliated organizations, or those of the publisher, the editors and the reviewers. Any product that may be evaluated in this article, or claim that may be made by its manufacturer, is not guaranteed or endorsed by the publisher.

frontiers | Frontiers in Physiology

ORIGINAL RESEARCH
published: 17 June 2022
doi: 10.3389/fphys.2022.921210

Cepstral Analysis for Scoring the Quality of Electrocardiograms for Heart Rate Variability

Paolo Castiglioni[1]*, *Gianfranco Parati*[2,3] and *Andrea Faini*[2]

[1]IRCCS Fondazione Don Carlo Gnocchi ONLUS, Milan, Italy, [2]IRCCS Istituto Auxologico Italiano, San Luca Hospital, Milan, Italy, [3]Department of Medicine and Surgery, University of Milano-Bicocca, Milan, Ital

Mobile-health solutions based on heart rate variability often require electrocardiogram (ECG) recordings by inexperienced operators or real-time automatic analyses of long-term recordings by wearable devices in free-moving individuals. In this context, it is useful to associate a quality index with the ECG, scoring the adequacy of the recording for heart rate variability to identify noise or arrhythmias. Therefore, this work aims to propose and validate a computational method for assessing the adequacy of single-lead ECGs for heart rate variability analysis that may run in real time on wearable systems with low computational power. The method quantifies the ECG pseudo-periodic structure employing cepstral analysis. The cepstrum (spectrum of log-spectrum) is estimated on a running ECG window of 10 s before and after "liftering" (filtering in the cepstral domain) to remove slower noise components. The ECG periodicity generates a dominant peak in the liftered cepstrum at the "quefrency" of the mean cardiac interval. The Cepstral Quality Index (CQI) is the ratio between the cepstral-peak power and the total power of the unliftered cepstrum. Noises and arrhythmias reduce the relative power of the cepstral peak decreasing CQI. We analyzed a public dataset of 6072 single-lead ECGs manually classified in normal rhythm or inadequate for heart rate variability analysis because of noise or atrial fibrillation, and the CQI = 47% cut-off identified the inadequate recordings with 79% sensitivity and 85% specificity. We showed that the performance is independent of the lead considering a public dataset of 1,000 12-lead recordings with quality classified as "acceptable" or "unacceptable" by visual inspection. Thus, the cepstrum describes the ECG periodic structure effectively and concisely and CQI appears to be a robust score of the adequacy of ECG recording for heart rate variability analysis, evaluable in real-time on wearable devices.

Keywords: heart rate variability, fourier transform, EKG, power cepstrum, signal quality, premature beat, wearable system, mobile ECG monitoring

OPEN ACCESS

Edited by:
Gernot Plank,
Medical University of Graz, Austria

Reviewed by:
Ilija Uzelac,
Georgia Institute of Technology, United States
Youngsun Kong,
University of Connecticut, United States

***Correspondence:**
Paolo Castiglioni
pcastiglioni@dongnocchi.it

Specialty section:
This article was submitted to Cardiac Electrophysiology, a section of the journal Frontiers in Physiology

Received: *15 April 2022*
Accepted: *27 May 2022*
Published: *17 June 2022*

Citation:
Castiglioni P, Parati G and Faini A (2022) Cepstral Analysis for Scoring the Quality of Electrocardiograms for Heart Rate Variability. Front. Physiol. 13:921210. doi: 10.3389/fphys.2022.921210

1 INTRODUCTION

Advancements in sensors technology are making it possible to monitor the electrocardiogram (ECG) for long periods in unattended subjects through wearable systems, promoting solutions for telemonitoring, home rehabilitation, mobile health, and ambient-assisted living applications. Most of these applications quantify indexes of heart rate variability to provide information on the autonomic control and cardiorespiratory interactions, based on ECG recordings performed by

inexperienced users and on automatic analyses of ECG tracings. In these cases, it is important to associate a quality score with the recorded signals. In telemonitoring applications this would indicate to inexperienced operators the need to repeat the recording if the ECG quality is too low; in ambient assisted living applications, this would allow expert systems not to take decisions on the base of unreliable ECG signals. A further requirement is to exclude arrhythmias if the aim is to quantify heart rate variability, as during exercise-based rehabilitation programs for restoring the autonomic control in cardiac patients after heart surgery or in diabetic individuals with autonomic neuropathy. A normal rhythm is indeed necessary to correctly interpret the indices of heart rate variability.

In the frame of domotic applications aimed at developing a smart environment for elderly people, we had to deal with the definition of an automatic score of the ECG quality in normal rhythm. The domotic application consisted of a first layer of sensors and devices with low computational power to collect physiological and behavioral data to be sent to upper computational levels operating decisions in support of the assistance staff (Gower et al., 2011). In particular, the ECG had to be recorded for hours or days on freely moving subjects for a continuous assessment of heart rate variability with wearable ECG sensors (Di Rienzo et al., 2010). In this context, the occurrence of arrhythmic episodes, artifacts, and noise was expected, making important the dynamic assessment of data reliability in real-time automatically. These requirements demanded an algorithm working on different leads separately and running on low-power microprocessors on board the wearable devices, to score the ECG quality, select the best lead, and identify the presence of normal sinus rhythm for the online evaluation of heart rate variability. To deal with these requirements, we originally designed an algorithm to characterize the ECG quality from its periodic structure (Castiglioni et al., 2011).

We further developed the original algorithm and this work aims to illustrate the capability of cepstral analysis to characterize the pseudo-periodicity of the ECG and to propose and validate a cepstral method for devices with low-computing power that scores the quality of ECG leads for heart rate variability applications.

2 METHODS

2.1 The Power Cepstrum

The Power Spectrum *PS(f)* of a signal *s(t)* is the squared magnitude of its Fourier Transform:

$$PS(f) = |\mathcal{F}[s(t)]|^2 \tag{1}$$

The Power Cepstrum $PC(\tau)$ of *s(t)* is the power spectrum of the logarithm of *PS(f)*:

$$PC(\tau) = \left|\mathcal{F}[\log PS(f)]\right|^2 \tag{2}$$

The Power Cepstrum was introduced to identify signals echoes (Bogert et al., 1963; Oppenheim and Schafer, 2004). In fact, the Fourier spectrum of the superposition of a signal and its echo after τ seconds is the product between the spectrum of the signal and a periodic function with period $1/\tau$ Hertz. The logarithm converts the product into a sum and the following Fourier

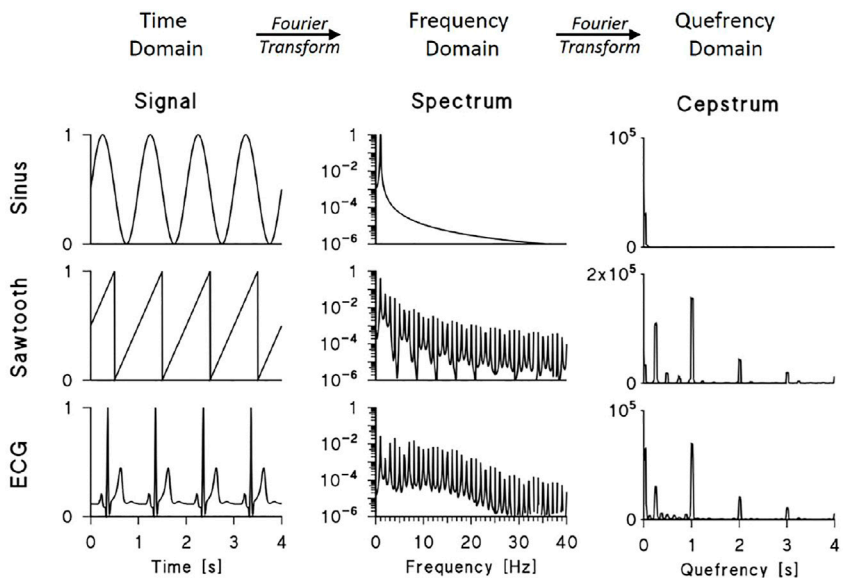

FIGURE 1 | Power spectra and power cepstra of a sinusoid, sawtooth function and synthesised ECG. The signals were sampled at 200 Hz, the spectra were calculated over 2048 points by Fast Fourier Transform (FFT) and the cepstra were calculated by FFT of the log-transformed spectra between 0 and 100 Hz (for clarity, spectra are plotted up to 40 Hz, signals and cepstra up to 4 s). The cepstra of the sawtooth function and synthesized ECG show peaks at 1, 2, and 3 s representing the train of power spectrum harmonics multiple of the fundamental frequency f_0 = 1 Hz; the sawtooth cepstrum also shows peaks at 0.24 s and its multiples representing the modulation with period of 4.2 Hz visible in its log-spectrum; the ECG cepstrum shows a large peak at the lowest quefrency representing the decreasing spectral trend.

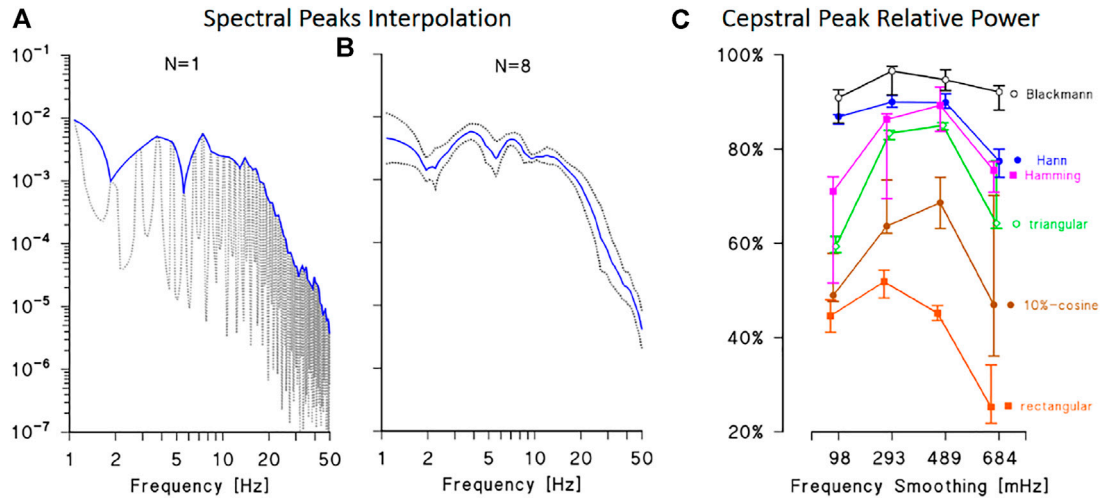

FIGURE 2 | Definition of data windows for ECG cepstral analysis. **(A)**: power spectrum of a synthesised ECG (dotted line) with interpolation of the maxima at the fundamental harmonic and its multiples (continuous line). **(B)**: average and 95% confidence interval of the lines interpolating the spectral maxima of 8 synthesised ECG. The average interpolating line is relatively constant up to 20 Hz and rapidly decreases at higher frequencies, suggesting to limit the length of the frequency-domain data window up to 20 Hz. **(C)**: relative power of the main cepstral peak: median and interquartile range over 8 synthesised ECGs calculated by six different time-domain data windows and by smoothing the spectral lines using moving average filters with bandwidth between 98 and 684 mHz. The best performance is obtained with the Blackmann window and smoothing bandwidth between 250 and 500 mHz.

analysis identifies the echo delay as a spectral peak at "frequency" τ. The domain of the spectrum of the log-spectrum is treated as a "frequency domain", but after two Fourier transforms its units are those of time, in seconds, not of frequency, in Hertz. For this reason, it is referred to as the "quefrency" domain. Like "cepstrum" and "liftering", this term was coined by interchanging consonants of familiar words ("frequency", "spectrum" and "filtering") to emphasize that time-domain methods are applied to functions of the frequency.

The cepstral approach, however, also gives us a concise way of describing the harmonic structure of periodic signals. This is illustrated in **Figure 1**, which compares power spectra and power cepstra of three periodic functions with a period of 1 s.

The first function is a sinusoid: its power spectrum is composed of a single peak at 1 Hz and, consequently, its cepstrum shows very-low quefrency power only. The second signal is a sawtooth function: the power spectrum consists of a sequence of harmonics at multiples of the fundamental frequency $f_0 = 1$ Hz. When plotted in a log scale, this train of peaks appears modulated by a slower oscillation with a "period" of 4.2 Hz. These components are clear in the cepstrum: harmonics at quefrencies τ multiples of $\tau_0 = 1/f_0$, i.e. at τ equal to 1, 2, and 3 s, represent the train of spectral peaks; and cepstral peaks at $\tau = 1/4.2$ Hz^{-1} (i.e., 0.24 s) and its multiples represent the slower spectral periodicity. The third periodic function is a synthesized ECG: in this case, the log-spectrum appears as a quasi-sinusoidal train of peaks that decays at frequencies higher than 20 Hz. Like the sawtooth cepstrum, the ECG cepstrum shows peaks at $\tau = 1$, 2, and 3 s that represent the train of harmonics.

2.2 Synthesized Electrocardiogram

To identify the parameters that better describe the cepstral peaks of the ECG, we made use of synthesized ECG signals. The same synthesized ECGs also allow us to quantify the effects of added noise and deviations from pseudo-periodicity. To synthesize ECG waves with realistic shapes, we started with real recordings. One lead ECG (Einthoven II lead, 200 Hz) was recorded in eight young volunteers (4 males/4 females, age 21–38 years) resting supine for 10 min by a Cardioline Delta 1 plus (REMCO ITALIA, Milan, Italy) electrocardiograph. An ECG template was obtained from each recording by R-peak synchronized average. About 600 beats were averaged for each template, virtually removing any type of noise asynchronous with the R peak (baseline drift, muscular noise, or 50/60 Hz power noise). A synthesized ECG was generated from each template sequentially appending copies of the template, spaced evenly. The mean R-R interval of the 8 recordings ranged between 738 and 1126 ms and the distance between consecutive R peaks was equal to the mean R-R interval of each original recording. In this way, the 8 synthesized signals preserved the original heart rate and ECG shape (see an example in the lower-left panel of **Figure 1**).

2.3 Electrocardiogram Cepstral Estimator

We first introduced the ECG cepstral analysis in a conference presentation as a new tool for assessing the quality of electrocardiographic recordings (Castiglioni et al., 2011). In the present work, we evaluate critically the performance of the cepstral approach by applying it to synthesized ECG signals, to a large number of real ECG recordings from public databases, and to specific ECG tracings selected from our previous works as being representative of specific physiological or pathological conditions. However, before applying the cepstral analyses on synthesized and real ECGs, this paragraph shows how we

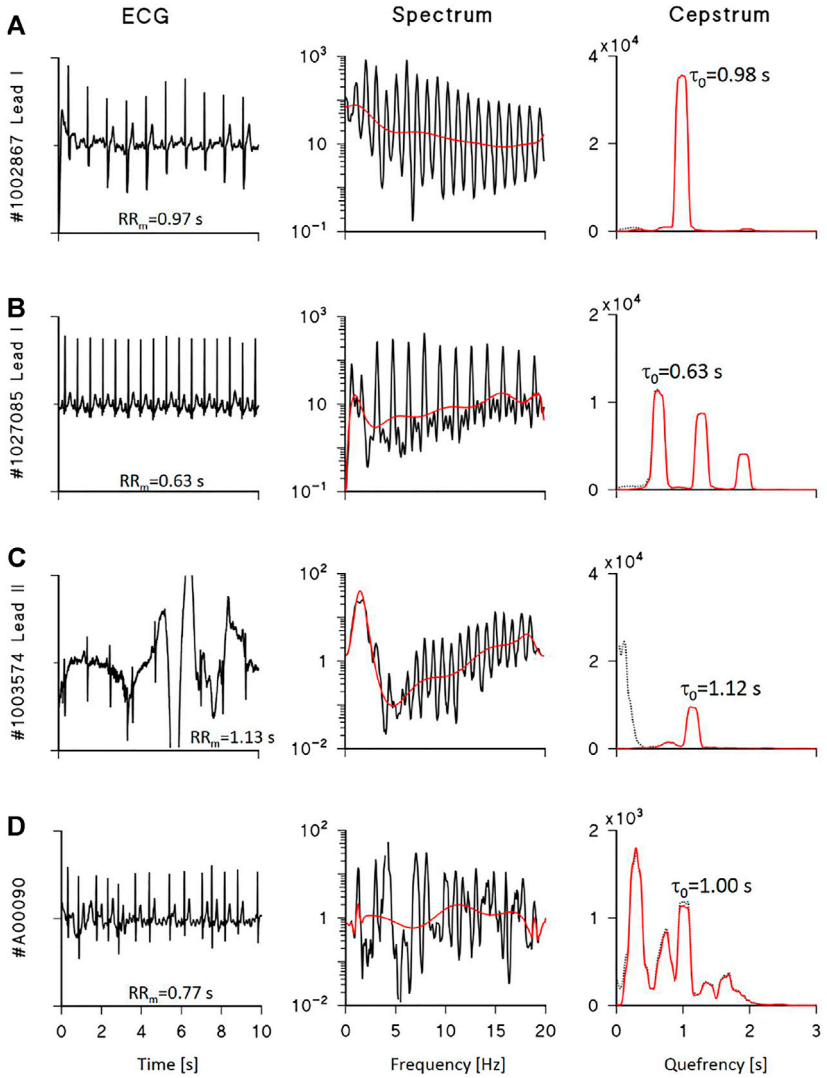

FIGURE 3 | Examples of ECG cepstral analysis. *Left*: 10-s ECG segments from the Physionet/Computing in Cardiology datasets of the 2011 **(A–C)** and 2017 **(D)** Challenges; *centre*: log-spectra with polynomial trends (red line); *right*: cepstra before (dotted black) and after (red) liftering by polynomial detrending, with τ_0 the quefrency of the estimated first harmonic. **(A)** shows a high quality ECG and a cepstrum with a single harmonic; the corresponding CQI is 91.1%. **(B)** shows a high quality ECG, its cepstrum with 3 harmonics multiple of τ_0, and CQI is 67.2%. **(C)** shows a low-quality ECG with a single harmonic identifiable in the liftered cepstrum and CQI is 29.3% due to consistent low-quefrency noise. **(D)** shows a high quality ECG during atrial fibrillation: the log-spectrum does not have a periodic structure, the liftered cepstrum does not show a clear first harmonic, and CQI is 22.1% only. When a clear cepstral first harmonic is identifiable **(A–C)**, its quefrency τ_0 practically coincides with the mean R-R interval, RR_m.

empirically optimized some parameters of the cepstral estimator. In particular, the power cepstrum estimator depends on the type of data windowing and spectral smoothing, like the traditional Fourier periodogram. Since the cepstrum consists of two consecutive Fourier spectra, the length of the data windows should be defined in the time domain for the first Fourier Transform, selecting the duration of the ECG segments, and in the frequency domain for the second Fourier Transform, selecting the frequency range of the log-spectrum. The window length in the time domain was set equal to 10 s as a trade-off between frequency resolution, which should be sufficiently high to distinguish ECG harmonics, and amplitude of heart rate changes, which should be relatively small to locally preserve the pseudo-periodicity of the signal.

The optimal window length in the frequency domain was identified as the frequency band where the height of ECG spectral peaks remains relatively constant. This choice avoids introducing very low quefrency components in the cepstrum due to slow decreasing trends in the train of harmonics. The band was identified by calculating the power spectrum for consecutive 10-s segments of each synthesized ECG and by interpolating the maxima (**Figures 2A,B**). The interpolating function is relatively stable below 20 Hz and decreases at higher frequencies, coherently with the literature (Golden et al.,

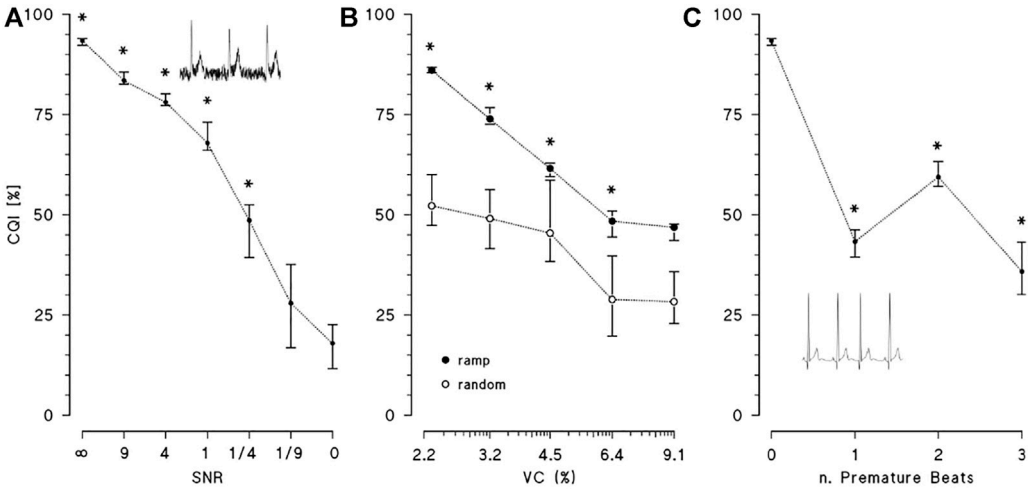

FIGURE 4 | Effects of noise and deviations from periodicity on CQI. CQI median and interquartile range over 8 synthesised ECGs. **(A)**: CQI at decreasing levels of signal-to-noise ratios, SNR (SNR = ∞ means no noise, SNR = 0 means noise only) with * indicating statistically significant difference vs. SNR = 0 at $p < 0.05$; the inset is an example of ECG with SNR = 4. **(B)**: CQI at increasing values of variation coefficient, VC, of R-R interval when the heart rate dynamics consists in monotonic ramps (solid circles) or random changes (open circles): median and interquartile range over 8 synthesised ECGs with * indicating statistically significant difference between ramp and random changes at $p < 0.05$. **(C)**: CQI without or with 1, 2 or 3 premature beats, with * indicating statistically significant difference vs. no premature beats at $p < 0.05$: inset is an example of simulated supraventricular premature beat.

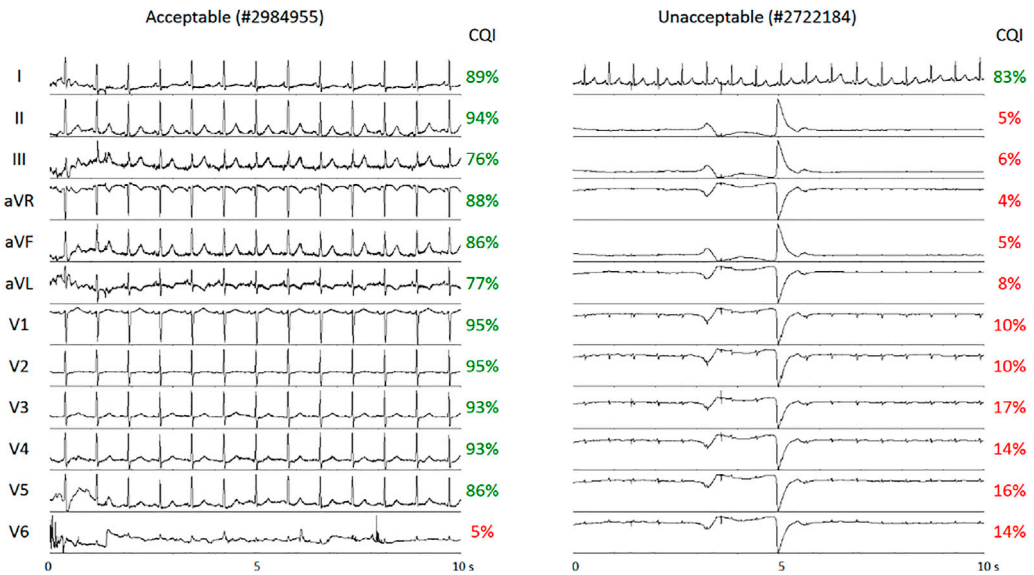

FIGURE 5 | Examples of multi-lead ECGs from the dataset of Physionet/Computing in Cardiology 2011 Challenge. The recordings were classified as "acceptable" (left) or "unacceptable" (right). CQI scores of individual leads correctly detect Lead I of sufficient quality for heart rate variability analysis in the "unacceptable" recording and Lead V6 as inadequate for heart rate variability analysis in the "acceptable" recording.

1973). This suggests setting the length of frequency-domain data windows between 0 and 20 Hz.

The type of window function critically defines the proper combination between power leakage and main-lobe amplitude of the Fourier spectrum (Marple, 1987), determining the relative power of the cepstral peak at the quefrency τ_0 corresponding to the mean R-R interval. To choose the time-domain data window, the relative amplitude of the main cepstral peak was calculated using six different windows (rectangular, triangular, 10%-cosine, Hann, Hamming, and Blackman) and by smoothing the resulting spectral lines with moving average filters of different orders. The best performance was obtained with the Blackmann window (**Figure 2C**): about 90% of the cepstral power is concentrated in the main cepstral peak if the Blackman window is used in the

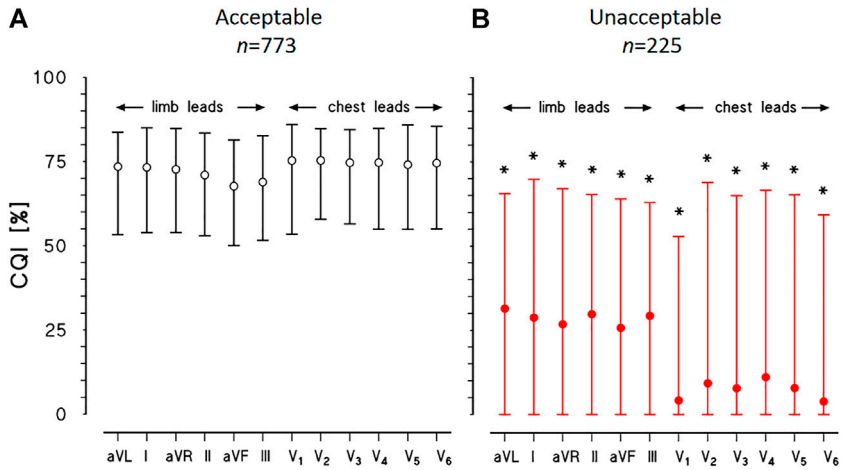

FIGURE 6 | Physionet/Computing in Cardiology Challenge 2011 datasets. CQI median and interquartile range for each of 12 leads of ECG recordings classified as "acceptable" **(A)** or "unacceptable" **(B)**: for each lead, the * indicates statistically significant difference between groups at $p < 0.01$.

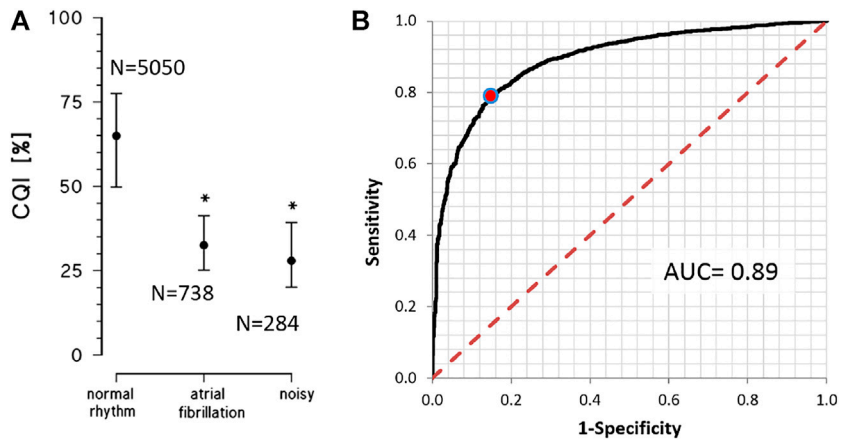

FIGURE 7 | Physionet/Computing in Cardiology Challenge 2017 datasets. **(A)** CQI as median and interquartile range for single-lead ECGs manually classified as in normal rhythm, atrial fibrillation or noisy recording. The * indicates a statistically significant difference vs. the normal rhythm group at $p < 0.01$ **(B)** ROC analysis on 5050 recordings adequate for heart rate variability analysis (normal rhythm) vs. 1022 recordings inadequate for heart rate variability analysis (in atrial fibrillation or noisy); the red dot on the curve identifies the classification cut-off (CQI > 47%) according to the Youden's criterion; AUC = Area Under the Curve.

time domain and the resulting spectral lines are smoothed with moving average filters of order between 250 and 500 mHz.

As regards the data window in the frequency domain, we selected the 10%-cosine taper (Bingham et al., 1967) because the window length is relatively short (up to 20 Hz only, implying a relatively large main lobe) and the cosine taper reduces leakage with a small increase only of the width of the main lobe.

2.4 A Cepstral Score of the Electrocardiogram Quality in Normal Sinus Rhythm

The evidence that the harmonic structure of synthesized ECGs produces cepstra with a dominant peak at the quefrency τ_0 corresponding to the average R-R interval, suggests taking the relative power of this cepstral peak (and its higher harmonics if present) as the index of ECG signal quality. To obtain a Cepstral Quality Index (CQI), first the ECG cepstrum and its total power are estimated as follows:

1. a 10-s ECG segment is selected, linearly detrended and Blackman windowed, $s(t)$;
2. the FFT power spectrum of $s(t)$ is calculated, $P(f)$;
3. $P(f)$ is truncated at 20 Hz, smoothed averaging contiguous lines over a frequency band of 300 mHz and log-transformed, log $P(f)$;
4. log $P(f)$ is linearly detrended by least-square fitting a regression line and windowed by the 10%-cosine taper, log $P(f)_{CT}$;

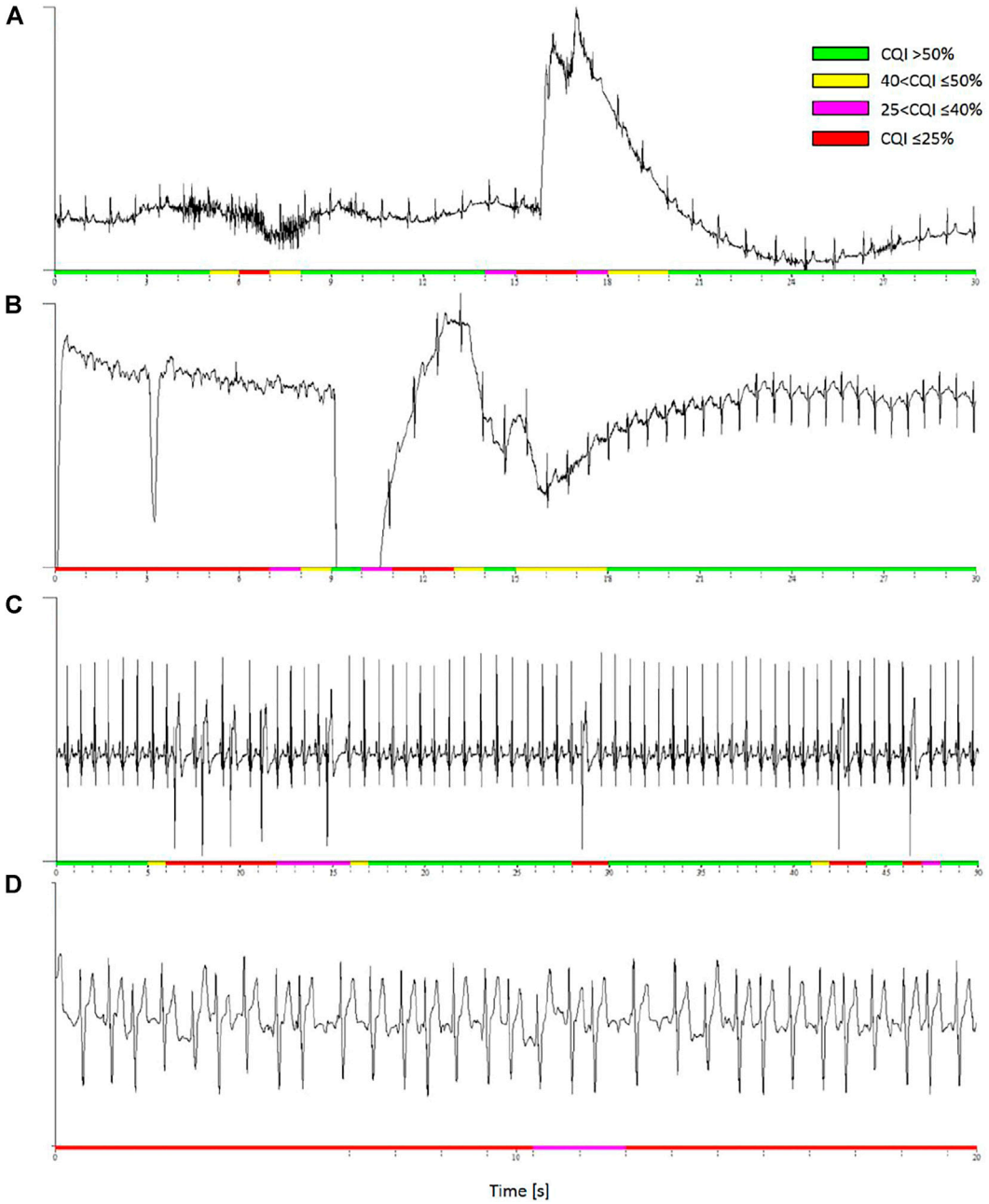

FIGURE 8 | Examples of discarded ECG segments by running cepstral analysis. Colors represent four CQI levels. **(A)***:* low CQI values identify a short burst of muscle noise and a following movement artefact. **(B)***:* low CQI values detect signal loss likely due to a poor contact between textile electrodes and skin. **(C)**: premature beats in a high quality recording are locally associated to low CQI values. **(D)***:* atrial fibrillation is associated to persistently low CQI even in high quality ECG recording.

5. the FFT power spectrum of log $P(f)_{CT}$ is calculated obtaining the cepstrum $CP(\tau)$ at quefrencies $\tau \geq 0.05$ s (inverse of 20 Hz, highest frequency in the log spectrum);

6. the total cepstral power TOT is calculated by integrating $CP(\tau)$ up to $\tau = 3$ s.

Figure 3 shows examples of power cepstra $CP(\tau)$ from real ECG recordings selected from the datasets of the PhysioNet/Computing in Cardiology 2011 Challenge (Silva et al., 2011) and 2017 Challenge (Clifford et al., 2017). **Figures 3A,B** show high-quality ECG in normal sinus rhythm: their cepstrum consists of the main harmonic at the quefrency of the mean R-R interval and possibly higher harmonics. By contrast, **Figure 3C** shows that noise may produce spurious cepstral peaks with larger power than the true ECG peak; in this case, high-pass "liftering" (i.e., filtering in the frequency domain) the log-spectra may help identifying the true peaks. Thus, to properly calculate the

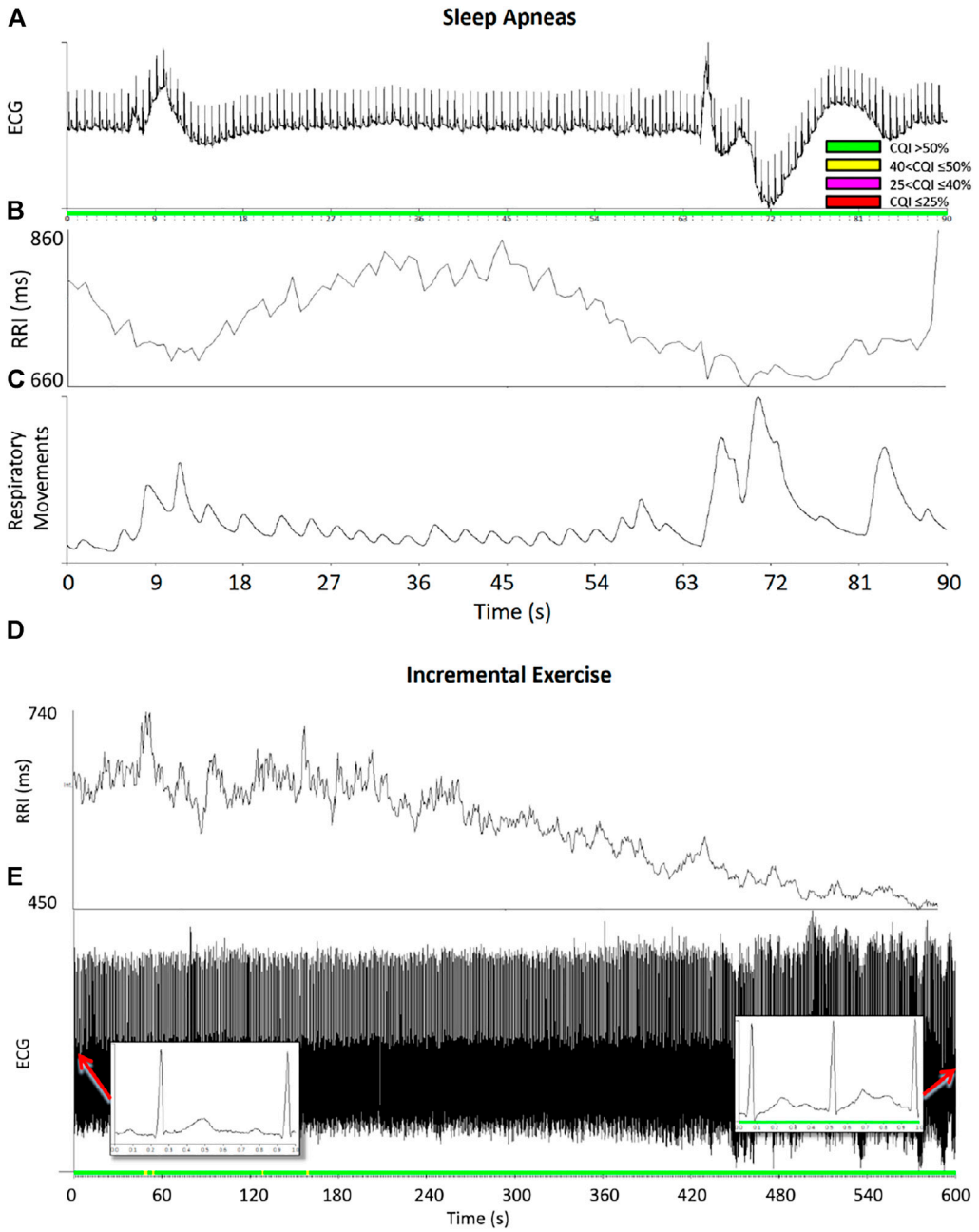

FIGURE 9 | Examples of running cepstral during ramp-like heart-rate changes. Upper panels: ECG **(A)**, R-R intervals, RRI **(B)**, and respiratory movements of the thorax **(C)** during sleep apneas; color codes represent the CQI levels. Even if apnea/deep breathing events produced large ramp-like changes of heart rate, the CQI score remained relatively high classifying the data segment of good quality for heart rate variability analysis. Lower panels: R-R intervals **(D)** and ECG **(E)** during an incremental exercise test on the cycloergometer: the ECG was in normal sinus rhythm (see insets) and the CQI score remained high even when RRI progressively decreased during the exercise.

power associated with the ECG cepstral harmonics, a liftered cepstrum is also estimated as follows:

7. log $P(f)$ (calculated at step 3) is "liftered" by least-square fitting and removing a polynomial of order 10, log $P(f)_L$;
8. the 10% cosine taper is applied to log $P(f)_L$ obtaining log $P(f)_{LCT}$;
9. the FFT of log $P(f)_{LCT}$ is calculated obtaining the liftered cepstrum $CP_L(\tau)$;
10. a moving average over a quefrency band of 0.20 s further improves the statistical consistency of $CP_L(\tau)$;

Figure 3 shows that liftering removes very-low quefrency power due to noise without affecting the true ECG cepstral

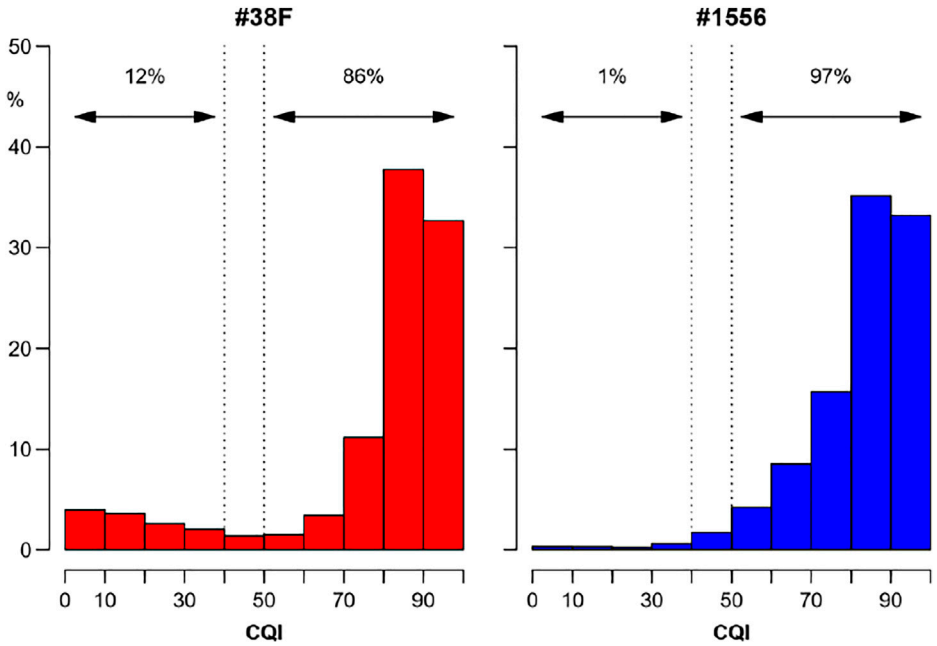

FIGURE 10 | Overall quality of very long-term ECG recordings from the distribution of running CQI values. Distributions (relative frequencies) of CQIs calculated second-by-second on ECG Holters recorded for 7 consecutive days continuously with a wearable device (RootiRx®, Rooti Labs Ltd., Taipei, Taiwan) at 250 Hz in two subjects. The recording of the subject on the right (#1556) is almost completely analysable having good quality (CQI > 50%) for 97% of the time; by contrast, assessing heart rate variability in the recording on the left (#38F) might be problematic for a not negligible fraction of the time, being the quality "very low" or "unacceptable" (CQI ≤ 40%) for 12% of the recording.

peaks. Readers may find a detailed description of the MATLAB code implementing steps from 1 to 10 in the **Supplemental Material**. We define the quality score as the power of the liftered cepstral peaks relative to the total power of the unliftered cepstrum as follows:

11. the power of $CP_L(\tau)$ first and second harmonics, H, is calculated;
12. the cepstral quality index is the ratio between H and TOT: CQI = H/TOT.

In our application, the main ECG peak is identified between $0.30 \leq \tau \leq 2.5$ s (the quefrency band where τ_0 corresponding to the average R-R interval is expected) by comparison with a threshold equal to the 90% percentile of the liftered cepstrum: the peak of the ECG first cepstral harmonic should overcross this threshold. A second cepstral peak that falls in the quefrency band corresponding to twice the band of the main harmonic is recognized as a genuine second harmonic. CQI may therefore range between 100% (when all the power of the cepstrum is contained in the first and second harmonics of the ECG cepstrum) and 0% (when no ECG peaks are identified in the cepstrum).

When the hypothesis of ECG pseudoperiodicity does not hold, as during arrhythmias episodes, a cepstral main harmonic might not be detected even in a high-quality ECG. **Figure 3D** shows an ECG segment during atrial fibrillation: the power spectrum does not have a periodic structure, cepstral harmonics cannot be correctly associated with a spectral periodicity, and the resulting CQI is remarkably low.

When the ECG recording is longer than 10 s, continuous, second-by-second CQI estimates are calculated for the whole duration of the recording performing the cepstral analysis on 90%-overlapped, running ECG segments of 10-s length.

2.5 Validation on Synthesized and Real Electrocardiograms

We quantified the effects of noise and deviations from pseudoperiodicity on CQI using the synthesized ECGs. The effect of broadband noise was evaluated by adding increasing levels of white noise to the synthesized ECGs, with signal-to-noise ratio, SNR (ratio between the ECG power and the power of added noise), between 9 and 1/9. The effects of deviations from periodicity were evaluated on synthesized ECGs appending the ECG templates at uneven periods. Two types of heart rate changes were simulated preserving the original mean heart rate: monotonic ramps, with R-R intervals increasing or decreasing linearly in time, and random fluctuations, with independent changes of R-R intervals from one beat to the next. Monotonic heart-rate ramps during normal sinus rhythm can be observed in 10-s ECG tracings following cardiac sympathetic or vagal activations, as well as during deep breathing episodes. Random heart-rate changes may somehow model the disordered cardiac rhythm in atrial fibrillation. The variation coefficient, VC (ratio between

standard deviation and mean) of the original R-R intervals in healthy volunteers was 4.5% when calculated over 10-s segments and the ECGs were synthesized with VC between half and twice this physiological value. Premature beats may also alter the ECG pseudo-periodicity. Supraventricular beats were simulated by removing the portion of the template before the QRS complex which includes the P wave. One, two, or three altered templates were added randomly to the equispaced sequence of synthesized ECGs.

To validate the proposed cepstral score on real ECG tracings, we considered recordings from two datasets provided by the Physionet Community at the MIT Laboratory for Computational Physiology (Goldberger et al., 2000). To test the effects of noise and artifacts on real ECG recordings, CQI was evaluated on "set-A" of ECG recordings made available for the Physionet/Computing in Cardiology 2011 Challenge (Silva et al., 2011). The recordings consisted of 12 ECG leads (I, II, III, aVR, aVF, aVL, V1-V6) sampled at 500 Hz, 16 bit with 5 μV resolution, and standard diagnostic bandwidth (0.05–100 Hz). The overall quality of each multi-lead recording was manually scored by a group of annotators. Combining their scores, ECG recordings were classified as having "acceptable" (n = 773) or "unacceptable" (n = 225) signal quality.

To systematically check how the CQI score detects arrhythmias, the cepstral analysis was applied to the training dataset of the PhysioNet/Computing in Cardiology 2017 Challenge (Clifford et al., 2017). The dataset is composed of single-channel (equivalent to lead I) ECGs recorded with the AliveCor devices at 300 Hz and 16 bit, with 0.5–40 Hz bandwidth, visually classified by experts into 4 groups: noisy, or in normal rhythm, or in atrial fibrillation, or in any "other" rhythm. From the whole dataset, we considered the 5050 normal-rhythm recordings, the 738 atrial fibrillation recordings, and the 284 noisy ECGs. Their duration ranged between 9 and 61 s, with a median value of 30 s. The running cepstral analysis was applied and the second-by-second estimates were averaged to obtain a single CQI score for each recording. The Area Under the Curve (AUC) of Receiver-Operator Characteristic (ROC) analysis measured how CQI classifies between cases for which heart rate variability analysis is feasible (i.e., normal rhythm recordings without excessive noise), and cases to be excluded from heart rate variability analysis (i.e., atrial fibrillation or too noisy recordings). The Youden index, calculated as in (Goksuluk et al., 2016), provided the cut-off value for the classification.

Statistical comparisons between groups were performed with the Wilcoxon matched-pairs test.

Additionally, we illustrated the performance of the proposed score by applying the running cepstral analysis on ECG tracings collected in our previous experiments, which included long-term recordings in free-moving volunteers at high altitudes (Lombardi et al., 2013; Caravita et al., 2015). The experiments were approved by the ethic committee of Istituto Auxologico Italiano, IRCCS (EudraCT No. 2010-019986-27) and conducted in agreement with the principles of the Declaration of Helsinki, after having received informed consent.

3 RESULTS

3.1 Validation on Synthesized Electrocardiograms

Figure 4A shows the effect of broadband noise on CQI. The index progressively decreases from values greater than 90%, when noise is absent, to 68% when SNR = 1. CQI falls more rapidly when SNR < 1 and at SNR = 1/9 it is statistically indistinguishable from CQI of pure noise. **Figure 4B** illustrates the effects of increasing levels of heart rate variability, quantified by VC, on CQI, comparing random changes with ramp-like changes. In both cases, CQI decreases with increasing levels of VC, but the effects depend on the type of heart rate dynamics, being more important for random than monotonic changes. As to the effects of premature beats on CQI, **Figure 4C** shows that even a single ectopic beat in the 10-s ECG segment reduces CQI importantly.

3.2 Validation on Real Electrocardiograms

3.2.1 Physionet/Computing in Cardiology 2011 Challenge

The effects of noise and artifacts on real ECG recordings were tested systematically on the Physionet/Computing in Cardiology 2011 Challenge dataset (Silva et al., 2011). **Figure 5** shows two examples of multi-lead ECGs, one classified as "unacceptable" and one as "acceptable"; the CQI of each lead is reported. Since the Physionet classification regards the quality of multi-lead ECGs as a whole, a single lead might have sufficient quality for heart rate variability analysis even in a multi-lead recording scored as globally unacceptable: this is the case of lead I of #2722184 recording. Similarly, individual leads may occasionally have poor quality even in globally "acceptable" recordings, such as lead V6 of #2984955 recording. In these two examples, the CQI scores allow automatically selecting the proper ECG leads for heart rate variability discarding inadequate leads.

Figure 6 shows the results of cepstral analysis for the whole dataset. The median CQI score of each lead is coherent with the manual classification through visual inspection of the recordings, being close to 70% for all the leads of the "acceptable" group and much lower for all the leads of the "unacceptable" group (close to 30% for limb leads, to 7% for chest leads).

However, the CQI interquartile range is remarkably wide for the "unacceptable" group, suggesting that leads with a sufficient CQI score for heart rate variability analysis may be identified in most cases even in this group, as the example of **Figure 5A** suggests.

3.2.2 Physionet/Computing in Cardiology 2017 Challenge

Figure 7A compares CQI values in the three groups of recordings of the PhysioNet/Computing in Cardiology 2017 Challenge (Clifford et al., 2017). These three groups were selected to quantify the effects of deviations due to noise or atrial fibrillation from the pseudoperiodicity of the normal rhythm. Most of the recordings in normal rhythm have CQIs greater than 50%, as the "acceptable" recordings of the 2011 Challenge. Atrial

fibrillation or noise substantially reduces CQI, which is lower than 40% in most of these recordings.

The ROC curve that was calculated to quantify the capability of CQI to identify an ECG recording as adequate for heart rate variability analysis, was associated with a consistently high AUC (**Figure 7B**). The Youden criterion identified in CQI > 47% the cut-off to classify an ECG recording as adequate, with 79.0% sensitivity and 85.2% specificity.

3.2.3 Running Cepstral Analysis

Figure 8 shows examples of running cepstral analysis on ECGs collected with wearable/mobile devices affected by different types of noise. A four-level color code is used to represent the CQI values estimated second by second. Based on the cut-off defined by ROC analysis (**Figure 7B**), we classified the ECG as having good quality when CQI > 50%, representing the time window in green color, and as having "acceptable quality" when 40 < CQI ≤ 50%, representing the time window in yellow. ECG classified with "very low" or "unacceptable" quality are associated with 25 < CQI ≤ 40% and CQI ≤ 25%, and are represented in magenta and red respectively.

Panel a) is a segment of 24-h ECG (250 Hz sampling, 16 bit) in a healthy volunteer during daily-life activities with a wearable device (Faros 360 Mega, Kuopio, Finland). The ECG shows a short burst of muscular noise followed by a movement artifact: the running analysis associates both the events with locally low CQI values.

Panel b) is a segment of ECG recorded in a healthy volunteer during night-time sleep at a high altitude (Lombardi et al., 2013). The ECG (200 Hz, 12 bit) was recorded with the MagIC device, a wearable system with woven ECG electrodes, a textile plethysmograph for measuring respiratory movements of the thorax, and a sternal accelerometer (Di Rienzo et al., 2010), connected to a pulse oximeter (Nonin Xpod®, Nonin Medical, Inc., Plymouth, MN, United States). The running analysis classified unacceptable (CQI ≤ 25%) a data segment with a temporary signal loss, likely due to a bad contact between textile electrodes and skin. The recovery of the ECG waveform was identified by classifying the signal as having CQI > 50%.

Panel c) is a high-quality ECG with frequent premature beats recorded by MagIC in a volunteer resting at a high altitude (Caravita et al., 2015). While most of the recording is associated with high CQI values, each premature beat causes a dramatic local fall in the quality score. These beats are classified as "unacceptable" for heart rate variability analysis.

Panel d) is an example of running cepstral analysis during random heart-rate variations due to the lack of normal sinus rhythm. The ECG was recorded with a mobile electrocardiograph (AliveCor Inc., Mountain View, CA, United States) by a patient in atrial fibrillation (#A00027 of the PhysioNet/Computing in Cardiology Challenge 2017 dataset). The whole signal is associated with very low CQI values indicating that it is unacceptable for heart rate variability.

Figure 9 shows examples of running cepstral analysis on ECG tracings in normal sinus rhythm with large ramp-like changes in heart rate. The upper panels regard a segment of a sleep recording at a high altitude by the MagIC device. The low barometric pressure at high altitude induced frequent apneas/hypopneas events followed by deep breathing, which caused wide ramp-like changes in R-R intervals and fluctuations of the ECG baseline. These wide heart rate fluctuations occurred in normal sinus rhythm and did not prevent the cepstral analysis to quantify high CQI scores and classify the segment as acceptable for heart rate variability analysis.

The lower panels of **Figure 9** regard an ECG recording (1000 Hz sampling rate, PowerLab 8/35 Bioamp—Data Acquisition System, ADInstruments, Dunedin, New Zealand) during an incremental exercise test up to exhaustion on the cycle ergometer (Ergoselect 100, ergoline GmbH, Bitz, Germany). The test was performed by a 14-year-old male participant with an increasing exercise load at 12 W/min. Even if the R-R intervals decreased progressively during the test with a ramp-like pattern as the load increased, the CQI score remained sufficiently high and classified the ECG quality as "good" or "acceptable" throughout the test.

4 DISCUSSION AND CONCLUSION

In the last years, several methods have been proposed for evaluating the quality of ECG recordings: the principles on which they are defined and comparisons among methods are reported in two recent reviews (Satija et al., 2018; Rahman et al., 2022). These reviews highlight that the accuracy of each method depends on the medical context for which it is proposed. Therefore, while some methods are aimed at the correct identification of the QRS complex only, others require a more detailed morphological identification of specific ECG features, like amplitudes and intervals between waves (Satija et al., 2018). Furthermore, the accuracy depends on the testing dataset because the type of artifacts and noises affecting mobile ECGs for telemonitoring applications differ from those expected for wearable ECG devices or ECGs recorded in the doctor's office or in intensive care units (Rahman et al., 2022). In this context, the usefulness of our cepstral approach is to address a specific aspect of the ECG signal quality that has not been explicitly considered by other methods: the acceptability of ECG recordings for heart rate variability analysis. In this frame, an ECG segment should be considered not acceptable even in absence of noise components or artifacts if it does not occur during normal sinus rhythm, a condition not considered by other indexes of signal quality. In addition, our work was motivated by the need to evaluate the ECG adequacy for heart rate variability analysis continuously onboard wearable devices with low computational power. We found the cepstral analysis to be a promising approach because the power cepstrum describes the periodic structure of ECG recordings in a simple way (i.e., with the main harmonic at τ_0 and very few multiples at most) that can be calculated and interpreted easily. This makes the power cepstrum a potentially useful tool in heart rate variability studies to identify and discard noisy ECG recordings or recordings not in normal sinus rhythm. The estimation of the power cepstrum does not require important computational resources and consent defining a simple score,

CQI, evaluable by the wearable systems themselves. In multi-lead ECG recordings, CQI could allow selecting and transmitting the ECG lead with the best quality only (that is the lead with the highest CQI), reducing the flow of redundant information within the monitoring system and the power consumption for signal transmission.

The dataset of the Physionet/Computing in Cardiology 2017 Challenge demonstrated that CQI is useful to distinguish ECGs in normal rhythm from unacceptable recordings due to noise or arrhythmias, and provided us with an objective cut-off threshold for the classification. In ambient-assisted living applications, thresholds on running CQI estimates may be employed to send alerts from the wearable device to upper computational levels, which may apply more sophisticated analysis tools, possibly integrating other physiological, behavioral, and environmental signals, to properly manage the alarm. On very-long term monitoring, comparing the distribution of CQI values with cut-off thresholds provides an effective way to summarize the overall quality of the ECG recording, as in the example of **Figure 10**.

It is worth noting that deviations from the ECG periodicity may occur also in normal sinus rhythm due to physiological changes in heart rate. Even if most applications of heart rate variability require stationarity, which assures a stable mean heart rate, time-varying methods are employed to describe autonomic activations that induce rapid changes in the cardiac rhythm. These changes appear as heart-rate ramps in the short running window used for cepstral analysis and they should not be excluded from the evaluation of heart rate variability. Results on synthesized ECGs (**Figure 4B**) showed that a chaotic heart-rate pattern decreases CQI significantly more than a ramp-like pattern with the same variation coefficient. As **Figure 9** exemplifies, this means that even marked ramp-like changes in the heart rate may be correctly classified as adequate for evaluating the heart rate variability if they occur in normal sinus rhythm, in absence of artifacts or noise.

4.1 Limitations and Future Perspectives

We defined CQI to assess recordings in adults or the elderly during daily activities. Therefore, the parameters defining our method should be modified to properly monitor subjects with much higher heart rates, such as neonates or young athletes during maximal exercise. This can be done easily because the parameters are easily interpretable. For instance, let's consider the frequency data window we defined between 0 and 20 Hz and the cepstral band for identifying the peak at τ_0 between 0.3 and 2.5 s; if the heart rate is 180 bpm, only 6 harmonics fall in the frequency data window and τ_0 is very close to the lower limit of the cepstral band. Thus, if such high average heart rates are expected, it may be desirable to increase the upper limit of the frequency window above 20 Hz and to shift the cepstral band toward quefrencies lower than 0.3 s to better capture the cepstral power around the mean R-R interval. Moreover, a limit of CQI is that it does not distinguish between noise and arrhythmias, being similarly low in the case of noise and atrial fibrillation (**Figure 7A**), even if the causes for the deviations from the ECG periodicity are rather different in the two cases. More detailed quantification of the cepstral morphology than CQI might better characterize the chaotic rhythm of atrial fibrillation, possibly integrating traditional spectral methods to distinguish among types of atrial fibrillation and between atrial fibrillation and noise.

DATA AVAILABILITY STATEMENT

Publicly available datasets were analyzed in this study. This data can be found here: Physionet https://physionet.org/about/challenge/moody-challenge. The Matlab code described in the Supplemental Material can be accessed at doi:10.5281/zenodo.6552328.

ETHICS STATEMENT

The studies involving human participants were reviewed and approved by Ethical Committee of the Istituto Auxologico Italiano (Milan, Italy), approval number 2010_04_13_01. Written informed consent to participate in this study was provided by the participants' legal guardian/next of kin.

AUTHOR CONTRIBUTIONS

PC and AF developed the methodology, wrote the software, designed the algorithm validation with synthesized series, performed the validation on real signals, and lead the manuscript writing. GP provided real ECG signals. All the authors interpreted the results and critically revised the manuscript.

FUNDING

Research funded by the Italian Ministry of Health.

SUPPLEMENTARY MATERIAL

The Supplementary Material for this article can be found online at: https://www.frontiersin.org/articles/10.3389/fphys.2022.921210/full#supplementary-material

REFERENCES

Bingham, C., Godfrey, M., and Tukey, J. (1967). Modern Techniques of Power Spectrum Estimation. *IEEE Trans. Audio Electroacoust.* 15, 56–66. doi:10.1109/TAU.1967.1161895

Bogert, B. P., Healy, M. J., and Tukey, J. W. (1963). The Quefrency Analysis of Time Series for Echoes : Cepstrum, Pseudo-autocovariance, Cross-Cepstrum and Saphe Cracking. *Proc. symposium time Ser. analysis* 15, 209–243.

Caravita, S., Faini, A., Lombardi, C., Valentini, M., Gregorini, F., Rossi, J., et al. (2015). Sex and Acetazolamide Effects on Chemoreflex and Periodic Breathing during Sleep at Altitude. *Chest* 147, 120–131. doi:10.1378/chest.14-0317

Castiglioni, P., Meriggi, P., Faini, A., and Rienzo, M. D. (2011). "Cepstral Based Approach for Online Quantification of ECG Quality in Freely Moving Subjects," in 2011 Computing in Cardiology, Hangzhou, China, 18-21 Sept. 2011, 625–628.

Clifford, G., Liu, C., Moody, B., Lehman, L.-w., Silva, I., Li, Q., et al. (2017). AF Classification from a Short Single Lead ECG Recording: The Physionet Computing in Cardiology Challenge 2017," in Computing in Cardiology Conference (CinC),2017 Computing in Cardiology Conference (CinC). doi:10.22489/CinC.2017.065-469

Di Rienzo, M., Meriggi, P., Rizzo, F., Castiglioni, P., Lombardi, C., Ferratini, M., et al. (2010). Textile Technology for the Vital Signs Monitoring in Telemedicine and Extreme Environments. *IEEE Trans. Inf. Technol. Biomed.* 14, 711–717. doi:10.1109/TITB.2010.2048921

Goksuluk, D., Korkmaz, S., Zararsiz, G., and Karaagaoglu, A. E.(2016). easyROC: An Interactive Web-Tool for ROC Curve Analysis Using R Language Environment. *R J.* 8, 213. doi:10.32614/RJ-2016-042

Goldberger, A. L., Amaral, L. A., Glass, L., Hausdorff, J. M., Ivanov, P. C., Mark, R. G., et al. (2000). PhysioBank, PhysioToolkit, and PhysioNet: Components of a New Research Resource for Complex Physiologic Signals. *Circulation* 101, E215–E220. doi:10.1161/01.cir.101.23.e215

Golden, D. P., Wolthuis, R. A., and Hoffler, G. W. (1973). A Spectral Analysis of the Normal Resting Electrocardiogram. *IEEE Trans. Biomed. Eng.* BME-20, 366–372. doi:10.1109/TBME.1973.324231

Gower, V., Andrich, R., Braghieri, P., and Susi, A. (2011). "An Advanced Monitoring System for Residential Care Facilities," in *Everyday Technology for Independence and Care Assistive Technology Research Series (Gert Jan Gelderblom, Mathijs Soede, Leon Adriaens, Klaus Miesenberger)*, 57–64. doi:10.3233/978-1-60750-814-4-57

Lombardi, C., Meriggi, P., Agostoni, P., Faini, A., Bilo, G., Revera, M., et al. (2013). High-altitude Hypoxia and Periodic Breathing during Sleep: Gender-Related Differences. *J. Sleep. Res.* 22, 322–330. doi:10.1111/jsr.12012

Marple, S. L. (1987). *Digital Spectral Analysis: With Applications*. Englewood Cliffs, N.J: Prentice-Hall.

Oppenheim, A. V., and Schafer, R. W. (2004). Dsp History - from Frequency to Quefrency: A History of the Cepstrum. *IEEE Signal Process. Mag.* 21, 95–106. doi:10.1109/MSP.2004.1328092

Rahman, S., Karmakar, C., Natgunanathan, I., Yearwood, J., and Palaniswami, M. (2022). Robustness of Electrocardiogram Signal Quality Indices. *J. R. Soc. Interface.* 19, 20220012. doi:10.1098/rsif.2022.0012

Satija, U., Ramkumar, B., and Manikandan, M. S. (2018). A Review of Signal Processing Techniques for Electrocardiogram Signal Quality Assessment. *IEEE Rev. Biomed. Eng.* 11, 36–52. doi:10.1109/RBME.2018.2810957

Silva, I., Moody, G. B., and Celi, L. (2011). "Improving the Quality of ECGs Collected Using Mobile Phones: The PhysioNet/Computing in Cardiology Challenge 2011," in 2011 Computing in Cardiology, 273–276.

Conflict of Interest: The authors declare that the research was conducted in the absence of any commercial or financial relationships that could be construed as a potential conflict of interest.

frontiers | Frontiers in Physiology

ORIGINAL RESEARCH
published: 07 July 2022
doi: 10.3389/fphys.2022.873630

Non-Contact Intracardiac Potential Mapping Using Mesh-Based and Meshless Inverse Solvers

Shu Meng[1], Judit Chamorro-Servent[2], Nicholas Sunderland[1,3], Jichao Zhao[1], Laura R. Bear[4,5,6], Nigel A. Lever[1,7,8], Gregory B. Sands[1], Ian J. LeGrice[1,9], Anne M. Gillis[10], David M. Budgett[1] and Bruce H. Smaill[1]*

[1]Auckland Bioengineering Institute, University of Auckland, Auckland, New Zealand, [2]Department of Mathematics, Universitat Autònoma de Barcelona, Bellaterra, Spain, [3]Bristol Heart Institute, University of Bristol, Bristol, United Kingdom, [4]HU Liryc, Electrophysiology and Heart Modeling Institute, Fondation Bordeaux Université, Bordeaux, France, [5]Centre de Recherche Cardio-Thoracique de Bordeaux, Université Bordeaux, Bordeaux, France, [6]INSERM, Centre de Recherche Cardio-Thoracique de Bordeaux, Bordeaux, France, [7]Auckland City Hospital, Auckland, New Zealand, [8]Department of Medicine, University of Auckland, Auckland, New Zealand, [9]Department of Physiology, University of Auckland, Auckland, New Zealand, [10]Libin Cardiovascular Research Institute, Calgary University, Calgary, AB, Canada

Atrial fibrillation (AF) is the most common cardiac dysrhythmia and percutaneous catheter ablation is widely used to treat it. Panoramic mapping with multi-electrode catheters has been used to identify ablation targets in persistent AF but is limited by poor contact and inadequate coverage of the left atrial cavity. In this paper, we investigate the accuracy with which atrial endocardial surface potentials can be reconstructed from electrograms recorded with non-contact catheters. An *in-silico* approach was employed in which "ground-truth" surface potentials from experimental contact mapping studies and computer models were compared with inverse potential maps constructed by sampling the corresponding intracardiac field using virtual basket catheters. We demonstrate that it is possible to 1) specify the mixed boundary conditions required for mesh-based formulations of the potential inverse problem fully, and 2) reconstruct accurate inverse potential maps from recordings made with appropriately designed catheters. Accuracy improved when catheter dimensions were increased but was relatively stable when the catheter occupied >30% of atrial cavity volume. Independent of this, the capacity of non-contact catheters to resolve the complex atrial potential fields seen in reentrant atrial arrhythmia depended on the spatial distribution of electrodes on the surface bounding the catheter. Finally, we have shown that reliable inverse potential mapping is possible in near real-time with meshless methods that use the Method of Fundamental Solutions.

Keywords: atrial fibrillation, open basket catheters, inverse problem, non-contact mapping, endocardial potentials

OPEN ACCESS

Edited by:
Matthijs Cluitmans, Maastricht University, Netherlands

Reviewed by:
Jake Bergquist, The University of Utah, United States
Peter Michael Van Dam, University Medical Center Utrecht, Netherlands

****Correspondence:***
Shu Meng
shu.meng@auckland.ac.nz

Specialty section:
This article was submitted to Cardiac Electrophysiology, a section of the journal Frontiers in Physiology

Received: *11 February 2022*
Accepted: *07 June 2022*
Published: *07 July 2022*

Citation:
Meng S, Chamorro-Servent J, Sunderland N, Zhao J, Bear LR, Lever NA, Sands GB, LeGrice IJ, Gillis AM, Budgett DM and Smaill BH (2022) Non-Contact Intracardiac Potential Mapping Using Mesh-Based and Meshless Inverse Solvers. Front. Physiol. 13:873630. doi: 10.3389/fphys.2022.873630

INTRODUCTION

Intracardiac catheters can acquire electrograms simultaneously at multiple sites on or close to the heart wall and have been used to construct panoramic maps of electrical activity in patients during persistent atrial fibrillation (AF) (Narayan et al., 2012; Pathik et al., 2018). While macro-scale atrial activation is disorganized in AF, it is argued that repeated patterns of local electrical reentry in such maps may provide targets for the percutaneous catheter ablation procedures used to treat this

dysrhythmia (Narayan et al., 2012; Haissaguerre et al., 2016). Effective contact mapping with multi-electrode catheters presents challenges. The spatial distribution of electrodes in the 8-spline basket catheters that have been used for intra-atrial mapping is inherently non-uniform, with greater density along splines than around the equator of these devices when fully deployed (Pathik et al., 2018). Deformation of basket catheter splines in contact with the wall can exacerbate sampling heterogeneity (Pathik et al., 2018). Furthermore, experimental and modelling studies indicate incomplete wall coverage, with ~50% only of electrodes close to the atrial wall (<5 mm from endocardium) in typical studies of the left atrium (LA) (Oesterlein et al., 2016; Martinez-Mateu et al., 2018; Pathik et al., 2018).

Inverse methods can be used to reconstruct potential maps on the heart surface from electrograms recorded with electrodes that are not in contact with it (Johnson and Bronzino, 2000; Pullan et al., 2005). This requires information about the geometry of the heart surface, the 3D locations of the electrodes and the electrical properties of the volume between them. Mesh-based solutions of the inverse potential problem have been widely used for non-invasive electrocardiographic imaging (ECGi) (Barr et al., 1977; Johnson and Bronzino, 2000; Ramanathan and Rudy, 2001; Pullan et al., 2005; Cluitmans et al., 2017; Duchateau et al., 2019) but also for non-contact intracardiac potential mapping with electrodes arrays mounted on the surface of inflatable balloons (Khoury et al., 1995). To solve this problem, it is necessary to specify Cauchy boundary conditions; that is to assign both potentials and normal potential gradients at points across the boundary on which electrical recordings are made (Johnson and Bronzino, 2000; Pullan et al., 2005). This presents no difficulties for ECGi or for intracardiac inverse potential mapping if electrodes are mounted on an inflatable balloon. Sampling surfaces are insulating in both instances and the normal potential gradient is zero everywhere on them. This is not the case, however, for a multi-electrode basket catheter and normal potential gradients must be estimated on the virtual surface that bounds the electrodes to solve mesh-based formulations of the inverse potential problem. While reliable solutions of the inverse potential problem can in principle be obtained with mesh-based methods such as the finite element method (FEM) or boundary element method (BEM) if appropriate input information is provided (Johnson and Bronzino, 2000; Pullan et al., 2005), meshless methods that employ the Method of Fundamental Solutions (MFS) (Fairweather and Karageorghis, 1998) offer a simpler alternative. The latter approach has been used for ECGi (Wang and Rudy, 2006; Bear et al., 2018) and was recently proposed for non-contact intracardiac potential mapping (Meng et al., 2022).

Here, we provide a systematic *in silico* analysis of mesh-based and meshless methods for solving the intracardiac inverse potential problem—for the first time as far as we are aware. The mathematical bases of the approaches used in this setting are summarized and a simple method for estimating Cauchy boundary conditions from electrograms recorded with a multi-electrode basket catheter is outlined. This is tested in a simplified 2D domain and then used for an FEM-based investigation of inverse potential mapping in the 3D atria. The extent to which accuracy is affected by catheter dimensions, electrode distribution and noise are considered. Finally, we compare the efficacy of this mesh-based approach with meshless methods that use the MFS.

This study demonstrates that reliable non-contact potential mapping can be achieved across a wide range of basket catheter dimensions using mesh-based inverse methods if the electrode distribution is sufficient to provide representative samples of the intracardiac potential field. It also shows that the MFS is equally accurate over most of this range but computationally more efficient.

MATHEMATICAL BACKGROUND

The electrostatic potential ϕ in a biological volume conductor is typically represented as

$$\nabla \cdot \sigma \nabla \phi = -I_v \tag{1}$$

where σ is the electrical conductivity tensor and I_v is the current per unit volume defined within the solution domain Ω. Electrostatic potentials associated with cardiac electrical activity flow are caused by current flow *via* transmembrane ion channels and transporters in heart muscle cells, but there is no nett current flow elsewhere in the domain. Therefore,

$$\nabla \cdot \sigma \nabla \phi = 0 \text{ in } \Omega_H \tag{2}$$

where Ω_H is a heart cavity.

A Mesh-Based Inverse Approach

A representation of the potential problem is given in **Figure 1A**. If the potential on the endocardial surface Γ_H is specified (Dirichlet boundary conditions), ϕ can be estimated throughout Ω_H by solving the forward problem **Eq. 2**.

The objective of the corresponding inverse problem is to reconstruct ϕ on Γ_H from potentials recorded with an array of electrodes introduced into the cavity on a catheter. This can be expressed as a boundary value problem by defining a surface Γ_C that bounds the electrodes on the catheter and encloses the domain Ω_C. We seek to define a set of linear equations that satisfies Eq. 2 in $\Omega_H - \Omega_C$ and can be reformulated as

$$\mathbf{A}\phi_H = \phi_C \tag{3}$$

where ϕ_H is a vector of data on Γ_H and ϕ_C is a vector of data on Γ_C. The inverse problem is to determine ϕ_H given ϕ_C.

Both problems can be solved numerically using *finite difference*, *finite element* and *finite volume* methods or, because the problem can be reduced to the boundaries alone since σ is uniform and isotropic throughout Ω_H, using *boundary integral* and *boundary element* methods (Oostendorp and van Oosterom, 1991; Johnson and Bronzino, 2000; Pullan et al., 2005). To do so, it is first necessary to discretize the solution domain with an appropriate mesh. Because the inverse problem is ill-posed, solutions are not unique and this amplifies the effects of noise. Tikhonov regularization (Johnson and Bronzino, 2000) is widely used in this setting to reduce instability. It seeks to identify the regularization parameter λ that optimises the objective function

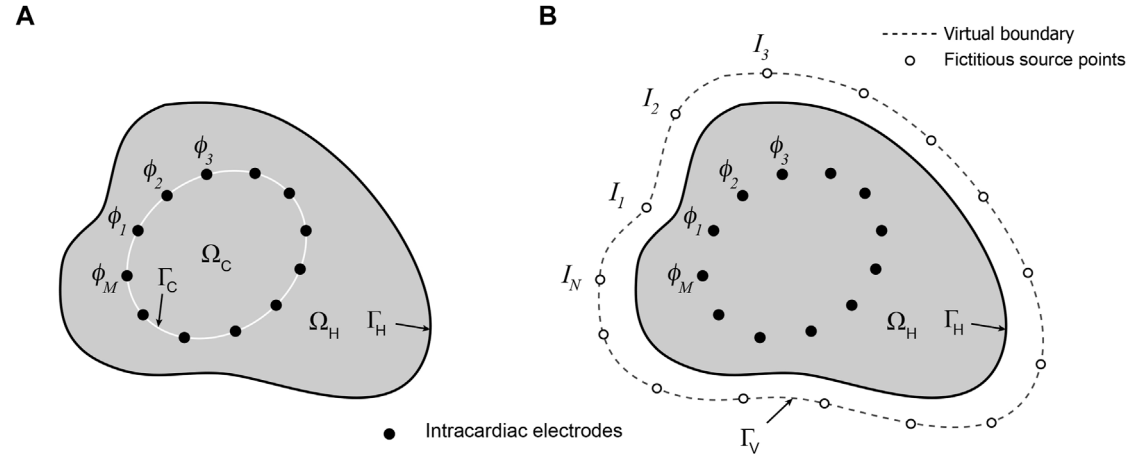

FIGURE 1 | Schematic representations of **(A)** mesh-based and **(B)** meshless/MFS formulations of the intracardiac inverse potential problem which seeks to map the potential distribution on the surface Γ_H that bounds a heart cavity Ω_H from a set of M potentials $\phi_C(\boldsymbol{x})$ sampled at electrodes inside Ω_H. In **(A)** potentials and normal potential gradients on the surface Γ_C that bounds the electrodes are related to the potential distribution on Γ_H and in solution domain $\Omega_H - \Omega_C$. In **(B)** N fictitious sources I_i (open circles) distributed around a virtual boundary Γ_V outside Γ_H generate the current flux that gives rise to the potential distribution in Ω_H. These are matched to the sampled potentials $\phi_C(\boldsymbol{x})$ enabling potential distribution on Γ_H to be estimated.

$$\left\|\mathbf{A}\phi_H - \phi_C\right\|^2 + \lambda\left\|\mathbf{L}\phi_H\right\|^2 \tag{4}$$

where the first term is the sum of squared residuals from **Eq. 3** and the second penalizes lack of smoothness of the solution vector. With zero-order Tikhonov regularization **L** is the identity matrix (Tikhonov and Arsenin, 1977). The closely related inverse problem of electrocardiography ECGi, in which voltages measured on the torso are used to calculate voltages on the surface of the heart, has been solved using all the numerical methods above (Barr et al., 1977; Johnson and Bronzino, 2000; Pullan et al., 2005; Cluitmans et al., 2017; Bear et al., 2018).

To solve the intracardiac inverse problem, it is necessary to specify appropriate boundary conditions at Γ_C. Continuity of potential and normal current flow is maintained on both sides of the interface (Pullan et al., 2005).

That is

$$\begin{aligned} \phi_C^{in} &= \phi_C^{out} \\ \sigma_{in}\nabla\phi_C^{in}\cdot\boldsymbol{n} &= \sigma_{out}\nabla\phi_C^{out}\cdot\boldsymbol{n} \end{aligned} \tag{5}$$

where *in* and *out* indicate inner and outer sides of Γ_C respectively.

For a balloon catheter, $\sigma_{in} = \infty$ and $\nabla\phi_C\cdot\boldsymbol{n} = 0$, and the inverse problem for this case has been solved using a boundary element method very similar to equivalent approaches used for ECGi (Khoury et al., 1995; Pullan et al., 2005). However, current flows freely across Γ_C with a basket catheter and the dispersion of current in $\Omega_H - \Omega_C$ can vary substantially between these cases depending on the geometry of Γ_H and Γ_C. The distribution of ϕ in $\Omega_H - \Omega_C$ reflects this and it follows that ϕ cannot be estimated adjacent to Γ_C unless Cauchy boundary conditions which specify both ϕ_C and $\nabla\phi_C.\boldsymbol{n}$ are used. A simple way to set these boundary conditions is to solve the forward problem **Eq. 2** for the subdomain Ω_C using ϕ_C recorded on Γ_C as Dirichet boundary conditions so that ϕ^{in} adjacent to Γ_C can be estimated. Provided that ϕ_C samples the potentials on Γ_C adequately, $\nabla\phi_C\cdot\boldsymbol{n}$ can be estimated enabling Cauchy boundary conditions to be specified.

Meshless Inverse Methods That Use the Method of Fundamental Solutions

The Method of Fundamental Solutions (MFS) provides a means of solving partial differential equations such as the Laplace equation without the need to set up connected internal meshes in the solution domain (Fairweather and Karageorghis, 1998). This approach was applied to ECGi by Wang and Rudy (Wang and Rudy, 2006) and here we extend it to intracardiac inverse potential mapping.

The meshless/MFS formulation of the intracardiac problem is presented in **Figure 1B**. Potentials $\phi(\boldsymbol{x})$ at points $\boldsymbol{x}$ in Ω_H are approximated as the linear superposition of source functions positioned at locations $\{\xi_i\}_{i=1}^N$ around a virtual surface Γ_V that encloses Ω_H. It is assumed that the conductivity σ throughout the extended domain bounded by Γ_V is uniform and isotropic, and that the electrical properties of the basket catheter can be neglected.

At any instant, the potential $\phi_C(\boldsymbol{x})$ at each of the M electrodes at $\boldsymbol{x}$ in Ω_H is estimated as

$$\phi(\boldsymbol{x}) = \sum_{i=1}^{N}\sigma I_i G(\xi_i, \boldsymbol{x}) \tag{6}$$

where $I_i = (I_1, \ldots, I_N)$ are the source current magnitudes at $\{\xi_i\}_{i=1}^N$ and G is the fundamental solution of the 3D Laplace operator at each point. That is,

$$G(\xi, \boldsymbol{x}) = \frac{1}{4\pi|\xi - \boldsymbol{x}|} \tag{7}$$

where $|\xi - \boldsymbol{x}|$ is the Euclidean distance between $\boldsymbol{x}$ and ξ.

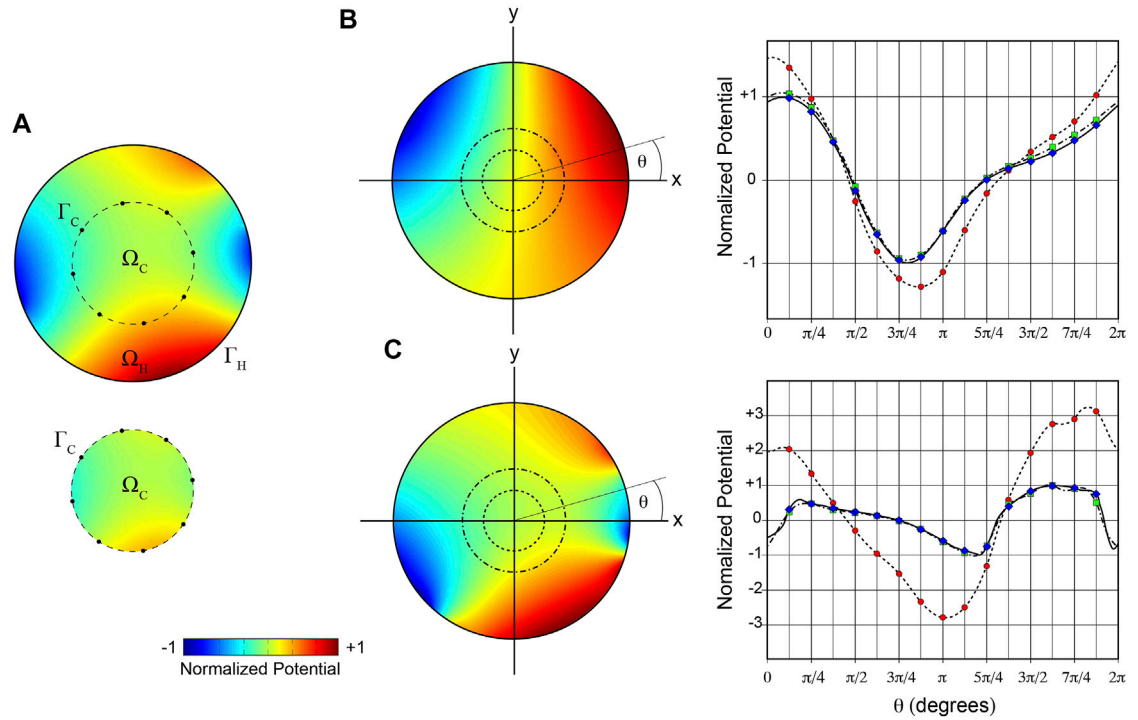

FIGURE 2 | 2D illustration of mesh-based inverse potential mapping. **(A)** Schematic of steps in specifying Cauchy boundary conditions on Γ_C. The potential distribution in Ω_H (upper panel) is sampled at 8 recording electrodes (black dots). Potentials around Γ_C are reconstructed from these samples with radial basis interpolation and used as Dirichlet boundary conditions in numerical solution of potential distribution in Ω_C (lower panel). This enables estimation of potentials and normal potential gradients around Γ_C. **B** and **(C)** Potential distributions on Γ_H reconstructed from potentials sampled in Ω_H for **(B)** relatively simple, and **(C)** more complex potential fields in Ω_H. Ground-truth potential distributions in Ω_H are given on left and the broken circles indicate the internal boundaries around which samples are acquired (16 sites in both cases). Potentials on Γ_H are reconstructed using Cauchy boundary conditions on Γ_C and compared with ground-truth potentials in the graphs at right. Normalized ground truth surface potentials (solid line, blue diamonds), and surface potentials reconstructed from samples acquired on internal boundaries with relative radii 0.469 (dashed line, green squares) and 0.375 (dotted line, red circles) are plotted as functions of angular coordinate θ.

This results in an $M \times N$ system of equations and solution of the inverse problem yields the source current magnitudes that best match the $\phi_C(\boldsymbol{x})$ recorded with the catheter. The corresponding endocardial potentials $\phi_H(\boldsymbol{x})$ can then be reconstructed by evaluating **Eq. 6** $\forall\, \boldsymbol{x} \in \Gamma_H$.

This system is inherently under-determined because the number of electrodes M is generally less than N, the number of fictitious sources needed to map potentials faithfully onto Γ_H.

METHODS

A well-established computational approach (Ramanathan and Rudy, 2001) was used to quantify the accuracy with which potentials around an external boundary can be reconstructed from non-contact potentials sampled within the corresponding domain using inverse solution methods. The basic steps were as follows. First, "ground-truth" potential distributions, one simple and one more complex, were specified on the external boundary. The corresponding internal field was then determined by numerical solution of Laplace's equation and this potential field was sampled at points corresponding to different catheter dimensions and electrode distributions. Finally, potentials on the outer boundary were reconstructed using the sampled potentials and compared with ground-truth potentials to assess the accuracy of inverse mapping. Key features of our mesh-based inverse approach were tested first with simple 2D problems and then extended to a more realistic 3D FEM analysis using atrial endocardial boundary geometry and representative potential distributions on this anatomy based on experimental measurement and simulation. Finally, the efficacy of inverse potential mapping using a meshless/MFS approach was compared with a representative mesh-based FEM analysis.

2D Analysis

Aspects of the approach employed here are illustrated in **Figure 2**. Two different arbitrary ground-truth potential distributions were specified on the boundary Γ_H of the circular domain Ω_H and the associated potential fields in Ω_H were constructed by solving Laplace's equation with these boundary conditions (**Figure 2A**) using the finite difference method (FDM) on a polar grid centered on the origin.

Cauchy boundary conditions on Γ_C were determined as shown in **Figure 2A**. Potentials were sampled at discrete points distributed uniformly on Γ_C which bounds the circular interior domain Ω_C. Potentials around Γ_C were reconstructed using

radial-based interpolation and the corresponding potential field in Ω_C was estimated by solving Laplace's equation with a polar finite difference scheme. Gradients normal to Γ_C were estimated using the FDM with a polar grid centered on the origin of the domains. Transfer **Eq. 3** relating ϕ_H and ϕ_C were formulated using the boundary integral approach developed by Barr et al. (1977) (Barr et al., 1977), then discretized and evaluated as outlined by this group. The inverse problem was solved employing zero-order Tikhonov regularization (Tikhonov and Arsenin, 1977) with the regularization parameter selected using a U-curve algorithm (Chamorro-Servent et al., 2019) based on the discrete Picard condition (Hansen, 2010). This optimizes the singular value decomposition associated with the regularization problem.

3D Analyses

Anatomic and experimental data used for 3D analyses were acquired from an anesthetized closed-chest sheep employing methods summarized below. All procedures were approved by the Animal Ethics Committee of the University of Auckland and conform to the Guide for the Care and Use of Laboratory Animals (National Institutes of Health publication no. 85–23).

Gadolinium-enhanced (Gd-DTPA 0.2 mmol kg) ECG-gated magnetic resonance images (MRIs) of the atria ($1.0\,mm^2 \times 1.0\,mm^2$ in-plane resolution approximately parallel to the atrio-ventricular valve plane and 1.6 mm between slices) were acquired with a 3T Siemens Magnetom Skyra scanner in late diastole with lungs inflated. Atrial electrical activation was subsequently mapped using 38 and 48 mm 64-electrode Constellation™ catheters (Boston Scientific) introduced percutaneously into the atria *via* the jugular vein under fluoroscopic guidance. Catheters were positioned in the LA using a guide wire and sheath introduced by trans-septal puncture. Electrograms from LA catheters (bandlimited to 0.5–1,500 Hz and sampled at 3 kHz) were recorded simultaneously in sinus rhythm (SR) using a multi-channel acquisition system (UnEmap, Auckland UniServices) with catheters in different locations. Serial biplane ciné X-ray views of the catheters (LAO/RAO, 25 frames/second, with concurrent Lead II ECG added for synchronization) were acquired immediately after each electrical recording. The ventilator was switched off during fluoroscopy to minimize respiratory motion.

Endocardial surface geometry from a representative LA was segmented from serial MRI using Amira 5.4 (Thermo Fisher Scientific) and reconstructed in 3D with the atrial appendage cropped (see **Figure 2**). LA electro-anatomic maps were reconstructed for this heart from recordings in SR with 3D electrode locations estimated from biplane X-ray records (Meng et al., 2017). Ground-truth potential distributions in SR were constructed at selected activation times by interpolating potentials around the activation wavefront from recorded electrograms. Ground truth data representing reentrant atrial activation were simulated. Meandering spiral wave reentry was simulated on an isotropic 2D monodomain with Fenton Karma activation kinetics (Fenton and Karma, 1998) using a standard cross-field S1-S2 stimulus protocol (Pandit et al., 2005). Points on the 2D domain were sampled and mapped onto the 3D surface mesh so that surface area was similar in both, with a contour adjacent to the boundary in the former assigned to the mitral valve orifice. Extracellular potentials were approximated from the transmembrane currents computed at each 3D point at a sampling rate of 1 kHz.

The open-source software environment SCIRun (Burton et al., 2011) was used for FEM solutions of 3D forward problems. A triangular surface mesh (1,529 nodes) was fitted to the LA and Ω_H was discretized using tetrahedral elements. Intracardiac potential fields were computed from the ground-truth surface potential distributions by solving Laplace's equation throughout Ω_H. The intracardiac field was sampled at points corresponding to electrodes on two basket catheter configurations with 1) 64 channels with 8 equally spaced electrodes along 8 splines at equal radial angles, and 2) 130 channels with 8 equally spaced electrodes along 16 splines at equal radial angles and electrodes at upper and lower poles. Basket dimensions were uniformly scaled to vary the ratio of catheter volume to LA volume. The centroids of catheters and the LA chamber were aligned to allow maximum catheter expansion and to ensure reproducibility between results. Noise was imposed by adding Gaussian noise independently to the electrograms recorded at each electrode with power set at realistic levels. Signal-to-noise ratio (SNR) is quantified as the ratio of root-mean-squared (RMS) voltages of reconstructed electrograms and noise.

SCIRun was also used for FEM solutions of 3D inverse problems. The methods outlined above for estimating Cauchy boundary conditions for the 2D case were extended to 3D as follows. Intracardiac fields were sampled at points corresponding to electrodes on specified intracardiac catheters. A triangular mesh was fitted to Γ_C (6,720 nodes) and the potential field on this surface was reconstructed from the sampled data using radial-based interpolation. Laplace's equation was solved in Ω_C using these potentials as Dirichlet boundary conditions and $\nabla\phi \cdot \boldsymbol{n}$ was estimated on Γ_C with the FDM using a polar grid centered on the catheter. Finally, the volume between boundaries Γ_C and Γ_H was discretized with a tetrahedral mesh. The inverse problem was solved subject to the potential and normal potential gradient boundary conditions specified on it using zero-order Tikhonov regularization (Tikhonov and Arsenin, 1977) employing the L-curve method to calculate the regularization parameter (Hansen, 2010).

Inverse solutions with the MFS were run with purpose-written code and a more detailed account of the methods used is given in Meng et al. (Meng et al., 2022). In brief, the virtual boundary Γ_v was formed by uniform radial inflation of the atrial surface mesh Γ_H by 6% and individual sources were associated with each of its nodes. Inverse endocardial potential distributions for intracardiac potentials "sampled" with virtual catheters were obtained using zero-order Tikhonov regularization (Tikhonov and Arsenin, 1977) employing the L-curve method to calculate the regularization parameter (Hansen, 2010). Comparisons between FEM and MFS inverse solutions were made at common points on Γ_H.

Correspondence between ground-truth and reconstructed potential maps were quantified by evaluating normalized root-mean-squared error (nRMSE) and correlation coefficient (CC).

TABLE 1 | Effects of number of points on sampling boundary Γ_C represented in **Figure 2A** and its location relative to outer boundary Γ_H on the accuracy with which potentials and normal potential gradients on Γ_C are reconstructed. Potential distribution in Ω_H shown in **Figure 2A**. Γ_C is concentric with Γ_H and the radius of the former is increased as indicated by the area ratio Ω_C relative to Ω_H. Samples are acquired at 8,16 and 32 uniformly spaced points around Γ_C.

Area ratio		0.049	0.195	0.346	0.541	0.779	0.914	Samples
$\phi(x_j)$	CC	0.9999	0.9995	0.9991	0.9989	0.9984	0.9970	8
	nRMSE	0.0041	0.0101	0.0128	0.0137	0.0170	0.0241	
$\frac{\partial\phi(x_j)}{\partial n}$	CC	0.9996	0.9961	0.9947	0.9977	0.9879	0.9689	
	nRMSE	0.0078	0.022	0.0263	0.0268	0.0280	0.0428	
$\phi(x_j)$	CC	1.0000	1.0000	1.0000	0.9999	0.9997	0.9986	16
	nRMSE	0.0022	0.0020	0.0023	0.0031	0.0078	0.0161	
$\frac{\partial\phi(x_j)}{\partial n}$	CC	0.9998	0.9996	0.9994	0.9989	0.9949	0.9797	
	nRMSE	0.0049	0.0061	0.0079	0.0105	0.0184	0.0347	
$\phi(x_j)$	CC	1.0000	1.0000	1.0000	1.0000	1.0000	0.9999	32
	nRMSE	0.0014	0.0017	0.0020	0.0023	0.0027	0.0046	
$\frac{\partial\phi(x_j)}{\partial n}$	CC	0.9999	0.9997	0.9995	0.9996	0.9996	0.9996	
	nRMSE	0.0030	0.0055	0.0074	0.0062	0.0055	0.0156	

$$nRMSE = \sqrt{\frac{\sum_{i=1}^{N}(\phi_{GT}^{i} - \phi_{R}^{i})^{2}}{\sum_{i=1}^{N}(\phi_{GT}^{i})^{2}}} \text{ and}$$
$$CC = \frac{\sum_{i=1}^{N}(\phi_{GT}^{i} - \mu_{GT})(\phi_{R}^{i} - \mu_{R})}{\sqrt{\sum_{i=1}^{N}(\phi_{GT}^{i} - \mu_{GT})^{2}}\sqrt{\sum_{i=1}^{N}(\phi_{R}^{i} - \mu_{R})^{2}}} \quad (8)$$

where N is the number of surface points compared, ϕ_{GT}^{i} and ϕ_{R}^{i} are ground-truth and reconstructed potentials at surface point i, while μ_{GT} and μ_{R} are mean values for ground-truth and reconstructed potentials, respectively, across the surface.

Activation times (ATs) for ground-truth and reconstructed electrograms were estimated as maximum negative rate of potential change and the activation time difference ΔT at each surface point was evaluated as the difference between the ground-truth and reconstructed ATs

$$\Delta T = |\mathrm{AT}_{GT} - \mathrm{AT}_{R}| \quad (9)$$

SCIRun was used for 3D FEM forward and inverse calculations and for visualization of all 3D results. Meshless/MFS inverse solutions were run in purpose-written C code. All other computation (2D analysis, estimation of potential gradients, regularization and evaluation of correspondence measures), was implemented in the MATLAB programming language (The Mathworks, Natick, Massachusetts).

RESULTS

2D Analysis of Mesh-Based Intracardiac Potential Mapping

We used a simple 2D analysis initially to test the feasibility of our methods for estimating intracardiac Cauchy boundary conditions. **Figure 2A** illustrates the steps involved. It shows that the ground truth potential field in Ω_C (upper panel) is replicated qualitatively in the lower panel using a limited set of samples around Γ_C. **Table 1** presents corresponding median CC and nRMSE for ϕ and $\nabla\phi \cdot \boldsymbol{n}$ around Γ_C and demonstrates that both can be estimated with good accuracy in this case. Error increased as Γ_C was enlarged relative to Γ_H but was offset by increasing the number of samples.

In this figure, we also compare ground-truth potentials on Γ_H with corresponding inverse results reconstructed from samples around internal circles in simple (**Figure 2B**) and more complex (**Figure 2C**) fields. Surface potentials reconstructed from samples around an internal radius of 0.469 relative to Γ_H were close to ground-truth (nRMSE 0.02 and 0.06, CC 1.0 and 0.99 for simple and more complex fields, respectively). However, error increased when the dimension of Γ_C was reduced further. With a relative radius of 0.375 (~14% of the domain area), reconstructed surface potentials were overestimated, and the complex surface potential distribution captured less well (nRMSE 0.14 and 0.48, CC 0.99 and 0.70 for simple and more complex fields, respectively). These results demonstrate that mesh-based inverse potential mapping can be used to reconstruct surface potential distributions, but that accuracy is influenced by the dimension of the surface relative to the solution domain.

3D Analysis of Mesh-Based Intracardiac Potential Mapping Accuracy

Figure 3 presents the results of an *in silico* analysis of the accuracy with which LA surface potential distributions can be reconstructed from non-contact electrograms recorded in SR using 64-channel basket catheters. The ground truth endocardial potential distribution at one instant (43.9 msec after onset of atrial activation) is shown in **Figure 3A** with the 3D locations of basket catheter electrodes superimposed (the volume ratio of the catheter with respect to LA cavity was 0.67). The corresponding inverse reconstruction of atrial surface potentials in **Figure 3B** is qualitatively similar to the ground-truth map, while reference and inverse electrograms at a representative site (point 1 in **Figure 3B**) correspond closely throughout the activation cycle (**Figure 3C**). **Figures 3D–F** show acceptable non-contact mapping accuracy for a wide range of catheter dimensions (median: CC >0.96; nRMSE <0.12; ΔT = 3 ms for catheter-atrial volume ratios >0.3). However, error accumulates progressively when catheter dimensions are decreased below this range.

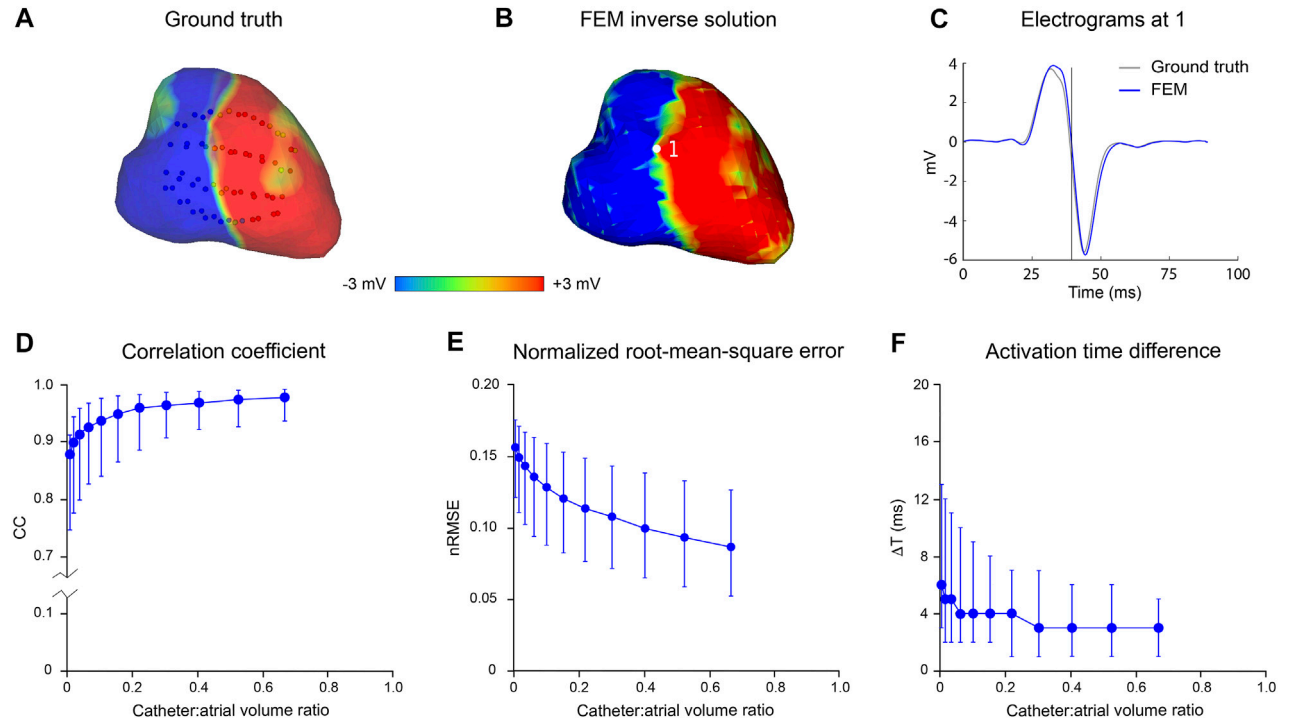

FIGURE 3 | Effect of catheter size on accuracy of inverse potential mapping. Comparison of ground truth potential maps on endocardial surface of LA in SR with inverse maps reconstructed using FEM. Inverse potential maps were reconstructed from electrograms "sampled" using a 64-electrode basket catheter, with centroids of catheter and LA chamber aligned. The upper panel presents typical results for a catheter which bounds a volume fraction of 0.67 relative to LA volume. These include **(A)** ground-truth surface potential distribution 43.9 msec after onset of activation with basket catheter superimposed, and **(B)** corresponding potential maps reconstructed using FEM. Finally, in **(C)** a ground-truth electrogram (black) at point 1 is compared with corresponding electrograms reconstructed using FEM (blue). In the lower panel, **(D)** correlation coefficient (CC) **(E)** normalized root-mean-squared error (nRMSE), and **(F)** activation time difference (ΔT) are presented as functions of relative catheter volume for FEM. Median values and interquartile range are given. Abbreviations: FEM, finite element method; SR sinus rhythm.

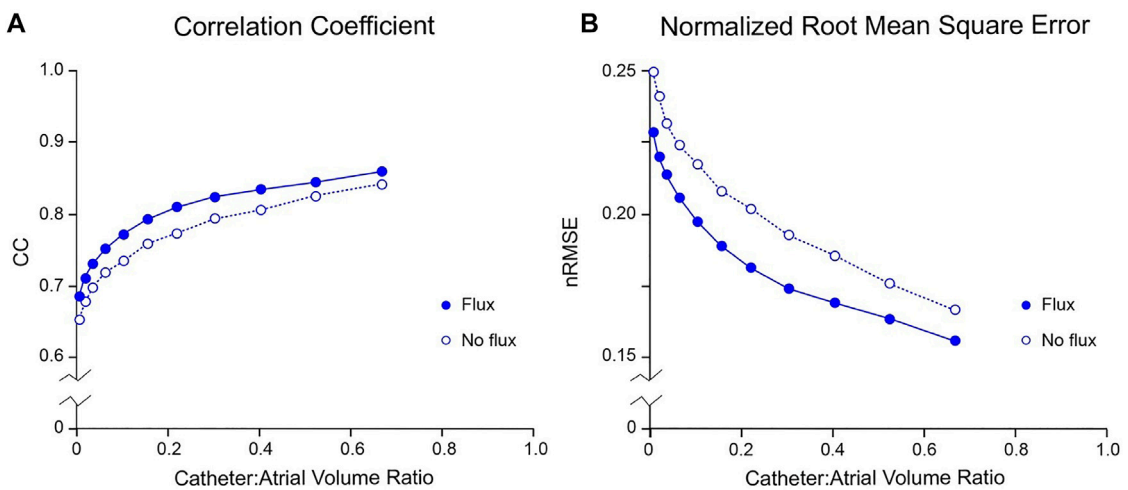

FIGURE 4 | Effect of boundary value specification on accuracy of inverse potential mapping using FEM. Comparison of ground truth potential maps on endocardial surface of LA in SR 43.9 msec after onset of activation with inverse maps reconstructed using FEM from potentials sampled with centrally located internal basket catheters with 64 equi-spaced electrodes. In **(A)** and **(B)**, respectively, relative root-mean-squared error (nRMSE) and correlation coefficient (CC) are presented as functions of catheter volume relative to LA. Additional error introduced by not estimating normal potential gradients on the virtual surface bounding electrodes is indicated by the no flux results (open circles) in which normal potential gradients are set to zero. Abbreviations: FEM, finite element method; SR, sinus rhythm.

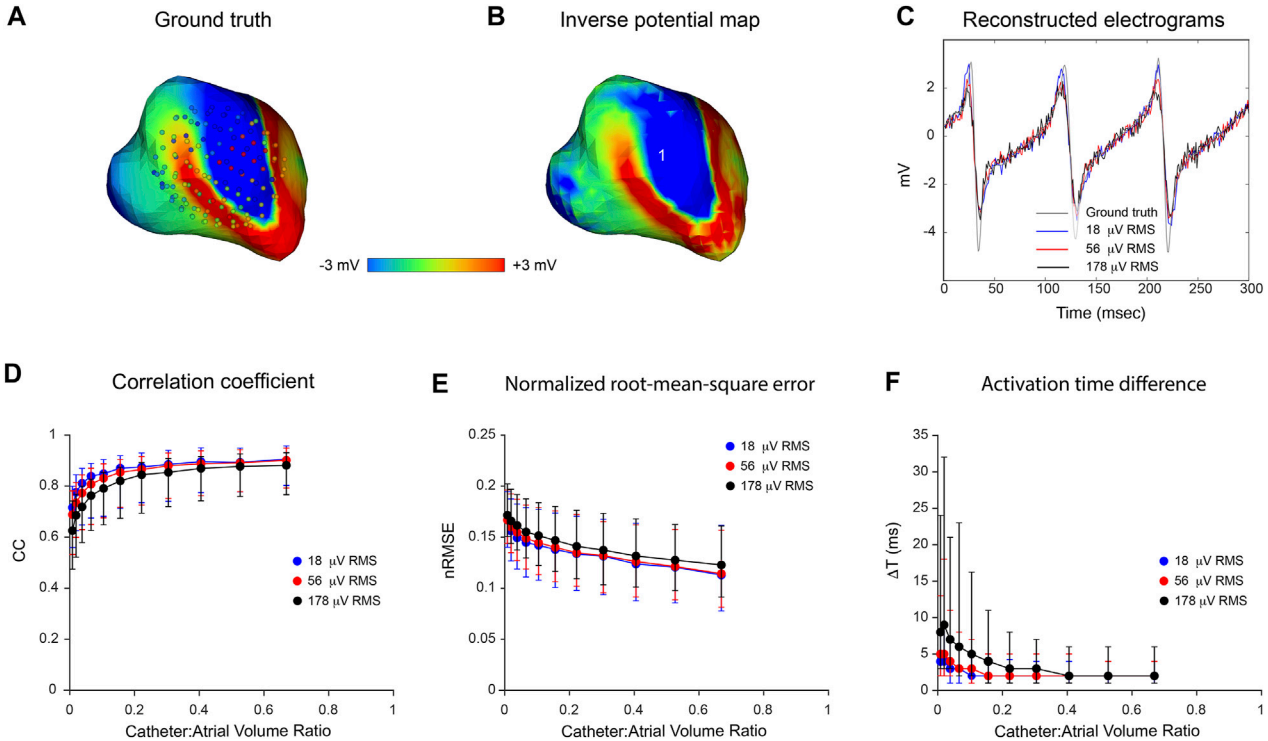

FIGURE 5 | Effects of catheter dimension and noise on inverse potential maps reconstructed during macro-reentry using FEM. LA surface potentials during 3 cycles of simulated atrial flutter are reconstructed from electrograms sampled inside the LA cavity with 130-electrode basket catheters and compared with ground-truth data. The upper panel presents typical results for catheters that bound a volume fraction of 0.67 relative to LA volume. These include **(A)** the ground-truth surface potential distribution at one instant with catheter electrodes overlaid **(B)** corresponding potential map reconstructed using electrograms "sampled" with a 130-electrode basket catheter, and **(C)** electrograms reconstructed at location 1 from sampled records with 18 μV RMS (blue), 56 μV RMS (red) and 178 μV RMS (black) of added Gaussian noise compared with the ground truth electrogram (grey) at the same site. In the lower panel, **(D)** correlation coefficient (CC) **(E)** normalized root-mean-squared error (nRMSE), and **(F)** activation time difference (ΔT) are presented as functions of catheter-atrial volume ratio for these levels of added noise. Median values and interquartile range are given. Abbreviation: FEM, finite element method.

Figure 4 presents the error introduced when the normal potential gradient on the surface bounding the electrodes, Γ_C, is not accounted for. In this example, one time-point only is considered (43.9 msec after onset of atrial activation). $\frac{\partial\phi(x_j)}{\partial n}$ is assumed to be zero which corresponds to a no-flux condition at Γ_C. Incorporation of realistic estimates of normal potential gradients on Γ_C reduces nRMSE, with greatest absolute reduction in error for the intermediate range of relative volume ratios. The effects are modest with ~9% reduction in CC and ~10% increase in nRMSE at a catheter-atrial volume ratio of 0.3 and absolute error appears to be reduced at the extremes of the relative volume ratio range.

Results of an analysis of inverse mapping accuracy for more complex atrial rhythms in the presence of noise are presented in **Figure 5**. In this case, a simulated rotor with a moving core was used as ground-truth. Three activation cycles were sampled with a 130-electrode basket catheter and Gaussian noise at RMS voltages of 18, 56 and 178 μV was added to these records. The upper panel shows representative results for a catheter-atrial volume ratio of 0.67. Ground-truth surface potential maps (**Figure 5A**) were reconstructed with reasonable accuracy in the absence of noise (see **Figure 5B**). Median results were CC = 0.92, nRMSE = 0.11 and ΔT = 2 ms; clearly better than the corresponding result with a 64-electrode catheter (CC = 0.83, nRMSE = 0.14 and ΔT = 3 ms). At this catheter dimension also, inverse mapping was robust in the presence of realistic levels of electrical noise. Results with systematic variation of relative catheter dimension and noise are shown in **Figures 5D–F**. Accuracy was relatively invariant despite increasing noise as catheter-atrial volume ratio was reduced from 0.67 to ~0.2. At dimensions less than this, however, there was a progressive increase in error which scaled with noise level. It is noteworthy that activation time estimates were markedly degraded by noise at reduced catheter dimensions.

An important final observation is that the transfer matrices used for 3D FEM analyses were over-determined in all cases, with the LA represented by a 1529-node triangular surface mesh while a 6720-node triangular mesh was fitted to the catheter. This was necessary to achieve stable solutions.

Comparison of FEM and MFS Inverse Solutions

In **Figure 6**, we compare the performance of mesh-based inverse mapping employing a FEM solver with a meshless approach that

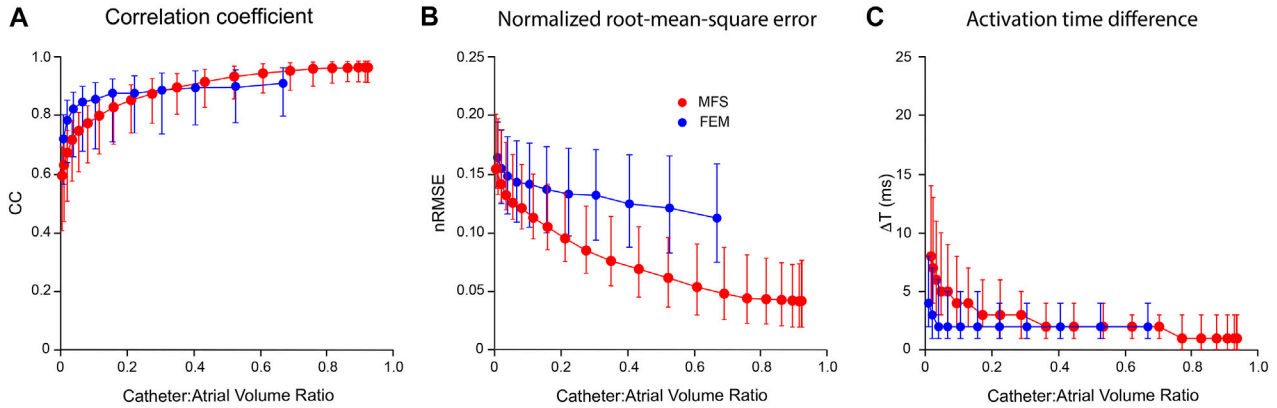

FIGURE 6 | Comparison of inverse potential maps reconstructed during macro-reentry using FEM and meshless methods that employ the MFS. LA surface potentials throughout 3 activation cycles in simulated atrial flutter reconstructed from electrograms sampled inside LA cavity with 130-electrode basket catheters and compared with ground-truth data. **(A)** Correlation coefficient (CC) **(B)** normalized root-mean-squared error (nRMSE), and **(C)** activation time difference (ΔT) are presented as functions of catheter-atrial volume ratio for FEM (blue) and meshless/MFS (red). Median values and interquartile range are given. Abbreviations: FEM, finite element method; MFS method of fundamental solutions.

employs the MFS. We used the simulated rotor in **Figure 5** as ground-truth and again "sampled" 3 activation cycles with 130-electrode basket catheters of different dimensions. FEM inverse solutions matched ground-truth maps quite well, with median values of CC = 0.91 and nRMSE = 11.3% across the activation sequence at a catheter-atrial volume ratio of 0.67. Corresponding results for the meshless/MFS approach were 0.95 and 4.9%, but activation time differences with ground truth were the same for both. While CC was marginally better with MFS than FEM for catheter-atrial volume ratios >0.3, this measure decreased more rapidly with the MFS when catheter dimensions were reduced further (see **Figure 6A**). Likewise, ΔT was greater with the MFS for catheter-atrial volume ratios <0.3. In contrast, nRMSE was substantially less for MFS than FEM inverse results across the full volume range.

The main difference between methods was that the MFS was much more efficient computationally than the FEM in our hands. Transfer matrices were simple to set up and inverse solutions were obtained in near real-time using purpose-written code. Finally, the meshless/MFS formulation was robust, with stable inverse solutions despite the fact that transfer matrices were inherently under-determined.

DISCUSSION

Summary

In this paper, we present the results of a computational analysis of the accuracy with which endocardial potential maps can be reconstructed from non-contact multi-electrode basket catheter recordings. This inverse problem is addressed initially using a mesh-based approach where transfer relationships are formulated between potentials on the two boundaries involved. This is accurate in principle because assumptions made about the electrical properties of the solution domain are limited (and inherently realistic). However, it requires Cauchy conditions to be specified on the surface Γ_C that bounds the electrodes. A simple and robust way of doing this is outlined and used to solve representative 2D and 3D problems. We demonstrate that effective non-contact intracardiac potential mapping can be achieved using mesh-based methods and that accuracy is determined by 1) the spatial complexity of the intracardiac potential field, 2) the dimensions of the catheter relative to those of the cavity, 3) the distribution of electrodes on the catheter, and 4) the signal-to-noise ratio of the potentials acquired. Finally, we show that a much simpler meshless method which uses the MFS is at least as accurate as mesh-based inverse potential mapping over a wide range of catheter dimensions and computationally far more efficient. This work addresses an important problem in cardiac electrophysiology and is the first *in silico* investigation of this topic, as far as we are aware.

Mesh-Based Inverse Potential Mapping

With the mesh-based inverse solvers used in this analysis, it is necessary to specify potentials at sufficient points on the surface Γ_C that bounds the electrodes to ensure that the transfer matrices are well-determined. These boundary potentials can be faithfully reconstructed by interpolation if their distribution is represented by the data sampled. This is not sufficient here for complete specification of boundary conditions. It is evident that current flux through an open basket catheter affects the distribution of potentials across the heart cavity and with mesh-based inverse solvers this is captured by specifying normal potential gradients on Γ_C as outlined in the Mathematical Background.

Our 2D analysis demonstrates that intracardiac potential fields in the vicinity of Γ_C can be reconstructed accurately from a relatively small number of potentials sampled uniformly around this boundary. The difference between estimated and expected potentials and normal potential gradients on Γ_C depended on matching the number of electrodes to the spatial complexity of the potential distribution, and correspondence improved as the

distance between Γ_C and heart surface Γ_H increased. These findings indicate that it is possible to specify the boundary conditions necessary for non-contact potential mapping using mesh-based inverse solution methods. We have demonstrated that normal potential gradients on Γ_C can be estimated with acceptable accuracy and have shown in **Figure 4** that inclusion of this information improves the accuracy of 3D non-contact potential mapping with mesh-based inverse solvers. The robustness of this approach is confirmed by the precision of non-contact potential mapping across a wide range of catheter dimensions in complex rhythms and in the presence of noise (**Figures 3**, **5**).

Our analyses show that the accuracy of inverse potential mapping decreases when catheter dimensions are reduced and this becomes more marked as noise levels are increased. In the 3D examples presented here (**Figures 3**, **5**), error remains relatively low as catheter-atrial volume ratios decrease to ~0.3 but increases exponentially with further reduction. These findings are intuitively reasonable. With increasing distance from the heart surface, intracardiac potentials are progressively attenuated and smoothed. The extent to which high temporal frequencies on Γ_H can be recovered depends on the regularization method used, but the presence of noise introduces additional problems (Johnson and Bronzino, 2000; Pullan et al., 2005). Because the magnitude of intracardiac electrograms decreases toward the center of Γ_H, the signal-to-noise ratio of records sampled with a small catheter is reduced and the noise is amplified by inverse mapping. Finally, if the catheter is too small it cannot provide an adequate representation of the potentials distributed throughout the cavity, particularly when they are complex spatially.

The 3D analyses above also show that the accuracy with which potentials on Γ_H are reconstructed is improved by matching the number of electrodes to the spatial complexity of the "ground truth" potential distribution. While acceptable non-contact mapping accuracy was achieved in SR using a 64-electrode basket catheter (see **Figure 3**), a 130-electrode catheter was needed to achieve similar performance for non-stationary reentrant activity (see **Figure 5** and related text). If the electrode distribution is not sufficiently dense, high spatial frequencies cannot be recovered and low frequency artefacts (aliasing) may occur (Rice, 1950). This holds for both non-contact and contact mapping.

Comparison of Mesh-Based and Meshless Inverse Potential Mapping

As noted at the start of the Discussion, we opted to use mesh-based inverse potential mapping as the reference method in this study because assumptions made about the electrical properties of the solution domain with this approach are minimal. We argue that the correspondence of the 3D FEM solutions presented here with ground truth and the stability of these results support this strategy. In contrast, the meshless/MFS alternative with which it is compared employs a much simpler representation of the intracardiac forward problem but introduces additional assumptions about the current sources that give rise to intracardiac potential distributions. The fact that the MFS approach performs better for catheter-atrial volume ratios >0.3 (**Figure 6**) warrants further consideration. It is likely that much of the apparent improvement with meshless/MFS is due to the compact support for linear interpolation in the FEM implementation used. This gives rise to discontinuities across element boundaries (see **Figure 5B**) whereas potentials on the heart surface are continuous with meshless inverse mapping. We note that there is no difference in ΔT for catheter-atrial volume ratios >0.3 and argue that meshless/MFS inverse potential mapping is at least as accurate as mesh-based inverse methods over this range.

The major advantage of meshless/MFS methods in this setting is that the forward transfer function is computationally simple and can be assembled very rapidly. In contrast, with mesh-based alternatives, such as FEM, the forward transfer function is complex and time consuming to assemble and invert. Furthermore, our results indicate that the meshless/MFS representation of the intracardiac problem is much better conditioned and therefore more robust than FEM. This is reflected by the fact that an over-determined transfer matrix was needed for stable inverse solutions with FEM, whereas accurate solutions were obtained with MFS despite the fact that transfer matrices were under-determined.

Potential Clinical Impact of These Findings

Non-contact intracardiac mapping systems that have been used clinically have utilized balloon-mounted multi-electrode array for potential mapping (Khoury et al., 1995; Khoury et al., 1998; Schilling et al., 1999) or have reconstructed membrane charge density from electrograms recorded with an open basket catheter (Willems et al., 2019). While the inverse problem techniques used are different, one would expect the information recovered to be affected similarly by electrode density and positioning, and catheter size, i.e. the number of recording electrodes, their physical spacing on the catheter and proximity of the electrodes to the atrial wall once the catheter is fully deployed. Validation studies have shown that the accuracy with which endocardial electrograms are constructed with the first of these approaches is inversely related to the distance from the electrodes array to corresponding points on the cavity surface (Earley et al., 2006). As far as we are aware, an equivalent systematic validation has not been completed for the second. This study indicates that reliable non-contact potential mapping can also be performed using multi-electrode catheters and could be carried out in near real-time using meshless methods that employ the MFS.

In terms of optimal catheter design, greater electrode density and more uniform distribution would be expected to provide higher resolution. However, the question of how much is enough has only started to be addressed recently. Martinez et al. (Martinez-Mateu et al., 2018) showed computationally that methods used to transform basket electrogram signals back into catheter surface potential maps may result in the creation of fictitious repetitive activation patterns resembling AF rotors when the input information was too sparsely sampled. Williams et al. (Williams et al., 2018) on the other hand defined optimal endocardial sampling densities, both computationally and *in-vivo*, required to resolve activation patterns of varying

complexities. They report that a minimum endocardial sampling density of 1.0–1.5 points/cm^2 is required, with higher densities needed to resolve spiral wave activity. Whilst they were looking at endocardial interpolation of contact recordings not inverse solutions, it is evident from our work here that potential pitfalls in inverse mapping also need to be addressed with good catheter design and mechanistic insight.

Limitations

It could be argued that the BEM is better matched to the mesh-based inverse potential problem addressed here (Oostendorp and van Oosterom, 1991; Johnson and Bronzino, 2000; Pullan et al., 2005). The FEM generates sparse transfer matrices and is computationally expensive, while BEMs reduce the solution domain to the boundaries only giving rise to compact transfer matrices that can reduce computational overheads and improve accuracy (Johnson and Bronzino, 2000; Pullan et al., 2005). However, our purpose here was to benchmark the mesh-based approach and we opted to use FEM to avoid possible instability that can occur when boundaries are geometrically complex as is the case in the atria. We note that our mesh-based analysis has proved stable and that the meshless/MFS methods with which they are compared are much more efficient computationally than either FEM or BEM. A further limitation is that although our ground-truth data represent atrial rhythms of increasing complexity they do not replicate the spatio-temporal disorder that characterizes AF.

CONCLUSION

This computational analysis indicates that potentials on the endocardial surface of a cardiac chamber can be reconstructed with intracardiac multi-electrode basket catheters using inverse solution methods provided that the boundary geometry is specified and the 3D location of catheters with respect to it are known. These data are now available clinically. Panoramic electro-anatomic maps can therefore be generated at successive time steps from non-contact recordings. Mapping accuracy is determined by 1) the distance of recording electrodes from the endocardium, 2) their distribution within the subdomain sampled, and 3) rhythm complexity. These issues should be factored into the design of future non-contact multi-electrode basket catheters. We conclude that reliable non-contact potential mapping can be carried out in near real-time using meshless methods that employ the MFS.

DATA AVAILABILITY STATEMENT

The original contributions presented in the study are included in the article/Supplementary Material, further inquiries can be directed to the corresponding author.

ETHICS STATEMENT

The animal study was reviewed and approved by the All procedures were approved by the Animal Ethics Committee of the University of Auckland and conform to the Guide for the Care and Use of Laboratory Animals (National Institutes of Health publication no. 85–23).

AUTHOR CONTRIBUTIONS

SM and NS jointly completed all aspects of the analyses presented here and developed the computational pipeline used. JC-S is responsible for our use of MFS, completed 2D prototype studies using this approach and was influential in the direction taken in this work. LB wrote our initial 3D MFS code. SM, BS, IL, NL, AG, GS, and JZ designed, performed and analyzed animal experiments which provided data for this study. JZ contributed to the simulation of reentrant arrhythmia and provided phase mapping code. SM, NS and BS generated the figures. SM, NS, GS, and BS wrote the manuscript. BS and DB were responsible for funding and direction of the project. All authors contributed to manuscript revision, read, and approved the version submitted.

FUNDING

This work was supported in part by the Health Research Council of New Zealand (NZ) under Programme Grant 13-799, by the NZ Ministry of Business and Innovation Endeavour Fund Grant CONT-50916-ENDSI-UOA and by Return on Sciences, NZ.

REFERENCES

Barr, R. C., Ramsey, M., and Spach, M. S. (1977). Relating Epicardial to Body Surface Potential Distributions by Means of Transfer Coefficients Based on Geometry Measurements. *IEEE Trans. Biomed. Eng.* 24, 1–11. doi:10.1109/TBME.1977.326201

Bear, L. R., LeGrice, I. J., Sands, G. B., Lever, N. A., Loiselle, D. S., Paterson, D. J., et al. (2018). How Accurate Is Inverse Electrocardiographic Mapping? *Circ Arrhythmia Electrophysiol.* 11, e006108. doi:10.1161/CIRCEP.117.006108

Burton, B. M., Tate, J. D., Erem, B., Swenson, D. J., Wang, D. F., Steffen, M., et al. (2011). "A Toolkit for Forward/inverse Problems in Electrocardiography within the SCIRun Problem Solving Environment," in Proceedings of the Annual International Conference of the IEEE Engineering in Medicine and Biology Society EMBS, Boston, MA, USA, 30 August 2011-03 September 2011, 267–270. doi:10.1109/IEMBS.2011.6090052

Chamorro-Servent, J., Dubois, R., and Coudière, Y. (2019). Considering New Regularization Parameter-Choice Techniques for the Tikhonov Method to Improve the Accuracy of Electrocardiographic Imaging. *Front. Physiol.* 10, 273. doi:10.3389/fphys.2019.00273

Cluitmans, M. J. M., Bonizzi, P., Karel, J. M. H., Das, M., Kietselaer, B. L. J. H., de Jong, M. M. J., et al. (2017). *In Vivo* Validation of Electrocardiographic Imaging. *JACC Clin. Electrophysiol.* 3, 232–242. doi:10.1016/j.jacep.2016.11.012

Duchateau, J., Sacher, F., Pambrun, T., Derval, N., Chamorro-Servent, J., Denis, A., et al. (2019). Performance and Limitations of Noninvasive Cardiac Activation Mapping. *Heart rhythm.* 16, 435–442. doi:10.1016/j.hrthm.2018.10.010

Earley, M. J., Abrams, D. J. R., Sporton, S. C., and Schilling, R. J. (2006). Validation of the Noncontact Mapping System in the Left Atrium during Permanent Atrial Fibrillation and Sinus Rhythm. *J. Am. Coll. Cardiol.* 48, 485–491. doi:10.1016/j.jacc.2006.04.069

Fairweather, G., and Karageorghis, A. (1998). The Method of Fundamental Solutions for Elliptic Boundary Value Problems. *Adv. Comput. Math.* 9, 69–95. doi:10.1023/A:1018981221740

Fenton, F., and Karma, A. (1998). Vortex Dynamics in Three-Dimensional Continuous Myocardium with Fiber Rotation: Filament Instability and Fibrillation. *Chaos* 8, 20–47. doi:10.1063/1.166311

Haissaguerre, M., Shah, A. J., Cochet, H., Hocini, M., Dubois, R., Efimov, I., et al. (2016). Intermittent Drivers Anchoring to Structural Heterogeneities as a Major Pathophysiological Mechanism of Human Persistent Atrial Fibrillation. *J. Physiol.* 594, 2387–2398. doi:10.1113/JP270617

Hansen, P. C. (2010). "Front Matter," in Discrete Inverse Problems *(Society for Industrial and Applied Mathematics)* (Philadelphia: Society for Industrial and Applied Mathematics), i–xii. doi:10.1137/1.9780898718836.fm

Johnson, C. R. (2000). "Numerical Methods for Bioelectric Field Problems," in *T*he Biomedical Engineering Handbook. Editor J. D. Bronzino. 2nd Edition (Boca Raton: CRC Press LLC).

Khoury, D. S., Berrier, K. L., Badruddin, S. M., Zoghbi, W. A., and Zoghbi, W. A. (1998). Three-dimensional Electrophysiological Imaging of the Intact Canine Left Ventricle Using a Noncontact Multielectrode Cavitary Probe: Study of Sinus, Paced, and Spontaneous Premature Beats. *Circulation* 97, 399–409. doi:10.1161/01.cir.97.4.399

Khoury, D. S., Taccardi, B., Lux, R. L., Ershler, P. R., and Rudy, Y. (1995). Reconstruction of Endocardial Potentials and Activation Sequences from Intracavitary Probe Measurements: Localization of Pacing Sites and Effects of Myocardial Structure. *Circulation* 91, 845–863. doi:10.1161/01.CIR.91.3.845

Martinez-Mateu, L., Romero, L., Ferrer-Albero, A., Sebastian, R., Rodríguez Matas, J. F., Jalife, J., et al. (2018). Factors Affecting Basket Catheter Detection of Real and Phantom Rotors in the Atria: A Computational Study. *PLoS Comput. Biol.* 14, e1006017. doi:10.1371/journal.pcbi.1006017

Meng, S., Sunderland, N., Chamorro-Servent, J., Bear, L. R., Lever, N. A., Sands, G. B., et al. (2022). Intracardiac Inverse Potential Mapping Using the Method of Fundamental Solutions. *Front. Physiol.* 13, 873049. doi:10.3389/fphys.2022.873049

Meng, S., Zhao, J., Lever, N., Sands, G., Bear, L., Gillis, A., et al. (2017). "Atrial Electro-Anatomic Mapping with a Novel Noncontact Approach," in Computing in Cardiology, Rennes, France, 24-27 September 2017, 1–4. doi:10.22489/CinC.2017.105-291

Narayan, S. M., Krummen, D. E., and Rappel, W.-J. (2012). Clinical Mapping Approach to Diagnose Electrical Rotors and Focal Impulse Sources for Human Atrial Fibrillation. *J. Cardiovasc Electrophysiol.* 23, 447–454. doi:10.1111/j.1540-8167.2012.02332.x

Oesterlein, T., Frisch, D., Loewe, A., Seemann, G., Schmitt, C., Dössel, O., et al. (2016). Basket-type Catheters: Diagnostic Pitfalls Caused by Deformation and Limited Coverage. *BioMed Res. Int.* 2016, 1–13. doi:10.1155/2016/5340574

Oostendorp, T., and van Oosterom, A. (1991). The Potential Distribution Generated by Surface Electrodes in Inhomogeneous Volume Conductors of Arbitrary Shape. *IEEE Trans. Biomed. Eng.* 38, 409–417. doi:10.1109/10.81559

Pandit, S. V., Berenfeld, O., Anumonwo, J. M. B., Zaritski, R. M., Kneller, J., Nattel, S., et al. (2005). Ionic Determinants of Functional Reentry in a 2-D Model of Human Atrial Cells During Simulated Chronic Atrial Fibrillation. *Biophysical J.* 88, 3806–3821. doi:10.1529/biophysj.105.060459

Pathik, B., Kalman, J. M., Walters, T., Kuklik, P., Zhao, J., Madry, A., et al. (2018). Absence of Rotational Activity Detected Using 2-dimensional Phase Mapping in the Corresponding 3-dimensional Phase Maps in Human Persistent Atrial Fibrillation. *Heart rhythm.* 15, 182–192. doi:10.1016/j.hrthm.2017.09.010

Pullan, A. J., Cheng, L. K., and Buist, M. L. (2005). *Mathematically Modelling the Electrical Activity of the Heart: From Cell to Body Surface and Back Again*. Singapore: World Scientific Publishing Company Pte Ltd. ISBN: 978-981-256-373-6. doi:10.1142/5859

Ramanathan, C., and Rudy, Y. (2001). Electrocardiographic Imaging: II. Effect of Torso Inhomogeneities on Noninvasive Reconstruction of Epicardial Potentials, Electrograms, and Isochrones. *J. Cardiovasc. Electrophysiol.* 12, 241–252. doi:10.1046/j.1540-8167.2001.00241.x

Rice, S. O. (1950). Communication in the Presence of Noise-Probability of Error for Two Encoding Schemes. *Bell Syst. Tech. J.* 29, 60–93. doi:10.1002/j.1538-7305.1950.tb00933.x

Schilling, R. J., Peters, N. S., and Davies, D. W. (1999). Feasibility of a Noncontact Catheter for Endocardial Mapping of Human Ventricular Tachycardia. *Circulation* 99, 2543–2552. doi:10.1161/01.CIR.99.19.2543

Tikhonov, A. N., and Arsenin, V. Y. (1977). *Solutions of Ill-Posed Problems*. Washington DC: Winston and Sons. Available at: https://www.ams.org/bull/1979-01-03/S0273-0979-1979-14602-0/(Accessed May 4, 2021).

Wang, Y., and Rudy, Y. (2006). Application of the Method of Fundamental Solutions to Potential-Based Inverse Electrocardiography. *Ann. Biomed. Eng.* 34, 1272–1288. doi:10.1007/s10439-006-9131-7

Willems, S., Verma, A., Betts, T. R., Murray, S., Neuzil, P., Ince, H., et al. (2019). Targeting Nonpulmonary Vein Sources in Persistent Atrial Fibrillation Identified by Noncontact Charge Density Mapping: UNCOVER AF Trial. *Circ Arrhythmia Electrophysiol.* 12, e007233. doi:10.1161/CIRCEP.119.007233

Williams, S. E., Harrison, J. L., Chubb, H., Whitaker, J., Kiedrowicz, R., Rinaldi, C. A., et al. (2018). Local Activation Time Sampling Density for Atrial Tachycardia Contact Mapping: How Much Is Enough? *Europace* 20, e11–e20. doi:10.1093/europace/eux037

Conflict of Interest: The authors declare that the research was conducted in the absence of any commercial or financial relationships that could be construed as a potential conflict of interest.

Publisher's Note: All claims expressed in this article are solely those of the authors and do not necessarily represent those of their affiliated organizations, or those of the publisher, the editors and the reviewers. Any product that may be evaluated in this article, or claim that may be made by its manufacturer, is not guaranteed or endorsed by the publisher.

frontiers | Frontiers in Physiology

TYPE Original Research
PUBLISHED 12 August 2022
DOI 10.3389/fphys.2022.909372

OPEN ACCESS

EDITED BY
Gernot Plank,
Medical University of Graz, Austria

REVIEWED BY
Caroline Helen Roney,
Queen Mary University of London, United Kingdom
Simone Pezzuto,
University of Italian Switzerland, Switzerland
Linwei Wang,
Rochester Institute of Technology, United States
Karli Gillette,
Medical University of Graz, Austria

*CORRESPONDENCE
Ruben Doste,
ruben.doste@cs.ox.ac.uk

SPECIALTY SECTION
This article was submitted to Cardiac Electrophysiology, a section of the journal Frontiers in Physiology

RECEIVED 31 March 2022
ACCEPTED 07 July 2022
PUBLISHED 12 August 2022

CITATION
Doste R, Lozano M, Jimenez-Perez G, Mont L, Berruezo A, Penela D, Camara O and Sebastian R (2022), Training machine learning models with synthetic data improves the prediction of ventricular origin in outflow tract ventricular arrhythmias.
Front. Physiol. 13:909372.
doi: 10.3389/fphys.2022.909372

Training machine learning models with synthetic data improves the prediction of ventricular origin in outflow tract ventricular arrhythmias

Ruben Doste[1]*, Miguel Lozano[2], Guillermo Jimenez-Perez[3], Lluis Mont[4], Antonio Berruezo[5], Diego Penela[5], Oscar Camara[3] and Rafael Sebastian[2]

[1]Department of Computer Science, University of Oxford, Oxford, United Kingdom, [2]Computational Multiscale Simulation Lab (CoMMLab), Department of Computer Science, Universitat de Valencia, Valencia, Spain, [3]Physense, BCN Medtech, Department of Information and Communication Technologies, Universitat Pompeu Fabra, Barcelona, Spain, [4]Arrhythmia Section, Cardiology Department, Cardiovascular Clinical Institute, Hospital Clínic, Universitat de Barcelona - IDIBAPS, Barcelona, Spain, [5]Cardiology Department, Heart Institute, Teknon Medical Center, Barcelona, Spain

In order to determine the site of origin (SOO) in outflow tract ventricular arrhythmias (OTVAs) before an ablation procedure, several algorithms based on manual identification of electrocardiogram (ECG) features, have been developed. However, the reported accuracy decreases when tested with different datasets. Machine learning algorithms can automatize the process and improve generalization, but their performance is hampered by the lack of large enough OTVA databases. We propose the use of detailed electrophysiological simulations of OTVAs to train a machine learning classification model to predict the ventricular origin of the SOO of ectopic beats. We generated a synthetic database of 12-lead ECGs (2,496 signals) by running multiple simulations from the most typical OTVA SOO in 16 patient-specific geometries. Two types of input data were considered in the classification, raw and feature ECG signals. From the simulated raw 12-lead ECG, we analyzed the contribution of each lead in the predictions, keeping the best ones for the training process. For feature-based analysis, we used entropy-based methods to rank the obtained features. A cross-validation process was included to evaluate the machine learning model. Following, two clinical OTVA databases from different hospitals, including ECGs from 365 patients, were used as test-sets to assess the generalization of the proposed approach. The results show that V2 was the best lead for classification. Prediction of the SOO in OTVA, using both raw signals or features for classification, presented high accuracy values (>0.96). Generalization of the network trained on simulated data was good for both patient datasets (accuracy of 0.86 and 0.84, respectively) and presented better values than using exclusively real ECGs for classification (accuracy of 0.84 and 0.76 for each dataset). The use of simulated ECG data for training machine learning-based classification algorithms is critical to obtain good SOO predictions in

OTVA compared to real data alone. The fast implementation and generalization of the proposed methodology may contribute towards its application to a clinical routine.

KEYWORDS

machine learning, electrophysiological simulations, outflow tract ventricular arrhythmias, synthetic databases, virtual population, digital twin

1 Introduction

In structurally healthy hearts, ventricular tachycardia (VT) occurs primarily as a consequence of abnormal ectopic foci in the ventricles, overtaking sino-atrial activation and leading to premature ventricular complexes. The most common type of idiopathic ventricular arrhythmias originates from the outflow tract, and shows a high incidence in young population (Sirichand et al., 2017). For this group of patients, a catheter ablation of the tissue that triggers the ectopic focus is indicated, which shows low procedural complications and a high success rate. However, it is key to previously determine the site of origin (SOO) of the outflow tract ventricular arrhythmia (OTVA) to plan the intervention and the catheter approach. In particular, the differentiation between left and right ventricular (LV and RV, respectively) origin is crucial for the electrophysiologist, being the involved risk and time greatly different.

It is common to obtain recordings of the focal VT in the form of an electrocardiogram (ECG) prior to a radiofrequency ablation (RFA) procedure, which contain important information related to the OTVA and its origin. It is known that the majority of OTVAs originates from the RVOT (70–80%) (Srivathsan et al., 2005). Clinicians have developed several algorithms based on manual feature detection from ECGs (Lerman, 2015) to help determine the SOO. For a review on the classical ECG signatures proposed to determine the SOO of OTVAs, see Anderson et al. (2019). One of the main drawbacks of traditional ECG features is that they are complex to implement in daily clinical practice due to the large number of specific rules that have to be checked, which entail detailed measurements and visual comparison between precordial transitions, signal notches, and other features. In addition, they are usually based on observations on small cohorts of patients from a single-center study. In consequence, the whole process is too dependent on the clinician's experience. We recently showed that patient-specific simulations can reproduce the ECG signatures of OTVA, being able to predict the SOO in a small cohort of patients from a single center (Doste et al., 2020). However, processing patient data and performing patient-specific simulations requires very specific expertise and it is very time consuming, limiting its implementation in clinical routine.

We propose the application of machine learning (ML) techniques on ECGs from OTVA patients to guide their treatment. The use of ML and deep learning (DL) algorithms to learn from ECG data and provide predictions is becoming very popular in the medical field (Attia et al., 2021; Nagarajan et al., 2021). One particularly successful application is the use of ML for ECG analysis of cardiac arrhythmias, as recently reviewed in Minchole et al. (2019). For instance, ML was applied to classify different types of ventricular arrhythmias by a combination of support vector machine (SVM), with the help of grid search, and waveform morphological analysis (Li et al., 2022). ML has also being used to predict the LVOT versus RVOT SOO of VT in a clinical database of 420 patients with a high accuracy (Zheng et al., 2021), and to localize premature ventricular complexes from ECG using simulated databases (Yang et al., 2017; Alawad and Wang, 2019). Beyond patient stratification, DL has also been used for risk prediction of drug-induced arrhythmias and diagnosis of long QT syndrome (Prifti et al., 2021), or for finding an optimal lead subset of the 12-lead ECG to eliminate the redundancy, improving the generalizability of DL-based models (Lai et al., 2021).

ML and DL techniques rely on the quality of training datasets, which should represent the target population and be balanced. In the particular case of OTVAs, there are different locations for the SOOs (transmurally distributed in several anatomical regions of the LV and RV), and other co-variables such as the ventricular anatomy, its orientation, or the presence of pathological tissue (scar) that affect the ECG morphology. Since there are not large public labelled databases of OTVA patients available (largest in the order of 350 cases), the solution could be the use of computational models, e.g., digital twins (Corral-Acero et al., 2020) to build large virtual datasets where all the variables are under control. These virtual hearts are electrophysiological twins to the patient's heart on which various stimulation protocols can be applied to, for instance, in our case induce OTVAs from different SOO. Such an approach has been successfully applied to several medical applications, such as drug screening (Costabal et al., 2019), anatomical modelling of pathological populations (Romero et al., 2021; O'Hara et al., 2022), therapy planning of catheter ablation (Ferrer et al., 2015; Ferrer-Albero et al., 2017; Prakosa et al., 2018; Lopez-Perez et al., 2019), or ECG simulation (Cardone-Noott et al., 2016).

In this paper, we propose the use of ML models trained with large synthetic datasets of simulated ECG data obtained from biophysical electrophysiology simulations of OTVAs on digital twins. We present results on the prediction of SOO using different approaches in which we train ML models with a virtual population of synthetic simulated data, validating them

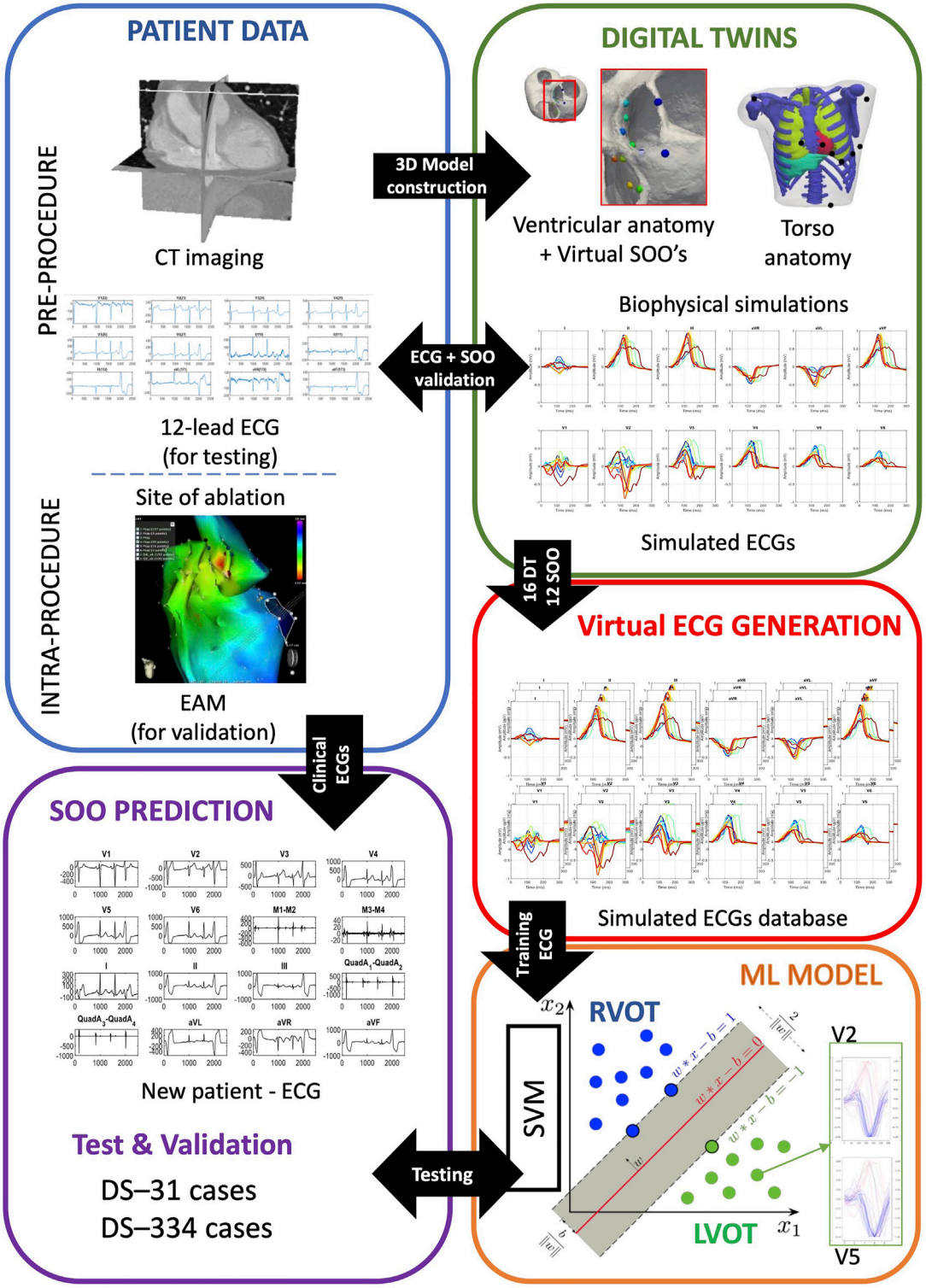

FIGURE 1
Scheme of the proposed methodology. Patient data was used to build ventricular digital twins for the 16 patients. Biophysical simulations were run in the different anatomies, using 12 different sites of origin (SOO), to generate a database of 12-lead electrocardiograms (ECGs). The database of simulated ECGs was finally used to train a ML algorithm to predict the SOO (Right ventricle outflow tract (RVOT) vs. Left ventricle outflow tract (LVOT)) of real patients ECGs from two different clinical datasets (DS-334 and DS-31). Abbreviations used in the image: CT: computed tomography; EAM: electroanatomical mapping; ML: machine learning; SVM: support vector machine.

with real clinical datasets from different centers, also evaluating combinations of synthetic and real data for training and validation. We also evaluated the best precordial leads and the signal features that produced a better LVOT/RVOT classification. This approach in which all the simulations have been performed beforehand and only ML models are used to predict the SOO of new patients permits its translation to daily clinical routine.

2 Materials and methods

We have developed a computational pipeline to build and validate our approach, from clinical data to final ML-based predictions, summarized in Figure 1. It starts with the generation of ventricular digital twins, built with patient-specific heart meshes together with their cellular and tissue electrical properties. All the digital twins include outflow tracts from both ventricles up to the valve planes, with the estimated myocardial fiber orientation as in Doste et al. (2019), and no structural disease. Biophysical simulations of ventricular cardiac electrophysiology were run from different SOO to compute the ECGs. Subsequently, simulated ECGs were compared and validated against the available patient data and used to generate a database of synthetic ECGs. This database was later used to perform a supervised training of a ML model to predict the SOO of an ectopic beat, and was tested against two clinical OTVA ECG databases from different hospitals. In the following subsections we describe the different clinical datasets and the methodology used for simulating the ECGs. The next subsection is then focused on the data pre-processing and homogenization for both clinical and simulated signals. Final subsection contains all the information about the support vector machine used for classification between RV and LV SOO. Two different strategies for reducing the dimensionality of the data (downsampling the raw ECG signal and extracting ECG-based features) are introduced. We also applied a data augmentation algorithm to improve the performance of the classification. Finally, the different scenarios used for the signal classification are described.

2.1 Clinical datasets for testing

We included two different clinical ECG datasets from OTVA patients for the validation of the proposed approach. The first dataset consisted of 31 ECGs (DS-31) that were prescribed for catheter ablation procedure at the Hospital Clinic, Barcelona. All patients underwent a electro-anatomical mapping study by CARTO three navigation system (Biosense Webster, Diamond Bar, CA, United States) with a 3.5 mm irrigated tip catheter (NaviStar, Biosense Webster). During the procedure, 12-lead surface ECG and intracardiac recordings were obtained and displayed by an electrophysiology data acquisition system (Bard LabSystem, CR Bard Inc., Lowell, MA, United States ; or EP-Tracer, CardioTek, Maastricht, Netherlands). Ablation was considered successful if the targeted OTVA was eliminated and it was noninducible after isoproterenol infusion. The site where RFA application eliminated the OTVA was considered the SOO and was labelled and saved in the electroanatomical mapping data for validation purposes. The study was approved by the local ethics committee and written informed consent was obtained from all participants. The second dataset was an open-source 12-lead ECG database of 334 OTVA patients (DS-334) published by Zheng et al. (2020). The database was composed of 257 patients that had arrhythmias originated in the RVOT and 77 patients with an LVOT origin, which were treated at the Ningbo First Hospital of Zhejiang University (China). ECG signals were obtained at a sampling rate of 2 kHz. Details about the RFA procedure, ECG acquisition or ethical committee can be found in the original study (Zheng et al., 2020).

2.2 Virtual electrocardiogram generation

In this work, we constructed ventricular digital twins from 16 different biventricular geometries built from patient-specific computed tomography (CT) scans. Each model was represented by a volumetric 3D mesh made of hexahedral elements with an average resolution of 400 μm. Every element was labeled according to its cellular properties as, endocardial, midmyocardial or epicardial cells. As described in Doste et al. (2020), for each digital twin, we simulated OTVAs from 12 different SOOs (see Figure 1, digital twins, spheres on biventricular geometry) chosen following clinical observations (Anderson et al., 2019), seven from the LVOT and five from the RVOT.To perform the simulations at the organ level, we used the software ELVIRA (Heidenreich et al., 2010), which solves the anisotropic reaction-diffusion equation of the monodomain model for cardiac EP using finite element methods. For the numerical solution of our simulations, we applied the conjugate gradient method with an integration time step of 0.02 ms, using implicit integration for the parabolic partial differential equation of monodomain model and explicit integration with adaptive time stepping for ordinary differential equation of the ionic model (ten Tusscher et al., 2004). Each simulation consisted in a train of four beats with a cycle length of 800 ms followed by an ectopic focus simulated during a time window of 300 ms. Extracellular potentials at the heart were approximated from transmembrane potentials previously computed, and propagated by using the finite element method to solve a Laplace equation over the volume mesh of a generic 3D torso model (Lopez-Perez et al., 2019). Torso anatomy included the lungs, ribs, liver, atria and a cavity where each biventricular model was fitted. To add extra variability on the simulated ECG that can be produced by

different lead placement or heart orientation, we shifted precordial leads around the standard position to have 13 different lead configurations. Consequently, we built a database of a total of 2,496 12-lead simulated ECGs (16 patients, with 12 different SOO and with 13 different electrode placements). ECGs were validated against patient data using the 12 lead correlation coefficient and the LV/RV ratio (Doste et al., 2020). This ratio was calculated by dividing the mean of the 12 lead correlation coefficient values of all the SOO simulations with origin in the LVOT by the one corresponding to the SOO simulations originated in the RVOT. A LV/RV ratio larger and smaller than one will indicate a LVOT and RVOT origins, respectively.

2.3 Data pre-processing

We performed data homogenization to facilitate the data processing by the ML algorithm and a better comparison of the results. In particular, we classified all the ECGs (real and simulated) according to the SOO provided in the work by Zheng et al. (2020). All the OTVA ECGs were divided in two main groups as a function of the origin: LVOT or RVOT. The SOO were also distributed in different sublocations. LVOT cases were classified into six regions: Left coronary cusp (LCC), right coronary cusp (RCC), LCC-RCC commissure, non-coronary cusp (NCC), aortomitral continuity (AMC) and LV epicardial summit. RVOT cases were divided in anteroseptal RV, posteroseptal RV and right ventricular free wall (RFW). These regions can be visualized in the geometry shown in Figure 4. Only the QRS complex of the ECGs was evaluated. To standardize the input to the ML models, each 12-lead ECG amplitude was max-abs normalized (i.e., normalized in the range [-1, 1]) and the onset and offset of the QRS complexes were obtained using a DL-based ECG delineator (Jimenez-Perez et al., 2021a; Jimenez-Perez et al., 2021b) for posteriorly using them in raw- and feature-based approaches (Section 2.4). In feature-based approaches, the signal was further zero-corrected to remove baseline wander, and transformed using the wavelet transform (Martinez et al., 2004) and Welch's periodogram (Welch, 1967) for the feature extraction pipeline.

2.4 Machine learning model

We chose support vector machines (SVM) to classify patient arrhythmias as a function of the SOO. An SVM is a well-known learning algorithm (Cristianini and Shawe-Taylor, 2000) that has extensively been used in many clinical areas, such as ECG classification (Attia et al., 2021), due to a remarkably robust performance when working with sparse and noisy data. SVMs tries to separate a given labeled training set (LVOT vs. RVOT origin) with a hyper-plane that is maximally distant from them. In our case, we use radial basis function kernels that will produce non-linear decision boundaries. We have applied two strategies for reducing the dimensionality of the data used for model training, since high dimensionality directly affects the classification performance by introducing unwanted noise. These strategies included downsampling the raw ECG signal and using this morphology directly (Section 2.4.1) and extracting ECG-based features (Section 2.4.2). The final number of features and samples in the down-sampled signal was chosen by evaluating the cumulative variance against the number of principal components of the training signals. We also evaluated the information carried in each lead by analyzing the classification performance of using specific lead combinations.

2.4.1 Raw signals

Since all ECG signals were conveniently normalized and aligned, segmented QRS complexes could be directly treated as patterns and also as feature vectors, where the pseudo-features correspond to the ECG amplitude at each time point. Given that the changes in the voltage convey the most important information of the ECG, we simply consider that the down-sampled raw signal (dimensionality reduction) is a set of features that represent the data at specific time points around the R-peak. Therefore, after studying the cumulative variance of the principal components, the signals were down-sampled to 10 samples (see Figure 2).

We used this down-sampled raw signal representation to determine the best lead combinations as well as the most important lead in terms of classification. This exploration was carried out exhaustively, that is, for each one of the possible lead combinations (4,095). Therefore, a SVM classification model was trained with the corresponding lead combinations and then evaluated with the two test datasets. To obtain the feature vector of a lead combination we simply concatenate the corresponding signal leads (increasing the number of dimensions associated to the classification tasks). Finally, we computed the accuracy distribution associated to each lead by considering all the accuracy obtained from any lead combination that contain that particular lead.

The signal low dimension representation can also be used to determine what part of the signal is the most important in terms of classification. To assess this issue, we calculate a feature importance ranking based on *extra – trees* classifier models. In this kind of forests, the importance of the features are computed as the mean and standard deviation of accumulation of the impurity decrease within each tree (entropy based) and it is provided by the fitted model. The feature importance is specially interesting for raw signals as each feature covers a short time interval of the beat, so that the most important features correspond with the time intervals used by the classifier that better explain its predictions.

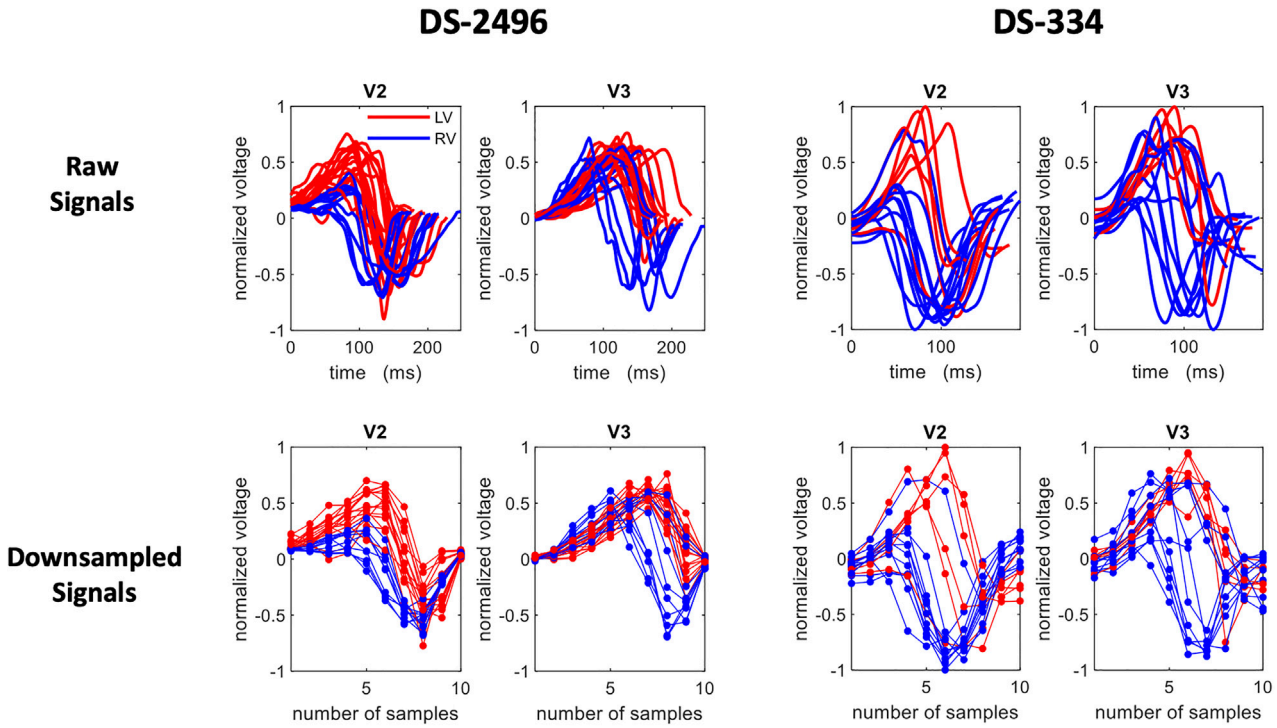

FIGURE 2
A set of selected ECG traces from the simulated (DS-2496) and the DS-334 datasets. The extracted QRS of the V2 and V3 precordial leads are shown in the top row and their corresponding down-sampled traces (10 samples) in the bottom row. Right Ventricle (RV) signals are plotted in blue, whereas left ventricle (LV) signals are in red.

2.4.2 Feature-based signals

2.4.2.1 Feature extraction

Previous studies have reported a decrease in generality when using the raw ECG trace as opposed to ECG-derived features (Minchole et al., 2019). To address this, feature extraction was performed on the QRS complex as an alternative representation of its morphology. A total of 356 features were extracted, based on measurements on the raw ECG, its wavelet transform and its power spectral density. Some features were computed using single leads (e.g. maximum of lead V3), whereas other features performed pairwise comparisons of leads (e.g. area under the curve of lead II with respect to lead III). To avoid too high dimensionality, comparative features were only computed within three subsets of leads: limb leads (I, II and III), augmented leads (aVR, aVF and aVL) and precordial leads (V1 to V6), with a total of 21 comparisons per extracted feature. Finally, some features explored the effect of many leads (e.g. precordial transition explores the lead where the polarity changes, taking all precordial leads). Some of the extracted features were inspired in the methodology presented by Maršánová et al. (2017), which provided high accuracy when classifying heartbeat types. A schematic representation of the extracted features is depicted in Figure 3.

The signal-based features consisted in the computation of several markers from the raw ECG. Firstly, two all-lead features were considered: the QRS′ total activation time (QRS_{end} – QRS_{start}) and the localization of the precordial transition. The precordial transition was computed via retrieving the signed maximum of each precordial lead and selecting the first lead where the QRS complex changed polarity, codified as a decimal point value within zero (V1) and one (V6). Secondly, eight per-lead features are extracted. These comprise the polarity of the lead's signed maximum ($\{-1, 1\}$), the lead's maximum and minimum voltage, its absolute maximum voltage (signed and unsigned), the lead's amplitude and its area (both raw and taking the absolute value). Finally, three comparative features were computed: the signed maximum voltage of the difference between the leads, the area of the difference between the leads and the cross-correlation between the leads.

Wavelet-based features were computed with the mother wavelet designed by Martinez et al. (2004), which has a frequency response that is optimal for QRS complexes. The wavelet transform is used in this work as a robust surrogate of the original signal's derivatives, and was employed to locate

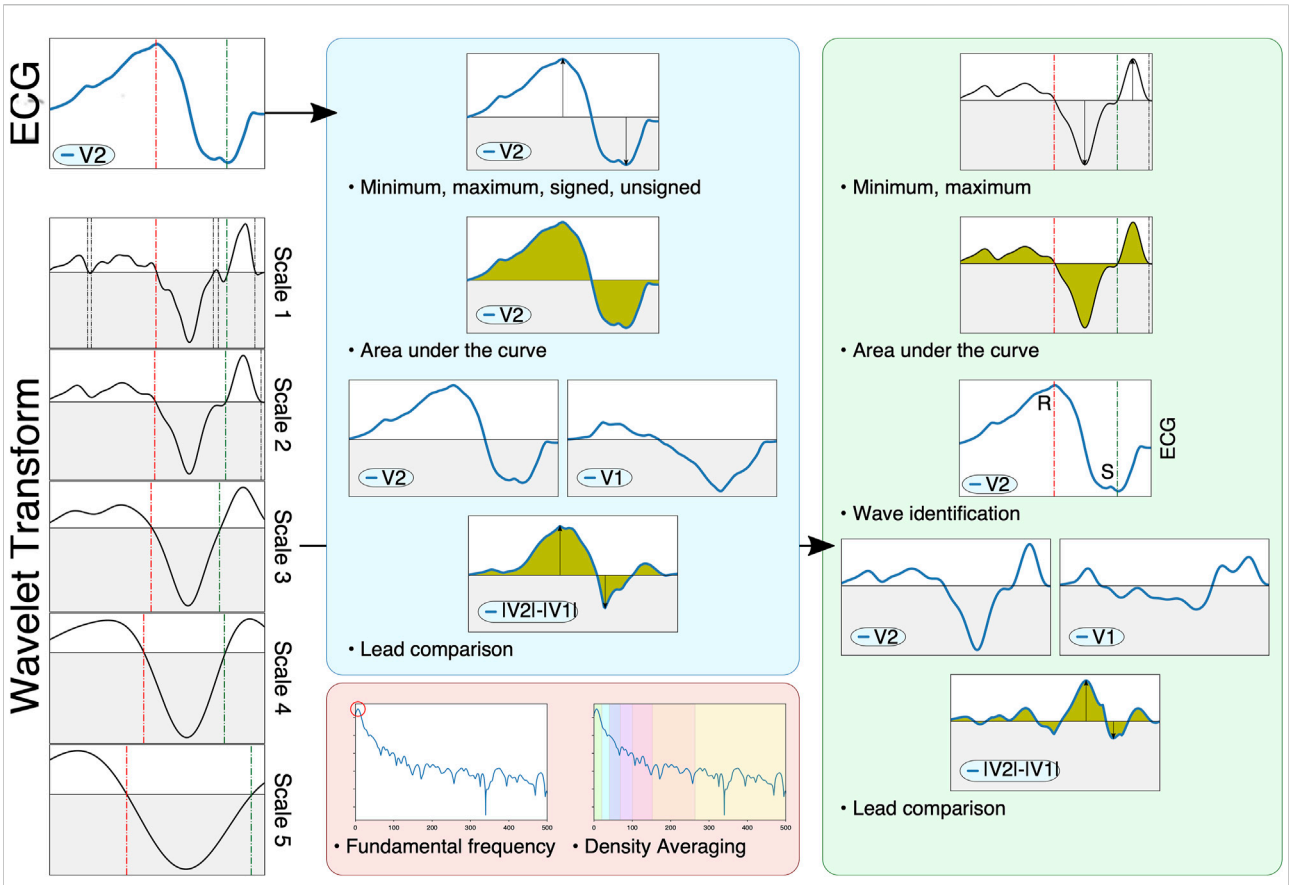

FIGURE 3
Schematic representation of the feature extraction pipeline. The ECG (left, top) and its wavelet transform (left, scales one through 5) are used to compute signal-based (blue), wavelet-based (green) and spectral-based (red) features. Signal-based features measure the raw ECG, computing extrema, areas or characteristics computed through pairwise lead comparison. Wavelet-based features also compute said markers, but also identify important fiducials through zero-crossings (e.g. different QRS waves such as the R and S waves, shown on the left as green and red dotted lines). Finally, spectral information employs Welch's periodogram to obtain features based on the signal's power spectral density.

different fiducials in the signal (Q, R and S wave peaks) through the identification of zero crossings across multiple wavelet scales (Figure 3, bottom-left). This allowed a better characterization of important clinical markers such as the ratio between the R and S waves or the maximum signal velocity. Firstly, a single all-lead feature was extracted, the precordial transition, by estimating the moment where the precordial leads changed polarity. Secondly, six per-lead features were computed, comprising the maximum and minimum amplitude values, the mean amplitude of the wavelet, its area under the curve, the signal fragmentation (estimated as the ratio between the wavelet's area and its absolute area) and the R/S amplitude ratio. Finally, three comparative features were extracted, consisting in the area under the curve, the maximum difference and the cross-correlation between two leads. Although the identification of important fiducials was performed by propagating the information across different wavelet scales, only the first wavelet scale was employed for the above computations.

Finally, seven per-lead spectral features were extracted. For that purpose, the power spectral density of the QRS complex was computed with the method proposed by Welch (1967). After computing the power spectra (Figure 3, red block), the fundamental frequency was estimated by computing the frequency with the highest power, and six spectral density bands were computed by averaging the signal's power between (0.3) (3.6) (6.9) (9.12) (12.25) and (25.50) Hz.

2.4.2.2 Feature importance

When working with the 356-featured training set, the selection of the best features for classification has been carried out using *extra – trees* classifier models (Geurts et al., 2006). The model consists on a meta estimator that fits a number of unpruned randomized decision trees (*extra – trees*) on various sub-samples of the training set. Then, predictions are made by majority voting from the trees. Similar methods like bagging and random forest develop each decision tree from a bootstrap

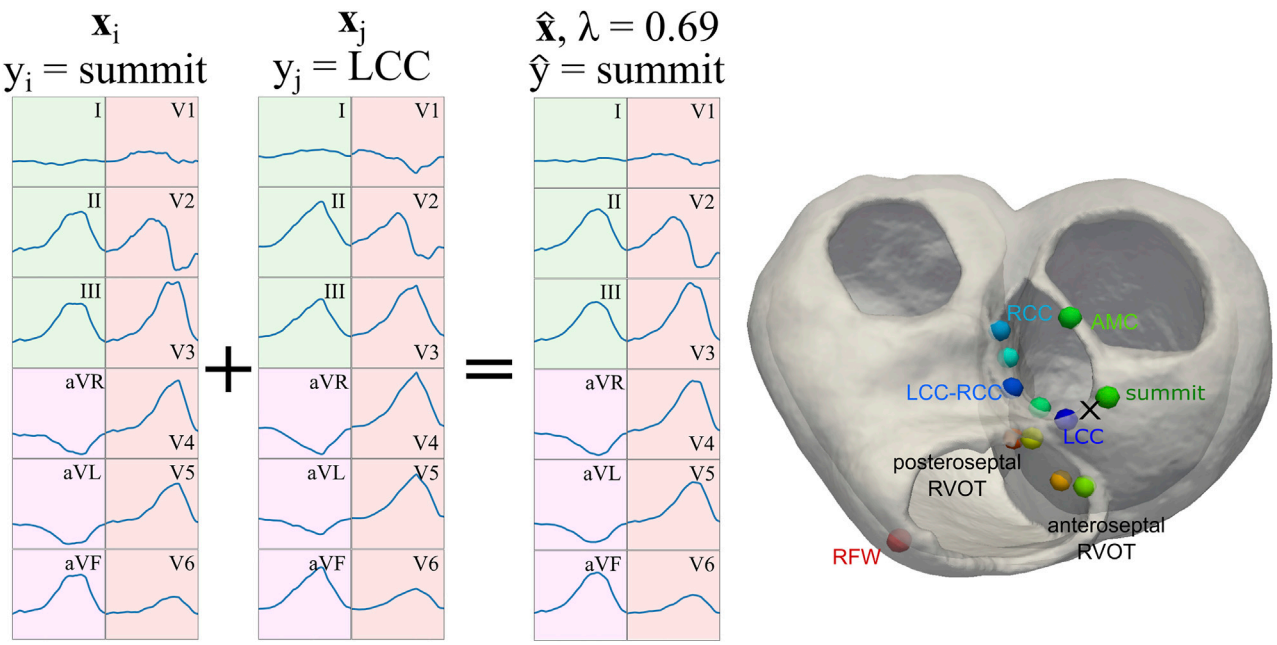

FIGURE 4
Representation of the signal augmentation process. Two samples $\mathbf{x}_i$ and $\mathbf{x}_j$ are linearly combined with $\lambda \sim \mathcal{B}(\alpha, \beta)$. The label of $\mathbf{x}_i$ is adopted, given that $\lambda > 0.5$. In the right, marked with a cross, the approximated location of the augmented sample. LCC: left coronary cusp; RCC: right coronary cusp; RFW: right free wall; AMC: aortomitral continuity; RVOT: right outflow tract.

sample of the training set, while the *extra − trees* algorithm fits each decision tree on the whole training set. Furthermore, similarly to the random forest method, the *extra − trees* model will randomly sample the features at each split point of a decision tree. However, random forest uses a greedy algorithm to select an optimal split point, while the *extra − trees* model selects a split point at random. All the features extracted from the simulated dataset (DS-2496) were ranked according with the results of the *extra − trees* classifier. A variance analysis was also conducted to evaluate the minimum number of features that optimizes the classification performance.

2.4.3 Data augmentation

In order to improve the performance of the classification task, the simulated dataset was augmented using mixup, as described by Zhang et al. (2018). This technique allowed for smoother decision boundaries when training a classifier on augmented data: augmented samples are generated by randomly selecting two samples ($\mathbf{x}_i$ and $\mathbf{x}_j$) and performing a linear combination of the two ($\hat{\mathbf{x}} = \lambda \mathbf{x}_i + (1 - \lambda)\mathbf{x}_j$), given a parameter generated by a beta distribution ($\lambda \sim \mathcal{B}(\alpha, \beta), \lambda \in [0, 1]$). In the same signal generation process, the corresponding label (y_i or y_j) was fixed through the λ parameter: y_i was adopted if $\lambda > 0.5$, and y_j was selected otherwise.

In this work, we employed single 12-lead QRS complexes as samples $\mathbf{x}_i$, and the labels y_i were the ground-truth SOO (either LVOT vs. RVOT or the nine finer SOO sublocations). For the purposes of this work, $\alpha = 5$ and $\beta = 1.5$ were selected as hyperparameters. The λ parameter was saved to be used as sample weight in the classification process. In the case of the finer sublocations, and to avoid issues with labels corresponding to distant sublocalizations (e.g. mixing Anteroseptal and AMC SOO samples), mixup was only applied when $\mathbf{x}_i$ and $\mathbf{x}_j$ were neighboring segments in a spatial sense, as can be seen in Figure 4. Finally, the generated QRS complexes were in turn employed for classification with the raw signal, as described in Section 2.4.1, and with the feature extraction pipeline explained in Section 2.4.2. In total, 7,488 augmented QRS complexes were generated for the virtual ECG population described in Section 2.2. A table with comparison metrics of the different databases, including the augmented database, can be found in the Supplementary Material S1.

2.4.4 Classification and validation

To evaluate the degree of generalization achieved by the SVM models and to exploit the datasets used in this work, we considered the following scenarios (See Table 1):

As we manage four datasets, namely DS-2496 (simulated signals), DS-7488 (simulated augmented signals), DS-334 (real patient signals), and DS-31 (real patient signals), the test-set(s) used for the assessment of each learning scenario are those not employed in training. Furthermore, cross validation (CV)

TABLE 1 Description of the different classification scenarios.

Scenario	Training	Classification Strategy
Scenario 1 (Sc1)	SVM model trained with simulated signals (DS-2496) or augmented simulated signals (DS-7488)	down-sampled raw signal; feature-based ECG signals; 10 best features
Scenario 2 (Sc2)	SVM model trained with real signals (DS-334; DS-31)	down-sampled raw signal; feature-based ECG signals
Scenario 3 (Sc3)	SVM model trained with a hybrid training set (DS-334) + (DS-2496); (DS-31) +(DS-2496)	down-sampled raw signal; feature-based ECG signals

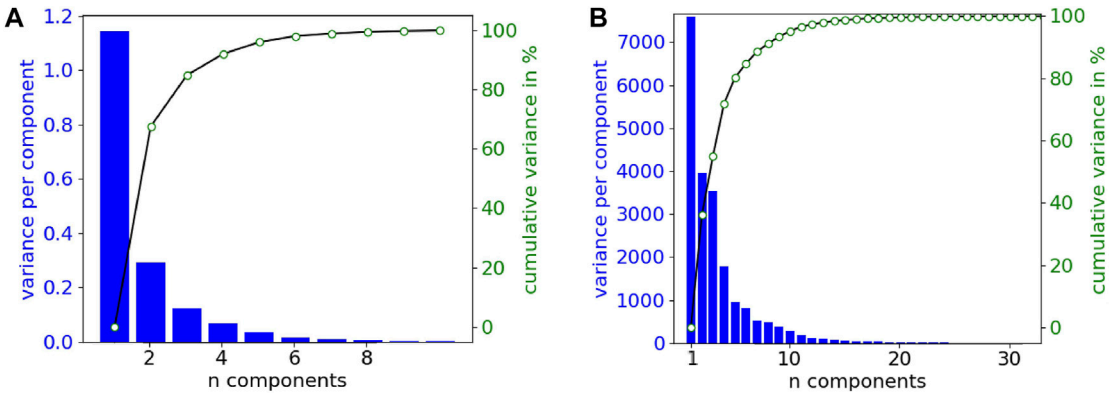

FIGURE 5
Variance explained by the principal components from the simulated dataset (DS-2496). **(A)** Down-sampled raw signals (10 samples or features). **(B)** Featured signals (356 features).

techniques (folds = 5) in the domain of the training set are also included. Accuracy values obtained for the DS-334 and DS-31 datasets were computed as balanced accuracy. More information about the classification of the main Scenarios (confusion matrix and accuracy per class) is attached in the Supplementary Material S1.

3 Results

3.1 Variance analysis

Figure 5 shows the variance explained by a principal component analysis (PCA) of the simulated dataset (DS-2496) according to the number of components, in the two signal representations handled in this work; raw (a) and featured (b). In both cases, the number of features required to cover almost 100% of the variance is low (10 features). Therefore, the down-sampling of the raw signals allows to easily reduce the number of features of the dataset in similar way to PCA, although in this case the new features are directly related with the electrical potential mean values of time intervals.

3.2 Best lead combination for classification with raw data

Using the down-sampled simulated raw data (10 equidistant samples from the voltage ECG traces), we explored which were the lead combinations that showed a better performance for ECG classification. A total of 4,095 different models were trained using all the possible lead combinations. Figure 6A shows the best 24 combinations that presented the highest classification results. The accuracy distribution associated to each lead is presented in Figure 6B. Lead V2 is the lead that presents higher accuracy in both testing sets (followed by lead V3), and is also present in all the best lead combinations for DS-334. When comparing the different accuracy obtained with both datasets, DS-31 presents overall lower accuracy values.To uncover the characteristics of V2 that might be responsible for the higher classification accuracy, we evaluated the importance of each samples in the downsampled raw signal. The results are depicted in Figure 7A. The importance of each of the 10 samples is represented by the red bars, being the seventh sample the most important one. Figure 7B depicts a small subset of V2 traces from the LVOT (red) and RVOT (blue) simulations overlaid to the down-sampled signal samples (red and

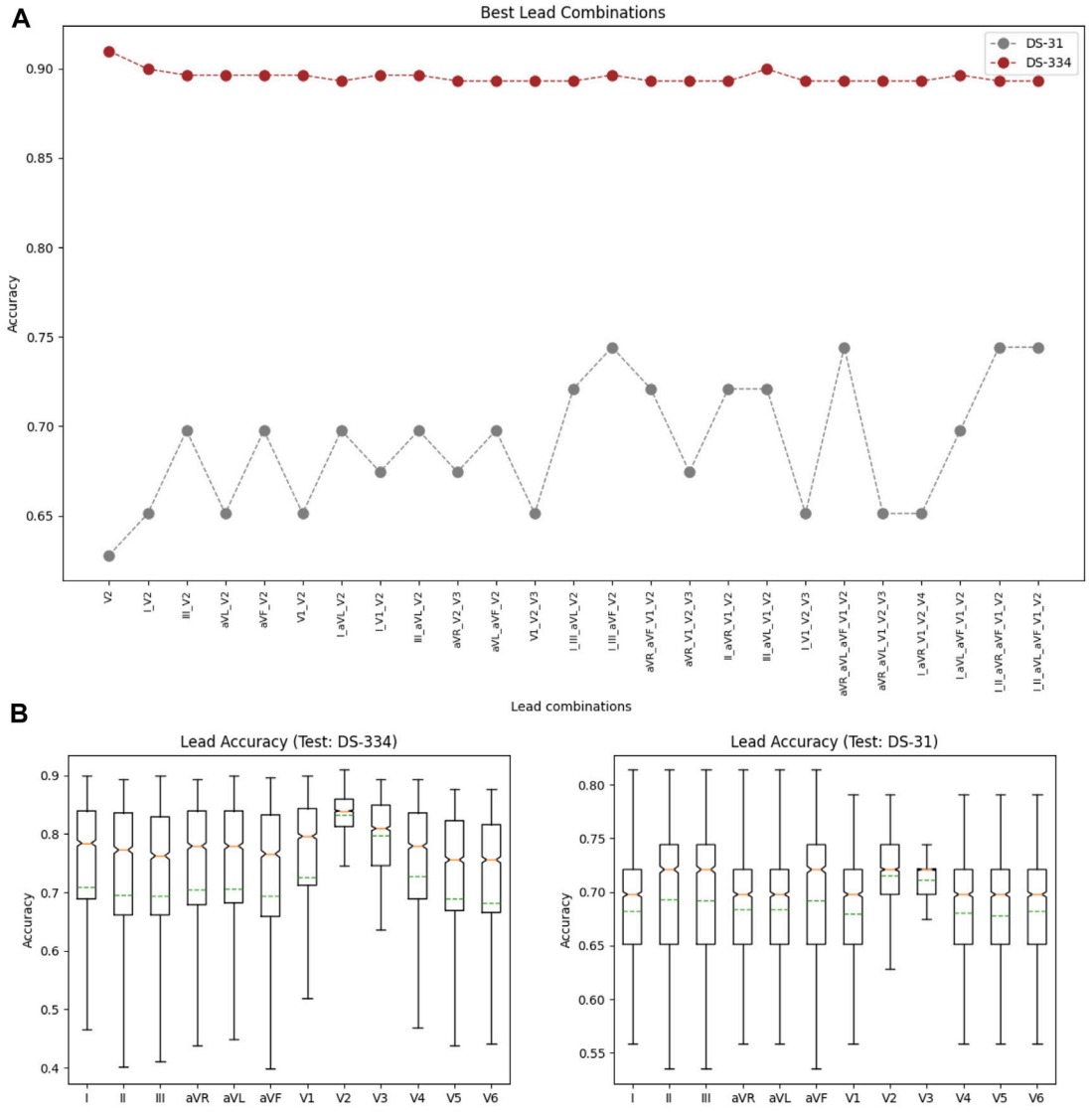

FIGURE 6
(A) Lead combinations that presented the best classification results for both datasets. **(B)** Distribution of the classification accuracies associated to each lead for the DS-334 (left) and DS-31 (right) datasets.

blue dots). Results show that the seventh bin samples, where differences in voltage between LVOT and RVOT simulated traces are clearly seen, are the most important for the classification. The second most important bin is the second, where traces show a positive or negative slope. The adjacent samples to the second and seventh bins continue the order of descending sample relevance.

3.3 Feature selection

Figure 8A shows the ten most important features obtained using the introduced *extra – trees* model. As can be seen, the most important features were signal-based features extracted from the V2 and V3 leads. In addition, the panel on the right shows the accuracy scores obtained by the SVM-classifier by varying the number of features used in the training set. The calculated scores are the accuracy from a cross validation process (folds = 5) and the predictions of the datasets employed for model testing (DS-334, DS-31).

3.4 Classification results

Table 2 shows the classification performance of the different scenarios described in the methodology. The cross-validation analysis of the classification with each of the datasets, using five

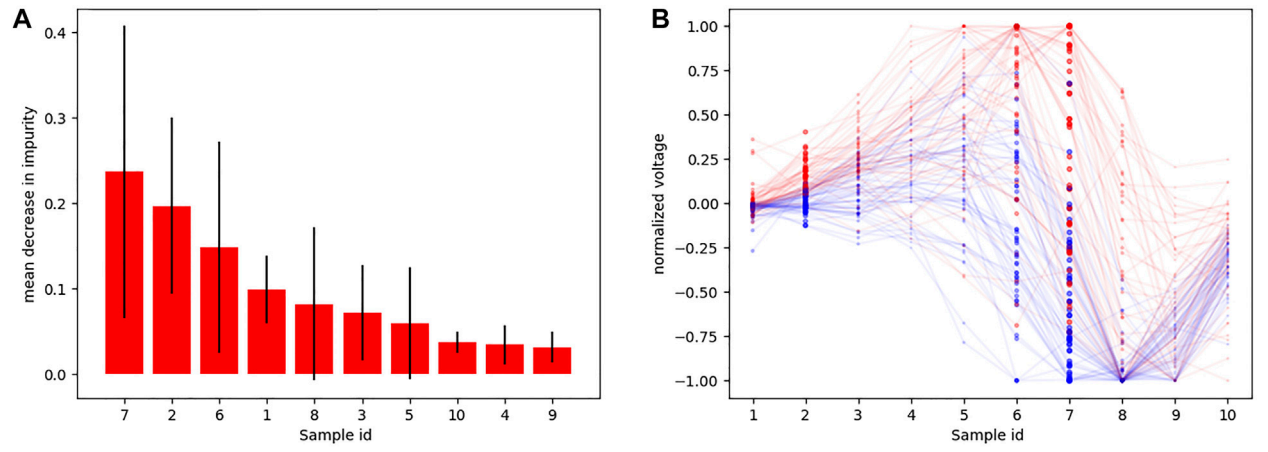

FIGURE 7
(A) Sample importance obtained using raw down-sampled signals; **(B)** Ten samples (red and blue dots) corresponding to signal time intervals obtained from a subset of V2 signals, together with their corresponding traces (transparent) so that they could be easily interpreted. Red traces correspond to LVOT and blue traces to RVOT.

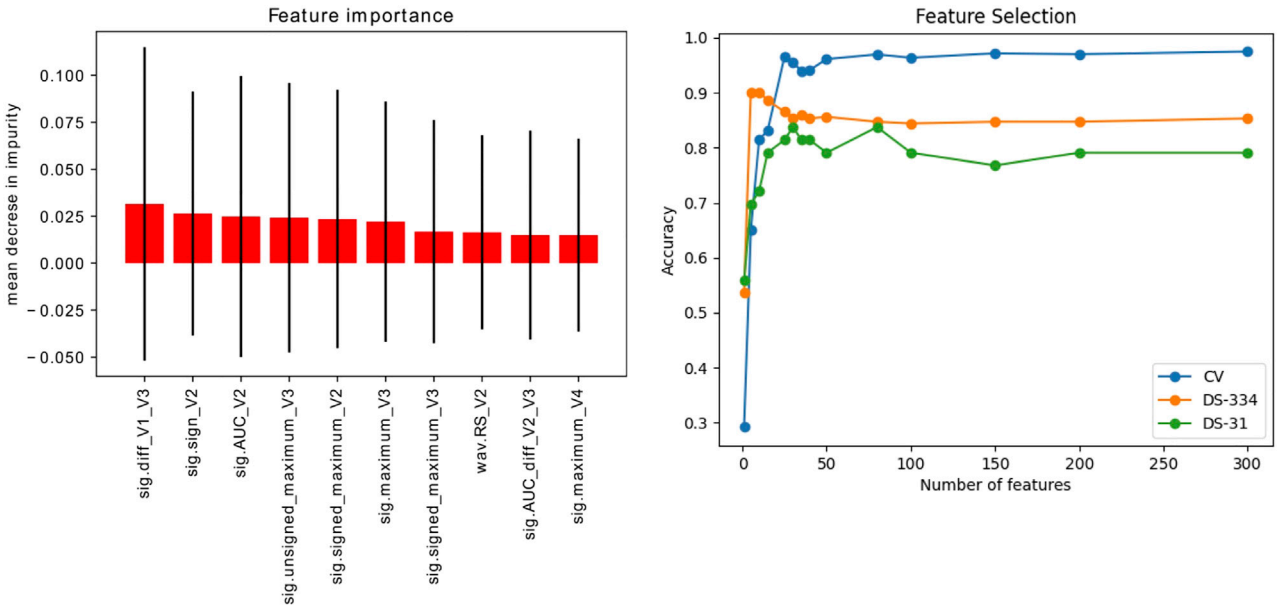

FIGURE 8
Left: Ranking of the 10 most important signal features (out of 356) for signal classification, extracted using the extra-trees classifier method. Right: Evolution of the accuracy scores vs. the number of features used for training. The accuracy was evaluated in the simulated signals through a cross validation (CV) process and in the clinical datasets (DS-334 and DS-31).

folds, provided high accuracies between 0.82 and 0.96 for the simulated data, and low accuracies for the clinical datasets, that were between 0.60 and 0.92. DS-31 was particularly complex to classify due to its reduced size and high data variability.

Scenario 1, where only simulated signals were considered for training, presents the highest accuracy values in the classification. Raw down-sampled signals were able to classify the clinical signals of the DS-334 with an accuracy of 0.86, whereas the DS-31 presented lower values (0.71). Results did not improve significantly when we made use

TABLE 2 SVM accuracy results.

Scenario	Training Set	Accuracy		
		CV (folds = 5)	Test (DS-334)	Test (DS-31)
Sc1	Simulated Raw Signals (DS-2496)	0.96	0.86	0.71
Sc1	Augmented Simulated Raw Signals (DS-7488)	0.98	0.86	0.71
Sc1	Featured Simulated Signals (DS-2496)	0.97	0.85	0.84
Sc1	Featured Augmented Simulated Signals (DS-7488)	0.98	0.86	0.84
Sc1	10 Best Features Simulated Signals (DS-2496)	0.82	0.88	0.77
Sc1	10 Best Features Augmented Simulated Signals (DS-7488)	0.87	0.86	0.77
Sc2	Real Raw Signal (DS-334)	0.88	-	0.57
Sc2	Real Featured Signal (DS-334)	0.92	-	0.76
Sc2	Real Raw Signal (DS-31)	0.62	0.84	-
Sc2	Real Featured Signal (DS-31)	0.60	0.74	-
Sc3	Hybrid: Simulated + Real Raw Signals (DS-334)+(DS-2496)	0.90	-	0.71
Sc3	Hybrid: Simulated + Real Featured Signals (DS-334)+(DS-2496)	0.96	-	0.81
Sc3	Hybrid: Simulated + Real Raw Signals (DS-31)+(DS-2496)	0.95	0.86	-
Sc3	Hybrid: Simulated + Real Featured Signals (DS-31)+(DS-2496)	0.97	0.85	-

of augmented simulated data for training (DS-7488). The use of signal features also presented good classification values. Although the accuracy slightly decreased in the DS-334 with respect to the raw data (0.85 vs. 0.86, featured-based vs. raw data), the accuracy for dataset DS-31 was considerably higher (0.84 vs. 0.71, featured-based vs. raw data). As with the case of raw data, augmented feature data barely increased the accuracy values. Furthermore, as shown in the cumulative variance plot, classification with only 10 features was also performed. Results showed that a classification using the best 10 features, determined in Figure 8, provided good accuracy values, although the cross-validation accuracy values were slightly lower than the ones obtained using all the features (356).

Scenario 2, which was calculated using only real data for training, served as a good comparison of the classification performance of the simulated data versus the real data. It can be seen that, when using signals from different clinical datasets for training and classification, the accuracy in the prediction of the SOO decreases significantly, being inferior to the values of Scenario one in all cases. Scenario 3, on its behalf, used a mix of simulated and real data for training. All the accuracies (using raw data and featured data) surpassed the values of the Scenario 2, showing that the use of simulated data in the training can considerably improve the classification results.

4 Discussion

In this work, we have presented a methodology to automatically classify ECGs from patients that suffer OTVAs by a ML model purely trained with synthetic data from biophysical simulations carried out on ventricular digital twins. To this end, we trained SVMs classifiers that were able to determine the SOO of the arrhythmia, differentiating between LVOT and RVOT. We have validated the method with two clinical datasets acquired in different clinical centers. In particular, we show that this method can predict the SOO with an accuracy of 0.86 in a clinical database of 334 patients, and 0.84 in a second clinical database of 31 patients, without the need of performing any manual analysis on the ECG signals. This is key, since other algorithms in the literature require an electrophysiologist to extract a considerable number of the features from the 12-lead ECG signals and perform several calculations on them to predict the SOO (Anderson et al., 2019). Further, we have been able to show that a ML model for ECG classification can be trained on virtual ECGs, eliminating the need to collect and curate large clinical databases (Zheng et al., 2020). Another advantage of this simulation strategy is that the signals are noise free, and the location of the SOO is determined without any error in position. Finally, the dataset built to train the ML model can include a balanced number of samples that represent properly all the SOOs, and possible variations of the heart with respect to the torso, such as rotations, which is really complex to achieve with clinical data due to the incidence of the pathology in the population (70% of cases correspond to RVOT SOO) (Srivathsan et al., 2005).

Our analysis on the use of different combinations of signals to train the model and predict the SOO pointed out that V2 was the signal that convey more information followed by V3. This is in agreement with the results already reported in a few clinical studies (Hayashi et al., 2017; Kaypakli et al., 2018). A more exhaustive evaluation of the down-sampled version of the V2 lead, showed the most important signal samples used for the classification by the SVM. In particular, these positions, usually located after the R peak, corresponded with the signal parts that presented higher variability in voltage between RVOT and LVOT (once these signals have been aligned and normalized).

The obtained classification results had a similar level of accuracy than clinical algorithms used in the SOO prediction (Anderson et al., 2019; Mariani et al., 2021). From these results, we have been able to conclude that, although extracting signal features from ECG seems to be the best approach, there is not a large improvement with respect to simply use raw data as features (the potential of the signal at ten equally spaced time points), provided that all signals are aligned. That means that, if necessary, signals do not have to be processed, which could introduce errors and requires supervision during the feature extraction phase.

One of the most remarkable results of this work is that the use of simulated ECGs for training not only predicts the OTVA SOO with good accuracy, but it even surpasses the performance of the databases trained with real data, especially when they are used with a different database. This is due to the higher variability of the simulated data, which also presents less bias towards acquisition instruments or protocol. Consequently, as it is shown in Scenario 3, the addition of simulated data to real databases can improve the prediction of the SOO in any dataset when compared with the results obtained by training with only real data (Scenario 2). These results support the use of simulated signals for improving the performance of ML classifiers, as it has been done previously for atrial fibrillation (Luongo et al., 2021) or cardiac resynchronization therapy response (Khamzin et al., 2021). On the other hand, the inclusion of augmented simulated data (DS-7488) did not had a significant impact in the classification results, probably due to the high correlation of the data. We also analyzed why the DS-31 dataset presents lower classification accuracies than DS–334. An analysis of the classification results (see Supplementary Material S1) showed that some of the LV SOO were wrongly classified as RV SOO. This was caused by some LV signals presenting variability that could not be reproduced by the simulated ECGs used for training. Furthermore, the reduced sample size of this dataset negatively affected the computed accuracies.

It is important to note that the designed ML-based pipeline does not require any further complex and time-consuming simulations, unless there is a need to update the model with additional data. That is one of the main limitations of physics-based approaches, in which the construction of the patient digital twin, and the computation of electrophysiology simulations is complex and requires hours to days to produce the results (Prakosa et al., 2018). This makes the ML-based approach suitable to be transferred to the clinical routine, since it can make instantaneous predictions with the only requirement of accessing the 12-lead ECG. This is a critical step towards the implantation of computational techniques for therapy planning of catheter-based ablation, since they can help to reduce procedure times, improve the risk evaluation or identify arrhythmias that cannot be treated (e.g. inaccessible SOOs (Yamada et al., 2010)) before the intervention. There have been previous works that made use of ML models to predict the SOO using only clinical data for training with good accuracy (0.97) at the cost of having a large feature vector of 1.6 million size (Zheng et al., 2021), which could show problems to generalize for other databases.

4.1 Limitations

Even though our method shows promising results when compared to existing solutions, it presents some limitations. First of all, to build the database, digital twin models must be faithful representations of patients, and the biophysical simulations have to be properly calibrated to produce realistic simulations that provide ECGs comparable to those recorded in clinical practice (Lopez-Perez et al., 2015). Otherwise, the training dataset could represent only a subset of the population and have problems generalizing to other datasets and patients. We are aware that having a single torso geometry, where all the personalized ventricular anatomies are registered could also be a limitation, since it has been reported that changes in the orientation of the heart or disposition of pericardial fat could have important effects in the ECG (Bradley et al., 2000; Gyawali et al., 2020). In our models, we have not considered the inclusion of a personalized Purkinje system, which could interact with the electrical sequence of activation (Sebastian et al., 2011; Cárdenes et al., 2015).

In addition, although we include variability in our simulations (different electrode location, SOO or digital twin anatomy), simulated data still is highly dependent on the initial conditions of the model. Increasing the number of the simulations, and varying additional parameters (new torso geometry, SOOs, different ectopic coupling interval, conduction velocity or heart rate) could reduce the bias that the simulated data may present. The use of more anatomies could help to cover a wider range of anatomical variability. In this study we used 16 patient-specific anatomies that presented considerable differences in shape and volume, but including a greater inter-subject variability could also improve the simulated ECG data. However, the computational time necessary to build or extend the simulated database can increase considerably.

Finally, we have not explored the classification of the SOO in the nine sublocations (e.g., LCC, RFW or AMC). The available datasets did not produced enough well-labeled data, and some of these

sublocations were underrepresented (e.g., LCC-RCC commissure, AMC). This same limitation was present in other works that used similar datasets (Zheng et al., 2021). Richer clinical data for testing the ML models, together with more accessible OTVA datasets, will help in the prediction of the SOO with more accuracy.

5 Conclusion

We have shown a computational approach to predict the SOO of idiopathic ventricular tachycardia originated in the ventricular outflow tract. The method, that relies in biophysical simulation and machine learning techniques, is able to differentiate between LV or RV origin of the ectopic beat with an accuracy of 0.86 in a clinical database of 334 patients, and 0.84 in a second clinical database of 31 patients.

Since all the simulated training set was generated offline, the presented methodology could be transferred to a clinical environment, avoiding the need of time consuming tasks such as building computational models of the heart and performing electrophysiology simulations. Nevertheless, the simulated signals (DS-2496, DS-7488) achieved high performance in the test sets (DS-344 and DS-31), demonstrating the viability to produce good classification models for real data. Moreover, the methodology is not dependent on the expertise of the electrophysiologist, and it is consistent between cases, which could provide an additional tool to electrophysiologist to plan RFA interventions of this type of tachycardia. Future works will focus on improving the accurate determination of the exact SOO of the tachycardia within the ventricles, especially in the outflow tract sublocations.

Data availability statement

The raw data supporting the conclusion of this article will be made available by the authors, without undue reservation.

Author contributions

All authors have made substantial contributions to this study. Conceptualization: RD, OC, ML, and RS.; methodology: RD, ML, GJ-P, OC, and RS; software: RD, GJ-P, and ML; validation: RD, ML, DP, OC, and RS; resources: LM, AB, DP, OC, and RS; writing—original draft preparation: RD, ML, GJ-P, OC, and RS; writing—review and editing: RD, ML, GJ-P, OC, and RS; funding acquisition: OC and RS. All authors have read and agreed to the published version of the manuscript. All authors have also approved the final version to be published while agreeing to be accountable for all aspects of the work in ensuring that questions related to the accuracy or integrity of any part of the work are appropriately investigated and resolved.

Funding

This work has been funded by Generalitat Valenciana Grant AICO/2021/318 (Consolidables 2021) and Grant PID2020-114291RB-I00 funded by MCIN/10.13039/501100011033 and by “ERDF A way of making Europe”.

Conflict of Interest

The authors declare that the research was conducted in the absence of any commercial or financial relationships that could be construed as a potential conflict of interest.

Publisher’s note

Supplementary material

The Supplementary Material for this article can be found online at: https://www.frontiersin.org/articles/10.3389/fphys.2022.909372/full#supplementary-material

References

Alawad, M., and Wang, L. (2019). Learning domain shift in simulated and clinical data: Localizing the origin of ventricular activation from 12-lead electrocardiograms. *IEEE Trans. Med. Imaging* 38, 1172–1184. doi:10.1109/TMI.2018.2880092

Anderson, R. D., Kumar, S., Parameswaran, R., Wong, G., Voskoboinik, A., Sugumar, H., et al. (2019). Differentiating right- and left-sided outflow tract ventricular arrhythmias: Classical ECG signatures and prediction algorithms. *Circ. Arrhythm. Electrophysiol.* 12, e007392. doi:10.1161/CIRCEP.119.007392

Attia, Z. I., Harmon, D. M., Behr, E. R., and Friedman, P. A. (2021). Application of artificial intelligence to the electrocardiogram. *Eur. Heart J.* 42, 4717–4730. doi:10.1093/eurheartj/ehab649

Bradley, C. P., Pullan, A. J., and Hunter, P. J. (2000). Effects of material properties and geometry on electrocardiographic forward simulations. *Ann. Biomed. Eng.* 28, 721–741. doi:10.1114/1.1289467

Cárdenes, R., Sebastian, R., Soto-Iglesias, D., Berruezo, A., and Camara, O. (2015). Estimation of purkinje trees from electro-anatomical mapping of the left ventricle using minimal cost geodesics. *Med. Image Anal.* 24, 52–62. doi:10.1016/j.media.2015.05.007

Cardone-Noott, L., Bueno-Orovio, A., Mincholé, A., Zemzemi, N., and Rodriguez, B. (2016). Human ventricular activation sequence and the simulation of the electrocardiographic QRS complex and its variability in healthy and

intraventricular block conditions. *Europace* 18, iv4–iv15. doi:10.1093/europace/euw346

Corral-Acero, J., Margara, F., Marciniak, M., Rodero, C., Loncaric, F., Feng, Y., et al. (2020). The 'digital twin'to enable the vision of precision cardiology. *Eur. Heart J.* 41, 4556–4564. doi:10.1093/eurheartj/ehaa159

Costabal, F. S., Matsuno, K., Yao, J., Perdikaris, P., and Kuhl, E. (2019). Machine learning in drug development: Characterizing the effect of 30 drugs on the qt interval using Gaussian process regression, sensitivity analysis, and uncertainty quantification. *Comput. Methods Appl. Mech. Eng.* 348, 313–333. doi:10.1016/j.cma.2019.01.033

Cristianini, N., and Shawe-Taylor, J. (2000). *An introduction to support vector machines and other kernel-based learning methods*. Cambridge University Press.

Doste, R., Sebastian, R., Gomez, J. F., Soto-Iglesias, D., Alcaine, A., Mont, L., et al. (2020). *In silico* pace-mapping: Prediction of left vs. right outflow tract origin in idiopathic ventricular arrhythmias with patient-specific electrophysiological simulations. *Europace* 22, 1419–1430. doi:10.1093/europace/euaa102

Doste, R., Soto-Iglesias, D., Bernardino, G., Alcaine, A., Sebastian, R., Giffard-Roisin, S., et al. (2019). A rule-based method to model myocardial fiber orientation in cardiac biventricular geometries with outflow tracts. *Int. J. Numer. Method. Biomed. Eng.* 35, e3185. doi:10.1002/cnm.3185

Ferrer, A., Sebastian, R., Sánchez-Quintana, D., Rodríguez, J. F., Godoy, E. J., Martínez, L., et al. (2015). Detailed anatomical and electrophysiological models of human atria and torso for the simulation of atrial activation. *Plos One* 10, e0141573. doi:10.1371/journal.pone.0141573

Ferrer-Albero, A., Godoy, E. J., Lozano, M., Martínez-Mateu, L., Atienza, F., Saiz, J., et al. (2017). Non-invasive localization of atrial ectopic beats by using simulated body surface p-wave integral maps. *PLoS One* 12, e0181263. doi:10.1371/journal.pone.0181263

Geurts, P., Ernst, D., and Wehenkel, L. (2006). Extremely randomized trees. *Mach. Learn.* 63, 3–42. doi:10.1007/s10994-006-6226-1

Gyawali, P. K., Horacek, B. M., Sapp, J. L., and Wang, L. (2020). Sequential factorized autoencoder for localizing the origin of ventricular activation from 12-lead electrocardiograms. *IEEE Trans. Biomed. Eng.* 67, 1505–1516. doi:10.1109/TBME.2019.2939138

Hayashi, T., Santangeli, P., Pathak, R. K., Muser, D., Liang, J. J., Castro, S. A., et al. (2017). Outcomes of catheter ablation of idiopathic outflow tract ventricular arrhythmias with an R wave pattern break in lead V2: A distinct clinical entity. *J. Cardiovasc. Electrophysiol.* 28, 504–514. doi:10.1111/jce.13183

Heidenreich, E. A., Ferrero, J. M., Doblaré, M., and Rodríguez, J. F. (2010). Adaptive macro finite elements for the numerical solution of monodomain equations in cardiac electrophysiology. *Ann. Biomed. Eng.* 38, 2331–2345. doi:10.1007/s10439-010-9997-2

Jimenez-Perez, G., Acosta, J., Alcaine, A., and Camara, O. (2021a). Generalizing electrocardiogram delineation: Training convolutional neural networks with synthetic data augmentation. *ARXIV*. doi:10.48550/arXiv.2111.12996

Jimenez-Perez, G., Alcaine, A., and Camara, O. (2021b). Delineation of the electrocardiogram with a mixed-quality-annotations dataset using convolutional neural networks. *Sci. Rep.* 11, 863. doi:10.1038/s41598-020-79512-7

Kaypakli, O., Koca, H., Sahin, D. Y., Karataş, F., Ozbicer, S., Koç, M., et al. (2018). S-R difference in V1-V2 is a novel criterion for differentiating the left from right ventricular outflow tract arrhythmias. *Ann. Noninvasive Electrocardiol.* 23, e12516. doi:10.1111/anec.12516

Khamzin, S., Dokuchaev, A., Bazhutina, A., Chumarnaya, T., Zubarev, S., Lyubimtseva, T., et al. (2021). Machine learning prediction of cardiac resynchronisation therapy response from combination of clinical and model-driven data. *Front. Physiol.* 12, 753282. doi:10.3389/fphys.2021.753282

Lai, C., Zhou, S., and Trayanova, N. A. (2021). Optimal ecg-lead selection increases generalizability of deep learning on ecg abnormality classification. *Philos. Trans. A Math. Phys. Eng. Sci.* 379, 20200258. doi:10.1098/rsta.2020.0258

Lerman, B. B. (2015). Mechanism, diagnosis, and treatment of outflow tract tachycardia. *Nat. Rev. Cardiol.* 12, 597–608. doi:10.1038/nrcardio.2015.121

Li, H., An, Z., Zuo, S., Zhu, W., Cao, L., Mu, Y., et al. (2022). Classification of electrocardiogram signals with waveform morphological analysis and support vector machines. *Med. Biol. Eng. Comput.* 60, 109–119. doi:10.1007/s11517-021-02461-4

Lopez-Perez, A., Sebastian, R., and Ferrero, J. M. (2015). Three-dimensional cardiac computational modelling: Methods, features and applications. *Biomed. Eng. Online* 14, 35. doi:10.1186/s12938-015-0033-5

Lopez-Perez, A., Sebastian, R., Izquierdo, M., Ruiz, R., Bishop, M., Ferrero, J. M., et al. (2019). Personalized cardiac computational models: From clinical data to simulation of infarct-related ventricular tachycardia. *Front. Physiol.* 10, 580. doi:10.3389/FPHYS.2019.00580

Luongo, G., Azzolin, L., Schuler, S., Rivolta, M. W., Almeida, T. P., Martínez, J. P., et al. (2021). Machine learning enables noninvasive prediction of atrial fibrillation driver location and acute pulmonary vein ablation success using the 12-lead ECG. *Cardiovasc. Digit. Health J.* 2, 126–136. doi:10.1016/j.cvdhj.2021.03.002

Mariani, M. V., Piro, A., Della Rocca, D. G., Forleo, G. B., Pothineni, N. V., Romero, J., et al. (2021). Electrocardiographic criteria for differentiating left from right idiopathic outflow tract ventricular arrhythmias. *Arrhythm. Electrophysiol. Rev.* 10, 10–16. doi:10.15420/AER.2020.10

Maršánová, L., Ronzhina, M., Smíšek, R., Vítek, M., Němcová, A., Smital, L., et al. (2017). ECG features and methods for automatic classification of ventricular premature and ischemic heartbeats: A comprehensive experimental study. *Sci. Rep.* 7, 11239. doi:10.1038/s41598-017-10942-6

Martinez, J., Almeida, R., Olmos, S., Rocha, A., and Laguna, P. (2004). A wavelet-based ECG delineator: Evaluation on standard databases. *IEEE Trans. Biomed. Eng.* 51, 570–581. doi:10.1109/TBME.2003.821031

Minchole, A., AnaCamps, J., Lyon, A., and Rodriguez, B. (2019). Machine learning in the electrocardiogram. *J. Electrocardiol.* 57, S61–S64. doi:10.1016/j.jelectrocard.2019.08.008

Nagarajan, V. D., Lee, S.-L., Robertus, J.-L., Nienaber, C. A., Trayanova, N. A., Ernst, S., et al. (2021). Artificial intelligence in the diagnosis and management of arrhythmias. *Eur. Heart J.* 42, 3904–3916. doi:10.1093/eurheartj/ehab544

O'Hara, R. P., Binka, E., Prakosa, A., Zimmerman, S. L., Cartoski, M. J., Abraham, M. R., et al. (2022). Personalized computational heart models with t1-mapped fibrotic remodeling predict sudden death risk in patients with hypertrophic cardiomyopathy. *Elife* 11, e73325. doi:10.7554/eLife.73325

Prakosa, A., Arevalo, H. J., Deng, D., Boyle, P. M., Nikolov, P. P., Ashikaga, H., et al. (2018). Personalized virtual-heart technology for guiding the ablation of infarct-related ventricular tachycardia. *Nat. Biomed. Eng.* 2, 732–740. doi:10.1038/s41551-018-0282-2

Prifti, E., Fall, A., Davogustto, G., Pulini, A., Denjoy, I., Funck-Brentano, C., et al. (2021). Deep learning analysis of electrocardiogram for risk prediction of drug-induced arrhythmias and diagnosis of long qt syndrome. *Eur. Heart J.* 42, 3948–3961. doi:10.1093/eurheartj/ehab588

Romero, P., Lozano, M., Martínez-Gil, F., Serra, D., Sebastián, R., Lamata, P., et al. (2021). Clinically-driven virtual patient cohorts generation: An application to aorta. *Front. Physiol.* 12, 713118. doi:10.3389/fphys.2021.713118

Sebastian, R., Zimmerman, V., Romero, D., and Frangi, A. F. (2011). Construction of a computational anatomical model of the peripheral cardiac conduction system. *IEEE Trans. Biomed. Eng.* 58, 3479–3482. doi:10.1109/TBME.2011.2166553

Sirichand, S., Killu, A. M., Padmanabhan, D., Hodge, D. O., Chamberlain, A. M., Brady, P. A., et al. (2017). Incidence of idiopathic ventricular arrhythmias: A population-based study. *Circ. Arrhythm. Electrophysiol.* 10. doi:10.1161/CIRCEP.116.004662

Srivathsan, K., Lester, S. J., Appleton, C. P., Scott, L. R. P., and Munger, T. M. (2005). Ventricular tachycardia in the absence of structural heart disease. *Indian Pacing Electrophysiol. J.* 5, 106–121.

ten Tusscher, K., Noble, D., Noble, P. J., and Panfilov, A. V. (2004). A model for human ventricular tissue. *Am. J. Physiol. Heart Circ. Physiol.* 286, H1573–H1589. doi:10.1152/ajpheart.00794.2003

Welch, P. (1967). The use of fast fourier transform for the estimation of power spectra: A method based on time averaging over short, modified periodograms. *IEEE Trans. Audio Electroacoust.* 15, 70–73. doi:10.1109/TAU.1967.1161901

Yamada, T., McElderry, H. T., Doppalapudi, H., Okada, T., Murakami, Y., Yoshida, Y., et al. (2010). Idiopathic ventricular arrhythmias originating from the left ventricular summit anatomic concepts relevant to ablation. *Circ. Arrhythm. Electrophysiol.* 3, 616–623. doi:10.1161/CIRCEP.110.939744

Yang, T., Yu, L., Jin, Q., Wu, L., and He, B. (2017). Localization of origins of premature ventricular contraction by means of convolutional neural network from 12-lead ecg. *IEEE Trans. Biomed. Eng.* 9294, 1662–1671. doi:10.1109/TBME.2017.2756869

Zhang, H., Cisse, M., Dauphin, Y. N., and Lopez-Paz, D. (2018). "mixup: Beyond empirical risk minimization," in 6th International Conference on Learning Representations (Vancouver, Canada: ICLR 2018). doi:10.48550/arXiv.1710.09412

Zheng, J., Fu, G., Abudayyeh, I., Yacoub, M., Chang, A., Feaster, W. W., et al. (2021). A high-precision machine learning algorithm to classify left and right outflow tract ventricular tachycardia. *Front. Physiol.* 12, 641066. doi:10.3389/fphys.2021.641066

Zheng, J., Fu, G., Anderson, K., Chu, H., and Rakovski, C. (2020). A 12-lead ecg database to identify origins of idiopathic ventricular arrhythmia containing 334 patients. *Sci. Data* 7, 98–10. doi:10.1038/s41597-020-0440-8

frontiers | Frontiers in Physiology

TYPE Original Research
PUBLISHED 29 August 2022
DOI 10.3389/fphys.2022.908364

OPEN ACCESS

EDITED BY
Gernot Plank,
Medical University of Graz, Austria

REVIEWED BY
Mark Potse,
UMR5251 Institut de mathématiques de Bordeaux (IMB), France
Danila Potyagaylo,
EPIQure GmbH, Germany

*CORRESPONDENCE
Rubén Molero,
rumoal1@itaca.upv.es

†These authors have contributed equally to this work and share first authorship

SPECIALTY SECTION
This article was submitted to Cardiac Electrophysiology, a section of the journal Frontiers in Physiology

RECEIVED 30 March 2022
ACCEPTED 01 August 2022
PUBLISHED 29 August 2022

CITATION
Molero R, González-Ascaso A, Hernández-Romero I, Lundback-Mompó D, Climent AM and Guillem MS (2022), Effects of torso mesh density and electrode distribution on the accuracy of electrocardiographic imaging during atrial fibrillation. *Front. Physiol.* 13:908364. doi: 10.3389/fphys.2022.908364

Effects of torso mesh density and electrode distribution on the accuracy of electrocardiographic imaging during atrial fibrillation

Rubén Molero[1†*], Ana González-Ascaso[1†], Ismael Hernández-Romero[1], David Lundback-Mompó[2], Andreu M. Climent[1] and María S. Guillem[1]

[1]ITACA Institute, Universitat Politècnica de València, València, Spain, [2]Corify Care SL, Madrid, Spain

Introduction: Electrocardiographic Imaging (ECGI) allows computing the electrical activity in the heart non-invasively using geometrical information of the patient and multiple body surface signals. In the present study we investigate the influence of the number of nodes of geometrical meshes and recording ECG electrodes distribution to compute ECGI during atrial fibrillation (AF).

Methods: Torso meshes from 100 to 2000 nodes heterogeneously and homogeneously distributed were compared. Signals from nine AF realistic mathematical simulations were used for computing the ECGI. Results for each torso mesh were compared with the ECGI computed with a 4,000 nodes reference torso. In addition, real AF recordings from 25 AF patients were used to compute ECGI in torso meshes from 100 to 1,000 nodes. Results were compared with a reference torso of 2000 nodes. Torsos were remeshed either by reducing the number of nodes while maximizing the overall shape preservation and then assigning the location of the electrodes as the closest node in the new mesh or by forcing the remesher to place a node at each electrode location. Correlation coefficients, relative difference measurements and relative difference of dominant frequencies were computed to evaluate the impact on signal morphology of each torso mesh.

Results: For remeshed torsos where electrodes match with a geometrical node in the mesh, all mesh densities presented similar results. On the other hand, in torsos with electrodes assigned to closest nodes in remeshed geometries performance metrics were dependent on mesh densities, with correlation coefficients ranging from 0.53 $\pm$ 0.06 to 0.92 $\pm$ 0.04 in simulations or from 0.42 $\pm$ 0.38 to 0.89 $\pm$ 0.2 in patients. Dominant frequency relative errors showed the same trend with values from 1.14 $\pm$ 0.26 to 0.55 $\pm$ 0.21 Hz in simulations and from 0.91 $\pm$ 0.56 to 0.45 $\pm$ 0.41 Hz in patients.

Conclusion: The effect of mesh density in ECGI is minimal when the location of the electrode is preserved as a node in the mesh. Torso meshes constructed without imposing electrodes to constitute nodes in the torso geometry should contain at least 400 nodes homogeneously distributed so that a distance between nodes is below 4 cm.

KEYWORDS
electrocardiographic imaging, geometry, torso, atrial fibrillation, mesh density

1 Introduction

Electrocardiographic imaging (ECGI) is a non-invasive technique that can be used to estimate the electrical activity of the heart from surface electrocardiographic signals. ECGI offers multiple clinical applications, such as ablation guidance in atrial fibrillation (AF) patients. ECGI requires to use torso and heart geometries together with electrical recordings from the patient. Firstly, surface electrodes placed over the torso are used to record electrical signals. Additionally, the heart geometry is usually obtained from medical images (magnetic resonance imaging or axial computerized tomography) (Salinet et al., 2021), and the torso geometry can be derived from photogrammetry (Rodrigo et al., 2018), with latter reconstruction creating triangular or polygonal meshes (van der Graaf et al., 2016). Once these elements are acquired, the inverse problem can be solved and epicardial potentials are estimated, which can be used to compute dominant frequencies or rotor-related metrics (Rodrigo et al., 2017a).

The properties of the 3D torso geometry have been proven to affect the calculation of the ECGI. Accurate reconstructions (Messinger-Rapport and Rudy, 1990) of the anatomy of the patient's body and the use of real dimensions in the torso model (Jamison et al., 2011) show more precise results. Incorporation of inner organs into the geometry of the problem has not shown a major impact on the shape of ECGI potentials (Ramanathan and Rudy, 2001). However, additional geometrical effects should be carefully considered in order to achieve a sufficient resolution.

The objective of this study is to evaluate the repercussion of the number of nodes of the torso geometry mesh and their distribution on the resolution of the ECGI using both AF simulations and real recordings from AF patients. We hypothesized that there is an effect on the ECGI reconstruction quality related to the number of nodes on the torso mesh used independently of the number of ECG electrodes that record the signal. A careful analysis will allow us to establish a threshold to ensure good performance while keeping the computing time as low as possible. We studied two different remeshing situations based on the positioning of body surface electrodes. The first was maintaining the electrodes in the original position while remeshing the rest of the torso to quantify the effect of mesh density and distribution on the morphology of ECGI signals, and our second remeshing alternative was to remesh the whole torso surface to maximize resemblance between original and remeshed volumes, and then we reassign the electrode nodes as those with the smallest Euclidean distance between the original and remeshed torso geometries, in order to quantify the effect of electrode displacement as a consequence of remeshing. We compared the electrocardiographic signals (ECGI) using time metrics: the Pearson's correlation coefficient (CC), the relative difference measurement (RDM*) and errors in dominant frequency estimation. To obtain the ECGI potentials, we used real torso geometries from AF patients with different geometrical resolutions, 9 electrophysiological AF simulations, and 25 ECGI recordings from AF patients.

2 Materials and methods

To analyze the effect related with node variations of torso geometry on the ECGI, we first created the torso models with different numbers and distribution of nodes, then computed the respective inverse electrograms, and finally compared the results using time metrics (CC and RDM*) and dominant frequencies related maps and metrics.

2.1 Study population—Data acquisition

2.1.1 Simulation data

Cardiac electrophysiological simulations lasting for 10 s included in this study were created using the same cardiac geometry and different AF episodes. A realistic 3D model of the atrial anatomy composed of 284,578 nodes and 1,353,783 tetrahedrons was used for creating the simulations (Rodrigo et al., 2017b). Variation of ionic current parameters was introduced in $I_{k,ACH}$, I_{K1}, $I_{Na,}$ and ICaL to simulate electrical remodeling and allow the maintenance of atrial fibrillation. Fibrotic tissue was modeled by disconnecting a percentage of nodes between 20% and 60% and scar tissue by disconnecting 100% of nodes in the scar region. The system of differential equations was solved by using Runge–Kutta integration on a graphic processors unit (NVIDIA Tesla C2075 6G), (Rodrigo et al., 2017b). AF was induced by implementing an S1 S2 protocol, with the S2 stimulus applied at different locations in the atria, thus producing different AF patterns.

2.1.2 Patient data

The electrical recordings from 25 atrial fibrillation patients from Hospital Gregorio Marañón, Madrid, Spain (Ethics Committee Approval 475/14) described elsewhere (Rodrigo et al., 2020; Molero et al., 2021) were used. To record the signals 57 electrodes distributed on the torso of the patients were employed. The atrial geometries were also obtained from the same patients using Magnetic Resonance Imaging, and the 3D models were segmented through ITK-Snap (Yushkevich et al., 2006) and Autodesk Meshmixer (Schmidt and Singh, 2010). Furthermore, the torso models were obtained from

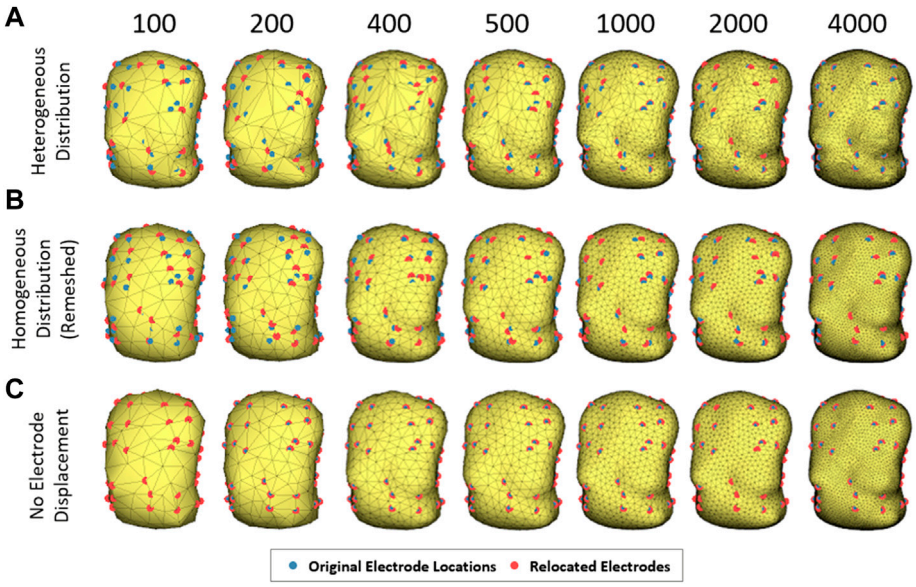

FIGURE 1
Example of torso models with different number of nodes and node distribution. The electrodes relocated appear in blue and the original locations in red. **(A)** illustrates torsos with irregular mesh distribution, **(B)** with homogeneous distribution and **(C)** torsos maintaining the electrodes in the original position.

photogrammetry, and 3D geometries consisting of triangular meshes were constructed (Remondino, 2004) and refined with Autodesk Meshmixer.

2.2 Data processing

2.2.1 Torso remeshing

In order to evaluate the effect of torso mesh density on the morphology of the electrograms after resolution of the inverse problem of electrocardiography, we constructed torso meshes with a reduced number of nodes departing from the finest torso meshes available. We used as reference the torso meshes constructed for each patient, constituted of at least 2000 nodes. The epicardial potentials computed for each of the electrophysiological models were placed in the same position as the original heart inside the thorax. In order to calculate body surface potentials for the computer model simulations, we chose 10 different patient meshes of 4,000 nodes. An inhomogeneous remeshing of torso geometries down to 100, 200, 400, 500, and 1,000 nodes for patients (plus a 2000 nodes mesh for cardiac simulations), maximizing shape preservation was performed with MATLAB built-in functions (see Figure 1A). In order to quantify the impact on ECGI resolution of the homogeneity of the distance of the nodes in the mesh, we also constructed meshes with a homogeneous distribution of nodes based on an iterative approach (Manu, 2022) (see Figure 1B). Properties of the different torso meshes used with simulations and patients are displayed in Figures 2, 3, respectively.

For solving the inverse problem of electrocardiography, electrodes have to be located in the torso mesh. We chose the node with the smallest Euclidean distance from each electrode to relocate electrodes on the mesh. In order to evaluate separately the effect of mesh density and electrode relocation, we also constructed downsampled meshes without electrode relocation. For imposing the electrode position in all the meshes, the closest face of the geometry to each electrode was triangulated again, and three new triangles were included joined by the original electrode position (see Figure 1C).

2.2.2 Processing of surface potentials and Electrocardiographic Imaging calculation

In mathematical models, the forward problem of the simulated electrograms was calculated using the boundary element method (BEM) (Pedrón-Torrecilla et al., 2016). Noise was added to the computed surface potentials to obtain a 20 dB signal to noise ratio emulating the noise present in real recordings. The baseline was subtracted, and a low pass filter of 40 Hz was applied. The electrical information related to the nodes representing the 57 electrodes was selected, and the inverse problem was calculated through the BEM, using zero-order Tikhonov regularization and L-curve optimization (Pedrón-Torrecilla et al., 2016).

Body surface signals obtained from each patient with surface electrodes were pre-processed by selecting 5 s and removing the

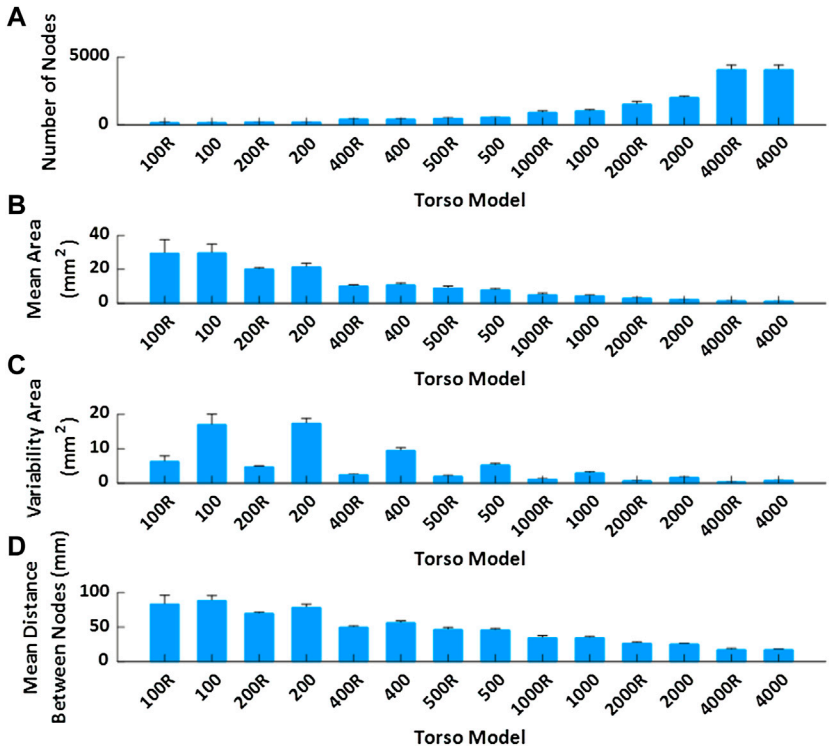

FIGURE 2
Mean value and standard deviation of torso model properties of the geometries used in the simulation study represented. **(A)**. Mean number of nodes depending on the model. **(B)**. Mean area of the faces. **(C)**. Variability of the area of the faces. **(D)**. Mean distance between nodes of the same triangle.

baseline. A 10th order Butterworth was used to band-pass filter between 2 and 45 Hz to eliminate the noise. The Principal Component Analysis (PCA) approach was performed electrode by electrode to cancel the ventricular activity (QRST segment), (Castells et al., 2005).

Once the recorded or simulated body surface signals were processed, the inverse computed electrograms were calculated through BEM using zero-order Tikhonov regularization and L-curve optimization (Pedrón-Torrecilla et al., 2016).

2.3 Quality of mesh evaluation metrics

To evaluate the effect of the mesh in the reconstruction of ECGI potentials, the similarity between ECGI signals obtained with finest and sparser torso meshes was evaluated.

Specifically, we used Pearson's correlation coefficient (CC) and the relative difference measurement (RDM*) (Meijs et al., 1989; Figuera et al., 2016). For both metrics, the temporal version was used (for each node, the CC and RDM* were computed using all the time instants, and the mean and standard deviation across nodes are then calculated).

$$\mathrm{RDM}^{*} = \sqrt{\sum_{k}\left(\frac{x_k}{\|x^2\|} - \frac{\hat{x}_k}{\|\hat{x}^2\|}\right)^2}$$

2.4 Frequency metrics

The dominant frequency (DF) of each node of the cardiac geometry was estimated after the calculation of ECGI using Welch periodogram (2-s Hamming window with a 25% overlap) (Rodrigo et al., 2017a). The absolute difference in DF for each atrial node between the reference and the other models was calculated for both AF simulations and AF patient studies (Figuera et al., 2016).

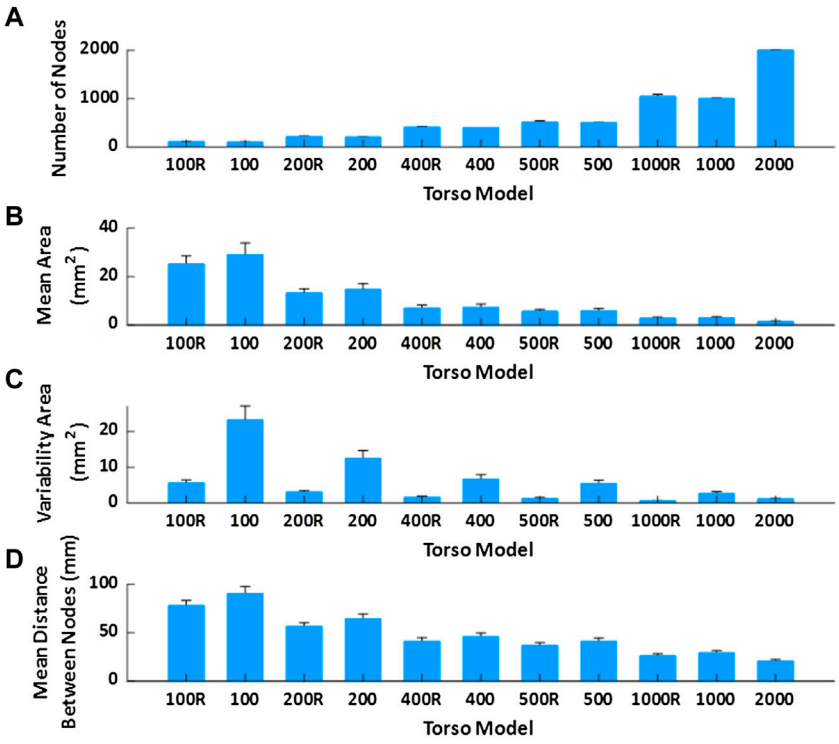

FIGURE 3
Mean value and standard deviation of torso model properties of the geometries used in the real patient's study. **(A)**. Mean number of nodes depending on the model. **(B)**. Mean area of the faces. **(C)**. Variability of the area of the faces. **(D)**. Mean distance between nodes of the same triangle.

3 Results

3.1 Impact of mesh density on Electrocardiographic Imaging reconstruction

Mesh density alone -without electrode relocation-had a limited impact on ECGI signals. In Figure 4A, reconstructed signals with different mesh densities for a sample epicardial node show only subtle differences. Average correlation coefficients remain above 0.96 even for torso meshes with just 100 nodes, and relative errors are below 0.3%, with the lowest CC values of 0.93, Figures 4B,C. The effect of the torso's node density in the dominant frequencies is depicted in Figure 4D. The observed absolute error decreases with the number of nodes of the mesh, and errors are stabilized below 0.2 Hz with torso meshes with at least 400 nodes.

The same analysis on real AF patient data is shown in Figure 5. Again, CCs were above 0.99 even for meshes with 100 nodes, relative errors were below 0.1 and errors in DF were below 0.2 Hz. CC values for low-density meshes presented very high values, even higher than those obtained for the simulated data. This was because when solving the inverse problem in patients, the optimal regularization parameter was higher than in the simulated cases ($\sim10^{-5}$ vs. $\sim10^{-8}$), likely because of the presence of spatial uncertainties in ECGI reconstruction and the presence of different sources of noise on the recorded signals. These larger values of regularization parameters in patients result in smoother ECGI solutions that make the ECGI signal estimation less dependent on mesh resolution.

In addition to the effect of the number of nodes, the type of remeshing affected the quality of the ECGI signal. Results showed that homogenous meshes present lower values of CC and higher values of RDM* and DF errors compared to the heterogeneous distribution of the mesh, which could be attributed to a poorer shape preservation in the homogeneous meshes.

3.2 Impact of electrode relocation in low-density torso meshes on Electrocardiographic Imaging reconstruction

ECGI signals obtained from cardiac electrophysiological simulations and using different torso meshes where the electrode position was relocated to match a mesh node after remeshing present noticeable differences with the reference ECGI signals with the finest torso meshes without electrode

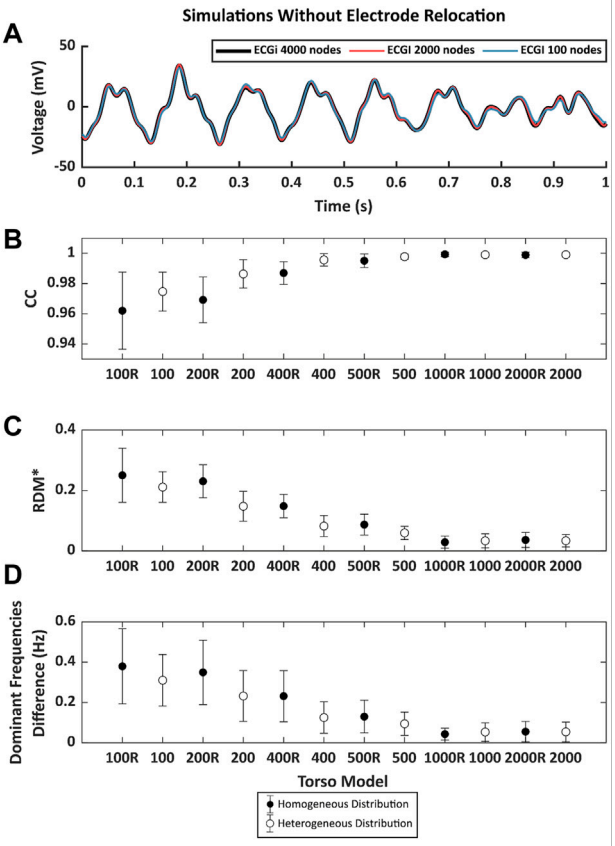

FIGURE 4
(A). Example of 1 s of inverse computed electrograms obtained with different torso models and the same simulation signals for torsos without electrode relocation. Signal in black was obtained with the reference 4000-node torso, red and blue signals correspond to the ones obtained with torsos of 2000 and 100 nodes respectively. **(B)**. Pearson's correlation coefficient (CC), **(C)**. relative measurement (RDM*) and **(D)**. mean absolute difference between the reference dominant frequencies (DF) between torso models and from 100 to 2000 nodes. Points in black represent the mean value of the metrics torsos in which the distribution of the nodes is homogeneous and white points represent the torso with nodes heterogeneously placed. Whiskers represent the standard deviation.

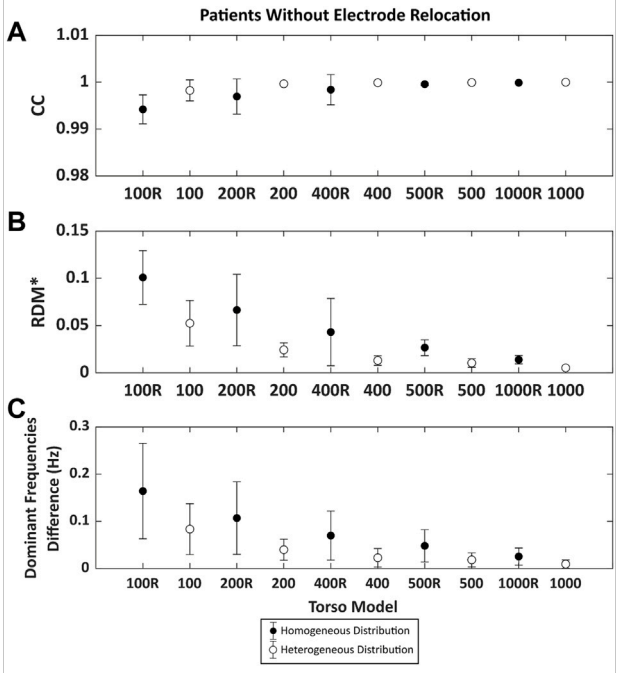

FIGURE 5
Time metrics obtained comparing the inverse computed electrograms 25 atrial fibrillation patients of the reference and the signals obtained with different torso models without electrode relocation. Points in black represent the torsos in which the distribution of the nodes is homogeneous and white points represent the torso with nodes heterogeneously placed. **(A)**. Pearson's correlation coefficient (CC) and **(B)**. Relative difference measurement (RDM*). **(C)**. Mean absolute difference between the reference dominant frequencies (DF) between torso models and from 100 to 1,000 nodes.

relocation (Figure 6). First, an example of simulated ECGI signals of the reference torso with coarser meshes is presented in panel Figure 6A. Although the overall shape of the inversely computed electrograms is preserved for lower mesh densities, some impact of shape morphology can be observed, especially for the sparser meshes (blue line). A global comparison between the signals measured through time-metrics is represented in Figures 6B,C for all the models. The CC and the RDM* show a strong dependency on torso mesh density. A progressive increase is shown for the CC as the number of nodes increases, from 0.53 ± 0.06 for the 100 mesh to 0.92 ± 0.04 for the 2000 node mesh. Besides, the RDM* decreases when the torso is composed with a higher number of vertices from 0.96 ± 0.07 for the 100 mesh down to 0.38 ± 0.09 for the 2000 node mesh. Regular meshes do show better correlation coefficients and RDM* values than irregular meshes with a similar number of nodes, especially for the meshes with a lower number of nodes. For the finer meshes and, therefore, smaller areas of the geometrical faces, slightly better results are observed for the irregular meshes.

Figure 6D shows the differences in DF between the ECGI signals calculated with the torso meshes with 4,000 nodes homogeneously distributed and the remaining models. The largest difference can be observed for the torso with 100 nodes (1.14 ± 0.26 Hz), and it decreases as the number of nodes increases. Differences in the frequencies show higher values when a homogeneous distribution of the electrodes is presented for models with fewer than 1,000 nodes. However, when the number of nodes was 1,000 or higher, these differences were higher in the case of the homogeneous models.

The results of the CC and RDM* of the ECGI computed with each torso mesh from real AF patient data are presented in Figure 7. As observed with the computer simulations, the CC values increased, and the RDM* decreased with the number of

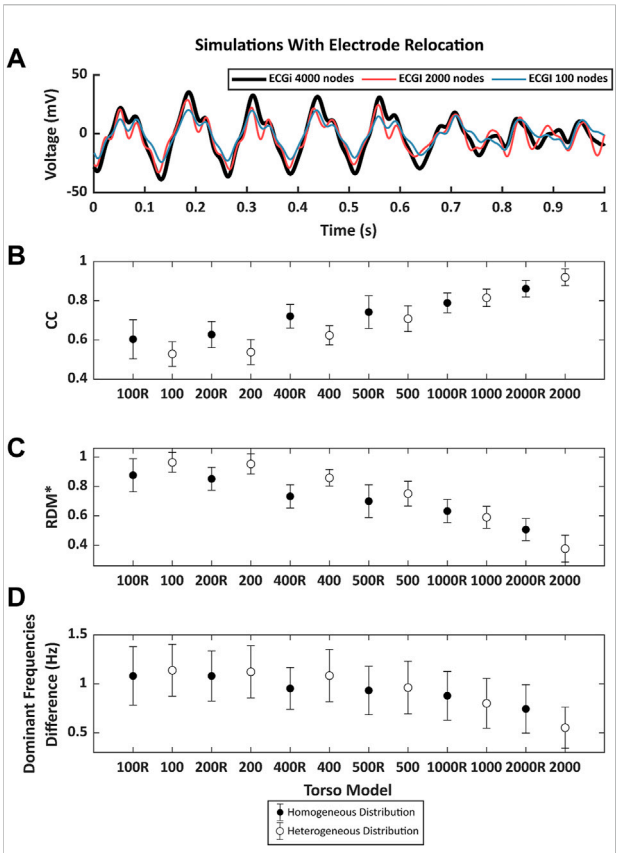

FIGURE 6
(A). Example of 1 s of inverse computed electrograms obtained with different torso models and the same simulation signals for torsos with the node of the electrode displaced by the remeshing. Signal in black was obtained with the reference 4000-node torso, red and blue signals correspond to the ones obtained with torsos of 2000 and 100 nodes respectively. **(B)**. Pearson's correlation coefficient (CC), **(C)**. relative measurement (RDM*) and **(D)**. mean absolute difference between the reference DF between torso models and from 100 to 2000 nodes. Points in black represent the mean value of the metrics torsos in which the distribution of the nodes is homogeneous and white points represent the torso with nodes heterogeneously placed. Whiskers represent the standard deviation.

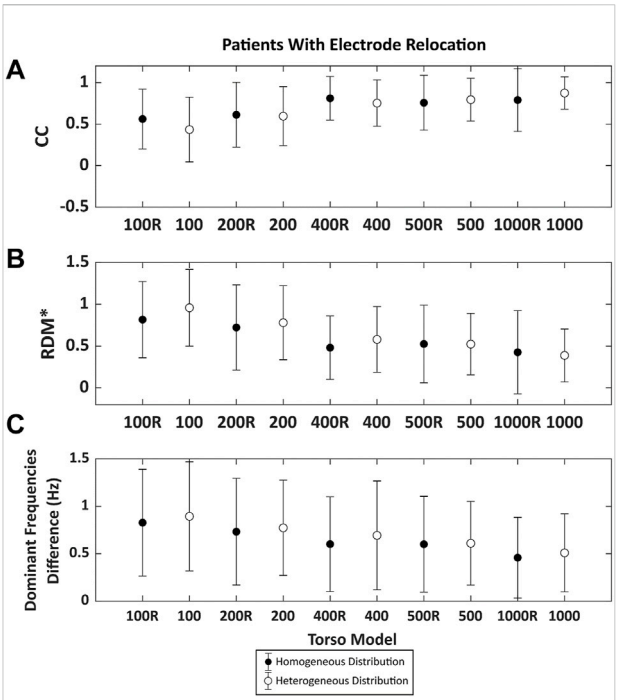

FIGURE 7
Time metrics obtained comparing the inverse computed electrograms 25 atrial fibrillation patients of the reference and the signals obtained with different torso models with the node of the electrode displaced by the remeshing. Points in black represent the torsos in which the distribution of the nodes is homogeneous and white points represent the torso with nodes heterogeneously placed. **(A)**. Pearson's correlation coefficient (CC) and **(B)**. Relative difference measurement (RDM*). **(C)**. Mean absolute difference between the reference DF between torso models and from 100 to 1,000 nodes.

nodes. Even though the trend is the same as presented in Figure 6, differences are more prominent using real AF signals from patients as compared to simulation data. The correlation coefficient ranged from 0.42 ± 0.38 using the 100 nodes torso and up to 0.87 ± 0.2 with the 1,000 mesh. The RDM* decreases from 0.98 ± 0.45 (100 nodes) to 0.40 ± 0.33 (1000R). Although the results show a more marked effect of the remeshing in real AF signals, both CCs and RDM* values showed a stabilization for torsos above 400 nodes, as in Figure 6.

The calculation of differences in dominant frequencies is shown in Figure 7C. The results presented the same trend as the findings for simulations, and the difference in DF decreases with increasing number of nodes. The largest difference is found for the torso with 100 nodes (0.91 ± 0.56 Hz), while the lowest difference is obtained using the 1000-node torso (0.45 ± 0.41 Hz). In this case we could observe that differences in DFs were lower for the homogeneous torso meshes than their inhomogenous counterparts. DF maps for a sample patient are shown in Figure 8. As the number of vertices increased, the maps looked more similar to the one obtained with the reference torso mesh (2000 nodes). Torso meshes constituted by 400 nodes or less didn't allow to determine the site with the highest DF, present in the right atrium. In addition, in torso meshes with nodes from 400 to 1,000, the location and extension of the highest dominant frequency area are more similar to the reference ECGI 2000-nodes torso.

4 Discussion

In this study, we explored the effect of torso mesh density and homogeneity on ECGI signals for atrial fibrillation simulations and real signals. Firstly, we studied the effect of the number of

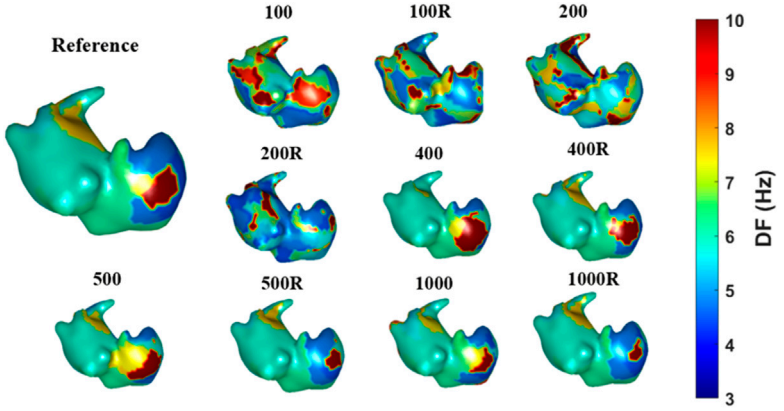

FIGURE 8
Dominant frequency maps obtained with different torso models for one real patient case.

nodes on torso meshes with imposed nodes matching with the location of the electrodes so that they don't need to be relocated. For both simulations and real signals, the number of nodes had little effect in the ECGI solution, especially for torsos with more of 400 nodes, where the trend in the studied metrics was stabilized. This suggests that torso meshes built upon the restriction of including the electrodes as nodes in the torso mesh are reliable even for very low densities. Furthermore, we observed that irregular meshes presented better results in terms of metrics compared to regular meshes for finer geometries, likely because of a better shape preservation.

Additionally, we explored the effect of node distribution and density, considering that the remeshing affects the position of the nodes that corresponded to electrodes. This analysis is relevant in the context of building first a torso mesh and later assigning the nodes corresponding to recording electrodes in a second step. Under these constraints, the effect of torso density is no longer negligible, and CC can decrease down to 0.5 for meshes with 100 nodes in simulations when there are no further spatial uncertainties and noise is limited to 20 dB SNR. The impact of mesh density on real patient data, when different sources of uncertainty are present, is less relevant because correlations are lower than in the computer simulations even for torso meshes with 1,000 nodes. In either case, correlation coefficients are affected, and decrease from 0.87 ± 0.2 for 1,000 node meshes down to 0.42 ± 0.38.

The effect of the node density of the meshes of the torsos has not been widely studied. Nevertheless, an accurate torso geometry has been reported as necessary to obtain precise inverse electrograms (Messinger-Rapport and Rudy, 1990). Our study uses torso models obtained with photogrammetry, which presented realistic results but not as precise as those obtained with medical imaging techniques, which were reported to be very important for correct inverse results (Svehlikova et al., 2012). Previous studies addressed that as long as geometrical parameters are captured with local details, the significant impact on the inverse electrogram is minimal (Wang et al., 2010), which is in accordance with the presented results, especially with a larger number of nodes. Likewise, torso reshaping and remeshing with a different number of nodes affected the quality of the signals, with 400 nodes being the minimum necessary to obtain a reliable result. Torso reshaping and smoothing the geometry have been reported to produce less accurate results when computed inverse electrograms (Lenkova et al., 2012) were compared to real ones. Nevertheless, we demonstrated that a homogeneous distribution of the nodes improved the inverse solution for meshes of less than 1,000 nodes independently of the type of signal used (real or simulated) when the remeshing forced a relocation of the electrodes. Heterogenous distribution of the nodes improved the results compared to the homogeneous one for geometries of more than 1,000 nodes and torsos with the electrodes matching a node position. However, when number of nodes increased, the differences between the distribution of the nodes decrease, and we cannot ensure that homogeneous meshes are worse for higher number of nodes, most likely because electrode relocation is less relevant in homogenous torso meshes since the distance between the actual location of the electrode and its location in the relocated torso mesh is larger in heterogenous meshes than in their homogeneous counterparts.

The minimum number of electrodes for computing ECGI with AF signals needed has been studied previously, with 23 the minimum number for an accurate reconstruction, similar to a 12-lead ECG (Guillem et al., 2009). Although the number of electrodes remains critical for a proper inverse reconstruction, in this study, we used a reliable amount according to the literature. Notwithstanding, increasing the number may alleviate the misplacement effect and could be needed for a correct reconstruction of reliable torso meshes.

The position and displacement of the electrodes remain important, as shown in the results and described by van der Graaf et al., 2016. Nevertheless, some studies provided results that the optimal position for placing the electrodes is not unique, which matches the study (Lux et al., 1978). The possibility of a range of appropriate electrode positions allows the opportunity of having reliable ECGI reconstructions with different torso meshes and electrodes displacement as in the presented study. The remeshing influenced electrode location, but we could establish the maximum displacement tolerated of the electrodes as 2cm, the mean displacement of 400-nodes torsos, which is in accordance with what has been described *in vivo* studies previously (Cluitmans and Volders, 2017). This distance gives margin to consider as a good reconstruction of the location of the electrodes using photogrammetry. Furthermore, slightly displaced electrodes would not affect the results drastically. Despite that, results demonstrated that 400 nodes -or mean distance between nodes below 4 cm-is a good trade-off for torso geometry reconstruction; geometries with a higher number of nodes would alleviate electrode misplacement (Huiskamp and Van Oosterom, 1989).

4.1 Limitations

In this study, we compared real AF signals with ECGI reconstructed with a higher number of nodes in the mesh as a reference and with no intracardiac data. We considered a higher number of nodes models as a reference assuming that it will provide a better reconstruction. For this purpose, data from AF simulations were used, being the conclusions with simulations and real data in agreement.

For the used forward model, inner organs were not included. Our model may be simplistic, and for that reason, the observed results with relocated electrodes may be better in simulations than in patient analysis. Nevertheless, although the incorporation of inner organs has not shown a major impact on the shape of ECGI potentials (Ramanathan and Rudy, 2001), simulated body surface potentials are indeed affected by these torso inhomogeneities that we have not considered in the present study. Additionally, the lack of anisotropy of the forward model may influence our results because although it may not affect the ECGI resolution significantly, potential distributions that are more complex due to the anisotropy will complicate the resolution of the inverse model (Colli-Franzone et al., 1982; Hren et al., 1998; Potse et al., 2009). Furthermore, it should be noted that the presented results are not relevant to mesh-less solutions due to the influence of the BEM on the presented results. For simulations, the results for each torso geometry were compared with a reference ECGI of a 4000-nodes torso and not with the original electrogram due to the low similarity at the high-frequencies for the intrinsic smoothing of the ECGI. Nevertheless, this does not imply that we could define the effect of the quality of the mesh on the inverse solution. Finally, in the present study we have omitted the quantification of the impact of the epicardial mesh on the signals estimated by ECGI, which should be explored in future studies.

5 Conclusion

The present study shows that the effect of mesh density on ECGI signals has little effect when the original electrode position is respected, especially for geometries with more than 400 nodes. Nevertheless, if maintaining the original position of the electrode is not possible, a mesh of at least 400 nodes is recommended for solving the inverse problem of electrocardiography in the context of atrial fibrillation signals in order to achieve reliable results. Furthermore, a homogeneous distribution of the nodes showed to be convenient for computing the ECGI with a distance separation of nodes under 4 cm. A displacement of the nodes corresponding to the position of the electrodes higher than 2 cm should be avoided.

Data availability statement

The original contributions presented in the study are included in the article/supplementary material, further inquiries can be directed to the corresponding author.

Ethics statement

The studies involving human participants were reviewed and approved by Hospital Gregorio Marañón, Madrid, Spain (Ethics Committee Approval 475/14). The patients/participants provided their written informed consent to participate in this study.

Author contributions

RM and AG-A contributed to the experimentation, design of the figures and text. DL-M contributed to the design of the experiments. MG contributed to the design of the experiments and text. IH-R and AC contributed to the final manuscript.

Funding

This work was supported by: Instituto de Salud Carlos III, and Ministerio de Ciencia e Innovación (supported by FEDER Fondo Europeo de Desarrollo Regional PI17/01106, PEJ2018-003617 and RYC2018-024346-I), EIT Health (Activity code 220385, EIT Health is supported by EIT, a body of the

European Union), Generalitat Valenciana Conselleria d'Educació, Investigació, Cultura i Esport (ACIF/2020/265) and Spanish Agencia Estatal de Investigación (AEI), part of the Ministerio de Ciencia e Innovación, reference PID2020-119364RB-I00.

Conflict of interest

MG, IH-R, and AC are co-founders and shareholders of Corify Care SL. Author DL-M was employed by the company Corify Care SL.

The remaining authors declare that the research was conducted in the absence of any commercial or financial relationships that could be construed as a potential conflict of interest.

Publisher's note

All claims expressed in this article are solely those of the authors and do not necessarily represent those of their affiliated organizations, or those of the publisher, the editors and the reviewers. Any product that may be evaluated in this article, or claim that may be made by its manufacturer, is not guaranteed or endorsed by the publisher.

References

Castells, F., Mora, C., Rieta, J. J., Moratal-Pérez, D., and Millet, J. (2005). Estimation of atrial fibrillatory wave from single-lead atrial fibrillation electrocardiograms using principal component analysis concepts. *Med. Biol. Eng. Comput.* 43, 557–560. doi:10.1007/BF02351028

Cluitmans, M. J. M., and Volders, P. G. A. (2017). Influence of body-surface geometry accuracy on noninvasive reconstruction of electrical activation and recovery in electrocardiographic imaging. *Comput. Cardiol.* 44, 1–4. doi:10.22489/CinC.2017.243-189

Colli-Franzone, P., Guerri, L., Viganotti, C., Macchi, E., Baruffi, S., Spaggiari, S., et al. (1982). Potential fields generated by oblique dipole layers modeling excitation wavefronts in the anisotropic myocardium. Comparison with potential fields elicited by paced dog hearts in a volume conductor. *Circ. Res.* 51, 330–346. doi:10.1161/01.RES.51.3.330

Figuera, C., Suárez-Gutiérrez, V., Hernández-Romero, I., Rodrigo, M., Liberos, A., Atienza, F., et al. (2016). Regularization techniques for ECG imaging during atrial fibrillation: A computational study. *Front. Physiol.* 7, 466. doi:10.3389/fphys.2016.00466

Guillem, M. S., Bollmann, A., Climent, A. M., Husser, D., Millet-Roig, J., and Castells, F. (2009). How many leads are necessary for a reliable reconstruction of surface potentials during atrial fibrillation? *IEEE Trans. Inf. Technol. Biomed.* 13, 330–340. doi:10.1109/TITB.2008.2011894

Hren, R., Nenonen, J., and Horáček, B. M. (1998). Simulated epicardial potential maps during paced activation reflect myocardial fibrous structure. *Ann. Biomed. Eng.* 26, 1022–1035. doi:10.1114/1.73

Huiskamp, G., and Van Oosterom, A. (1989). Tailored versus realistic geometry in the inverse problem of electrocardiography. *IEEE Trans. Biomed. Eng.* 36, 827–835. doi:10.1109/10.30808

Jamison, C., Navarro, C., Turner, C., Shannon, J., Anderson, J., and Adgey, J. (2011). The inverse problem utilizing the boundary element method for a nonstandard female torso. *IEEE Trans. Biomed. Eng.* 58, 876–883. doi:10.1109/TBME.2010.2093525

Lenkova, J., Svehlikova, J., and Tysler, M. (2012). Individualized model of torso surface for the inverse problem of electrocardiology. *J. Electrocardiol.* 45, 231–236. doi:10.1016/j.jelectrocard.2012.01.006

Lux, R. L., Smith, C. R., Wyatt, R. F., and Abildskov, J. A. (1978). Limited lead selection for estimation of body surface potential maps in electrocardiography. *IEEE Trans. Biomed. Eng.* 25, 270–276. doi:10.1109/TBME.1978.326332

Manu (2022). Patch remesher. Available at: https://uk.mathworks.com/matlabcentral/fileexchange/49691-patch-remesher. MATLAB Central File Exchange. (Accessed April 13, 2021).

Meijs, J. W. H., Weier, O. W., Peters, M. J., Van Oosterom, A., and vAn Oosterom, A. (1989). On the numerical accuracy of the boundary element method. *IEEE Trans. Biomed. Eng.* 36, 1038–1049. doi:10.1109/10.40805

Messinger-Rapport, B. J., and Rudy, Y. (1990). Noninvasive recovery of epicardial potentials in a realistic heart-torso geometry. Normal sinus rhythm. *Circ. Res.* 66, 1023–1039. doi:10.1161/01.RES.66.4.1023

Molero, R., Torro, J. M. S., Alzamora, N. M., Climent, A. M., and Guillem, M. S. (2021). Higher reproducibility of phase derived metrics from electrocardiographic imaging during atrial fibrillation in patients remaining in sinus rhythm after pulmonary vein isolation. *Comput. Biol. Med.* 139, 104934. doi:10.1016/J.COMPBIOMED.2021.104934

Pedrón-Torrecilla, J., Rodrigo, M., Climent, A. M., Liberos, A., Pérez-David, E., Bermejo, J., et al. (2016). Noninvasive estimation of epicardial dominant high-frequency regions during atrial fibrillation. *J. Cardiovasc. Electrophysiol.* 27, 435–442. doi:10.1111/jce.12931

Potse, M., Dubé, B., and Vinet, A. (2009). Cardiac anisotropy in boundary-element models for the electrocardiogram. *Med. Biol. Eng. Comput.* 47, 719–729. doi:10.1007/s11517-009-0472-x

Ramanathan, C., and Rudy, Y. (2001). Electrocardiographic imaging: II. Effect of torso inhomogeneities on noninvasive reconstruction of epicardial potentials, electrograms, and isochrones. *J. Cardiovasc. Electrophysiol.* 12, 241–252. doi:10.1046/j.1540-8167.2001.00241.x

Remondino, F. (2004). 3-D reconstruction of static human body shape from image sequence. *Comput. Vis. Image Underst.* 93, 65–85. doi:10.1016/j.cviu.2003.08.006

Rodrigo, M., Climent, A. M., Hernández-Romero, I., Liberos, A., Baykaner, T., Rogers, A. J., et al. (2020). Non-invasive assessment of complexity of atrial fibrillation: Correlation with contact mapping and impact of ablation. *Circ. Arrhythm. Electrophysiol.* 13, e007700. doi:10.1161/CIRCEP.119.007700

Rodrigo, M., Climent, A. M., Liberos, A., Fernández-Avilés, F., Berenfeld, O., Atienza, F., et al. (2017a). Highest dominant frequency and rotor positions are robust markers of driver location during noninvasive mapping of atrial fibrillation: A computational study. *Heart Rhythm* 14, 1224–1233. doi:10.1016/j.hrthm.2017.04.017

Rodrigo, M., Climent, A. M., Liberos, A., Fernández-Avilés, F., Berenfeld, O., Atienza, F., et al. (2017b). Technical considerations on phase mapping for identification of atrial reentrant activity in direct-And inverse-computed electrograms. *Circ. Arrhythm. Electrophysiol.* 10, e005008. doi:10.1161/CIRCEP.117.005008

Rodrigo, M., Guillem, M. S., Climent, A. M., Liberos, A., Hernández-Romero, I., Arenal, Á., et al. (2018). Solving inaccuracies in anatomical models for electrocardiographic inverse problem resolution by maximizing reconstruction quality. *IEEE Trans. Med. Imaging* 37, 733–740. doi:10.1109/TMI.2017.2707413

Salinet, J., Molero, R., Schlindwein, F. S., Karel, J., Rodrigo, M., Rojo-Álvarez, J. L., et al. (2021). Electrocardiographic imaging for atrial fibrillation: A perspective from computer models and animal experiments to clinical value. *Front. Physiol.* 12, 653013. doi:10.3389/fphys.2021.653013

Schmidt, R., and Singh, K. (2010). "Meshmixer: an interface for rapid mesh composition," in ACM SIGGRAPH 2010 Talks. SIGGRAPH '10. doi:10.1145/1837026.1837034

Svehlikova, J., Lenkova, J., Turzova, M., Tysler, M., Kania, M., and Maniewski, R. (2012). Influence of individual torso geometry on inverse solution to 2 dipoles. *J. Electrocardiol.* 45, 7–12. doi:10.1016/j.jelectrocard.2011.07.012

van der Graaf, A. W. M., Bhagirath, P., de Hooge, J., de Groot, N. M. S., and Götte, M. J. W. (2016). A priori model independent inverse potential mapping: the impact of electrode positioning. *Clin. Res. Cardiol.* 105, 79–88. doi:10.1007/s00392-015-0891-7

Wang, L., Wong, K. C. L., Zhang, H., Liu, H., and Shi, P. (2010). How much geometrical detail do we need in cardiac electrophysiological imaging? A generic heart-torso representation for fast subject-specific customization. *Stat. Atlases Comput. Models Heart* 6364, 232–241. doi:10.1007/978-3-642-15835-3_24

Yushkevich, P. A., Zhang, H., and Gee, J. C. (2006). Continuous medial representation for anatomical structures. *IEEE Trans. Med. Imaging* 25, 1547–1564. doi:10.1109/TMI.2006.884634

frontiers | Frontiers in Physiology

TYPE Original Research
PUBLISHED 21 September 2022
DOI 10.3389/fphys.2022.939240

OPEN ACCESS

EDITED BY
Richard David Walton,
Université de Bordeaux, France

REVIEWED BY
Elias Karabelas,
University of Graz, Austria
Sing-Chien Yap,
Erasmus Medical Center, Netherlands
Uyen Chau Nguyen,
Maastricht University Medical Centre, Netherlands

*CORRESPONDENCE
Jacob Melgaard,
jm@hst.aau.dk

SPECIALTY SECTION
This article was submitted to Cardiac Electrophysiology, a section of the journal Frontiers in Physiology

RECEIVED 08 May 2022
ACCEPTED 29 August 2022
PUBLISHED 21 September 2022

CITATION
Melgaard J, van Dam PM, Sommer A, Fruelund P, Nielsen JC, Riahi S and Graff C (2022), Non-invasive estimation of QLV from the standard 12-lead ECG in patients with left bundle branch block. *Front. Physiol.* 13:939240. doi: 10.3389/fphys.2022.939240

Non-invasive estimation of QLV from the standard 12-lead ECG in patients with left bundle branch block

Jacob Melgaard[1]*, Peter M. van Dam[2,3], Anders Sommer[4], Patricia Fruelund[4], Jens Cosedis Nielsen[5], Sam Riahi[4] and Claus Graff[1]

[1]CardioTech Research Group, Department of Health Science and Technology, Faculty of Medicine, Aalborg University, Aalborg, Denmark, [2]Department of Cardiology, University Medical Center Utrecht, Utrecht, Netherlands, [3]Peacs BV, Nieuwerbrug Aan Den Rijn, Netherlands, [4]Department of Cardiology, Aalborg University Hospital, Aalborg, Denmark, [5]Department of Cardiology, Aarhus University Hospital, Aarhus, Denmark

Background: Cardiac resynchronization therapy (CRT) is a treatment for patients with heart failure and electrical dyssynchrony, i.e., left bundle branch block (LBBB) ECG pattern. CRT resynchronizes ventricular contraction with a right ventricle (RV) and a left ventricle (LV) pacemaker lead. Positioning the LV lead in the latest electrically activated region (measured from Q wave onset in the ECG to LV sensing by the left pacemaker electrode [QLV]) is associated with favorable outcome. However, optimal LV lead placement is limited by coronary venous anatomy and the inability to measure QLV non-invasively before implantation. We propose a novel non-invasive method for estimating QLV in sinus-rhythm from the standard 12-lead ECG.

Methods: We obtained 12-lead ECG, LV electrograms and LV lead position in a standard LV 17-segment model from procedural recordings from 135 standard CRT recipients. QLV duration was measured post-operatively. Using a generic heart geometry and corresponding forward model for ECG computation, the electrical activation pattern of the heart was fitted to best match the 12-lead ECG in an iterative optimization procedure. This procedure initialized six activation sites associated with the His-Purkinje system. The initial timing of each site was based on the directions of the vectorcardiogram (VCG). Timing and position of the sites were then changed iteratively to improve the match between simulated and measured ECG. Noninvasive estimation of QLV was done by calculating the time difference between Q-onset on the computed ECG and the activation time corresponding to centroidal epicardial activation time of the segment where the LV electrode is positioned. The estimated QLV was compared to the measured QLV. Further, the distance between the actual LV position and the estimated LV position was computed from the generic ventricular model.

Results: On average there was no difference between QLV measured from procedural recordings and non-invasive estimation of QLV

(Δ_{QLV} = −3.0 ± 22.5 ms, p = 0.12). Median distance between actual LV pacing site and the estimated pacing site was 18.6 mm (IQR 17.3 mm).

Conclusion: Using the standard 12-lead ECG and a generic heart model it is possible to accurately estimate QLV. This method may potentially be used to support patient selection, optimize implant procedures, and to simulate optimal stimulation parameters prior to pacemaker implantation.

KEYWORDS

cardiac modeling, electrophysiology, ventricular activation, left bundle branch block, cardiac resynchronization therapy

Introduction

Cardiac resynchronization therapy (CRT) is a treatment option intended for patients with heart failure and reduced ejection fraction (HFrEF) and wide QRS on the electrocardiogram (ECG) (Glikson et al., 2021). The therapy was developed in the 1990s (Leclercq et al., 1998) and gained widespread use in the early 2000s. It is known that response varies greatly from patient to patient, with some improving much in both symptoms and survival, while others see no or even a negative response (Ypenburg et al., 2009). This has entailed great interest in finding markers for positive response. Initially, a stricter definition of the ECG criteria for left bundle branch block (LBBB) was proposed (Strauss et al., 2011), but still, about one third of these patients do not experience improvement in symptoms. Lack of response is most likely multifactorial, including patient selection, presence of large areas of myocardial scarring, implantation site of the left ventricular (LV) pacing lead, and timing of the stimulus impulse. Further, CRT has been shown to be beneficial in some subgroups of patients with HF and non-LBBB ECG, e.g. Right Bundle Branch Block (RBBB) or non-specific Intra-Ventricular Conduction Delay (IVCD), stressing that other factors than solely QRS duration or LBBB morphology determine outcome (Salden et al., 2020). Therefore, more knowledge about the activation sequence of the heart prior to CRT implantation may impact selection of the best CRT candidates and be valuable in planning CRT implantation.

Inverse ECG computer modeling is a means for relating ECG signals measured on the body surface to the cardiac electrical activation through equations governed by physical laws. Computing the ECG from a cardiac activation pattern is termed the forward problem, while going from ECG to myocardial activation is termed the inverse problem, or often simply electrocardiographic imaging (ECGi). The inverse problem in electrocardiography cannot be solved uniquely, and generally recordings from much more than the 10 electrodes used for measuring the 12-lead ECG are used when solving the inverse problem. Such recordings are termed body surface potential maps (BSPM). A computationally efficient way of solving the inverse problem is to define a fixed set of activation sites and minimize the error between simulated and measured ECGs or BSPMs (van Dam, Oostendorp, Linnenbank, et al., 2009). Given fixed activation sites, forward models have been able to accurately simulate LBBB ECGs (Galeotti et al., 2013; van Dam et al., 2014). Similarly, a fastest route algorithm optimizing the activation pattern with regard to the error between the simulated and measured 12-lead ECG, by moving and delaying a number of activation sites, was able to simulate the ECG accurately (Roudijk et al., 2021; Boonstra et al., 2022). Ideally, an individual geometric model should be made for each patient, to improve simulation accuracy. However, this requires CT or MRI scans of the patient, and time-consuming manual work to segment the heart, lungs and thorax. Hence, this is often not possible in standard clinical practice.

In this study we use an inverse ECG algorithm together with a generic geometric model and the standard 12-lead surface ECG to estimate the activation sequence of the heart for LBBB patients. Further, we estimate QLV from a given anatomical location and compare with procedurally measured QLV in patients with sinus rhythm and LBBB undergoing CRT implantation.

Methods

Study population

The study population consisted of 182 patients included in the Empiric Versus Imaging Guided Left Ventricular Lead Placement in Cardiac Resynchronization Therapy (ImagingCRT) study (Clinical Trials record NCT01323686); a double-blinded, randomized controlled trial. The design and results of the study have previously been published (Sommer et al., 2013, 2016). Briefly, the study investigated if imaging guided optimal left ventricular (LV) lead placement targeting the latest mechanically activated non-scared segment improved the response rate to cardiac resynchronization therapy (CRT) compared with standard LV lead placement. A 12-lead surface ECG and bipolar electrograms were recorded during the implantation procedure (CardioLab, GE Medical, Milwaukee, MN). At the time of collection, 31 records could not be retrieved

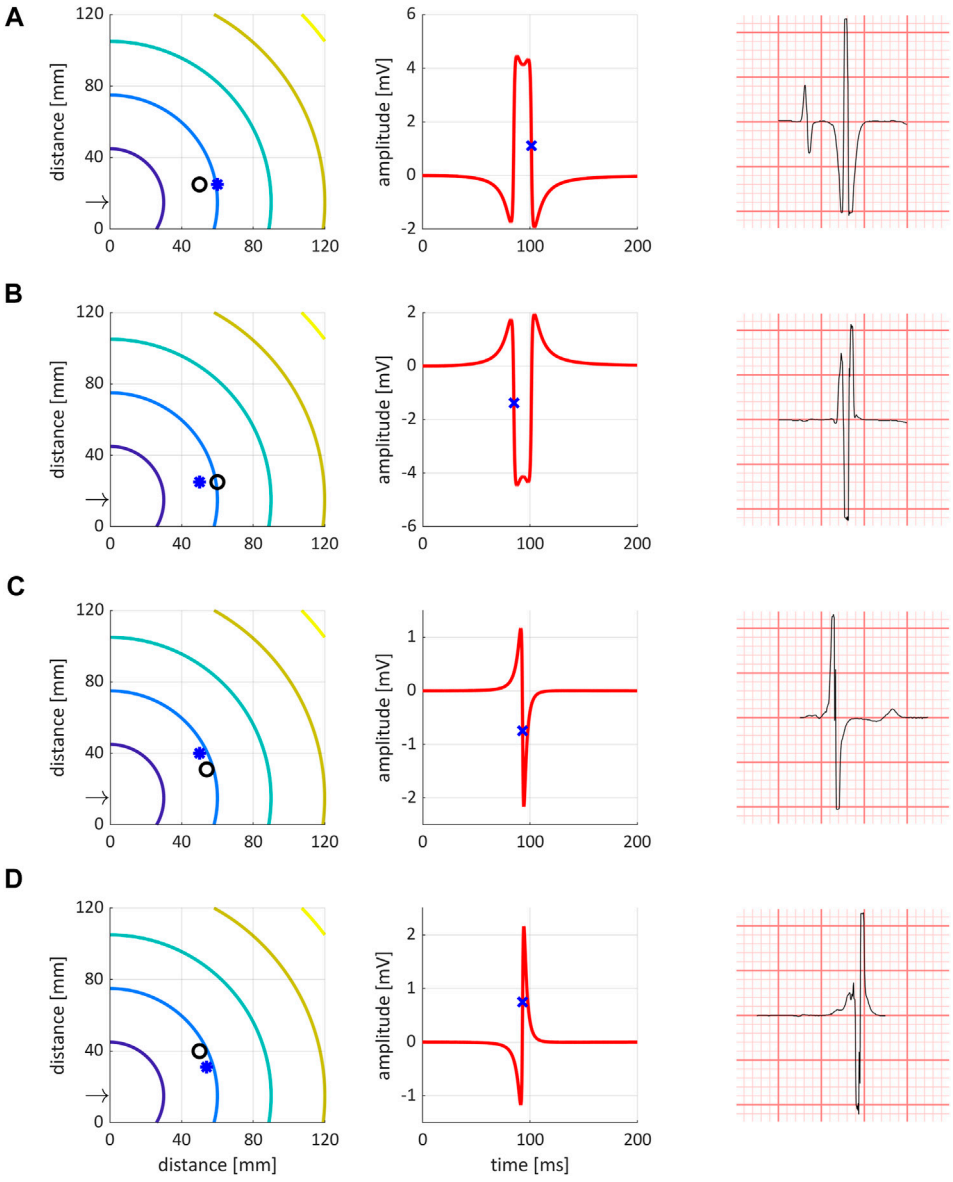

FIGURE 1
The four bipolar electrogram phenotypes identified and simulated. Left column are simulated isochrones, with the ring denoting the negative electrode, and the star denoting the positive catheter tip electrode. The arrow points to the stimulation site at (x = 0 mm, y = 15 mm). Middle column shows simulated bipolar electrograms. Right column shows representative examples from the data. **(A–D)** (horizontal) show the four different configurations. Please refer to the text for further details.

from CardioLab, 15 records had no sinus rhythm ECG (patients were pacemaker dependent), and one showed a normal QRS duration of 84 ms and was therefore excluded. The remaining 135 patients were included in this study.

The included 135 patients all had simultaneous 12-lead surface ECG and bipolar right ventricular (RV) and LV pacing lead electrograms measured at the final implant site. Data was exported as two paired files per patient, one with the 12-lead ECG, and one where lead V1 was exchanged for the bipolar LV sense signal (ECG/LV). QRS duration was measured manually by one reviewer (C.G.) with digital calipers on the ECGs with magnification 200%, and the QRS onset and offset points were transferred to the ECG/LV files. QLV was then measured on the ECG/LV files by two reviewers (C.G. and J.M.), also using a digital caliper at a magnification of 500%. Any discrepancies were resolved by consensus. AHA17 segment

location (Cerqueira et al., 2002) for the LV electrode was evaluated by post-implant cardiac computed tomography (A.S.) and was available for all 135 patients from study records.

QLV measurement

The morphology of bipolar electrograms depend on both the direction of the activation wave front and the tissue-electrode distances (Bakker, 2019). We identified four different QLV morphology phenotypes in our data. Bipolar electrograms are simulated using a moving circular dipole layer in an infinite medium approximated by triangulated rings. Simulations were done in an infinite 3D slab of homogenous isotropic tissue with thickness of 4 mm. We visualize the wavefront only for a 120 mm by 120 mm region of this slab. The simulated sensing catheter has electrode spacing of 10 mm. The stimulus origin was at $x = 0$ mm and $y = 15$ mm (referenced to the visualized region), with the catheter electrodes placed approximately 40 mm away from this origin. We first computed the activation map analytically with a conduction velocity of 0.6 m/s. Then, with a time sampling of 0.1 ms, we computed the total solid angle (van Oosterom and Strackee, 1983) per time step of the triangulated circular ring (400 triangles); this being a scaled version of the local infinite medium potential at one measuring electrode (the unipolar electrogram). The bipolar electrogram is then the subtraction of the two simulated electrograms from the two differently located electrode positions. As the electrodes are relatively close together, the approximation of the volume conductor as being an infinite medium is approximately valid. A limitation of these simulations is that the local heart curvature and anisotropy is not taken into account, because this data was not available Also, bath loading effects were not including is this simulation. For different electrode orientations the electrogram could be simulated as shown in Figure 1. One bipolar electrogram simulation takes approximately 4 s on a standard office pc (Intel core i7 3 GHz running Windows). Panel (A) shows propagation along the catheter direction, with the tip closest to activation origin. In this case, activation at the catheter tip causes the first negative deflection in the bipolar ECG. Hence, to reflect local activation time (LAT) at the catheter tip, we measure the first negative slope of the signal. Panel (B) also shows propagation along the catheter, but in the opposite direction. In this case, the second leg (but still the steepest negative slope) represents LAT at the tip. Panel (C) shows electrodes nearly perpendicular to the activation wavefront, giving rise to a biphasic signal. In this case, the steepest negative slope is measured as representative for LAT at the electrode tip. Finally, panel (D) shows a situation similar to (C), but with the electrodes interchanged with respect to the activation wavefront. In this case, the steepest positive deflection is representative of LAT at the tip. The four phenotypes are denoted configuration one to four, for (A)-(D), respectively.

To reflect local activation time (LAT) at the catheter tip, all EGMs were first classified as one of the four phenotypes, and based on this configuration the QLV was determined accordingly.

The mapper

The Mapper is a modeling approach that aims to estimate the cardiac activation initiated from the His-Purkinje system by optimizing a forward solution to best match the ECG. The mapper has previously been validated using both endocardial and epicardial recordings (Roudijk et al., 2021; Boonstra et al., 2022), and has also been shown to accurately show PVC foci (Potyagaylo et al., 2019) and general morphological changes occurring with LBBB (Galeotti et al., 2013). The steps involved in The Mapper algorithm are shown in Figure 2. Briefly, a generic geometry and a patient-specific ECG are used as input. Using this data, the major QRS axis is computed. Depending on the QRS axis and QRS duration, an initial activation time is set for each of the "His-Purkinje" nodes, or the nodes are "disabled". In the final optimization step, timing and position of the "His-Purkinje" nodes are changed to best fit the patient specific ECG. The human His-Purkinje system distributes the electrical activation to a large part of the endocardial surface of the myocardium. In this study the initial activation from a branch of the His-Purkinje system is approximated by an endocardial surface being activated almost simultaneously, attributed to the density of the local available Purkinje-myocardial junctions located on the endocardial surface. Thus, the Purkinje initiated ventricular activation is modelled by a combination of multiple breakthroughs in different parts of the left and right ventricular myocardium.

Activation sequence construction

The fastest route algorithm is used to compute the activation propagation from the initial sites of activation (van Oosterom and van Dam, 2005; van Dam, Oostendorp, and van Oosterom, 2009b). The fastest route algorithm computes the (virtual) distances in the geometric heart model between a node and all other nodes on a closed triangulated myocardial surface. The propagation velocity within the myocardium is anisotropic, i.e., velocities perpendicular to the myocardial fiber direction is about 2 times slower than along the fiber direction. To take this anisotropic propagation velocity into account the (virtual) distance for transmural connections is made 2.5 times longer, as the transmural connections are by definition perpendicular to the local fiber direction (van Dam, Oostendorp, and van Oosterom, 2009b; van Dam, Oostendorp, Linnenbank, et al., 2009). To mimic the surface activation from the Purkinje system, the local velocity around a node on the ventricular surface is set to 1.7 m/s with a radius of 15 mm. The Mapper is described in detail by Roudijk et al. (Roudijk et al., 2021), especially in the

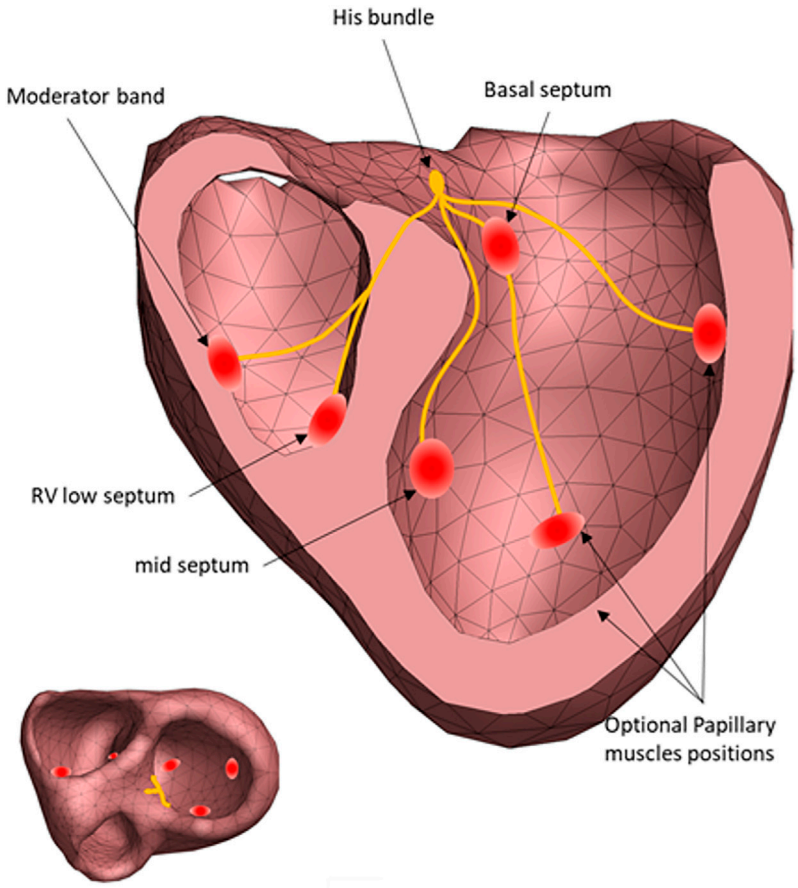

FIGURE 2
The regional sites of early activation associated with the Purkinje activation. Each red circle identifies a position of the initial estimation of the cardiac activation. The exact position of the His-Purkinje system is unknow, only the effect of the His-Purkinje system on cardiac activation is simulated (left panel).[15].

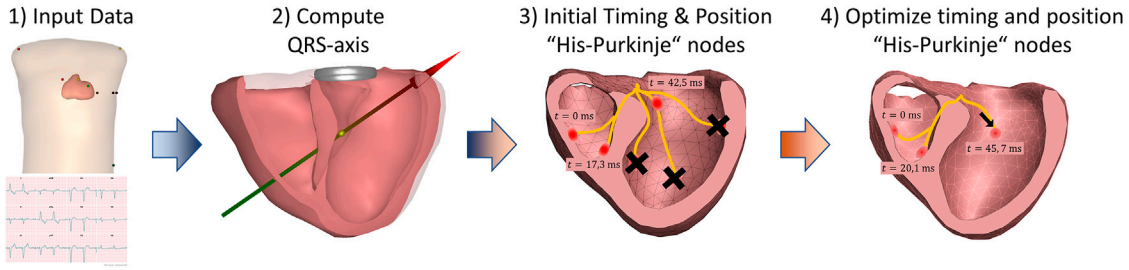

FIGURE 3
The steps involved in The Mapper algorithm. 1) First, a geometry (generic or patient specific) and a patient specific 12-lead ECG is used as input. 2) Initial analysis of the QRS axis and QRS duration determines gross activation pattern, and based on this 3) pre-defined times are set for the six His-Purkinje activation sites (or sites are "disabled"). Finally, 4) both the position and the activation times of the His-Purkinje activation sites are changed to best fit the ECG.

supplementary material, and by Boonstra et al. (Boonstra et al., 2022).

The geometric model used in this study to estimate the cardiac activation is from a 58-year-old male which we find to have typical body build and heart orientation. The source method used to simulate the equivalence of the cardiac activity is the equivalent dipole layer (EDL) (van Dam, Oostendorp, & van Oosterom, 2009a; van Dam, Oostendorp, Linnenbank, et al., 2009; van Oosterom, 2011; van Dam et al., 2013; Janssen et al., 2018). This model is used to compute the ECG given the activation time at each of the nodes of the ventricular mesh (Figure 3). Several methods exist to account for the volume conductor effect and compute the ECG from local activation times, for instance the Lead Field approach (Potse, 2018), or the commonly used Boundary Element Method. In this research the Boundary Element Method was used. The volume conductor model uses the geometries of the thorax, ventricles, and ventricular blood cavities. The conductivity of the blood was set to be 3 times the value of the rest of the thorax geometry (Roudijk et al., 2021).

TABLE 1 Baseline characteristics.

	All
Subjects, n	135
Female sex, n (%)	32 (24)
Age	70 ± 9 years
Height	174 ± 9 cm
Weight	80 ± 16 kg
BMI	26.3 ± 4.5 kg m^{-2}
Ischemic Heart Disease, n (%)	63 (47)
Pacemaker, n (%)	6 (4)
QRS Duration	163 ± 21 ms
QLV	135 ± 28.6 ms
LVEF	25 ± 5.7%
LV EDF	259 ± 83.3 ml
LV ESV	196 ± 71.2 ml

Phenomenological estimation of His-Purkinje system activation

To estimate the His-Purkinje activation sequence from a patient's ECG, an initial activation sequence is generated to simulate ECG signals. This initial sequence uses six different anatomical locations of potential Purkinje activations sites (Figure 2), based qualitatively of the activation sequence described by Durrer et al. They described that initial activation was typically found on the anterior left septum, with later local breakthroughs in the left and right apical regions as well as the right free wall (Durrer et al., 1970). Hence, for the LV septum, two sites are located basal and mid septum. Two more locations were selected on the left free wall, associated with papillary muscle locations and thus with potential sites of early His-Purkinje activation. The two positions on the endocardial RV wall represent the entry of the moderator band (Ho et al., 2003) associated with the papillary muscles, and a site at the right apical septum. This approach was previously validated (Roudijk et al., 2021; Boonstra et al., 2022).

The initial timing of each of these six locations depend on the morphology of an ECG waveform and they are used as an initial guess for subsequent iterative optimization procedures. For normal ECG morphology, the initiation times of the left septal wall was set to 0 ms, i.e. equal to the QRS onset, while the RV and LV initiation times are set to 15 ms. For ECGs with an LBBB pattern (QRS duration >120 ms) the initial timing of the left regions, is delayed to 40 ms for the septal regions and 45 ms for the free wall regions. Similarly, for RBBB ECG waveforms (QRS duration >120 ms), the initial activation of the RV septal region is set to 45 ms, and the RV free wall to 65 ms.

In the subsequent optimization procedure, the timing and position of these six early sites of activation can be changed to obtain the best match between the simulated ECG and measured ECG. The total activation duration for each constructed sequence is matched to the QRS duration by adapting the overall used propagation velocity. The used propagation velocity is maintained within the physiological range of the myocardial velocity, i.e., between 0.6 and 0.85 m/s (Roberts et al., 1979; Spach and Kootsey, 1983; Kléber and Rudy, 2004; Cantwell et al., 2015; Good et al., 2020).

Analysis of activation times and LV pacing site

For each patient, the mapper estimates the activation sequence of the heart based on the 12-lead ECG. The mesh-model of the heart is divided into the AHA 17 defined segments on a node level, and the geometric mean of the segment containing the LV pace electrode is computed. Since the pacing site within an AHA 17 segment is not known, we set the LV pacing site to be in the center of the myocardial segment assessed by cardiac computed tomography. The estimated activation time at this location is found by linear interpolation within the triangle encompassing the geometric mean of the segment. The time difference between the measured and estimated activation time, denoted Δ_{QLV}, is given in milliseconds.

From the estimated activation of the whole heart, we also determined the distance between the LV electrode position (defined and computed as above) and the closest point which is estimated to activate at the measured QLV time. This is done by first searching for the nearest triangulated surface element containing an activation time equal to the measured QLV. For this triangular element, the precise location activating at this time is found by linear interpolation within the triangle. All distances between points are given in millimeters. Finally, we compared the

10.3389/fphys.2022.939240

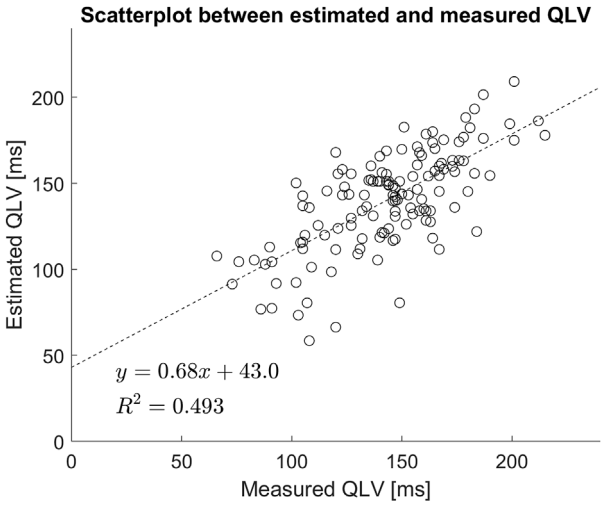

FIGURE 4
Scatter plot of estimated vs. measured QLV. Included is also a linear regression analysis.

segment of the estimated QLV position to the segment containing the LV lead. We report the fraction that is placed within the same segment.

Statistical analysis

Continuous variables are reported as mean ± SD unless severely skewed. Categorical values are reported as absolute numbers and percentages. For analysing associations, unpaired *t*-test was used for continuous independent variables. $p < 0.05$ was considered statistically significant. Matlab 2021b was used to perform the statistical analyses.

Results

Baseline patient characteristics are shown in Table 1. The Mapper successfully estimated activation sequences for all patients. The mean difference between estimated and measured QRS duration was -0.7 ± 3.3 ms (mean ± SD). For 125 cases out of the 135, the QRS difference was within -2 ms to $+4$ ms; the remaining 10 cases were outliers with a difference between -2 and -20 ms. Median correlation between simulated and recorded ECGs was 0.73. The Mapper runs in near real-time, with an execution time of approximately 1 s (and always less than 2 s) on a standard office PC (2018 Intel core i7, 3 GHz) running Windows.

On average there was a small and not statistically significant difference between measured and estimated QLV ($\Delta_{QLV} = -3.0 \pm 22.5$ ms; mean ± SD, $p = 0.119$). Regression between estimated and measured QLV is highly significant and shows $R^2 = 0.49$. A scatterplot together with the regression line is shown in Figure 4. All estimated QLV values are shown in the AHA 17-segment illustration in Figure 5.

Overall distribution of LV pacing site given as AHA 17 segments is shown in Table 2, while overall distribution of EGM configurations is shown in Table 3. The overall median distance between measured and estimated LV pacing site was 18.6 mm (IQR = 17.3 mm). In Tables 2, 3 we also present the fraction of correctly estimated QLV segments.

Similarly, there was no systematic difference or proportional bias between measured QLV and Δ_{QLV} (Figure 6).

Figure 7 shows the distances between LV pacing site and the nearest point activating at the measured QLV time also using the AHA 17-segment model.

Figure 8 illustrates, for all 135 patients, the distance between the LV catheter position (defined as the geometric center of the segment it was found to be in), and the closest point of the epicardium that is estimated to activate at this time. The markers are 8 mm in diameter.

Discussion

In this retrospective study based on 135 patients undergoing CRT, we estimated QLV using a standard 12-lead ECG. There was no statistical difference between non-invasively estimated QLV and QLV measured during the implant procedure. The median distance between measured and estimated LV pacing site was 18.6 mm (IQR 17.3 mm). However, the location of LV pacing site was known with segment-level precision; LV pacing site was always placed in the segment center. For reference, in the generic model, the mean epicardial area of the defined segments is 601 mm^2. If the segments were perfectly square in shape, this would correspond to a side length of approximately 25 mm. This is an adequate approximation for all segments except the apex which is circular and even larger; it has a mean diameter of 47 mm.

We presented four phenotypes of bipolar electrograms and show from a theoretical standpoint how local activation should be measured differently in the four situations. To our knowledge, such categorization and presentation is novel.

Since we are using a generic geometry with uniform conduction velocity for the whole heart, it is not always possible to match the ECG exactly. One measure of the goodness of fit for the model is the error in matching QRS duration (Δ_{QRS}). We divided Δ_{QRS} into three groups representing underestimation of QRS ($\Delta_{QRS} < -1$ ms), exact estimation of QRS (-1 ms $\leq \Delta_{QRS} \leq +1$ ms) and overestimation of QRS ($\Delta_{QRS} > +1$ ms). These groups were compared with a one-way ANOVA analysis, and the group representing QRS underestimation was significantly different from the other two

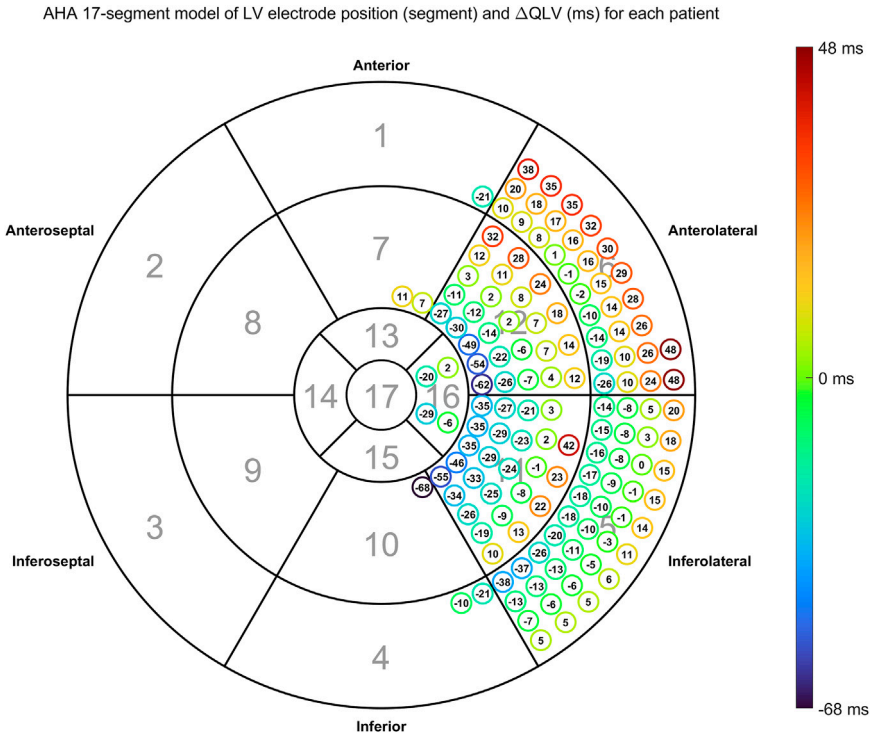

FIGURE 5
Time difference between estimated and measured QLV (Δ_{QLV}) according to anatomical LV lead position. The encircled numbers show Δ_{QLV} for each patient. The color of the circle is a visual representation of the Δ_{QLV} value.

TABLE 2 Overall distribution of LV pacing site in terms of AHA17 segments and associated Δ_{QLV}.

LV pacing site [AHA17 segment]	*n*	Δ_{QLV}	*p*-value	Mean distance [mm]	Fraction correct
		μ (± SD) [ms]			
1	1	-21		17	1/1 (100%)
4	2	-15		25	1/2 (50%)
5	40	-6 ± 14	*0.012*	15	32/40 (80%)
6	32	16 ± 18	*0.000*	22	24/32 (75%)
7	2	+9		12	2/2 (100%)
10	1	-68		58	0/1 (0%)
11	26	-15 ± 23	*0.003*	28	8/26 (31%)
12	27	-5 ± 24	*0.294*	23	15/27 (56%)
16	4	-13		18	3/4 (75%)

n: number of patients with LV pacing site at the given segment. Δ_{QLV} μ and SD: mean and standard deviation of Δ_{QLV} for all patients with LV pacing site in the given segment. In groups with four patients or less, no standard deviation was computed, and hence no *p*-value could be computed. *p*-value: test for the hypothesis $\mu = 0$. Mean distance: distance between LV pacing site and the nearest site estimated to activate at the measured QLV time. Fraction correct: The fraction of estimated QLV locations in the same segment as LV lead. Please refer to Figure 3 or five for anatomical location of AHA segment number.

($p < 0.05$). Figure 9 shows a boxplot with median and IQR for each group. Since the QRS duration imposes an upper limit of the QLV estimate, it is not surprising that QRS underestimation also (on average) leads to QLV underestimation. However, it is only in four cases that QRS underestimation exceeds -4 ms, and these cases are the main drivers of this group. The largest Δ_{QRS} was

TABLE 3 Overall distribution of EGM configurations and associated Δ_{QLV}.

Configuration	n	Δ_{QLV}	p	Mean distance [mm]	Fraction correct
		$\mu \pm$ SD [ms]			
1	24	-8 ± 24	*0.101*	23	15/24 (62%)
2	19	+8 ± 22	*0.137*	19	13/19 (68%)
3	45	-4 ± 25	*0.294*	23	28/45 (62%)
4	47	-4 ± 19	*0.151*	19	30/47 (64%)

n: number of patients with ECG configuration as defined in Figure 1. Δ_{QLV} μ and SD: mean and standard deviation of Δ_{QLV} for all patients with LV pacing site in the given segment. In groups with four patients or less, no standard deviation was computed, and hence no p-value could be computed. p-value: test for the hypothesis $\mu = 0$. Mean distance: distance between LV pacing site and the nearest site estimated to activate at the measured QLV time. Fraction correct: The fraction of estimated QLV locations in the same segment as LV lead.

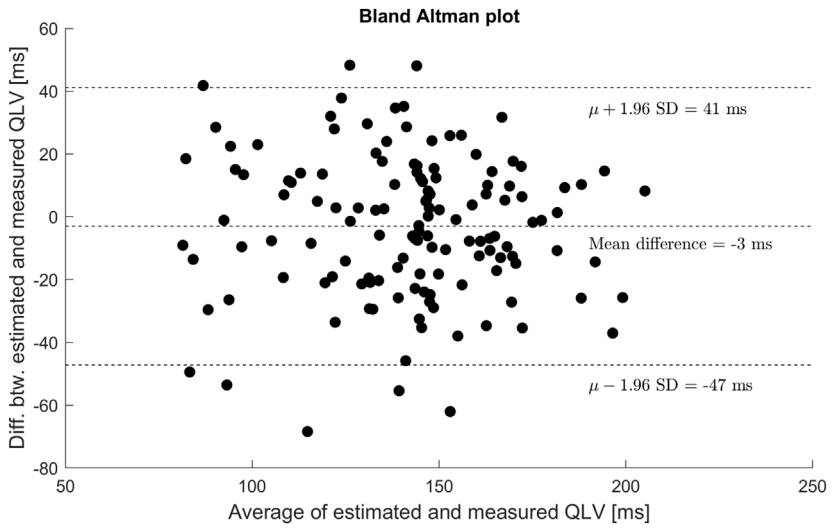

FIGURE 6
Bland-Altman plot showing agreement between estimated and measured QLV. No general trends were identified from the plot.

4 ms; for the 125 of 135 cases with Δ_{QRS} between -1 ms and +4 ms, there was no relation between Δ_{QRS} and Δ_{QLV}.

The varying response to CRT treatment between patients has led to an immense number of studies investigating both patient selection and optimal treatment. Positioning of the LV electrode has long been a main concern for response and is still reported to be associated with outcome (Kutyifa et al., 2018). Further it is suggested that having an overview of the myocardial substrate in terms of fibrosis and scarring (Butter et al., 2021), as well as myocardial activation and coronary venous anatomy before the procedure would be beneficial. This makes it possible to plan the procedure and to aim for placing the LV lead in a coronary sinus branch over a viable myocardial region with late electrical activation. There are several steps in this process. Firstly, the activation pattern of the heart needs to be mapped. This is the aim of this study. Secondly, information on myocardial scarring and cardiac venous anatomy obtained through cardiac imaging (e.g., magnetic resonance imaging and cardiac computed tomography) should be fused with the model. Then, the optimal pacing site can be determined based on simulations and be provided to the physician prior to CRT implantation. However, possible challenges with achieving a stable LV lead position with acceptable pacing thresholds and no phrenic nerve stimulation may still exist.

The largest drawback of the approach described above is that it works in research settings but is too elaborate for normal clinical practice. This is the reason we explore the use of generic models and use of the 12-lead ECG only. Our results indicate that QLV, and likely the entire activation sequence, may be estimated non-invasively from a standard 12-lead ECG, potentially solving the inherent problem that QLV cannot be measured until the patient is undergoing CRT implantation. However, The Mapper

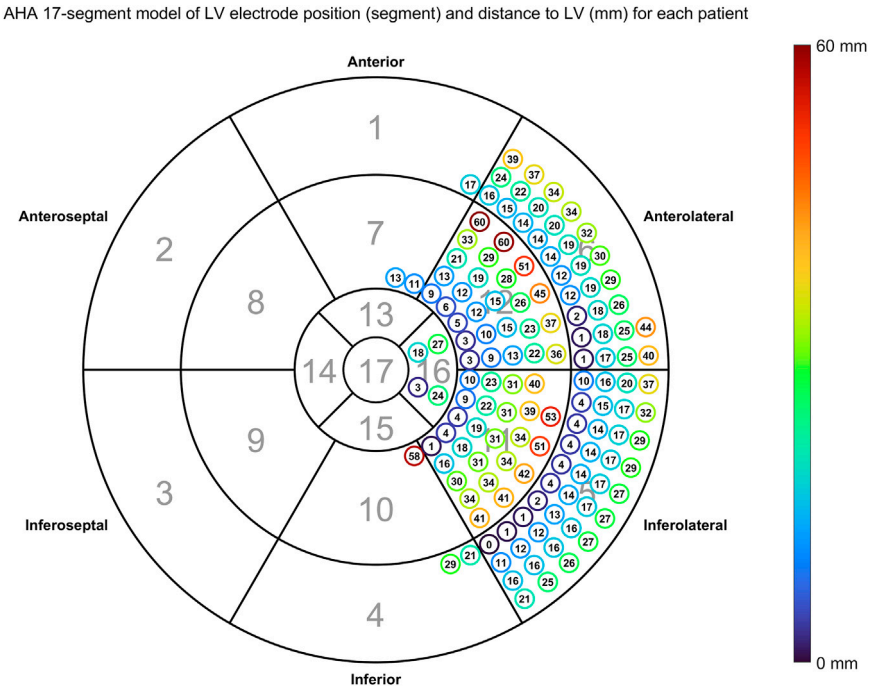

FIGURE 7
Distance between anatomical LV pacing site and nearest node activating at the measured Δ_{QLV}. Each encircled number shows the computed distance between estimated position and position determined by physician. The color of a circle is a visual representation of these distances.

is not constrained in positioning the latest activating site. In practice, LV lead placement is limited by coronary vein anatomy, presence of scar tissue, or unintentional phrenic nerve pacing in which case the lead should be repositioned. This will inherently lead to differences between estimated and measured QLV. Still, knowing the activation sequence of the heart and hence the latest activating site may provide a more narrow and targeted area to map during LV lead implantation. Precision could possibly be improved by using more patient specific anatomical models obtained e.g. from statistical shape modeling, which could be done automatically or semi-automatically with little physician effort. This, however, requires a large library of segmented CT/MRI images. We are currently building such a library to enable this.

An intrinsic difficulty with CRT patients is that they often also suffer from ischemic heart disease (IHD) and have areas of myocardial scarring. Especially scarring is a poor tissue substrate for stimulation and should be avoided. In the present study we used a generic model and did not take ischemia or scarring into account. However, the precision was practically the same whether patients were considered to have ischemic heart disease or not (+IHD: $\Delta_{QLV} = +2$ ms, SD = 24 ms, median distance 22 mm, −IHD: $\Delta_{QLV} = -8$ ms, SD = 20 ms, median distance 21 mm). We expect the reason for this to be the implicit incorporation of ischemia or scarring through adjustment of the propagation velocity. Ischemia causes slower conduction than healthy tissue. When computing the activation sequence of the heart, the overall QRS duration must be matched, and thus ischemia is indirectly taken into consideration, however without location or extent. If data on scarring or ischemia is available, it would be possible to transfer this information to the generic model in a segment-wise manner. This will be investigated in a future study.

It is well known that the bipolar electrogram changes configuration depending on the position and angle to the wavefront, making measurement of local activation time difficult. The variations theoretically constitute a continuous spectrum of morphological changes. However, in practice we identified only four different phenotypes, corresponding to wavefronts along the axis or transverse to the axis of the bipolar lead, each in both directions. This is an important result that demonstrates the feasibility of measuring bipolar EGMs and how they can be used similarly to unipolar EGMs to measure local activation time consistently.

Limitations

The Mapper is limited in that it has up to six initial activation sites that can change in timing and position, and a uniform (but

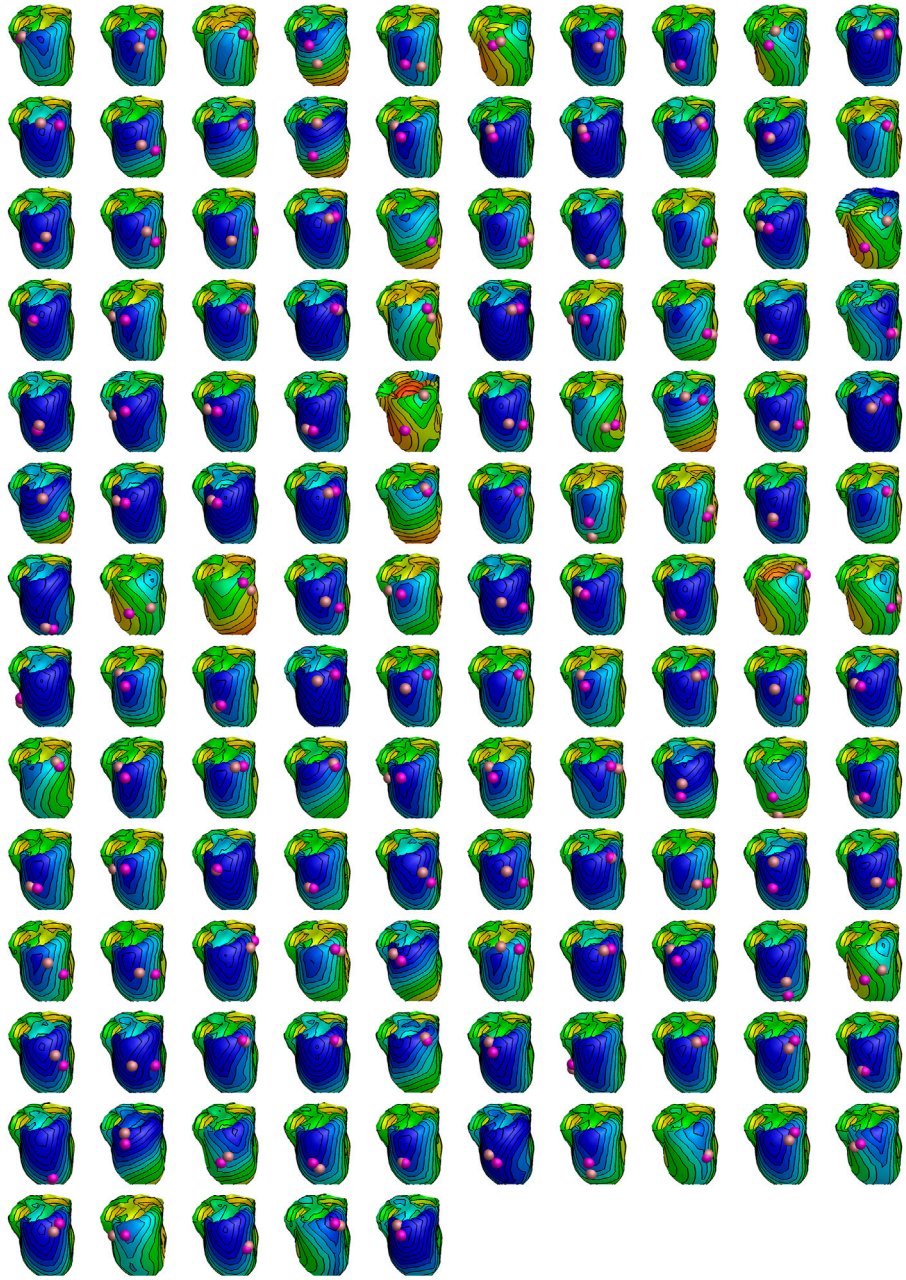

FIGURE 8
Estimated activation patterns for all 135 patients in the study. All hearts are oriented similarly independent of LV pacing site. Early to late activation is coded with red (earliest) over yellow and green to blue (latest) colors. The coloring is normalized to the patient specific QRS duration. The purple sphere shows the LV pacing site determined by physician by cardiac computed tomography (always in the center of a segment), while the bronze-colored sphere shows the nearest site activating at the measured QLV time. Both spheres are drawn with a diameter of 8 mm.

anisotropic) conduction velocity. On this basis, the Mapper tries to match both the activation pattern (as governed by correlation between measured and simulated ECG) and QRS duration (by adjusting conduction velocity within certain physiological limits). Hence, it may be necessary to make a trade-off between the two. This is especially true in cases where the generic geometry is a poor match for the actual heart, and in cases where ischemia or scarring results in non-uniform conduction velocity. The limitation in the number of possible activation sites are most important in cases with complex activation sequences, where they may limit the accuracy of the solution.

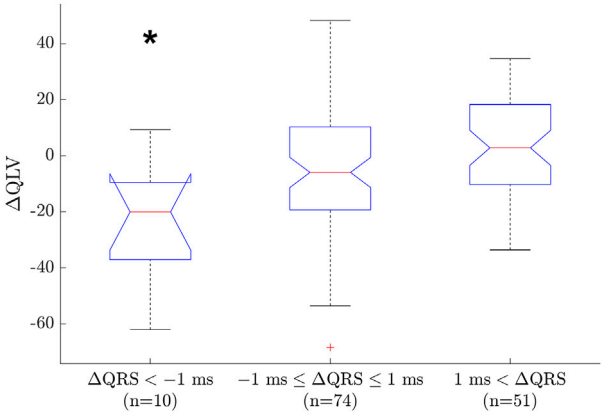

FIGURE 9
Boxplot between groups of Δ_{QRS} and Δ_{QLV}. The plot shows mean and IQR, with one outliers marked as a cross. The group representing QRS underestimation showed a statistically significant (negative) error in QLV estimation (*$p < 0.05$). This may be explained by the QRS duration imposing an upper bound on the QLV estimate.

Conclusion

We demonstrated a novel non-invasive method for estimating QLV, based on the standard 12-lead ECG. On average, the method estimates myocardial activation and QLV with a small error, and may potentially be used to support patient selection, optimize implant procedures, and to simulate optimal stimulation parameters before the procedure. The use of a generic model has limitations that in some cases lead to considerable errors. This has to be taken into account when using The Mapper. Adding patient specific data, like electrode positions and body build might be necessary.

Data availability statement

Due to confidentiality agreements, supporting data cannot be made available.

Ethics statement

The studies involving human participants were reviewed and approved by the Central Denmark regional committee on health research ethics (file no. 20100245). The patients/participants provided their written informed consent to participate in this study.

Author contributions

JM: Conceptualization, Methodology, Formal analysis, Data Curation, Writing—Original Draft, Visualization. PvD: Conceptualization, Methodology, Software, Visualization, Writing—Review and Editing. AS: Investigation, Resources, Writing—Review and Editing. PF: Conceptualization, Writing—Review and Editing. JN: Investigation, Resources, Writing—Review and Editing. SR: Conceptualization, Writing—Review and Editing. CG: Conceptualization, Methodology, Data Curation, Writing—Review and Editing.

Conflict of interest

PvD is an owner of ECG Excellence BV and Peacs BV.

The remaining authors declare that the research was conducted in the absence of any commercial or financial relationships that could be construed as a potential conflict of interest.

Publisher's note

All claims expressed in this article are solely those of the authors and do not necessarily represent those of their affiliated organizations, or those of the publisher, the editors and the reviewers. Any product that may be evaluated in this article, or claim that may be made by its manufacturer, is not guaranteed or endorsed by the publisher.

References

Bakker, J. M. de. (2019). Electrogram recording and analyzing techniques to optimize selection of target sites for ablation of cardiac arrhythmias. *Pacing Clin. Electrophysiol.* 42 (12), 1503–1516. doi:10.1111/PACE.13817

Boonstra, M. J., Roudijk, R. W., Brummel, R., Kassenberg, W., Blom, L. J., Oostendorp, T. F., et al. (2022). Modeling the his-purkinje effect in non-invasive estimation of endocardial and epicardial ventricular activation. *Ann. Biomed. Eng.* 50 (3), 343–359. doi:10.1007/S10439-022-02905-4

Butter, C., Georgi, C., and Stockburger, M. (2021). Optimal CRT implantation-where and how to place the left-ventricular lead? *Curr. Heart Fail. Rep.* 18, 329–344. doi:10.1007/s11897-021-00528-9

Cantwell, C. D., Roney, C. H., Ng, F. S., Siggers, J. H., Sherwin, S. J., and Peters, N. S. (2015). Techniques for automated local activation time annotation and conduction velocity estimation in cardiac mapping. *Comput. Biol. Med.* 65, 229–242. doi:10.1016/J.COMPBIOMED.2015.04.027

Cerqueira, M. D., Weissman, N. J., Dilsizian, V., Jacobs, A. K., Kaul, S., Laskey, W. K., et al. (2002). & (American heart association writing group on myocardial segmentation and registration for cardiac Imaging)Standardized myocardial segmentation and nomenclature for tomographic imaging of the heart. A statement for healthcare professionals from the cardiac imaging committee of the council on clinical cardiology of the American heart association. *Circulation* 105 (4), 539–542. doi:10.1161/HC0402.102975

Durrer, D., van Dam, R. T., Freud, G. E., Janse, M. J., Meijler, F. L., and Arzbaecher, R. C. (1970). Total excitation of the isolated human heart. *Circulation* 41 (6), 899–912. doi:10.1161/01.CIR.41.6.899

Galeotti, L., van Dam, P. M., Loring, Z., Chan, D., and Strauss, D. G. (2013). Evaluating strict and conventional left bundle branch block criteria using electrocardiographic simulations. *Europace* 15 (12), 1816–1821. doi:10.1093/EUROPACE/EUT132

Glikson, M., Nielsen, J. C., Kronborg, M. B., Michowitz, Y., Auricchio, A., Barbash, I. M., et al. (2021). 2021 ESC Guidelines on cardiac pacing and cardiac resynchronization therapy: Developed by the Task Force on cardiac pacing and cardiac resynchronization therapy of the European Society of Cardiology (ESC) with the special contribution of the European Heart Rhythm Association (EHRA). *Eur. Heart J.* 42 (35), 3427–3520. doi:10.1093/eurheartj/ehab364

Good, W. W., Zenger, B., Bergquist, J. A., Rupp, L. C., Gillette, K., Plank, G., et al. (2020). Quantifying the spatiotemporal influence of acute myocardial ischemia on volumetric conduction velocity. *Comput. Cardiol.* 47. doi:10.22489/CINC.2020.279

Ho, S. Y., McCarthy, K. P., Ansari, A., Thomas, P. S., and Sánchez-Quintana, D. (2003). Anatomy of the atrioventricular node and atrioventricular conduction system. *Int. J. Bifurc. Chaos* 13 (12), 3665–3674. doi:10.1142/S0218127403008879

Janssen, A. M., Potyagaylo, D., Dössel, O., and Oostendorp, T. F. (2018). Assessment of the equivalent dipole layer source model in the reconstruction of cardiac activation times on the basis of BSPMs produced by an anisotropic model of the heart. *Med. Biol. Eng. Comput.* 56 (6), 1013–1025. doi:10.1007/S11517-017-1715-X

Kléber, A. G., and Rudy, Y. (2004). Basic mechanisms of cardiac impulse propagation and associated arrhythmias. *Physiol. Rev.* 84 (2), 431–488. doi:10.1152/PHYSREV.00025.2003

Kutyifa, V., Kosztin, A., Klein, H. U., Biton, Y., Nagy, V. K., Solomon, S. D., et al. (2018). Left ventricular lead location and long-term outcomes in cardiac resynchronization therapy patients. *JACC. Clin. Electrophysiol.* 4 (11), 1410–1420. doi:10.1016/J.JACEP.2018.07.006

Leclercq, C., Cazeau, S., le Breton, H., Ritter, P., Mabo, P., Gras, D., et al. (1998). Acute hemodynamic effects of biventricular DDD pacing in patients with end-stage heart failure. *J. Am. Coll. Cardiol.* 32 (7), 1825–1831. doi:10.1016/S0735-1097(98)00492-6

Potse, M. (2018). Scalable and accurate ECG simulation for reaction-diffusion models of the human heart. *Front. Physiol.* 9 (370). doi:10.3389/fphys.2018.00370

Potyagaylo, D., Chmelevsky, M., van Dam, P., Budanova, M., Zubarev, S., Treshkur, T., et al. (2019). ECG adapted fastest route algorithm to localize the ectopic excitation origin in CRT patients. *Front. Physiol.* 10 (MAR), 183. doi:10.3389/fphys.2019.00183

Roberts, D. E., Hersh, L. T., and Scher, A. M. (1979). Influence of cardiac fiber orientation on wavefront voltage, conduction velocity, and tissue resistivity in the dog. *Circ. Res.* 44 (5), 701–712. doi:10.1161/01.RES.44.5.701

Roudijk, R. W., Boonstra, M. J., Brummel, R., Kassenberg, W., Blom, L. J., Oostendorp, T. F., et al. (2021). Comparing non-invasive inverse electrocardiography with invasive endocardial and epicardial electroanatomical mapping during sinus rhythm. *Front. Physiol.* 12, 730736. doi:10.3389/FPHYS.2021.730736

Salden, O. A. E., Vernooy, K., van Stipdonk, A. M. W., Cramer, M. J., Prinzen, F. W., and Meine, M. (2020). Strategies to improve selection of patients without typical left bundle branch block for cardiac resynchronization therapy. *JACC. Clin. Electrophysiol.* 6 (2), 129–142. doi:10.1016/J.JACEP.2019.11.018

Sommer, A., Kronborg, M. B., Nørgaard, B. L., Poulsen, S. H., Bouchelouche, K., Böttcher, M., et al. (2016). Multimodality imaging-guided left ventricular lead placement in cardiac resynchronization therapy: A randomized controlled trial. *Eur. J. Heart Fail.* 18 (11), 1365–1374. doi:10.1002/ejhf.530

Sommer, A., Kronborg, M. B., Poulsen, S. H., Böttcher, M., Nørgaard, B. L., Bouchelouche, K., et al. (2013). Empiric versus imaging guided left ventricular lead placement in cardiac resynchronization therapy (ImagingCRT): Study protocol for a randomized controlled trial. *Trials* 14, 113. doi:10.1186/1745-6215-14-113

Spach, M. S., and Kootsey, J. M. (1983). The nature of electrical propagation in cardiac muscle. *Am. J. Physiol.* 244 (1), H3–H22. doi:10.1152/AJPHEART.1983.244.1.H3

Strauss, D. G., Selvester, R. H., and Wagner, G. S. (2011). Defining left bundle branch block in the era of cardiac resynchronization therapy. *Am. J. Cardiol.* 107 (6), 927–934. doi:10.1016/J.AMJCARD.2010.11.010

van Dam, P. M., Oostendorp, T. F., Linnenbank, A. C., and van Oosterom, A. (2009). Non-invasive imaging of cardiac activation and recovery. *Ann. Biomed. Eng.* 3737 (99), 1739–1756. doi:10.1007/S10439-009-9747-5

van Dam, P. M., Oostendorp, T. F., and van Oosterom, A. (2009b). Application of the fastest route algorithm in the interactive simulation of the effect of local ischemia on the ECG. *Med. Biol. Eng. Comput.* 47 (11), 4711–4720. doi:10.1007/S11517-008-0391-2

van Dam, P. M., Oostendorp, T. F., and van Oosterom, A. (2009a). "Non-invasive cardiac imaging based on just the standard 12-lead signals?," in 36th Annual Computers in Cardiology Conference (CinC), Park City, UT, USA, 13-16 September 2009. Available at: https://ieeexplore.ieee.org/document/5445443?arnumber=5445443.

van Dam, P. M., Proniewska, K., Maugenest, A.-M., van Mieghem, N. M., Maan, A. C., de Jaegere, P. P. T., et al. (2014). Electrocardiographic imaging-based recognition of possible induced bundle branch blocks during transcatheter aortic valve implantations. *Europace* 16 (5), 750–757. doi:10.1093/EUROPACE/EUU071

van Dam, P. M., Shivkumar, K., and Laks, M. (2013). Non-invasive myocardial imaging of PVCs and Pacemakers using the 12 lead ECG. *J. Electrocardiol.* 46 (4), e20. doi:10.1016/J.JELECTROCARD.2013.05.073

van Oosterom, A. (2011). "The equivalent double layer; source models for repolarization," in *Basic electrocardiology*. Editors P. W. Macfarlane, A. van Oosterom, M. C. Janse, P. Kligfield, J. Camm, and O. Pahlm (Springer), 227–246.

van Oosterom, A., and Strackee, J. (1983). The Solid Angle of a Plane Triangle. *IEEE Trans. Biomed. Eng.* BME-30 (2), 125–267. doi:10.1109/TBME.1983.325207

van Oosterom, A., and van Dam, P. M. (2005). The intra-myocardial distance function used in inverse computations of the timing of depolarization and repolarization. *Comput. Cardiol.* 32, 567–570. doi:10.1109/cic.2005.1588164

Ypenburg, C., van Bommel, R. J., Borleffs, C. J. W., Bleeker, G. B., Boersma, E., Schalij, M. J., et al. (2009). Long-term prognosis after cardiac resynchronization therapy is related to the extent of left ventricular reverse remodeling at midterm follow-up. *J. Am. Coll. Cardiol.* 53 (6), 483–490. doi:10.1016/J.JACC.2008.10.032

frontiers | Frontiers in Physiology

TYPE Original Research
PUBLISHED 23 September 2022
DOI 10.3389/fphys.2022.907190

OPEN ACCESS

EDITED BY
David Christini,
Downstate Health Sciences University,
United States

REVIEWED BY
Michael Clerx,
University of Nottingham,
United Kingdom
Peter Michael Van Dam,
University Medical Center Utrecht,
Netherlands

*CORRESPONDENCE
Gernot Plank,
gernot.plank@medunigraz.at

SPECIALTY SECTION
This article was submitted to Cardiac Electrophysiology,
a section of the journal
Frontiers in Physiology

RECEIVED 29 March 2022
ACCEPTED 15 August 2022
PUBLISHED 23 September 2022

CITATION
Gillette K, Gsell MAF, Strocchi M, Grandits T, Neic A, Manninger M, Scherr D, Roney CH, Prassl AJ, Augustin CM, Vigmond EJ and Plank G (2022), A personalized real-time virtual model of whole heart electrophysiology.
Front. Physiol. 13:907190.
doi: 10.3389/fphys.2022.907190

A personalized real-time virtual model of whole heart electrophysiology

Karli Gillette[1,2], Matthias A. F. Gsell[1,3], Marina Strocchi[4], Thomas Grandits[1,3], Aurel Neic[5], Martin Manninger[6], Daniel Scherr[6], Caroline H. Roney[7], Anton J. Prassl[1,2], Christoph M. Augustin[1,2], Edward J. Vigmond[8] and Gernot Plank[1,2]*

[1]Gottfried Schatz Research Center—Biophysics, Medical University of Graz, Graz, Austria, [2]BioTechMed-Graz, Graz, Austria, [3]NAWI Graz, Institute of Mathematics and Scientific Computing, University of Graz, Graz, Austria, [4]King's College London, London, United Kingdom, [5]NumeriCor GmbH, Graz, Austria, [6]Division of Cardiology, Department of Internal Medicine, Medical University of Graz, Graz, Austria, [7]Queen Mary University of London, London, United Kingdom, [8]Electrophysiology and Heart Modelling Institute, Bordeaux, France

Computer models capable of representing the intrinsic personal electrophysiology (EP) of the heart *in silico* are termed virtual heart technologies. When anatomy and EP are tailored to individual patients within the model, such technologies are promising clinical and industrial tools. Regardless of their vast potential, few virtual technologies simulating the entire organ-scale EP of all four-chambers of the heart have been reported and widespread clinical use is limited due to high computational costs and difficulty in validation. We thus report on the development of a novel virtual technology representing the electrophysiology of all four-chambers of the heart aiming to overcome these limitations. In our previous work, a model of ventricular EP embedded in a torso was constructed from clinical magnetic resonance image (MRI) data and personalized according to the measured 12 lead electrocardiogram (ECG) of a single subject under normal sinus rhythm. This model is then expanded upon to include whole heart EP and a detailed representation of the His-Purkinje system (HPS). To test the capacities of the personalized virtual heart technology to replicate standard clinical morphological ECG features under such conditions, bundle branch blocks within both the right and the left ventricles under two different conduction velocity settings are modeled alongside sinus rhythm. To ensure clinical viability, model generation was completely automated and simulations were performed using an efficient real-time cardiac EP simulator. Close correspondence between the measured and simulated 12 lead ECG was observed under normal sinus conditions and all simulated bundle branch blocks manifested relevant clinical morphological features.

KEYWORDS

His-Purkinje system, virtual heart technology, cardiac electrophysiology, 12 lead electrocardiogram, cardiac personalization, cardiovascular disease

1 Introduction

Many virtual heart technologies aim to represent the entire organ-scale EP of the heart *in silico* in full mechanistic detail and accordingly provide information of the intrinsic cardiac sources that drive electrical activation and repolarization of the heart. As such, these technologies have the potential to serve not only as surrogates for human clinical and experimental studies, but be a powerful tool within both industrial and clinical applications (Abadi et al., 2020; Corral-Acero et al., 2020). More efficient development of medical devices at cheaper costs, for example, is possible by reducing the number of necessary animal experiments and allowing automated testing of alternative design and deployment variations during the design process. Furthermore, virtual heart technologies could allow optimization of clinical trials and provide patient-tailored therapeutic options (Viceconti et al., 2016). Most importantly, the models can be a transformative tool in clinical diagnostics, prognostics, and treatment planning (Corral-Acero et al., 2020) when personalized. Personalization is performed according to electrical recordings such as the 12 lead ECG and electro-anatomical mappings (EAMs) that are ideally acquired non-invasively.

Despite their potential, current realizations of such technologies fall short in various regards, significantly limiting the scope for potential industrial or clinical applications. Major limitations are the 1) significant computational costs involved in carrying out *in silico* EP studies; 2) the difficulty of personalizing the EP; 3) lack of compelling validation, that is, to demonstrate that simulated EP correlates closely to the physical reality; 4) little proof of predictive capabilities; and, 5) inability to provide estimates of model uncertainties. Furthermore, most reported current technologies focus only on specific chambers of the heart. Namely, studies have reported on either the ventricles (Arevalo et al., 2016; Lopez-Perez et al., 2019) or the atria (Ali et al., 2019; Nagel et al., 2021; Roney et al., 2022), and only a few technologies representing whole heart EP are reported (Strocchi et al., 2020; Gerach et al., 2021; Moss et al., 2021).

We report on the development of our novel virtual technology of whole-heart EP aiming to address these limitations. Our cardiac EP simulator, comprising a whole heart EP model, is able to mechanistically represent the full spectrum of known organ-scale EP under both normal sinus rhythm and bundle branch blocks (BBBs). In previous work, a trimmed down ventricular and torso model of a healthy volunteer was personalized under sinus conditions (Gillette et al., 2021a) and subsequently equipped with a topologically realistic model of the His-Purkinje system (HPS) (Gillette et al., 2021b). Within this study, the model was extended to the whole heart by accounting for atrial EP and adding an atrio-ventricular node (AVN) connected to the HPS facilitating atrio-ventricular conduction. 12 lead ECGs and body surface potential maps (BSPMs) on the torso surface, as well as EAMs recovered through electrocardiographic imaging (ECGi) within the entirety of the heart, were simulated using an efficient and real-time EP simulator first under normal sinus rhythm. The ability of the model to reproduce known ECG features under pathological conditions, which the model was not parameterized for, was then tested. BBBs in the (left and right ventricles LV, RV) were generated. To account for possible remodeling and alterations in the electrical substrate of the ventricles under such conditions (Vernooy et al., 2005; Valenti et al., 2012; Michalski et al., 2022), a lowered (conduction velocity CV) within the associated ventricle was also applied. Close correspondence between simulated and measured 12 lead ECGs is shown under sinus conditions. 12 lead ECGs simulated under pathological conditions under complete BBB are validated based on standard clinical ECG diagnostics (Surawicz et al., 2009).

2 Materials and methods

An anatomically-personalized model of a single subject (male, 45 years of age) was built from imaging data and the non-invasive 12 lead ECG, extending on our previous work (Gillette et al., 2021a; Gillette et al., 2021b). Segmentation and meshing was performed semi-automatically to generate a model that explicitly represents all four chambers of the heart, blood volumes, lungs, and torso. Highly automated workflows relying on abstract anatomical reference frames defined within the ventricles and atria separately were then used to define complex space-varying parameters governing cardiac EP over the whole heart. Parameters governing ventricular EP were previously introduced and fitted using a five-fascicular model to represent the HPS (Gillette et al., 2021a). The simplified model was subsequently replaced by an equivalent topologically realistic representation of the HPS to produce a corresponding 12 lead ECG (Gillette et al., 2021b). Atrial EP was prescribed according to experimental and clinical observations. To generate a complete human heartbeat, the proximal HPS was electrically connected to a model of the AVN that was electrically paired to tissue in the basal right atrium (RA). Methodological steps are described in detail below.

2.1 Model generation

2.1.1 Anatomical model

An anatomically-specific model of a human whole heart for the single subject was generated from clinical magnetic resonance

MRI data (Gillette et al., 2021a). Two separate MRI scans of the full torso and whole heart were sequentially acquired using standardized protocols at 3T (Magnetom Skyra, Siemens Healthcare, Erlangen, Germany). The full torso MRI was attained in four overlapping stacks using a non-ECG gated 3D T1-weighted gradient-echo sequence during expiration at a lower resolution of $1.3 \times 1.3 \times 3.0$ mm^3. A lower resolution is acceptable as the scan is used purely to construct the volume-conductor model. To preserve anatomical structures of the heart for subsequent segmentation, the whole heart MRI was attained using an ECG-gated, fat-saturated, T2-prepared, isotropic 3D gradient-echo to give a higher output resolution of $0.7 \times 0.7 \times 0.7$ mm^3. The scan was attained in an expiratory state during free breathing by employing navigators. All subjects gave written and informed consent at the time of the study that was approved by ethical review board at the Medical University of Graz (EKNr: 24–126 ex 11/12).

At the time of image acquisition, a 12 lead ECG was recorded in the supine position using MRI-compatible electrodes. The measured 12 lead ECG had been filtered with a 150 Hz low-pass filter, 0.5 Hz high-pass filter, and a band-stop filter of 50 Hz to remove electrical noise (Kligfield et al., 2007). Electrode positions were later recovered during segmentation.

Four chamber heart segmentation including blood pools from the iso-volumetric cardiac MRI was automatically performed using a two-kernel convolutional neural network originally trained on computed tomography images and boosted for application on MRIs (Payer et al., 2018). The torso MRI was semi-automatically segmented using intensity thresholding in open-source *Seg3D* (CIBC, 2016) into heart, lungs, and general torso tissue. Registration using an iterative closest point algorithm was performed to automatically register the four-chamber heart with the heart in the torso segmentation (Chetverikov et al., 2002). Anatomical meshes of all four cardiac chambers were generated from volumetric segmentations using the software *CARPentry-Pro Studio* (NumeriCor GmbH, Graz, Austria). Target resolutions of 1.2 and 4 mm were prescribed for cardiac and torso surfaces, respectively.

2.1.2 Anatomical reference frames

Anatomical reference frames were computed for the ventricles and the atria to facilitate control over spatially-varying EP parameters and to map tissue properties such as fibers. Surfaces and interfaces that were required to define boundary conditions for the computation of the reference frames were automatically extracted from the model using tissue labels and the *meshtool* (Neic et al., 2020) software package. For the ventricles, universal ventricular coordinates (UVCs) were computed within the meshed ventricles according to (Bayer et al., 2018) and modified as discussed in (Gillette et al., 2021a). Universal atrial coordinates (UACs) were assigned to the endocardial surface of the left and right atria as introduced in (Roney et al., 2019; Roney et al., 2021).

2.1.3 Ventricular and atrial fiber architecture

Within the ventricles, fiber architecture was auto-generated using a rule-based method as presented in (Bayer et al., 2012). Ventricular fibers were generated to rotate from $+60^\circ$ on the endocardium to -60° on the epicardium (Streeter et al., 1969). Within the atria, a two-step UAC-based mapping was used to incorporate fiber architecture from an endocardial fiber atlas as in (Roney et al., 2021). In a first step, fibers were mapped from the fiber altas onto the endocardial surface of left and right atria utilizing the UACs generated for our model. In a second step, the fibers were extended transmurally to the volumetric mesh defining the atria. For this reason, a *k*d-tree was generated to map each volumetric cell element in the atrial mesh to the closest surface element on the atrial endocardium. This map was then used to assign the fibers of the surface elements to the related volumetric cell elements. Processing steps of anatomical reference frame generation and fiber integration were also carried out in *CARPentry-Pro Studio* (NumeriCor GmbH, Graz, Austria).

2.2 Cardiac electrophysiology

We subsequently detail the EP within the various chambers of the heart, as well as the subsequent simulation of both the cardiac sources and 12 lead ECGs. The pipeline for personalizing and constructing the whole heart model of EP was implemented within the publicly-available *openCARP* simulation framework (Plank et al., 2021). Cardiac simulation was performed in *CARPentry* (Vigmond et al., 2008), which includes implementations and components not available in the *openCARP* simulator, but utilized within this work. Simulation, however, could still be performed using a traditional bidomain simulation approach within the *openCARP* simulator.

2.2.1 His-Purkinje system

A simplified fascicular-based model comprising disk-like root sites embedded in a fast-conducting sub-endocardial layer, representing the fascicles of the HPS in the sub-endocardium, was previously optimized for single subject's measured 12 lead ECG (Gillette et al., 2021a) and slightly modified within this work. Such a representation modulates the fast spread of activation mediated by the subendocardial Purkinje network, but lacks the ability to capture complex mechanisms during certain disease pathologies and pacing (Gillette et al., 2021b). Therefore, the fitted fascicular-based model was replaced by an auto-generated topologically realistic representation of the HPS. It was previously shown

that the 12 lead ECG is preserved during substitution within sinus rhythm (Gillette et al., 2021b).

Improvements were made on the implementation of topologically realistic representation of the HPS to make it compatible for whole heart simulations. Namely, 1) extending the input of the His bundle to include an AVN, 2) alternative branching parameters of 45° repulsion and a mean cable length of 6 mm resulted in a less-dense network allowing faster computation, and 3) incorporating cable-wise tuning of conduction parameters as subsequently described. All fascicles within the HPS were confined to the subendocardium, apart from the fascicle of the RV moderator band, which was allowed to transmurally penetrate up to 50% in the RV free wall to obtain realistic amplitudes in the precordial leads. After discretization to 500 μm, the final HPS contained 958 Purkinje-myocardial junctions and a total of $\approx 32k$ nodes. Antegrade and retrograde delays of the HPS were respectively prescribed at 8 and 3 ms (Evans et al., 1984).

CV within the fast-conducting HPS was assumed to be 2.0 m s^{-1} (Kassebaum and Van Dyke, 1966). To ensure activation timings comparable with those directly prescribed in the fascicular-based model, CVs were tuned within the last cable of the HPS preceding the root site of each fascicular branch. In more detail, an initial Eikonal activation map of the HPS was pre-computed to determine the activation timings in the root sites without CV tuning. CVs within each cable preceding a root site were then computed as the Euclidean distance over desired activation delay as prescribed. General myocardial CVs along the longitudinal myocardial fiber orientations were assigned 0.6 m s^{-1} with an off-axis ratio of 4:2:1 (Taggart et al., 2000). Conductivity within the ventricles was set according to (Roberts and Scher, 1982).

2.2.2 Atrial electrophysiology

During sinus rhythm, activation was assumed to start from the sino-atrial node (SAN) placed high on the posteriorly-located crista terminalis (CT) on the roof of the RA after an initial electrical baseline of 25 ms. Within the atrial myocardium, CVs of 1.2 m s^{-1} along the fiber axes with an off-axis value of 0.6 m s^{-1} was assigned in both the RA and the LA. Conductivity values were set using ratios reported in (Roberts and Scher, 1982), but scaled to account for the higher atrial CVs (Roberts and Scher, 1982). To facilitate coordinated activation of the LA and RA, a Bachmann's bundle (BB) was incorporated into the model that linked the RA from the SAN to the roof of the LA. Between the LA and the RA, the BB wraps between the superior vena cava and the left ventricular outflow tract (LVOT). A higher CV of 2.25 m s^{-1} with an off-axis value of 0.8 m s^{-1} assigned within this region (Nagel et al., 2021). A pathway on the rim of the foramen ovale (Fossa Ovalis (FO)-RIM) was also included on the atrial septum. Additional structures of the SAN block (SAN-B), the pectinate muscles (PMs), and the CT were included, but assigned default EP in accordance with the atrial myocardium.

2.2.3 Cellular electrophysiology and ventricular repolarization

With the aim of keeping simulation times compatible with real-time scales, cellular EP dictating action potential morphology was defined using the Mitchell-Schaeffer phenomenological model within the entirety of the heart (Mitchell and Schaeffer, 2003). This is motivated by the fact that ECG morphology is governed by the spatio-temporal distribution of cardiac electrical sources, which is essentially determined by the CV of travelling depolarization wavefronts and the intrinsic duration of the action potential at a given location in the heart. The Mitchell-Schaeffer model was tuned to the more physiologically detailed Ten-Tusscher model (ten Tusscher et al., 2004; Gillette et al., 2021a). Resulting base parameter values of ν_{gate}, τ_{close}, τ_{in}, and τ_{out} were respectively 0.13, 175.0, 0.3, and 5.4. A prescribed resting membrane potential of −86.2 mV and a peak potential of 40 mV were applied.

To establish a physiological T-wave, gradients in the activation recovery intervals (ARIs) across the ventricles were computed assuming a linear mapping with the Eikonal activation map AT($\mathbf{x}$) dictated by ventricular EP,

$$\mathrm{ARI}(\mathbf{x}) = m \cdot \mathrm{AT}(\mathbf{x}) + b. \tag{1}$$

The Eikonal activation sequence of only the ventricles was therefore precomputed using the tuned HPS. To compute ARI, a slope of $m = -0.66$ was then used according to (Opthof et al., 2009) and intersect value of $b = 215$ ms was chosen based on the ST interval manually extracted from the measured 12 lead ECG of the subject.

The ARI must then be prescribed using variations in ionic model parameters. The τ_{close} parameter of the Mitchell-Schaeffer ionic model primarily dictates maximal action potential duration (APD_{max}), a surrogate for the ARI. A relationship between τ_{close} and APD_{max} is derived from Eq. (13) in (Mitchell and Schaeffer, 2003), such that

$$\tau_{\text{close}}(\mathbf{x}) = \frac{\text{APD}_{\text{max}}(\mathbf{x})}{\ln\left(4\frac{\tau_{\text{in}}}{\tau_{\text{out}}}\right)} \approx \frac{\mathrm{ARI}(\mathbf{x})}{\ln\left(4\frac{\tau_{\text{in}}}{\tau_{\text{out}}}\right)}. \tag{2}$$

2.2.4 Atrio-ventricular conduction

Atria and ventricles were separated at the base by nodal splitting (Costa et al., 2014) to enforce electrical isolation of the intracellular space. Atrio-ventricular conduction was then mediated by a ventricular conduction system comprising an AVN and a HPS. A topologically simple 1D model of an AVN

was incorporated and electrically connected to tissue in the basal RA. CV within the AVN was determined to obtain a physiological PR interval of 200 ms matching the subject's 12 lead ECG. The CV within the AVN was tuned to a value of 0.07 m s^{-1} to delay the onset of ventricular activation (Efimov et al., 2004). The fast and slow conducting pathways of the AVN were not accounted for. The distal exit of the AVN was connected to the His bundle, mediating propagation into fascicles and Purkinje network. This model of atrial-ventricular conduction facilitates bidirectional electrical conduction across the atrio-ventricular base.

2.2.5 Torso volume conductor model

The lungs, blood pools, and general tissue in the torso volume conductor were set according to 0.0389 S m^{-1}, 0.7 S m^{-1}, and 0.22 S m^{-1}, respectively (Keller et al., 2010). Both the trunk of the aorta and the right ventricular outflow track (RVOT) were integrated into the general torso tissue and electrically inhibited. Electrode placements corresponding to the measured 12 lead ECG were localized to nodes on the torso surface.

2.3 Bundle branch block

Disease pathologies of left bundle branch block (LBBB) and right bundle branch block (RBBB) were modeled alongside sinus rhythm under two different CV setups. In both setups, the respective branch of the HPS was inhibited to cause a complete branch block in each case. First, the standard myocardial CV settings were used. As BBBs often cause underlying structural changes or result in cardiac remodelling (i.e. dilation in dyssynchrony) altering activation and conduction within myocardial tissue (Vernooy et al., 2005; Breithardt and Breithardt, 2012; Valenti et al., 2012; Michalski et al., 2022), the longitudinal CV was then reduced to 0.3 m s^{-1} within the affected ventricle while maintaining off-axis ratios. In both conditions, all other EP was assumed to be the same as under sinus rhythm.

2.4 Cardiac simulation

Cardiac sources and the potentials at every electrode position for the 12 lead ECG were simulated using the reaction-Eikonal method and lead fields implemented within *CARPentry* (Vigmond et al., 2008; Neic et al., 2017; Potse, 2018; Gillette et al., 2021a). The right leg (RL) electrode was prescribed as an electrical ground for computation. Lead fields were precomputed once for the model and utilized in every pathological simulation. Simulations were conducted for a single heart beat assumed to last 700 ms, in agreement with the subject's heart rate. A desktop machine with 8 cores was utilized. All simulated ECGs were filtered with a 150 Hz low-pass filter and a high-pass filter of 0.5 Hz to correspond to the measured 12 lead ECG (Kligfield et al., 2007). Note that the 12 lead ECGs are represented in the rotational-axis view.

The reaction-Eikonal simulations were also run in pseudo-bidomain mode to compute extracellular potential fields throughout the heart and torso needed for EAMs. The pseudo-bidomain simulation method, described in great detail elsewhere (Bishop and Plank, 2011; Neic et al., 2017), couples an augmented monodomain model with the elliptic portion of the bidomain model to achieve faster computation of potentials within a bounded simulation domain such as the torso. Speedup is achieved as the elliptic portion is only solved at infrequent time instances dictated by the desired temporal frequency of the electrical signal.

2.5 ECG analysis

The 12 lead ECG during sinus rhythm was compared against the measured signal of the subject. For this purpose, the measured signal of 10 s was split into the individual beats by identifying the QRS peaks on lead I and aligning them using a simple thresholding value of 0.2 mV. This allowed us to compute the statistical mean beat against which we compared the simulated ECG. The loss metrics of average L2-norm and the average Pearson correlation coefficient (correlation coefficient (CC)) across all leads in the 12 lead ECG were computed between simulated and mean signals to give an indication of the overall agreement in the signals achieved from the personalization. Scaling of 0.32 is performed to align the signals in terms of amplitude (Gillette et al., 2021a). As no recordings of LBBB and RBBB were available for the healthy subject, QRS duration was computed and the signals were analyzed for standard clinical recommendations set by the American Heart Association for complete LBBB and complete RBBB as reported in (Surawicz et al., 2009). The same scaling is applied under these conditions.

3 Results

3.1 Workflow performance

All anatomical entities facilitating cardiac EP could be integrated using abstract reference frames (Figure 1). Due to such high automation in model construction and use of an efficient simulator for cardiac EP, a single human heart beat could therefore be simulated in around 2 min on a desktop machine with 8 cores. Pure model construction time amounted to around 1.5 min, with 9 s denoted to mapping of repolarization heterogeneity and 70 s denoted to

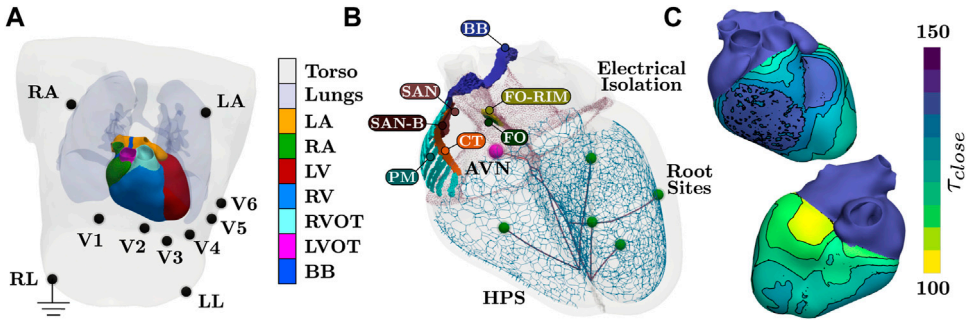

FIGURE 1
Setup of the torso and whole heart EP simulations. **(A)** Tissue labels present within the model. Blood pools within the heart are not visualized. All electrodes for 12 lead ECG are recovered from the MRI image of the subject, with RL electrode serving as electrical ground. **(B)** Anatomical structures pertaining to cardiac EP. Structures of SAN block (SAN-B), pectinate muscles (PM), and CT are assigned generic EP. The AVN and the SAN facilitate activation, where the BB is assigned a higher CV to facilite coordinate activation of the atria. Each terminal cable before a root site is applied a different CV to control activation timings of the fascicles of the HPS. **(C)** Prescribed τ_{close} parameters of the Mitchell-Schaeffer model needed to facilitate a physiological T-wave. Values within the ventricles are computed from the Eikonal activation map. Both atrial tissues and the HPS are assigned the maximal value. Isolines and binning of the color bar indicates 5 ms.

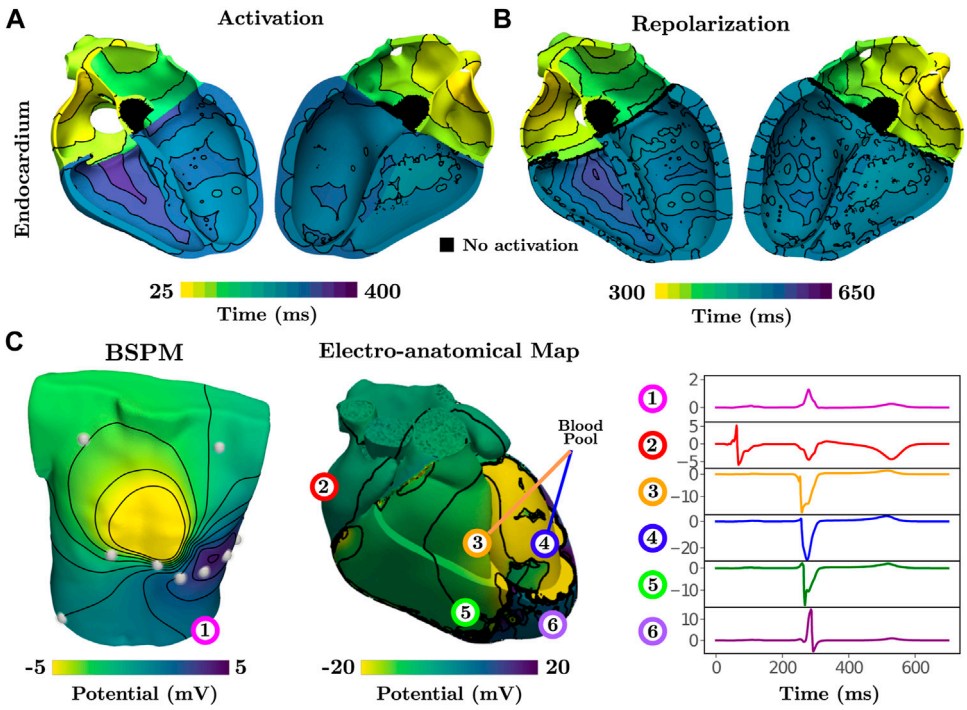

FIGURE 2
Activation and repolarization patterns during normal sinus rhythm underlying simulated ECGi information of BSPMs and EGMs. **(A)** Activation initiates from fascicular root sites and spreads into the fast-conducting Purkinje network. Latest activation is seen on the posterior RV free wall. **(B)** Repolarization is linearly dependent on activation, thus exhibiting a similar pattern. **(C)** The BSPM and EAM are visualized at a time point of 275 ms. Electrical potentials at 6 recording locations on the torso, on the epicardium, and in the blood pool next to the endocardium are shown for the single heart beat.

construction of the HPS including fascicular CV tuning to keep activation timing optimal at root sites. The remaining model construction time was allocated general setup time. In terms of simulation, computation of all lead fields required a one-time computational cost of around 72 s. Subsequent simulation using the reaction-Eikonal method with the lead fields

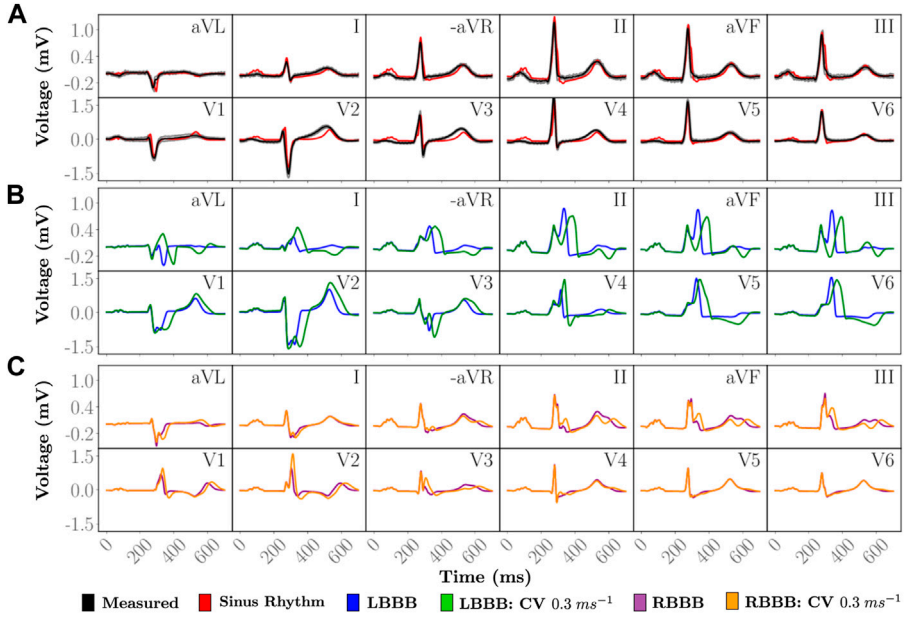

FIGURE 3
Simulated 12 lead ECGs of a single heartbeat. **(A)** The personalized heartbeat (red) during normal sinus rhythm is compared to an average heart beat in the measured data (black). Gray indicates 2 standard deviations from the average measured signal. Disease pathologies of **(B)** LBBB and **(C)** RBBB are compared to the simulated 12 lead ECG under sinus rhythm. The simulated and measured signals under sinus rhythm have a QRS duration of 85 ms. Simulated LBBB ECGs have QRS durations of 127 and 178 ms with a ...longitudinal CV of 0.6 m/s and 0.3 m/s, respectively, within the LV. Simulated RBBB ECGs have QRS durations of 121 and 148 ms with a longitudinal CV of 0.6 m/s and 0.3 m/s, respectively, within the RV.

required approximately 30 s with 10 s purely for mesh IO. Running in pseudo-bidomain mode to recover extracellular potential fields needed for construction of EAMs led to an increased simulation time of 35 min.

3.2 Whole heart electrophysiology under sinus rhythm

Activation of the atria is initiated at the SAN and spreads from the RA to the LA. Inter-atrial conduction within the model is predominately dictated by the BB that leads to earlier conduction on the LA roof. Latest activation is observed in the left-atrial appendage and within the LA just above the base at the LV free wall. Synchronous activation of the LV and RV then ensues due to rapid breakthrough of the fascicles with the myocardium stemming from the root locations. Latest activation occurs on the posterior RV wall due to a lack of Purkinje network within this region (Figure 1B), which is in agreement with reported physiology (Durrer et al., 1970). Due to the dependence of repolarization on activation, similar patterns are observed albeit an inverse relationship (Figure 2B).

Electrical potentials in the form of EGMs reveal the underlying cardiac electrical sources and temporal time sequence when an activation wave-front passes by a given region within the heart. Electrical potentials can also be recovered within the entirety of the model, including on the blood pool and torso surface, to generate information for ECGi, namely BSPMs and EAMs (Figure 2) to replicate all clinically observable EP data.

Close agreement between simulated and measured ECGs across all 12 leads is attained (Figure 3A). The personalized signal resulted in an average L2-norm difference of 0.08 and a CC of 0.89. Visually, only very minor discrepancies are observed such as the onset of the T-wave in lead V2 or a less pronounced R progression in the precordial leads.

3.3 Manifestation of bundle branch block

Within all cases of BBB, atrial SAN driven activation and associated P-wave remained unaltered. Morphological differences within the 12 lead ECG from normal sinus rhythm (Figure 3) therefore predominantly arise from asynchronous activation of the ventricles as can be observed within the time-course of transmembrane voltages for every pathology (Figure 4). Videos of cellular membrane voltage for both healthy sinus rhythm and BBBs at different CVs are provided that demonstrate the spread of the activation and repolarization wavefronts within the heart. Every video has a temporal rate of 25 frames per second with a total of 700 frames, thus lasting a total

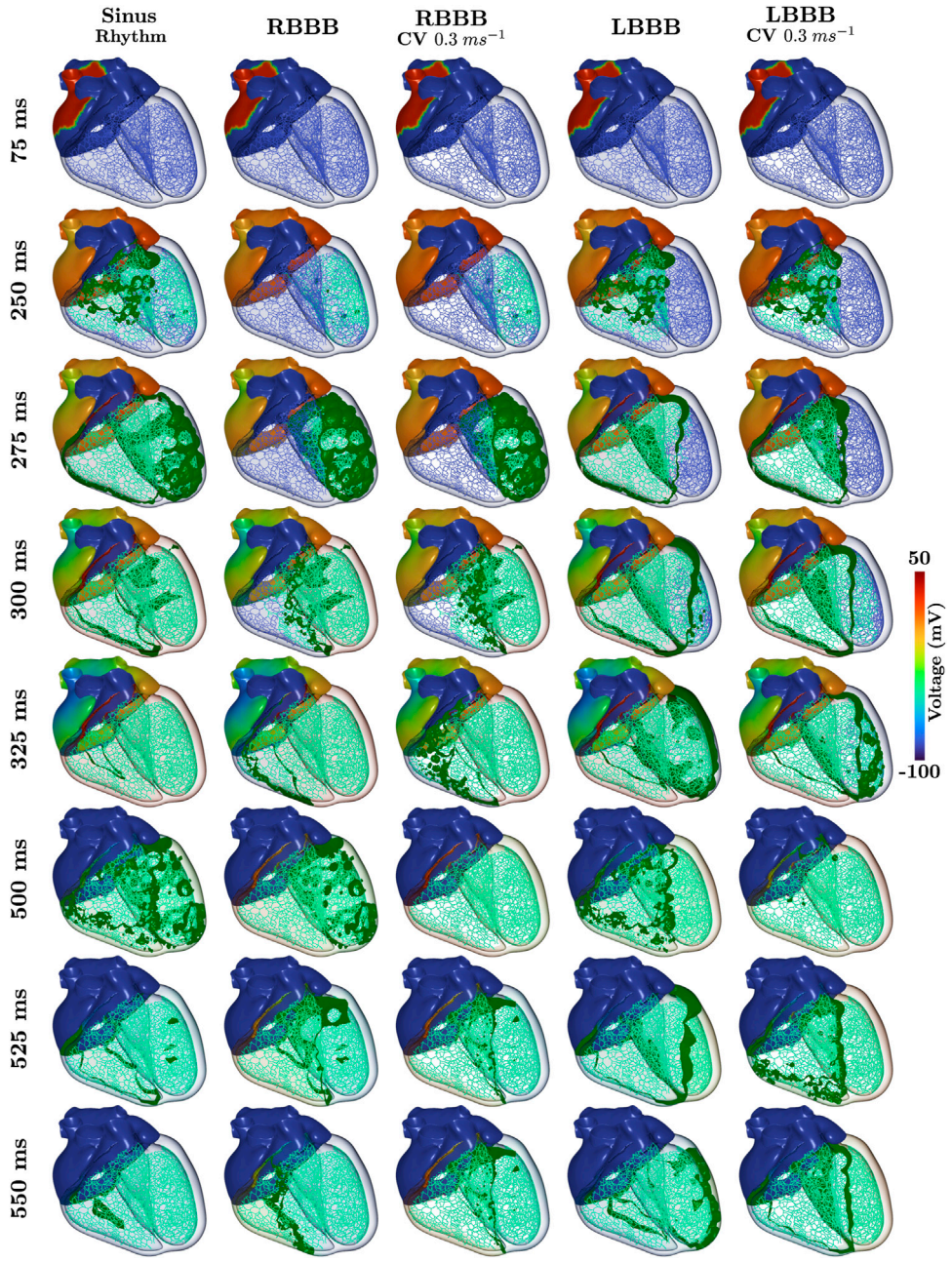

FIGURE 4
Time-course of the transmembrane voltage within the heart for sinus rhythm and BBBs with both normal and halfed CV in the respective affected ventricle. Green isosurfaces within the ventricles correspond to a membrane voltage of −40 mV and the color map corresponds to the atrial trans-membrane voltages.

of 28.0 s. These videos correspond to Figure 4 within the main text. Corresponding full videos of the membrane voltage through the heart beat are included in the Supplementary Material. While underlying cardiac electrical sources are only shown under sinus rhythm, the same information is available across all pathologies. Standard empirical ECG diagnostics (Surawicz et al., 2009) under complete BBB were used as a metric to gauge the fidelity of the model under disease conditions.

3.3.1 Left bundle branch block

All propagation into the left bundle branch was interrupted to generate a complete LBBB. Activation of the ventricles

therefore initiates from the RV. Retrograde activation of the left bundle branch and associated HPS led to a significantly slower activation of the LV as compared to sinus under both CV settings (see 275 ms panels in Figure 4). Apparent morphological features in the 12 lead ECG meet all clinical diagnostic criteria of a LBBB (Figure 3B), and are exaggerated by a reduction in CV within the LV. A prolonged QRS duration of 150 ms (> 120 ms) is attained under LBBB with normal CV that is extended to 195 ms with reduced CV. A deep and broad S with a notch resembling a "W" in leads V1 and V2 and a completely positive and notched R-wave in leads V5 and V6 is also observed. Furthermore, leads I and aVL appear similar to leads V5 and V6. During repolarization, T-wave inversion and ST-segment depression in leads V5, V6, I and aVL in contrast to ST-segment elevation and positive T-waves in leads V1-V3 is also observed.

3.3.2 Right bundle branch block

RBBB was initiated by inhibiting propagation of the right bundle branch of the HPS. Activation within the RV was therefore facilitated by a retrograde activation of the HPS and general myocardial tissues that passes from the LV through the septum (see 300 ms panels in Figure 4). This activation pattern is manifested within the 12 lead ECG (Figure 3C) by a monophasic R in leads V1 and V2, slight slurring of S waves in leads aVL and I, and a QRS duration of 150.0 ms (> 120 ms). With lowered CV within the RV, an inversion in the T-wave in leads V1 and V2 becomes more drastic, as well as an increasing amount of fractionation is observed in leads II, aVL, and III. QRS duration is also extended to 180 ms under reduced CV conditions.

4 Discussion

This study reports on the development of a novel torso and whole heart model of EP that is able to compute EGMs and ECGs with real-time performance, thus mitigating typical costs associated with *in silico* EP studies. Anatomically and structurally accurate representations of atria and ventricles were used, which were electrically isolated at the base. A topologically realistic cardiac conduction system was incorporated to electrically connect atria and ventricles, thus mediating bidirectional atrio-ventricular conduction. Personalization of the model was based primarily on the recorded ECG, as well as some experimental and clinical measurements. This novel virtual technology of the whole heart thus constitutes a fully mechanistic model of whole heart EP.

As most current virtual heart technologies reported in the literature do not relate simulated EP to clinically observable data, our novel virtual heart technology constitutes an important advancement towards clinical and industrial *in silico* applications in terms of model fidelity (Viceconti et al., 2016). Mechanistic completeness is demonstrated by modeling two pathologies of the cardiac conduction system, LBBB and RBBB, the model was not parameterized for. Our model is able to replicate intricate morphological features of the 12 lead ECG during both normal sinus rhythm, as well as during LBBB and RBBB according to standard clinical guidelines (Figure 3). The underlying cardiac EP of the given subject must therefore be accounted for to a great extent (Figure 3A). We were able to replicate observable data under sinus rhythm with high fidelity and meet all clinical criteria under BBB, thus building an important foundation for future use of cardiac digital twins (Corral-Acero et al., 2020).

Our methodology of personalizing cardiac digital twins under sinus rhythm and then adapting the model to disease condition could have important implications for predictive and preemptive medicine. The mechanistic completeness endows the model with predictive capabilities, that is, the model can be used under scenarios to which it was not calibrated for, without the need of model re-fitting. Further, model predictions are testable and can be validated by comparing directly to both non-invasive data acquired in clinical routine, or invasive measurements as acquired during an intervention. These capabilities combined facilitate the generation of high fidelity digital twin hearts from a physical patient, open new perspectives in industry, e.g. in the development of device therapies, and in the clinic, for advanced model-based clinical data analysis to support diagnosis, and predictive modeling for planning of optimal therapies.

4.1 Workflow performance

Personalization of parameters relating to the QRS complex was previously performed on the simpler BiV model assuming a fasicular-based representation of the His-Purkinje system embedded in a fast-conducting sub-endocardial layer well-suited for efficient simulations at large scale. Extending this representation to the whole heart model, necessary for modeling various disease pathologies, was entirely automatic and required an additional construction time of only 1.5 min. Extension included construction of a detailed His-Purkinje system modulating the same personalized activation pattern under sinus rhythm, and inclusion of the parameters dictating atrial electrophysiology.

In general, lightweight and efficient simulation models are needed to render whole heart simulations tractable and clinically relevant. Simulations of cardiac sources for a single heart beat using the reaction-Eikonal method with lead fields were computationally inexpensive. Recovery of 12 lead ECGs was possible in around 30 s after precomputation of the lead fields requiring approximately 1.5 min. Body surface potential maps and electro-anatomical maps, as well as cardiac sources, needed in various clinical applications, could be computed using reaction-Eikonal in pseudo-bidomain mode in approximately 35 min on a normal desktop machine with 8 cores. Validation of the underlying simulation in previous work reported in Gillette

et al., 2021 (Gillette et al., 2021a) showed that ECGs acquired using the reaction-Eikonal method paired with lead fields gave comparable ECG morphologies to a traditional high-resolution, full bidomain simulation at a fraction of the costs. Such fine-detailed full bidomain simulations on even a simpler bi-ventricular setup without a physiologically-detailed His-Purkinje system lasting only 150 ms, required 30 min min on a HPC with 240 computing cores to compute both cardiac sources and potentials used to generate the same 12 lead ECG (Gillette et al., 2021a).

4.2 Clinical ECG interpretation

The ECG during sinus rhythm was assessed by making a comparison with the ECG measured from the healthy subject. Close correspondence between the measured and simulated 12 lead ECG could be obtained under normal sinus conditions. As pathological ECGs were not available for healthy volunteer subject, the effect of conduction disturbances, specifically, LBBB and RBBB, was assessed to ascertain the model's mechanistic completeness. It was demonstrated that all relevant clinical morphological features manifest in the ECG consistent with clinical ECG diagnostic criteria.

4.2.1 Sinus rhythm

The simulated ECGs under sinus rhythm matched the recorded ECG with high fidelity. A very close agreement in ECG morphology across all 12 lead could be attained (Figure 3A) in terms of the averaged L2-norm of 0.08 and CC of 0.89, with all complexes matching in terms of polarity and shape. In the simulated healthy ECG known features manifest such as R-wave progression or the S-wave disappearing between leads V3 to V4. Nonetheless, minor discrepancies are also witnessed that provide hints towards missing features of the model or sub-optimal model parameterization. Overall, QRS morphology is well captured, but R-progression in the precordial leads is slower, with R peaking in V5, not in V4. More striking discrepancies relate to ST-segment and T-wave. Modelled ST-segments differ from clinical ones largely in their slope that is close to zero over prolonged periods. This is less the case with measured ST-segments where a non-zero slope early after QRS initiates a smooth transition to the T-wave. Similarly, the T-wave in the precordial leads features a spikier morphology, with sharper deflections as compared to the ECG.

Discrepancies are anticipated to some extent due to a number of factors. These comprise technological factors related to ECG acquisition such as anatomical uncertainties due to breathing, electrode placement, and signal processing in terms of noise. Modeling factors related to the choice of action potential shape, tissue conductivities, and neglect of structures such as bones, muscle or skin) may also play a role. Finally, the measurement of similarity between ECGs is influenced by the scaling applied (Gillette et al., 2021a). The flat slope of the ST-segment is likely to be related to the Mitchell-Schaeffer model used to model the action potential that lacks features such as early repolarization or a spike-and-dome morphology. In absence of these features, during the plateau phase there is no change in transmembrane voltage, thus minimizing the dynamics of any gradients that could contribute towards an ST-segment slope.

4.2.2 Left bundle branch block

Interrupting the left bundle branch innervating all fascicles in the LV altered the ECG, leading to a morphology that was consistent with all empirically-based standard clinical diagnostic criteria. With LBBB alone, most diagnostic hallmark features could be identified in the simulated ECG, albeit some were borderline. For instance, QRS was prolonged to ≈120 ms, but not beyond to >120 ms, as anticipated from a full block of the entire left bundle branch. However, diagnostic criteria are built upon empirical observations from patients suffering from LBBB over prolonged periods of time, not from perfectly healthy subjects with a sudden acutely occurring LBBB, as simulated in this model. Such a persistent ventricular electrical dyssynchrony, associated with changes in electrical activation and repolarization patterns that impairs mechanical performance, triggers downstream remodelling processes (Vernooy et al., 2005; Valenti et al., 2012; Michalski et al., 2022) which may lead to alterations in anatomical shape, size and morphology, in structural changes related to fiber and sheet arrangement and fibrosis, and functional changes in EP affecting action potential shape and duration. These factors combined contribute to clinical LBBB ECGs, but have not been considered.

4.2.3 Right bundle branch block

Similarly to LBBB, interrupting the right bundle branch led to an ECG morphology that was mostly consistent with the ECG criteria for diagnosing RBBB, albeit to a lesser degree than LBBB. In the RBBB case not all diagnostic features manifested after acutely blocking the right bundle branch. For instance, the criterion of a QRS complex in leads V1 and V2 resembling the letter M displaying a rsr', rsR' or rSR' pattern, with rSR‘ being the most common, is not readily apparent. S often does not reach baseline in V1 and V2 which is not the case either. A broad S-wave, with S being longer than R, is only observed in aVL and I, but not in V5 and V6, and S is >40 ms in I, but not in V6. Downsloping ST-segments and inverted T-waves are present in leads V1 and V2, but the shape of the T-wave is biphasic, also featuring a positive component. The leads V5, V6, aVL and I all show positive T-waves, consistent with the diagnostic criterion. These discrepancies are explained, analog to the LBBB case, by additional factors beyond the

interruption of conduction in the right bundle branch that contribute to the clinical RBBB ECG, but remain unaccounted for in the model.

4.3 Validation

Validation of the cardiac sources under all conditions is required. Comparison between the simulated and measured 12 lead ECG signal was only made against the statistical mean beat recorded over 10 s which slightly differs as indicated in Figure 3A. As the inverse problem of cardiac EP is ill-posed, different activation sequences might produce the same ECG. That is, the observation that the computed ECG under a sinus activation replicates the measured ECG of the subject with remarkable fidelity suggests a close relationship in EP between virtual and physical heart, but does not imply that the EP must be the same.

Furthermore, predictive capabilities were only illustrated by assessing the effect of a complete bundle branch block in the virtual heart of a healthy subject according to standard diagnostic criteria as such data cannot be acquired from healthy volunteers. Simulating a wider range of activation sequences under pathologies such as bundle branch blocks that activate the HPS differently, with a fusion of orthodromic and antidromic conduction, is thus required to better interrogate fascicular and network structure of the HPS. While BBB was explored under two different conduction velocity settings, accounting for ventricular hypertrophy, dilation, and remodeling must be explored to better understand the capabilities of the model, as seen in (Galeotti et al., 2013). Simulation of either Wolff-Parkinson-White syndrome or premature ventricular contractions leading to retrograde activation, for example, could also provide valuable insight.

A thorough clinical validation of our model should be performed in patients to better understand the ability to replicate the underlying EP. For example, in patients undergoing His-optimized (HOT) cardiac resynchronization therapy (CRT), a broader range of activation sequences is initiated during implantation, including RV and LV pacing as well as selective or non-selective His and left bundle branch pacing. Such validation is beyond the scope of this study, but digital twin modeling has the potential to revolutionize cardiac resynchronisation therapy by predicting activation patterns, as well as hemodynamics, under different pacing strategies before implantation which would facilitate response-prediction for such costly therapies.

A general limitation of clinical data, however, is related to the inability to observe electrical signals throughout the 3D myocardial muscle. Observations of electrical phenomenon are limited on specific manifolds, such as the body surface or the endocardia where EAMs of relatively high spatio-temporal resolution are recorded during routine clinical mapping procedures. More rigorous experimental validation to determine if the underlying EP is truly representative of the patient could be built on experimental animal studies that acquire electrical data invasively in 3D, throughout the myocardial walls, under a range of induced activation sequences as previously mentioned. Such invasive experimental studies offer a means to record within the entirety of the mammalian heart (Cluitmans et al., 2018; Zenger et al., 2020), and comparison of EGMs could reveal whether the underlying cardiac EP sufficiently approximates the mechanisms within the heart.

Furthermore, as the reported virtual technology of whole heart EP is only personalized for a single subject, however, further validation is required to ensure that the technique for generating a personalized model of cardiac EP is possible in additional subjects. This is particularly important for the generation of model cohorts that could be used for the applications of device development and clinical trials on larger patient groups. Ensuring underlying parameters are capable of representing variation in the patient population is therefore crucial and can be conducted by comparing simulation outputs against databases of 12 lead ECGs such as the publicly available PTB-XL dataset (Wagner et al., 2020). Global sensitivity analysis would also yield valuable information on the relationship between morphological elements in the 12 lead ECG and the input parameter space detailing cardiac EP.

4.4 Personalization of cardiac electrophysiology

Simulated physiology correlates closely to the physical reality within the signal subject based on the 12 lead ECG due to model personalization and fitting. Primarily, parameters relating to the location and initiation time of the fascicular sites of the His-Purkinje system had been previously personalized and shown to give improvement within the QRS complex in the 12 lead ECG over an initial fascicular setup (Gillette et al., 2021a). Comparison in activation sequences revealed the underlying differences in the 12 lead ECG were negligible when extending to a more sophisticated representation of the His-Purkinje system used in the study (Gillette et al., 2021b). Various parameters could be tuned using metrics directly taken from the measured 12 lead ECG Namely, the CV of the atrio-ventricular (AV) node, as well as the intersect parameter during ARI mapping for repolarization, could be extracted using the PR and QT intervals, respectively.

Several limitations still exist within this study in terms of modeling personalized cardiac EP, however, as many parameters were assigned based on physiological measurements. Primarily, little personalization of the parameters dictating atrial EP was performed. Locations of the AVN, SAN and atrial structures such as BB were not known within the subject, but were instead generically assigned based on physiological assumptions.

Further, the actual architecture and branching of the HPS is not known and was thus assigned generically. In theory, variation in CV with the branches as detailed in 2.2.1 should indirectly account for differing branching properties that may influence activation breakthrough. Many other components dictating ventricular activation, such as fibers, conductivities, and conduction velocities were also assigned generic values. Regarding the T-wave, the linear slope of the ARI mapping was taken from reported values (Opthof et al., 2009) and the general technique may only be applicable when information on the sinus ECG is available.

Data availability statement

Original contributions presented in the study are summarized in the article. Due to constraints of the IRB approval and subject consent, the ventriculartorso model is not publicly available. The simulation of electrophysiology can be replicated using various tools and simulation code available publicly as part of the open-source *openCARP* simulation framework. Further inquiries about previous work and model availability can be directed to the corresponding author.

Author contributions

KG was involved in all primary research including data acquisition, running simulations, mesh generation and manipulation, and all components associated with manuscript drafting. MAFG preformed aspects relating to the model generation and parameterisation, including various tools needed to automate the pipeline of fiber assignment and reference frame generation. He was also involved in manuscript drafting. MS provided the idea and general implementation of the CV tuning within the HPS. TG processed and filtered the ECGs, performed the loss comparison between the ECGs, and was involved in manuscript drafting. AN meshed and corrected the underlying anatomy after initial segmentation. MM and DS gave clinical guidance and feedback by interpreting the 12 lead ECGs and giving insight into the underlying anatomical and electrical basis for the manifestations of the modeled conditions. CHR laid the ground work, and provided guidance, for fiber generation within the atria. AJP contributed to the pipeline construction for the simulations. CMA participated in funding acquisition, as well as manuscript writing and reviewing. EJV provided the initial code for the HPS that was adapted and improved upon within this study and provided feedback on parameter alterations needed for modeling concordant atrial EP. GP served as a primary supervisor over all aspects of the work and manuscript drafting.

Funding

This research was supported by funds received from BioTechMed-Graz under the ILearnHeart Flagship Project and under grant I2760-B30 from the Austrian Science Fund to GP. This project conducted under MedalCare 18HLT07 has received funding from the EMPIR programme co-financed by the Participating States and from the European Union's Horizon 2020 research and innovation programme. This research has also received funding from the European Union's Horizon 2020 research and innovation programme under the ERA-NET co-fund action No. 680969 (ERA-CVD SICVALVES) funded by the Austrian Science Fund (FWF), Grant I 4652-B to CMA. For the purpose of open access, the author has applied a CC BY public copyright licence to any Author Accepted Manuscript version arising from this submission. EJV received financial support from the French Government as part of the "Investments of the Future" program managed by the National Research Agency (ANR), Grant reference ANR-10-IAHU-04.

Conflict of interest

This research was conducted in collaboration with the company Numericor GmbH with author affiliations of AN, EJV, GP, MAFG, and CMA. CHR provided advice on the implementation of the atrial coordinate software within Carpentry-Pro Studio software (NumeriCor Gmbh, Graz, Austria).

The remaining authors declare that the research was conducted in the absence of any commercial or financial relationships that could be construed as a potential conflict of interest.

All remaining authors declare no potential conflicts of interest.

Publisher's note

Supplementary material

The Supplementary Material for this article can be found online at: https://www.frontiersin.org/articles/10.3389/fphys.2022.907190/full#supplementary-material

SUPPLEMENTAL VIDEO S1
Normal Sinus Rhythm.

SUPPLEMENTAL VIDEO S2
Complete LBBB with a normal CV of 0.6 m/s along the longitudinal myocardial fiber orientation assigned in the LV.

SUPPLEMENTAL VIDEO S3
Complete LBBB with a reduced longitudinal CV of 0.3 m/s in the LV.

SUPPLEMENTAL VIDEO S4
Complete RBBB with a normal CV of 0.6 m/s along the longitudinal myocardial fiber orientation assigned in the RV.

SUPPLEMENTAL VIDEO S5
Complete RBBB with a reduced longitudinal CV of 0.3 m/s in the RV.

References

Abadi, E., Segars, W. P., Tsui, B. M., Kinahan, P. E., Bottenus, N., Frangi, A. F., et al. (2020). Virtual clinical trials in medical imaging: A review. *J. Med. Imaging* 7, 042805. doi:10.1117/1.JMI.7.4.042805

Ali, R. L., Hakim, J. B., Boyle, P. M., Zahid, S., Sivasambu, B., Marine, J. E., et al. (2019). Arrhythmogenic propensity of the fibrotic substrate after atrial fibrillation ablation: A longitudinal study using magnetic resonance imaging-based atrial models. *Cardiovasc. Res.* 115, 1757–1765. doi:10.1093/cvr/cvz083

Arevalo, H. J., Vadakkumpadan, F., Guallar, E., Jebb, A., Malamas, P., Wu, K. C., et al. (2016). Arrhythmia risk stratification of patients after myocardial infarction using personalized heart models. *Nat. Commun.* 7, 11437–11438. doi:10.1038/ncomms11437

Bayer, J., Prassl, A. J., Pashaei, A., Gomez, J. F., Frontera, A., Neic, A., et al. (2018). Universal ventricular coordinates: A generic framework for describing position within the heart and transferring data. *Med. Image Anal.* 45, 83–93. doi:10.1016/j.media.2018.01.005

Bayer, J. D., Blake, R. C., Plank, G., and Trayanova, N. A. (2012). A novel rule-based algorithm for assigning myocardial fiber orientation to computational heart models. *Ann. Biomed. Eng.* 40, 2243–2254. doi:10.1007/s10439-012-0593-5

Bishop, M. J., and Plank, G. (2011). Representing cardiac bidomain bath-loading effects by an augmented monodomain approach: Application to complex ventricular models. *IEEE Trans. Biomed. Eng.* 58, 1066–1075. doi:10.1109/TBME.2010.2096425

Breithardt, G., and Breithardt, O. A. (2012). Left bundle branch block, an old–new entity. *J. Cardiovasc. Transl. Res.* 5, 107–116. doi:10.1007/s12265-011-9344-5

Chetverikov, D., Svirko, D., Stepanov, D., and Krsek, P. (2002). The trimmed iterative closest point algorithm. Pattern Recognition, 2002. Proceedings. 16th International Conference on (IEEE), August 2002, Quebec City, QC, Canada, vol. 3, 545–548.

CIBC (2016). *Seg3D: Volumetric image segmentation and visualization*. [Dataset]. Scientific Computing and Imaging. Available at: http://www.seg3d.org.

Cluitmans, M., Brooks, D. H., MacLeod, R., Dössel, O., Guillem, M. S., Van Dam, P. M., et al. (2018). Validation and opportunities of electrocardiographic imaging: From technical achievements to clinical applications. *Front. Physiol.* 9, 1305. doi:10.3389/fphys.2018.01305

Corral-Acero, J., Margara, F., Marciniak, M., Rodero, C., Loncaric, F., Feng, Y., et al. (2020). The 'Digital Twin' to enable the vision of precision cardiology. *Eur. Heart J.* 41, 4556–4564. doi:10.1093/eurheartj/ehaa159

Costa, C. M., Campos, F. O., Prassl, A. J., dos Santos, R. W., Sánchez-Quintana, D., Ahammer, H., et al. (2014). An efficient finite element approach for modeling fibrotic clefts in the heart. *IEEE Trans. Biomed. Eng.* 61, 900–910. doi:10.1109/TBME.2013.2292320

Durrer, D., Van Dam, R. T., Freud, G., Janse, M., Meijler, F., and Arzbaecher, R. (1970). Total excitation of the isolated human heart. *Circulation* 41, 899–912. doi:10.1161/01.cir.41.6.899

Efimov, I. R., Nikolski, V. P., Rothenberg, F., Greener, I. D., Li, J., Dobrzynski, H., et al. (2004). Structure-function relationship in the av junction. *Anatomical Rec. Part A Discov. Mol. Cell. Evol. Biol.* 280, 952–965. An Official Publication of the American Association of Anatomists. doi:10.1002/ar.a.20108

Evans, J. J., Gilmour, R. F., Jr, and Zipes, D. P. (1984). The effects of lidocaine and quinidine on impulse propagation across the canine purkinje-muscle junction during combined hyperkalemia, hypoxia, and acidosis. *Circ. Res.* 55, 185–196. doi:10.1161/01.res.55.2.185

Galeotti, L., van Dam, P. M., Loring, Z., Chan, D., and Strauss, D. G. (2013). Evaluating strict and conventional left bundle branch block criteria using electrocardiographic simulations. *Europace* 15, 1816–1821. doi:10.1093/europace/eut132

Gerach, T., Schuler, S., Fröhlich, J., Lindner, L., Kovacheva, E., Moss, R., et al. (2021). Electro-mechanical whole-heart digital twins: A fully coupled multi-physics approach. *Mathematics* 9, 1247. doi:10.3390/math9111247

Gillette, K., Gsell, M. A., Bouyssier, J., Prassl, A. J., Neic, A., Vigmond, E. J., et al. (2021). Automated framework for the inclusion of a his–purkinje system in cardiac digital twins of ventricular electrophysiology. *Ann. Biomed. Eng.* 49, 3143–3153. doi:10.1007/s10439-021-02825-9

Gillette, K., Gsell, M. A., Prassl, A. J., Karabelas, E., Reiter, U., Reiter, G., et al. (2021). A framework for the generation of digital twins of cardiac electrophysiology from clinical 12-leads ecgs. *Med. Image Anal.* 71, 102080. doi:10.1016/j.media.2021.102080

Kassebaum, D. G., and Van Dyke, A. R. (1966). Electrophysiological effects of isoproterenol on purkinje fibers of the heart. *Circ. Res.* 19, 940–946. doi:10.1161/01.res.19.5.940

Keller, D. U., Weber, F. M., Seemann, G., and Dössel, O. (2010). Ranking the influence of tissue conductivities on forward-calculated ecgs. *IEEE Trans. Biomed. Eng.* 57, 1568–1576. doi:10.1109/TBME.2010.2046485

Kligfield, P., Gettes, L. S., Bailey, J. J., Childers, R., Deal, B. J., Hancock, E. W., et al. (2007). Recommendations for the standardization and interpretation of the electrocardiogram: Part i: The electrocardiogram and its technology a scientific statement from the American heart association electrocardiography and arrhythmias committee, council on clinical cardiology; the American college of cardiology foundation; and the heart rhythm society endorsed by the international society for computerized electrocardiology. *J. Am. Coll. Cardiol.* 49, 1109–1127. doi:10.1016/j.jacc.2007.01.024

Lopez-Perez, A., Sebastian, R., Izquierdo, M., Ruiz, R., Bishop, M., and Ferrero, J. M. (2019). Personalized cardiac computational models: From clinical data to simulation of infarct-related ventricular tachycardia. *Front. Physiol.* 10, 580. doi:10.3389/fphys.2019.00580

Michalski, B., Stankovic, I., Pagourelias, E., Ciarka, A., Aarones, M., Winter, S., et al. (2022). Relationship of mechanical dyssynchrony and lv remodeling with improvement of mitral regurgitation after crt. *JACC. Cardiovasc. Imaging* 15, 212–220. doi:10.1016/j.jcmg.2021.08.010

Mitchell, C. C., and Schaeffer, D. G. (2003). A two-current model for the dynamics of cardiac membrane. *Bull. Math. Biol.* 65, 767–793. doi:10.1016/S0092-8240(03)00041-7

Moss, R., Wülfers, E. M., Schuler, S., Loewe, A., and Seemann, G. (2021). A fully-coupled electro-mechanical whole-heart computational model: Influence of cardiac contraction on the ecg. *Front. Physiol.* 12, 778872. doi:10.3389/fphys.2021.778872

Nagel, C., Schuler, S., Dössel, O., and Loewe, A. (2021). A bi-atrial statistical shape model for large-scale *in silico* studies of human atria: Model development and application to ecg simulations. *Med. Image Anal.* 74, 102210. doi:10.1016/j.media.2021.102210

Neic, A., Campos, F. O., Prassl, A. J., Niederer, S. A., Bishop, M. J., Vigmond, E. J., et al. (2017). Efficient computation of electrograms and ecgs in human whole heart simulations using a reaction-eikonal model. *J. Comput. Phys.* 346, 191–211. doi:10.1016/j.jcp.2017.06.020

Neic, A., Gsell, M. A. F., Karabelas, E., Prassl, A. J., and Plank, G. (2020). Automating image-based mesh generation and manipulation tasks in cardiac modeling workflows using Meshtool. *SoftwareX* 11, 100454. doi:10.1016/j.softx.2020.100454

Niederer, S. A., Aboelkassem, Y., Cantwell, C. D., Corrado, C., Coveney, S., Cherry, E. M., et al. (2020). Creation and application of virtual patient cohorts of heart models: Virtual Cohorts of Heart Models. *Philos. Trans. A Math. Phys. Eng. Sci.* 378, 20190558. doi:10.1098/rsta.2019.0558

Opthof, T., Coronel, R., and Janse, M. J. (2009). Is there a significant transmural gradient in repolarization time in the intact heart? Repolarization gradients in the intact heart. *Circ. Arrhythm. Electrophysiol.* 2, 89–96. doi:10.1161/CIRCEP.108.825356

Payer, C., Štern, D., Bischof, H., and Urschler, M. (2018). "Multi-label whole heart segmentation using anatomical label configurations and cnns," in International workshop on statistical atlases and computational models of the heart. Springer, 190–198.

Plank, G., Loewe, A., Neic, A., Augustin, C., Gsell, M. A. F., Karabelas, E., et al. (2021). The openCARP simulation environment for cardiac electrophysiology. *Comput. Methods Prog. Biomed.* 208, 106223.

Potse, M. (2018). Scalable and accurate ecg simulation for reaction-diffusion models of the human heart. *Front. Physiol.* 9, 370. doi:10.3389/fphys.2018.00370

Roberts, D. E., and Scher, A. M. (1982). Effect of tissue anisotropy on extracellular potential fields in canine myocardium *in situ*. *Circ. Res.* 50, 342–351. doi:10.1161/01.res.50.3.342

Roney, C. H., Bendikas, R., Pashakhanloo, F., Corrado, C., Vigmond, E. J., McVeigh, E. R., et al. (2021). Constructing a human atrial fibre atlas. *Ann. Biomed. Eng.* 49, 233–250. doi:10.1007/s10439-020-02525-w

Roney, C. H., Pashaei, A., Meo, M., Dubois, R., Boyle, P. M., Trayanova, N. A., et al. (2019). Universal atrial coordinates applied to visualisation, registration and construction of patient specific meshes. *Med. Image Anal.* 55, 65–75. doi:10.1016/j.media.2019.04.004

Roney, C. H., Sim, I., Yu, J., Beach, M., Mehta, A., Alonso Solis-Lemus, J., et al. (2022). Predicting atrial fibrillation recurrence by combining population data and virtual cohorts of patient-specific left atrial models. *Circ. Arrhythm. Electrophysiol.* 15, e010253. doi:10.1161/CIRCEP.121.010253

Sharma, P. S., and Vijayaraman, P. (2021). Conduction system pacing for cardiac resynchronisation. *Arrhythm. Electrophysiol. Rev.* 10, 51–58. doi:10.15420/aer.2020.45

Streeter, D. D., Jr, Spotnitz, H. M., Patel, D. P., Ross, J., Jr, and Sonnenblick, E. H. (1969). Fiber orientation in the canine left ventricle during diastole and systole. *Circ. Res.* 24, 339–347. doi:10.1161/01.res.24.3.339

Strocchi, M., Augustin, C. M., Gsell, M. A., Karabelas, E., Neic, A., Gillette, K., et al. (2020). A publicly available virtual cohort of four-chamber heart meshes for cardiac electro-mechanics simulations. *PloS one* 15, e0235145. doi:10.1371/journal.pone.0235145

Surawicz, B., Childers, R., Deal, B. J., Gettes, L. S., Bailey, J. J., Gorgels, A., et al. (2009). Aha/accf/hrs recommendations for the standardization and interpretation of the electrocardiogram: Part iii: Intraventricular conduction disturbances a scientific statement from the American heart association electrocardiography and arrhythmias committee, council on clinical cardiology; the American college of cardiology foundation; and the heart rhythm society endorsed by the international society for computerized electrocardiology. *J. Am. Coll. Cardiol.* 53, 976–981. doi:10.1016/j.jacc.2008.12.013

Taggart, P., Sutton, P. M., Opthof, T., Coronel, R., Trimlett, R., Pugsley, W., et al. (2000). Inhomogeneous transmural conduction during early ischaemia in patients with coronary artery disease. *J. Mol. Cell. Cardiol.* 32, 621–630. doi:10.1006/jmcc.2000.1105

ten Tusscher, K. H., Noble, D., Noble, P. J., and Panfilov, A. V. (2004). A model for human ventricular tissue. *Am. J. Physiol. Heart Circ. Physiol.* 286, H1573–H1589. doi:10.1152/ajpheart.00794.2003

Valenti, V., Zia, M. I., Supariwala, A., Shubayev, L., Edelstein, S., Levin, M., et al. (2012). The differential impact of intraventricular and interventricular dyssynchrony on left ventricular remodeling and function in patients with isolated left bundle branch block. *J. Cardiovasc. Magn. Reson.* 14, Suppl. 1–P149. doi:10.1186/1532-429x-14-s1-p149

Vernooy, K., Verbeek, X. A., Peschar, M., Crijns, H. J., Arts, T., Cornelussen, R. N., et al. (2005). Left bundle branch block induces ventricular remodelling and functional septal hypoperfusion. *Eur. Heart J.* 26, 91–98. doi:10.1093/eurheartj/ehi008

Viceconti, M., Henney, A., and Morley-Fletcher, E. (2016). *In silico* clinical trials: How computer simulation will transform the biomedical industry. *Int. J. Clin. Trials* 3, 37. doi:10.18203/2349-3259.ijct20161408

Vigmond, E., Dos Santos, R. W., Prassl, A., Deo, M., and Plank, G. (2008). Solvers for the cardiac bidomain equations. *Prog. Biophys. Mol. Biol.* 96, 3–18. doi:10.1016/j.pbiomolbio.2007.07.012

Wagner, P., Strodthoff, N., Bousseljot, R. D., Kreiseler, D., Lunze, F. I., Samek, W., et al. (2020). PTB-XL, a large publicly available electrocardiography dataset. *Sci. Data* 7, 154. doi:10.1038/s41597-020-0495-6

Zenger, B., Good, W. W., Bergquist, J. A., Burton, B. M., Tate, J. D., Berkenbile, L., et al. (2020). Novel experimental model for studying the spatiotemporal electrical signature of acute myocardial ischemia: A translational platform. *Physiol. Meas.* 41, 015002. doi:10.1088/1361-6579/ab64b9

frontiers | Frontiers in Physiology

TYPE Original Research
PUBLISHED 08 November 2022
DOI 10.3389/fphys.2022.1030307

OPEN ACCESS

EDITED BY
Matthijs Cluitmans,
Maastricht University, Netherlands

REVIEWED BY
Tiantian Wang,
Maastricht University, Netherlands
Rafael Sebastian,
University of Valencia, Spain
João Salinet,
Federal University of ABC, Brazil

*CORRESPONDENCE
Cuiwei Yang,
yangcw@fudan.edu.cn

SPECIALTY SECTION
This article was submitted to Cardiac Electrophysiology,
a section of the journal
Frontiers in Physiology

RECEIVED 28 August 2022
ACCEPTED 20 October 2022
PUBLISHED 08 November 2022

CITATION
Zhong G, Feng X, Yuan H and Yang C (2022), A 3D-CNN with temporal-attention block to predict the recurrence of atrial fibrillation based on body-surface potential mapping signals. *Front. Physiol.* 13:1030307. doi: 10.3389/fphys.2022.1030307

A 3D-CNN with temporal-attention block to predict the recurrence of atrial fibrillation based on body-surface potential mapping signals

Gaoyan Zhong[1], Xujian Feng[1], Han Yuan[1] and Cuiwei Yang[1,2]*

[1]The Center for Biomedical Engineering, School of Information Science and Technology, Fudan University, Shanghai, China, [2]Key Laboratory of Medical Imaging Computing and Computer Assisted Intervention of Shanghai, Fudan University, Shanghai, China

Catheter ablation has become an important treatment for atrial fibrillation (AF), but its recurrence rate is still high. The aim of this study was to predict AF recurrence using a three-dimensional (3D) network model based on body-surface potential mapping signals (BSPMs). BSPMs were recorded with a 128-lead vest in 14 persistent AF patients before undergoing catheter ablation (Maze-IV). The torso geometry was acquired and meshed by point cloud technology, and the BSPM was interpolated into the torso geometry by the inverse distance weighted (IDW) method to generate the isopotential map. Experiments show that the isopotential map of BSPMs can reflect the propagation of the electrical wavefronts. The 3D isopotential sequence map was established by combining the spatial–temporal information of the isopotential map; a 3D convolutional neural network (3D-CNN) model with temporal attention was established to predict AF recurrence. Our study proposes a novel attention block that focuses the characteristics of atrial activations to improve sampling accuracy. In our experiment, accuracy (ACC) in the intra-patient evaluation for predicting the recurrence of AF was 99.38%. In the inter-patient evaluation, ACC of 3D-CNN was 81.48%, and the area under the curve (AUC) was 0.88. It can be concluded that the dynamic rendering of multiple isopotential maps can not only comprehensively display the conduction of cardiac electrical activity on the body surface but also successfully predict the recurrence of AF after CA by using 3D isopotential sequence maps.

KEYWORDS

atrial fibrillation recurrence, attention, body surface potential mapping, 3D convolutional neural network (3D CNN), isopotential map

1 Introduction

Atrial fibrillation (AF) is the most common cardiac arrhythmia with a prevalence of 10%–18% in people aged over 80 (Zoni-Berisso et al., 2014). Although catheter ablation (CA) therapy can effectively treat AF, the recurrence rate of AF is still high, and the mechanism of recurrence is not clear (Schotten et al., 2011; Calvo et al., 2018; McCann et al., 2021). At present, predicting postoperative recurrence in AF patients based on preoperative clinical baseline data would enable the selection of the best personalized treatment for AF patients.

Various body surface electrocardiogram (ECG) and intracardiac electrogram (EGM) predictors associated with AF recurrence after CA have been reported. Everett et al. (2001) concluded that the spectrum of AF signals contains information related to its tissue and can be used to predict the successful termination of AF in ten dogs. Takahashi et al. (2006) found that a higher organization index (OI) of atrial EGM was associated with the termination of AF during limited ablation; this parameter may be useful for anticipating the extent of ablation. Meo et al. (2013) argued that the amplitude variability of AF waves (f-waves) could be characterized by multi-lead ECG to predict the prognosis of CA. Szilágyi et al. (2018) used body-surface ECG and intracardiac EGM signals for spectrum analysis and found that dominant frequency (DF), regularity index (RI), and OI could be used to predict AF recurrence. Furthermore, most of the methods based on ECG complexity investigated to date have been determined both in the frequency (Alcaraz et al., 2016; Hidalgo-Muñoz et al., 2017) and time domain (Nault et al., 2009) or in AF cycle length (Matsuo et al., 2009), and a few by sample entropy (Alcaraz et al., 2011). Nevertheless, the acquisition of EGM is difficult for its trauma, and some body-surface ECG, like the standard 12-lead ECG or single-lead ECG, could not provide sufficient spatial–temporal information on atrial activity to predict AF recurrence.

Body-surface potential mapping signals (BSPM) can not only provide sufficient body surface information but also effectively characterize the atrial complexity of patients with AF. Bonizzi et al. (2010) demonstrated that BSPMs outperform standard single-lead analysis and proposed a novel automated approach to quantitatively assess the degree of the spatial–temporal organization of atrial activity (AA) during AF. Zhang et al. (2018) suggested that the fast Fourier transform (FFT) algorithm is a useful and convenient way to evaluate the rhythm of BSPMs in AF patients, which is important for identifying some hypotheses to predict the recurrence of AF. Their study also demonstrated that multi-channel mapping is superior to standard 12-lead ECG. Meo et al. (2018) proposed a marker from BSPMs to quantify AF complexity that could be used to select patients eligible for AF ablation. Marques et al. (2020) used frequency and phase analyses of BSPM maps to reveal distinct behavior between arrhythmias. Li et al. (2018) proposed a deep learning algorithm based on BSPMs to predict AF recurrence after CA. However, most studies quantify AF complexity using traditional machine-learning methods, and few studies use deep learning to predict AF recurrence after CA based on the three-dimensional (3D) spatial–temporal features of BSPMs.

Due to the volume of BSPMs and the difficulty of distinguishing and quantifying important features, electrical image sequence representation is a common visualization tool in evaluating and understanding BSPMs (Brook and MacLeod, 1997). Common methods include isochrone maps, isopotential maps, integral maps, isoarea or isointegral maps, and phase maps (Brook and MacLeod, 1997; Rogers et al., 1998). Isopotential maps are obtained by directly plotting the mapped ECG data—the voltage amplitude—on the model without modification. This drawing will not add any additional information nor any data processing, so it will not lose any mapping information.

In this study, 3D visualization techniques were used to deeply explore the temporal evolution of BSPMs to predict the recurrence of AF. It takes a step from previous research and proposes a noninvasive isopotential map-based approach for the evaluation of AF complexity. We here propose a new method for extracting the spatial–temporal characteristics of cardiac activations during AF and realize the prediction of AF recurrence by inputting 3D isopotential sequence maps into a 3D convolutional neural network (3D-CNN). This method not only provides the overall propagation pattern of ECG signals on the body surface but also successfully predicts the recurrence of AF. At the same time, the innovative temporal-attention block solves the problem of the 3D input signal not being able to effectively extract important information based on time series.

2 Material and methods

2.1 Data collection

BSPM data from 33 patients with clinical AF were collected before and after macrovascular surgery at West China Hospital of Sichuan University; 14 AF patients with radiofrequency surgery ablations and successful electrical cardioversion within 3–4 weeks had been the subject of continuous follow-up studies for 1 year. The study was approved by the ethics review board of West China Hospital, Sichuan University, and written informed consent was obtained from all patients upon admission. Moreover, their personal information was anonymized and de-identified prior to analysis. Table 1 lists their clinical characteristics and the basic information.

A 128-lead vest connected by elastic bands constitutes the front-end signal acquisition equipment. Every electrode is gold-plated copper, and all electrodes were gathered on a soft PCB board. Figure 1A illustrates how the electrodes were distributed on a patient's body surface. There were 74 electrodes distributed

TABLE 1 Fundamental information and clinical characteristics of subjects.

ID	Age	Sex	Height	Weight	Preoperative rhythm	Description	Surgical process and treatment plan	Recurrence	Segments
13	53	Male	170	66	AF	RHD[a]: MS[b], MR[c], TR[d]	MVR[g], TVP[h], Maze[j]	No	72
14	52	Male	—	—	AF	RHD[a]: MS[b], MR[c], TR[d]	MVR[g], Maze[j]	No	106
16	50	Male	164	58	AF	RHD[a]: MS[b], AS[f], AR[e]	MVR[g], Maze[j]	No	86
17	50	Male	170	68	AF	RHD[a]: MS[b], MR[c], AR[e]	MVR[g], Maze[j]	No	82
18	69	Male	173	56	AF	RHD[a]: MS[b], TR[d]	MVR, Maze[j]	Yes	69
19	46	Female	156	55	AF	RHD[a]: MS[b], MR[c], TR[d]	MVR[g], TVR[h], Maze[j]	Yes	62
20	44	Female	155	55	AF	RHD[a]: MS[b], MR[c], TR[d]	MVR[g], TVR[h], Maze[j]	No	68
21	50	Female	155	45	AF	RHD[a]: MS[b], TR[d]	MVR[g], TVR[h], Maze[j]	No	74
22	46	Male	173	67	AF	RHD[a]: MS[b], TR[d]	MVR[g], TVR[h], Maze[j]	No	91
23	65	Female	156	57	AF	RHD[a], MS[b], MR[c], TR[d]	MVR[g], TVR[h], Maze[j]	No	70
24	42	Female	157	80	AF	RHD[a]: MR[c], TR[d]	MVR[g], TVR[h], Maze[j]	Yes	108
25	62	Female	152	55	AF	RHD[a]: MS[b], AR[e]	MVR[g], TVP[h], Maze[j]	No	88
26	43	Female	153	49	AF	RHD[a]: MS[b], TR[d]	MVR[g], AVR[i], TVR[h], Maze[j]	No	76
30	50	Female	154	47	AF	RHD[a]: MS[b], MR[c], TR[d]	MVR[g], TVR[h], Maze[j]	Yes	120

[a]RHD, rheumatic heart disease.
[b]MS, mitral valve stenosis.
[c]MR, mitral valve regurgitation.
[d]TR, tricuspid valve regurgitation.
[e]AR, aortic valve regurgitation.
[f]AS, aortic stenosis.
[g]MVR, mitral valve replacement.
[h]TVR, tricuspid valve replacement.
[i]AVR, aortic valve replacement.
[j]Maze, surgical maze surgery of AF.

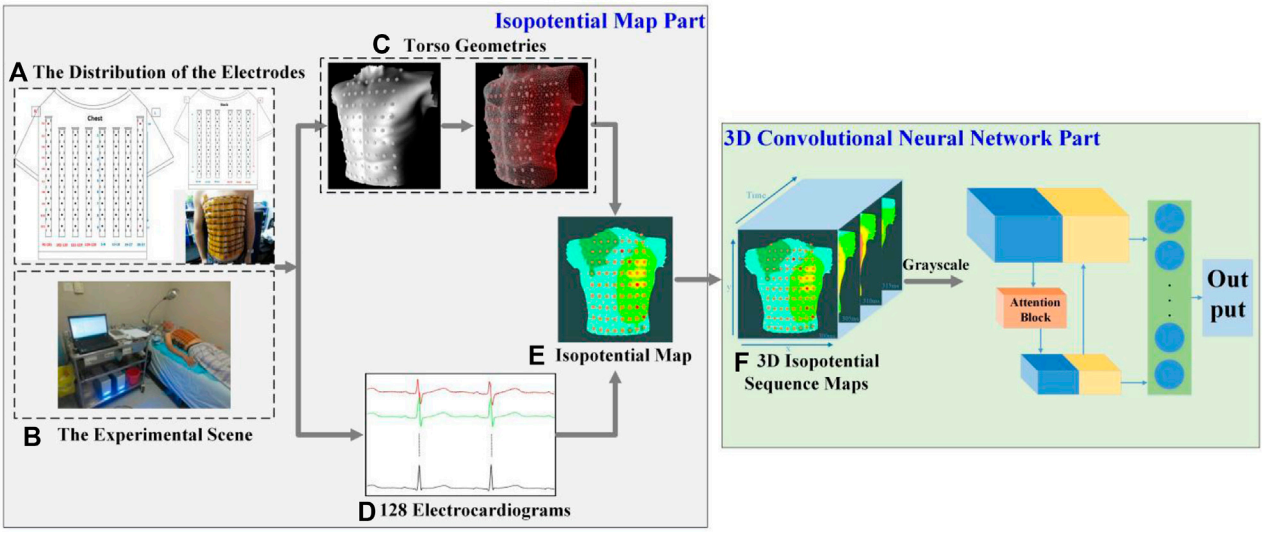

FIGURE 1
Framework of our prediction model of AF recurrence. **(A)** The distribution of the electrodes. There are 128 electrodes, including 74 on the chest and 54 on the back. **(B)** The experimental scene. **(C)** Torso geometries. Torso geometries consist of 128 body surface electrodes and a body torso geometry. **(D)** 128 electrocardiograms. Different colors show the BSPM of different channels, and there are 128 channels in total. **(E)** Isopotential map. Different colors indicate different voltage amplitudes, and the darker the color, the lower the voltage. **(F)** 3D isopotential sequence maps. y and x are the height and width of isopotential map, and time is consistent with the time of the BSPMs.

on the anterior body surface, while 54 were distributed on the posterior body surface. Two adjacent electrodes belonging to the same column were 3.5 cm apart. At the same time, three electrode points were located in a triangular shape to construct the Wilson's center terminal as the reference point. This reference point should be subtracted by the voltage value acquired at other points to obtain the ultimate voltage value. Data recording and storage uses the multi-channel electrophysiological signal acquisition and recording system NeuroScan (ESI-128, Compumedics Ltd., Australia) (Zhang et al., 2018). Figure 1B depicts the experimental scene.

The entire experiment was verified on the AF signals database before surgery; this is different from other work which used sinus rhythm before AF (Sahadevan et al., 2004), and where patient follow-up was conducted by the same doctor performing the same surgical procedure, which can ensure that the initial conditions of sample are the same. In this study, preoperative signals were used to predict postoperative AF recurrence, and postoperative sinus rhythm signals were used to analyze the conduction law of AF cardiac activation on BSPMs.

2.2 Framework overview

As shown in Figure 1, the two parts of this study were an isopotential map and a 3D-CNN. In the former, the data analyzed in this study were all BSPMs of patients with AF and were filtered by the NeuroScan system at a 1–40 Hz band-pass. After obtaining the torso geometry by pre-processing technology based on a point cloud from a laser scanning system (Guo et al., 2020), the BSPMs were interpolated to 3D displacement by inverse distance weighting (IDW). The patient's isopotential map was displayed at the same time, and the conduction law of cardiac electrical activity was analyzed by BSPM. At the same time, the noise of baseline wander (in record "bw") (Goldberger et al., 2000) with a signal-to-noise ratio of 12 dB was added to the original signal. In the 3D-CNN part of this study, the isopotential map was generated from the signal and transformed into 3D isopotential sequence maps by combining time information. A temporal-attention block for ECG signals was designed to predict the recurrence of AF. Figure 1F shows the 3D isopotential sequence maps. In order to process 3D isopotential sequence map information more efficiently, the original isopotential map was transformed into a gray-scale image with only one channel, whereas the color image has three (RGB). The image input to the CNN is significantly increased if a color image is employed, as it is three times larger than a gray-scale image. A more effective gray-scale image was employed because it can capture different potentials at different pixel values; this can already reflect the conduction of the ECG signal. The deep CNN is used to train the processed 3D isopotential sequence maps.

The 128-channel unipolar BSPMs at about 3 min per patient were collected, and the BSPMs were sampled at 1000 Hz. Afterward, the original signal was cut into 2 s for analysis. Segments with extremely poor signal quality were manually eliminated due to circumstances such as patient movement during the acquisition process. Consequently, the number of segments saved varies for each patient, as shown in Table 1 with specific subject information. The ratio of non-recurrent to recurrent segments is 813:359. There is a great imbalance in the amount of data. The overlap method is used to deal with recurrent samples. It should also be noted that the shift between two segments is equal to 175 points (Oliver et al., 2018; Andersen et al., 2019). Thereafter, the total data were 1627 segments, including 814 recurrent and 813 non-recurrent segments.

The development environment of this research is the Win 10 system, 64 GB memory, i7-8700 CPU, and RTX2080 GPU. The isopotential map compiler using the C++ development language adopts Visual Studio 2013, and the deep learning framework is the Tensorflow framework based on Python.

2.3 Isopotential map

Using the scanning platform, the 3D model of the torso geometry is reconstructed by point-cloud technology (Chen et al., 2013). The hardware is based on a Raspberry PI 3B + microcontroller, stepper motor and laser drive circuit, scanning tables, and optical sensor. Depth information is point-cloud information, which had to be collected at different sites of the torso by infrared cameras around the body. Then, the data collected in the space were processed and recovered by software, and the geometric shape of the torso geometry and the position of the surface electrodes were finally obtained. The format of the point cloud information is an obj file containing 83,184 vertices and 39,504 faces. There were a total of 129 meshes representing 128 body surface electrodes and a body torso geometry (for the latter, see Figure 1C).

IDW is a computational method based on the geometric relationship between interpolated objects (Shepard, 1968). The distance between the known point and the point to be interpolated is the "weight value", and the interpolation points can be estimated by a weighted average. Assuming the known point is $D_i(x_i, y_i)$, whose value is represented by $z_i(x_i, y_i)$, the point to be interpolated is $P(x, y)$, while d_i represents the distance between the two points $P(x, y)$ and $D_i(x_i, y_i)$. The interpolation function can therefore be expressed as

$$f_{1,x}(x,y) = \frac{\sum_{i=1}^{N}\sum_{j=1,i\neq j}^{N}(\boldsymbol{d_i})^{-(u-2)}\left(\boldsymbol{d_j}\right)^{-u}(\boldsymbol{x}-\boldsymbol{x_i})\boldsymbol{z_i}\left(\boldsymbol{z_i}-\boldsymbol{z_j}\right)}{\left|\sum_{i=1}^{N}(\boldsymbol{d_i})^{-u}\right|^2} \quad (1)$$

By replacing $(x - x_i)$ with $(y - y_i)$, the interpolation of the $f_{1,y}(x, y)$ can be calculated. The weight of the distance is as follows:

$$(d_i)^{-2} = \frac{1}{\left[(x - x_i)^2 + (y - y_i)^2\right]} \quad (2)$$

Empirically, with the increase of the coefficient u, the interpolation points become smooth, but the computational overhead increases significantly. Usually, the parameter u is taken to be 2.

The different potential in the isopotential map was rendered as different colors filling the vertex coordinates at the same time (Abildskov et al., 1976). The 3D characterization process of the ECG data from the BSPMs is principally divided into the following steps:

1) Collect the synchronous BSPMs with a certain sampling frequency = 1000 Hz , as shown in Figure 1A, according to the placement location of the acquisition electrode.
2) Remove noise or interference from power frequency, breathing or muscle power from the ECG signal collected in Step 1), and normalize the signal amplitude.
3) Based on the voltage amplitude after normalizing each of the ECG data obtained in Step 2), draw the isopotential map according to the IDW interpolation algorithm and estimate the voltage. Then map the actual or interpolated voltage values to the corresponding spatial coordinates, with different voltage values rendered into different colors according to the voltage level.
4) Repeat Step 3) to obtain the isopotential map of each sampling time by the sampling interval $1/fs$ and complete the dynamic rendering, then render one image at each sampling interval and save the isopotential map of each sampling time.
5) Within the period of time l, the isopotential map obtained in Step 4) is synthesized to a 3D isopotential sequence map at a fixed time interval Δt. The 3D isopotential sequence map retains the color information contained in each isopotential map rendering. Multiple series of time dimensions are merged into a 3D isopotential sequence map. The fixed time interval is $\Delta t = 1/fs$, for a certain period of time $l = K \cdot \Delta t$, where K is the number of isopotential maps included in each synthesized 3D excited sequence map. In this study, $l = 2$ s, $\Delta t = 1$ ms, $K = 2000$.
6) Repeat Step 5) to obtain the 3D isopotential sequence maps until all isopotential maps are traversed.

We give different colors to different voltage values according to the voltage level: the darker the color, the lower the voltage. Red represents a wave crest, and blue represents a wave trough. The research uses the OpenGL graphics interface in Visual Studio 2013 software to load the 3D torso model, obtain the isopotential map at each sampling time at a time interval of 1 ms (i.e., $1/fs$), and use the screen capture function glReadPixels in OpenGL to save the image at each sampling time.

In our study, we use a CNN to analyze the 3D isopotential sequence maps, as too much input will increase the difficulty of network convergence. Thus, only the isopotential map from the front part of the torso is included, and the information from the back part is totally ignored.

2.4 Architecture and training of the prediction model

We used 3D-CNN to predict AF recurrence. The architecture of the network is shown in Figure 2. The network takes 3D isopotential sequence maps as input and the vector representing recurrence or non-recurrence as output. The 3D isopotential sequence maps generated by a series of 2D isopotential maps as the dataset is input into the 3D-CNN. The size of the 3D isopotential sequence maps is $W \times H \times T$, where W indicates its width, H its height, and T is the number of frames of the 3D isopotential sequence maps. We arrive at an architecture consisting of eight convolutional layers, three fully connected layers, and a Softmax.

2.4.1 3D-CNN

In order to make the optimization of such a network tractable, we employed skip connections in a similar manner to those found in the U-Net architecture (Ronneberger et al., 2015). The skip connections between neural network layers optimize training by allowing the information of low- and high-resolution features to propagate effectively in different layers of a neural network. The network architecture is illustrated in Figure 2, including Blocks 1–3 and the temporal-attention block. Block 3 is the full connection layer block. The structures of other parts consist of a contracting path as shown in Block 1 and an expansive path as shown in Block 2. The contracting path follows the typical architecture of a convolutional network. At each down-sampling step, we doubled the number of feature channels. Every step in the expansive path consists of an up-sampling of the feature map followed by a 2 × 2 convolution (“up-convolution”) that halves the number of feature channels. Based on the U-Net architecture, the model extracts the feature on the output of the multi-scale convolutional layer in the contraction path and inputs to the fully connected layer. The prediction result is obtained through Softmax. In Figure 2, C indicates the channel of the network and Dense 256 indicates that the length of the output feature vector is 256.

In the output part, the deep and shallow features of the network can be fused by fusing the information of different layers of the network. Among them, the network parameter F1 is the output after the fifth convolution layer, F2–F4 process the features after using up-convolution fusion on deep and shallow features, and the deep and shallow features are fused again through concatenating.

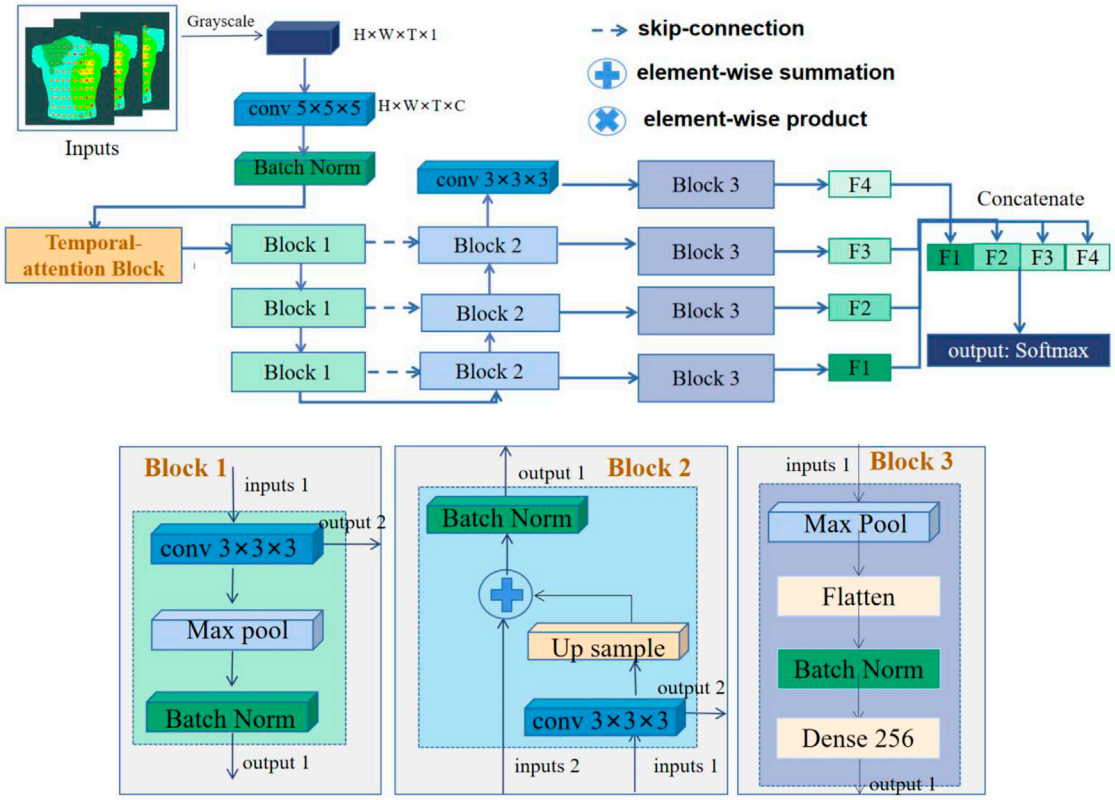

FIGURE 2
Structure diagram of the 3D-CNN classification framework.

2.4.2 Temporal attention

The temporal-attention block presented was mainly inspired by SENet in 2017 (Hu et al., 2018) and the characteristics of ECG. The prediction of AF recurrence mainly focuses on the signals within a particular time. For example, for AF recurrence, we mainly focused on the characteristics of atrial activations (Heijman et al., 2021). The data used in this study include ventricular and atrial activations. However, we paid more attention to the atrial signal for the recurrence of AF. In order to better identify the characteristics of atrial activation, we added a temporal-attention block to the network so that the signal can pay attention to K of $W \times H \times T \times C$. For AF recurrence, the temporal-attention block should give greater weight to the time period of atrial activation, so that the network can pay more attention to the time period related to AF recurrence.

A temporal-attention block is a computational unit which can be built upon a transformation F_{tr} mapping an input $X \in R^{H^{2032} \times W' \times T'^{\times} C'}$ to feature maps $U \in R^{H \times W \times T \times C}$. In the following notation, we take F_{tr} to be a convolutional operator and use $V = [vs_1, vs_2, \cdots, vs_c]$ to denote the learned set of filter kernels, where vs_c refers to the parameters of the cth filter. We can then write the outputs as us_l, and us_l refers to the parameters of the l-th part of feature maps. That means $vs_l \in R^{a \times b \times c}$ and $X_l \in R^{a \times b \times c}$, where:

$$us_l = vs_l {}^{*} X_l = \sum_{k=1}^{C} \left(\sum_{i=1}^{i=a} \sum_{j=1}^{j=b} \sum_{z=1}^{z=c} vs_{ijz} \times X_{ijz} \right)_k \tag{3}$$

For a temporal feature, the traditional 3D convolution is the convolution sum of the length, width, and time dimensions of the signal. The characteristic relationship of the temporal and spatial information is thus learned by the convolution kernel, and even channel information will be mixed together through summation. The purpose of temporal attention is to extract the temporal information from this mixture so that the model can learn the temporal information more directly.

The 4D features are passed through a $1 \times 1 \times 1$ convolution kernel, and the channel number is adjusted to 1 to obtain F through a reshape operation, where $F \in R^{H \times W \times T}$ (Szegedy et al., 2015). Since convolution is only operated in a local space, it is difficult to observe the relationship between the local and global space. Using the squeeze operation proposed by SENet, we encode all spatial features at a time into a global feature, which is generated into temporal-wise

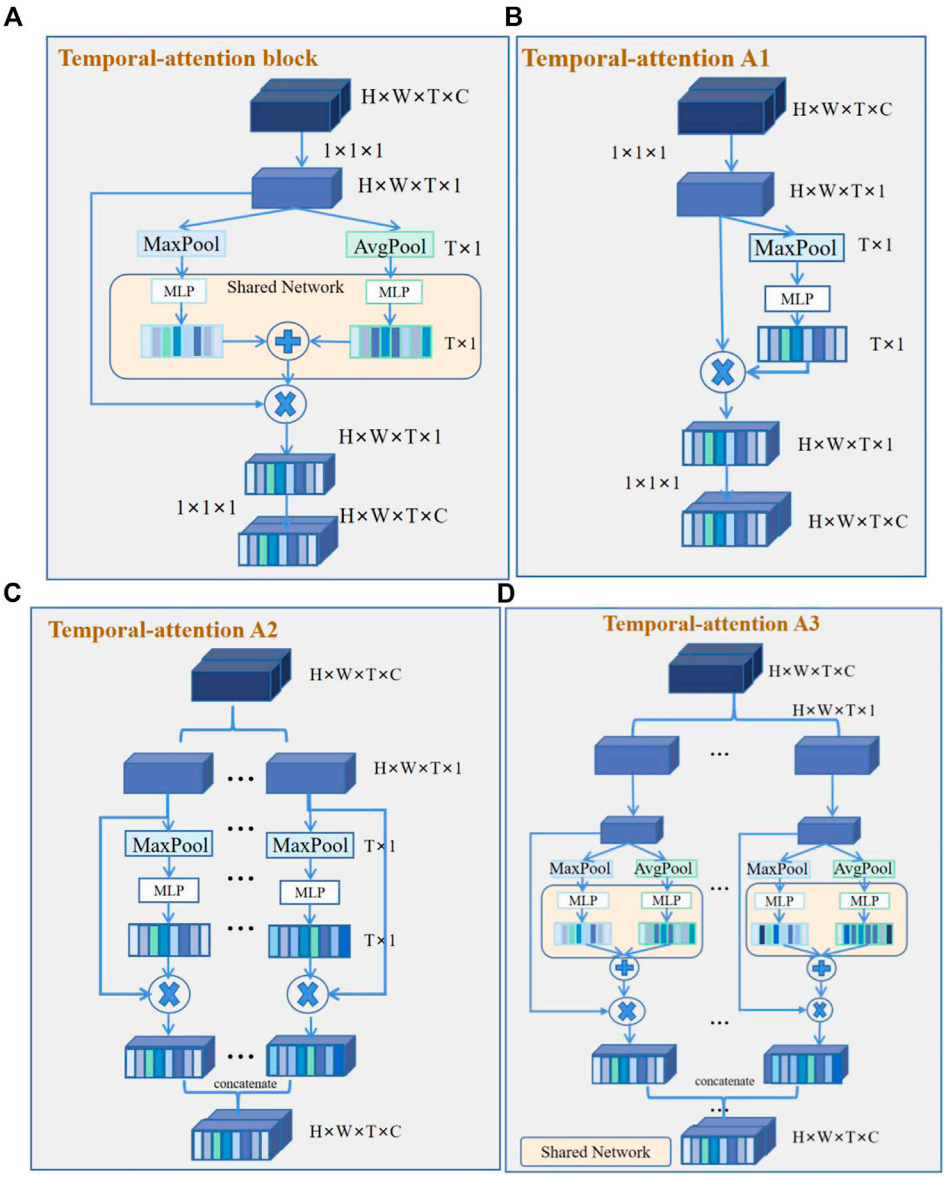

FIGURE 3
Temporal-attention block and its variants. **(A)** Temporal-attention block. Two groups of features were obtained by global average pooling (AvgPool) and maximum average pooling (MaxPool), then get the sum of the different features matrices. **(B)** Temporal-attention A1. Feature acquisition contains only MaxPool. **(C)** Temporal-attention A2. Different channel features were obtained by MaxPool, and use concatenation to fuse different channel features. **(D)** Temporal-attention A3. Different channel features were obtained by AvgPool and MaxPool, and use concatenation to fuse different channel features.

statistics by global average pooling (AvgPool) and maximum average pooling (MaxPool) (Woo et al., 2018). The temporal weight M_T is obtained by fusing the features of global average pooling and max average pooling. M_T goes through a sequence and excitation operation. The shared network is composed of a multi-layer perceptron (MLP) with one hidden layer. After the shared network is applied to the block, we merge the output feature vectors using element-wise summation. The formula of the temporal weight M_T is as follows:

$$\begin{aligned} M_T(F) &= \sigma\left(MLP\left(AvgPool(F)\right) + MLP\left(MaxPool(F)\right)\right) \\ &= \sigma\left(W_2 ReLU\left(W_1\left(F_{avg}^{sq}\right)\right) + W_2 ReLU\left(W_1\left(F_{max}^{sq}\right)\right)\right) \end{aligned} \tag{4}$$

where σ denotes the Sigmoid function, $W_1 \in R^{T/r \times T}$ and $W_2 \in R^{T \times T/r}$. The formula of AvgPool F_{avg}^{sq} and MaxPool F_{max}^{sq} are as follows:

$$F_{avg}^{sq} = \frac{1}{H \times W} \sum_{i=1}^{H} \sum_{j=1}^{w} f_t(i,j) \tag{5}$$

$$F_{max}^{sq} = max(f_t(i,j)) \tag{6}$$

As with SENet, r is a super parameter for dimensionality reduction. In this experiment, $r = 4$ is taken. The weighted temporal attention is obtained by summing up the elements to map the features and multiplying this by the original signal F. Finally, the number of channels is adjusted to C using a $1 \times 1 \times 1$ convolution kernel. The temporal-attention block structure is shown in Figure 3A, while Figures 3B–D are all variants of the structure. The temporal attention A1 structure includes a $1 \times 1 \times 1$ convolution kernel and just uses MaxPool to generate temporal-wise statistics. Temporal attention A2 and A3 structures use concatenation to fuse different channel features instead of a $1 \times 1 \times 1$ convolution kernel.

2.5 Optimization

There are more non-recurrent than recurrent samples, which causes data imbalance. Therefore, the model fails to learn the features of fewer classes and is trained with low efficiency, as most locations are easy negatives that contribute no useful learning signal. The purpose of using focal loss is to solve the serious imbalance in the proportion of non-recurrent and recurrent samples (Lin et al., 2017) and to reduce the weight of a large number of easy-to-classify samples in training. Focal loss reduces the contribution of samples which are easy to classify to loss and makes the model attend more to the hard-to-classify samples. The formula is as follows:

$$L_{fl} = \begin{cases} -\alpha\left(1-y'\right)^{\gamma} log\left(y'\right), & y = 1 \\ -(1-\alpha)y'^{\gamma} log\left(1-y'\right), & y = -1 \end{cases} \tag{7}$$

As aforementioned, $y \in \{\pm 1\}$ specifies the ground-truth class and $y' \in [0, 1]$ is the model's estimated probability for the class with label $y = 1$, which means recurrent samples. When $\gamma = 0$, L_{fl} is equivalent to cross entropy (CE) and as γ is increased, the effect of the modulating factor is likewise increased. The γ reduces the contribution of easy-to-classify samples to loss. The α can be used to balance the uneven number of non-recurrent and recurrent samples. In our study, we set γ to 2 and α to 0.25.

After each convolutional layer, we applied batch normalization (Ioffe and Szegedy, 2015) and a rectified linear activation. We also applied dropout (Srivastava et al., 2014) between the skip-connection layers and the fully-connected layers. We used the Adam (Kingma et al., 2014) optimizer with default parameters and reduced the learning rate by $1/t$ decay, where t denoted the training step. During optimization, we saved the best model as an evaluation of the validation set.

2.6 Evaluation index of performance

In our study, we used two dataset evaluation methods to test performance. One is inter-patient evaluation, which strictly requires that the training set and testing set data come from different patients (Nguyen et al., 2019). The other is intra-patient evaluation, which completely ignores the individual differences. The training set and testing set can come from the same patient to achieve higher performance. At this time, the negative impact of individual differences is the least, as is the difficulty of realization.

For the two different data-set division methods, we used four main statistical indicators to evaluate this prediction model: sensitivity (*SE*), specificity (*SP*), positive predictive value (*PPV*), and accuracy (*ACC*). These expressions are given as follows:

$$SE = \frac{TP}{(TP+FN)} \times 100\% \tag{8}$$

$$SP = \frac{TN}{(TN+FP)} \times 100\% \tag{9}$$

$$PPV = \frac{TP}{(TP+FP)} \times 100\% \tag{10}$$

$$ACC = \frac{(TP+TN)}{(TP+FN+FP+FN)} \times 100\% \tag{11}$$

where *TP* is the amount of AF recurrence samples that were correctly predicted, *TN* is the AF non-recurrence samples which were predicted as non-recurrence, *FP* indicates the AF non-recurrence samples that were wrongly predicted as recurrent, and *FN* is the recurrence samples that were wrongly predicated as non-recurrent. Another quality of the prediction model is measured by the area under curve (*AUC*) of its receiver operating characteristic (ROC) curve based on maximized *SE* and *SP* (Fawcett, 2006).

3 Experimental results and discussion

3.1 Cardiac axis

The signal of normal sinus rhythm is selected to calculate the cardiac axis. The conduction law of cardiac activations in the BSPMs is that these conduct along the direction of the cardiac axis, allowing the cardiac electrical signals of different propagation orders to be extracted through the BSPMs.

According to the electrode distribution of the anterior chest mapped on the body surface (Figure 4), we use channels 93, 29, and 37 to approximately calculate leads I and III. Lead I is approximately the difference between channels 29 and 93 and lead III is approximately the difference between channels 37 and 29. Its formula is as follows:

$$U_{\mathrm{I}} \sim U_{29} - U_{93} \tag{12}$$

$$U_{\mathrm{III}} \sim U_{37} - U_{29} \tag{13}$$

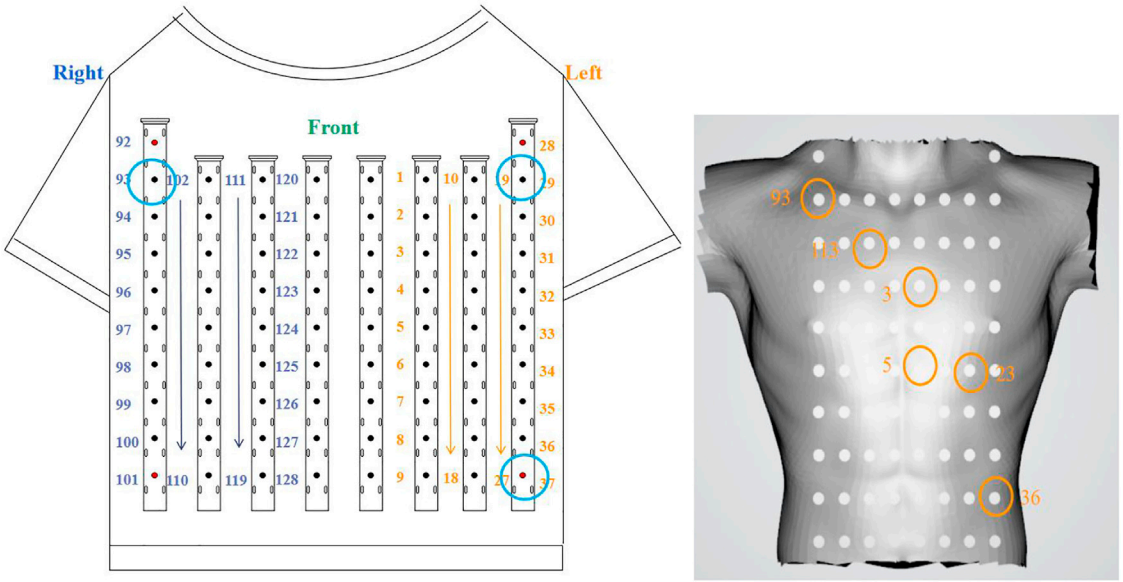

FIGURE 4
Position of six electrode reference points.

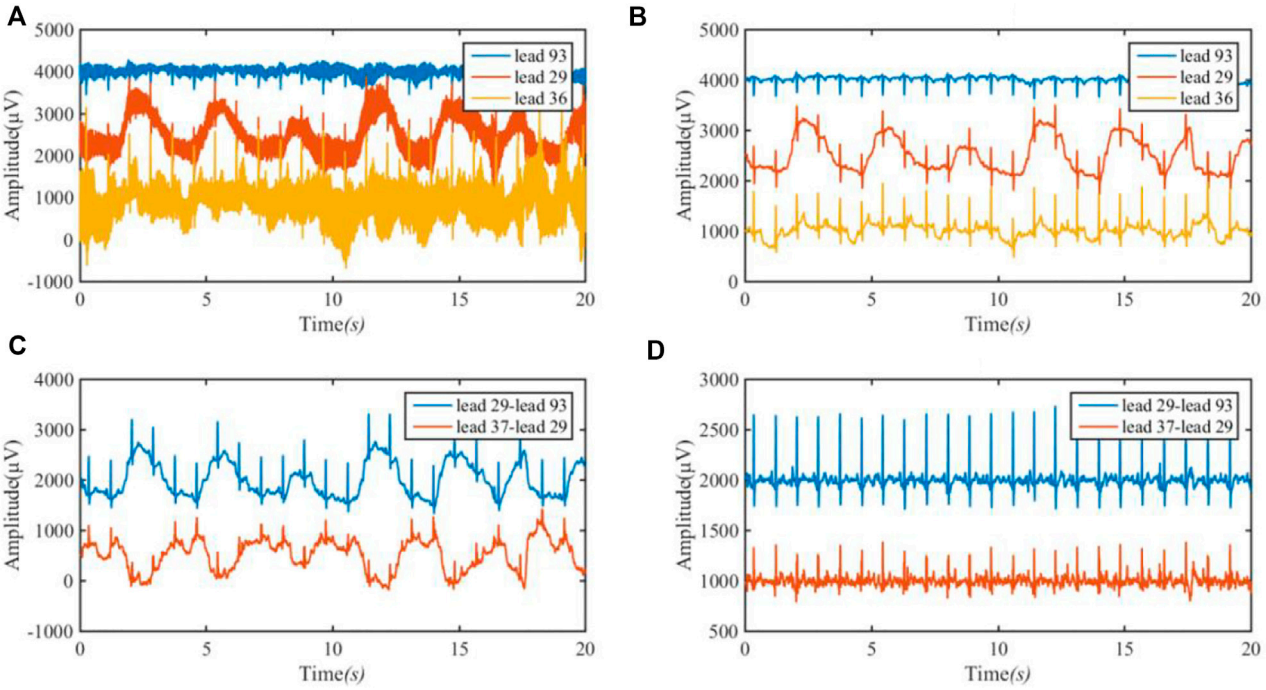

FIGURE 5
ECG of lead I (29–93) and lead III (37–29) achieved from BSPM. **(A)** the original BSPM. The blue line is 93 lead (channel); the red line is 29 lead (channel); and the orange line is 36 lead (channel). **(B)** The ECG after band-pass filtering. **(C)** The approximate ECG of lead I and III. The blue line is the approximate ECG of lead I by subtracting lead (channel) 93 amplitude from lead (channel) 29 amplitude; the red line is the approximate ECG of lead III by subtracting lead (channel) 29 amplitude from lead (channel) 37 amplitude; **(D)** The signal after removing the baseline wander.

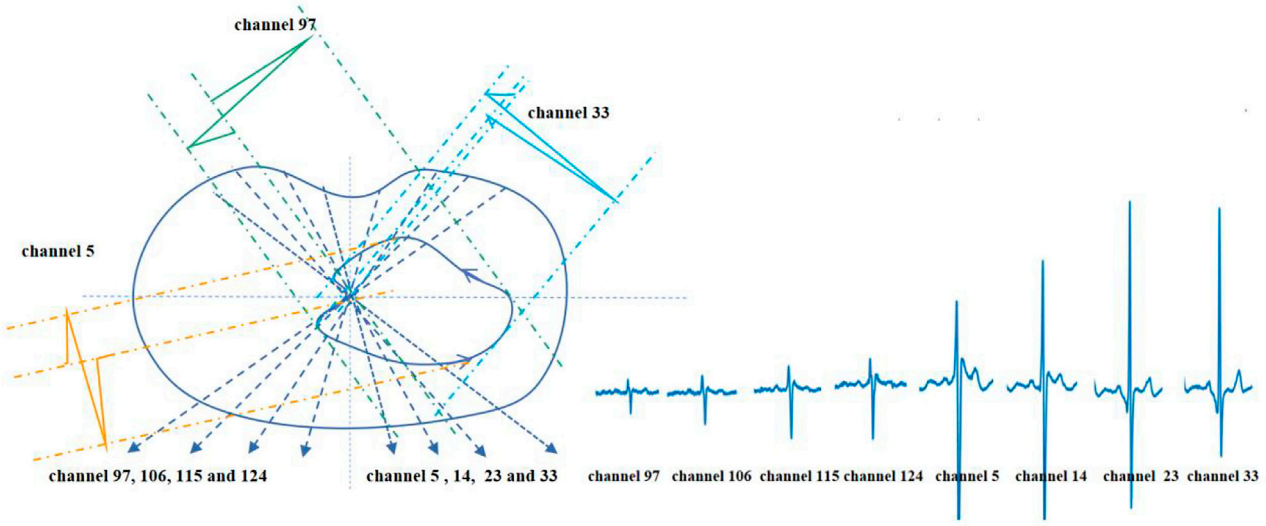

FIGURE 6
Projection and waveform formation of the transverse plane vectorcardiographic loop of BSPM.

Figure 5 shows the approximate ECG of leads I and III achieved from BSPMs. Figure 5A is the original BSPM, Figure 5B is the ECG after band-pass filtering at 1–40 Hz, Figure 5C is the approximate ECG of lead I obtained by subtracting the corresponding lead, and Figure 5D is the signal after removing the baseline wander using the low-pass filter of 3 Hz (first-order Butterworth filter).

We calculated the amplitude of positive and negative R waves in 80 s signals to obtain the patient's cardiac axis. The sum of the amplitude of a QRS wave of U_{I} is U_{I} = 383.7130 and the sum of the amplitude of a QRS wave of U_{III} is U_{III} = 176.5790. The cardiac axis angle is 47.9516°, which is in normal range.

On the transverse plane, the projection of the vectorcardiographic loop of the BSPMs is shown in Figure 6. Electrodes 97–33 in the same row of BSPMs are selected, and the propagation law of BSPMs is obtained through a two-step projection of a spatial vector cardiogram, as shown in Figure 6. By comparing the BSPMs collected in Figure 6, it is evident that the BSPMs follow the pattern of the conduction law of cardiac activations and that the peak value of the R wave follows the propagation order from left to right.

3.2 Verification isopotential map

For postoperative sinus rhythm, a total of 80 s sinus mapping signals (including 92 heartbeats) are included to verify the performance of the rendered dynamic mapping data. Six electrode reference points—nearly consistent with the normal electrical axis of the heart (Figure 4)—are channels 93, 112, 3, 5, 24 and 36, respectively. These channels are numbered 93 (①), 112 (②), 3 (③), 5 (④), 25 (⑤), and 36 (⑥) from small to large, and the chronological order of the QRS complex received at these six electrodes is also counted. Table 2 shows numbers and arrows being used to indicate the order of the body surface activation sequence during sinus rhythm. For example, ①→②→③→④→⑤→⑥ indicates that the activation sequence is conducted from right to left, from the top to bottom, and from channel 92 (①) to channel 36 (⑥).

The delay time is used to represent the difference between the time when the electrodes with a different activation sequence receive the ECG activation and when they receive the ECG activation under normal conditions. It can be seen from Table 2 that an activation delay was detected in electrodes ② and ⑥. The longest activation delay was less than 3 ms. It is found that the delay time is short and will not have a great impact on the model rendering. Compared with the 14 times of activation delay, the difference is not obvious; this indicates that the isopotential map can approximately represent the conduction law of cardiac electrical activity on BSPMs.

For preoperative AF, the BSMPs of the five selected electrode points (channels 2, 12, 23, 25, and 36) in the normal activation sequence and the rendered isopotential map are shown in Figures 7 and 8. In Figure 7, the ECG signals of the five selected channels within 3 s are arranged in parallel from top to bottom. The dotted line indicates that the time from channel 2 to the QRS complex peak is 362 ms, corresponding to the first isopotential map of Figure 8. It is evident that channel 2 first detected the moment of excitation and that the other channels also detected excitation after a certain delay—consistent with the conduction results shown in Figure 8. It can be seen from Figure 8 that the color of the place near channel 2 changes first, indicating that the excitement is first transmitted to this place. Then, along the

TABLE 2 Statistics for the excitement sequence of sinus rhythm.

Activation sequence	The number of heartbeats	Delay time	The proportion of the number of heartbeats in the delay time	
①→②→③→④→⑤→⑥[a]	78	0	—	
②→①→③→④→⑤→⑥	11	1–3 ms	1 ms	91.67%
			3 ms	8.33%
⑥→①→②→③→④→⑤	2	>3 ms	100.00%	
②→①→⑥→③→④→⑤	1	1 ms	100.00%	

[a]①→②→③→④→⑤→⑥ indicates that activation sequence is conducted from channels 93 (①) to 36 (⑥).
The bold values represents the optimal result of different algorithms.

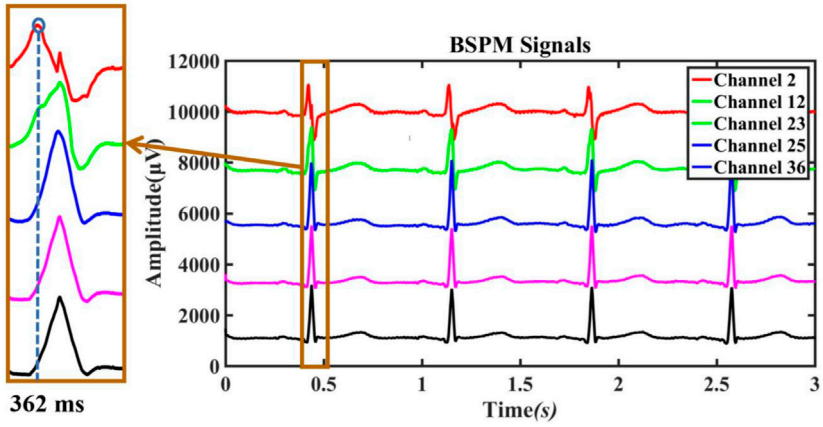

FIGURE 7
Original ECG data collected by channels 2, 12, 23, 25, and 36.

electrical axis, the color of the lower-left area of the torso turns from yellow to red and spreads out, indicating that the excitement is transmitted to this area later.

3.3 3D-CNN in the intra-patient evaluation

In our study, a 3D isopotential sequence map was used to predict the recurrence of AF, and the 3D-CNN structure was used for prediction. In the meanwhile, the classification performance of four classic network structures of image was compared. Four common network training models—LeNet (Lecun et al., 1998), AlexNet (Krizhevsky et al., 2012), VGGNet-16 (Simonyan and Zisserman, 2014), and ResNet (He et al., 2016)—were selected for comparison with the 3D-CNN classification model in this study. The input of LeNet, AlexNet, and VGGNet-16 was 3D isopotential sequence maps changed from a traditional 2D image; ResNet was changed from ResNet 50 and had 16 convolution layers and 1 max average pooling layer.

In our experiment, different sizes of 3D isopotential sequence maps were reserved to compare the prediction results. Because the data size is too large when $K = 2000$, in order to save training time and improve network performance, the network input size $W \times H \times T$ is $32 \times 32 \times 128$, $64 \times 64 \times 256$, and $64 \times 64 \times 400$, respectively. We randomly divided the dataset (training set: validation set: testing set = 7: 2: 1). The results of the comparison of five different 3D network models and four different input sizes are shown in Table 3.

It can be seen from Table 2 that the performance of different models for data differs. Compared with other models, AlexNet and VGGNet-16 have insufficient memory when the input size of the model is larger than $64 \times 64 \times 256$. This is because the model parameters are too large. From the results in the table, we can see that the training speed of the $32 \times 32 \times 128$ model is obviously faster than that of other sizes. For the other three networks, the performance of LeNet and ResNet is unstable, while the result of 3D-CNN is the best and is relatively stable.

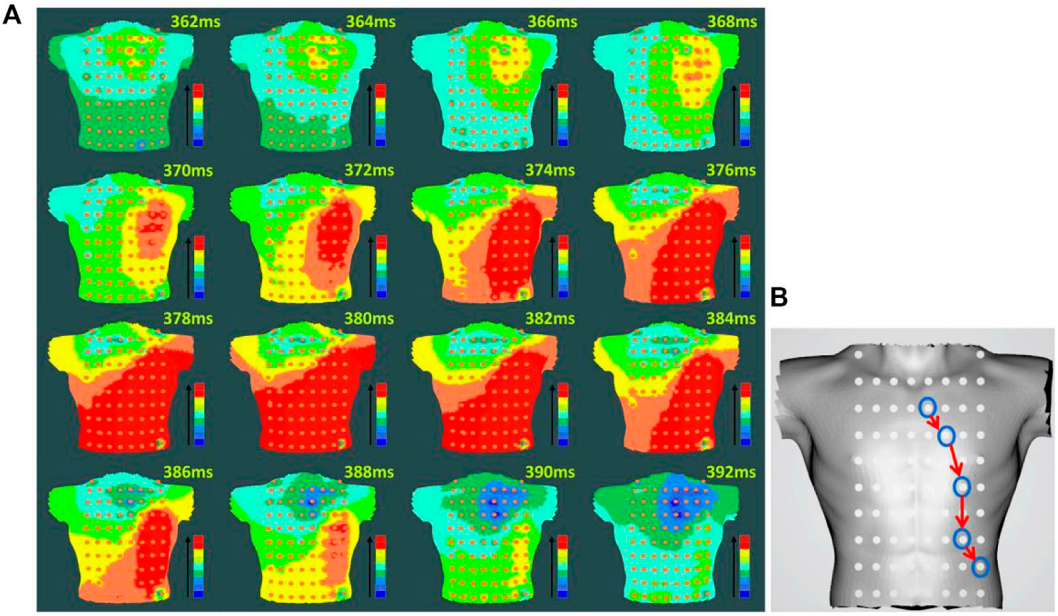

FIGURE 8
Rendering of the isopotential map of preoperative AF **(A)** Rendering of the isopotential map at different times. The time in this figure means each sampling time of the isopotential map and the color of each isopotential map represents the magnitude of the voltage amplitude: red represents the maximum relative amplitude, and blue represents the minimum. **(B)** Conduction order of Torso geometries. Blue circular lines are the location of the different electrodes; red arrow indicate the order of cardiac activations.

TABLE 3 Comparison of balanced random prediction performance with different network structures.

Size	Model	PPV(%)	SP(%)	SE (%)	ACC(%)	Time s/epoch	Batch size
32 × 32×128	LeNet	96.34	96.29	97.53	96.91	5 s/epoch	16
	AlexNet	65.85	48.14	100.00	74.07	11 s/epoch	16
	VGGNet-16	100.00	100.00	93.82	96.91	26 s/epoch	16
	ResNet	100.00	100.00	97.53	98.76	3 s/epoch	16
	Proposed	98.77	100.00	100.00	**99.38**	8 s/epoch	16
64 × 64 × 256	LeNet	92.11	92.59	86.42	89.51	8 s/epoch	16
	AlexNet	OOM[a]					16
	VGGNet-16	OOM[a]					16
	ResNet	97.18	97.53	85.19	91.36	19 s/epoch	16
	Proposed	100.00	100.00	96.30	**98.14**	52 s/epoch	16
64 × 64 × 400	LeNet	98.77	98.76	98.77	98.77	14 s/epoch	8
	AlexNet	OOM[a]					8
	VGGNet-16	OOM[a]					8
	ResNet	100.00	100.00	97.53	98.76	31 s/epoch	8
	Proposed	100.00	100.00	98.77	**99.38**	85 s/epoch	8

[a]Out of memory.
The bold values represents the optimal result of different algorithms.

TABLE 4 Inter-patient prediction performance of the five-fold cross-validation model.

Model	Indicator	Fold 1	Fold 2	Fold 3	Fold 4	Fold 5	Average
LeNet	ACC(%)	51.85	43.30	82.02	70.30	76.27	64.75
	SE (%)	0.00	11.79	79.49	63.31	71.43	45.20
	SP(%)	100.00	97.89	86.34	76.22	83.34	88.56
	PPV(%)	0.00	90.62	90.79	69.29	87.05	67.55
ResNet	ACC(%)	51.85	36.60	37.10	93.39	39.47	51.68
	SE (%)	0.00	0.00	0.00	94.24	0.00	18.85
	SP(%)	100.00	100.00	100.00	92.68	100.00	**98.52**
	PPV(%)	0.00	0.00	0.00	91.61	0.00	18.32
Proposed	ACC(%)	51.85	91.75	95.16	95.71	72.94	**81.48**
	SE (%)	0.00	91.87	95.97	90.65	60.07	**67.71**
	SP(%)	100.00	91.55	93.79	100.00	95.69	95.69
	PPV(%)	0.00	94.96	96.32	100	92.66	**76.79**

The bold values represents the optimal result of different algorithms.

TABLE 5 Performance of up-convolution model on five-fold cross-validation.

Model	PPV	SP	SE	ACC	AUC
VGG-5	**69.82**	87.08	56.66	71.48	**0.7958**
VGG-8	49.79	**96.65**	11.30	54.27	0.5370
3D-CNN + F4	64.98	82.66	**63.27**	**73.09**	0.7634

The bold values represents the optimal result of different algorithms.

3.4 3D-CNN in the inter-patient evaluation

A training set and testing set can be derived from the same patient, so the accuracy of using neural networks to predict recurrence is very close. In order to better verify that the network proposed in this study can effectively distinguish spatial–temporal features, in the later experiments we used the inter-patient method: the method of distinguishing patients to verify the model. The experiment uses five-fold cross-validation to characterize the experimental results. Since there are only four recurrent patients, one was randomly selected for training.

The 3D 32 × 32 × 128 isopotential sequence map was selected as the input to the network, and LeNet, ResNet, and 3D-CNN were selected for comparison. Table 4 shows that, in the case of a small amount of data, the accuracy of inter-patient in predicting the recurrence of AF has reached 81.48%. It can be seen from Table 3 that the 3D-CNN performs better than the three classic image network structures with an SE of 67.71%, SP of 95.69%, and PPV of 76.79%, based on the same dataset in inter-patient prediction of AF recurrence.

3.5 Effectiveness of temporal-attention block in the inter-patient evaluation

To verify the effectiveness of the proposed components of our model, we conducted control experiments with fine-tuned models on the inter-patient dataset using five-fold cross-validation. In the control experiment, we selected 64 × 64 × 256 as the input size. The baseline represents the CNN architecture using VGGNet-5. The 3DCNN + F4 represents the proposed model with up-convolution. The results of the control experiment are shown in Table 5; the proposed 3DCNN + F4 model outperforms the traditional VGGNet structure. It can also be seen that up-convolution has excellent performance on the inter-patient dataset, which demonstrates that up-convolution can effectively expand the difference between the recurrence and non-recurrence samples.

To more intuitively show the advantages of fusing the deep and shallow features model in the full connection layer, we calculated the performance of the validation set a on five-fold cross-validation. As shown in Table 6, only adding the fully connected layer of F2 or F3 could not improve the network identification accuracy of recurrent AF. We speculate that F2 or F3 might contain limited information in the middle layer of the network, so it could not bring gain to the network. However, when F1 and F4 were concatenated, the model contained the fusing deep and shallow features and performed better. Furthermore, when F1–F4 were concatenated, the model contained features of different depth and achieved best performance. The focal loss is widely used in class-imbalanced classification; in our work, the default-loss function is set to focal loss in a structure containing the F1–F4 methods. Overall, these results indicate that the network model combined with features of different depths can perform better.

TABLE 6 Performance of fusing the deep and shallow features model on five-fold cross-validation.

Model	PPV(%)	SP(%)	SE (%)	ACC(%)	AUC
3D-CNN + F1+F4	70.37	86.96	60.26	74.19	0.8214
3D-CNN + F4+F2	67.83	**88.56**	43.58	63.74	0.7757
3D-CNN + F4+F3	67.21	81.37	54.76	67.30	0.7385
3D-CNN + F4+F1+F2+F3	**72.48**	71.59	62.10	74.81	0.8459
3D-CNN + F4+F1+F2+F3+FOCAL	71.49	85.36	**65.80**	**76.36**	**0.8766**

The bold values represents the optimal result of different algorithms.

TABLE 7 Performance of adding attention block model on five-fold cross-validation.

Model	PPV(%)	SP(%)	SE (%)	ACC(%)	AUC
Temporal-attention A1	69.86	68.02	**70.67**	73.24	0.7583
Temporal-attention A2	68.09	80.07	63.70	72.92	0.7798
Temporal-attention A3	65.05	82.41	51.53	66.26	0.7041
Temporal-attention block (Proposed)	**76.79**	**95.69**	67.71	**81.48**	**0.8850**

The bold values represents the optimal result of different algorithms.

In addition, as shown in Table 7, our experiment analyzed the network with temporal-attention structure. By comparing the attention structures of temporal-attention A1 and other structures, it is found that the $1 \times 1 \times 1$ structure can bring gain to the network. We can see that the network model combined with temporal-attention A1 or temporal-attention block can achieve better results. It can also be seen that temporal-attention block (proposed) by fusing the features of global average pooling and max average pooling can effectively expand the difference between the recurrence samples and non-recurrence samples. Temporal-attention A3 is the most complex attention block in our experiment, while the results are not satisfactory. According to the results for temporal-attention A2 and A3, it seems that the attention-block parameters need not be too complex; otherwise, difficulties in network training will result.

4 Discussion

4.1 Isopotential map and its clinical significance

Many clinical indicators have been proposed to measure the recurrence of AF, such as CAAP-AF score (Winkle et al., 2016), while there is still a lack of a standard to evaluate the recurrence of AF by preoperative ECG. In this study, a new method based on 3D isopotential sequence maps is proposed to non-invasively evaluate the complex cardiac electrical activity of AF before CA.

The isopotential map shows the difference of the potential distribution of body surface ECG activity, which is a direct manifestation of the ECG conduction pathway. Over time, a series of isopotential maps on the torso geometry form the fluctuation map that represents the conduction path of cardiac electrical activity in the torso across the body surface. The experimental results show that fluctuations in the isopotential map can reveal some regularities of the conduction of the cardiac electrical activity. The 3D-CNN model could extract features of 3D isopotential sequence maps through the convolution layer. As an isopotential map is rich in spatial and temporal information, 3D-CNN can combine the spatial–temporal information using the unique skip-connections. Through the convolution layer, the detailed features reflecting the conduction of cardiac electrical activity in the isopotential map can be extracted to accurately predict the recurrence of AF.

4.2 Comparison with other studies

Based on the same dataset in the intra patient evaluation, the 3D-CNN performed better than the CNN approach of amplitude of discrete ECG signal, with SE of 83.50% and SP of 95.99% in predicting AF recurrence (Li et al., 2018), with SE of the proposed approach increasing by almost 15%.

Due to the lack of a public database for the study of AF recurrence, we can only make comparison with research in different datasets. Compared with the traditional approach of the P wave signal-averaged ECG method (Aytemir et al., 1999) with SE of 70% and SP of 76%, and based on the different dataset in the inter-patient evaluation, our model can achieve better prediction results by inputting 3D isopotential sequence maps that combine temporal information and spatial characteristics. Our method associates the

higher spatial-temporal characteristics complexity of BSPM with successful CA procedures, even though the interclass has statistically significant differences which are not verified on the signals we examined.

4.3 Benefits of the classification method

Experiments show that up-convolution and skip connections can promote the network compared with the traditional VGG network. The skip connections between the neural network layers of the dense layer can also make the network integrate features of different depth and can improve the accuracy of the network in identifying the recurrence of AF. Focal loss makes the model attend better to difficult samples and can solve the problem of data imbalance, thus improving the accuracy of identifying the recurrence of AF.

Our research proposes a novel attention block—temporal attention—which captures the importance of features of the local space of ECG signals in a period of time. Temporal attention uses an efficient attention-computation method that does not have any information bottlenecks. By comparing other attention blocks, we find that, for long time-series data, the temporal-attention block we propose can effectively extract temporal information and improve the accuracy of prediction. Our experiments demonstrate that temporal attention improves the baseline performance of architectures like 3D-CNN on tasks like ECG classification or other physiological signals, while only introducing a minimal computational overhead. We suggest that this temporal-attention block can achieve good results for any type of time series.

4.4 General remarks and limitation

Our experiment included 14 patients in the intra-patient evaluation. We used random shuffling to choose partial segments of 14 patients to build the network model and another to test it. This method ignores patient-specific differences because training segments and test segments are probably from the same patient—leading to relatively decent results—while other patients not involved in the network model training (non-participants) will have very poor test outcomes. In order to avoid this situation, this study used the inter-patient evaluation method, where the segments participating in the network training and the tested segments come from different patients, thus avoiding the aforementioned situation.

The lack of comparison with endocardial recording has hampered our research. A global overview of cardiac electrical activity is provided by BSPMs, while endocardial signals account for local information. Nevertheless, we propose a noninvasive analysis method. The superiority of our method over conventional CA outcome predictors has been demonstrated. Furthermore, the conclusion of this study is based on the BSPMs of 1627 segments from 14 patients with AF, and there is no available public database in regard to postoperative detailed information for patients with AF. For further research, we need to gradually collect more clinical BSPM data of AF patients to further verify the reliability of the proposed methods.

5 Conclusion

BSPMs combined with 3D isopotential sequence maps can be used as a tool for the clinical diagnosis and treatment of AF. Isopotential maps can express the conduction law of cardiac electrical activity on the body surface. Furthermore, 3D isopotential sequence maps can obtain the spatial information of conduction. Temporal-attention block is easy to use, can be embedded in any layer of the network, and has fewer parameters. The 3D-CNN with temporal-attention block can extract the features of 3D isopotential sequence maps, and the network is shown to be robust. The optimal network combination confirmed its excellent intra-patient prediction performance with 99.38% of ACC, 98.77% of SE, 100.00% of SP, and 100.00% of PPV. In intra-patient evaluation, 3D-CNN achieved 81.48% of ACC, 67.71% of SE, 76.79% of SP, 95.69% of PPV, and 0.8850 of AUC. A 3D-CNN with temporal-attention block can provide relevant insights for selecting patients with low recurrence risk and suitability for surgery for radiofrequency ablation, thus providing better treatment for them.

Data availability statement

The original contributions presented in the study are included in the article/supplementary material; further inquiries can be directed to the corresponding author.

Ethics statement

The studies involving human participants were reviewed and approved by the ethics review board of West China Hospital, Sichuan University. The patients/participants provided their written informed consent to participate in this study.

Author contributions

CY: conceptualization, resources, data curation, and supervision; GZ: methodology, investigation, software, formal analysis, and writing—review and editing; XF: methodology, conceptualization, and visualization; HY: methodology and writing.

Funding

This work was supported by Shanghai Municipal Special Project of Industry Transformation and Upgrading (GYQJ-2020-1-31), Shanghai Science and Technology Support Project (18441900900), and Shanghai Municipal Science and Technology Major Project (2017SHZDZX01).

Acknowledgments

The authors would like to thank Professor Zhong Wu from West China Hospital of Sichuan University, Dr. Xiliang Zhu, who now serves as the cardiothoracic physician of the People's Hospital in Henan Province, for their support in signal acquisition.

Conflict of interest

The authors declare that the research was conducted in the absence of any commercial or financial relationships that could be construed as a potential conflict of interest.

Publisher's note

All claims expressed in this article are solely those of the authors and do not necessarily represent those of their affiliated organizations, or those of the publisher, the editors, and the reviewers. Any product that may be evaluated in this article, or claim that may be made by its manufacturer, is not guaranteed or endorsed by the publisher.

References

Abildskov, J. A., Burgess, M. J., Lux, R. L., and Wyatt, R. F. (1976). Experimental evidence for regional cardiac influence in body surface isopotential maps of dogs. *Circ. Res.* 38 (5), 386–391. doi:10.1161/01.res.38.5.386

Alcaraz, R., Hornero, F., and Rieta, J. J. (2016). Electrocardiographic spectral features for long-term outcome prognosis of atrial fibrillation catheter ablation. *Ann. Biomed. Eng.* 44 (11), 3307–3318. doi:10.1007/s10439-016-1641-3

Alcaraz, R., Hornero, F., and Rieta, J. J. (2011). Noninvasive time and frequency predictors of long- standing atrial fibrillation early recurrence after electrical cardioversion. *Pacing Clin. Electrophysiol.* 34 (10), 1241–1250. doi:10.1111/j.1540-8159.2011.03125.x

Andersen, R. S., Peimankar, A., and Puthusserypady, S. (2019). A deep learning approach for real-time detection of atrial fibrillation. *Expert Syst. Appl.* 115, 465–473. doi:10.1016/j.eswa.2018.08.011

Aytemir, K., Naksoyek, S., Yildirir, A., and Oto, A. (1999). Prediction of atrial fibrillation recurrence after cardioversion by P wave signal-averaged electrocardiography. *Int. J. Cardiol.* 70 (1), 15–21. doi:10.1016/s0167-5273(99)00038-8

Bonizzi, P., Guillem, M., Climent, A. M., Millet, J., Zarzoso, V., Castells, F., et al. (2010). Noninvasive assessment of the complexity and stationarity of the atrial wavefront patterns during atrial fibrillation. *IEEE Trans. Biomed. Eng.* 57 (9), 2147–2157. doi:10.1109/TBME.2010.2052619

Brook, D. H., and MacLeod, R. S. (1997). Electrical imaging of the heart: Electrophysical underpinnings and signal processing opportunities. *IEEE Signal Process. Mag.* 14 (1), 24–42. doi:10.1109/79.560322

Calvo, D., Filgueiras-Rama, D., and Jalife, J. (2018). Mechanisms and drug development in atrial fibrillation. *Pharmacol. Rev.* 70 (3), 505–525. doi:10.1124/pr.117.014183

Chen, B., Deng, K., Fan, H., and Hao, M. (2013). Large-scale deformation monitoring in mining area by D-In SAR and 3D laser scanning technology integration. *Int. J. Min. Sci. Technol.* 23, 555–561. doi:10.1016/j.ijmst.2013.07.014

Everett, T. H., Kok, L. C., Vaughn, R. H., Moorman, J. R., and Haines, D. E. (2001). Frequency domain algorithm for quantifying atrial fibrillation organization to increase defibrillation efficacy. *IEEE Trans. Biomed. Eng.* 48 (9), 969–978. doi:10.1109/10.942586

Fawcett, T. (2006). An introduction to ROC analysis. *Pattern Recognit. Lett.* 27 (8), 861–874. doi:10.1016/j.patrec.2005.10.010

Goldberger, A. L., Amaral, L., Glass, L., Hausdorff, J. M., Ivanov, P. C., Mark, R. G., et al. (2000). PhysioBank, PhysioToolkit, and PhysioNet: Components of a new research resource for complex physiologic signals. *Circulation* 101 (23), e215–e220. doi:10.1161/01.cir.101.23.e215

Guo, Y., Wang, H., Hu, Q., Liu, H., Liu, L., and Bennamoun, M. (2020). Deep learning for 3D point clouds: A survey. *IEEE Trans. Pattern Anal. Mach. Intell.* 43 (12), 4338–4364. doi:10.1109/TPAMI.2020.3005434

He, K., Zhang, X., Ren, S., and Sun, J. (2016). "Deep residual learning for image recognition," in Proceedings of the IEEE conference on computer vision and pattern recognition, CVPR 2016, Las Vegas, USA, June 26–July 1, 2016, 770–778.

Heijman, J., Luermans, J. G. L. M., Linz, D., van Gelder, I. C., and Crijns, H. J. (2021). Risk factors for atrial fibrillation progression. *Card. Electrophysiol. Clin.* 13 (1), 201–209. doi:10.1016/j.ccep.2020.10.011

Hidalgo-Muñoz, A. R., Latcu, D. G., Meo, M., Meste, O., Popescu, I., Saoudi, N., et al. (2017). Spectral and spatiotemporal variability ECG parameters linked to catheter ablation outcome in persistent atrial fibrillation. *Comput. Biol. Med.* 88, 126–131. doi:10.1016/j.compbiomed.2017.07.004

Hu, J., Shen, L., and Sun, G. (2018). "Squeeze-and-excitation networks," in Proceedings of the IEEE conference on computer vision and pattern recognition, CVPR 2018, Salt Lake, USA, June 18–21, 2018, 7132–7141.

Ioffe, S., and Szegedy, C. (2015). "Batch normalization: Accelerating deep network training by reducing internal covariate shift," in International conference on machine learning (ICML), ICML 2015, Lile, France, July 6–11, 2015, 448–456.

Kingma, D. P., and Ba, J. (2014). A method for stochastic optimization. arXiv preprint arXiv:1412.6980. Available at: https://arxiv.org/abs/1412.6980 (Accessed Dec 22, 2014).

Krizhevsky, A., Sutskever, I., and Hinton, G. E. (2012). Imagenet classification with deep convolutional neural networks. *Adv. Neural Inf. Process. Syst.* 25, 1097–1105. NIPS. doi:10.1145/3065386

Lecun, Y., Bottou, L., Bengio, Y., and Haffner, P. (1998). Gradient-based learning applied to document recognition. *Proc. IEEE* 86 (11), 2278–2324. doi:10.1109/5.726791

Li, Z., Yang, C., and Zhang, Q. (2018). "Noninvasive prediction of atrial fibrillation recurrence based on a deep learning algorithm," in Proceedings of the 2018 2nd International Conference on Computational Biology and Bioinformatics, ICCBB 2018, Bari, Italy, Oct. 2018, 6711–7113. ACM International Conference Proceeding Series.

Lin, T. Y., Goyal, P., Girshick, R., He, K., and Dollár, P. (2017). "Focal loss for dense object detection," in Proceedings of the IEEE international conference on computer vision, Venice Italy, October 24–27, 2017, 2980–2988.

Marques, V. G., Rodrigo, M., de la Salud Guillem, M., and Salinet, J. (2020). Characterization of atrial arrhythmias in body surface potential mapping: A computational study. *Comput. Biol. Med.* 127, 103904. doi:10.1016/j.compbiomed.2020.103904

Matsuo, S., Lellouche, N., Wright, M., Bevilacqua, M., Knecht, S., Nault, I., et al. (2009). Clinical predictors of termination and clinical outcome of catheter ablation for persistent atrial fibrillation. *J. Am. Coll. Cardiol.* 54 (9), 788–795. doi:10.1016/j.jacc.2009.01.081

McCann, A., Vesin, J. M., Pruvot, E., Roten, L., Sticherling, C., and Luca, A. (2021). ECG-based indices to characterize persistent atrial fibrillation before and during stepwise catheter ablation. *Front. Physiol.* 12, 654053. doi:10.3389/fphys.2021.654053

Meo, M., Pambrun, T., Derval, N., Dumas-Pomier, C., Puyo, S., Duchateau, J., et al. (2018). Noninvasive assessment of atrial fibrillation complexity in relation to ablation characteristics and outcome. *Front. Physiol.* 9, 929. Heart Rhythm Society. doi:10.3389/fphys.2018.00929

Meo, M., Zarzoso, V., Meste, O., Latcu, D. G., and Saoudi, N. (2013). Spatial variability of the 12-lead surface ECG as a tool for noninvasive prediction of catheter ablation outcome in persistent atrial fibrillation. *IEEE Trans. Biomed. Eng.* 60 (1), 20–27. doi:10.1109/TBME.2012.2220639

Nault, I., Lellouche, N., Matsuo, S., Knecht, S., Wright, M., Lim, K. T., et al. (2009). Clinical value of fibrillatory wave amplitude on surface ECG in patients with persistent atrial fibrillation. *J. Interv. Card. Electrophysiol.* 26 (1), 11–19. doi:10.1007/s10840-009-9398-3

Nguyen, T-N., Nguyen, M. H., Tran, V-H., and Nguyen, T. H. (2019). A deep learning framework for inter-patient ECG classification. *Int. J. Comput. Sci. Netw. Secur.* 19 (1), 74–84. doi:10.5555/2627435.2670313

Oliver, F., Alex, S., Murtadha, K., San, T. R., Fujita, H., and Acharya, U. R. (2018). Automated detection of atrial fibrillation using long short-term memory network with RR interval signals. *Comput. Biol. Med.* 102, 327–335. doi:10.1016/j.compbiomed.2018.07.001

Rogers, J. M., Bayly, P. V., Ideker, R. E., and Smith, W. M. (1998). Quantitative techniques for analyzing high-resolution cardiac-mapping data. *IEEE Eng. Med. Biol. Mag.* 17 (1), 62–72. doi:10.1109/51.646223

Ronneberger, O., Fischer, P., and Brox, T. (2015). "U-Net: Convolutional networks for biomedical image segmentation," in International Conference on Medical image computing and computer-assisted intervention, October 5-9, 2015, Munich, Germany (Springer), 234–241.

Sahadevan, J., Ryu, K., Peltz, L., Khrestian, C. M., Stewart, R. W., Markowitz, A. H., et al. (2004). Epicardial mapping of chronic atrial fibrillation in patients: Preliminary observations. *Circulation* 110 (21), 3293–3299. doi:10.1161/01.CIR.0000147781.02738.13

Schotten, U., Verheule, S., Kirchhof, P., and Goette, A. (2011). Pathophysiological mechanisms of atrial fibrillation: A translational appraisal. *Physiol. Rev.* 91 (1), 265–325. doi:10.1152/physrev.00031.2009

Shepard, D. (1968). "A two-dimensional interpolation function for irregularly-spaced data," in Proceedings of the 1968 23rd ACM national conference (ACM), New York, USA, August 27–29, 1968, 517–524.

Simonyan, K. K., and Zisserman, A. (2014). Very deep convolutional networks for large-scale image recognition. Computer Science. Available at: https://arxiv.org/abs/1409.1556 (Accessed Sep 4, 2014).

Srivastava, N., Hinton, G., Krizhevsky, A., Sutskever, I., and Salakhutdinov, R., (2014). Dropout: A simple way to prevent neural networks from overfitting. *J. Mach. Learn. Res.* 15 (1), 1929–1958. doi:10.5555/2627435.2670313

Szegedy, C., Wei, L., Jia, Y., Sermanet, P., Reed, S., Anguelov, D., et al. (2015). "Going deeper with convolutions," in 2015 IEEE Conference on Computer Vision and Pattern Recognition (CVPR), CVPR 2015, Boston, MA, June 7, 2015 (IEEE), 1–9.

Szilágyi, J., Walters, T. E., Marcus, G. M., Vedantham, V., Moss, J. D., Badhwar, N., et al. (2018). Surface ECG and intracardiac spectral measures predict atrial fibrillation recurrence after catheter ablation. *J. Cardiovasc. Electrophysiol.* 29, 1371–1378. doi:10.1111/jce.13699

Takahashi, Y., Sanders, P., Jais, P., Hocini, M., Dubois, R., Rotter, M., et al. (2006). Organization of frequency spectra of atrial fibrillation: Relevance to radiofrequency catheter ablation. *J. Cardiovasc. Electrophysiol.* 17 (4), 382–388. doi:10.1111/j.1540-8167.2005.00414.x

Winkle, R. A., Jarman, J. W. E., Mead, R. H., Engel, G., Kong, M. H., Fleming, W., et al. (2016). Predicting atrial fibrillation ablation outcome: The CAAP-AF score. *Heart rhythm.*. 13 (11), 2119–2125. doi:10.1016/j.hrthm.2016.07.018

Woo, S., Park, J., Lee, J. Y., and Kweon, I. S. (2018). "Cbam: Convolutional block Attention module," in *European conference on computer vision (ECCV)*. Editors V. Ferrari, M. Hebert, C. Sminchisescu, and Y. Weiss (Cham: Springer), 3–19.

Zhang, Q., Yang, C., Wang, D., Li, Z., Wu, Z., Zhu, X., et al. (2018). Atrial fibrillation prediction based on the rhythm analysis of body surface potential mapping signals. *J. Med. Imaging Health Inf.* 8 (1), 145–150. doi:10.1166/jmihi.2018.2248

Zoni-Berisso, M., Lercari, F., Carazza, T., and Domenicucci, S. (2014). Epidemiology of atrial fibrillation: European perspective. *Clin. Epidemiol.* 6, 213–220. doi:10.2147/CLEP.S47385

frontiers | Frontiers in Physiology

TYPE Original Research
PUBLISHED 22 November 2022
DOI 10.3389/fphys.2022.939350

OPEN ACCESS

EDITED BY
Gernot Plank,
Medical University of Graz, Austria

REVIEWED BY
Oleg Aslanidi,
King's College London, United Kingdom
Raúl Alcaraz,
University of Castilla-La Mancha, Spain

*CORRESPONDENCE
Wouter-Jan Rappel,
rappel@physics.ucsd.edu

†These authors have contributed equally to this work

SPECIALTY SECTION
This article was submitted to Cardiac Electrophysiology, a section of the journal Frontiers in Physiology

RECEIVED 09 May 2022
ACCEPTED 10 November 2022
PUBLISHED 22 November 2022

CITATION
Kappel C, Reiss M, Rodrigo M, Ganesan P, Narayan SM and Rappel W-J (2022), Predicting acute termination and non-termination during ablation of human atrial fibrillation using quantitative indices.
Front. Physiol. 13:939350.
doi: 10.3389/fphys.2022.939350

Predicting acute termination and non-termination during ablation of human atrial fibrillation using quantitative indices

Cole Kappel[1†], Michael Reiss[2†], Miguel Rodrigo[3], Prasanth Ganesan[4], Sanjiv M. Narayan[4] and Wouter-Jan Rappel[2*]

[1]Department of Physics, UC Irvine, Irvine, CA, United States, [2]Department of Physics, UC San Diego, La Jolla, CA, United States, [3]CoMMLab, Electronic Engineering Department, Universitat de Valencia, Valencia, Spain, [4]Stanford Cardiovascular Institute, Stanford University School of Medicine, Stanford, CA, United States

Background: Termination of atrial fibrillation (AF), the most common arrhythmia in the United States, during catheter ablation is an attractive procedural endpoint, which has been associated with improved long-term outcome in some studies. It is not clear, however, whether it is possible to predict termination using clinical data. We developed and applied three quantitative indices in global multielectrode recordings of AF prior to ablation: average dominant frequency (ADF), spectral power index (SPI), and electrogram quality index (EQI).

Methods: In N = 42 persistent AF patients (65 ± 9 years, 14% female) we collected unipolar electrograms from 64-pole baskets (Abbott, CA). We studied N = 17 patients in whom AF terminated during ablation ("Term") and N = 25 in whom it did not ("Non-term"). For each index, we determined its ability to predict ablation by computing receiver operating characteristic (ROC) and calculated the area under the curve (AUC).

Results: The ADF did not differ for Term and Non-term patients at 5.28 ± 0.82 Hz and 5.51 ± 0.81 Hz, respectively ($p = 0.34$). Conversely, the SPI for these two groups was. 0.85 (0.80–0.92) and 0.97 (0.93–0.98) and the EQI was 0.61 (0.58–0.64) and 0.56 (0.55–0.59) ($p < 0.0001$). The AUC for predicting AF termination for the SPI was 0.85 ([0.68, 0.95] 95% CI), and for the EQI, 0.86 ([0.72, 0.95] 95% CI).

Conclusion: Both the EQI and the SPI may provide a useful clinical tool to predict procedural ablation outcome in persistent AF patients. Future studies are required to identify which physiological features of AF are revealed by these indices and hence linked to AF termination or non-termination.

KEYWORDS

atrial fibrillation, ablation, termination, computational analysis, electrograms

Introduction

Atrial fibrillation (AF) is the most common cardiac arrhythmia in the world and currently affects more than five million people in the United States alone (Chugh et al., 2014; Calkins et al., 2018). AF is associated with increased risk for stroke and morbidity. There is increasing evidence that early intervention for AF, either by drug therapy or ablation, can reduce long-term adverse outcomes (Kirchhof et al., 2020), yet both forms of therapy are suboptimal. Pulmonary vein isolation (PVI) to electrically isolate the pulmonary veins is the cornerstone of ablation treatment (Haissaguerre et al., 1998), but is only modestly effective with a 1-year success rate in persistent AF patients of 50–60% (Calkins et al., 2017). Several additional ablation procedures have been proposed yet with varying outcomes, such as targeting complex fractionated electrograms (Nademanee et al., 2004; Knecht et al., 2008), rotational and focal sources (Narayan et al., 2012; Ramirez et al., 2017; Baykaner et al., 2018), posterior wall isolation (Lee et al., 2019; Pothineni et al., 2021; Chieng et al., 2022) and others. It would be useful to track AF ablation intraprocedurally, to determine if the current strategy is effective in this patient or whether additional lesions are warranted.

Currently, there is no quantitative metric that can reliably predict whether ablation will result in AF termination or not. Such a metric may be procedurally useful. In addition, some studies have shown that acute termination during ablation is associated with improved long-term outcome (O'Neill et al., 2009; Scherr et al., 2015; Heist et al., 2012; Zhou et al., 2013; Park et al., 2012; Schreiber et al., 2015; Rostock et al., 2011). Furthermore, a reliable metric may provide insights into the spatio-temporal activation patterns that underlie AF.

In this study, we developed and compared the ability of three different quantitative indices to predict whether a uniform ablation strategy resulted in AF termination to either sinus rhythm (SR) or atrial tachycardia (AT), or failed to terminate AF. Our indices were computed using unipolar electrograms from 64-pole baskets, measured over a prolonged time (60 s). The indices consisted of the average dominant frequency (ADF), the DF averaged over all electrograms, the spectral power index (SPI), a measure of the power contained in the power spectrum close to the dominant frequency relative to the total power in the spectrum, and a novel electrogram quality index (EQI), a measure of the relative amplitude of the most prominent peak of the time derivative of electrograms in repeated intervals. These indices were tested in N = 42 patients, divided into N = 17 patients that did ("Term") and N = 25 patients that did not ("Non-term") terminate during the procedure.

Methods

We studied 42 patients with persistent AF (defined as patients in whom AF lasted longer than 7 days) referred for ablation at Stanford University Hospital, Palo Alto, CA for standard indications. Of these patients, N = 17 terminated acutely during the ablation procedure, while N = 25 did not. All patients had failed at least one anti-arrhythmic medication, were >18 years and none had contra-indications to ablation. All patients provided written informed consent and this study was approved by our Institutional IRB.

Data acquisition

No electrical cardioversion was applied at the beginning of the procedure and patients who presented in sinus rhythm were paced into AF. AF was mapped using 64 pole contact baskets (FIRMap, Abbott) for 60 s. The baskets were positioned in LA for AF mapping, based upon 3-dimensional electroanatomic imaging (NavX, St Jude Medical, Sylmar, CA; or Carto, Biosense-Webster, Diamond Bar, CA). This catheter consists of eight splines, each with eight electrodes, totaling 64 electrodes, which improves over older designs and covers >70% of the LA (Honarbakhsh et al., 2017). Within a spline, electrodes are separated by 4–6 mm, and spacing between splines is mostly within 20% of that range (Honarbakhsh et al., 2017). Ablation was guided prospectively at regions of interest identified by a commercial system (RhythmView™, Abbott, Inc.).

Endocardial ablation was used using 3.5 mm irrigated-tip catheters (SmartTouch®, Biosense Webster; FlexAbilityTM, Abbott) targeting 30–35 W at 10–20 g force. The primary goal was to perform pulmonary vein isolation assessed by the endpoint of entrance block. Additional lesions were patient-tailored. Selected sites were ablated to cover 2–3 cm regions, to an endpoint of voltage < 0.5 mV. Ablation at any site was abandoned if the esophagus was heated by > 1.5 C despite reduced power or high power short-duration lesions (50W, 6 s), or that overlay regions of phrenic nerve capture. Electrical cardioversion was applied if AF had not terminated (non-termination group).

Data export

Unipolar electrograms were recorded at 1 kHz sampling and the QRS complex was removed by computing an average QRS complex and subtracting it from electrograms as detailed before (Alhusseini et al., 2017).

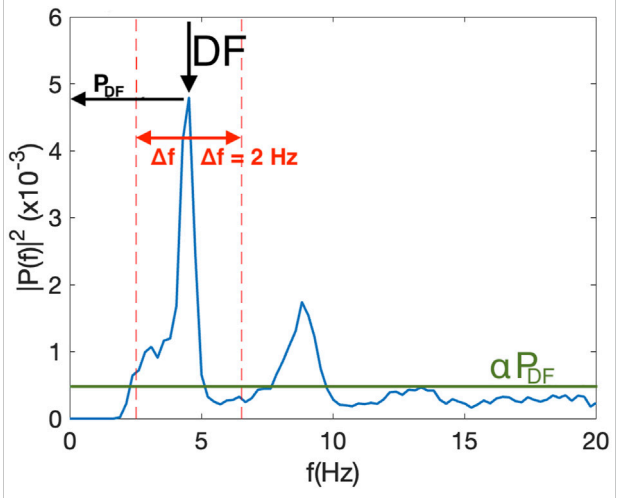

FIGURE 1
Example of the single sided power spectrum of one of the electrograms used to calculate the DF and the SPI. The threshold, a fraction α of the peak at the DF, αP_{DF}, is plotted as a green line using α = 0.1 while the interval around the DF, indicated by the arrow, is plotted as dashed red lines, and shown using Δf = 2 Hz. In this example, SPI = 0.67 and DF = 4.53 Hz.

Data analysis

The Dominant Frequency (DF) was computed for each electrode from the Power Spectral Density (PSD) of the unipolar electrogram using a Welch Periodogram (50% overlapping, 4 s length Hamming window) and a frequency interval between 0 and 20 Hz. The ADF for each patient was then computed as the mean of the DF of all 64 electrodes.

To compute the Spectral Power Index (SPI) of an electrogram (Figure 1), we first determined the spectral power of the DF (P_{DF}) and defined a threshold αP_{DF}, where α is a value between 0 and 1. This threshold was introduced to remove the noise floor in the signal. Second, we determined all frequencies with a power larger than αP_{DF} and within an interval of width 2Δf symmetrically located around the DF: DF±Δf. The sum of the power for these frequencies was computed as P_{int}. The SPI was then defined as the ratio of P_{int} and the sum of the power for all frequencies between 0 and 20 Hz that were above αP_{DF}, P_{all}: SPI = P_{int}/P_{all}. This procedure is shown in Figure 1, where we have plotted a sample power spectrum of one of the electrograms. The threshold, here taken to be $\alpha = 0.1$, is shown as a green line while the interval around the DF is indicated as dashed red lines and shown using Δf = 4 Hz. Note that the SPI can take on values between 0 and 1. Specifically, for noisy signals, with a broad peak, we expect that most power is concentrated around the DF. This signal will have a high SPI value. For more regular signals, we expect a narrow peak and more power in harmonics (corresponding to whole number multiples the peak frequency), resulting in a low SPI value. Figure 2A shows a power spectrum of an electrogram with a high SPI (SPI = 0.95). In this case, all power above the threshold, here chosen to be $\alpha = 0.2$, resided within the interval DF±Δf, with Δf = 3 Hz. As a comparison, Figure 2B shows a power spectrum of an electrogram with the low SPI value (SPI = 0.65). In this case, for the same values of the parameters α and Δf, significant amount power is distributed at frequencies outside the interval around DF.

For the Electrogram Quality Index (EQI), we processed each electrogram v(t) with a bandpass filter from 2.5 Hz to 30 Hz as a combination of a low-pass and a high-pass Butterworth filter of fourth order, respectively. Additionally, we applied a fourth order Butterworth notch filter between 55 and 65 Hz to eliminate 60 Hz noise. To calculate the period T of the signal, we used the first peak in the autocorrelation at non-zero time of v(t), smoothed using a zero-phase digital filter. We computed the first derivate with respect to time, $\frac{dv}{dt}$, and the resulting time trace was divided into N consecutive intervals with width T. This procedure is illustrated in Figure 3 for two sample electrograms and where the intervals are marked by dashed red lines. In these, and other patients, T was around 200 ms, resulting in approximately 300 intervals. We computed for each interval i the difference, Q_i, between the maximum value of $\frac{dv}{dt}$, β, and the sum of all other (n) positive maxima within that interval, γ, normalized by β: $Q_i = (\beta - \frac{1}{n}\sum_{j=1}^{n}\gamma_j)/\beta$. In Figure 3, the maximum value β for the first intervals is marked by a magenta dot, while all other positive maxima in the same interval are marked by black dots. For an electrogram with a single peak in its time derivate, the value of Q_i will equate to 1. On the other hand, a value of 0 corresponds to a signal with equal valued maxima of $\frac{dv}{dt}$ in the interval. Thus, Q_i quantifies the ease with which a large $\frac{dv}{dt}$ can be identified in the interval. Examples of intervals with large values of Q_i are shown in Figure 3A: for every interval, the maximum $\frac{dv}{dt}$ is well separated from smaller peaks in $\frac{dv}{dt}$ and clearly distinguishable. As a result, Q_i, which quantifies the normalized difference between the value of this peak and the sum of all other positive peaks within each interval, is close to one In contrast, the intervals presented in Figure 3B all have multiple peaks with almost identical amplitudes, resulting in much smaller values of Q_i.

The electrogram quality index was then calculated as the average of Q_i over all N intervals: $EQI = \sum_{i=1}^{N} Q_i/N$. In summary, the EQI can also take on values between 0 and 1 with large values of EQI corresponding to $\frac{dv}{dt}$ traces with a clear maximum in each interval and small values corresponding to signals that have multiple and almost equally valued peaks in $\frac{dv}{dt}$ for the majority of its time.

Statistics

Data are reported as mean ± standard deviation for normally distributed data and statistical significance was calculated using a

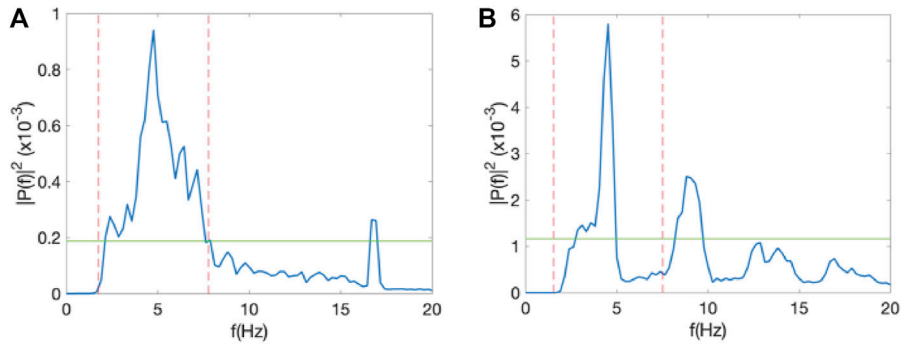

FIGURE 2
SPI analysis. **(A)** Power spectrum of one of the electrodes of a 55 year-old female in which AF did not terminate during the procedure, corresponding to an SPI value of 0.95, computed using $\alpha = 0.2$ and $\Delta f = 3$ Hz. **(B)** As in A, but for a 51 year-old male in which AF terminated during the procedure with an SPI value of 0.65.

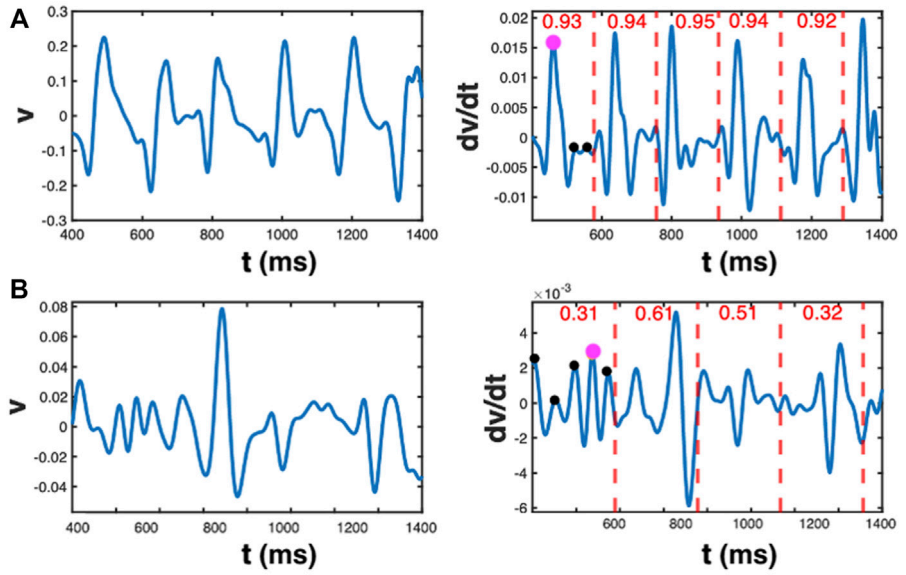

FIGURE 3
EQI analysis. **(A)** Unipolar trace (left panel) and its time derivative (right panel) for an electrogram with large values of Q_i. The value of Q_i is reported in the right panel for each time interval, indicated by the red dashed lines. It quantifies the normalized difference between the maximum value of dv/dt and the sum of all other positive maxima within the interval. These dots are marked for the first interval in magenta and black, respectively. The EQI is computed as the average value of Q_i for each time interval. **(B)** As in A, but now for an electrogram with small values of Q_i (reported in the right panel).

two tailed *t*-test. For data that were not normally distributed, data are reported as median (interquartile 1 - inter quartile 3) and the significance was evaluated with the Wilcoxon rank sum test using the "ranksum" function in MATLAB. A *p*-value < 0.05 was considered statistically significant. Receiver Operating Characteristic Curves (ROC curves) were computed using the built in MATLAB "perfcurve" function and confidence intervals (CIs) of the area under curve (AUC) values were estimated using a non-parametric bootstrap algorithm, using 10,000 iterations.

As a sensitivity analysis, the AUC values were also computed by performing 5,000 iterations in which 5 randomly selected patients were removed from the total cohort. Results form this analysis are reported as median

TABLE 1 Patient details.

	Term (n = 17)	*Non-term (n = 25)*	*p-value*
Age in years	62.08 ± 10.98	66.92 ± 8.02	0.11
Female	17.6% (3)	12% (3)	0.61
Non-paroxysmal AF	100% (17)	100% (25)	1
Normal LA Size	29.4% (5)	12% (3)	0.16
LVEF %	52.88 ± 12.93	55.04 ± 12.44	0.60
Hypertension	64.7% (11)	60% (15)	0.76
Coronary artery disease	5.88% (1)	24% (6)	0.12
Diabetes mellitus	29.4% (5)	16% (4)	0.30
Transient ischemia attack/stroke	0% (0)	8% (2)	0.50
CHADS2-VASc	1.82 ± 1.33	2.32 ± 1.46	0.27
Previous AF ablation	52.94% (9)	32% (8)	0.18
On Anti Arrhythmic Drug(s)	64.7% (11)	44% (11)	0.19

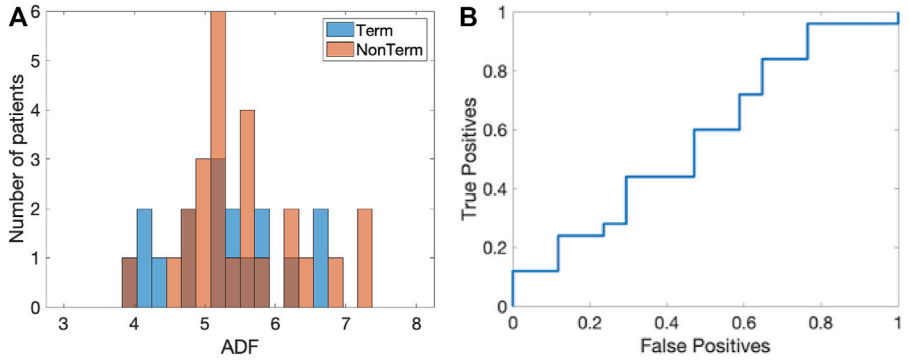

FIGURE 4
ADF analysis. **(A)** Histogram of the ADF value for the Term (blue) and Non-term groups (red). **(B)** Corresponding ROC curve with an AUC = 0.57 ([0.38, 0.75] 95% CI).

(interquartile 1 - inter quartile 3). Finally, the ROC analysis was repeated by removing outliers in the data set, defined as values that were either 3 standard deviations from the mean (for normal distributions) or 1.5 times the interquartile range (IQR) above the third quartile or below the first quartile (for non-normal distributions).

Results

Patient demographics

Table 1 provides the clinical details for the patients in the termination and non-termination cohort. The two groups did not differ significantly in any characteristic.

Average dominant frequency (ADF)

We first determined the ADF using the PSD of the electrograms. The histograms of the ADF values, averaged over all electrograms for each patient, are shown in Figure 4A for both the Term (blue) and Non-term groups (red). For the termination patients, we found that the ADF was 5.28 ± 0.82 Hz while for the non-termination patients this value was 5.51 ± 0.81 Hz ($p = 0.34$). These histograms did not contain any outliers (Methods).

To determine whether this quantity was able to distinguish between termination and non-termination patients, we computed the corresponding receiver operating characteristic (ROC) (Figure 4B). We calculated the area under the curve (AUC) and found that it was 0.57 ([0.38, 0.75] 95% CI). The

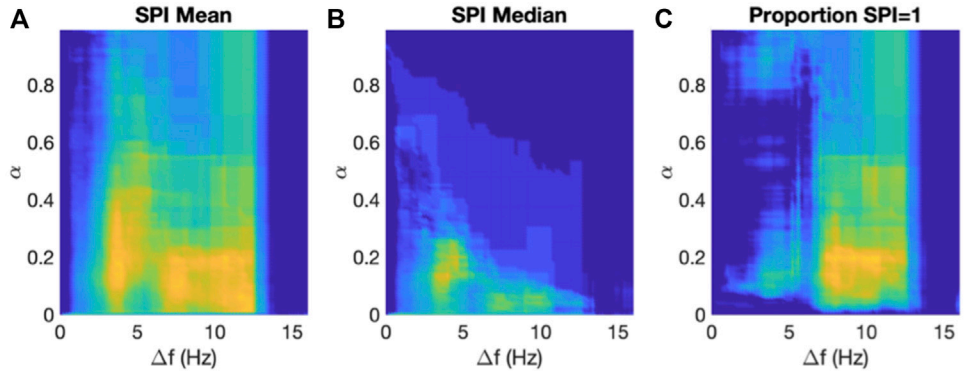

FIGURE 5
Results of the SPI analysis. **(A)** The AUC of the ROCs computed using the mean SPI as a function of the two parameters in the algorithm, α and Δf, plotted using a color scale with AUC = 0.5 corresponding to blue and AUC = 0.9 corresponding to yellow. **(B)** As in A but now using the median value of the SPI. **(C)** As in A but now using the proportion of channels with SPI = 1.

sensitivity analysis (Methods) resulted in a median AUC that was unaltered, with a small IQR: 0.57 (0.55–0.60).

Spectral power index (SPI)

We next determined whether the shape of the peak in the power spectrum was significantly different between the termination and non-termination patients. For this, we computed the SPI, which ranges between 0 and one and which represents a measure of the power around the DF relative to the total power (Methods).

We computed the SPI for each patient as the mean value over all electrograms as a function of the two parameters α and Δf in the analysis (Methods). After having obtained the SPI values for both patient groups, we determined the ROC and corresponding AUC. The result of this grid search is presented in Figure 5A, where we plot the AUC using a color scheme with low/high values shown in blue/yellow. The maximum AUC value was found to be 0.85 ([0.68, 0.95] 95% CI) corresponding to a threshold of α = 0.18 and a frequency interval around the DF of Δf = 3.6 Hz. For these parameter values, the mean SPI for the termination patients was 0.85 (0.80–0.92) while for the non-termination patients it was 0.97 (0.93–0.98) ($p < 0.001$). This significance was retained when adding any of the patient characteristics to the SPI in a logistic regression model. After removing one outlier in each data set, the AUC only changed to 0.86 while the sensitivity analysis resulted in an identical AUC with a small IQR: AUC = 0.85 (0.83–0.87). We also performed this grid search using the median value of the SPI of all electrograms, with the results illustrated in Figure 5B. Using this median value, we found a maximum AUC of 0.82 ([0.65, 0.93] 95% CI) using a threshold α = 0.14 and a frequency interval of Δf = 4.0 Hz.

Finally, we asked whether the termination patients had more electrograms with SPI = 1 than non-termination patients. To address this question, we calculated for each patient the proportion of electrograms with an SPI value equal to 1, again using a grid search in threshold and frequency interval. For this comparison, we found a maximum AUC of 0.86 (([0.71, 0.95] 95% CI) using a threshold of α = 0.2 and a frequency interval of Δf = 10.4 Hz (Figure 5C). For these parameters, the average proportion of electrograms with SOI = 1 in termination patients was 0.91 (0.65–0.96) while this value was 1.00 (0.96–1.00) for non-termination patients ($p < 0.001$).

Electrogram quality index (EQI)

As a final quantity, we computed the EQI for each patient, averaged over all electrograms. The histograms of the EQI for the termination (blue) and non-termination patients (red) are shown in Figure 6A. The median EQI for the termination group was 0.61 (0.58–0.64) while that for the non-termination group was 0.56 (0.55–0.59) ($p < 0.0001$). As was the case for the SPI, this significance was retained when combining the EQI and any single patient characteristic in a logistic regression model. The ROC curve for this analysis is plotted in Figure 6B and has an AUC of 0.86 ([0.72, 0.95] 95% CI). Finally, one outlier was identified in the Term patients and removing this outlier did not change the AUC while the sensitive analysis resulted in an AUC value of 0.86 (0.85–0.88).

Discussion

In this study we show that novel indices of electrograms in patients with persistent AF can identify those in whom AF did or did not terminate by ablation.

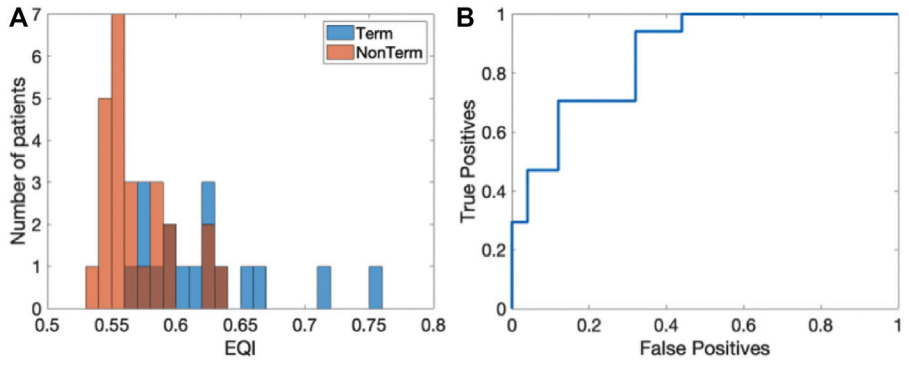

FIGURE 6
Results of the EQI analysis. **(A)** Histograms of EQI for the termination (blue) and non-termination patients (red). **(B)** ROC curve for the EQI analysis (AUC = 0.86 ([0.72,0.95] 95% CI)).

Usefulness of AF termination

While the utility of AF termination during ablation is debated, there are few other procedural endpoints beyond isolation of the pulmonary veins. AF termination has been shown in several studies to be associated with improved long-term outcome (O'Neill et al., 2009; Scherr et al., 2015; Heist et al., 2012; Zhou et al., 2013; Park et al., 2012; Schreiber et al., 2015; Rostock et al., 2011). For example, using a stepwise ablation procedure that involved pulmonary vein isolation, electrogram-guided, and linear ablation, it was shown that inability to terminate AF during ablation was the strongest predictor of arrhythmia recurrence (Scherr et al., 2015). Other studies have failed to show this association and that further studies are required to reconcile the divergent clinical outcomes (Estner et al., 2008; Elayi et al., 2010; Wang et al., 2018). Nevertheless, termination remains the only acute endpoint that correlates with long-term outcome and knowing whether termination is achievable could enable an electrophysiologist to add or constrain lesion sets accordingly.

Previous studies predicting AF termination

A number of previous studies have investigated whether patient characteristics can predict acute AF termination in catheter ablation. In one study, a cohort of persistent AF patients with a similar size to the current study (N = 38, with 18 termination patients) was examined (Combes et al., 2013). Several patient characteristics were found to be significantly associated with AF termination during ablation, including left ventricular ejection fraction and left atrial area. However, in a multivariable analysis, only the left atrial appendage peak flow velocity remained significant, with the termination group having a larger velocity ($p = 0.04$). The corresponding AUC was found to be 0.81. In another study, N = 70 persistent AF patients, of whom 14 terminated, were investigated (Kumagai et al., 2013). Again, it was found that the left atrial appendage contraction velocity was significantly decreased in the non-termination group and was an independent predictor of termination. No AUC value was reported but this study also showed that patients that terminated during ablation had a higher AF-free survival after 1 year than patients that needed cardioversion. In future studies, it would be interesting to combine this patient characteristic with our newly developed indices.

Indices in our study

The ADF metric, which quantifies the frequency of the peak in the power spectrum, averaged over all electrograms, was not able to distinguish between the two patient groups. This suggests that the overall average 'rate' of AF within the atrium may not separate patient groups. The average DF value between the two groups (5.28 Hz vs 5.51 Hz) was not significantly different and the AUC value of the ROC was close to 0.5 (0.57). These ADF values were consistent with those reported in a recent previous study (Rodrigo et al., 2021). Note that we did not use the location of DF sites to guide ablation (Atienza et al., 2009).

Contrary to the ADF index, both the SPI and EQI had average values that differed significantly between patients with and without AF termination. These indices provided promising AUCs (0.85 and 0.86, respectively), indicating that they may be clinically useful. The SPI quantifies the amount of power contained within a certain frequency band around the DF relative to the power contained in the entire 0–20Hz interval. This SPI is a function of two parameters: the width of this frequency band and the threshold value above which the power is considered.

SPI is distinct from previous spectral organizational indices, such as those which computed a regularity index that involved the power within a fixed interval around the DF (Skanes et al., 1998; Sanders et al., 2005; Rodrigo et al., 2021). Using a systematic search, in which we varied the values of these two parameters, we found a set of parameters that optimized the AUC of the ROC. Our results indicated that, on average, the Term patients had more power in their PSD outside the interval around the DF than Non-term patients. In other words, the Non-term patients had more noisy signals, resulting in a broad peak within the interval around the DF while the Term patients had narrower peaks, with more power in harmonics that were outside this interval.

The newly introduced EQI is computed using the time derivative of the electrogram and quantifies the amplitude of the peak, relative to all other peaks in intervals of length T, the correlation time. This is equivalent to the magnitude of the slope of the electrogram, which has long been used to identify tissue activation (Colli-Franzone et al., 1982; Steinhaus, 1989; Kuklik et al., 2015). EQI is determined by first computing T in the electrogram and then, using contiguous windows of size T, determining the value of the maximum amplitude of the derivative relative to all other maxima of the derivative. Thus, an electrogram with either several near-equal valued maxima or with poorly identifiable peak values of the derivative in most intervals will have a small EQI. In contrast, very regular electrograms with a clearly identifiable and large derivative peak will result in a large EQI. We have verified that this computation is insensitive to the start time of the first time window (Supplementary Figure S1). In contrast to the SPI, the EQI does not depend on adjustable parameters and did not require fine tuning to achieve an optimal AUC. The EQI was significantly higher in the Term compared to the Non-term patients, indicating that the electrogram shapes of the Term group exhibited peaks in their time derivative that were more clearly identifiable. Activation patterns in this group determined using algorithms based on electrogram shapes may therefore be less prone to noise. This could result in better identification of rotational sources, better guidance for targeted ablation, and could result in acute termination.

Our results were computed using the simultaneous recordings from 64 electrograms, obtained from a basket catheter inserted into the left atrium. Thus, and distinct from other studies that used single recording electrodes, we were able to obtain spatially averaged quantities since this basket covers >70% of the atrium. It would be interesting, however, to apply our indices to electrograms that are collected in a pointwise fashion. Furthermore, we used recordings with a prolonged duration (60s), which reduces the likelihood of spurious results.

Our results indicate that both the SPI and the EQI may be a useful tool to predict whether ablation results in acute termination or not. Furthermore, our finding that the SPI and EQI are significantly different in Term than in Non-term patients may indicate a difference in atrial organization in these patient groups.

Limitations

Our cohort size was moderate (N = 42) and replication in larger samples with external validation is needed. We are currently planning to expand the analysis to larger patient groups. Furthermore, we did not use the indices to prospectively predict outcome, or to guide ablation strategy. In addition, although studies have shown that acute termination during ablation correlates with long-term outcome, this study did not report any follow-up results. We are currently planning to determine whether the metrics are able to predict long-term outcome in AF patients.

Data availability statement

The raw data supporting the conclusion of this article will be made available by the authors, without undue reservation.

Ethics statement

The studies involving human participants were reviewed and approved by Institutional IRB Board, Stanford University. The patients/participants provided their written informed consent to participate in this study.

Author contributions

CK and MR performed the computational analysis. SN provided the clinical data. PG and MR organized the data base. W-JR designed the study and wrote the first draft. All authors contributed to manuscript revision, read, and approved the submitted version.

Funding

This work was supported in part by grants from the National Institutes of Health to W-JR (HL122384) and SN (HL149134 and HL83359).

Acknowledgments

We thank Paul Clopton for many valuable discussions.

Conflict of interest

The authors declare that the research was conducted in the absence of any commercial or financial relationships that could be construed as a potential conflict of interest.

Publisher's note

All claims expressed in this article are solely those of the authors and do not necessarily represent those of their affiliated organizations, or those of the publisher, the editors and the reviewers. Any product that may be evaluated in this article, or claim that may be made by its manufacturer, is not guaranteed or endorsed by the publisher.

Supplementary material

The Supplementary Material for this article can be found online at: https://www.frontiersin.org/articles/10.3389/fphys.2022.939350/full#supplementary-material

References

Alhusseini, M., Vidmar, D., Meckler, G. L., Kowalewski, C., Shenasa, F., Wang, P. J., et al. (2017). Two independent mapping techniques identify rotational activity patterns at sites of local termination during persistent atrial fibrillation. *J. Cardiovasc. Electrophysiol.* 28, 615–622. doi:10.1111/jce.13177

Atienza, F., Almendral, J., Jalife, J., Zlochiver, S., Ploutz-Snyder, R., Torrecilla, E. G., et al. (2009). Real-time dominant frequency mapping and ablation of dominant frequency sites in atrial fibrillation with left-to-right frequency gradients predicts long-term maintenance of sinus rhythm. *Heart rhythm.* 6, 33–40. doi:10.1016/j.hrthm.2008.10.024

Baykaner, T., Rogers, A. J., Meckler, G. L., Zaman, J., Navara, R., Rodrigo, M., et al. (2018). Clinical implications of ablation of drivers for atrial fibrillation: A systematic review and meta-analysis. *Circ. Arrhythm. Electrophysiol.* 11, e006119. doi:10.1161/CIRCEP.117.006119

Calkins, H., Hindricks, G., Cappato, R., Kim, Y-H., Saad, E. B., Aguinaga, L., et al. (2018). 2017 HRS/EHRA/ECAS/APHRS/SOLAECE expert consensus statement on catheter and surgical ablation of atrial fibrillation: Executive summary. *Europace* 20, 157–208. doi:10.1093/europace/eux275

Calkins, H., Hindricks, G., Cappato, R., Kim, Y. H., Saad, E. B., Aguinaga, L., et al. (2017). 2017 HRS/EHRA/ECAS/APHRS/SOLAECE expert consensus statement on catheter and surgical ablation of atrial fibrillation: Executive summary. *Heart rhythm.* 14, e445–e494. doi:10.1016/j.hrthm.2017.07.009

Chieng, D., Sugumar, H., Ling, L-H., Segan, L., Azzopardi, S., Prabhu, S., et al. (2022). Catheter ablation for persistent atrial fibrillation: A multicenter randomized trial of pulmonary vein isolation (PVI) versus PVI with posterior left atrial wall isolation (PWI)-The capla study. *Am. Heart J.* 243, 210–220. doi:10.1016/j.ahj.2021.09.015

Chugh, S. S., Havmoeller, R., Narayanan, K., Singh, D., Rienstra, M., Benjamin, E. J., et al. (2014). Worldwide epidemiology of atrial fibrillation: A global burden of disease 2010 study. *Circulation* 129, 837–847. doi:10.1161/CIRCULATIONAHA.113.005119

Colli-Franzone, P., Guerri, L., Viganotti, C., Macchi, E., Baruffi, S., Spaggiari, S., et al. (1982). Potential fields generated by oblique dipole layers modeling excitation wavefronts in the anisotropic myocardium. Comparison with potential fields elicited by paced dog hearts in a volume conductor. *Circ. Res.* 51, 330–346. doi:10.1161/01.res.51.3.330

Combes, S., Jacob, S., Combes, N., Karam, N., Chaumeil, A., Guy-Moyat, B., et al. (2013). Predicting favourable outcomes in the setting of radiofrequency catheter ablation of long-standing persistent atrial fibrillation: A pilot study assessing the value of left atrial appendage peak flow velocity. *Arch. Cardiovasc. Dis.* 106, 36–43. doi:10.1016/j.acvd.2012.09.002

Elayi, C. S., Di Biase, L., Barrett, C., Ching, C. K., Al Aly, M., Lucciola, M., et al. (2010). Atrial fibrillation termination as a procedural endpoint during ablation in long-standing persistent atrial fibrillation. *Heart rhythm.* 7, 1216–1223. doi:10.1016/j.hrthm.2010.01.038

Estner, H. L., Hessling, G., Ndrepepa, G., Luik, A., Schmitt, C., Konietzko, A., et al. (2008). Acute effects and long-term outcome of pulmonary vein isolation in combination with electrogram-guided substrate ablation for persistent atrial fibrillation. *Am. J. Cardiol.* 101, 332–337. doi:10.1016/j.amjcard.2007.08.053

Haissaguerre, M., Jais, P., Shah, D. C., Takahashi, A., Hocini, M., Quiniou, G., et al. (1998). Spontaneous initiation of atrial fibrillation by ectopic beats originating in the pulmonary veins. *N. Engl. J. Med.* 339, 659–666. doi:10.1056/NEJM199809033391003

Heist, E. K., Chalhoub, F., Barrett, C., Danik, S., Ruskin, J. N., and Mansour, M. (2012). Predictors of atrial fibrillation termination and clinical success of catheter ablation of persistent atrial fibrillation. *Am. J. Cardiol.* 110, 545–551. doi:10.1016/j.amjcard.2012.04.028

Honarbakhsh, S., Schilling, R. J., Providência, R., Dhillon, G., Sawhney, V., Martin, C. A., et al. (2017). Panoramic atrial mapping with basket catheters: A quantitative analysis to optimize practice, patient selection, and catheter choice. *J. Cardiovasc. Electrophysiol.* 28, 1423–1432. doi:10.1111/jce.13331

Kirchhof, P., Camm, A. J., Goette, A., Brandes, A., Eckardt, L., Elvan, A., et al. (2020). Early rhythm-control therapy in patients with atrial fibrillation. *N. Engl. J. Med.* 383, 1305–1316. doi:10.1056/NEJMoa2019422

Knecht, S., Hocini, M., Wright, M., Lellouche, N., O'Neill, M. D., Matsuo, S., et al. (2008). Left atrial linear lesions are required for successful treatment of persistent atrial fibrillation. *Eur. Heart J.* 29, 2359–2366. doi:10.1093/eurheartj/ehn302

Kuklik, P., Zeemering, S., Maesen, B., Maessen, J., Crijns, H. J., Verheule, S., et al. (2015). Reconstruction of instantaneous phase of unipolar atrial contact electrogram using a concept of sinusoidal recomposition and Hilbert transform. *IEEE Trans. Biomed. Eng.* 62, 296–302. doi:10.1109/TBME.2014.2350029

Kumagai, K., Sakamoto, T., Nakamura, K., Hayano, M., Yamashita, E., and Oshima, S. (2013). Pre-procedural prediction of termination of persistent atrial fibrillation by catheter ablation as an indicator of reverse remodeling of the left atrium. *Circ. J.* 77, 1416–1423. CJ-12-0934. doi:10.1253/circj.cj-12-0934

Lee, J. M., Shim, J., Park, J., Yu, H. T., Kim, T-H., Park, J-K., et al. (2019). The electrical isolation of the left atrial posterior wall in catheter ablation of persistent atrial fibrillation. *JACC. Clin. Electrophysiol.* 5, 1253–1261. doi:10.1016/j.jacep.2019.08.021

Nademanee, K., McKenzie, J., Kosar, E., Schwab, M., Sunsaneewitayakul, B., Vasavakul, T., et al. (2004). A new approach for catheter ablation of atrial fibrillation: Mapping of the electrophysiologic substrate. *J. Am. Coll. Cardiol.* 43, 2044–2053. doi:10.1016/j.jacc.2003.12.054

Narayan, S. M., Krummen, D. E., Shivkumar, K., Clopton, P., Rappel, W-J., and Miller, J. (2012). Treatment of atrial fibrillation by the ablation of localized sources: CONFIRM (conventional ablation for atrial fibrillation with or without focal impulse and rotor modulation) trial. *J. Am. Coll. Cardiol.* 60, 628–636. doi:10.1016/j.jacc.2012.05.022

O'Neill, M. D., Wright, M., Knecht, S., Jaïs, P., Hocini, M., Takahashi, Y., et al. (2009). Long-term follow-up of persistent atrial fibrillation ablation using termination as a procedural endpoint. *Eur. Heart J.* 30, 1105–1112. doi:10.1093/eurheartj/ehp063

Park, Y. M., Choi, J. I., Lim, H. E., Park, S. W., and Kim, Y. H. (2012). Is pursuit of termination of atrial fibrillation during catheter ablation of great value in patients with longstanding persistent atrial fibrillation? *J. Cardiovasc. Electrophysiol.* 23, 1051–1058. doi:10.1111/j.1540-8167.2012.02370.x

Pothineni, N. V. K., Lin, A., Frankel, D. S., Supple, G. E., Garcia, F. C., Lin, D., et al. (2021). Impact of left atrial posterior wall isolation on arrhythmia outcomes in patients with atrial fibrillation undergoing repeat ablation. *Heart Rhythm O2* 2, 489–497. doi:10.1016/j.hroo.2021.07.004

Ramirez, F. D., Birnie, D. H., Nair, G. M., Szczotka, A., Redpath, C. J., Sadek, M. M., et al. (2017). Efficacy and safety of driver-guided catheter ablation for atrial fibrillation: A systematic review and meta-analysis. *J. Cardiovasc. Electrophysiol.* 28, 1371–1378. doi:10.1111/jce.13313

Rodrigo, M., Waddell, K., Magee, S., Rogers, A. J., Alhusseini, M., Hernandez-Romero, I., et al. (2021). Non-invasive spatial mapping of frequencies in atrial fibrillation: Correlation with contact mapping. *Front. Physiol.* 11, 611266. doi:10.3389/fphys.2020.611266

Rostock, T., Salukhe, T. V., Steven, D., Drewitz, I., Hoffmann, B. A., Bock, K., et al. (2011). Long-term single-and multiple-procedure outcome and predictors of success after catheter ablation for persistent atrial fibrillation. *Heart rhythm.* 8, 1391–1397. doi:10.1016/j.hrthm.2011.04.012

Sanders, P., Berenfeld, O., Hocini, M., Jais, P., Vaidyanathan, R., Hsu, L. F., et al. (2005). Spectral analysis identifies sites of high-frequency activity maintaining atrial fibrillation in humans. *Circulation* 112, 789–797. doi:10.1161/CIRCULATIONAHA.104.517011

Scherr, D., Khairy, P., Miyazaki, S., Aurillac-Lavignolle, V., Pascale, P., Wilton, S. B., et al. (2015). Five-year outcome of catheter ablation of persistent atrial fibrillation using termination of atrial fibrillation as a procedural endpoint. *Circ. Arrhythm. Electrophysiol.* 8, 18–24. doi:10.1161/CIRCEP.114.001943

Schreiber, D., Rostock, T., Fröhlich, M., Sultan, A., Servatius, H., Hoffmann, B. A., et al. (2015). Five-year follow-up after catheter ablation of persistent atrial fibrillation using the stepwise approach and prognostic factors for success. *Circ. Arrhythm. Electrophysiol.* 8, 308–317. doi:10.1161/CIRCEP.114.001672

Skanes, A. C., Mandapati, R., Berenfeld, O., Davidenko, J. M., and Jalife, J. (1998). Spatiotemporal periodicity during atrial fibrillation in the isolated sheep heart. *Circulation* 98, 1236–1248. doi:10.1161/01.cir.98.12.1236

Steinhaus, B. M. (1989). Estimating cardiac transmembrane activation and recovery times from unipolar and bipolar extracellular electrograms: A simulation study. *Circ. Res.* 64, 449–462. doi:10.1161/01.res.64.3.449

Wang, Yl, Liu, X., Zhang, Y., Jiang, Wf, Zhou, L., Qin, M., et al. (2018). Optimal endpoint for catheter ablation of longstanding persistent atrial fibrillation: A randomized clinical trial. *Pacing Clin. Electrophysiol.* 41, 172–178. doi:10.1111/pace.13221

Zhou, G., Chen, S., Chen, G., Zhang, F., Meng, W., Yan, Y., et al. (2013). Procedural arrhythmia termination and long-term single-procedure clinical outcome in patients with non-paroxysmal atrial fibrillation. *J. Cardiovasc. Electrophysiol.* 24, 1092–1100. doi:10.1111/jce.12193

Frontiers in Physiology

Understanding how an organism's components work together to maintain a healthy state

The second most-cited physiology journal, promoting a multidisciplinary approach to the physiology of living systems - from the subcellular and molecular domains to the intact organism and its interaction with the environment.

Discover the latest Research Topics

See more →

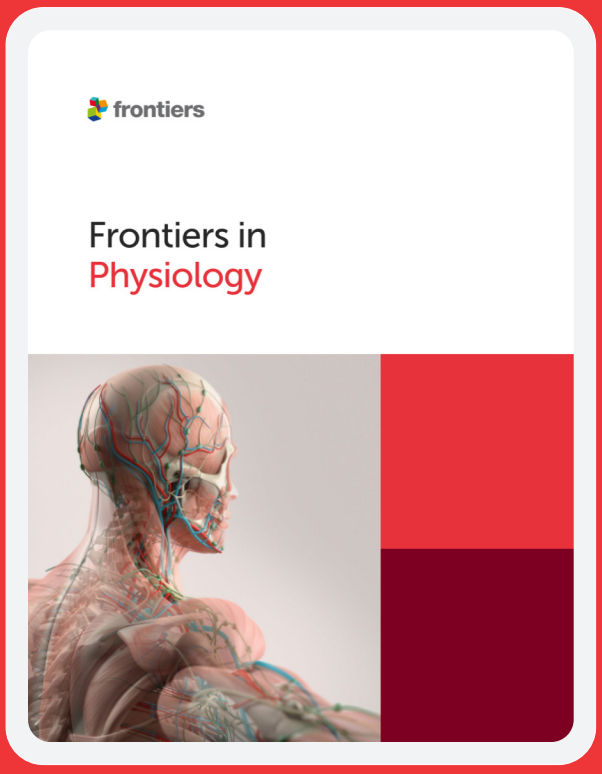

Frontiers

Avenue du Tribunal-Fédéral 34
1005 Lausanne, Switzerland
frontiersin.org

Contact us

+41 (0)21 510 17 00
frontiersin.org/about/contact